VNIVERSITAT DE VALÈNCIA

ANILATO-BASED MULTIFUNCTIONAL MOLECULAR MATERIALS

Patricia Gómez Claramunt

Tesis Doctoral

Doctorado en Nanociencia y Nanotecnología Molecular

Valencia, Enero de 2018

Directores:

Carlos J. Gómez García y Samia Benmansour Souilamas

Universitat de València

Instituto de Ciencia Molecular

D. Carlos José Gómez García, Catedrático de Química Inorgánica y **Dª. Samia Benmansour Souilamas**, Contratada Doctor del Instituto de Ciencia Molecular (ICMol) de la Universidad de Valencia,

CERTIFICAN:

Que el trabajo que presenta Dª. Patricia Gómez Claramunt en esta Memoria, bajo el título: "**Anilato-based Multifunctional Molecular Materials**" corresponde a su Tesis Doctoral y ha sido realizado bajo nuestra dirección en el Instituto de Ciencia Molecular (ICMol) de la Universidad de Valencia.

Y para que así conste, a efectos de su presentación para optar al Grado de Doctor en Nanociencia y Nanotecnología Molecular, se expide el presente documento.

Prof. Carlos José Gómez García — Director

Dra. Samia Benmansour Souilamas — Directora

Paterna (Valencia), Noviembre de 2017

A Víctor.

Por todo lo que somos.

Por todo lo que seremos.

En estas líneas, me gustaría agradecer su apoyo y colaboración a las personas que han hecho posible la realización de esta tesis doctoral acompañándome en este camino tanto profesional como personalmente.

En primer lugar, y como no podía ser de otra manera, tengo que darle las gracias a Víctor. Gracias, gracias y gracias. Por todo. Gracias por el tiempo. Por todo el apoyo, en los momentos buenos, no tan buenos, en los malos y en los peores. Gracias por estar siempre viendo la parte buena de las cosas, por hacerme creer en mí y por quererme tanto. Por no dejar que me rindiera nunca. Esta tesis es una parte tuya, porque has sido mi principal soporte durante todos estos años. No podría tener un compañero de vida mejor.

A Carlos y a Sam, por supuesto gracias también. Por enseñarme todo. Por guiar todos y cada uno de los pasos durante la tesis. Por todas las horas que habéis dedicado a este trabajo, intentando siempre hacerme mejor profesional. Muchas gracias por todo lo vivido. Siempre recordaré los años que pase en el ICMol con vosotros.

A mis padres. Todos mis estudios se los debo a ellos. Gracias por todo el esfuerzo y sacrificio. Por confirmar en mí y apoyarme en todas las decisiones que he tomado en mi vida. Gracias por toda la confianza que habéis depositado siempre en mí. Ha sido una suerte saber que podía contar con vosotros. Gracias por ser los mejores padres que se puede pedir.

A los que formáis o habéis formado parte del grupo M4, gracias por todos los momentos vividos, por las risas y por el ambiente tan bueno que habéis creado en ese laboratorio en el que pasábamos más horas que en casa. Muchas gracias por todo a todos.

A María, gracias por hacer de mi estancia una etapa que recuerde con tanto cariño. Gracias por acogerme allí y por hacerme sentir como en casa.

A Josep, por las medidas de luminiscencia y por estar siempre disponible para cada duda, para cada pregunta, para cada comentario. Que fácil y que agradable es trabajar contigo.

A Chema, a Gloria y a la gente del SCSIE, por el apoyo científico extra.

A mis amigas. Simplemente por vuestra bonita amistad. Por quererme bien. Por estar en lo bonito y en lo feo. Sois geniales.

A mis nuevos/as compañeras de trabajo. Por la piña tan increíble que hemos hecho. Por los cafés del área, por los jueves en tascas. Por hacer que no me haya sentido sola en ningún momento de estos ya varios meses. Por ser mi nueva familia. ¡Qué suerte haberos encontrado!

A los miembros del tribunal, gracias por acceder a serlo.

Sabéis que no soy una mujer con especial acierto a la hora de expresar sentimientos. Lo que digo aquí, no es comparable con lo que siento. A todos los anteriores. De verdad. Gracias por formar parte de mi vida. Gracias por hacer que esto sea posible. Gracias por hacer que cierre esta etapa con una sonrisa y que empiece una nueva con fuerza, alegría y recuerdos de momentos bonitos.

No te rindas, aun estás a tiempo
de alcanzar y comenzar de nuevo,
aceptar tus sombras, enterrar tus miedos,
liberar el lastre, retomar el vuelo.

No te rindas que la vida es eso,
continuar el viaje,
perseguir tus sueños,
destrabar el tiempo,
correr los escombros y destapar el cielo.

Mario Bennedetti

TABLE OF CONTENTS

Long summary of the thesis (in Spanish) 1

Preface 15

Introduction 18

1. Multifunctional hybrid materials 18
    1.1. Oxalato compounds: the predecessors to anilato-based compounds 19
2. Anilato-base Molecular Materials 22
    2.1. 0D anilato-based compounds 23
    2.2. 1D anilato-based compounds 26
    2.3. 2D anilato-based compounds 29
    2.4. Multifunctional materials based on the anilato ligand 39
    2.5. Anilato-based materials prepared in this thesis 40
3. References 67

Chapter 1: Monomeric building blocks of the type $A_3[M^{III}(C_6O_4X_2)_3]$

1. Introduction 99
2. Experimental Section 100
    2.1. Synthesis 100
    2.2. Physical Properties 107
    2.3. Structural Characterization 108
3. Results and Discussion 108
    3.1. Synthesis 108
    3.2. Infrared Spectroscopy 109
    3.3. X-Ray single crystal diffraction 111
        3.3.1. Discussion of the structures 117
    3.4. X-Ray Powder Diffraction 120
    3.5. Magnetic Properties 124
4. Conclusions and perspectives 127
5. References 129

Chapter 2: 2D/3D heterometallic networks with M^{III}/M^{I}

1. Introduction 131
2. Experimental Section 132
   - 2.1. Synthesis 132
   - 2.2. Physical Properties 133
   - 2.3. Structural Characterization 133
3. Results and Discussion 134
   - 3.1. Infrared Spectroscopy 134
   - 3.2. X-Ray Diffraction 136
     - 3.2.1. Discussion of the structures 141
   - 3.3. X-Ray Powder Diffraction 142
   - 3.4. Magnetic Properties 143
4. Conclusions and perspectives 145
5. References 146

Chapter 3: 2D heterometallic lattices with new template molecules

1. Introduction 149
2. Experimental Section 150
   - 2.1. Synthesis 150
   - 2.2. Physical Properties 151
   - 2.3. Structural Characterization 151
3. Results and Discussion 152
   - 3.1. X-Ray Diffraction 152
   - 3.2. X-Ray Powder Diffraction 161
   - 3.3. Magnetic Properties 163
4. Conclusions and perspectives 172
5. References 173

Chapter 4: Lanthanide compounds based on the anilato ligand

1. Introduction 177
2. Experimental Section 179
   - 2.1. Synthesis 179
   - 2.2. Structural Characterization 180
   - 2.3. Physical Properties 180
   - 2.4. Luminescent Properties 181

3. Results and Discussion 181
3.1. X-Ray Diffraction 181
3.2. X-Ray Powder Diffraction 194
3.3. Magnetic Properties 196
3.4. Luminescent Properties 197
4. Conclusions and perspectives 201
5. References 204
Chapter 5: Spin crossover compounds based on anilato ligand
1. Introduction 207
2. Experimental Section 209
2.1. Synthesis 209
2.2. Physical Properties 221
2.3. Structural Characterization 212
3. Results and Discussion 213
3.1. X-Ray Diffraction 213
3.2. X-Ray Powder Diffraction 224
3.3. Magnetic Properties 224
3.4. LIESST effect 229
4. Conclusions and perspectives 230
5. References 231
Chapter 6: Luminescent compounds based on anilato ligand
1. Introduction 235
2. Experimental Section 235
2.1. Synthesis 235
2.2. Physical Properties 237
2.3. Structural Characterization 237
2.4. Luminescent Properties 238
3. Results and Discussion 238
3.1. Infrared Spectroscopy 238
3.2. X-Ray Diffraction 242
3.3. X-Ray Powder Diffraction 252
3.4. Magnetic Properties 253
3.5. Luminescent Properties 261

4. Conclusions and perspectives 262
5. References 264
Chapter 7: Single Molecule Magnets inserted between anilato layers
1. Introduction 267
2. Experimental Section 267
2.1. Synthesis 267
2.2. Physical Properties 268
2.3. Structural Characterization 269
3. Results and Discussion 269
3.1. Infrared Spectroscopy 269
3.2. X-Ray Diffraction 272
3.3. X-Ray Powder Diffraction 278
3.4. Magnetic Properties 279
4. Conclusions and perspectives 284
5. References 285
Chapter 8: A bi-functional electrode based on anilato
1. Introduction 287
2. Experimental Section 290
2.1. Synthesis 290
2.2. Electrochemical measurements 291
3. Results and discussion 292
In-situ electro-synthesis of a new catalyst [$Fe_2(C_6O_4Cl_2)_3$] 295
4. Conclusions and perspectives 303
5. References 306
Short summary of the thesis (in English) 315
Short summary of the thesis (in Spanish) 319

Long summary of the thesis

(Spanish)

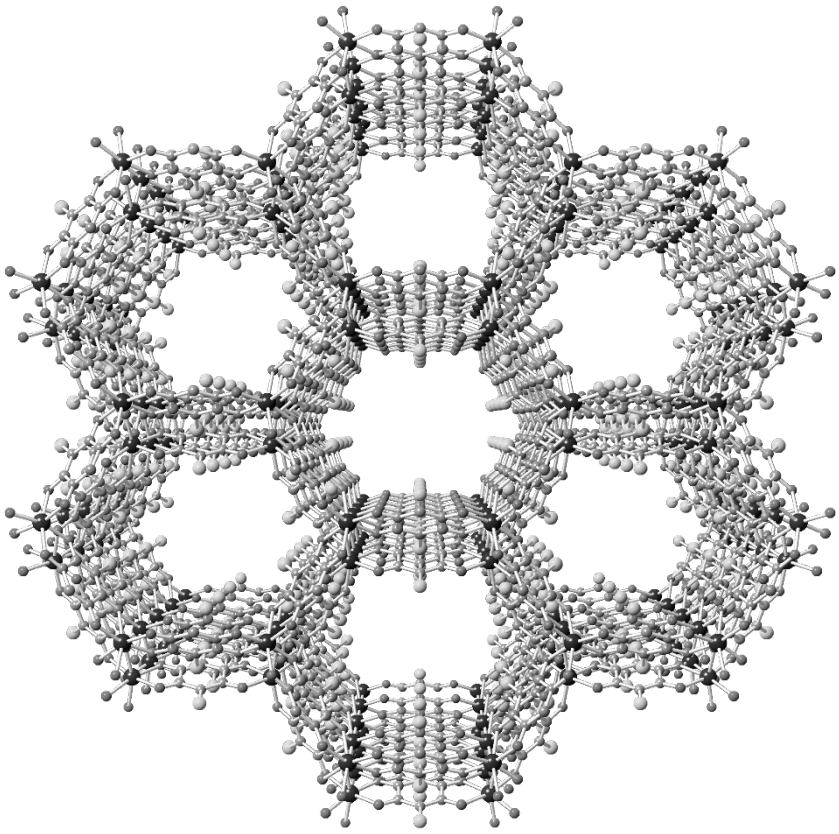

Objetivos, Metodología y Resumen de Resultados, Conclusiones y Perspectivas.

1. Objetivos.

El objetivo general de esta Tesis es la preparación de materiales moleculares multifuncionales basados en el ligando anilato ($C_6O_4X_2^{2-}$ donde X = Cl, Br, NO_2,…,) que combinen propiedades magnéticas con otras propiedades extra como pueden ser transición de espín, luminiscencia, propiedades de imán molecular,…. Otro de los objetivos, no menos importante y ambicioso, es lograr controlar, mediante la ingeniería cristalina y la correcta elección de los materiales de partida, la dimensionalidad y la estructura cristalina de nuestros compuestos.

2. Metodología.

2.1. Síntesis.

En esta Tesis los compuestos se han sintetizado mediante dos métodos de síntesis ampliamente conocidos: el conocido como el método “one pot”, que consiste en mezclar todos los compuestos de partida en un mismo vaso de precipitados para que tenga lugar la reacción y posteriormente dejar evaporar lentamente el disolvente para obtener monocristales. Aunque con este método de síntesis se han obtenido algunos monocristales válidos para medir mediante difracción de rayos X, la mayoría de los productos obtenidos por este método han sido polvos micro-cristalinos. El segundo método de síntesis que se ha usado ha sido el método de difusión lenta, en el que dos disoluciones de distinta densidad se colocan lentamente el uno sobre el otro para permitir la difusión lenta de sus compuestos a través de los disolventes. Este último método de síntesis se realiza en tubos finos y alargados, para promover que la difusión sea lo más lenta posible y así garantizar una mayor calidad en la obtención de cristales válidos para difracción de rayos X. Los inconvenientes de este método son el bajo rendimiento y los largos tiempos de cristalización en algunos casos.

2.2. Técnicas de Caracterización.

2.2.1. FT-IR.

FT-IR son las siglas de Fourier Transform Infrared. Es una técnica usada para obtener el espectro infrarrojo de un sólido, líquido o gas. El termino de transformada de Fourier se incluye en el nombre ya que este proceso matemático es necesario para convertir los datos obtenidos en el espectro. La técnica infrarrojo se divide en tres regiones: infrarrojo cercano, medio y lejano. Todos los espectros mostrados en este trabajo están realizados en la región del infrarojo medio.

Mediante esta técnica se obtienen espectros que muestran bandas a longitudes de onda específicas para ciertas vibraciones y rotaciones moleculares, por lo que se pueden asignar las bandas obtenidas en el espectro con los diferentes tipos de enlaces existentes en las moléculas del compuesto que hemos analizado.

2.2.2. Medidas Magnéticas.

Las medias magnéticas presentadas en esta Tesis se realizaron con un Magnetómetro de tipo SQUID “Quantum Desing MPMS-XL-5”. SQUID es el acrónimo ingles para “Superconducting Quantum Interference Device” cuya traducción seria “Dispositivo Superconductor de Interferencia Cuántica”. Estos susceptómetros son capaces de medir señales magnéticas muy pequeñas con muy poco ruido. Las medidas de este trabajo se realizaron en el intervalo de temperaturas entre 2 y 300 K y aplicando campos magnéticos de 0.1 ó 0.5 T sobre las muestras poli-cristalinas de los compuestos. Después de realizar las medidas, los datos de susceptibilidad se corrigen para eliminar la contribución del porta-muestras donde se mide y de las contribuciones diamagnéticas mediante las constantes de Pascal.

2.2.3. Cristalografía de Rayos X

La cristalografía de Rayos X nos permite obtener las estructuras cristalinas de los compuestos, siempre y cuando se disponga de mono-cristales que difracten los haces de rayos X. Esta técnica se basa en el principio que

supone que los rayos X son difractados por los electrones que se encuentran rodeando a los átomos de una molécula. El haz de rayos X que resulta de esta interacción y que es medido por el detector de rayos X contiene información sobre la posición y tipo de átomos encontrados en su camino. El análisis posterior por medios matemáticos permite obtener una representación a escala atómica de los átomos y con ello de las moléculas del compuesto estudiado.

En este trabajo, la difracción de rayos X se realizó a 120 K por regla general (aunque para ciertos compuestos se varió esta temperatura) con un difractómetro Supernova equipado con una fuente de rayos X de grafito monocromada (Mo). Para la resolución de estas estructuras por métodos directos se usaron los programas SIR92[1] y SHELXL-2014, utilizando la interfaz gráfica de usuario WinGX2014.1.15. Todos los átomos excepto los de hidrógeno se refinaron anisotrópicamente y los átomos de hidrógeno se colocaron en posiciones calculadas y se refinaron isotrópicamente. Los parámetros de recopilación y refinamiento de datos se muestran en cada capítulo, en las tablas de datos cristalográficos.

2.2.4. Difracción de Rayos X de polvo.

Esta técnica se ha usado para comprobar la pureza de las muestras obtenidas, es decir, para comprobar que el conjunto de la muestra presenta la misma estructura que el monocristal que se ha medido por difracción de rayos X y que no hay varias fases presentes.

Esta técnica se basa en la incidencia de la radiación de rayos X sobre una muestra localizada en un capilar de 0.5 mm de diámetro de vidrio, material amorfo y por lo tanto invisible a estos rayos X. El haz sale reflejado con un angulo θ de acuerdo con la ley de Bragg (sen $\theta = n\lambda/2d$). El detector de rayos X se mueve, variando el ángulo que forma con la muestra y registra el haz reflejado. El resultado de la intensidad en función del ángulo proporciona el difractograma de rayos X de polvo, que contiene la información sobre la estructura cristalina de la muestra. El equipo usado fue un Empyrean PANalytical difractómetro de polvo y las medidas se realizaron con un total de 3 barridos, a temperatura ambiente en el rango de 2θ de 2- 40º.

2.2.5. Microanálisis por Microscopia Electrónica de Barrido

Esta técnica se basa en el uso de electrones para formar imágenes de objetos de un tamaño muy reducido, mediante la emisión termoiónica de un haz de electrones, que bombardea la superficie de la muestra y genera señales que dan información morfológica o composicional del material analizado.

Además del uso para imágenes, este microscopio, en combinación con el sistema de microanálisis EDAX, también puede usarse para la realización de análisis químicos de elementos de número atómico Z > 11 y concentraciones superiores a 0.5 % en peso. En este trabajo, el equipo usado principalmente ha sido el Microscopio electrónico XL-30 y el S-4800 en menor medida.

3. Resultados, conclusiones y perspectivas.

En esta Tesis se presenta la síntesis y caracterización física y estructural de diferentes materiales multifuncionales basados en el ligando anilato. La memoria se divide en ocho capítulos: en los primeros siete capítulos se presentarán diferentes familias de materiales basado en el ligando anilato. Este estudio va un paso más allá en el campo de los materiales basados en anilato, dado que este campo estaba completamente inexplorado, exceptuando unos pocos trabajos.[2, 3] Este trabajo ha sido motivado por el amplio impacto de los materiales basados en el ligando oxalato en el campo de los materiales moleculares. La capacidad del ligando anilato para modular las propiedades del material final, que no posee el oxalato al no poderse funcionalizar químicamente, constituye un valor añadido de este ligando y lo hace un excelente candidato para sintetizar nuevos materiales multifuncionales.

En el **primer capítulo** se presenta la síntesis y la caracterización de una gran familia de complejos monoméricos de tris(anilato)metalato con fórmula $A_3[M^{III}(C_6O_4X_2)_3]$ preparados con diferentes ligandos anilato (X = Cl, Br y NO_2), diferentes iones metálicos trivalentes (M(III) = Cr, Fe y Ga) y diferentes cationes (A = PPh_3Et^+, PPh_3Pr^+, PBu_4^+, $Nhep_4^+$, PPh_4^+, K^+ y NBu_4^+). En concreto hemos preparado, de manera racional, la serie de compuestos de fórmula: $A_3[M^{III}(C_6O_4X_2)_3]$ donde A/M/X = PPh_3Et/Cr/Cl (**1**), PPh_3Et/Cr/Br (**2**), PPh_3Et/Ga/Br (**3**), PPh_3Et/Fe/NO_2 (**4**), PPh_3Pr/Cr/Cl (**5**), PPh_3Pr/Cr/Br (**6**),

$PPh_3Pr/Fe/NO_2$ (**7**), $PBu_4/Cr/NO_2$ (**8**), $PBu_4/Fe/NO_2$ (**9**), $Nhep_4/Cr/Cl$ (**10**), $Nhep_4/Cr/Br$ (**11**), $PPh_4/Fe/NO_2$ (**12**), K/Cr/Cl (**13**), K/Fe/Cl (**14**), K/Cr/CBr (**15**), K/Fe/Br (**16**), $NBu_4/Cr/Cl$ (**17**), $NBu_4/Fe/Cl$ (**18**), $NBu_4/Cr/Br$ (**19**) y $NBu_4/Fe/Br$ (**20**). Además de la síntesis racional, se ha realizado un estudio detallado sobre el papel clave de cationes considerados inocentes normalmente pero que en esta serie no lo son. La mayoría de los compuestos presentados en este capítulo ya han sido publicados.[4]

Hemos sintetizado hasta 20 nuevos compuestos de fórmula general $A_3[M(C_6O_4X_2)_3]$ siguiendo una reacción de un solo paso entre la sal de del metal M(III) (M(III) = Cr, Fe y Ga) y tres ligandos anilato con diferentes sustituyentes $[C_6O_4X_2]^{2-}$ (X = Cl, Br y NO_2). Hemos usado distintos cationes A^+ ($A = K^+$, $[PPh_3Et]^+$, $[PPh_3Pr]^+$, $[PBu_4]^+$, $[NBu_4]^+$, $[NHep_4]^+$ y $[PPh_4]^+$) para estudiar cómo las diferencias en la forma y en el tamaño afecta a la estructuras final de las correspondientes sales. Hemos demostrado el papel fundamental que juega el catión. Así, los compuestos que contienen el catión $[PPh_3Et]^+$, cristalizan en la fase I, en el grupo espacial quiral R3; Los compuestos de la fase II, que contienen el catión $[PPh_3Pr]^+$, cristalizan en el grupo espacial polar no quiral *P*2*cb* y, finalmente los compuestos de la fase III, que contienen el ligando no plano $[C_6O_4(NO_2)_2]^{2-}$ y un cation sin anillos aromáticos, cristalizan en el grupo espacial centrosimétrico, pero no polar ni quiral, *P*-1. Esta evolución de quiral y polar (fase I) a no quiral y polar (fase II) a centrosimétrica (fase III) se debe a la reducción de las interacciones π–π, que pasan de seis (fase I) a cuatro (fase II) a finalmente ninguna (fase III). Este ausencia de interacciones π-π es de esperar también para el resto de fases con cationes no aromáticos cuyas estructuras no hemos podido resolver dada la elevada dificultad de obtener monocristales de todas estas sales. Hemos observado que este papel clave de las interacciones π–π y depende fundamentalmente de la naturaleza del catión (excepto en el caso en que X = NO_2, ya que la falta de planaridad también juega un papel importante en la geometría final ya que impide la formación de interacciones π-π).

La cristalización de compuestos de la fase quiral I es un hecho inesperado y sin precedentes en los complejos de tris(anilato)metalato, y se ha atribuido a

la presencia de seis interacciones π–π, que se establecen entre el anillo aromático del ligando anilato del anión y los anillos fenilos del catión. Por el contrario, el uso de otros cationes voluminosos o el cambio del sustituyente X de Cl y Br a NO_2, da lugar a compuestos no quirales donde el número de interacciones π–π se reduce a cero debido a la falta de planaridad mencionada anteriormente. Aunque no se ha obtenido información estructural de ninguna sal con X = NO_2 y cationes con anillos aromáticos, es previsible la formación de cristales no quirales debido a la distorsión de los grupos nitro.

A pesar de que el importante papel que pueden jugar las interacciones π–π catión-anión en la estructura final ya era conocido, los compuestos que se presentan aquí muestran la capacidad de estas interacciones para formar cristales quirales y no quirales, aun cuando se parte de una mezcla racémica de cationes y aniones. Se ha usado esta serie de compuestos como precursores para la síntesis de diferentes familias de redes heterometálicas extendidas con ordenamiento magnéticos y otras propiedades interesantes, los cuales se presentaran en los siguientes capítulos.

Es bien sabido que el tamaño y la estructura del cation también afecta a la solubilidad de la sal resultante. Es por ello que decidimos preparar la serie de compuestos de fórmula $K_3[M^{III}(C_6O_4X_2)_3]$, las únicas sales de tris(anilato)metalato solubles en agua. Esta solubilidad puede ser usada para preparar las correspondientes sales de Ag^+ mediante una reacción de metátesis con $Ag(NO_3)$, una estrategia muy utilizada para preparar imanes multifuncionales 2D con el ligando oxalato.[5, 6]

En el **segundo capítulo** se presenta la síntesis y caracterización de redes anilato 2D y 3D con iones metálicos M(III)M(I). Se presenta también un ejemplo de polimorfismo 2D-3D sin precedentes en la química de coordinación del ligando anilato con los dos compuestos de fórmula $(NBu_3Me)_2[NaCr(C_6O_4Br_2)_3]$: uno de ellos presentan una estructura 2D tipo panal de abeja (compuesto **21**) y el otro polimorfo una estructura 3D quiral de tipo (10,3) (compuesto **22**), ambas obtenidas en la misma síntesis. Los compuestos presentados en este capítulo ya han sido publicados.[7] Este fenómeno de polimorfismo nunca había sido observado en la química del anilato ni en la del oxalato.

Estas estructuras muestran por primera vez la capacidad de los ligandos de tipo anilato para actuar como ligandos bis-bidentados, no sólo con parejas de metales M(II)M(II) y M(II)M(III), sino también con metales M(I)M(III), tal y como ya había sido observado en el ligandos oxalato. Esta capacidad debería de llevar hacia la síntesis de redes M(III)/M(II) 3D-(10-3) con ordenamiento magnético, que tras los resultados mostrados en este capítulo, es el único reto que queda por alcanzar en la analogía con el oxalato.[8]

Los estudios para tratar de encontrar una forma racional para obtener estas redes 3D M(III)/M(II), están actualmente en desarrollo. En los siguientes capítulos se mostrará un segundo avance en la serie de redes 2D, la inserción de cationes funcionales con una segunda propiedad interesante.

En el **tercer capítulo** se presenta la síntesis y caracterización de cinco compuestos basados en capas 2D tipo panal de abeja que contienen un metal trivalente (Cr^{III}) y uno divalente (Mn^{II}) con H_3O^+ o con NBu_4^+ como cation. Estos compuestos puede ser formulados como $(H_3O)[MnCr(C_6O_4X_2)_3]\cdot 2PhZ\cdot 6H_2O$ con X/Z = Cl/Cl (**23**), Br/Cl (**24**), Br/Br (**25**), Br/CH_3 (**26**) o bien como $(NBu_4)[MnCr(C_6O_4Br_2)_3]\cdot PhBr\cdot 5H_2O$ (**27**). En estos imanes 2D la inclusión de diferentes derivados del benceno favorece la disposición eclipsada de las capas, dando lugar a canales hexagonales ocupados por moléculas de disolvente, lo que da lugar a imanes porosos.

Esta estrategia ha permitido la síntesis de capas eclipsadas incluso con el catión NBu_4^+ (compuesto **27**), mejorando los resultados publicados en 2013,[2] donde las capas 2D hexagonales con el catión NBu_4^+ tienen una disposición alternada, lo que evita la formación de canales hexagonales. La formación de estos canales hexagonales puede posibilitar la absorción de moléculas gaseosas o de disolventes. En este capítulo proponemos el uso de diferentes derivados bencénicos para actuar como moléculas plantilla con el fin de obtener estructuras con disposición eclipsada de las capas y por lo tanto canales hexagonales y estructuras porosas. Además, mostramos el efecto de dichas moléculas plantillas derivadas del benceno en las propiedades magnéticas de estos imanes 2D posoros.

Los compuestos **23** y **27** presentan un ordenamiento ferrimagnético debido a un acoplamiento antiferrimagnético de los iones Cr(III) y Mn(II) a través de ligando anilato. Por el contrario, los compuestos **24**-**26**, presentan un comportamiento meta-magnético. Este comporatmiento se debe al hecho de que, aunque el acoplamiento Cr(III)-Mn(II) es antiferromagnético y debería dar lugar a un ordenamiento ferrimagnético (al igual que ocurre en los compuestos **23** y **27**), la presencia de un acoplamiento antiferromagnético débil entre las capas evita la aparición de dicho ordenamiento ferrimagnético. Este acoplamiento antiferromagnético débil sólo se puede cancelar con campos magnéticos por encima de aproximadamente 200 mT en las tres muestras, que es el campo crítico en las tres muestras. Este comportamiento es totalmente original en las capas magnéticas con anilato y sólo se observa en los tres compuestos (**24**-**26**) que poseen capas muy cercanas y además presentan ligandos bromanilato cuyos átomos de Br establecen enlaces de halógeno entre las capas. El compuesto **23** tiene el ligando cloranilato y el enlece de halógeno entre las capas es más débil. El compuesto **27** tiene cationes NBu_4^+ voluminosos entre la capas, lo que imposibilita la formación de interacciones entre capas.

En este campo el trabajo futuro se centrará en la síntesis de compuestos similares cambiando los grupos X y Z, para estudiar el papel de éstos grupos en las propiedades magnéticas de estos imanes porosos con el fin de poder modificar dichas propiedades. En el caso de los compuestos con el catión oxonio se estudiará la posibilidad de eliminar las moléculas de agua de los canales para comprobar la capacidad de estos materiales de albergar, de forma reversible, moléculas de gas o de otros disolventes, y por último, pero no menos importante, se estudiará si éstos huéspedes cambian las propiedades magnéticas de estos imanes porosos.

En el **cuarto capítulo** se presenta la familia de compuestos obtenidos con el ligando de tipo anilato asimétrico 2-cloro-5-ciano-3,6-dihidroxibenzoquinona e iones lantanoides con diferentes disolventes coordinantes. Dos de estos compuestos: $[Pr_2(C_6O_4(CN)Cl)_3(DMF)_6]$ (**28**) y $[Pr_2(C_6O_4(CN)Cl)_3(DMSO)_6]$ (**29**) contienen el ion Pr(III) y muestran estructuras bidimensionales con DMF o DMSO como disolventes coordinados. El tercer compuesto, de fórmula

$[Yb_2(C_6O_4(CN)Cl)_3(DMSO)_4]\cdot 2H_2O$ (**30**) tiene Yb(III) y, dado su menor tamaño, presenta un índice de coordinación menor, lo que da lugar a una estructura 2D menos distorsionada que la de los compuestos **28** y **29**. El cuarto compuesto: $[(H_3O)K][Yb_2(C_6O_4(CN)Cl)_3(\mu\text{-}OH)_2]$. (**31**) además de Yb(III) contiene K^+ y parejas de iones Yb(III) conectados por dobles puentes hidróxido que se encuentran conectados a otros dímeros por puentes anilato en una red 3D nunca observada en la química de los ligandos de tipo anilato ni en los oxalatos.

Como el ligando 2-cloro-5-ciano-3,6-dihidroxibenzoquinona es luminiscente, hemos realizado medidas de luminiscencia de los compuestos **28**-**30** para verificar el posible efecto antena de este ligando con los iones lantanoides. Estas medidas muestran una emisión intensa a aproximadamente 980 nm que corresponde a los iones Yb(III) en el compuesto **30** junto a una banda de emisión ancha localizada entre 600 y 800 nm. Esta banda es más intensa en el compuesto **28**. El análisis de estas bandas ha permitido una propuesta de diagrama de transferencia energética entre los niveles energéticos presentes en cada compuesto.

Como trabajo futuro en este campo, queremos extender esta serie de compuestos a todos los iones lantanoides y combinarlos con otros disolventes, para estudiar a fondo la capacidad de bloqueo de los diferentes disolventes con los diferentes iones lantanoides y así poder encontrar las mejores condiciones para obtener luminiscencia y preparar sensores luminiscentes para distintos disolventes.

En el **quinto capítulo** se presentan tres compuestos que combinan el ligando anilato con cationes que presentan una funcionalidad extra, como la transición de espín. Hemos usado el catión de transición de espín $[Fe(bpp)_2]^{2+}$ para preparar los compuestos $[NBu_4][Fe(3\text{-}bpp)_2][Cr(C_6O_4X_2)_3].H_2O$ con X = Cl (**32**) y Br(**33**) y $[Fe(3\text{-}bpp)_2]_3[Cr(C_6O_4Cl_2)_3]_2\cdot 6H_2O$ (**34**). Los compuestos **32** y **33** contienen una molécula de H_2O unida mediante enlace de hidrógeno al ligando bpp que juega un papel fundamental en las propiedades de transición de espín en los dos compuestos: tanto en la temperatura de transición de espín T_{SCO} como en la presencia/ausencia de histéresis durante el proceso de transición

de espín. En ambos casos, la eliminación de la molécula de agua incrementa la temperatura de transición de espín y da lugar a una pequeña histéresis de 6 K en la transición de espín del compuesto **33**. Además origina una transición de fase en las muestras deshidratadas, que pasan a tener dos centros de Fe(II) independientes: uno que muestra una transición de espín abrupta y otro que permanece en alto espín en todo el intervalo de temperaturas. También se ha demostrado que esta eliminación de agua (y por lo tanto el cambio de fase que genera) es un proceso reversible mediante inmersión del cristal en agua durante 48 horas. Curiosamente, las muestras rehidratadas recuperan la molécula de agua original y una adicional más. La molécula de agua que se recupera y que ya estaba presente inicialmente, se encuentra unida mediante un enlace de hidrógeno moderado a un ligando bpp, mientras que la segunda molécula de agua está unida mediante un enlace de hidrógeno débil. Esta segunda molécula de agua puede entrar en la estructura debido a que hay un espacio vacío de 224 $Å^3$.

El tercer compuesto de este capítulo: $[Fe(3\text{-bpp})_2]_3[Cr(C_6O_4Cl_2)_3]_2 \cdot 6H_2O$ (**34**) es un ejemplo interesante ya que tiene el mismo catión de transición de espín $[Fe(3\text{-bpp})_2]^{2+}$ que los compuestos **32** y **33**, y el mismo anión $[Cr(C_6O_4X_2)_3]^{3-}$, pero con una estequiometria diferente y sin catión NBu_4^+. Además, el compuesto **34** no tiene agua unida mediante enlaces de hidrógeno al ligando bpp del catión. Este hecho provoca un cambio brusco en las propiedades magnéticas ya que el compuesto **34** no muestra ninguna transición de espín. Este compuesto ilustra el papel clave que tienen las interacciones anión-catión y disolvente-catión en el fenómeno de la transición de espín.

Como perspectivas de futuro, se planea estudiar si la segunda molécula de agua que entra en los compuestos **32** y **33** podría entrar antes del proceso de deshidratación y estudiar si otros disolventes como el metanol, etanol o acetonitrilo pueden entrar en su estructura usando la misma estrategia de inmersión del cristal en el disolvente deseado, ya que es de esperar que éstas moléculas cambien drásticamente las propiedades de la transición de espín, lo que permitirá preparar sensores para estos disolventes.

En el **sexto capítulo** se presentan dos familias de compuestos basadas en el ligando anilato con el catión luminiscente $[Ir(ppy)_2(bpy)]^+$ (ppy = fenilpiridina y bpy = bipiridina). La primera familia contiene dos compuestos monoméricos: $[Ir(ppy)_2(bpy)]_2[(H_3O)[Cr(C_6O_4X_2)_3]\cdot H_2O$ con X = Cl **(35)** y Br **(36)** donde los aniones paramagnéticos $[Cr(C_6O_4X_2)_3]^{3-}$ aislados coexisten con cationes aislados $[Ir(ppy)_2(bpy)]^+$ formando compuestos paramagnéticos y que presentan la luminiscencia del catión $[Ir(ppy)_2(bpy)]^+$. Esta luminiscencia se caracteriza por una banda lo suficientemente ancha como para emitir luz blanca y con un máximo a unos 575 nm aproximadamente. Para este tipo de sistemas que contienen ligando neutros quelantes, como el $[Ir(ppy)_2(bpy)]^+$, hay dos posibles vías por las que se produce la luminsicencia. Uno de ellos es el conocido como “transferencia de carga metal-ligando” (^{3}MLCT) y la otra “transición de carga del ligando” (LC, $^3\pi-\pi^*$). Estas dos transiciones tienen energías similares, por lo que es difícil saber cuál de las dos está teniendo lugar.[9, 10]

La segunda familia está compuesta por seis compuestos basados en el ligando anilato que forman redes 2D de tipo panal de abeja con el catión luminiscente $[Ir(ppy)_2(bpy)]^+$ y que combinan Cr(III) y Mn(II). Estos compuestos se pueden formular como $[Ir(bpy)(ppy)_2][MnCr(C_6O_4X_2)_3]\cdot 2PhZ\cdot 2CH_3CN\cdot H_2O$ con X/G = Cl/PhF (**37**), Cl/PhCl (**38**), Cl/PhBr (**39**), Br/PhF (**40**), Br/PhCl (**41**) y Br/PhBr (**41**), donde los cationes $[Ir(ppy)_2(bpy)]^+$ se sitúan entre las capas aniónicas tipo panal de abeja. La estructura tipo panal de abeja de estos seis compuestos presenta, no obstante, una secuencia sin precedentes hasta la fecha: dos capas aniónicas de tipo $[MnCr(C_6O_4X_2)_3]^-$ por cada capa catiónica con los cationes $[Ir(ppy)_2(bpy)]^+$. El acoplamiento ferri-magnético de los iones Cr(III) y Mn(II) a través del ligando anilato da lugar al esperado ordenamiento ferrimagnético a aproximadamente 10 K para los tres compuestos con X = Cl y a unos 11.5 K para los tres compuestos con X = Br. Estas diferencias en la temperatura de orden (T_c) se explican por el efecto inductivo de los halógenos sobre el anillo aromático del ligando anilato. Por el contrario, el cambio de la molécula de halobenceno localizado en las cavidades hexagonales apenas afecta a la densidad electrónica en el ligando anilato y por lo tanto, no produce variaciones significativas en la T_c.

No se ha encontrado una luminiscencia significativa en estos compuestos. El espectro de emisión de los cuatro compuestos medidos (**38**, **40**, **41** y **42**) es muy débil en todos los casos, lo que sugiere que las capas anionicas de tipo $[MnCr(C_6O_4X_2)_3]^-$ bloquean la emisión del catión.

Como perspectivas de futuro, se plantea insertar otras especies luminiscentes entre las capas de anilato. En particular, resultarían interesantes otros derivados del $[Ir(ppy)_2(bpy)]^+$ que presentan diferentes espectro de emisión.[11-13] Además, se planea insertar el complejo neutro $[Ir(ppy)_3]$[14] entre capas neutras de anilato de tipo $[M^{III}M^{III}(C_6O_4X_2)_3]$ (M^{III} = Fe, Cr, Al, Ln; X = Cl, Br), usando derivados bencénicos como plantilla.

En el **séptimo capítulo**, se presentan cuatro compuestos en los que se ha insertado dos imanes mono-moleculares (SMM) entre las redes 2D de tipo panal de abeja basadas en ligandos de tipo anilato. Así, se han preparado los ferrimanes 2D de fórmula $[Mn(salpn)(H_2O)][CrMn(C_6O_4X_2)_3]$ con X = Cl (**43**) y Br (**44**) y $[Mn(salen)(H_2O)][CrMn(C_6O_4X_2)_3]$ con X = Cl (**45**) y Br (**46**). Aunque sólo se ha podido resolver la estructura de los compuestos que contienen el catión $[Mn(salpn)(H_2O)]^+$ (compuestos **4**3 y **44**), la presencia del catión $[Mn(salen)(H_2O)]^+$ entre las capas de anilato en los compuestos **45** y **46** se ha podido demostrar mediante otras técnicas. En este capítulo se detalla la caracterización estructural y magnética de los cuatro compuestos. Estos presentan un ordenamiento ferrimagnético con temperaturas de ordenamiento de 11.7 (**43**), 11.6 (**44**), 10.3 (**45**), y 11.5 K (**46**) y campos coercitivos 92 (**43**), 100 (**44**), 40 (**45**) y 22 mT (**46**) a 2 K. La falta de señal atribuible a los cationes SMM sugiere que los cationes no se encuentran aislados en la estructura de estos compuestos, sino interaccionando con las capas ferrimagnéticas. La presencia de una interacción π-π entre los anillos de anilato y los anillos aromáticos del ligando salpn del catión SMM en los compuestos **43** y **44** determina una posible vía para dicha interacción catión-anión.

Por último, en el **octavo capítulo** se presenta la preparación de un electrodo bifuncional de anilato (**47**) que funciona como batería de cationes alcalinos Na^+ y K^+, y además también es un catalizador para la producción de hidrógeno (reacción HER = hydrogen evolving reaction). Para explicar esta

bifuncionalidad, se propone el siguiente mecanismo: cuando los bloques de partida (Na^+ o K^+ y $[Fe^{III}(C_6O_4Cl_2)]^{3-}$) se encuentran en disolución y se aplica un potencial de 0 V durante 10 minutos se produce la reducción de los centros de Fe(III) a Fe(II). Esta reducción da lugar a la electrodeposición de un sólido con una estructura 2D de tipo panal de abeja con canales hexagonales como los ya vistos en otros muchos ejemplos de redes $[M^{II}_2(C_6O_4X_2)_3]^{2-}$. Para compensar la carga -2 de la red, los iones Na^+ o K^+ penetran en la estructura y se localizan en los canales hexagonales. Por lo tanto, se eletro-depositan compuestos del tipo $Na_2[Fe^{II}(C_6O_4Cl_2)]$ o $K_2[Fe^{II}(C_6O_4Cl_2)]$. Al ciclar el potencial, cuando se alcanza el voltaje adecuado, los centros de Fe(II) se oxidan a Fe(III) y los iones alcalinos son expulsados de los canales hexagonales para compensar esta oxidación. Este mecanismo propuesto explicaría los picos estrechos que aparecen cerca del voltaje característico del par redox Fe(III)/Fe(II). La rapidez con la que se produce la electrodeposición inicial al reducir los centros de Fe(III) a Fe(II) hace que la estructura de tipo panal de abeja tenga numerosos defectos y posiciones vacantes, por lo que algunos iones Fe(II) no se coordinan a tres ligandos anilato. Esto explica por qué el proceso de intercalación aumenta con el número de ciclos hasta que se observa saturación tras aproximadamente 60 ciclos. A partir de ese momento la intercalación empieza a disminuir posiblemente debido al hecho de que no todos los iones alcalinos que penetran en la red pueden abandonarla posteriormente, lo que dificulta la intercalación de más iones. A partir de ese momento, la compensación de carga se realiza mediante iones H_3O^+ que se colocan en las posiciones vacantes de los centros de Fe no hexa-coordinados, lo que cataliza su reducción a H_2, mejorando así el proceso HER. Estos dos procesos, la intercalación de iones y el HER son antagonistas pero también fuertemente dependientes uno del otro: solo cuando la intercalación alcanza el punto de saturación, se observa entonces el proceso HER. Esto sugiere que estos dos procesos no ocurren mediante el mismo mecanismo, independientemente de esto, el hecho de que la reacción HER evoluciona hacia potenciales más elevados (es decir, requiere potenciales menos reductores), sugiere que el electrodo **47** podría ser un buen catalizador para la formación de hidrógeno.

Otros posibles mecanismos incluyen: (i) la intercalación de los iones alcalinos entre las capas, en lugar de en los canales hexagonales o (ii) la unión de los iones alcalinos a los dos átomos de oxígeno terminales del ligando anilato del anión $[Fe(C_6O_4Cl_2)_3]^{3-}$. Este tercer mecanismo es el propuesto en la mayoría de baterías basadas en quinonas.[15-18] La determinación del mecanismo correcto requiere de un estudio electroquímico y estructural más detallado, que se esta llevando a cabo actualmente.

Las medidas realizadas en una disolución ácida (pH = 2) de KCl muestra una mejora progresiva del proceso HER, con una notable estabilidad. No obstante, estos resultados requieren un estudio mucho más riguroso y meticuloso, ya que el proceso HER también podría ser debido al carbón depositado en el GCE (Glassy Carbon Electrode).[19] Para caracterizar el material electrodepositado se llevarán a cabo experimentos con distintos electrodos para poder aislar los compuestos electrodepositados y poder realizar su caracterización estructural y magnética.

Como conclusión final de este capítulo, en línea con el objetivo principal de esta Tesis: la síntesis y caracterización de compuestos multifuncionales, basado en ligandos de tipo anilato, podemos afirmar que estos estudios preliminares muestran un compuesto bifuncional capaz de almacenar carga y electrocatalizar la formación de H_2.

Introduction

&

Preface

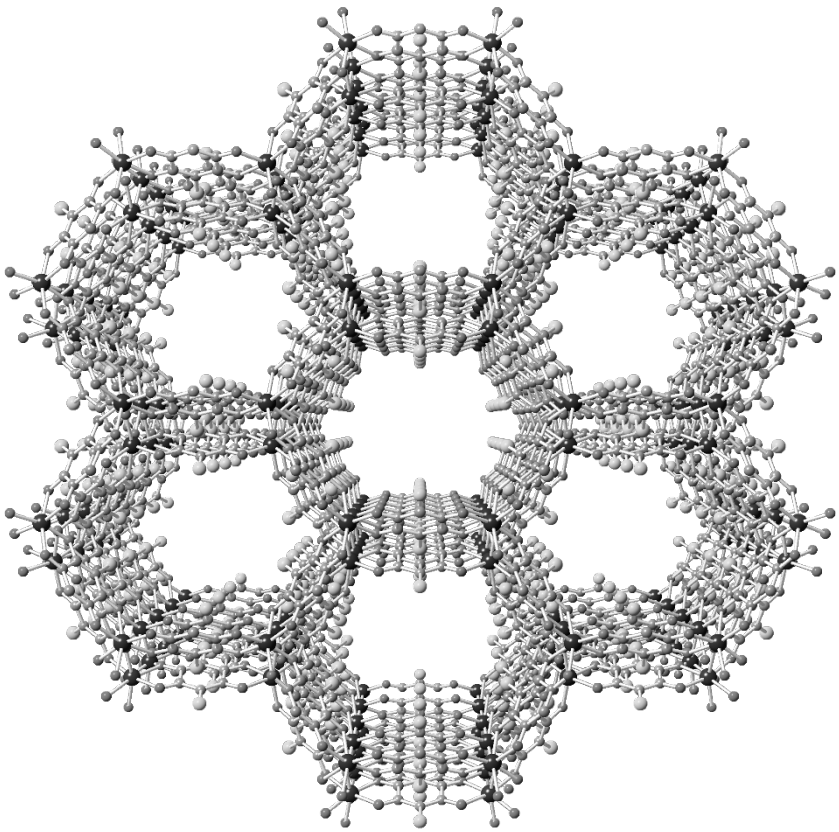

Preface

In this memory we will present the synthesis, structural and physical characterization of different anilato-based multifunctional molecular materials. The work will be divided in eight chapters: in the first seven chapters, different families of anilato-based materials will be presented. This study is a step further for the anilato-based materials, since the field of multifunctional anilato layers was completely unexplored, except for two exceptions.[1, 2] This work was motivated by the wide impact that oxalate-based multifunctional compounds had on the molecular materials field. The capacity to be modulated of the anilato-based ligands (absent in oxalato) constitutes an extra added value of the anilato ligands and makes them very good candidates for the synthesis of new multifunctional materials.

In **chapter one,** we present the synthesis and characterization of a large family of monomeric tris(anilato)metallate complexes formulated as $A_3[M^{III}(C_6O_4X_2)_3]$ prepared with different anilato ligands (X = Cl, Br and NO_2), different trivalent metal ions (M(III) = Cr, Fe and Ga) and different cations (A = PPh_3Et^+, PPh_3Pr^+, PBu_4^+, $Nhep_4^+$, PPh_4^+, K^+ and NBu_4^+). Thus, we have prepared in a rational way the following series of compounds formulated as $A_3[M^{III}(C_6O_4X_2)_3]$ with A/M/X = PPh_3Et/Cr/Cl (**1**), PPh_3Et/Cr/Br (**2**), PPh_3Et/Ga/Br (**3**), PPh_3Et/Fe/NO_2 (**4**), PPh_3Pr/Cr/Cl (**5**), PPh_3Pr/Cr/Br (**6**), PPh_3Pr/Fe/NO_2 (**7**), PBu_4/Cr/NO_2 (**8**), PBu_4/Fe/NO_2 (**9**), $Nhep_4$/Cr/Cl (**10**), $Nhep_4$/Cr/Br (**11**), PPh_4/Fe/NO_2 (**12**), K/Cr/Cl (**13**), K/Fe/Cl (**14**), K/Cr/CBr (**15**), K/Fe/Br (**16**), NBu_4/Cr/Cl (**17**), NBu_4/Fe/Cl (**18**), NBu_4/Cr/Br (**19**) and NBu_4/Fe/Br (**20**). A part from the rational synthesis, a comprehensive study about the key role of the, until now, innocent cations, is also discussed. Most of the compounds presented in this chapter have already been published.[3]

In **chapter two,** we present the synthesis and characterization of 2D and 3D anilato-based lattices with alternating M(III)M(I) metal ions. We present an unprecedented example of 2D-3D polymorphism in the anilato chemistry in two compounds formulated as $(NBu_3Me)_2[NaCr(C_6O_4Br_2)_3]$ that present a 2D honeycomb lattice (compound **21**) and a 3D chiral (10,3)-lattice (compound **22**), both obtained in the same synthesis. The compounds presented in this chapter have already been published.[4] This polymorphism phenomenon had never been observed in anilato and oxalato chemistry.

In **chapter three,** we report the synthesis and characterization of up to five 2D honeycomb layers containing a trivalent metal (Cr^{III}) and a divalent metal (Mn^{II}) with H_3O^+ formulated as $(H_3O)[MnCr(C_6O_4X_2)_3]\cdot 2PhZ\cdot 6H_2O$ with X/Z = Cl/Cl (**23**), Br/Cl (**24**), Br/Br (**25**), Br/CH_3 (**26**) and $(NBu_4)[MnCr(C_6O_4Br_2)_3]\cdot PhBr\cdot 5H_2O$ (**27**). Although these cations do not provide an extra functionality to these 2D ferrimagnets and metamagnets, the inclusion of different benzene derivative solvent molecules favours the eclipsed disposition of the layers, giving rise to hexagonal channels that contain the solvent molecules and originate porous magnets. This strategy has allowed the synthesis of eclipsed layers even with NBu_4^+ (compound **27**) improving the results published in 2013,[1] where the 2D hexagonal layers with $[NBu_4]^+$ were alternated, avoiding the formation of hexagonal channels. The formation of these hexagonal channels may enable the absorption of solvent or gas molecules. In this chapter, we propose the use of different benzene substituents to act as template molecules to achieve the eclipsed disposition. The template effect of these molecules and the importance of the porous magnets in the coordination chemistry field will be discussed in this chapter. Futhermore, we will show the key role played by the benzene derivative molecule in the magnetic properties of these 2D ferrimagnets or metamagnets.

In **chapter four**, we present four lanthanoid-containing luminescent anilato-based layered compounds formed with the heterosubstituted cyanochloroanilato ligand and Pr(III) or Yb(III): $[Pr_2(C_6O_4(CN)Cl)_3(DMF)_3]$ (**28**), $[Pr_2(C_6O_4(CN)Cl)_3(DMSO)_6]$ (**29**), $[Yb_2(C_6O_4(CN)Cl)_3(DMSO)_4]\cdot 2H_2O$ (**30**) and $[(H_3O)K][Yb_2(C_6O_4(CN)Cl)_3(\mu\text{-}OH)_2]$ (**31**). Since lanthanoid ions also present luminescent properties, the viability as antenna of this hetero-substituted ligand will be deeply studied. Furthermore, the structural impact of the added solvent is also studied. The luminescent properties and mechanism of the lanthanoid compound will be discussed.

In **chapter five,** we present three compounds prepared with the spin crossover (SCO) cation $[Fe(3\text{-}bpp)_2]^{2+}$ and two different monomeric tris(anilato)cromate complexes: $[NBu_4][Fe(3\text{-}bpp)_2][Cr(C_6O_4X_2)_3].H_2O$ with X = Cl (**32**) and Br (**33**) and $[Fe(3\text{-}bpp)_2]_3[Cr(C_6O_4Cl_2)_3]_2\cdot 6H_2O$ (**34**). Both compounds **32** and **33** present SCO and show the important role that may play a crystallization water molecule in determining the temperature of the transition and the presence/absence of hysteresis. Finally we

will show the presence of a reversible phase transition associated to the reversible loss of the crystallization water molecule in two of these compounds.

In **chapter six,** we present two different families of anilato-based compounds with the luminescent iridium-containing cation $[Ir(ppy)_2(bpy)]^+$. In the first series monomeric tris(anilato)cromate anions are combined with $[Ir(ppy)_2(bpy)]^+$ in comopunds $[Ir(ppy)_2(bpy)]_2[(H_3O)[Cr(C_6O_4X_2)_3]\cdot H_2O$ with X = Cl **(35)** and Br **(36)**. The second family consist of 2D honeycomb layers with the same iridium based luminescent cation inserted in between the layers formulated as $[Ir(bpy)(ppy)_2][MnCr(C_6O_4X_2)_3]\cdot 2G\cdot 2CH_3CN\cdot H_2O$ with X/G = Cl/PhF (**37**), Cl/PhCl (**38**), Cl/PhBr (**39**), Br/PhF (**40**), Br/PhCl (**41**) and Br/PhBr (**42**). These 2D layers show an unprecedented structure with two consecutive anionic layers. The structural, magnetic and luminescent properties of these two families will be presented.

In **chapter seven**, two different single molecule magnets (SMM) cations were inserted in between 2D anilato-based layers to obtain the series of 2D ferrimagnets formulated as $[Mn(salpn)(H_2O)][CrMn(C_6O_4X_2)_3]$ with X = Cl (**43**) and Br (**44**) and $[Mn(salen)(H_2O)][CrMn(C_6O_4X_2)_3]$ with X = Cl (**45**) and Br (**46**). Unfortunately, only the structure of the compounds containing the $[Mn(salpn)(H_2O)]^+$ cation could be solved, but the presence of the $[Mn(salen)(H_2O)]^+$ cation into the anilato-layers in compounds **45** and **46** was proved with other techniques. Structural and a detailed magnetic characterization of these four compounds will be described in this chapter.

In the last chapter, **chapter eight**, a bifunctional anilato-based electrode will be presented and the proposed mechanism will be discussed. This electrode seems to be a good charge storage for Na^+ and K^+ alkali cations and an unexpected HER (hydrogen evolving reaction) catalyst.

Introduction

1. Multifunctional hybrid materials.

The search of multifunctional molecule-based magnets is a very active area in molecular magnetism. Since the preparation, in the 1960s, of the first molecule-based magnets presenting low ordering temperatures,[5, 6] the search of new molecular-based magnets with higher ordering temperatures has stuck as one of the most active area in molecular magnetism.[7]

The versatility of molecular materials allows, with the appropriate selection of the initial building blocks, the rational preparation of compounds presenting cooperative magnetism or coexistence (or even a cooperativity) of magnetism with a second property. In these materials the crystalline structure has a critical importance since its control may allow the total control and tuning of their properties.

The best synthetic strategic for this goal is the “bottom-up” approach (Figure 1), which is based on the principle of starting from the simplest parts (bottom) and assemble them to obtain the more complex desired compound (up). Usually, the bottom-up approach entails an increase in dimensionality, and/or innuclearity

The challenging part is not only the choice of the building blocks but the selection of the synthetic conditions such as temperature or solvents. Sometimes, the preparation of molecular hybrid materials may depend on just one solvent, as we will show later. The advantage of this approach is that every building block that is being chosen could contribute with one property. So, the selection of these building blocks should be made taking into account the properties that they will present when assembled to form the final compound. Thereby, the combination of building blocks will yield a novel final material which may display all or some of the chosen properties.

Many multifunctional molecular materials have been synthesized following this strategy. The coexistence of many different properties is a fact in an enormous number of molecular materials, making the synthesis of materials with a new combination of properties an interesting challenge. Additionally, the improvement of these materials and their properties is always a goal to achieve for the scientific community.

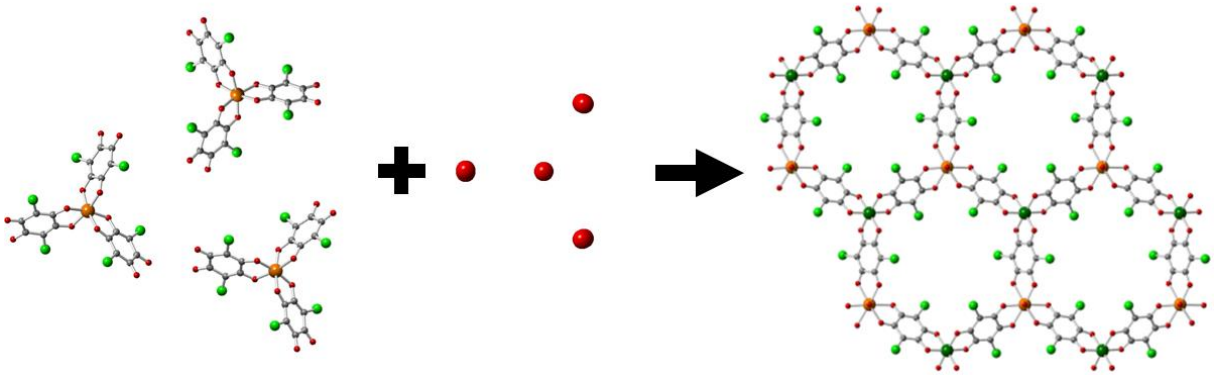

Figure 1. *The bottom-up approach.*

In this introductory chapter we will summarize the most important achievements on the molecular materials field.

1.1. oxalato compounds: the predecessors to anilato-based compounds

A milestone in the area of molecular magnetism was the preparation by Okawa et al. in the 1990s[8] of the family of heterometallic M^{III}-M^{II} hexagonal honeycomb oxalato layers with the formula $[NBu_4][M^{II}M^{III}(ox)_3]$ where M^{II} = Mn, Fe, Co, Ni, Zn and Cu; M^{III} = Cr and Fe and ox = oxalato ligand $(C_2O_4)^{2-}$. This family of layered compounds presents ferromagnetic ordering from 6 to 12 K when M^{III} = Cr, ferrimagnetic ordering with T_c up to 44 K when M^{III} = Fe and spin canting with T_c = 28 K for the couple $Mn^{II}Fe^{III}$. The initial publication was one of the most important breakthroughs in this area of the last decades,[8] as evidenced by the more than 700 citations that this publication has had to date.

oxalato-based compounds represent a very active area in molecular materials with up to 825 publications containing the keyword “oxalato” in 2015. Also in the same year, more than half (53 %) of publications containing the keywords “molecular materials” also contain the keyword “oxalato” (source: Scopus). The fact that more than half of all publications about molecular materials are based on oxalato compounds gives us an idea of the importance that this simple ligand still has.

Most of the oxalato-based molecular magnets have been synthetized with the bottom-up method described above. In this case, it is also called as the “complex-as-ligand approach”. For the oxalato-based compounds, the main building block is the monomeric $[M^{III}(ox)_3]^{3-}$ tris-oxalato metalate complex (a complex acting as a ligand).

This trivalent anion is used as a ligand towards divalent metal cations. Their combination results in the formation of the well-known bimetallic honeycomb layers (Figure 2a). As mentioned before, the first heterometallic oxalato network published by Okawa et al. consists of hexagonal layers with a bulky organic cation $[NBu_4]^+$ as counter-cation.

After Okawa's work, lots of publications modifying the original formula have been published. The first step was changing the trivalent metal combination in order to change the Curie temperature (T_c), obtaining analogous layered molecular magnets showing ferro-, ferri- and weak ferromagnetic ordering with T_c temperatures up to 45 K.[9-15] The second logical step was adding an extra functionality. Since these layers are negatively charged, a counter-cation is needed and soon others cations were used in order to not only act as charge-compensating counter-ions but also as templating agents that i) control the dimensionality of the final system and ii) add an extra functionality such as spin crossover (SCO)[16-27], single molecule magnets (SMM), etc.[28, 29] For example, the use of bulky cations such as $[Z^{II}(bpy)_3]^{2+}$, $[Ir(ppy)(bpy)_2]^+$ or $[Ir(ppy)_2(bpy)]^+$ where Z^{II} = Fe, Co, Ni, Ru; bpy = 2,2'-dipyridyl and ppy = phenylpyridine, led to the formation of three-dimensional oxalato-based enantiopure complexes (Figure 2b).[30-35] These 3D complexes are composed of homochiral units as a result of the intrinsic D_3 symmetry of the templating complexes which forces the monomeric tris-oxalato metallate to adopt a homochiral configuration, different to the alternating chirality shown in the honeycomb 2D layers. From the magnetic point of view, this increase in the structural dimensionality, makes ferro and ferrimagnets with lower T_c than their 2D analogues. This change can be understood thanks to the weaker magnetic exchange mediated by the longer metal-to-metal distances and the different relative orientation of the magnetic orbitals.[36]

It is possible to control the structure to make the dimensionality bigger, but also the opposite effect can be achieved. In fact, the use of capping ligands, which can cut the growth of the bimetallic complexes, leads to 1D oxalato-bridged chains or discrete polynuclear complexes such as dimers, trimers, tetramers,…[37-42]

Once the dimensionality was controlled, the main strategies have been addressed to include an additional property in these hybrid materials by playing with the functionality of the A^+ cations located in between the bimetallic layers. This simple

change has yielded large series of multifunctional molecular materials where the magnetic ordering of the bimetallic layer coexists and even interacts with other properties arising from the cationic layers.[16-29, 43-61]

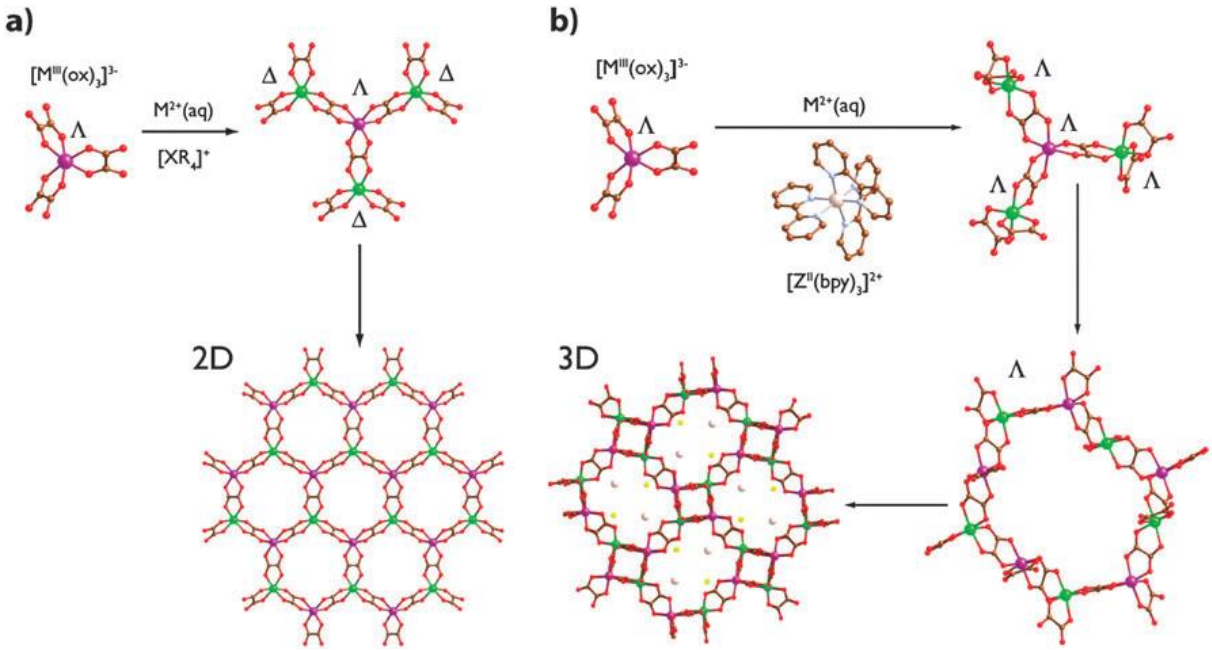

Figure 2: *Formation of the 2D heterochiral* ***(a)*** *and the 3D homochiral* ***(b)*** *oxalato-based architectures depending on the nature of the cation used to template their assembly.*[62]

Once the strategy to change the extra functionality was dominated, it seemed logical to try to modulate the magnetic properties, in order to increase the ordering temperatures. Since the nature of the inserted cation affects very little (if any) the magnetic properties of the resulting 2D hybrid material (emphasizing their 2D magnetic character),[12, 36, 43-47, 56, 63] the only way left to tune the magnetic properties of these compounds, is to act directly on the exchange pathways within the bimetallic layers. It has to be said that this affirmation is not only valid for 2D oxalato-based materials. As shown by Clemente et al.[30], it is possible to tune the T_c in 3D oxalato based materials by slightly changing the M^{III}-M^{II} separation when using cations of different sizes. In the 2D series, the change in the ordering temperatures can be done either by varying M^{II} and M^{III} (currently a highly exploited option already used by Okawa in 1992)[8-15, 62] or by changing the bridging ligand ($C_2O_4^{2-}$). Until date, just a few attempts have managed to replace the bridging oxalato ligand by the dithioxalato. In all these attempts the ordering temperatures remained almost equal to those of the oxalato lattices.[64-67] In our group, we have attempted the use of larger bis-bidentate bridging ligands such as the dianion of the 2,5-dihydroxy-1,4-benzoquinone ($H_2C_6O_4H_2$) and its derivatives

($C_6O_4X_2^{2-}$, Figure 3) since they show coordination modes similar to the oxalato ligand, but also, they present additional advantages: i) they are easy to functionalize in order to tune the exchange coupling through them by simply changing the X group, ii) their modification does not affect their coordination mode and iii) they are able to provide an effective pathway for the exchange interaction[68]. The easiness with which the ligand can be modulated is remarkable due to the fact that, with a little and easy variation, the magnetic exchange coupling and, therefore, the magnetic properties could change dramatically. As far as we know, this is the only ligand with this singularity.

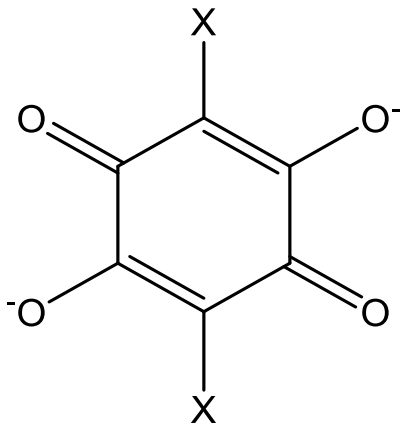

***Figure 3**: Anilato-derivate dianions used in this work (X = H, Cl, Br, NO_2, CN/Cl,...).*

2. Anilato-based Molecular Materials:

The coordination modes and ability to act as bridging ligands of these anilato derivatives to afford many different coordination frameworks have been summarized by Kitagawa and Kawata.[69] Derivatives of the $C_6O_4H_2^{2-}$ ligand (X = H) have been extensively studied (Table 1) to prepare several compounds with different dimensionalities and structures, ranging from isolated monomers, dimers and oligomers (0D) to extended 1D, 2D and 3D structures. In the following paragraphs we will present a little summary of the research done in this field of anilato-based compounds.

***Table 1**. Names and molecular formulas of the anilic acids reported in the literature.*[70]

Substituent X	Formula	Anilic Acid Name	Anilate dianion name
H	$H_4C_6O_4$	Hydranilic acid	Hydranilate
F	$H_2F_2C_6O_4$	Fluoranilic acid	Fluoranilate
Cl	$H_2Cl_2C_6O_4$	Chloranilic acid	Chloranilate
Br	$H_2Br_2C_6O_4$	Bromanilic acid	Bromanilate
I	$H_2I_2C_6O_4$	Iodanilic acid	Iodanilate
NO_2	$H_2N_2C_6O_8$	Nitranilic acid	Nitranilate
OH	$H_4C_6O_6$	Hydroxyanilic acid	Hydroxyanilate
CN	$H_2N_2C_8O_4$	Cyananilic acid	Cyananilate
Cl/CN	$H_2ClNC_7O_4$	Chlorocyananilic acid	Chlorocyananilate
NH_2	$H_6N_2C_6O_4$	Aminanilic acid	Aminanilate
CH_3	$H_8C_8O_4$	Methylanilic acid	Methylanilate
CH_2CH_3	$H_{12}C_{10}O_4$	Ethylanilic acid	Ethylanilate
iso-C_3H_7	$H_{16}C_{12}O_4$	Isopropylanilic acid	Isopropylanilate
C_6H_5	$H_{12}C_{18}O_4$	Phenylanilic acid	Phenylanilate
C_4H_3S	$H_8C_{14}O_4S_2$	Thiophenylanilic acid	Thiopehenylanilate
$C_6H_5O_2S$	$H_{12}C_{18}O_8S_2$	3,4-ethylenedioxy-thiophenylanilic acid	3,4-ethylenedioxy-thiophenylanilate
C_4H_9	$H_{20}C_{14}O_4$	2,3,5,6-tetrahydroxy-1,4-benzoquinone	2,3,5,6-tetrahydroxy-1,4-benzoquinonate

2.1. 0D anilato-based compounds:

The discrete (0D) anilato-based complexes can be classified according to the number of metal ions. The most abundant are, by far, the mononuclear complexes. These monomeric anilato-based compounds are usually obtained as mono-, bis- or tris-complexes of $C_6O_4X_2^{2-}$ dianions, depending of the oxidation state, the coordination number of the metallic centre and the presence of other co-ligands.[71-91] We will focus our study on the series of tris(anilato)metalate complexes with the general formula $[M^{III}(C_6O_4X_2)_3]^{3-}$ since they will be very useful as building blocks for the preparation of more complex structures as we will see in this Thesis.

Although the closely related tris(oxalato)metalate $[M^{III}(ox)_3]^{3-}$ complexes are known since the 1930's,[92] only two tris(anilato)metalate compounds were known before 2013. [93, 94] Both compounds were prepared with chloranilato ($C_6O_4Cl_2^{2-}$) combined with Fe(III)[87] or In(III)[93] and the Fe(III) compound was prepared by serendipity.[87] Compounds of this type with anilato ligands different from chloranilato ($C_6O_4X_2^{2-}$, X = Cl) were unknown until 2013.[1]

In the last years our group and Mercuri's group have published several articles including different families of these tris(anilato)metallate compounds. Two of them include the series of compounds with general formula $A_3[M^{III}(C_6O_4X_2)_3]$ where A = $[NBu_4]^+$, $[PPh_4]^+$ and $[(Et)_3NH_4]^+$ (only for X = Cl), M(III) = Cr and Fe and X = Cl, Br and I (Figure 4a).[1, 95] Later, another one focused on the $C_6O_4H_2^{2-}$ (X = H, $dhbq^{2-}$) ligand with A = $[PPh_4]^+$ and M(III) = Cr and Fe. These two dhbq-based compounds had a slightly different structure since they present a H-bonded network (Figure 4b). DFT theoretical calculations of the compounds show that the H substituent modulates the electron density of the anilato aromatic ring in favouring the electron delocalization toward the peripheral oxygen atoms.[96] Another article reported the family of tris(anilato)metallate complexes formulated as $[NBu_4]_3[M^{III}(C_6O_4(CN)Cl)_3]$ with M(III) = Cr, Fe and Al.[97] This family contains an unsymmetrically substituted anilato containing a Cl and a CN groups and present luminescent properties.

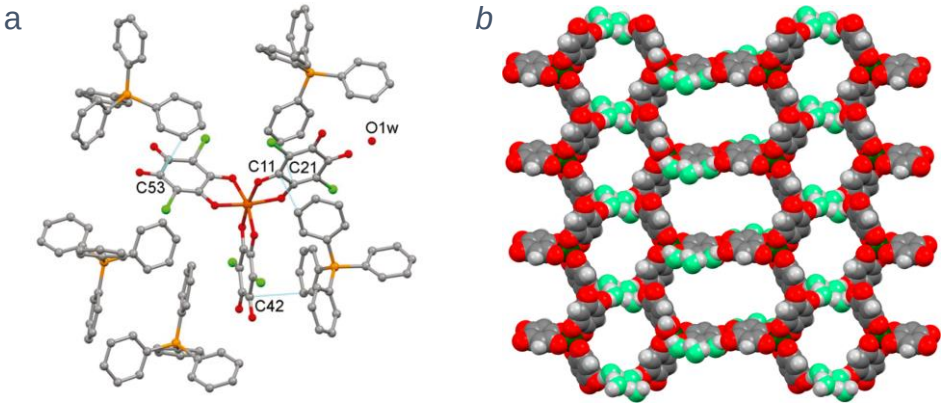

***Figure 4**: **(a)** Molecular packing of compound $[Ph_4P]_3[Fe(C_6O_4Cl_2)_3]$ showing the interactions between the anions and the surronding cations.[95] **(b)** View of the crystal packing of $[(Ph)_4P]_3[Fe(C_6O_4H_2)_3]\cdot 6H_2O$ with metal complexes and water molecules in spacefill model highlighting the supramolecular topology.[96]*

In the beginning of 2016 our group published[3] eighteen new monomeric complexes formulated as $[PPh_3Et]_3[M^{III}(C_6O_4X_2)_3]^{3-}$ with M/X = Cr/Cl, Fe/Cl, Ga/Cl, Cr/Br, Fe/Br, Ga/Br and Fe/NO_2, $[PPh_3Pr]_3[M^{III}(C_6O_4X_2)_3]$ with M/X = Cr/Cl, Fe/Cl, Ga/Cl, Cr/Br, Ga/Br and Fe/NO_2, $[PBu_4]_3[M^{III}(C_6O_4X_2)_3]$ with M/X = Cr/NO_2 and Fe/NO_2, $[NHep_4]_3[M^{III}(C_6O_4X_2)_3]$ with M/X = Cr/Cl and Cr/Br and $[PPh_4]_3[Fe(C_6O_4(NO_2)_2)_3]$. The six compounds with the cation $[PPh_3Et]^+$ and X = Cl or Br are chiral and crystallize in the chiral and polar *R*3 space group. These mixtures of enantio-pure chiral crystals are obtained using a racemic mixture of the anions and cations. When X = NO_2 or when

the cation is changed then the salts are achiral and crystallize in the polar but not chiral *P*2*cb* space group (for X = NO_2) or in the centro-symmetric (which is neither chiral nor polar) *P*-1 space group. This work showed the key role of the symmetry of the counter-cation in the chirality of the obtained salt and also showed the first examples of $[M(C_6O_4X_2)_3]^{3-}$ anions with Ga(III) and also the first ones with X = NO_2. These 18 compounds will be presented in chapter one in detail.

A second step in the family of 0D mononuclear tris(anilato)metallate compounds has been the recent incorporation of a second functionality. This aim was achieved with the cation BEDT-TTF (bis(ethylenedithio)tetrathiafulvalene or ET) that adds electrical conductivity. The first reported example of that kind is compound $(ET)_6[Fe(C_6O_4Cl_2)_3]\cdot(H_2O)_{1.5}\cdot(CH_2Cl_2)_{0.5}$, reported by our group in 2016.[98] This compound shows the typical layered structure found in many radical salts of ET (Figure 5a) and presents a high room-temperature electrical conductivity of *ca*. 10 S cm^{-1} and a semiconducting behaviour below 340 K with a very low activation energy of *ca*. 60 meV (Figure 5b). A few months later Avarvari et al. published three closely related 0D tris(chloranilato)metallate complexes also with ET, all of them showing a semiconducting behaviour.[99]

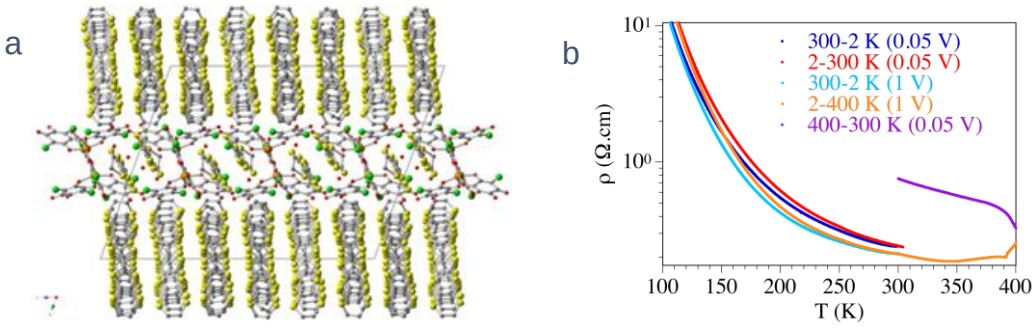

***Figure 5**: Structure of compound $(ET)_6[Fe(C_6O_4Cl_2)_3]\cdot(H_2O)_{1.5}\cdot(CH_2Cl_2)_{0.5}$ showing **(a)** The packing of the anionic and cationic layers and **(b)** the thermal variation of the resistivity in different scans.*

Besides the monomeric complexes, there are also several dimeric anilato-based complexes. These dimers can be classified, depending on the coordination type of the anilato-based ligand, into anilato-bridged and terminal anilato complexes and can be formulated as $[(L)_nM(C_6O_4X_2)M(L)_n]$ and $[(C_6O_4X_2)_nM(L)M(C_6O_4X_2)_n]$, respectively.[71, 78-81, 84, 88, 89, 91, 100-103] All these dimers have been prepared with transition metal ions

except for the lanthanoid-based family of dimers formulated as $[(H_2O)_5(C_6O_4(NO_2)_2)Ln(C_6O_4(NO_2)_2)Ln(C_6O_4(NO_2)_2)(H_2O)_5]$ (Ln(III) = Sm. Gd, Tb, Dy, Ho and Er) that has been recently reported by our group (Figure 6).[101]

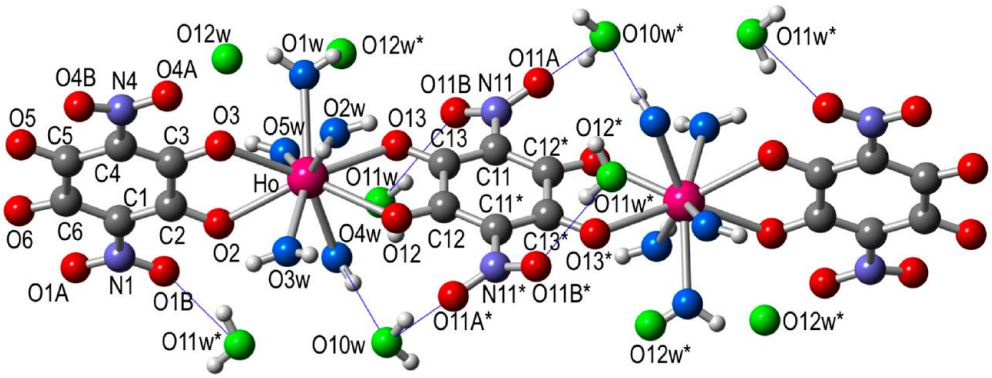

***Figure 6**: Structure of the dimer unit in $[Ho_2(C_6O_4(NO_2)_2)_3(H_2O)_{10}]\cdot 6H_2O$ ($C_6O_4(NO_2)_2$ = nitranilato).*[101]

2.2. 1D anilato-based compounds:

There are two main kinds of anilato-based chains: straight and zigzag chains. With *3d* transition metals the chain structures are formed when the metal centres are only coordinated by two bis-bidentate anilato-based ligands and the remaining coordination sites are occupied with terminal ligands (usually solvent molecules as H_2O, CH_3OH, CH_3CN,...).[104-110] The linear chains (Figure 7) are formed when the two terminal ligands are coordinated in *trans* whereas the zigzag chains are formed when the terminal ligands occupy *cis* positions (Figure 8a). For some divalent metal ions as Fe^{2+}, Cu^{2+}, Mn^{2+} and Co^{2+}, these chains may intercalate small molecules as in $[M(C_6O_4Cl_2)(H_2O)_2](G)$, G = phenazine (phz) and H_2O.[104,111]

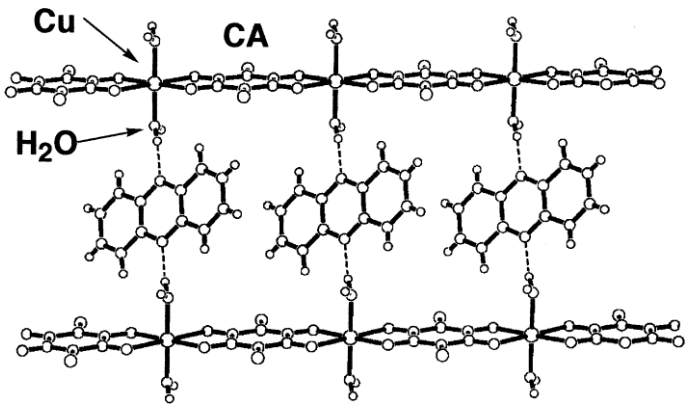

***Figure 7**: Structure of $[Cu(C_6O_4Cl_2)(H_2O)](phz)$ showing anilato-based linear chains.*[104]

A chain with formula $[Mn(C_6O_4Cl_2)(terpy)]$ (terpy = terpyridine) made up of neutral $[Mn(C_6O_4Cl_2)(terpy)]$ units with heptacoordinated Mn^{2+} ions was published by Kitagawa et al. in 2002.[109]

Besides transition metal ions, anilato based complexes with alkali metals (Na^+ ions) have also been described in compounds $[Na_2(C_6O_4Cl_2)(H_2O)_3]$[112, 113] and $[Na_2(phen)(C_6O_4Cl_2)](H_2O)_2]$[108] (phen = phenantroline).

In 2016, Robson et al. presented a family of chains based on dihydroxybenzoquinone (dhbq = $C_6O_4H_2$) formulated as *cis*-$M^{II}(C_6O_4H_2)(H_2O)_2 \cdot 2H_2O \cdot x$ROH ($M^{II}$ = Mg or Zn) presenting unexpected gas sorption properties (Figure 8b).[114] These *cis* chains contrast with the trans-$M^{II}(C_6O_4H_2) \cdot nH_2O$ (M^{II} = Mg, Mn, Co, Ni, Zn) published by Kitagawa et al. in 2010, which present a straight geometry.

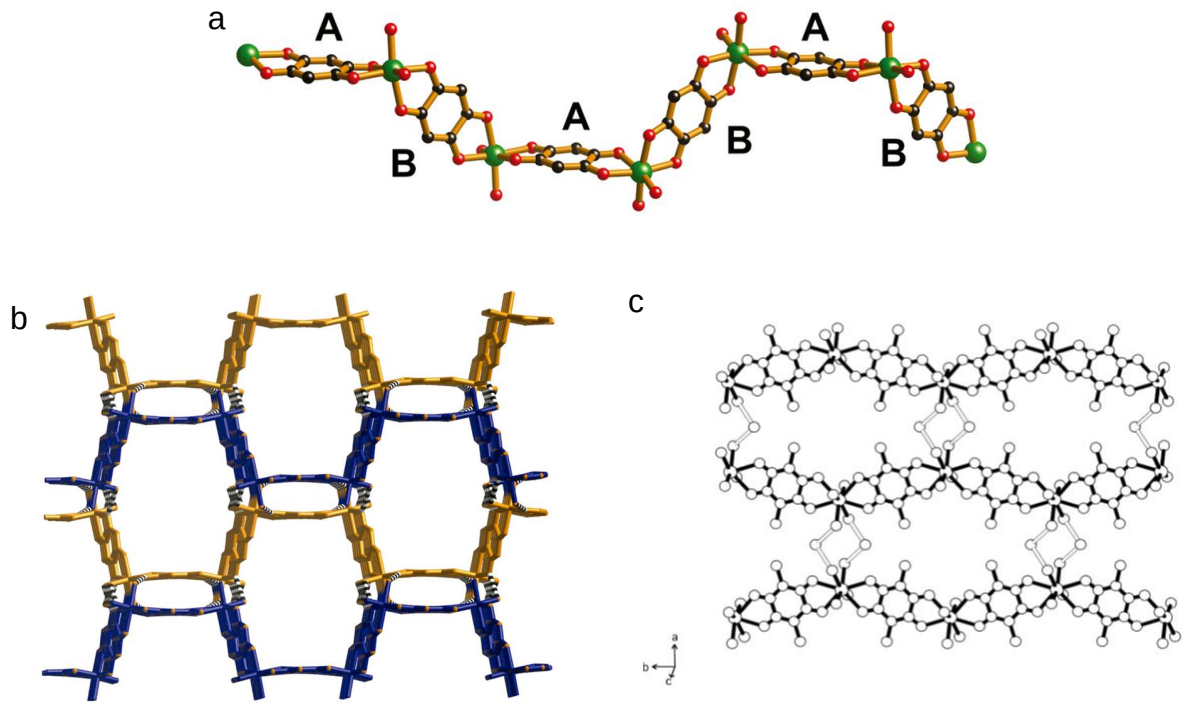

Figure 8: (a) *A fragment of a zigzag cis-$Mg(C_6O_4H_2)(H_2O)_2$ coordination polymer* ***(b)*** *Extended 3D hydrogen bonded network of $Mg(C_6O_4H_2)(H_2O)_2$ containing spacious channels were gas-sorption occurs*[114] ***(c)*** *Hydrogen bonded sheet structure of the anion layer in $Lu(C_6O_4Cl_2) \cdot 12H_2O$*[100]

Finally, also lanthanoid-based chains with anilato ligands formulated as $Ln_2(C_6O_4Cl_2)_3 \cdot 12H_2O$ (Ln = Yb, Lu) have been reported by Robson et al. (Figure 8c).[100] In this case, due to the larger size of the lanthanoid ions, their coordination number is eight. In these structures, a $[Ln(C_6O_4Cl_2)_2(H_2O)_4]^-$ monoanion is the counterion of the cationic chain formulated as $[Ln(C_6O_4Cl_2)(H_2O)_4]^+$.

In some cases the chains are linked by hydrogen bonds to form 2D H-bonded sheets (Figure 9a).[104, 115] The space between these H-bonded layers may be filled with different molecules as in the previously mentioned $[Cu(C_6O_4Cl_2)(H_2O)](phz)$].[104] The study was extended in 2002 also by Kawata et al. playing with the size of the inserted cation in between the "pseudo" 2D structure.[116] Thus, besides phenazine (phz), other molecules as ferrocene ($[Fe(Cp)_2]$, decamethylferrocene ($[Fe(Cp^*)_2]$ and tetrathiafulvalene (TTF) were inserted in between the "pseudo" 2D structure of the type $[Fe(C_6O_4Cl_2)_2(H_2O)_2]^-$ (Fe(II) or Fe(III)], demonstrating the flexibility of these layers (Figure 9b).

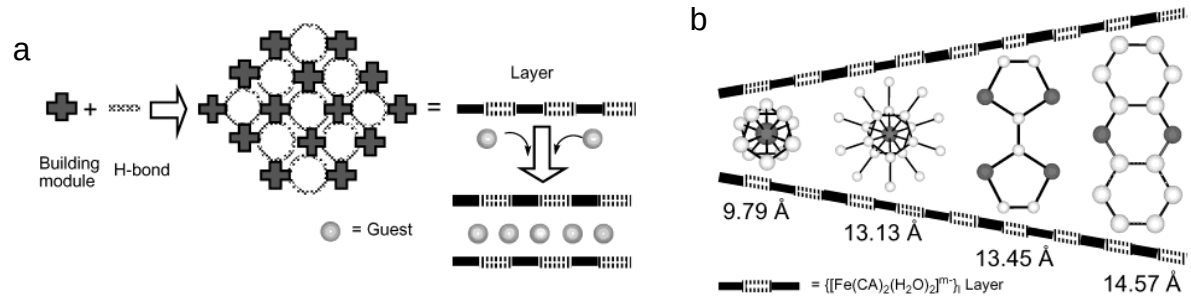

Figure 9: (a) *Scheme of the layers formed by H-bonded anilato chains.* ***(b)*** *Insertion of different guest molecules in between the* $[Fe(C_6O_4Cl_2)_2(H_2O)_2]^-$ *layers.*[116]

Only one heterometallic chain has been reported, a Cr^{III}/Mn^{II} chain with formula $[Fe^{II}(tren\text{-}(imid))_3)]_2[MnCl_2Cr(C_6O_4Cl_2)_3]Cl \cdot (CH_3OH) \cdot (CH_2Cl_2)_3 \cdot (CH_3CN)_{0.5}$ published in 2014 by Clemente et al.[117] (Figure 10). In this compound the $[Fe^{II}(tren\text{-}(imid)_3)]^+$ complex is a spin crossover (SCO) cation and half of the inserted Fe(II) cations undergo a complete and gradual spin crossover from 280 to 90 K that coexists with a magnetic ordering below 2.5 K.

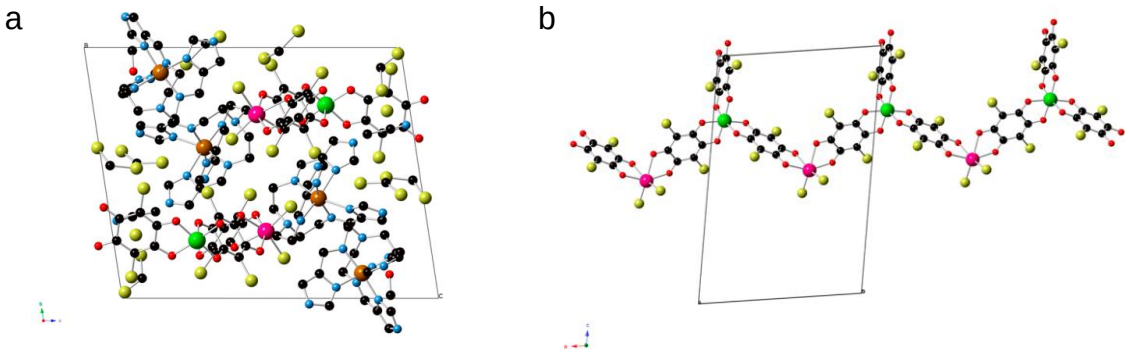

Figure 10: (a) *Projection of* $[Fe^{II}(tren(imid))_3)]_3[MnCl_2Cr(C_6O_4Cl_2)_3]_2$ *complex in the bc plane and* ***(b)*** $[MnCl_2Cr(C_6O_4Cl_2)_3]^{3-}$ *chains in the structure of* $[Fe^{II}(tren(imid))_3)]_3[MnCl_2Cr(C_6O_4Cl_2)_3]_2$*. Hydrogen atoms have been omitted for clarity.*[117]

2.3. 2D anilato-based compounds:

2.3.1. Homometallic 2D anilato-based compounds:

The 2D homometallic layered structures may be classified into two main groups (excluding few exceptions): hexagonal layers and rectangular layers.

The most common ones are the 2D honeycomb hexagonal lattices. These structures are based on infinite layers of coordination frameworks with transition metal ions and, more recently, with rare earths.

2.3.1.1. Homometallic 2D Honeycomb hexagonal networks:

The first examples were published in 1986 by Weis, Riegler and Robl[118] and consisted of infinite layers with Mn^{2+} and Cd^{2+} coordinated with $C_6O_4H_2^{2-}$, leading to $Na_2(H_2O)_{24}[M_2(C_6O_4H_2)_3]$ structures (Figure 14a). The octahedral $M(C_6O_4H_2)_3$ modules are connected to give a honeycomb-type layered network formulated as $[M_2(C_6O_4H_2)_3]^{2-}$. One of the Na^+ ions is located in the anionic layer and the other lies midway between two anionic layers. The water molecules coordinate the Na^+ ions and tie the layers together by hydrogen bonds of interstitial molecules. The layers are stacked in an eclipsed way, leading to the formation of hexagonal channels.[118] The second work showing 2D layers was published in 1987 by Robl[119] and is based on a nine coordinate Y^{3+} module with a tricapped trigonal prism geometry. Two isostructural compounds were published: $[Y_2(C_6O_4Br_2)_3(H_2O)_6]\cdot 6H_2O$ and $[Y_2(C_6O_4Cl_2)_3(H_2O)_6]\cdot 6.6H_2O$. In this particular case, the higher size of Y^{3+} ions leads to a higher coordination number (9 *vs*. 6 for the *3*d transition metals) that induces the

formation of infinite corrugated layers. The three additional coordination positions are occupied by three water molecules. The layer stacking yields cage-like cavities occupied by water molecules. Hydrogen bonds stabilise the structure by interlinking adjacent layers.[119] Robson et al. published in 1996 the fist rare earth 2D anilato based compound with formula $[Ce_2(C_6O_4H_2)_3]\cdot 24H_2O$ (Figure 11a).[120] This compound is formed by infinite corrugated layers formed by Ce^{3+} and the bis-chelating anion $C_6O_4H_2^{2-}$. Again, due to the higher size of Ce^{3+} *vs*. 3d transitions metals, the coordination number is nine and not six, and, again, the three coordination positions that remain after the Ce^{3+} ions are bonds to the three $C_6O_4H_2^{2-}$ ligands are filled with three water molecules, leading to a honeycomb-type network. It contains dodecahedral $Ce_2(H_2O)_{18}$ cages linking non consecutive layers (Figure 11b).[120] A slightly different kind of 2D network was published in 2002 by Kitagawa et al.[109] They presented a honeycomb structure where each hexagon consists of six Mn^{2+} ions, four $C_6O_4Cl_2^{2-}$ and two 2,2'-bipyrimidine (bipym) ligands with formula $[Mn(C_6O_4Cl_2)(bipym)_{0.5}(H_2O)](H_2O)(C_2H_5OH)$. This compound is made up of neutral $[Mn(C_6O_4Cl_2)(bipym)_{0.5}(H_2O)]$ units and interstitial water and ethanol molecules. In this example, Mn^{+2} ions are hepta-coordinated, with two nitrogen atoms of bipym, four oxygen atoms of two $C_6O_4Cl_2^{2-}$ anions and one oxygen from a water molecule.[109] This case would be later found in other anilato-based 2D networks.

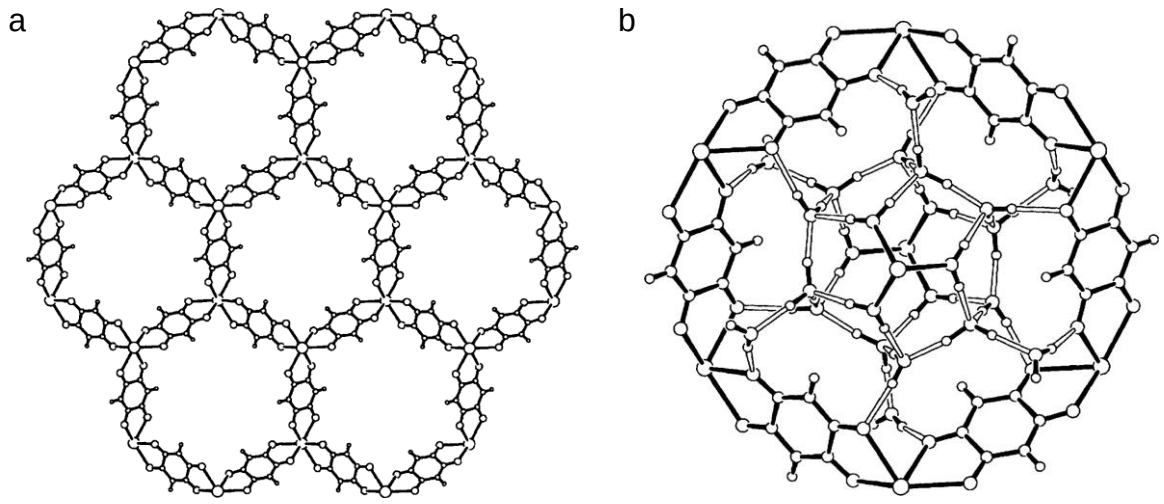

Figure 11: (a) *the two-dimensional honeycomb structure of* $Ce_2(C_6O_4H_2)_3\cdot 24H_2O$ ***(b)*** *The* $Ce_2(H_2O)_{18}$ *cage and the encompassing* $Ce_6(C_6O_4H_2)_6$ *ring to which it is hydrogen bonded.*[100, 120]

In 2002, Robson et al. published more 2D networks based on the $C_6O_4H_2^{2-}$ ligand and rare earth metals[100] to complete the family that they started in 1996 with the $[Ce_2(C_6O_4H_2)_3]\cdot 24H_2O$ compound.[120] They synthesized analogous compounds to the cerium one, all with the same formula $[Ln_2(C_6O_4H_2)_3]$ (Ln = La, Gd, Y, Yb and Lu) and isostructural. Due to the size difference in all these Ln^{3+} ions, the fact that they all present nine-coordination and the same structure suggests that hydrogen bonding within the crystal plays a major stabilizing role. When we move from $C_6O_4H_2^{2-}$ anion to $C_6O_4Cl_2^{2-}$, the isostructurality in-between all the chloranilato-based lanthanoid compound is remarkably missing, raising up to 4 different types of structures: dimers, chains and 2D structures: hexagonal and rectangular. In this section, we are only going to comment the 2D hexagonal lattices. Dimers and chains were commented previously and 2D rectangular lattices will be commented below. Hexagonal honeycomb layers with $C_6O_4Cl_2^{2-}$ and Y or Ln^{3+} = Ce, Pr, Nd, Tb, Gd, Eu, Yb have a 6,3 topology and the metal centre is nine coordinated (Figure 12).[100] They can be divided into three sub-classes (i) Ce, Pr, Nd and Tb; (ii) Y, Gd and Eu and (iii) Yb; differing in the coordination environment of the metal and the orientation of the chloranilato ligands relative to the plane of the polymeric sheet.

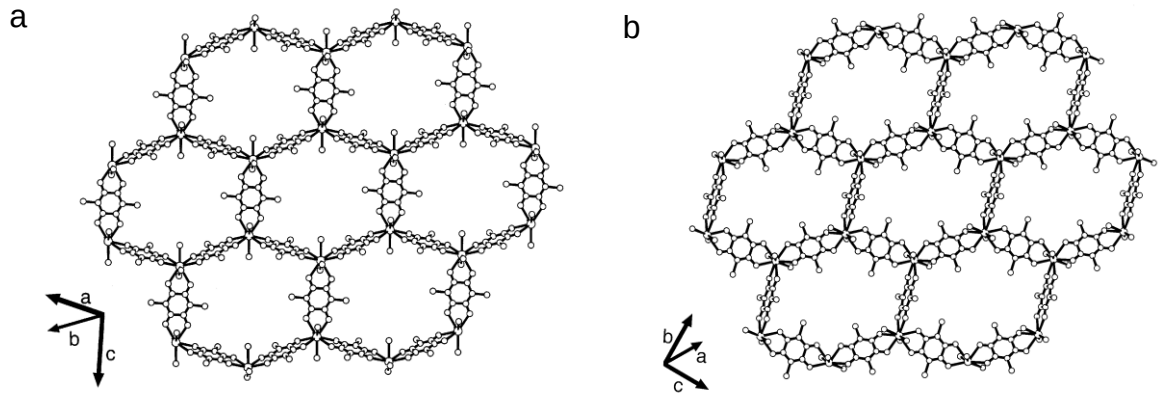

Figure 12: (a) *the sheet structure of* $Pr_2(C_6O_4Cl_2)_3\cdot 18H_2O$ ***(b)*** *the sheet structure of* $Y_2(C_6O_4Cl_2)_3\cdot 16H_2O$[100]

In 2004, Lu et al. published the first 2D honeycomb lattice using phenazine as template[121]. Phenazine is a neutral molecule which, thanks to the two pyridine donor sites is capable of participating in coordination and hydrogen-bonding interactions. Thus, three pyridine surround one oxonium cation, originating a $[(H_3O)(phz)_3]^+$ cation (Figure 13) that acts as (i) template, facilitating the π–π stacking interaction and (ii)

counteranion of the $[M_2(C_6O_4Cl_2)_3]^{2-}$ layers (M = Cu, Cd, Zn and Co). The compounds have a general formula $[(H_3O)_2(phz)_3][M_2(C_6O_4Cl_2)_3]\cdot 2CH_3COCH_3\cdot 2H_2O$ and are positioned in a eclipsed way, generating hexagonal channels where the acetone and water molecules are located.[121] Seven years later, Shilov et al. published the same 2D networks with M = Fe and Mn.[122]

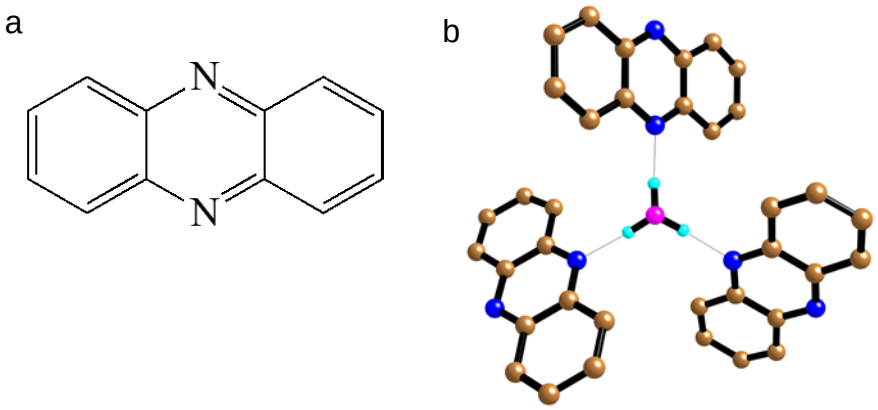

Figure 13: (a) *structure of phenazine* ***(b)*** *$[(H_3O)(phz)_3]^+$ unit.*

Very recently Harris et al.[123] have published two more 2D hexagonal networks formulated as $(Me_2NH_2)_2[M_2L_3]\cdot 2H_2O\cdot 6DMF$ (M = Fe^{3+} and Zn^{2+}; L = $C_6O_4Cl_2^{2-}$) In the Fe^{3+} case two of the three chloranilato ligands are serendipitiously reduced by the Fe^{2+} ions used as reagent. The presence of the reduced chloranilato ligands in the semiquinone radical form gives rise to a strong ferromagnetic coupling between the Fe(III) centres and to a long range ordering at 80 K that decreases to 26 K when the DMF molecuels are removed. At the beginning of this year, an extended study of this same compound was published.[124] In this publication, they proved that, soaking in a DMF solution of Cp_2Co, the compound suffers a single-crystal-to-single-crystal one-electron reduction to give $(Cp_2Co)_{1.43}(Me_2NH_2)_{1.57}[Fe_2L_3]\cdot 4.9DMF$; $[Fe_2L_3]$ = $[Fe^{III}_2(L_3^{-\bullet})_3]_3$. Magnetic measurements results in a T_c of *ca*. 105 K, the highest ordering temperature reported for a MOF.

The last 2D homometallic hexagonal networks, with formula $[NEt_4]_2[M_2(C_6O_4X_2)_3]$ (X/M = Cl/Mg, Cl/Mn, Cl/Fe, Cl/Co, Cl/Ni, Cl/Cu, Cl/Zn and F/Zn, have been very recently published by Robson et al. (Figure 14).[125] All these compounds are isostructural and present an eclipsed disposition of the layers with hexagonal channels occupied by the cations and some solvents that can be removed.

After desolvation, the structure does not collapse and the void space is *ca*. 39%-43% (depending on the compound). CO_2 can be more or less effectively absorbed at room temperature.[125]

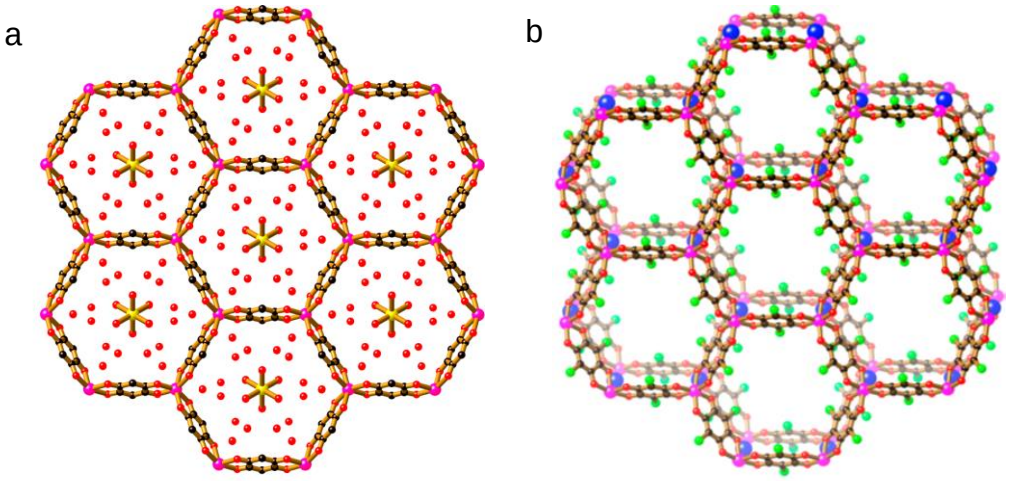

Figure 14: (a) *Structure of* $[Na(\mu_2\text{-}H_2O)_3]_2[Mn_2(C_6O_4H_2)_3]\cdot 18H_2O$ *viewed perperdicular to the (6,3) sheet. Isolated red circles represent lattice water molecules.* ***(b)*** *Structure of* $(Et_4N)_2[Zn_2(C_6O_4Cl_2)_3]$*, two* $[Zn_2(C_6O_4Cl_2)_3]_n^{2-}$ *sheets, showing the positions of the N centres of the* Et_4N^+ *cations (blue spheres). The ethyl groups are omitted for clarity.*[125]

2.3.1.2. 2D Homometallic square/rectangular networks

In 1994, Kitagawa et al. published one of the few 2D rectangular networks reported to date,[115] the lattice $[Cu(C_6O_4Cl_2)(pz)]$ (pz = pyrazine). The structure shows parallel sheets, which consist of square arrays of Cu^{II} ions bridged by $C_6O_4Cl_2^{2-}$ ligands and pyrazine ligands (Figure 15).[115] In 2002, they extended the family publishing the same $[M(C_6O_4Cl_2)(pz)]$ structure with M = Mn^{2+} and Co^{2+}.[126] Another 2D rectangular network, quite different to the previous one, was reported in 2002 by Robson et al.[100] The compound $La_2(C_6O_4Cl_2)_3\cdot 13H_2O$ is a ten-coordinate lanthanum based structure. Due to the higher size of the La versus the rest of Ln, its coordination number could be higher. In this structure two types of four-membered rings were observed in the sheet: $La_4(C_6O_4Cl_2)_4$ and $La_4(C_6O_4Cl_2)_2[(H_2O)_2]_2$.

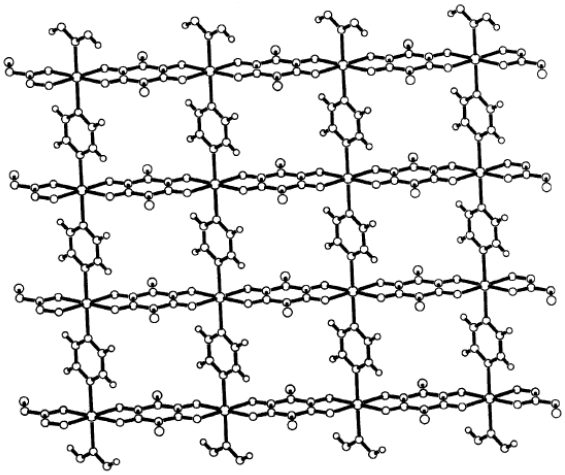

Figure 15: *Crystal structure of the 2D homometallic rectangular [Mn($C_6O_4Cl_2$)(pz)] lattice onto the bc plane.*[126]

2.3.2. Heterometallic 2D anilato-based compounds:

2.3.2.1. Heterometallic 2D Honeycomb hexagonal networks:

The first heterometallic 2D anilato-based networks were published by our group in 2013 (Figure 16).[1] In this publication, we presented three structures very similar to the ones published in 2004 by Lu et al.[121] but combining trivalent metals (M^{III} = Cr, Fe) with Mn^{2+} and using, not only $C_6O_4Cl_2^{2-}$ but also $C_6O_4Br_2^{2-}$, with general formula $[(H_3O)(H_2O)(phz)_3][M^{III}Mn(C_6O_4X_2)_3]$ (M^{III} = Cr, Fe and X = Cl, Br). These 2D lattices are also positioned in an eclipsed way, generating hexagonal channels. This structural eclipsed distribution is due to the templating effect of the $[(H_3O)(phz)_3]^+$ cation. When M(III) = Cr and X = Cl or Br, the difference in the metal spins leads to a ferrimagnetic long-range ordering at low temperatures.[1]

In this same publication,[1] the family of ferrimagnets $[NBu_4][CrMn(C_6O_4X_2)_3]$ (X = Cl, Br, I, H) was also presented. With this family, it was confirmed that in anilato-based magnets, a change of the X group changes the ordering temperature, obtaining, thus, a family of tuneable magnets. In these layers there is no π–π stabilization since there is no phenazine and, accordingly, the lattices in this family are alternated, precluding the formation of hexagonal channels.

Another heterometallic 2D network, this time combining M^{III} and M^{I} metals was published by Mercuri et al. and is formed by Fe^{3+} and K^{+} ions with the conducting cation ET as counterion.[127]

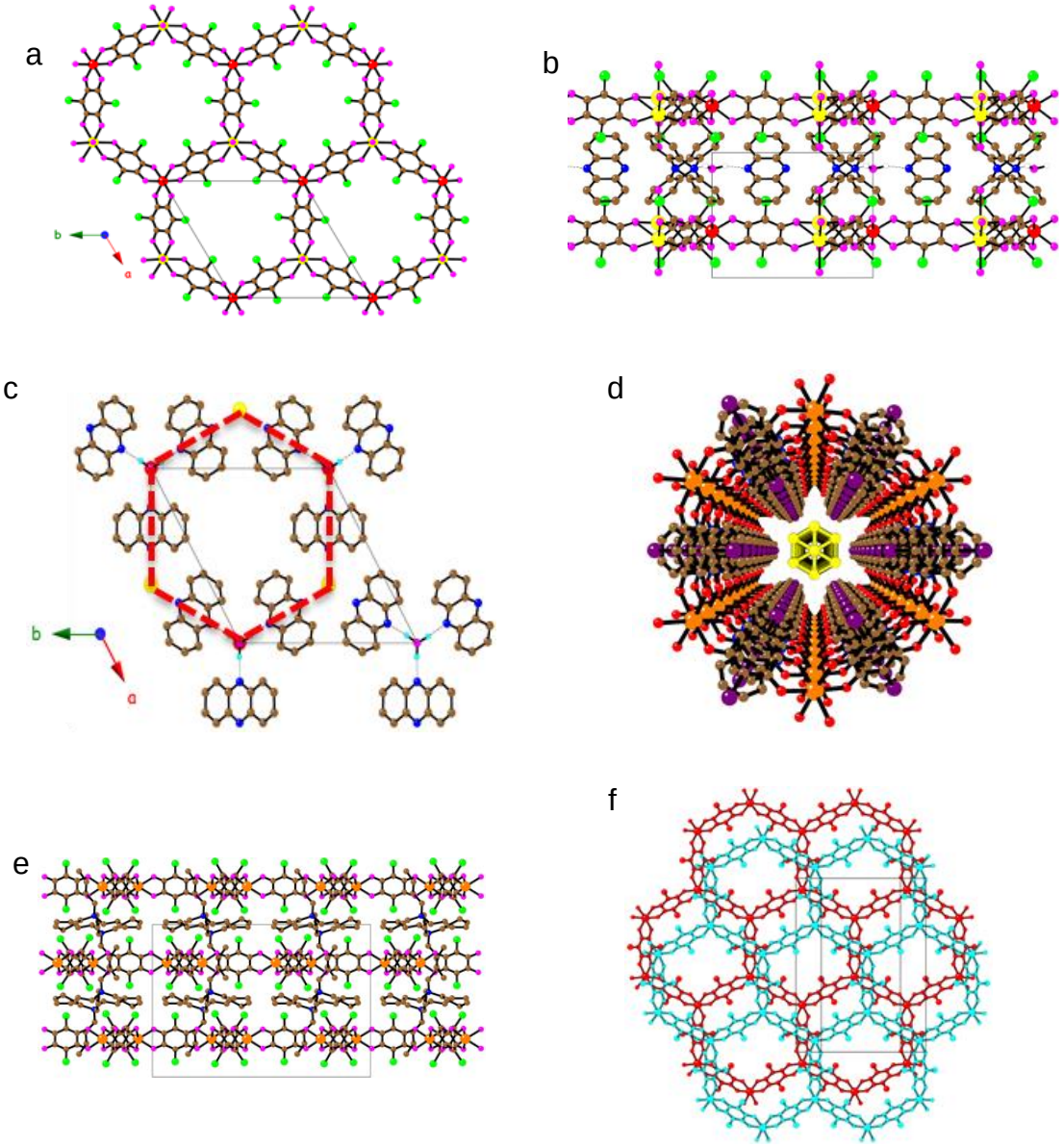

***Figure 16: (a), (b), (c)** and **(d)** show the crystal structure of $[(H_3O)(phz)_3][CrMn(C_6O_4Cl_2)_3]$ and **(e)** and **(f)** show the crystal structure of $(NBu_4)[CrMn(C_6O_4Cl_2)_3]$. **(a)** view of the anionic layer **(b)** view of the alternated anionic and cationic layers **(c)** view of the cationic layer showing the $[(H_3O)(phz)_3]^+$ entities and the position of the M(II) and M(III) in the vertices of the red hexagon **(d)** view in perspective of the hexagonal channels **(e)** view of the anionic and cationic layers **(f)** view of eclipsed layers.[1]*

Other 2D heterometallic honeycomb layers were published by Clemente et al. in 2014.[117, 128] They consist of the same $[CrMn(C_6O_4X_2)_3]^-$ (X = Cl, Br) anionic layers but with a cation presenting an extra property, in this case, spin crossover (SCO):

$[Fe^{III}(sal_2\text{-trien})][MnCr(C_6O_4Cl_2)_3]\cdot(CH_2Cl_2)_{0.5}\cdot(CH_3OH)\cdot(H_2O)_{0.5}\cdot(CH_3CN)_5$, $[Fe^{III}(4\text{-OH-}sal_2\text{-trien})][MnCr(C_6O_4Cl_2)_3]$, $[Fe^{III}(sal_2\text{-epe})][MnCr(C_6O_4Br_2)_3]\cdot(CH_3CN)_4$ and $[Fe^{III}(5\text{-Cl-}sal_2\text{-trien})][MnCr(C_6O_4Br_2)_3]\cdot(CH_2Cl_2)\cdot(CH_3OH)\cdot(H_2O)_4\cdot(CH_3CN)_{1.5}$. This series was enlarged with three more examples a year later: $[Fe^{III}(acac_2\text{-trien})][MnCr(C_6O_4Cl_2)_3]\cdot(CH_3CN)_2$, $[Fe^{III}(acac_2\text{-trien})][MnCr(C_6O_4Br_2)_3]\cdot(CH_3CN)_2$ and $[Ga^{III}(acac_2\text{-trien})][MnCr(C_6O_4Br_2)_3]\cdot(CH_3CN)_2$. In these last three structures, the SCO cations are located inside the hexagonal channels. Sadly, none of them present SCO behaviour.

In 2016, our group published a heterometallic Fe-Na 2D structure similar to the 2D honeycomb layers but with some interesting differences (Figure 17)[129]: (i) the vertices of the hexagons contain dimers of Na^+ cations connected through four oxygen atoms from two $[C_6O_4(NO_2)_2]^{2-}$ ligands, resulting in a 3,6-connected anionic layers and (ii) an additional $[Fe(C_6O_4(NO_2)_2)_3]^{3-}$ anion is located in the centre of the hexagons with the three nitranilato ligands pointing towards the Na^+ pairs, resulting in an unprecedented lattice formulated as $[Na_2Fe_2(C_6O_4(NO_2)_2)_6]^{4-}$ with DAMS as counterion (DAMS = $C_{16}H_{17}N_2^+$ = 4-[4-(dimethylamino)-α-styryl]-1-methylpyridinium).

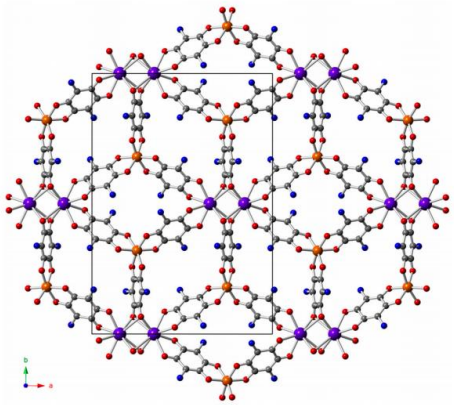

Figure 17: *View of the 3,6-connected anionic layers $[NaFe(C_6O_4(NO_2)_2)_3]^{2-}$ generated with Fe(III) and pairs of Na^+ cations (the oxygen atoms of the NO_2 groups have been omitted for clarity).*[129]

2.3.2.2. Heterometallic square/rectangular networks

Only one example of this kind of networks has been found and it was presented in 2011 by Robson et al. with formula $(Et_4N)_2[Sn^{IV}Ca^{II}(C_6O_4Cl_2)_4]\cdot 2Me_2CO$ (Figure 18).[130] In this compound both metals are octacoordinated and act as 4-connecting nodes to form a square grid containing “square” holes.

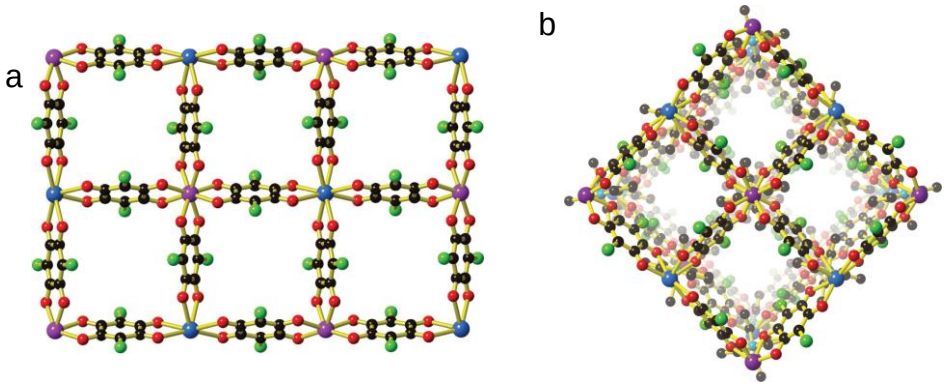

Figure 18: (a) *The 2D squared grid $[Sn^{IV}Ca^{II}(C_6O_4Cl_2)_4]^{2-}$ coordination network in $(Et_4N)_2[Sn^{IV}Ca^{II}(C_6O_4Cl_2)_4]\cdot Me_2CO\cdot 2H_2O$* ***(b)*** *A view down the channels in $(Et_4N)_2[Sn^{IV}Ca^{II}(C_6O_4Cl_2)_4]\cdot Me_2CO\cdot 2H_2O$. Acetone and water molecules are omitted for clarity.*[130]

2.3.3. 3D anilato based compounds:

Based on chloranilic acid, two 3D structures have been reported: one is a 3D network of alternating $C_6O_4Cl_2^{2-}$ dianions and Pr^{3+} ions.[131] Due to the fact that Pr^{3+} ions have nine coordination positions, six of them are occupied by three chloranilato ligand and the remaining three are occupied by ethanol molecules, giving rise to the formula $[Pr_2(C_6O_4Cl_2)_3(C_2H_5OH)_6]$. The other 3D network reported has alternating $C_6O_4Cl_2^{2-}$ dianions and K^+ ions, leading to a $[K_2(C_6O_4Cl_2)]$ structure.[132]

More recently, in 2011, Robson et al. synthesized a family of 3D homometallic network with formula $(NBu_4)_2[M_2(C_6O_4H_2)_3]$ where M = Mn^{II}, Fe^{II}, Co^{II}, Ni^{II}, Zn^{II} and Cd^{II}.[133] The structure presents two interpenetrating $[M_2(C_6O_4H_2)_3]^{2-}$ coordination 3D networks, each with the chiral (10,3)-a topology, with the two independent nets being of opposite quirality (Figure 19).

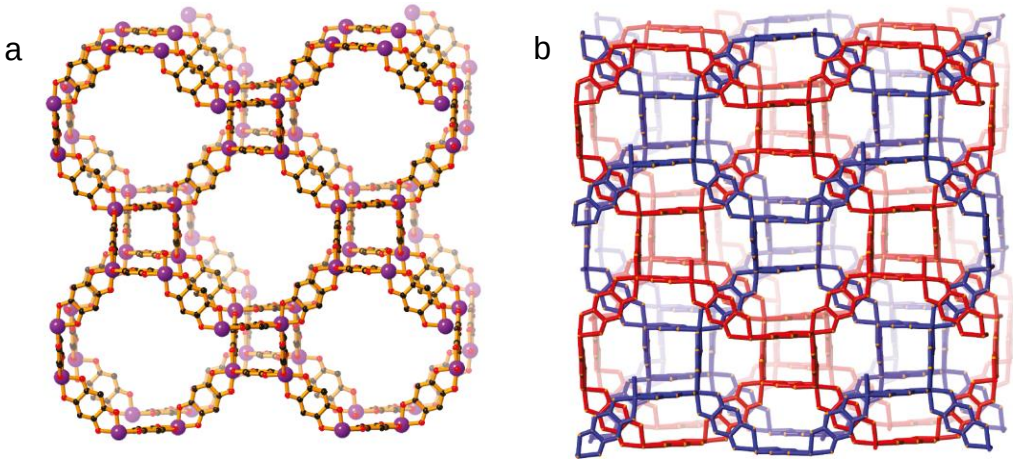

Figure 19: *Different views of $(NBu_4)_2[Fe^{II}_2(C_6O_4H_2)_3]$* ***(a)*** *one of the two $[Fe^{II}_2(C_6O_4H_2)_3]^{2-}$ networks with (10,3)-a topology* ***(b)*** *two independent, enantiomeric, interpenetrating $[Fe^{II}_2(C_6O_4H_2)_3]^{2-}$ networks.*[133]

At the end of 2015, Harris et al.[134] published a 3D new structure formulated as $(NBu_4)_2[Fe^{III}_2(C_6O_4H_2)_3]$ (Figure 20). This compound exhibits a conductivity value of 0.16 S/cm at 298 K, one of the highest values observed for a MOF. This conductivity is produced by the partial reduction of the anilato ligand, in the same serendipitousway as in the 2D anilato-based compound $(Me_2NH_2)_2[M_2L_3]\cdot 2H_2O\cdot 6DMF$.[123]

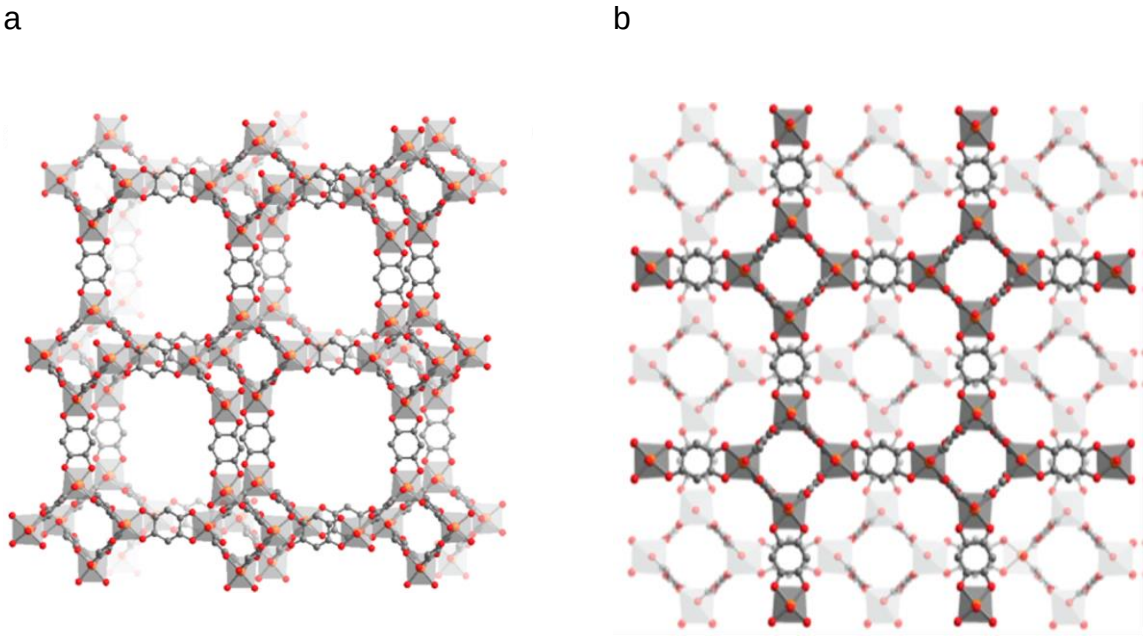

Figure 20: (a) *Crystal structure of $(NBu_4)_2[Fe^{III}_2(C_6O_4H_2)_3]$, showing one of the two interpenetrated (10,3)-a nets that together generate the porous three-dimensional structure.* ***(d)*** *The two interpenetrated (10,3)-a lattices of opposite chiralities that together compose $(NBu_4)_2[Fe^{III}_2(C_6O_4H_2)_3]$. Charge-balancing NBu_4^+ cations are not depicted for clarity.*

2.4. Multifunctional materials based on the anilato ligand

Multifunctional anilato-based compounds could be prepared by “simple” intercalation of cations presenting properties such as SCO, single molecule magnets (SMM), luminescence, etc. The word “simple” has quotation marks due to the difficulty in crystallizing the desired compound. In fact, until now only a few papers presenting 2D networks combining ferromagnetic ordering with functional cations have been published and, sadly, the compounds presented by Clemente et al. did not show spin-crossover.[117, 128] The first report showing ferrimagnetic anilato-based networks was published by our group.[1] In these compounds the cationic layers are formed by three phenazines surrounding one oxonium cation. This cation acts as a chiral template to yield chiral crystals in one case but shows no further functionality. There are no further examples of multifunctional 2D hexagonal layers.

In conclusion, from its easy chemical tuneability to its bigger size, the anilato ligand has several advantages versus the classical oxalate, which have motivated its use in this thesis work. Its bigger size implies bigger hexagonal channels in the honeycomb 2D layers, which enables the insertion of a larger family of cations whilst maintaining the 2D structure. Moreover, anilato compounds show higher T_c and have a less emphasized 2D magnetic character than their homologous oxalato ones. Thus, whilstfor 2D oxalato-based layers changing the inserted cation does not significantly affect the T_c, for 2D anilato-based magnets, this has a noteworthy effect. For instance, the$[(H_3O)(phz)_3][CrMn(C_6O_4X_2)]$ compounds reported in 2013 by our group[1] present T_c of *ca*. 5.5-6.3 K and the ones reported in 2014 by Clemente et al.[117] have a T_c of *ca*. 10 K. This tuning of the T_c with the inserted cations represents an additional advantage provided by the use of the anilato ligand. In another 2D compound presented by Clemente et al.,[128] the fact than the cation is inserted into the hexagonal cavity of the honeycomb layer, allows the anilato layers to be closer to one another than when the cation is placed in-between the layers. This also changes the T_c, making it higher (T_c ≈ 11 K). The change of X not only changes the T_c but also some more physical properties of the final compound like its hydrophobicity and the size of the channels. Finally, as we will see in this Thesis, it is even possible to prepare 2D magnets with very short interlayer separation that results in a weak interlayer interaction with a metamagnetic behaviour.

2.5. Anilato-based materials prepared in this Thesis

2.5.1. Monomeric building blocks of the type $A_3[M^{III}(C_6O_4X_2)_3]$

Among the many mononuclear anilato-based compounds reported to date,[69, 71-91] in the first chapter we will focus just on the tris(anilato)metalate complexes with general formula $[M^{III}(C_6O_4X_2)_3]^{3-}$ since we will use them as building blocks for the synthesis of structures with higher dimensionality and nuclearity.

As in the oxalato series, to synthesize families of 2D anilato-based layered heterometallic compounds (as will be described in chapters 3, 5, 6 and 7) it is necessary to start with monomeric tris(anilato)metallate complexes of the type $[M^{III}(C_6O_4X_2)_3]^{3-}$ as precursors. These precursors, in contrast with the related tris(oxalato)metallate complexes $[M^{III}(C_2O_4)_3]^{3-}$ that are known since the 1930s,[92, 135] were unknown until recently[3, 95, 97-99] except for two reported structures with In(III) and Fe(III).[93, 94]

In 2013, our group published the first examples of 2D M^{III}/M^{II} layered heterometallic anilato-based compounds with two different charge-compensating cations: $[NBu_4]^+$ and $[(H_3O)(phz)_3]^+$ (phz = phenazine). This $[(H_3O)(phz)_3]^+$ cation is generated *in situ* when the phenazine molecules, added as templates, surround a H_3O^+ cation present in the medium and establish moderate H-bonds. The templating effect of this cation leads to an eclipsed disposition of the layers, thus generating hexagonal channels capable of hosting solvent molecules. In this publication, the synthesis of the first four tris(anilato)metallate complexes of the type $[M^{III}(C_6O_4X_2)_3]^{3-}$, with M^{III}/X = Cr/Cl, Cr/Br, Cr/I, Fe/Br and $[NBu_4]^+$ as counterion was described.[1] This was the first report of the rational synthesis of the complexes of the type $A_3[M^{III}(C_6O_4X_2)_3]$.

The rational design of synthetic methods for the preparation of molecular materials has been key for obtaining many materials prepared with the proper choice of molecular precursors (building blocks). For this reason, and in order to prepare a complete series of anilato-bridged 2D heterometallic multifunctional magnets with M^{III} and M^{II} (as was done for the oxalato ligand), we have performed a systematic study to synthesize and characterize monomeric tris(anilato)metalate compounds $A_3[M^{III}(C_6O_4X_2)_3]$ with M^{III} = Cr, Fe and Ga; X = Cl, Br and NO_2 with a wide variety of cations: A = K^+, PPh_4^+, PPh_3R^+ (R = Me, Et, Pr), PBu_4^+, NBu_4^+ and $Nhep_4^+$.

In chapter 1 we report the synthesis, spectroscopic, magnetic and structural characterization of a total of 20 new compounds formulated as $A_3[M^{III}(C_6O_4X_2)_3]$ (M^{III} = Cr, Fe and Ga; X = Cl, Br and NO_2; A = K^+, PPh_3Et^+, PPh_3Pr^+, PBu_4^+, $NHep_4^+$, NBu_4^+ and PPh_4^+. The non-innocent role played by the cation in determining the presence or absence of chirality in the single crystals obtained will be described. We explore the idea that cations with C_3 symmetry, particularly the ones of the type PPh_3R^+ with aromatic rings, can stabilise the structure by extra π-π interactions with the anilato rings, facilitating the, otherwise very difficult, crystallization of these monomeric anilato precursors. Thus, only the six compounds prepared with PPh_3Et^+ and X = Cl and Br are chiral and crystallize as enantiomerically pure crystals (half of the crystals present one chirality and the other half the opposite one). On the other hand, when a different cation was used or when X = NO_2, the monomeric compounds are achiral and present a racemic mixture of both enantiomers in each crystal. Some studies about the role of the cation reveal that the counter-anions may play an important role in the final structure in some coordination compounds. However this role is basically based on the coordination ability of the anion.[136] In the compounds we are presenting, the key role of the cation is much more subtle due to the fact that, in all compounds, the obtained anionic part is the same, and only presents different spatial distributions and may or may not present chirality depending on the number of π–π anion-cation interactions.

The nature, size and presence or not of aromatic rings in the cations also significantly affects the solubility of the final compounds, changing radically between inorganic cations as K^+ and organic bulky cations as NBu_4^+, PBu_4^+ and $PPhR_3^+$, for example. Solubility also slightly changes between the organic cations depending on the size and the presence of π–π interactions, being more difficult to dissolve in the common solvents (such as alcohols, acetonitrile, acetone….) the compounds with more phenyl groups present in the cation.

2.5.2. 2D/3D heterometallic networks with M^{III}/M^{I}

As discussed in previous pages, 2D-(6,3) honeycomb and 3D-(10,3) homometallic anilato-based networks were published some years ago.[4] Albeit, since anilato ligands usually give rise to antiferromagnetic interactions,[69, 100, 121, 122, 133] all these homometallic compounds are not interesting from the magnetic point of view. Therefore, we decided to prepare the same 2D and 3D networks but with two different

metal ions to promote ferrimagnetic couplings and possible long range ordering. This possibility opens up the possible synthesis of the same kind of structures with the anilato ligand that were prepared with oxlato. Although $M^{III}M^{II}$ hexagonal layers are the most common oxalato layers, hexagonal layers combining $M^{III}M^{I}$ metal ions have also been prepared,[137-142] yielding paramagnetic molecular semiconductors, metals and superconductors.[141, 143, 144] Heterometallic 3D chiral lattices are also known in the oxalato family. In these lattices all the metal centres in the $[MM'(C_2O_4)_3]^{n-}$ lattice possess the same chirality and, therefore, the spatial disposition of the metals forms a 3D structure with non-planar rings of 10 metals atoms, each connected to three different rings, giving rise to a (10,3) network. These 3D lattices were first observed for $M^{I}M^{III}$ ions[145, 146] and later were prepared for $M^{II}M^{III}$ ions where, as expected, long range ferromagnetic ordering is observed.[147]

The most common building block used in coordination chemistry are the magnetic d- or f- block metal ions with anionic ligands. In the second chapter, Fe^{3+} and Cr^{3+} based building blocks will be combined with Na^{+} and K^{+} ions. In this chapter two missing links in the oxalato-anilato analogy are solved since the first heterometallic anilato-based $M^{I}M^{III}$ 2D lattices and the first heterometallic anilato-based 3D lattices are presented.

2.5.3. 2D heterometalic honeycomb lattices with new template molecules

In chapter 3, 2D layers combining trivalent and divalent metals in order to achieve ferrimagnetic order will be presented. Since these ligands mediate antiferromagnetic exchange interactions, we can anticipate that the 2D heterometallic lattices of the type $[M^{II}M^{III}(C_6O_4X_2)_3]^{-}$ should afford ferrimagnetic couplings and possibly long range ferrimagnetic order. Furthermore, if, as expected, the magnetic coupling depends on the substituent groups X of the ligand, a change in X is expected to modify the magnetic coupling and the T_c. To prove this idea, 2D heterometallic lattices with different anilato ligands (X = Cl, Br) have been synthesized.

The change of the ligand not only leads to a modification of the magnetic ordering and the possibility to tune it. Due to the bigger size of the ligand, the hexagonal 2D layers formed would be bigger than those obtained in the oxalato series, opening the possibility to obtain permanent channels big and stable enough to act as MOFs.

The search for new porous coordinaton polymers (PCPs) has been increasing exponentially during the last years, as shown in several bibliographic databases such as Scopus or Web of Science. These 21st century materials have a porous ordered network that allows its use in gas storage and gas separation[148-151], water adsorption[152], sensors[153, 154], catalysis[155], photocatalysis for water splitting[156], luminescence,[157] energy storage and transfer,[158-160] biomedical applications[161], etc. In order to favour these applications, a higher pore size is required: a big pore size is a clear advantage for the previously mentioned applications. But, this bigger pore size entails a drawback to add other cooperative properties, like magnetic ordering. It is well known that porosity leads to the isolation of the active building units, and, hence, to a decrease of the cooperative effect between them.[162-164] For this reason, the synthesis of PCPs with cooperative magnetic properties constitutes a fascinating challenge in Materials Chemistry and very few porous materials with long range magnetic order have been reported.

The first step to achieve the synthesis of porous magnets is the control of the final honeycomb lattices, to “force them” to crystallize in an eclipsed way in order to obtain networks with hexagonal channels. The most challenging part for a synthetic chemist is to achieve the total control of the final product. Crystal engineering, the design and synthesis of molecular solid state structures with desired properties, based on a rational and coherent choice of the starting building blocks and their possible interactions, is the base to accomplish maximum control.

In the article of our group in 2013[1] two different kinds of $[M^{II}M^{III}(C_6O_4X_2)_3]^-$ layers were presented: the first one with the cation $[(H_3O)(phz)_3]^+$ formed by phenazine in presence of oxonium, adopting a propeller-like structure, and a second one with NBu_4^+. In the first case, the crystallization process leads to high quality crystals. The oxonium surrounded by three phenazine molecules acts as a template in the crystallization process, enabling the eclipsed orientation in the 2D honeycomb layers. This role is clearly due to the aromatic rings of the phenazine that establish strong π-π interactions with the anilato rings and stabilize the eclipsed configuration. Curiously, in the case of the second type of layers, the formation of the first salt with formula $[NBu_4][M^{II}M^{III}(C_6O_4X_2)_3]$ (M^{III} = Cr, M^{II} = Mn and X = Cl) happened in a serendipitous way while trying to introduce a SCO cation after many attempts to obtain it in a rational

way. This structure is based on alternating layers with a shifted disposition, avoiding the formation of hexagonal channels.

To test the importance of the templating molecules, we have chosen benzene derivative molecules to create a rational way to obtain eclipsed layers with hexagonal channels. We have selected benzene derivatives (PhX where X = Cl, Br, I, F, CH_3, OH, NO_2, CN) anticipating an extra stabilization thanks to the π–π stacking that may occur between benzene derivatives and the aromatic ring of the anilato ligand. Very recently, Robson et al. published a new family of eclipsed 2D network with hexagonal channels with the NEt_4^+ cation.[125] In this case, obviously, the cation does not favour the eclipsed orientation thanks to the formation of π–π stacking, but to hydrogen bonding interactions, which were impossible (or almost impossible) to predict beforehand. In fact the butyl groups of the NBu_4^+ cations used in the first published family might also establish similar C-H···O to those observed in the NEt_4^+ example but in the NBu_4^+ compounds the anionic lattices present alternating orientation.

This thesis also explores the value of benzene derivatives as template molecules for obtaining eclipsed 2D networks with NBu_4^+ as cation. Thus, we have prepared the same $[MnCr(C_6O_4X_2)_3]^-$ lattices with NBu_4^+ in which the 2D anilato layers adopt either an eclipsed or a parallel orientation depending on the inclusion or not of benzene derivatives in the reaction mixture. This indicates that the benzene derivatives could be effectively used as a potential scaffold for the design of eclipsed networks with other cations.

The second example confirming the importance of the π–π interactions created between the benzene derivatives and the aromatic rings of the anilato ligand to favour the formation of the eclipsed configuration instead of the alternated one, is the preparation of 2D hexagonal networks with the oxonium cation as the only cation. Each hexagonal channel is filled with one oxonium, water and benzene derivatives. An analogous structure without benzene derivatives has not been reported so far.

Further studies on this last family of templates has to be done to fully understand all the advantages that they provide and if it is possible to remove them from the channels without collapsing the crystal structure. If this was the case, a door would be

open to the possible use of these lattices with empty holes as PCPs for gas or solvent absorption, separation, etc.

2.5.4. Lanthanoid compounds:

In all the anilato-based compounds previously named, only anilato ligands with the same X group were used (X = H, Cl, Br, I, NO_2)[1, 4, 129], while the possibility of using heterosubstituted ligands $(C_6O_4XX')^{2-}$ remains unexplored.

In 1966, the 2-chloro-5-cyano-3,6-dihydroxybenzoquinone molecule and its absorption spectra was reported.[165] In 2015 Mercuri et al. further extended the luminescent study in solution of this ligand,[97] showing the effect in the luminescence caused by the change of one of the substituents. This functional asymmetric ligand opens de door, not only to synthesize the equivalent 2D molecular magnets and extend the T_c range, but also to adding an extra functionality as the luminescence, besides the extra functionality provided by the cation as SCO,[166] SMM,[167] porosity,[168] etc. Up to now, using this assymetric anilato ligand only tris(anilato)metallate complexes with Cr(III), Fe(III) and Al(III) are known.[97] Unfortunately, the Cr(III) and Fe(III) complexes show a quenching of the luminescence that precludes the preparation of luminescent ferrimagnets with Cr(III)-M(II) or Fe(III)-M(II) anionic layers.

Therefore, in order to improve the luminescent properties of 2-chloro-5-cyano-3,6-dihydroxybenzoquinone ligand we have decided the use of trivalent lanthanoid ions. Publications based on lanthanoid ions have increased dramatically in the past few years due to their structural versatility[169] and wide potential to form luminescent compounds.[170] These lanthanoid ions are characterized by the availability of the 4f orbitals, from $4f^0$ to $4f^{14}$ (from La^{+3} to Lu^{+3}). This configuration results in a wide variety of electronic energy levels that can give rise to luminescent properties[171-177] and, in some cases, also interesting magnetic properties.[178-180] The energies of these levels are well defined due to the shielding of the 4f orbitals by the filled sublevels. These levels are extremely sensitive to the chemical environment of the lanthanoid ion. Therefore, a small change in this environment can drastically affect the luminescence properties.

Nevertheless, due to the parity-forbidden f-f transitions, the direct excitation of the lanthanoid ions does not lead to a strong luminescence. A solution to this problem is the use of “antennas” (also known as luminescence sensitizers). The antenna acts absorbing the incident light and transferring this excitation to one of the excited states of the lanthanoid metal by intramolecular transfer and, finally, if there is no quenching process, luminescence is produced. This is a very reduced summary about the sensitization process. In fact, the sensitization of Ln(III) luminescence by organic ligands is an intricate process, so it will not be fully discussed here, as it has already been widely discussed in various articles and books.[173, 181, 182]

Compounds combining Ln(III) ions with oxalato[183-186] and with anilato ligands[100] with X = H, Cl were previously reported, but no luminescent measurements were performed. Lanthanoid coordination anilato-based 2D and 3D polymers have already been presented (see above).

Our group has recently prepared dimers of Ln(III) with nitranilato ligand (X = NO_2) that show luminescent properties.[101] In the case of nitranilato, the luminescence of the ligand dominates over the luminescence of the lanthanoid ions. The most likely explanation for this fact is its shorter lifetime and higher oscillator strength.[187, 188] Dimers with oxalato were also published in 2010. In this case, no luminescence properties were described but SMM behaviour was found instead.[189]

The perfect scenario for this kind of compounds is not a hegemony of one of the building block versus the other, but a synergy of both to improve the luminescence that they can both show separately. This fact may allow the use of these luminescence lanthanoid compounds in many technological applications, like imaging probes (MRI) in biomedicine[190-201], fabrication of OLED’s[202-204] or sensors.[172, 205-207]

Very recently our group has published a study showing the key role played by the solvent in the synthesis of these anilato-based 2D networks with lanthanoids. This study was performed with Er(III) and the ligand bromanilato ($C_6O_4Br_2$) with three different coordinating solvents[208] as H_2O, DMSO (dimethylsulfoxide) and DMF (dimethylformamide).[209] The different sizes and shapes of the solvent molecules led to three different 2D compounds formulated as: $[Er_2(C_6O_4Br_2)_3(H_2O)_6]\cdot 12H_2O$,

$[Er_2(C_6O_4Br_2)_3(DMSO)_4]\cdot 2DMSO\cdot 2H_2O$ and $[Er_2(C_6O_4Br_2)_3(DMF)_6]$, where the coordination number and geometry change depending on the solvent (Figure 21).

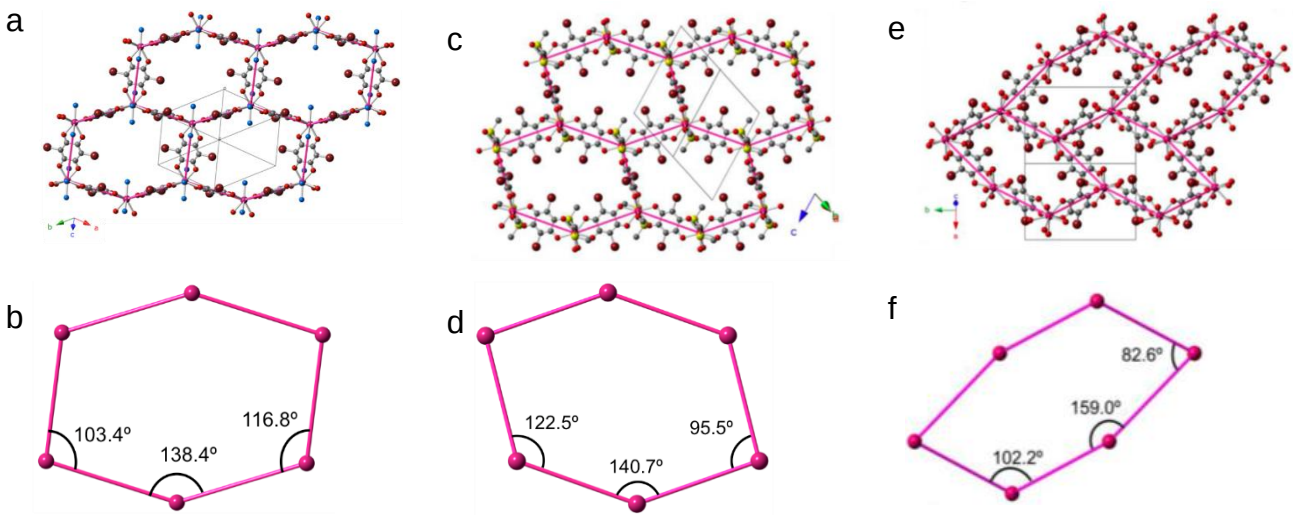

Figure 21: (a) *Hexagonal layer viewed along the [-1,-1,1] direction and* ***(b)*** *distorted hexagon in compound* $[Er_2(C_6O_4Br_2)_3(H_2O)_6]\cdot 12H_2O$ ***(c)*** *Hexagonal layer viewed along the [1,-1,0] direction and* ***(d)*** *distorted hexagonal ring in compound* $[Er_2(C_6O_4Br_2)_3(DMSO)_4]\cdot 2DMSO\cdot 2H_2O$ ***(e)*** *Hexagonal layer viewed along the [1,0,1] direction and* ***(f)*** *distorted hexagonal ring in compound* $[Er_2(C_6O_4Br_2)_3(DMF)_6]$.[209]

Since the three compounds are prepared under the same conditions, the changes between them are only attributable to the solvent used in each case. Four crystallization characteristics are analysed to widely depend on the solvent: i) the available space for the crystallization solvent molecules into the hexagonal cavities, ii) the distortions presented in the hexagonal cavities, iii) the coordination number and geometry of the lanthanoid ions and iv) the layer-layer separation. Thus, even though the three compounds present a (6,3)-2D honeycomb lattice, some important differences are found between them. Thus, the remaining empty space in the hexagonal cavities follows the logical trend, the smaller the solvent molecule, the more space remains available. The distortions of the hexagonal cavities increase as the size of the solvent molecule increases. The coordination number decreases using solvent with higher steric hindrance (DMSO) and the interlayer space increases with the size of the solvent molecule.

In this Thesis, the viability as antenna of the heterosubstituted chlorocyananilato 2-chloro-5-cyano-3,6-dihydroxybenzoquinone ligand is used with different lanthanoid ions and various solvents coordinated to these ions. The key role of the solvent in

these compounds will also be analysed. Since these solvent molecules fill the channels of the structure, preventing the absorption of gases or other solvent molecules, we will explore the possibility to remove these solvent molecules under vacuum, heat or a combination of both in order to determine if these compounds could be categorized as luminescent MOFs, which would be an important achievement.[171, 172, 175, 210-220]

2.5.5. Spin Crossover (SCO) compounds:

Under certain conditions, some coordination compounds of transition-metal ions may exhibit a switching phenomenon where the central metal ions change the spin state from high spin (HS) to low spin (LS). This change occurs under the influence of external perturbations such as a change of temperature, application of pressure or an external magnetic field and irradiation with light.[221-226] The name of this particular phenomenon is spin transition (ST) or, how it is commonly known, spin crossover (SCO). These SCO metal centres show, under external alterations[227, 228], a change in electronic structure, provoking structural changes in the whole molecule. For a simple and complete change in spin state, the spin crossover temperature (T_{SCO} or $T_{1/2}$) is the temperature at which the two states of different spin multiplicity are equally present. Sometimes, the transitions are not simple and happen in several steps. In these cases, the previous definition of T_{SCO} is not applicable. Moreover, SCO complexes may be classified into two groups depending on the shape of the SCO curve: complexes where the spin transition between HS and LS state occurs abruptly within a few Kelvin and SCO complexes where the spin transition occurs gradually over a wide temperature range.[229-231] In this Thesis, we are going to focus in simple spin transitions, so we are not going to go into deeper details about multi-step spin transitions. When the transition is incomplete, in either low or higher temperatures (residual low spin or high spin fractions), the T_{SCO} is defined as the temperature at which 50 % of the SCO active metal centres have changed their spin state.[222, 223]

The spin-crossover effect should be observed in *d*-block metal complexes for metal ions with d^4-d^7 configurations. The largest number of compounds with SCO is found for d^6 configuration, more specifically six-coordinate iron (II).[221, 227, 229, 232-236] Recently, iron (III) compounds exhibiting SCO effect are being extensively studied.[230, 235-237]

The spin state of a metal centre depends on the nature of the ligand field.[238] In weak fields, the ground state stabilized is the HS and, on the contrary, the LS is favoured by strong fields. For an octahedral *d*-block metal, the splitting of the energy of the d orbitals in the t_{2g} and e_g sets allows for HS and LS configurations to exist. In HS, the multiplicity is maximum and the d electrons are distributed over the t_{2g} and e_g sets. In the LS state, the minimum multiplicity is found: the t_{2g} set has to be completely full before electrons start filling the e_g set. If we focus on iron (II) ions with a d^6 configuration, four unpaired electrons will be found in HS ($t_{2g}^4e_g^2$) whereas there are no unpaired electrons in LS ($t_{2g}^6e_g^0$) (Figure 22).[229, 238]

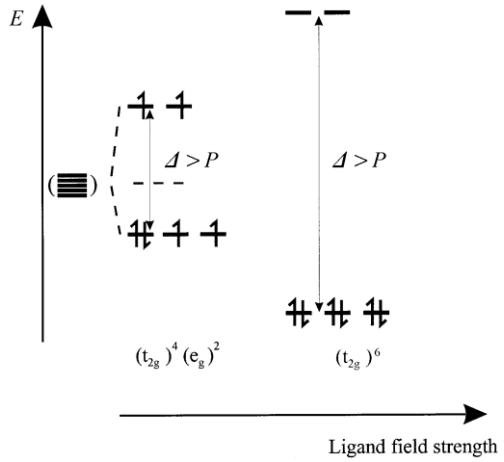

Figure 22: *Electronic configuration for a d^6 iron (II) ion, in the LS state, in the HS state and equilibrium between these two states in the case of thermal spin crossover. Δ stands for the cubic ligand field parameter and P for the mean spin-pairing energy.*[229, 238]

Fe(II) ions have a relative low charge and, therefore, the ligand field is relatively weak with many ligands, thus, spin pairing is not very favoured and it is possible to play with many ligands to obtain relatively stable HS or LS complexes, depending if those ligands favour a weak or a strong ligand field. Similarly, it is relatively easy to find ligands that provide an intermediate ligand field, therefore producing a SCO complex (Figure 22).

For these intermediate ligand fields, the energy difference between the two states is very small and an external change provokes a change in the state configuration, generating the SCO effect. The most usual external change used to provoke this transition is a change in temperature.[223]

Other d-block metal ions in which is common to found the SCO effect, although less usual than in Fe(II) ions are Fe(III) complexes, [221, 227, 229, 230, 232-237] with a d^5 configuration and Co(II) ions, with a d^7 configuration.[236, 239-241]

Some of the most important consequences of a spin transition are the changes produced in the metal-ligand bond distances due to the change in the occupancies of the t_{2g} and e_g orbitals and changes in the magnetic properties, resulting in a clear increase in the magnetic moment of the system when the spin configuration changes from low spin to high spin. Conventional spin transition curves are obtained by measuring the high spin fraction (γ_{HS}) *vs*. temperature (Figure 23). The γ_{HS} parameter can be obtained from magnetic measurements, Mössbauer, electronic and vibrational spectroscopies or single-crystal X-ray diffraction (metal-ligand bond distances).[242]

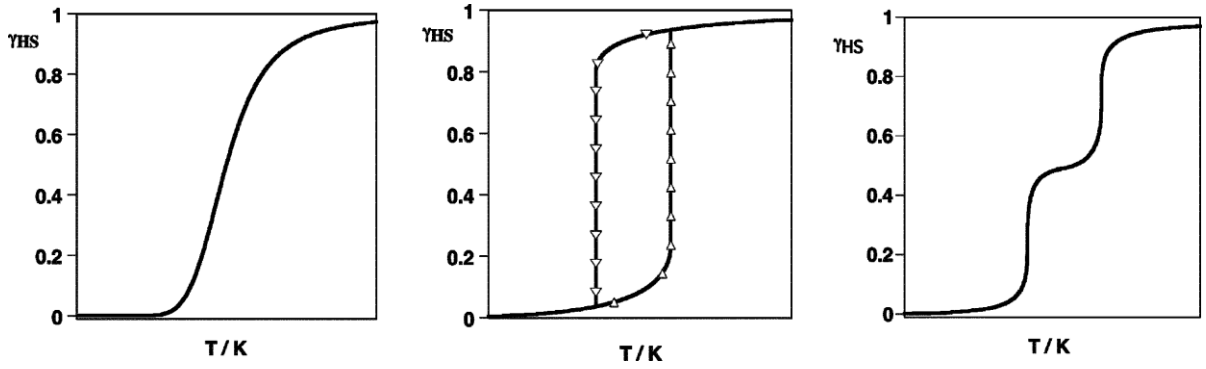

Figure 23: *Different types of spin transition curves representing the high-spin molar fractions vs. temperature. From left to right: gradual, abrupt with hysteresis and multistep.* [242]

Nowadays, the challenge is not only to obtain SCO complexes but to synthesise them rationally, with control of their T_{SCO} and transition curve form. The curve form is determined by the cooperativity in the solid lattice (the efficiency by which structural changes at every single SCO metal sites are transmitted through the bulk material) which its fundamental in the final SCO material since it determines it potential applicability.[224, 243] Structural changes depend on the metal ion and on the metal-ligand combination.[244] In octahedral metal ions with d^6 (S = 0 → S = 2) and d^5 (S = 1/2 → S = 5/2) configurations, the structural changes are bigger than for d^4 (S = 1 → S = 2) or d^7 (S = 1/2 → S = 3/2) since the increase of the electron density in the antibonding e_g orbital is more pronounced. Furthermore, the shape of the SCO transition also depends on the dimensionality and strength of the inter-molecular interactions in the bulk solid.[233, 245] For instance, planar wedge shaped aromatic ligand donor groups with

intermolecular π-π interactions are quite effective in inducing cooperativity because they present a large contact surface area between them and its neighbours molecules. Moreover, since hydrogen bonding, as well as other short intermolecular contacts, transmit structural changes through the bulk materials with high efficiency, then changes in molecular conformation during SCO are easily propagated between molecules.

Regarding the experimental techniques used to identify the SCO effect, measurements of the magnetic susceptibility as a function of temperature, $\chi_m(T)$ *vs*. T, is the main technique used (Figure 24).

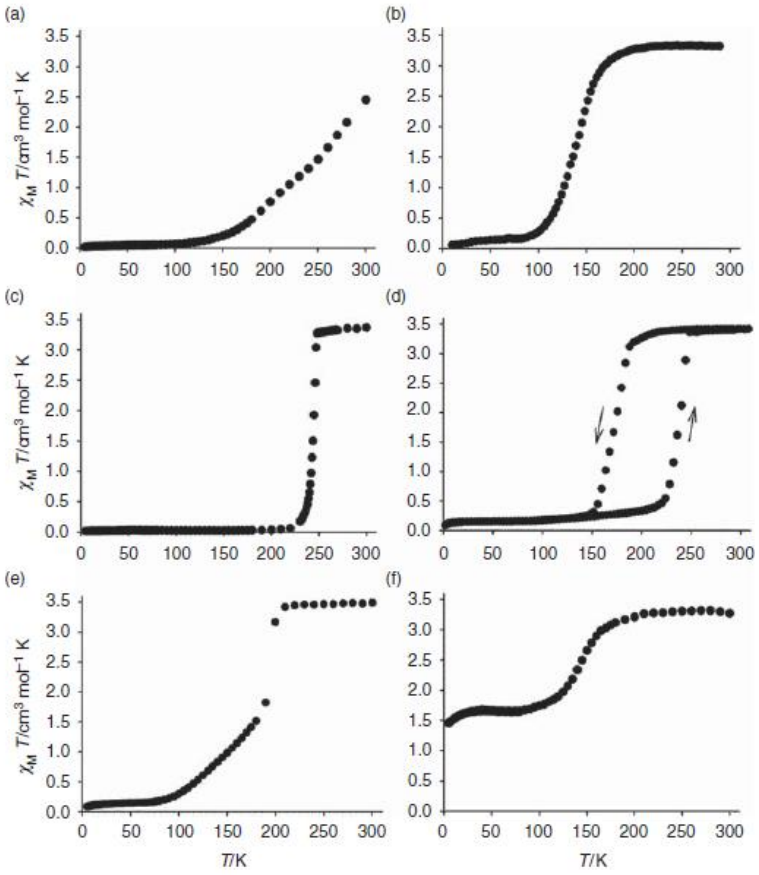

Figure 24: *Representative SCO transitions: from* ***(a)*** *to* ***(c)****: increasing degrees of abruptness;* ***(d)****: thermal hysteresis;* ***(e)****: discontinuous transition;* ***(f)****: incomplete transition.*[222, 246-249]

The spin transition from a diamagnetic LS state to a paramagnetic HS one is easily detected by a change in the magnetic susceptibility. The product of $\chi_m T$ for a SCO material is determined by the temperature dependent contributions of χ^{HS} and χ^{LS}. This result can be compared with the X-ray structural studies (as will be seen in chapter 5).

These materials are considered binary switches and are potentially useful materials for many applications such as memories, switching devices, sensors, MRI contrast agents,…[250, 251] Some advantages of these materials are, for example, the easiness to functionalize them, which allows to prepare SCO compounds with a wide range of flexibility. Moreover, the presence of a hysteresis, which is a must for molecular bistability and to make SCO compounds potential candidates for applications in memory and data storage devices (even though, for their exploitation in memory devices the bistability must be associated with a response function). In addition, those SCO compounds in which the transition is accompanied by a change in colour are well suited for the development of display devices. Despite this, not all SCO complexes are useful since the switching should occur at technologically relevant temperatures in order to qualify for potential real application, and that means that the hysteresis loop should fall approximately at room temperature. All the potential applications of SCO compounds generate a huge interest for these materials and for the understanding and control of the SCO process.[229]

2.5.5.1. LIESST: Light-Induced Excited Spin-State Trapping Effect:

In the mid-eighties, the LIESST effect was first observed accidentally in solution by McGarvey et al.[252] and, shortly after, in solid state by Decurtins et al.[253] In these first examples, a Fe(II) SCO compound in the LS state was converted by light irradiation into the metastable HS state, which has a virtually infinite lifetime at low enough temperatures.[229, 253, 254] If temperature is gradually increased, the complexes remain in the metastable HS state for a short time but, they eventually come back to the stable LS state.[255] In a later experiment, it was discovered that the opposite process is also possible and photoswitching from HS to LS state may also occur when a complex is irradiated with light (reverse-LIESST).[256] Green light of 514 nm from an Ar ion laser is the most widely used light to irradiate SCO complexes and the Fe(II)-based SCO complexes are the most usual compounds presenting LIESST.[233, 257-259]

When irradiating a Fe^{II}-based sample at low temperatures with an Ar ion laser, a transition between the $^1A_1$ ground state and ^1T_n state occurs (Figure 25). The excited singlet state occupation is very brief and quickly decays to the ground state. However, an alternative pathway to the decay is possible due to spin orbit coupling. Thus, an intersystem crossing step to the triplet states $^3T_1$ or $^3T_2$ and then another either to the

$^1A_1$ ground state or to the $^5T_2$ metastable state is possible. The system remains trapped in the HS state with a considerable long lifetime if the temperature is kept low enough in order not to surpass the energy barrier between the HS and the LS potential surfaces.[233, 257-259]

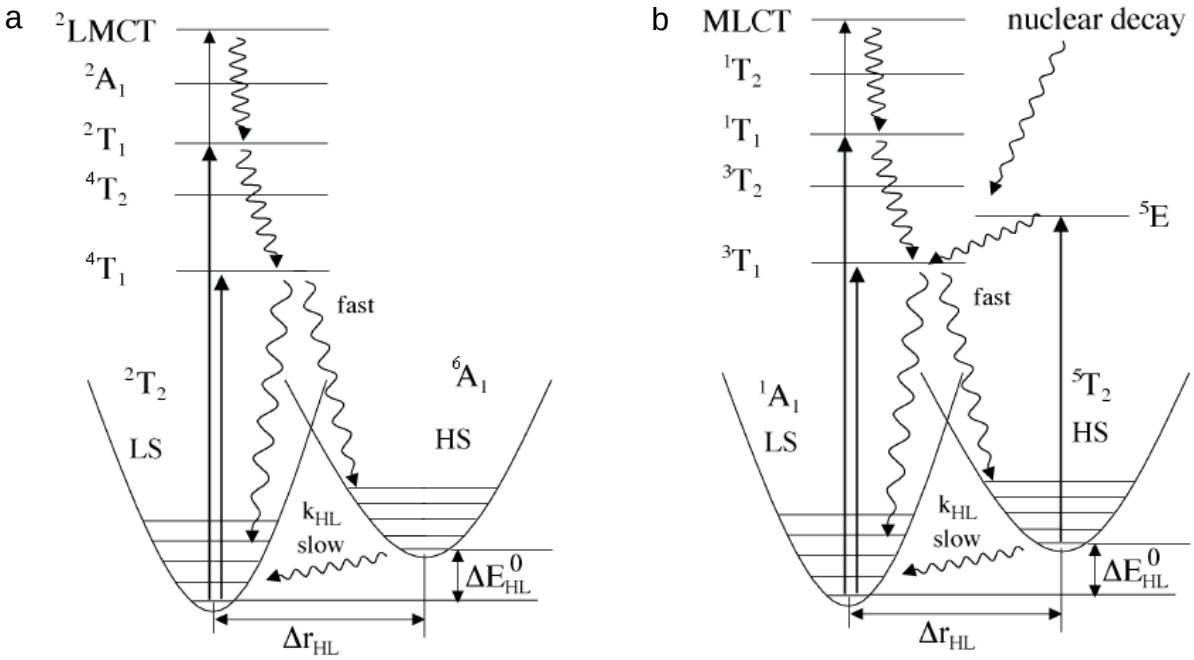

***Figure 25**: Jablonski diagrams of: **(a)** d^5 SCO system (Fe^{III}) and **(b)** d^6 SCO system (Fe^{II})*

The most usual way to measure photomagnetic properties of SCO complexes is by irradiating the sample at very low temperatures (usually 10 K) with an optical source coupled to a SQUID magnetometer. When the magnetic signal saturates, the irradiation is stopped. At this point, the equilibrium between the population and relaxation of the excited state reaches a maximum. Then, temperature is slowly increased (usually at a rate of 0.3-0.4 K/min). The compound remains in the metastable HS state until the thermal energy barrier between HS and LS is overcome and the magnetic signal drastically decreases and quickly recovers its initial value. The inflexion point of this decay, measured as the maximum of the $\delta\chi_M T/\delta T$ *vs*. T curve, determines the so-called T_{LIESST} temperature (Figure 26).

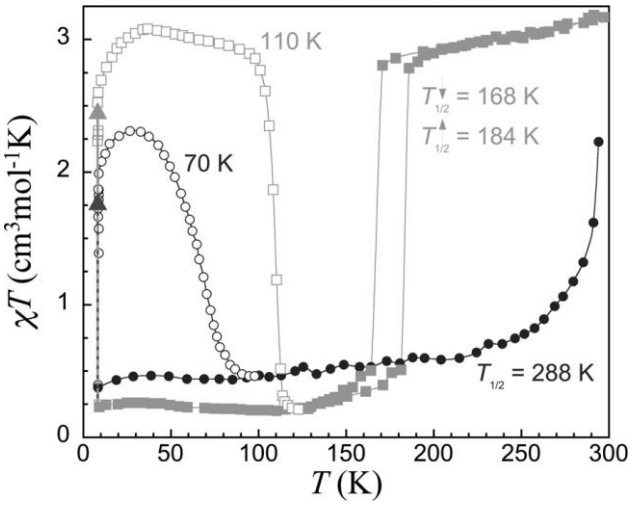

Figure 26: *Spin transition curves and LIESST properties of the compound [Fe(3-bpp)$_2$](BF$_4$)$_2$·xH$_2$O; for x = 3 white circles: LIESST experimental and subsequent heating, full circles: cooling mode; for x = 0: white squares: LIESST experiment and subsequent heating mode, full squares: cooling and heating mode prior to photo-excitation*[260]

Compounds presenting LIESST effect are gaining a lot of importance with the goal of obtaining suitable materials for technical applications such as displays, information storage, sensors, optical switchers, etc.[250] The main handicap to achieve this application is the LIESST temperature domain. The lifetime of the photoinduced HS state could be long enough at low temperatures, but the relaxation process thermally activates as the temperature increases and, in a very short time, the stored light-induced information disappears. To overcome this drawback, it was recently proposed to produce the light-induced phenomenon in the centre of a thermal hysteresis in some iron(II) molecular materials.[261-263] The main disadvantage is that this technique requires to use an iron(II) SCO material with a thermal hysteresis of around 100 K (with typical working temperatures from *ca*. 250 K up to *ca*. 350 K), a value not yet reached.

Hybrid materials with SCO cations and oxalato-based anions are well-known in the molecular materials community. Most of them were prepared with the [Fe(3-bpp)$_2$]$^{2+}$ cation (Figure 27) by Giménez-López et al.[17, 20, 25, 27, 264] Few years later, many different SCO cations based on Fe(II) and Fe(III) were inserted into 2D and 3D oxalato networks by Clemente et al.[16, 18, 19, 21-24, 26, 265, 266] Interestingly, the [Fe(3-bpp)$_2$]$^{2+}$ cation presents SCO in all the reported examples with oxalato-contanining anions, showing the robustness of the SCO in this cation. Moreover, this SCO behaviour changes when the sample is heated to remove the solvent molecules

and later rehydrated.[17, 20, 27, 264] This is a well-characterized behaviour in $[Fe(3\text{-}bpp)_2]^{2+}$-based compound with oxalato-contaning anions that is also found in discrete compounds formed by $[Fe(3\text{-}bpp)_2]^{2+}$ cations and $[Cr(C_6O_4X_2)_3]^{3-}$ units (X = Cl, Br), as will be shown in chapter 5 of this Thesis. In contrast, when the $[Fe(3\text{-}bpp)_2]^{2+}$ cations are inserted into 3D oxalato-based networks, the magnetic order in the 3D lattice at *ca*. 3 K is maintained but the SCO is lost. This fact does not change with desolvation.[25]

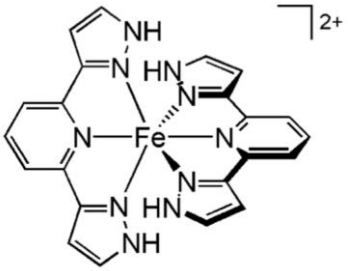

***Figure 27**: Structure of $[Fe(3\text{-}bpp)_2]^{2+}$ cation.* [231]

Other Fe(II)-based SCO cations inserted into oxalato networks are: $[Fe^{II}(imid_2\text{-}trien)]^{2+}$, $[Fe^{II}(trend(6\text{-}CH_3\text{-}py)_3]^{2+}$, $[Fe^{II}(trend(imid)_3)]^{2+}$ and $[Fe^{II}(pyimH)_3]^{2+}$, all of them gave rise to 3D oxalato-based magnets and all of them (except the second one) present SCO behaviour in the final oxalato compound.[26, 265]

Fe(III)-based SCO cations are, undoubtedly, the most used family of SCO cations to insert into oxalato networks. Clemente et al. made a thorough study including, not only different cations but also different solvents. The most used cation is the $[Fe(sal_2\text{-}trien)]^+$ which gave rise to a lot of different structures: 2D structures with CH_2Cl_2, $CHCl_3$, CH_2Br_2 and $CHBr_3$ as solvents and a 3D structure with CH_3OH. 2D structures showed complete photoinduced SCO transitions and the 3D structure showed a more gradual transition.[19, 21, 24] Also a $[Mn^{II}_2(ox)_3]^{2-}$ 2D layer with the above mentioned cation, showing a gradual SCO transition, has been reported.[16] Other cations derived from $[Fe(sal_2\text{-}trien)]^+$ have also been used: $[Fe(5\text{-}NO_2sal_2\text{-}trien)]^+$, $[Fe(5\text{-}CH_3Osal_2\text{-}trien)]^+$, $[Fe(5\text{-}Brsal_2\text{-}trien)]^+$, $[Fe(5\text{-}Clsal_2\text{-}trien)]^+$, $[Fe(4\text{-}Brsal_2\text{-}trien)]^+$, $[Fe(3\text{-}Brsal_2\text{-}trien)]^+$, $[Fe(3\text{-}Clsal_2\text{-}trien)]^+$, $[Fe(5\text{-}CH_3Osal_2\text{-}trien)]^+$ originating 2D and 3D oxalato-based structures with a wide variety of SCO transitions: complete, partial and no SCO behaviour (the Fe(III) centres remain in HS or in LS)[18, 22, 23] In all these examples the oxalato-based layers with SCO cations inserted are of the type Cr^{III}-Mn^{II}.

2.5.6. Luminescent Compounds:

The preparation of multifunctional compounds, being magnetic ordering one of these properties, is the main aim of this thesis.

One of the properties which has been attracting more interest in the past years is luminescence. In consonance with this emerging interest, 2015 was proclaimed The International Year of Light and Light-based Technologies (IYL 2015) by the United Nations General Assembly (http://www.light2015.org/Home.html). The energy demand is increasing year after year, with the direct consequence of global warming and CO_2 emissions. In order to start reversing climate change and to reach a sustainable energy model, one of the principal milestones is the development of high-efficiency light sources like solid-state lighting (SSL), light-emitting diodes (LEDs) and organic light-emitting diodes (OLEDs) that can convert electricity into light with a much higher efficiency than conventional lighting sources.[267] LEDs are formed by inorganic semiconductors containing a combination of different elements and provide highly efficient and convenient light sources of different colours.[267-282] OLEDs are flat light sources where the photon output is generated applying electric energy inside a multilayered thin film structure.[283-291] Research on light emitting devices, preferably white light emission, is continuously increasing in search for high quality solid-state LEDs and OLEDs that can beat the incandescent and mercury-containing fluorescent lighting. Mercury-based fluorescents are the most commonly used white-light sources nowadays. This systems are based on mercury releasing vapours to excite phosphor semiconductors, achieving white composite photoluminescence.[292, 293] But the negative environmental and human health consequences of the continued use and exposition to mercury are widely known. Tremendous efforts are being dedicated to the search of, not only more energy efficient and cheaper but also safer and environmentally friendly, white phosphor materials.[267, 270, 272, 273, 277, 278, 280]

The most common type of white phosphor materials are three: (i) monochromatic emitters (which emit in the whole visible spectrum), (ii) dichromatic emitters (that mix blue and yellow light) and (iii) trichromatic emitters (that mix red, green and blue light). Dichromatic and trichromatic emitters are the most efficient ones and show higher luminescence, and thus are the most studied ones.[293, 294]

In the field of phosphor emitters, heavy metal complexes have an important role due to their rich excited state properties and their wide applicability for the preparation of organic light-emitting diodes, electro-chemo-luminescence, photovoltaics, chemical sensors and bioimaging probes.[295-302] For the heavy-metal complexes with a d^6, d^8 and d^{10} electron configuration, Ir(III) complexes (d^6) have been proven to show important phosphorescent emission at room temperature. This intense phosphorescence is due to the many types of excited states that can be formed depending on the metal centres and ligands, such as metal-to-ligand charge transfer (MLCT), intraligand charge-transfer (ILCT), ligand-to-ligand charge-transfer (LLCT), metal-centred (MC) excited states, metal-metal-to-ligand charge-transfer (MMLCT), ligand-to-metal-metal charge-transfer (LMMCT) and metal-to-ligand-ligand charge transfer (MLLCT) states. The phosphorescence of heavy-metal coordination compounds is complex and almost unpredictable as it strongly depends on the metal centre, the ligands, the intramolecular and intermolecular interactions, the environment…[286, 300, 303-308] But, amongst heavy metal complexes, cyclometallate iridium (III) complexes are taking on greater importance as one of the most potential luminous component of OLEDs and LEDs due to, among other characteristics, their wide chemical modifications, short triplet lifetime and colour adjustability.[309-313]

The cyclometalated iridium (III) complexes can be classified into two main groups: (i) the neutral complexes containing cyclometalated ligands and other anionic ligands and (ii) the cationic complexes containing bidentate ligands like bipyridine and phenantroline. An important compound of this family is the one formed by two phenyl-pyridine and one bi-pyridine ligands ($[Ir(ppy)_2(bpy)]^+$), which emits in the yellow part of the visible spectra.[314-316] The most significant property of this compound is the photophysical changes induced by a slight modification in the bi-pyridine ligand.[317, 318] This fact allows the preparation of a whole family of very similar compounds emitting in different parts of the visible spectra.

2.5.7. Single Molecule Magnet (SMM) Compounds:

Since the discovery of single molecule magnets (SMM) in the 90's,[319] the molecular nanomagnets' area has been continuously developing. A SMM is a molecule that can be magnetised in a magnetic field and that will remain magnetised even after switching off the magnetic field. The first SMM was presented in 1991 and it was

composed by dodecametallic manganese cages {Mn_{12}}, with formula $[Mn_{12}O_{12}(O_2CCH_3)_{16}(H_2O)_4]\cdot 4H_2O\cdot 2CH_3CO_2$ with a spin ground state of S = 10 and presented magnetic hysteresis of molecular origin at low temperature.[320, 321] Due to the fact that this behaviour had only been reported for bulk ferromagnets or in magnetic nanoparticles, this discovery was a turning point in molecular magnetism. SMMs become magnetized in presence of a magnetic field and show slow relaxation when the magnetic field is removed. Moreover, the fact that every single molecule functions as a nanoscale, single-domain magnetic particle exhibiting the classical macroscale property of one traditional magnet made the publication of this family a significant development, since the magnetic "response" comes from individual and non-interacting molecules and each molecule has a magnetic moment and magnetic anisotropy large enough to function as a magnet. This means that the magnetic properties of SMM are not due to cooperative effects within magnetic domains, but to the molecule itself. Before this, magnets were based on metallic and ionic lattices.

The magnetic moment of the SMM molecule can be magnetized in response to an external magnetic field, and its spin can be either "up" or "down" along the axial magnetic anisotropic axis. One of the most important physical properties present in SMMs is the slow magnetization (*M*) relaxation at low temperature leading to a blocking of the magnetization below a specific temperature, "blocking temperature" (T_B), provoking a hysteretic behaviour. This magnetization occurs because of the large energy barrier between the spin-up and the spin-down state that allows that, below the blocking temperature, the system can be trapped in one of the high-spin energy wells. SMM molecules can be considered as single domains since the magnetic order exists solely within them. There are some characteristics that every molecule must have to present SMM behaviour: i) a very high spin (HS) ground state (S_T) and ii) a large magnetic anisotropy (*D*). The combination of these two properties may create an energy barrier between positive and negative m_s states, creating a superparamagnetic blocking at low temperatures. In the dodecametallic manganese cages {Mn_{12}} the ground state is very anisotropic, and, this anisotropy of the spin introduces an energy barrier to reorientation of the magnetisation of the molecule. The behaviour of the SMMs molecules is analogous to the previously known superparamagnets, but it occurs in a single molecule, which much smaller than a nanoparticle.[322-324]

The magnetization of SMM molecules can relax through an under-barrier mechanism via quantum tunnelling by the mixing of the “up” and “down” states. If we focus on the Mn_{12}-acetate hysteresis loop (Figure 28), we can observe steps at regular intervals in the plot of magnetization versus magnetic field. These steps correspond to an increase in the rate of change in magnetization occurring when there is an energy coincidence of the levels on the opposite parts of the double well potential (Figure 28). For these coincidence levels field values, tunnelling of the magnetization is allowed and, therefore the relaxation rate increases. These coincidences in the “up” and “down” states could be caused by low symmetry components of the crystal field or by an external magnetic field (i.e: a magnetic order in the 2D network where the SMM cation is inserted).[319]

The fact that the molecule “remembers” the direction of the applied field makes these molecules potential candidates for information storage. Since in SMMs molecules the magnetic information is being stored at a molecular level, this means several orders of magnitude smaller than the magnetic grains used in magnetic memory devices, the density of information being stored could also be increased by several orders of magnitude. The problem is the working temperature: in this particular $\{Mn_{12}\}$ cage, the temperature at which it could store information for a significant time is less than 4 K. Only below this T_B, the slow magnetic relaxation occurs.[320, 321, 325, 326]

The first SMMs molecules reported contained Mn^{III} ions and were $\{Mn_{12}\}$ cages. Right after, Milios et al.[327, 328] reported a family of $\{Mn_6\}$ cages. The record in the energy barrier (86 K) for loss of magnetization of any *3d*-based SMMs was reported in one of these $\{Mn_6\}$ cages. The largest known SMM has the formula $[Mn_{84}O_{72}(O_2CCH_3)_{78}(OCH_3)_{24}(OH)_6(CH_3OH)_{12}(H_2O)_{42}]$.[329] SMMs molecules were published during next years, but, until 2003, all of them consisted of molecules with several metallic centres. In 2003, the first example of SMMs containing only a single paramagnetic metal ion was reported by Ishikawa, a lanthanoid based complex with a phtalocyanine ligand.[330]

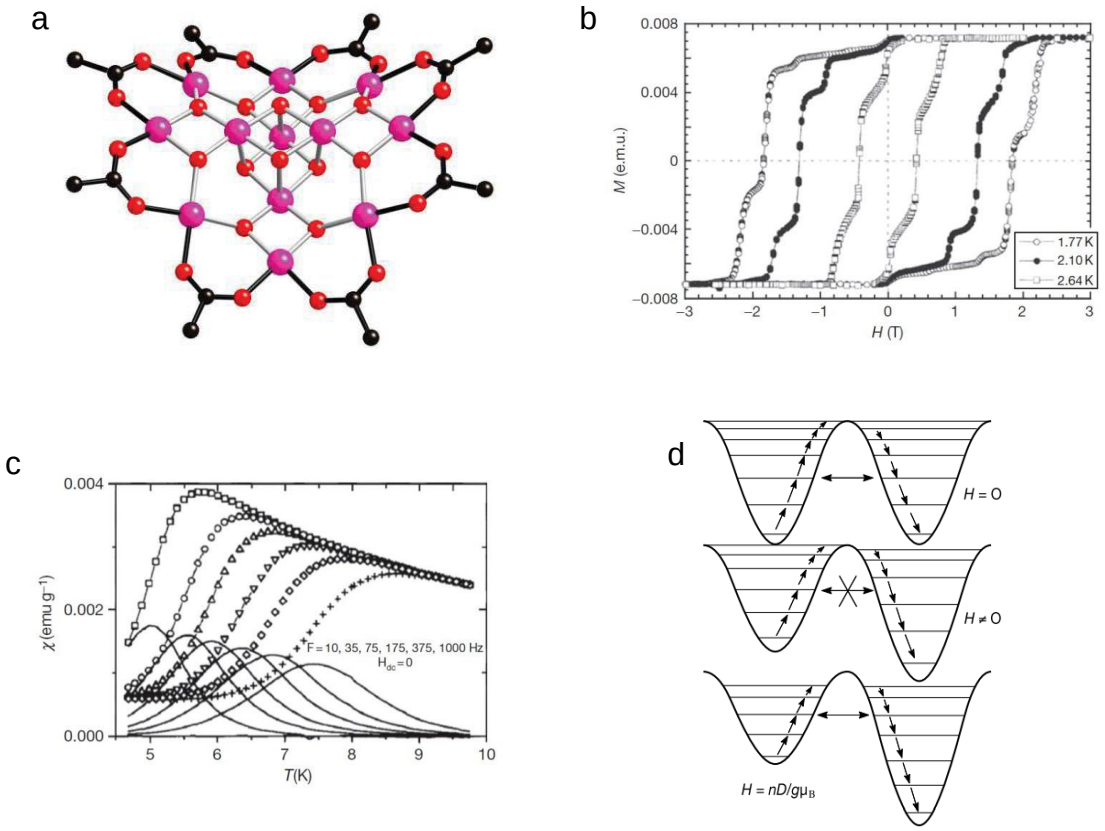

Figure 28: (a) *Crystal structure of $[Mn_{12}O_{12}(O_2CCH_3)_{16}(H_2O)_4]\cdot 4H_2O\cdot 2CH_3CO_2H$* ***(b)*** *M(H) curves, showing magnetic hysteresis for a single crystal of $[Mn_{12}O_{12}(O_2CCH_3)_{16}(H_2O)_4]\cdot 4H_2O\cdot 2CH_3CO_2H$ with the applied field along the easy axis of magnetization* ***(c)*** *in-phase and out-of-phase (solid lines) components of the AC magnetic susceptibility of $[Mn_{12}O_{12}(O_2CCH_3)_{16}(H_2O)_4]\cdot 4H_2O\cdot 2CH_3CO_2H$.* ***(d)*** *Drawing showing how the potential-energy diagram of an SMM changes as the magnetic field is swept. Resonant magnetization tunnelling occurs when the energy levels are aligned between the two halves of the diagram.* [319-321, 325, 326]

These molecules were also known as single-ion magnets (SIMs) and are based on a magnetically anisotropic single metal ion. In 2010, the first SIM based on a *3d* transition-metal center was reported by Long et al.,[331] a Fe(II) based complex with trigonal-pyramidal structure. After the publication of this Fe(II)-based SIM, *3d* transition-metal based SIMs have proliferated,[332] including Fe(II), Co(II)[333] and Mn(III)-based complexes.[334-341]

In this work, we will focus on Mn(III)-based SMM, more specifically in the "salen" derivatives family (Figure 29). Tetradentate Schiff base "salen" ligands (H_2salen, H_2salpn, H_2-5-Br-salen, etc) are ligands derived from the condensation of the corresponding salicylaldehyde or its derivatives with the corresponding amine and

reacted with Mn(III) acetate to produce dimeric complexes with two Mn(III) centers (Figure 30).[336, 337, 341, 342]

Several Mn(III)-salen binuclear SMM have been published, like $[Mn(salen)(H_2O)]_2(ClO_4)_2$ (salen = 2,2′-ethylenebis(nitrilomethylidene)diphenol),[341] $[Mn(salpn)(H_2O)]^+$ (salpn = N,N'-(propane)bis(salicyldeneiminate))[336] or $[Mn_2(saltmen)_2](ReO_4)_2$ complex (saltmen = 1,1,2,2-tetramethylene)bis(salicylideneiminate)), published in 2004.[343] In 2007, a very complete report about Mn(salen) derivatives was published by Abe and Miyasaka.[343] These Mn(III)-salen complexes were chosen to be inserted in between the anilato layers because of its cationic character, its stability and the precedent of 2D oxalato-based networks with these cationic complexes inserted in between the layers.[28, 29]

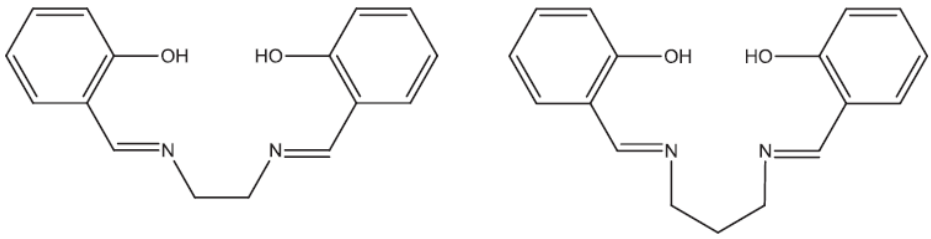

***Figure 29**: Scheme of the H_2salen ligand (left) and H_2salpn ligand (right)*

The SMM behaviour of some of the Mn(III)-salen complexes is mainly due to two facts i) the Jahn-Tellen distortion axis in the binuclear compound fits with the magnetic anisotropy axis ii) the two Mn^{III} in the binuclear compounds present ferromagnetic intramolecular interactions with a ground spin state $S_T = 4$.

Five different Mn(III)-salen type compounds have been inserted in between oxalato layers: i) $[Mn((R)\text{-salmen})]^+$, ii) $[Mn((S)\text{-salmen})]^+$, iii) $[Mn(salpn)]^+$, iv) $[Mn(saltmen)]^+$, and v) $[Mn(salen)]^+$.[28, 29] Only the $[Mn(salen)]^+$ compound presented SMM behaviour. This fact is particularly curious since the Mn(III)-salen precursor itself does not shows SMM behaviour because of the influence of inter-dimer interactions. When this cation is inserted in the 3D oxalato lattice, the network isolates the dimeric cations reducing the interdimer interactions and making possible the SMM behaviour (Figure 31).[29]

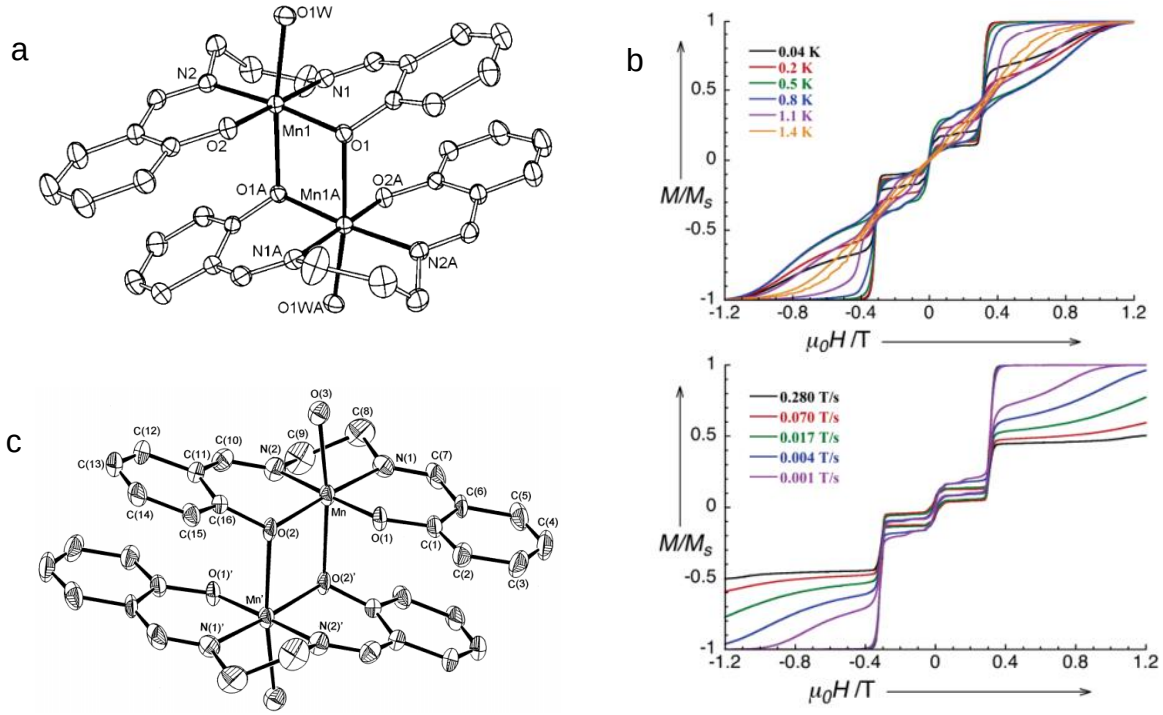

Figure 30: (a) *ORTEP drawing of the cationic part of $[Mn(salpn)(H_2O)]_2(ClO_4)_2$* ***(b)*** *Field dependence of the normalized magnetization performed on an oriented single crystal of $[Mn(salpn)(H_2O)]_2(ClO_4)_2$ at different temperatures with a sweep-field rate of 0.002 T/s (top) and with different sweep-field rate at 0.04 K (bottom). The field was applied in the easy direction of the crystal (along the c* axis)*[336] ***(c)*** *ORTEP drawing of the cationic part of $[Mn(salen)(H_2O)]_2(ClO_4)_2$.*[343]

If $[Mn_2(salpn)_2(H_2O)_2](ClO_4)_2$ is used instead, despite it shows an intermediate SMM and SCM (Single Chain Magnet) behaviour due to the magnetic interaction through the hydrogen bonds,[336, 344] the resulting oxalato-based compound with Mn(III)-salpn inserted in between the layer does not show SMM behaviour. All these differences are due to the fact that in the Mn(III)-salpn and the others cations the dimeric structure was not preserved (Figure 31), preventing any SMM behaviour.[28, 29] In this study, the difficulty in predicting the final properties of a molecular material is manifested since SMM behaviour depends on many factors and predicting them beforehand is impossible.

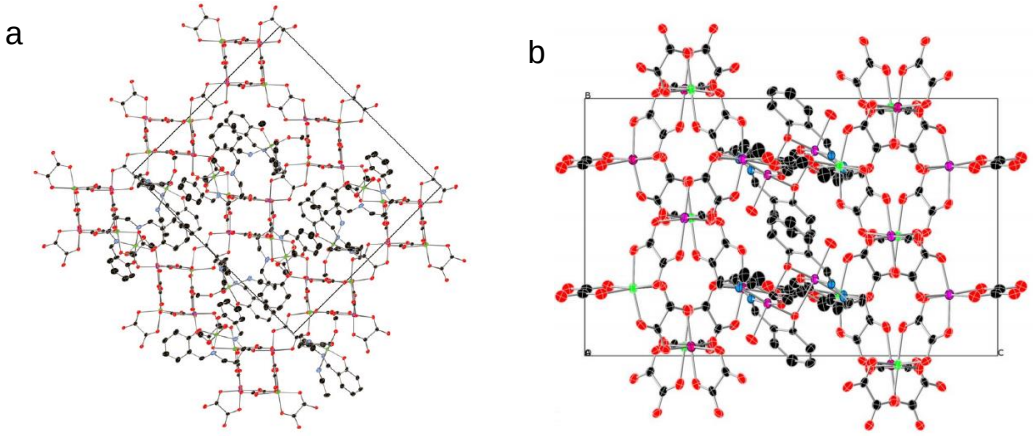

Figure 31: (a) *projection in the bc plane of the 3D oxalato network with M^{III}-salpn monomeric unit inserted* ***(b)*** *projection in the bc plane of oxalato 3D network with M^{III}-salen dimeric unit.*[28, 29]

When the chiral cations [Mn((*R*)-salmen)]$^+$ and [Mn((*S*)-salmen)]$^+$ are used, the final structure strongly depends on the solvent. In acetonitrile, a chiral 2D bimetallic oxalato network is obtained whereas using a different solvent like dichloromethane, nitromethane or acetone, yields a novel 3D achiral network, different from the previously reported 10,3 network. When using the achiral templating cations [Mn(salpn)]$^+$ and [Mn(saltmen)]$^+$, a chiral 3D network and an achiral 2D network, respectively, are obtained. In all these cases, only monomeric cations were inserted into the oxalato network. When using the [Mn(salen)]$^+$ cation, the dimeric form was inserted into an achiral 3D oxalato network.

In this Thesis we will show that [Mn(salen)(H_2O)](ClO_4) and [Mn(salpn)(H_2O)](ClO_4) (salpn = N,N'-(propane)bis(salicyldeneiminate)) could be successfully inserted in between anilato layers.

2.5.8. Applicability of anilato-based molecular materials:

Fossil fuels have been our main energy source since the industrial revolution. Over the years, the energy demand has widely increased, leading humanity to a critical situation due to the pauperization of the fossil fuel deposits and the dangerous increase of atmospheric pollution and global warming.

The escalating CO_2 emissions is one of the main causes of global warming. These emissions, the dangerous amount of pollution in our environment and its health

consequences require the development of new energy sources that allow humanity to evolve into a new era with efficient and carbon-neutral energies and fuels. Wind and solar energy currently contribute ~ 4 % of the total global electricity production and this is expected to increase to ~ 25 % by 2030.[345, 346] These renewable energies are the perfect alternative to produce electricity and supply it for household energy needs, but they cannot solve the fuel crisis by themselves due to their variability and the enormous difficult to store the energy they produce, among others aspects.

Hydrogen could be the perfect alternative due to his renewable nature and cleanliness.[347] Whereas burning fossil fuels emits a large amount of CO_2 into the atmosphere, the combustion of hydrogen produces pure water, so it is considered a sustainable storage form of energy to attend the energy demand in a non-pollutant way.

Since the electrolysis of water or others solvents to produce H_2 is not a naturally occurring process, the search for new efficient catalysts for this purpose is a hot topic in the research of new energies sources. Noble-metal catalysts (like platinum) are splendid H_2-evolution catalysts,[348, 349] but the cost of these compounds is elevated and O_2 reduction should also be catalysed, decreasing the yield of H_2 production. So, even though platinum is nowadays the best electrocatalyst for hydrogen formation, its high cost and low availability have slowed the implementation of hydrogen as an alternative fuel. In order to solve the noble-metal catalyst problem, many advances were reported in last few years in the development of small molecules which can catalyse H_2 from water and other solvents.[350-364]

Unfortunately, an efficient water splitting method to produce hydrogen on a large scale, preferably using the sunlight as energy source (solar fuels)[365-368], is still far away from being a reality. Up to now, few compounds have shown efficient catalysis properties in presence of O_2.[369, 370]

Notwithstanding, not only the development of renewable energy sources is important, also the development of low cost, clean and sustainable energy storage systems based on electrochemical processes is crucial.

One example of batteries which store electrical energy in a clean and sustainable way that are attracting much attention are the redox flow batteries (RFBs).

They employ reduction and oxidation reactions to store energy in liquid electrolyte solutions which flow through a battery of electrochemical cells during the charge and the discharge processes. Their ability to store large amounts of energy, their flexibility of design and their long lifetimes makes these RFBs particularly promising. The most popular electrolyte for these batteries is the vanadium redox flow battery systems (VRFBs) ,invented by Skyllas-Kazacos, that contain the same element in the positive and negative electrolytes, minimizing the effects of cross contamination.[345, 371, 372]

But, among the rise of the RFB, the best known and used batteries are the alkaline ion intercalation ones, such as rechargeable lithium-ion (Li^+) batteries, which are widely used for power conversion and storage systems.[373-380] However, the main problem with these Li-ion batteries is the high cost of large-scale energy storage due to the risk of explosion. Sodium (Na^+) and Potassium (K^+) batteries could be the perfect choice due to their low cost and the massive abundance of these elements[381-387]. This work focuses on the alkaline cations intercalation-based batteries (Na^+ and K^+). In these alkaline-ion intercalation batteries, not only the alkaline-ion is important for the intercalation reaction, the anionic lattice that host these cations is also a key element. The geometry of the lattice, its ability to establish bonds and the size of the holes or the separation in between the lattices are decisive characteristics for intercalation reactions to occur. Depending on the geometry of the anionic part of these compounds, 2D or 3D metal-organic frameworks (materials with permanently porous structures that can host molecules inside) could be found.[383, 388-391]

Two-dimensional (2D) inorganic nanomaterials offer a wide platform to achieve high-performance active materials. The use of 2D materials for electrochemical energy conversion and storage has being increasing recently.[389, 390] This interest is due to the large contacting areas for electrolytes and high number of active sites, which means an increase of reaction activity of inorganic lattices during the electrochemical process. Besides, the 2D geometry allows the assembly, layer by layer, into thin films for the preparation of electrochemical devices.

Di-substituted benzoquinones (anilato) derivatives compounds have been extensively studied[1, 4, 69, 99, 117] from the magnetic point of view, but, until now, there are no electrochemical studies of the extended 2D layers based on anilato ligand to determine their ability to act as electrocatalysts for hydrogen formation or as porous

materials for batteries.[392-407] Organic compounds present promising possibilities to act as such due to their high energy density,[408, 409] but practical applications have been unsuccessful to date because they normally present low discharge plateaus and poor cycling performances. However, some electrochemical studies of discrete quinone derivatives have shown promising results. In some of these studies the proposed mechanism is that the alkaline ion is coordinated by the quinone in a bis-bidentate way, which is the same coordination mode the anilato ligand adopts to form extended 2D layers.[392, 395, 398, 399]

References.

(1) Atzori, M.; Benmansour, S.; Mínguez Espallargas, G.; Clemente-León, M.; Abhervé, A.; Gómez-Claramunt, P.; Coronado, E.; Artizzu, F.; Sessini, E.; Deplano, P.; Serpe, A.; Mercuri, M. L.; Gómez García, C. J. A Family of Layered Chiral Porous Magnets Exhibiting Tunable Ordering Temperatures. *Inorg. Chem.* **2013***, 52*, 10031-10040.

(2) Abhervé, A.; Clemente-León, M.; Coronado, E.; Gómez-Garcia, C. J.; Verneret, M. One-Dimensional and Two-Dimensional Anilate-Based Magnets with Inserted Spin-Crossover Complexes. *Inorg. Chem.* **2014***, 53*, 12014-12026.

(3) Benmansour, S.; Gómez-Claramunt, P.; Vallés-García, C.; Mínguez Espallargas, G.; Gómez García, C. J. Key Role of the Cation in the Crystallization of Chiral Tris(Anilato)Metalate Magnetic Anions. *Cryst. Growth Des.* **2016***, 16*, 518-526.

(4) Benmansour, S.; Vallés-García, C.; Gómez-Claramunt, P.; Mínguez Espallargas, G.; Gómez-García, C. J. 2D and 3D Anilato-Based Heterometallic M(I)M(III) Lattices: The Missing Link. *Inorg. Chem.* **2015***, 54*, 5410-5418.

(5) Wickman, H. H.; Trozzolo, A. M.; Williams, H. J.; Hull, G. W.; Merritt, F. R. Spin-3/2 Iron Ferromagnet: Its Mössbauer and Magnetic Properties. *Phys. Rev.* **1967***, 155*, 563-566.

(6) Hoskins, B. F.; White, A. H. Crystal and Molecular Structure of Monochlorobis(Diethyldithiocarbamato)Iron(III). *J. Chem. Soc. A* **1970**, 1668-1674.

(7) Miller, J. S.; Gatteschi, D. Molecule-Based Magnets. *Chem. Soc. Rev.* **2011***, 40*, 3065-3066.

(8) Tamaki, H.; Zhong, Z. J.; Matsumoto, N.; Kida, S.; Koikawa, M.; Achiwa, N.; Hashimoto, Y.; Okawa, H. Design of Metal-Complex Magnets. Syntheses and Magnetic Properties of Mixed-Metal Assemblies $\{NBu_4[MCr(ox)_3]\}X$ (NBu_4^+ = Tetra(N-Butyl)Ammonium Ion; ox^{2-} = oxalate Ion; M = Mn^{2+}, Fe^{2+}, Co^{2+}, Ni^{2+}, Cu^{2+}, Zn^{2+}). *J. Am. Chem. Soc.* **1992***, 114*, 6974-6979.

(9) Carling, S. G.; Mathoniere, C.; Day, P.; Malik, K. M. A.; Coles, S. J.; Hursthouse, M. B. Crystal Structure and Magnetic Properties of the Layer Ferrimagnet n(N-C_5H_{11})4$MnFe(C_2O_4)_3$. *J. Chem. Soc. , Dalton Trans.* **1996**, 1839-1843.

(10) Coronado, E.; Galán-Mascaros, J. R.; Martí-Gastaldo, C. oxalate-Based 2D Magnets: The Series $[NBu_4]M^{II}Mn^{III}(ox)_3$] (MII = Fe, Co, Ni, Zn; ox = oxalate Dianion). *J. Mater. Chem.* **2006***, 16*, 2685-2689.

(11) Mathoniere, C.; Carling, S. G.; Yusheng, D.; Day, P. Molecular-Based Mixed Valency Ferrimagnets $(XR_4)FeFe(C_2O_4)_3$(X = N, P; R =,N-Propyl, N-Butyl, Phenyl): Anomalous Negative Magnetisation in the Tetra-N-Butylammonium Derivative. *J. Chem. Soc. , Chem. Commun.* **1994**, 1551-1552.

(12) Mathoniere, C.; Nuttall, C. J.; Carling, S. G.; Day, P. Ferrimagnetic Mixed-Valency and Mixed-Metal Tris(oxalato)Iron(III) Compounds: Synthesis, Structure, and Magnetism. *Inorg. Chem.* **1996***, 35*, 1201-1206.

(13) Min, K. S.; Miller, J. S. Synthesis of Layered (2-D) V-Based Bimetallic oxalates from Non-Aqueous Media that Cannot be Synthesized from Aqueous Media. *Dalton Trans.* **2006**, 2463-2467.

(14) Okawa, H.; Matsumoto, N.; Tamaki, H.; Ohba, M. Ferrimagnetic Mixed-Metal Assemblies $\{NBu_4MFe(ox)_3]\}X$. *Molecular Crystals and Liquid Crystals Science and Technology. Section A. Molecular Crystals and Liquid Crystals* **1993***, 233*, 257-262.

(15) Pellaux, R.; Schmalle, H. W.; Huber, R.; Fischer, P.; Hauss, T.; Ouladdiaf, B.; Decurtins, S. Molecular-Based Magnetism in Bimetallic Two-Dimensional oxalate-Bridged Networks. an X-Ray and Neutron Diffraction Study. *Inorg. Chem.* **1997***, 36*, 2301-2308.

(16) Clemente-León, M.; Coronado, E.; Carmen Giménez-López, M.; Soriano-Portillo, A.; Waerenborgh, J. C.; Delgado, F. S.; Ruiz-Pérez, C. Insertion of a Spin Crossover Fe-III Complex into an oxalate-Based Layered Material: Coexistence of Spin Canting and Spin Crossover in a Hybrid Magnet. *Inorg. Chem.* **2008***, 47*, 9111-9120.

(17) Clemente-León, M.; Coronado, E.; Giménez-López, M. C.; Romero, F. M.; Asthana, S.; Desplanches, C.; Létard, J. F. Structural, Thermal and Photomagnetic Properties of Spin Crossover $[Fe(bpp)_2]^{2+}$ Salts Bearing $[Cr(L)(ox)_2]$- Anions. *Dalton Trans.* **2009**, 8087-8095.

(18) Clemente-León, M.; Coronado, E.; López-Jordà, M. 2D and 3D Bimetallic oxalate-Based Ferromagnets Prepared by Insertion of Different Fe^{III} Spin Crossover Complexes. *Dalton Trans.* **2010***, 39*, 4903-4910.

(19) Clemente-León, M.; Coronado, E.; López-Jordà, M.; Desplanches, C.; Asthana, S.; Wang, H.; Letard, J. F. A Hybrid Magnet with Coexistence of Ferromagnetism and Photoinduced Fe(III) Spin-Crossover. *Chem. Sci.* **2011***, 2*, 1121-1127.

(20) Clemente-León, M.; Coronado, E.; Giménez-López, M. C.; Romero, F. M. Structural, Thermal, and Magnetic Study of Solvation Processes in Spin-Crossover $[Fe(bpp)_2]Cr(L)(ox)_2]_2 \cdot nH2O$ Complexes. *Inorg. Chem.* **2007***, 46*, 11266-11276.

(21) Clemente-León, M.; Coronado, E.; López-Jordà, M.; Mínguez Espallargas, G.; Soriano-Portillo, A.; Waerenborgh, J. Multifunctional Magnetic Materials obtained by Insertion of a Spin-Crossover Fe^{III} Complex into Bimetallic oxalate-Based Ferromagnets. *Chem. Eur. J.* **2010***, 16*, 2207-2219.

(22) Clemente-León, M.; Coronado, E.; López-Jordà, M.; Waerenborgh, J. C. Multifunctional Magnetic Materials obtained by Insertion of Spin-Crossover Fe^{III} Complexes into Chiral 3D Bimetallic oxalate-Based Ferromagnets. *Inorg. Chem.* **2011***, 50*, 9122-9130.

(23) Clemente-León, M.; Coronado, E.; López-Jordà, M. 2D Bimetallic oxalate-Based Ferromagnets with Inserted [Fe(4-Br-Sal_2-Trien)]+ and $[Fe(3\text{-}R\text{-}Sal_2\text{-}Trien)]^+$ (R = Br, Cl and CH_3O) Fe^{III} Spin-Crossover Complexes. *Eur. J. Inorg. Chem* **2013***, 2013*, 753-762.

(24) Clemente-León, M.; Coronado, E.; López-Jordà, M.; Waerenborgh, J. C.; Desplanches, C.; Wang, H.; Létard, J. F.; Hauser, A.; Tissot, A. Stimuli Responsive Hybrid Magnets: Tuning the Photoinduced Spin-Crossover in Fe(III) Complexes Inserted into Layered Magnets. *J. Am. Chem. Soc.* **2013***, 135*, 8655-8667.

(25) Coronado, E.; Galán Mascarós, J. R.; Giménez-López, M. C.; Almeida, M.; Waerenborgh, J. C. Spin Crossover Fe^{II} Complexes as Templates for Bimetallic oxalate-Based 3D Magnets. *Polyhedron* **2007***, 26*, 1838-1844.

(26) López-Jordà, M.; Giménez-Marqués, M.; Desplanches, C.; Mínguez Espallargas, G.; Clemente-León, M.; Coronado, E. Insertion of a $[Fe^{II}(pyimH)_3]^{2+}$ [pyimH = 2-(1H-Imidazol-2-Yl)Pyridine] Spin-Crossover Complex Inside a Ferromagnetic Lattice Based on a Chiral 3D Bimetallic oxalate Network. *Eur. J. Inorg. Chem* **2016***, 2016*, 2187-2192.

(27) Giménez-López, M. C.; Clemente-León, M.; Coronado, E.; Romero, F. M.; Shova, S.; Tuchagues, J. P. Structural Transformations and Magnetic Effects Induced by Solvent Exchange in the Spin Crossover Complex $[Fe(bpp)_2][Cr(bpy)(ox)_2]_2$. *Eur. J. Inorg. Chem* **2005***, 2005*, 2783-2787.

(28) Clemente-León, M.; Coronado, E.; López-Jordà, M. 2D and 3D Bimetallic oxalate-Based Ferromagnets Prepared by Insertion of Mn^{III}-Salen Type Complexes. *Dalton Trans.* **2013***, 42*, 5100-5110.

(29) Clemente-León, M.; Coronado, E.; Gómez-García, C. J.; López-Jordà, M.; Camón, A.; Repollés, A.; Luis, F. Insertion of a Single-Molecule Magnet Inside a Ferromagnetic Lattice Based on a 3D Bimetallic oxalate Network: Towards Molecular Analogues of Permanent Magnets. *Chemistry - A European Journal* **2014***, 20*, 1669-1676.

(30) Clemente-León, M.; Coronado, E.; Gómez-García, C. J.; Soriano-Portillo, A. Increasing the Ordering Temperatures in oxalate-Based 3D Chiral Magnets: the series $[Ir(ppy)_2(bpy)]M^{II}M^{III}(ox)_3]\cdot 0.5H_2O$ ($M^{II}M^{III}$ = MnCr, FeCr, CoCr, NiCr, ZnCr, MnFe, FeFe); bpy = 2,2-bipyridine; ppy = 2-phenylpyridine; ox = oxalate Dianion). *Inorg. Chem.* **2006***, 45*, 5653-5660.

(31) Coronado, E.; Galán-Mascarós, J. R.; Gómez-García, C. J.; Martínez-Agudo, J. M. Molecule-Based Magnets Formed by Bimetallic Three-Dimensional oxalate Networks and Chiral tris(bipyridyl) Complex Cations. the Series $Z^{II}(bpy)_3]ClO_4]M^{II}Cr^{III}(ox)_3]$ (Z^{II} = Ru, Fe, Co, and Ni; M^{II} = Mn, Fe, Co, Ni, Cu, and Zn; ox = oxalate Dianion). *Inorg. Chem.* **2001***, 40*, 113-120.

(32) Decurtins, S.; Schmalle, H. W.; Schneuwly, P.; Oswald, H. R. Photochemical Synthesis and Structure of a 3-Dimensional Anionic Polymeric Network of an Iron(II) oxalato Complex with Tris(2,2'-bipyridine)Iron(II) Cations. *Inorg. Chem.* **1993***, 32*, 1888-1892.

(33) Decurtins, S.; Schmalle, H. W.; Schneuwly, P.; Ensling, J.; Guetlich, P. A Concept for the Synthesis of 3-Dimensional Homo- and Bimetallic oxalate-Bridged Networks $M_2(ox)_3]N$. Structural, Moessbauer, and Magnetic Studies in the Field of Molecular-Based Magnets. *J. Am. Chem. Soc.* **1994***, 116*, 9521-9528.

(34) Hernández-Molina, M.; Lloret, F.; Ruiz-Pérez, C.; Julve, M. Weak Ferromagnetism in Chiral 3-Dimensional oxalato-Bridged Cobalt(II) Compounds. Crystal Structure of $[Co(bpy)_3]Co_2(ox)_3]ClO_4$. *Inorg. Chem.* **1998***, 37*, 4131-4135.

(35) Pointillart, F.; Train, C.; Gruselle, M.; Villain, F.; Schmalle, H. W.; Talbot, D.; Gredin, P.; Decurtins, S.; Verdaguer, M. Chiral Templating Activity of Tris(Bipyridine)Ruthenium(II) Cation in the Design of Three-Dimensional (3D) Optically Active oxalate-Bridged $\{Ru(bpy)_3]Cu_2xNi_{2(1-X)}(C_2O_4)_3]\}_n$ ($0 \le x \le 1$; bpy = 2,2-bipyridine): Structural, Optical, and Magnetic Studies. *Chem. Mater.* **2004***, 16*, 832-841.

(36) Fishman, R. S.; Clemente-León, M.; Coronado, E. Magnetic Compensation and Ordering in the Bimetallic oxalates: Why are the 2D and 3D Series so Different? *Inorg. Chem.* **2009***, 48*, 3039-3046.

(37) Coronado, E.; Galán-Mascaros, J. R.; Martí-Gastaldo, C. Design of Bimetallic Magnetic Chains Based on oxalate Complexes: Towards Single Chain Magnets. *CrystEngComm* **2009***, 11*, 2143-2153.

(38) Coronado, E.; Giménez, M. C.; Gómez-García, C. J.; Romero, F. M. Synthesis, Crystal Structure and Magnetic Properties of $[Cr_2Cu_2(bpy)_4(ox)_5]\cdot 2H_2O$: an oxalato-Bridged Heterometallic Tetramer. *Polyhedron* **2003***, 22*, 3115-3122.

(39) Marinescu, G.; Andruh, M.; Lescouezec, R.; Munoz, M. C.; Cano, J.; Lloret, F.; Julve, M. $[Cr(phen)(ox)_2]^-$: A Versatile Bis-oxalato Building Block for the Design of Heteropolymetallic Systems. Crystal Structures and Magnetic Properties of $AsPh_4Cr(phen)(ox)_2]\cdot H2O$, $[NaCr(phen)(ox)_2(H_2O)]\cdot 2H_2O$ and $\{Cr(phen)(ox)_2]_2Mn_2(bpy)_2(H_2O)_2(ox)]\}\cdot 6H_2O$. *New J. Chem.* **2000***, 24*, 527-536.

(40) Stanica, N.; Stager, C. V.; Cimpoesu, M.; Andruh, M. Synthesis and Magnetic Properties of a New oxalato-Bridged Heterotrinuclear Complex, $[NiCr_2(bipy)_2(C_2O_4)_4(H_2O)_2]\cdot H_2O$. A Rare Case of Antiferromagnetic Coupling between Cr(III) and Ni(II) Ions. *Polyhedron* **1998***, 17*, 1787-1789.

(41) Triki, S.; Bérézovsky, F.; Sala Pala, J.; Coronado, E.; Gómez-García, C. J.; Clemente, J. M.; Riou, A.; Molinié, P. oxalato-Bridged Dinuclear Complexes of Cr(III) and Fe(III): Synthesis, Structure, and Magnetism of $(C_2H_5)_4N]_4MM'(ox)(NCS)_8]$ with MM' = CrCr, FeFe, and CrFe. *Inorg. Chem.* **2000***, 39*, 3771-3776.

(42) Rochon, F. D.; Melanson, R.; Andruh, M. $[Cr(bipy)(C_2O_4)_2]^-$: A Versatile Building Block for the Design of Heteropolymetallic Systems. Crystal Structures of $BaCr_2(bipy)_2(C_2O_4)_4(H_2O)]_n\cdot nH_2O$, $MnCr_2(bipy)_2(C_2O_4)_4]N$, and $CoCr_2(bipy)_2(C_2O_4)_2(C_2O_4)_2(H_2O)_2]\cdot H_2O$. *Inorg. Chem.* **1996***, 35*, 6086-6092.

(43) Coronado, E.; Galán-Mascaros, J. R.; Gómez-García, C. J.; Martínez-Agudo, J. M. Increasing the Coercivity in Layered Molecular-Based Magnets $A[M(III)M(II)(ox)_3]$ (M(II) = Mn, Fe, Co, Ni, Cu; M(III) = Cr, Fe; ox = oxalate; A = Organic Or Organometallic Cation). *Adv Mater* **1999***, 11*, 558-561.

(44) Clemente-León, M.; Coronado, E.; Galán Mascaros, J. R.; Gómez-García, C. J. Intercalation of Decamethylferrocenium Cations in Bimetallic oxalate-Bridged Two-Dimensional Magnets. *Chem. Commun.* **1997**, 1727-1728.

(45) Coronado, E.; Clemente-León, M.; Galán-Mascaros, J. R.; Giménez-Saiz, C.; Gómez-García, C. J.; Martínez-Ferrero, E. Design of Molecular Materials Combining Magnetic, Electrical and Optical Properties. *J. Chem. Soc. Dalton Trans.* **2000**, 3955-3961.

(46) Coronado, E.; Galán-Mascaros, J. R.; Gómez-García, C. J.; Ensling, J.; Gutlich, P. Hybrid Molecular Magnets obtained by Insertion of Decamethyl-Metallocenium Cations into Layered, Bimetallic oxalate Complexes: $[Z(III)Cp_2^*][M(III)M(II)(ox)_3]$ (Z(III) = Co, Fe; M(III) = Cr, Fe; M(II) = Mn, Fe, Co, Cu, Zn; ox = oxalate; Cp* = Pentamethylcyclopentadienyl). *Eur. J. Inorg. Chem.* **2000***, 6*, 552-563.

(47) Coronado, E.; Galán-Mascaros, J. R.; Gómez-García, C. J.; Martínez-Agudo, J. M.; Martínez-Ferrero, E.; Waerenborgh, J. C.; Almeida, M. Layered Molecule-Based Magnets Formed by Decamethylmetallocenium Cations and Two-Dimensional Bimetallic Complexes $[M(II)Ru(III)(ox)_3]^-$ (M(II) = Mn, Fe, Co, Cu and Zn; ox = oxalate). *J. Solid State Chem.* **2001***, 159*, 391-402.

(48) Benard, S.; Riviere, E.; Yu, P.; Nakatani, K.; Delouis, J. F. A Photochromic Molecule-Based Magnet. *Chem. Mater.* **2001***, 13*, 159-162.

(49) Bénard, S.; Yu, P.; Audière, J. P.; Rivière, E.; Clément, R.; Guilhem, J.; Tchertanov, L.; Nakatani, K. Structure and NLO Properties of Layered Bimetallic oxalato-Bridged Ferromagnetic Networks Containing Stilbazolium-Shaped Chromophores. *J. Am. Chem. Soc.* **2000***, 122*, 9444-9454.

(50) Coronado, E.; Galán-Mascaros, J. R.; Gómez-García, C. J.; Laukhin, V. Coexistence of Ferromagnetism and Metallic Conductivity in a Molecule-Based Layered Compound. *Nature* **2000***, 408*, 447-449.

(51) Alberola, A.; Coronado, E.; Galán-Mascaros, J. R.; Giménez-Saiz, C.; Gómez-García, C. J. A Molecular Metal Ferromagnet from the Organic Donor Bis(Ethylenedithio)Tetraselenafulvalene and Bimetallic oxalate Complexes. *J. Am. Chem. Soc.* **2003***, 125*, 10774-10775.

(52) Aldoshin, S. M.; Nikonova, L. A.; Shilov, G. V.; Bikanina, E. A.; Artemova, N. K.; Smirnov, V. A. The Influence of an N-Substituent in the Indoline Fragment of Pyrano-Pyridine Spiropyran Salts on their Crystalline Structure and Photochromic Properties. *J. Mol. Struct.* **2006***, 794*, 103-109.

(53) Aldoshin, S. M.; Sanina, N. A.; Minkin, V. I.; Voloshin, N. A.; Ikorskii, V. N.; Oveharenko, V. I.; Smirnov, V. A.; Nagaeva, N. K. Molecular Photochromic Ferromagnetic Based on the Layered Polymeric Tris-oxalate of Cr(III), Mn(II) and 1-[(1 ',3 ',3 '-Trimethyl-6-nitrospiro[2H-1-benzopyran-2,2'-indoline]-8-yl)methyl]pyridinium. *J. Mol. Struct.* **2007***, 826*, 69-74.

(54) Kida, N.; Hikita, M.; Kashima, I.; Okubo, M.; Itoi, M.; Enomoto, M.; Kato, K.; Takata, M.; Kojima, N. Control of Charge Transfer Phase Transition and Ferromagnetism by Photoisomerization of Spiropyran for an Organic-Inorganic Hybrid System, (SP)[$Fe^{II}Fe^{III}(dto)_3$] (SP = Spiropyran, dto = $C_2O_2S_2$). *J. Am. Chem. Soc.* **2009***, 131*, 212-220.

(55) Sieber, R.; Decurtins, S.; Stoeckli-Evans, H.; Wilson, C.; Yufit, D.; Howard, J. A. K.; Capelli, S. C.; Hauser, A. A Thermal Spin Transition in [$Co(bpy)_3$][$LiCr(ox)_3$] (ox = $C_2O_4^{2-}$; bpy = 2,2 '-Bipyridine). *Chem. Eur. J.* **2000***, 6*, 361-368.

(56) Gruselle, M.; Train, C.; Boubekeur, K.; Gredin, P.; Ovanesyan, N. Enantioselective Self-Assembly of Chiral Bimetallic oxalate-Based Networks. *Coord. Chem. Rev.* **2006***, 250*, 2491-2500.

(57) Brissard, M.; Gruselle, M.; Malezieux, B.; Thouvenot, R.; Guyard-Duhayon, C.; Convert, O. An Anionic {[$MnCo(ox)_3]^-$}$_n$ network with Appropriate Cavities for the Enantioselective Recognition and Resolution of the Hexacoordinated Monocation [$Ru(bpy)_2(ppy)]^+$ (bpy = bipyridine, ppy = phenylpyridine). *Eur. J. Inorg. Chem.* **2001***, 2001*, 1745-1751.

(58) Train, C.; Gheorghe, R.; Krstic, V.; Chamoreau, L.; Ovanesyan, N. S.; Rikken, G. L. J. A.; Gruselle, M.; Verdaguer, M. Strong Magneto-Chiral Dichroism in Enantiopure Chiral Ferromagnets. *Nature Materials* **2008***, 7*, 729-734.

(59) Clemente-León, M.; Coronado, E.; Dias, J. C.; Soriano-Portillo, A.; Willett, R. D. Synthesis, Structure, and Magnetic Properties of [(S)-[PhCH(CH_3)N(CH_3)$_3$]][Mn(CH_3CN)$_{2/3}$Cr(ox)$_3$].(CH_3CN)·(Solvate), a 2D Chiral Magnet Containing a Quaternary Ammonium Chiral Cation. *Inorg. Chem.* **2008***, 47*, 6458-6463.

(60) Sadakiyo, M.; Okawa, H.; Shigematsu, A.; Ohba, M.; Yamada, T.; Kitagawa, H. Promotion of Low-Humidity Proton Conduction by Controlling Hydrophilicity in Layered Metal-Organic Frameworks. *J. Am. Chem. Soc.* **2012***, 134*, 5472-5475.

(61) Okawa, H.; Shigematsu, A.; Sadakiyo, M.; Miyagawa, T.; Yoneda, K.; Ohba, M.; Kitagawa, H. oxalate-Bridged Bimetallic Complexes {NH(Prol)$_3$}[MCr(ox)$_3$] (M = Mn^{II}, Fe^{II}, Co^{II}; NH(prol)$_3^+$ = tri(3-Hydroxypropyl)Ammonium) Exhibiting Coexistent Ferromagnetism and Proton Conduction. *J. Am. Chem. Soc.* **2009***, 131*, 13516-13522.

(62) Clemente-León, M.; Coronado, E.; Martí-Gastaldo, C.; Romero, F. M. Multifunctionality in Hybrid Magnetic Materials Based on Bimetallic oxalate Complexes. *Chem. Soc. Rev.* **2011***, 40*, 473-497.

(63) Clement, R.; Decurtins, S.; Gruselle, M.; Train, C. Polyfunctional Two- (2D) and Three-(3D) Dimensional oxalate Bridged Bimetallic Magnets. *Monats. Chem.* **2003***, 134*, 117-135.

(64) Bradley, J. M.; Carling, S. G.; Visser, D.; Day, P.; Hautot, D.; Long, G. J. Structural and Physical Properties of the Ferromagnetic Tris-Dithiooxalato Compounds, A[$M^{II}Cr^{III}$($C_2S_2O_2$)$_3$], with A^+ = n(n-C_nH_{2n+1})$_4$ + (n = 3 - 5) and P(C_6H_5)$^{4+}$ and M^{II} = Mn, Fe, Co, and Ni. *Inorg. Chem.* **2003***, 42*, 986-996.

(65) Carling, S. G.; Bradley, J. M.; Visser, D.; Day, P. Magnetic and Structural Characterisation of the Layered Materials AMnFe($C_2S_2O_2$)$_3$. *Polyhedron* **2003***, 22*, 2317-2324.

(66) Kojima, N.; Aoki, W.; Itoi, M.; Ono, Y.; Seto, M.; Kobayashi, Y.; Maeda, Y. Charge Transfer Phase Transition and Ferromagnetism in a Mixed-Valence Iron Complex, (N-C_3H_7)$_{4n}$[$Fe^{II}Fe^{III}$(dto)$_3$] (dto=$C_2O_2S_2$). *Solid State Commun.* **2001***, 120*, 165-170.

(67) Okawa, H.; Mitsumi, M.; Ohba, M.; Kodera, M.; Matsumoto, N. Dithiooxalato(Dto)-Bridged Bimetallic Assemblies {NPr_4MCr(dto)$_3$]}X (M = Fe, Co, Ni, Zn; NPr_4 = Tetrapropylammonium Ion): New Complex-Based Ferromagnets. *Bull. Chem. Soc. Jpn.* **1994***, 67*, 2139-2144.

(68) Benmansour, S.; Abhervé, A.; Gómez-Claramunt, P.; Vallés-García, C.; Gómez-García, C. J. Nanosheets of Two-Dimensional Magnetic and Conducting Fe(II)/Fe(III) Mixed-Valence Metal-Organic Frameworks. *ACS Appl. Mater. Interfaces* **2017***, 9*, 26210-26218.

(69) Kitagawa, S.; Kawata, S. Coordination Compounds of 1,4-Dihydroxybenzoquinone and its Homologues. Structures and Properties. *Coord. Chem. Rev.* **2002***, 224*, 11-34.

(70) Mercuri, M. L.; Congiu, F.; Concas, G.; Sahadevan, S. A. Recent Advances on Anilato-Based Molecular Materials with Magnetic and/Or Conducting Properties. *Magnetochemistry* **2017***, 3*.

(71) Abrahams, B. F.; Lu, K. D.; Moubaraki, B.; Murray, K. S.; Robson, R. X-Ray Diffraction and Magnetic Studies on a Series of Isostructural Divalent Metal Chloranilates with Zigzag Polymeric Chain Structures and on a Dinuclear Iron(III) Chloranilate. *J. Chem. Soc. Dalton Trans.* **2000**, 1793-1797.

(72) Abrahams, B. F.; Hoskins, B. F.; Robson, R. Mer-Triaqua(Chloranilato-O-O')Chloroiron(III) Pentahydrate. *Acta Cryst. C* **1996***, 52*, 2766-2768.

(73) Bessire, A. J.; Whittlesey, B. R.; Holwerda, R. A. Linkage Isomerization Equilibria in (Chloranilato)Palladium(II) Complexes with Amine Ligands. Crystal Structure of (Chloranilato)Bis(Acetonitrile)Palladium(II). *Inorg. Chem.* **1995***, 34*, 622-627.

(74) Bram, A.; Bruederl, G.; Burzlaff, H.; Lange, J.; Rothammel, W.; Spengler, R.; Karayannis, M. I.; Veltsistas, P. G. Disodium Bis(O-Chloranilato)Uranyl(VI) Hexahydrate. *Acta Cryst. C* **1994***, 50*, 178-180.

(75) Burzlaff, H.; Lange, J.; Spengler, R.; Karayannis, M. I.; Veltsistas, P. G. Bis(hexadecylpyridinium) Bis(3,6-Dichloro-4,5-Dihydroxy-3,5-Cyclohexadiene-1,2-Dionato-k_2O_4,O_5)Beryllium. *Acta Cryst. C* **1995***, 51*, 190-193.

(76) Calvo, M. A.; Manotti Lanfredi, A. M.; Oro, L. A.; Pinillos, M. T.; Tejel, C.; Tiripicchio, A.; Ugozzoli, F. Synthesis and Properties of Rhodium(I) Chloranilate and 2,5-Dihydroxy-1,4-Benzoquinonate Complexes. Crystal Structures of the Binuclear Rh_2(CA)(Cod)2] and Tetranuclear Rh4(.Mu.-CA)2(cod)4] Complexes (CA = Chloranilate Anion). *Inorg. Chem.* **1993***, 32*, 1147-1152.

(77) Decurtins, S.; Schmalle, H. W.; Schneuwly, P.; Zheng, L. M. Two 2,5-Dihydroxy-1,4-benzoquinonate-O,O'-Containing Mononuclear Complexes: [Cu($C_6H_2O_4$)($C_8H_6N_4$)(H_2O)].5H_2O and [Ni($C_6H_2O_4$)($C_{12}H_{12}N_2$)$_2$].H_2O ($C_8H_6N_4$ = 2,2'-Bipyrimidine, $C_{12}H_{12}N_2$ = 4,4'-Dimethyl-2,2'-bipyridine). *Acta Cryst. C* **1996***, 52*, 561-566.

(78) Folgado, J. V.; Ibanez, R.; Coronado, E.; Beltran, D.; Savariault, J. M.; Galy, J. Extremely Weak Magnetic Exchange Interactions in terpy-containing Copper(II) Dimer. Crystal and Molecular Structure of Cu(terpy)(CA).H_2O and Cu_2(terpy)$_2$(CA)](PF_6)$_2$ Complexes (terpy = 2,2':6',2''-Terpyridine, CA = Dianion of Chloranilic Acid). *Inorg. Chem.* **1988***, 27*, 19-26.

(79) Fujii, C.; Mitsumi, M.; Kodera, M.; Motoda, K. I.; Ohba, M.; Matsumoto, N.; Okawa, H. Structure and Magnetic Properties of New Dinuclear Copper(II) Complexes Bridges by Chloranilate Or Bromanilate Dianions. *Polyhedron* **1994***, 13*, 933-938.

(80) Gallert, S.; Weyhermüller, T.; Wieghardt, K.; Chaudhuri, P. Exchange Coupling Across Multiple-Atom Bridges: Crystal Structure and Magnetic Properties of a Chloranilate Bridged Dicopper(II) Complex. *Inorg. Chim. Acta* **1998***, 274*, 111-114.

(81) Heinze, K.; Huttner, G.; Zsolnai, L.; Jacobi, A.; Schober, P. Electron Transfer in Dinuclear Cobalt Complexes with “Non-Innocent” Bridging Ligands. *Chem. Eur. J.* **1997***, 3*, 732-743.

(82) Johnston, R. F.; Gupta, P. K. S.; Ossain, M. B.; van der Helm, R.; Jeong, W. Y.; Holwerda, R. A. Structure of (Chloranilato)Bis(Tri-Tolylphosphine)Palladium(II). *Acta Cryst. C* **1990***, 46*, 1796-1799.

(83) Johnston, R. F.; VanDer Veer, D. G.; Holwerda, R. A. Structure of (Chloranilato)Bis(Tri-N-Butylphosphine)Palladium(II). *J. Cryst. Spectrosc. Res.* **1992***, 22*, 755-759.

(84) Krasochka, O. N.; Avilov, V. A.; Otovmyan, L. O. *Zh. Struckt. Khim.* **1974***, 15*, 1140.

(85) Liu, S.; Shaikh, S. N.; Zubieta, J. Polyoxomolybdate-O-Benzoquinone Interactions. Synthesis and Structure of a Diacetal Derivative, $Mo_4O_{15}(OH)(C_{14}H_8)]^{3-}$, from 9,10-Phenanthrenequinone Carbonyl Insertion. Comparison to the Reaction Products with Tetrachloro-1,2-Benzoquinone, the Ligand-Bridged Binuclear Complexes $(MoO_2Cl_2)_2L]^{2-}$, L = $(C_6Cl_2O_4)^{2-}$ and $(C_2O_4)^{2-}$, Formed Via Carbonyl Insertion and Chloride Transfer. *Inorg. Chem.* **1988***, 27*, 3064-3066.

(86) Shaikh, S. N.; Zubieta, J. A Binuclear Dioxomolybdate Chloranilate Complex $[(MoO_2Cl_2)_2(C_6O_4Cl_2)]^{2-}$, Prepared from the Reaction of a Polyoxomolybdate Anion with Tetrachloro- 1,2-Benzoquinone. *Inorg. Chim. Acta* **1988***, 146*, 149-150.

(87) Spengler, R.; Lange, J.; Zimmermann, H.; Burzlaff, H.; Veltsistas, P. G.; Karayannis, M. I. Structure of $C_{36}H_{52}ClI_6InN_3O_{14}$. *Acta Cryst. B* **1995***, 51*, 174-177.

(88) Tinti, F.; Verdaguer, M.; Kahn, O.; Savariault, J. M. Interaction between Copper(II) Ions Separated by 7.6 .ANG.. Crystal Structure and Magnetic Properties of (μ-Iodanilato)Bis(N,N,N',N'-tetramethylethylenediamine)Copper(II)] Diperchlorate. *Inorg. Chem.* **1987***, 26*, 2380-2384.

(89) Xiang, D. F.; Duan, C. Y.; Tan, X. S.; Liu, Y. J.; Tang, W. X. Syntheses, Crystal Structures and Properties of Two Chloranilate-Bridging Dinuclear Mn (II) Compounds with Different Lattice Solvate Molecules : $[Mn_2(TPA)_2(CA)](ClO_4)_2{\cdot}3H_2O$ and $[Mn_2(TPA)_2(CA)](ClO_4)_2{\cdot}2CH_3CN$ (TPA = Tris (2-Pyridylmethyl) Amine ; CA = Dianion of Chloranilic Acid). *Polyhedron* **1998***, 17*, 2647-2653.

(90) Zheng, L. M.; Schmalle, H. W.; Ferlay, S.; Decurtins, S. Aqua(4,4'-Dicarbomethoxy-2,2'-Bipyridine-NN')(3,6-Dichloro-4,5-Dihydroxy-1,2-Benzoquinonato-O^4O^5)Copper(II) Acetonitrile Hemisolvate. *Acta Cryst. C* **1998***, 54*, 1578-1580.

(91) Pierpont, C. G.; Francesconi, L. C.; Hendrickson, D. N. Magnetic Exchange Interactions in Transition Metal Dimers. 11. Structural and Magnetic Characterization of $Ni_2(tren)_2(C_6O_4Cl_2)](BPh_4)_2$ and $Cu_2(Me_5dien)_2(C_6O_4Cl_2)](BPh_4)_2$. Magnetic Exchange Interactions Propagated by the Dianions of 2,5-Dihydroxy-1,4-Benzoquinones. *Inorg. Chem.* **1977***, 16*, 2367-2376.

(92) Bailar, J. C.; Jones, E. M.; Booth, H. S.; Grennert, M. Trioxalato Salts (Trioxalatoaluminiate, -Ferriate, -Chromiate, and -Cobaltiate). **1939**, 35-38.

(93) Spengler, R.; Lange, J.; Zimmermann, H.; Burzlaff, H.; Veltsistas, P. G.; Karayannis, M. I. Structure of $C_{36}H_{52}Cl_6InN_3O_{14}$. *Acta Cryst. B* **1995***, 51*, 174-177.

(94) Min, K. S.; Rhinegold, A. L.; Miller, J. S. Tris(Chloranilato)Ferrate(III) Anionic Building Block Containing the (Dihydroxo)oxodiiron(III) Dimer Cation: Synthesis and Characterization of $[(TPA)(OH)Fe^{III}OFe^{III}(OH)(TPA)][Fe(CA)_3]_{0.5}(BF_4)_{0.5}{\cdot}1.5MeOH{\cdot}H_2O$ [TPA = Tris(2-Pyridylmethyl)Amine; CA = Chloranilate]. *J. Am. Chem. Soc.* **2006***, 128*, 40-41.

(95) Atzori, M.; Artizzu, F.; Sessini, E.; Marchio, L.; Loche, D.; Serpe, A.; Deplano, P.; Concas, G.; Pop, F.; Avarvari, N.; Mercuri, M. L. Halogen-Bonding in a New Family of Tris(Haloanilato)Metallate(III) Magnetic Molecular Building Blocks. *Dalton Trans.* **2014***, 43*, 7006-7019.

(96) Atzori, M.; Marchiò, L.; Clérac, R.; Serpe, A.; Deplano, P.; Avarvari, N.; Mercuri, M. L. Hydrogen-Bonded Supramolecular Architectures Based on Tris(Hydranilato)Metallate(III) (M = Fe, Cr) Metallotectons. *Crystal Growth & Design* **2014***, 14*, 5938-5948.

(97) Atzori, M.; Artizzu, F.; Marchio, L.; Loche, D.; Caneschi, A.; Serpe, A.; Deplano, P.; Avarvari, N.; Mercuri, M. L. Switching-on Luminescence in Anilate-Based Molecular Materials. *Dalton Trans.* **2015***, 44*, 15786-15802.

(98) Benmansour, S.; Coronado, E.; Giménez-Saiz, C.; Gómez-García, C. J.; Rößer, C. Metallic Charge-Transfer Salts of Bis(Ethylenedithio)Tetrathiafulvalene with Paramagnetic Tetrachloro(oxalato)Rhenate(IV) and Tris(Chloranilato)Ferrate(III) Anions. *Eur. J. Inorg. Chem* **2014***, 2014*, 3949-3959.

(99) Atzori, M.; Pop, F.; Auban-Senzier, P.; Gómez-Garcia, C. J.; Canadell, E.; Artizzu, F.; Serpe, A.; Deplano, P.; Avarvari, N.; Mercuri, M. L. Structural Diversity and Physical Properties of Paramagnetic Molecular Conductors Based on Bis(Ethylenedithio)Tetrathiafulvalene (BEDT-TTF) and the Tris(Chloranilato)Ferrate(III) Complex. *Inorg. Chem.* **2014***, 53*, 7028-7039.

(100) Abrahams, B. F.; Coleiro, J.; Ha, K.; Hoskins, B. F.; Orchard, S. D.; Robson, R. Dihydroxybenzoquinone and Chloranilic Acid Derivatives of Rare Earth Metals. *J. Chem. Soc. Dalton Trans.* **2002**, 1586-1594.

(101) Benmansour, S.; López-Martínez, G.; Canet-Ferrer, J.; Gómez-García, J. C. A Family of Lanthanoid Dimers with Nitroanilato Bridges. *Magnetochemistry* **2016***, 2*, 32.

(102) Casas, J. M.; Falvello, L. R.; Forniés, J.; Mansilla, G.; Martín, A. Synthesis and Structural Characterization of Platinum and Palladium Complexes Containing O-Donor $C_6X_2O_4^{2-}$ Ligands. *Polyhedron* **1998***, 18*, 403-412.

(103) Elduque, A.; Garces, Y.; Oro, L. A.; Pinillos, M. T.; Tiripicchio, A.; Ugozzoli, F. oxidative-Addition Reactions on Planar Chloranilate Rhodium Systems. Crystal Structure of $[Rh_2C_6Cl_2O_4)Me_2I_2(CO)_2(PPh_3)_2]$. *J. Chem. Soc. , Dalton Trans.* **1996**, 2155-2158.

(104) Kawata, S.; Kitagawa, S.; Kumagai, H.; Kudo, C.; Kamesaki, H.; Ishiyama, T.; Suzuki, R.; Kondo, M.; Katada, M. Rational Design of a Novel Intercalation System. Layer-Gap Control of Crystalline Coordination Polymers, $\{[Cu(CA)(H_2O)_M](G)\}_N$ (M = 2, G = 2,5-Dimethylpyrazine and Phenazine; M = 1, G = 1,2,3,4,6,7,8,9-Octahydrophenazine). *Inorg. Chem.* **1996***, 35*, 4449-4461.

(105) Decurtins, S.; Schmalle, H. W.; Zheng, L. M.; Ensling, J. A New Polymeric Compound Containing Copper(II)-Chloranilate Chains: Synthesis, Crystal Structure and Magnetic Properties of $[Cu(DCMB)(CA)]_n$ (DCMB = 3,3′-Dicarbomethoxy-2,2′-Bipyridyl; CA = Dianion of 3,6-Dichloro-2,5-Dihydroxy- 1,4-Benzoquinone). *Inorg. Chim. Acta* **1996***, 244*, 165-170.

(106) Zheng, L. M.; Schmalle, H. W.; Huber, R.; Decurtins, S. Synthesis, Crystal Structure and Magnetic Properties of a Chloranilate-Bridged Manganese(II) Chain Compound: $[Mn(Bipy)(CA)]_n$ (Bipy = 2,2′-Bipyridine, CA = Chloranilate Anion). *Polyhedron* **1996***, 15*, 4399-4405.

(107) Frenzer, W.; Wartchow, R.; Bode, H. Crystal Structure of Disilver 2,5-Dichloro-[1,4]Benzoquinone-3,6-Diolate, $Ag_2(C_6O_4Cl_2)$. *Z. Kristallogr.* **1997***, 212*, 237-237.

(108) Kabir, M. K.; Kawata, S.; Adachi, K.; Kumagai, H.; Kitagawa, S. Crystal Structure and Magnetic Property of Cobalt(II) Assembled Compound, {Co(CA)(Bipym)]($H_2O)_2$}N (H_2CA = Chloranilic Acid, Bipym = 2,2-Bipyrimidine). *Mol. Cryst. Liq. Cryst. Sci. Technol. Sect. A. Mol. Cryst. Liq. Cryst.* **2000***, 342*, 211-216.

(109) Kabir, M. K.; Kawahara, M.; Kumagai, H.; Adachi, K.; Kawata, S.; Ishii, T.; Kitagawa, S. The Rational Syntheses of Manganese–chloranilate Compounds: Crystal Structures and Magnetic Properties. *Polyhedron* **2001***, 20*, 1417-1422.

(110) Robl, C.; Weiss, A. Komplexe Mit Substituierten 2,5-Dihydroxy-P-Benzochinonen: Das Isotype Paar BaC_6X_{20} 4 • 3 H_20 (X = CI, Br). *Z. Naturforsch.* **1986***, 41*, 1495.

(111) Kawata, S.; Kitagawa, S.; Kumagai, H.; Ishiyama, T.; Honda, K.; Tobita, H.; Adachi, K.; Katada, M. Novel Intercalation Host System Based on Transition Metal (Fe^{2+}, Co^{2+}, Mn^{2+}) Chloranilate Coordination Polymers. Single Crystal Structures and Properties. *Chem. Mater.* **1998***, 10*, 3902-3912.

(112) Papadimitriou, C.; Veltsistas, P.; Marek, J.; Novosad, J.; Slawin, A. M. Z.; Derek Woollins, J. Chloranilate Bridged Sodium Chains. *Inorganic Chemistry Communications* **1998***, 1*, 418-420.

(113) Veltsistas, P.; Papadimitriou, C.; Arabatzis, Y.; Slawin, A. M. Z.; Woollins, J. D. oxamate and Chloranilate Bridges in Polymeric Networks. *Phosphorus, Sulfur, and Silicon and the Related Elements* **1997***, 124*, 407-411.

(114) Abrahams, B. F.; Dharma, A. D.; Dyett, B.; Hudson, T. A.; Maynard-Casely, H.; Kingsbury, C. J.; McCormick, L. J.; Robson, R.; Sutton, A. L.; White, K. F. An Indirect Generation of 1D M^{II}-2,5-Dihydroxybenzoquinone Coordination Polymers, their Structural Rearrangements and Generation of Materials with a High Affinity for H_2, CO_2 and CH_4. *Dalton Trans.* **2016***, 45*, 1339-1344.

(115) Kawata, S.; Kitagawa, S.; Kondo, M.; Furuchi, I.; Munakata, M. Two-Dimensional Sheets of Tetragonal Copper(II) Lattices: X-Ray Crystal Structure and Magnetic Properties of $[Cu(C_6O_4Cl_2)(C_4H_4N_2)]_n$. *Angew. Chem. Int. Ed.* **1994***, 33*, 1759-1761.

(116) Nagayoshi, K.; Kabir, M. K.; Tobita, H.; Honda, K.; Kawahara, M.; Katada, M.; Adachi, K.; Nishikawa, H.; Ikemoto, I.; Kumagai, H.; Hosokoshi, Y.; Inoue, K.; Kitagawa, S.; Kawata, S. Design of Novel Inorganic Organic Hybrid Materials Based on Iron-Chloranilate Mononuclear Complexes: Characteristics of Hydrogen-Bond-Supported Layers Toward the Intercalation of Guests. *J. Am. Chem. Soc.* **2003***, 125*, 221-232.

(117) Abhervé, A.; Clemente-León, M.; Coronado, E.; Gómez-García, C. J.; Verneret, M. One-Dimensional and Two-Dimensional Anilate-Based Magnets with Inserted Spin-Crossover Complexes. *Inorg. Chem.* **2014***, 53*, 12014-12026.

(118) Weiss, A.; Riegler, E.; Robl, C. Polymeric 2,5-Dihydroxy-1,4-Benzoquinone Transition-Metal Complexes $Na_2(H_2O)_{24}[M_2(C_6H_2O_4)_3]$ (M = Mn^{2+}, Cd^{2+}). *Z. Naturforsch. B: Chem. Sci.* **1986***, 41*, 1501-1505.

(119) Robl, C. Complexes with Substituted 2,5-Dihydroxy-P-Benzoquinones: The Inclusion Compounds $[Y(H_2O)_3]_2$ $(C_6Cl_2O_4)_3 \cdot 6.6H_2O$ and $[Y(H_2O)_3]_2$ $(C_6Br_2O_4)_3 \cdot 6H_2O$. *Mater. Res. Bull.* **1987***, 22*, 1483-1491.

(120) Abrahams, B. F.; Coleiro, J.; Hoskins, B. F.; Robson, R. Gas Hydrate-Like Pentagonal Dodecahedral $M_2(H_2O)_{18}$ cages (M = Lanthanide Or Y) in 2,5-Dihydroxybenzoquinone-Derived Coordination Polymers. *Chem. Commun.* **1996**, 603-604.

(121) Luo, T.; Liu, Y.; Tsai, H.; Su, C.; Ueng, C.; Lu, K. A Novel Hybrid Supramolecular Network Assembled from Perfect Stacking of an Anionic Inorganic Layer and a Cationic Hydronium-Ion-Mediated Organic Layer. *Eur. J. Inorg. Chem.* **2004***, 2004*, 4253-4258.

(122) Shilov, G. V.; Nikitina, Z. K.; Ovanesyan, N. S.; Aldoshin, S. M.; Makhaev, V. D. Phenazineoxonium Chloranilatomanganate and Chloranilatoferrate: Synthesis, Structure, Magnetic Properties, and Mossbauer Spectra. *Russ. Chem. Bull.* **2011***, 60*, 1209-1219.

(123) Jeon, I. R.; Negru, B.; Van Duyne, R. P.; Harris, T. D. A 2D Semiquinone Radical-Containing Microporous Magnet with Solvent-Induced Switching from T_c = 26 to 80 K. *J. Am. Chem. Soc.* **2015***, 137*, 15699-15702.

(124) DeGayner, J. A.; Jeon, I. R.; Sun, L.; D., M.; Harris, T. D. 2D Conductive Iron-Quinoid Magnets Ordering Up to Tc = 105 K Via Heterogenous Redox Chemistry. *J. Am. Chem. Soc.* **2017***, 139*, 4175-4184.

(125) Kingsbury, C. J.; Abrahams, B. F.; D'Alessandro, D. M.; Hudson, T. A.; Murase, R.; Robson, R.; White, K. F. Role of NEt^{4+} in Orienting and Locking Together $[M_2lig_3]_2$ (6,3) Sheets (H2lig = Chloranilic Or Fluoranilic Acid) to Generate Spacious Channels Perpendicular to the Sheets. *Dalt. Trans.* **2017***, 17*, 1465-1470.

(126) Kumagai, H.; Kawata, S.; Kitagawa, S. Fabrication of Infinite Two-Dimensional Sheets of Tetragonal Metal(II) Lattices: X-Ray Crystal Structures and Magnetic Properties of [M(CA)(pyz)]N (M^{2+}=Mn^{2+} and Co^{2+}; H_2CA=chloranilic Acid; pyz=pyrazine). *Inorg. Chim. Acta* **2002***, 337*, 387-392.

(127) Atzori, M.; Pop, F.; Auban-Senzier, P.; Clérac, R.; Canadell, E.; Mercuri, M. L.; Avarvari, N. Complete Series of Chiral Paramagnetic Molecular Conductors Based on Tetramethyl-Bis(Ethylenedithio)-Tetrathiafulvalene (TM-BEDT-TTF) and Chloranilate-Bridged Heterobimetallic Honeycomb Layers. *Inorg. Chem.* **2015***, 54*, 3643-3653.

(128) Abhervé, A.; Mañas-Valero, S.; Clemente-León, M.; Coronado, E. Graphene Related Magnetic Materials: Micromechanical Exfoliation of 2D Layered Magnets Based on Bimetallic Anilate Complexes with Inserted $[Fe^{III}(Acac_2\text{-Trien})]^+$ and $[Fe^{III}(Sal_2\text{-Trien})]^+$ Molecules. *Che. Sci.* **2015***, 6*, 4665-4673.

(129) Benmansour, S.; Gómez-García, J. C. A Heterobimetallic Anionic 3,6-Connected 2D Coordination Polymer Based on Nitranilate as Ligand. *Polymers* **2016***, 8*, 89.

(130) Abrahams, B. F.; Grannas, M. J.; Hudson, T. A.; Hughes, S. A.; Pranoto, N. H.; Robson, R. Synthesis, Structure and Host-Guest Properties of $(Et_4N)_2Sn^{IV}Ca^{II}(Chloranilate)_4]$, a New Type of Robust Microporous Coordination Polymer with a 2D Square Grid Structure. *Dalton Trans.* **2011***, 40*, 12242-12247.

(131) Riley, P. E.; Pecoraro, V. L.; Carrano, C. J.; Raymond, K. N. *Inorg. Chem.* **1983***, 22*, 3096.

(132) Bock, H.; Nick, S.; Näther, C.; Bats, J. W. *Z. Naturforsch. B: Chem. Sci.* **1994***, 49*, 1021-1030.

(133) Abrahams, B. F.; Hudson, T. A.; McCormick, L. J.; Robson, R. Coordination Polymers of 2,5-Dihydroxybenzoquinone and Chloranilic Acid with the (10,3)-a Topology. *Cryst. Growth Des.* **2011***, 11*, 2717-2720.

(134) Darago, L. E.; Aubrey, M. L.; Yu, C. J.; Gonzalez, M. I.; Long, J. R. Electronic Conductivity, Ferrimagnetic Ordering, and Reductive Insertion Mediated by Organic Mixed-Valence in a Ferric Semiquinoid Metal-Organic Framework. *J. Am. Chem. Soc.* **2015***, 137*, 15703-15711.

(135) Che, C. M.; Kwong, S. S.; Poon, C. K.; Lai, T. F.; Mak, T. C. W. Cis Ruthenium Complexes of 1,4,8,11-Tetraazacyclotetradecane (Cyclam): Crystal and Molecular Structure of Cis-[Ru(cyclam)Cl_2]Cl. *Inorg. Chem.* **1985***, 24*, 1359-1363.

(136) Mukherjee, P.; Drew, M. G. B.; Gómez-García, C. J.; Ghosh, A. The Crucial Role of Polyatomic Anions in Molecular Architecture: Structural and Magnetic Versatility of Five Nickel(II) Complexes Derived from A N,N,O-Donor Schiff Base Ligand. *Inorg. Chem.* **2009***, 48*, 5848-5860.

(137) Martín, L.; Day, P.; Horton, P.; Nakatsuji, S.; Yamada, J.; Akutsu, H. Chiral Conducting Salts of BEDT-TTF Containing a Single Enantiomer of Tris(oxalato)Chromate(III) Crystallised from a Chiral Solvent. *J. Mater. Chem.* **2010***, 20*, 2738-2742.

(138) Martín, L.; Day, P.; Nakatsuji, S.; Yamada, J.; Akutsu, H.; Horton, P. A Molecular Charge Transfer Salt of BEDT-TTF Containing a Single Enantiomer of Tris(oxalato)Chromate(III) Crystallised from a Chiral Solvent. *CrystEngComm* **2010***, 12*, 1369-1372.

(139) Suh, J. S.; Shin, J. Y.; Yoon, C.; Lee, K. W.; Suh, I. H.; Lee, J. H.; Ryu, B. Y.; Lim, S. S. The Crystal and Molecular Structure of Sodium Magnesium Tris(oxalato)Chromate(Ⅲ) Decahydrate, NaMg[Cr(ox)$_3$]·10H_2O. *Bull. Korean Chem. Soc.* **1994***, 15*, 245-249.

(140) Kurmoo, M.; Graham, A. W.; Day, P.; Coles, S. J.; Hursthouse, M. B.; Caulfield, J. L.; Singleton, J.; Pratt, F. L.; Hayes, W. Superconducting and Semiconducting Magnetic Charge Transfer Salts: (BEDT-TTF)$_4$AFe(C_2O_4)$_3$.Cntdot.C_6H_5CN (A = H2O, K, NH_4). *J. Am. Chem. Soc.* **1995***, 117*, 12209-12217.

(141) Coronado, E.; Curreli, S.; Giménez-Saiz, C.; Gómez-García, C. J. The Series of Molecular Conductors and Superconductors ET_4[AFe(C_2O_4)$_3$]·PhX (ET = bis(ethylenedithio)tetrathiafulvalene; $(C_2O_4)^{2-}$ = oxalate; $A^+ = H_3O^+, K^+$; X = F, Cl, Br, and I): Influence of the Halobenzene Guest Molecules on the Crystal Structure and Superconducting Properties. *Inorg. Chem.* **2012***, 51*, 1111-1126.

(142) Suh, M. P.; Jeon, J. W.; Moon, H. R.; Min, K. S.; Choi, H. J. Self-Assembly of Hybrid Solids Consisting of 2D Supramolecular Networks and Intercalated Metal Complexes. *Comptes Rendus Chim.* **2005***, 8*, 1543-1551.

(143) Graham, A. W.; Kurmoo, M.; Day, P. ß"-(bedt-ttf)$_4$[(H_2O)Fe(C_2O_4)$_3$]·PhCN: The First Molecular Superconductor Containing Paramagnetic Metal Ions. *J. Chem. Soc. , Chem. Commun.* **1995**, 2061-2062.

(144) Coronado, E.; Curreli, S.; Giménez-Saiz, C.; Gómez-García, C. J. A Novel Paramagnetic Molecular Superconductor Formed by bis(ethylenedithio)tetrathiafulvalene, tris(oxalato) Ferrate(III) Anions and Bromobenzene as Guest Molecule: ET_4[(H_3O)Fe(C_2O_4)$_3$]·C_6H_5Br. *J. Mater. Chem.* **2005***, 15*, 1429-1436.

(145) Butler, K. R.; Snow, M. R. Absolute Configuration of the Tris-(1,10-Phenanthroline)Nickel(II) and Tris(oxalato)cobaltate(III) Complex Ions by X-Ray Structure Analysis. *J. Am. Chem. Soc.* **1971**, 565-569.

(146) Decurtins, S.; Schmalle, H. W.; Schneuwly, P.; Ensling, J.; Guetlich, P. A Concept for the Synthesis of 3-Dimensional Homo- and Bimetallic oxalate-Bridged Networks $[M_2(ox)_3]_n$. Structural, Moessbauer, and Magnetic Studies in the Field of Molecular-Based Magnets. *J. Am. Chem. Soc.* **1994***, 116*, 9521-9528.

(147) Coronado, E.; Galán-Mascaros, J. R.; Gómez-García, C. J.; Martínez-Agudo, J. M. Molecule-Based Magnets Formed by Bimetallic Three-Dimensional oxalate Networks and Chiral tris(bipyridyl) Complex Cations. The Series $[Z^{II}(bpy)_3][ClO_4][M^{III}M^{II}(ox)_3]$ (Z^{II} = Ru, Fe, Co, and Ni; M^{II} = Mn, Fe, Co, Ni, Cu, and Zn; ox = oxalate Dianion). *Inorg. Chem.* **2001***, 40*, 113-120.

(148) Barea, E.; Montoro, C.; Navarro, J. A. Toxic Gas Removal--Metal-Organic Frameworks for the Capture and Degradation of Toxic Gases and Vapours. *Chem. Soc. Rev.* **2014***, 43*, 5419-5430.

(149) Pang, J.; Jiang, F.; Wu, M.; Liu, C.; Su, K.; Lu, W.; Yuan, D.; Hong, M. A Porous Metal-Organic Framework with Ultrahigh Acetylene Uptake Capacity Under Ambient Conditions. *Nat. Comm.* **2015***, 6*, 7575.

(150) Wang, B.; Cote, A. P.; Furukawa, H.; O'Keeffe, M.; Yaghi, O. M. Colossal Cages in Zeolitic Imidazolate Frameworks as Selective Carbon Dioxide Reservoirs. *Nature* **2008***, 453*, 207-211.

(151) Schoedel, A.; Ji, Z.; Yaghi, O. M. The Role of Metal–organic Frameworks in a Carbon-Neutral Energy Cycle. *Nature Energy* **2016***, 1*, 16034.

(152) Canivet, J.; Fateeva, A.; Guo, Y.; Coasne, B.; Farrusseng, D. Water Adsorption in MOFs: Fundamentals and Applications. *Chem. Soc. Rev.* **2014***, 43*, 5594-5617.

(153) Kreno, L. E.; Leóng, K.; Farha, O. K.; Allendorf, M.; Van Duyne, R. P.; Hupp, J. T. Metal-Organic Framework Materials as Chemical Sensors. *Chem. Rev.* **2012***, 112*, 1105-1125.

(154) Liu, D.; Lu, K.; Poon, C.; Lin, W. Metal-Organic Frameworks as Sensory Materials and Imaging Agents. *Inorg. Chem.* **2014***, 53*, 1916-1924.

(155) Nandasiri, M. I.; Jambovane, S. R.; McGrail, B. P.; Schaef, H. T.; Nune, S. K. Adsorption, Separation, and Catalytic Properties of Densified Metal-Organic Frameworks. *Coord. Chem. Rev.* **2016***, 311*, 38-52.

(156) Wang, S.; Wang, X. Multifunctional Metal-Organic Frameworks for Photocatalysis. *Small* **2015***, 11*, 3097-3112.

(157) Hu, Z.; Deibert, B. J.; Li, J. Luminescent Metal-Organic Frameworks for Chemical Sensing and Explosive Detection. *Chem. Soc. Rev.* **2014***, 43*, 5815-5840.

(158) Wang, L.; Han, Y.; Feng, X.; Zhou, J.; Qi, P. Metal–organic Frameworks for Energy Storage: Batteries and Supercapacitors. *Coord. Chem. Rev.* **2016***, 307*, 361-381.

(159) Furukawa, H.; Cordova, K. E.; O'Keeffe, M.; Yaghi, O. M. The Chemistry and Applications of Metal-Organic Frameworks. *Science* **2013***, 341*, 1230444.

(160) So, M. C.; Wiederrecht, G. P.; Mondloch, J. E.; Hupp, J. T.; Farha, O. K. Metal-Organic Framework Materials for Light-Harvesting and Energy Transfer. *Chem. Commun.* **2015***, 51*, 3501-3510.

(161) Horcajada, P.; Gref, R.; Baati, T.; Allan, P. K.; Maurin, G.; Couvreur, P.; Férey, G.; Morris, R. E.; Serre, C. Metal-Organic Frameworks in Biomedicine. *Chem. Rev.* **2012***, 112*, 1232-1268.

(162) Kurmoo, M. Magnetic Metal-Organic Frameworks. *Chem. Soc. Rev.* **2009***, 38*, 1353-1379.

(163) Stavila, V.; Talin, A. A.; Allendorf, M. D. MOF-Based Electronic and Opto-Electronic Devices. *Chem. Soc. Rev.* **2014***, 43*, 5994-6010.

(164) Li, J. R.; Yu, Q.; Sanudo, E. C.; Tao, Y.; Song, W. C. Three-Dimensional Homospin Inorganic–Organic Ferrimagnet Constructed from (VO) Chains Linking {[5-(Pyrimidin-2-Yl)Tetrazolato-(Cu)] } Layers. *Chem. Mater.* **2008***, 20*, 1218-1220.

(165) Rehwol, R. E.; Chasen, B. L.; Li, J. B. 2-Chloro-5-Cyano-3,6-Dihydroxybenzoquinone, a New Analytical Reagent for the Spectrophotometric Determination of Calcium(II). *Anal. Chem.* **1966***, 38*, 1018-1019.

(166) Halcrow, M. A. Structure:Function Relationships in Molecular Spin-Crossover Complexes. *Chem. Soc. Rev.* **2011***, 40*, 4119-4142.

(167) Williams, J. M.; Ferraro, J. R.; Thorn, R. J.; Carlson, K. D.; Geiser, U.; Wang, H. H.; Kini, A. M.; Whangbo, M. H. In *Organic Superconductors (Including Fullerenes), Synthesis, Structure, Properties and Theory;* Crimes, R. N., Ed.; Prentice Hall: Englewood Cliffs, NJ, 1992; .

(168) Zhou, H.; Long, J. R.; Yaghi, O. M. Introduction to Metal–Organic Frameworks. *Chem. Rev.* **2012***, 112*, 673-674.

(169) Alipour, M.; Akintola, O.; Buchholz, A.; Mirzaei, M.; Eshtiagh-Hosseini, H.; Görls, H.; Plass, W. Size-Dependent Self-Assembly of Lanthanide-Based Coordination Frameworks with Phenanthroline-2,9-Dicarboxylic Acid as a Preorganized Ligand in Hybrid Materials. *Eur. J. Inorg. Chem.* **2016***, 2016*, 5356-5365.

(170) Guillou, O.; Daiguebonne, C.; Calvez, G.; Bernot, K. A Long Journey in Lanthanide Chemistry: From Fundamental Crystallogenesis Studies to Commercial Anticounterfeiting Taggants. *Acc. Chem. Res.* **2016***, 49*, 844-856.

(171) Chandler, B. D.; Cramb, D. T.; Shimizu, G. K. H. Microporous Metal-Organic Frameworks Formed in a Stepwise Manner from Luminescent Building Blocks. *J. Am. Chem. Soc.* **2006***, 128*, 10403-10412.

(172) Harbuzaru, B. ; Corma, A.; Rey, F.; Atienzar, P.; Jordà, J. ; García, H.; Ananias, D.; Carlos, L. ; Rocha, J. Metal–Organic Nanoporous Structures with Anisotropic Photoluminescence and Magnetic Properties and their use as Sensors. *Angewandte Chemie International Edition* **2008***, 47*, 1080-1083.

(173) Binnemans, K. Lanthanide-Based Luminescent Hybrid Materials. *Chem. Rev.* **2009***, 109*, 4283-4374.

(174) Armelao, L.; Quici, S.; Barigelletti, F.; Accorsi, G.; Bottaro, G.; Cavazzini, M.; Tondello, E. Design of Luminescent Lanthanide Complexes: From Molecules to Highly Efficient Photo-Emitting Materials. *Coord. Chem. Rev.* **2010***, 254*, 487-505.

(175) Rocha, J.; Carlos, L. D.; Paz, F. A. A.; Ananias, D. Luminescent Multifunctional Lanthanides-Based Metal-Organic Frameworks. *Chem. Soc. Rev.* **2011***, 40*, 926-940.

(176) Senthil Kumar, K.; Schafer, B.; Lebedkin, S.; Karmazin, L.; Kappes, M. M.; Ruben, M. Highly Luminescent Charge-Neutral Europium(Iii) and Terbium(Iii) Complexes with Tridentate Nitrogen Ligands. *Dalton Trans.* **2015***, 44*, 15611-15619.

(177) Zhao, Y.; He, L.; Qin, S.; Tao, G. H. Tunable Luminescence of Lanthanide (Ln = Sm, Eu, Tb) Hydrophilic Ionic Polymers Based on Poly(N-Methyl-4-Vinylpyridinium-Co-Styrene) Cations. *Polym. Chem.* **2016***, 7*, 7068-7077.

(178) Pointillart, F.; Cador, O.; Le Guennic, B.; Ouahab, L. Uncommon Lanthanide Ions in Purely 4f Single Molecule Magnets. *Coord. Chem. Rev.* **2017***, in press*.

(179) Sorace, L.; Benelli, C.; Gatteschi, D. Lanthanides in Molecular Magnetism: Old Tools in a New Field. *Chem. Soc. Rev.* **2011***, 40*, 3092-3104.

(180) Long, J.; Habib, F.; Lin, P. H.; Korobkov, I.; Enright, G.; Ungur, L.; Wernsdorfer, W.; Chibotaru, L. F.; Murugesu, M. Single-Molecule Magnet Behavior for an Antiferromagnetically Superexchange-Coupled Dinuclear Dysprosium(III) Complex. *J. Am. Chem. Soc.* **2011***, 133*, 5319-5328.

(181) Bünzli, J. G.; Eliseeva, S. V. In *Basics of Lanthanide Photophysics*; Lanthanide Luminescence: Photophysical, Analytical and Biological Aspects; Springer Berlin Heidelberg: Berlin, Heidelberg, 2011; Vol. 7, pp 1-45.

(182) Eliseeva, S. V.; Bunzli, J. C. G. Lanthanide Luminescence for Functional Materials and Bio-Sciences. *Chem. Soc. Rev.* **2010***, 39*, 189-227.

(183) Wang, G. T.; Tang, Z. Y.; Zhou, H. T.; Zou, P.; Rao, H. B.; Zhang, Y. S.; Hou, G. F. Syntheses and Topological Structures of Four Luminescent Lanthanide Phosphonates Based on 2-(Pyridyl-N-oxide)Methylphosphonic Acid and oxalic Acid. *Polyhedron* **2016***, 117*, 259-264.

(184) Mohapatra, S.; Hembram, K. P. S. S.; Waghmare, U.; Maji, T. K. Immobilization of Alkali Metal Ions in a 3D Lanthanide-Organic Framework: Selective Sorption and H_2 Storage Characteristics. *Chem. Mater.* **2009***, 21*, 5406-5412.

(185) Decurtins, S.; Gross, M.; Schmalle, H. W.; Ferlay, S. Molecular Chromium(III)â^'Lanthanide(III) Compounds (Ln = La, Ce, Pr, Nd) with a Polymeric, Ladder-Type Architecture:Â€‰ A Structural and Magnetic Study. *Inorg. Chem.* **1998***, 37*, 2443-2449.

(186) Mao, J. G. Structures and Luminescent Properties of Lanthanide Phosphonates. *Coord. Chem. Rev.* **2007***, 251*, 1493-1520.

(187) Malinowski, M.; Frukacz, Z.; Szuflińska, M.; Wnuk, A.; Kaczkan, M. Optical Transitions of Ho^{3+} in YAG. *J. Alloys Compounds* **2000***, 300–301*, 389-394.

(188) Szostak, M. M.; Kozankiewicz, B.; Lipiński, J. Low-Temperature Photoluminescence of P-Nitroaniline and O-Methyl-P-Nitroaniline Crystals. *Spectrochimica Acta Part A: Molecular and Biomolecular Spectroscopy* **2007***, 67*, 1412-1416.

(189) Xu, G. F.; Wang, Q. L.; Gamez, P.; Ma, Y.; Clerac, R.; Tang, J.; Yan, S. P.; Cheng, P.; Liao, D. Z. A Promising New Route Towards Single-Molecule Magnets Based on the oxalate Ligand. *Chem. Commun.* **2010***, 46*, 1506-1508.

(190) Elbanowski, M.; Mąkowska, B. The Lanthanides as Luminescent Probes in Investigations of Biochemical Systems. *Journal of Photochemistry and Photobiology A: Chemistry* **1996***, 99*, 85-92.

(191) Yam, V. W. W.; Lo, K. K. W. Recent Advances in Utilization of Transition Metal Complexes and Lanthanides as Diagnostic Tools. *Coord. Chem. Rev.* **1999***, 184*, 157-240.

(192) Reichert, D. E.; Lewis, J. S.; Anderson, C. J. Metal Complexes as Diagnostic Tools. *Coord. Chem. Rev.* **1999***, 184*, 3-66.

(193) Selvin, P. R. Principles and Biophysical Applications of Lanthanide-Based Probes. *Annual Reviews* **2002***, 31*, 1-516.

(194) Hemmilä, I.; Laitala, V. Progress in Lanthanides as Luminescent Probes. *J. Fluoresc.* **2005***, 15*, 529-542.

(195) Faulkner, S.; Pope, S. J. A.; Burton-Pye, B. P. Lanthanide Complexes for Luminescence Imaging Applications. *Applied Spectroscopy Reviews* **2005***, 40*, 1-31.

(196) Bottrill, M.; Kwok, L.; Long, N. J. Lanthanides in Magnetic Resonance Imaging. *Chem. Soc. Rev.* **2006***, 35*, 557-571.

(197) Hermann, P.; Kotek, J.; Kubicek, V.; Lukes, I. Gadolinium(III) Complexes as MRI Contrast Agents: Ligand Design and Properties of the Complexes. *Dalton Trans.* **2008***, 23*, 3027-3047.

(198) Bünzli, J. C. G. Lanthanide Luminescence for Biomedical Analyses and Imaging. *Chem. Rev.* **2010***, 110*, 2729-2755.

(199) Heffern, M. C.; Matosziuk, L. M.; Meade, T. J. Lanthanide Probes for Bioresponsive Imaging. *Chem. Rev.* **2014***, 114*, 4496-4539.

(200) Dasari, S.; Singh, S.; Sivakumar, S.; Patra, A. K. Dual-Sensitized Luminescent Europium(III) and Terbium(III) Complexes as Bioimaging and Light-Responsive Therapeutic Agents. *Chem. Eur. J.* **2016***, 22*, 17387-17396.

(201) Tang, G.; Gao, J.; Wang, C.; Tan, H. Luminescent Lanthanide Coordination Polymer as a Platform for DNA Colorimetric Detection. *Sensors Actuators B: Chem.* **2017***, 244*, 571-576.

(202) Katkova, M. A.; Bochkarev, M. N. New Trends in Design of Electroluminescent Rare Earth Metallo-Complexes for OLEDs. *Dalton Trans.* **2010***, 39*, 6599-6612.

(203) Zhao, Y. W.; Zhang, F. Q.; Zhang, X. M. Single Component Lanthanide Hybrids Based on Metal-Organic Framework for Near-Ultraviolet White Light LED. *ACS Appl. Mater. Interfaces* **2016***, 8*, 24123-24130.

(204) Zinna, F.; Pasini, M.; Galeotti, F.; Botta, C.; Di Bari, L.; Giovanella, U. Design of Lanthanide-Based OLEDs with Remarkable Circularly Polarized Electroluminescence. *Adv. Funct. Mater.* **2017***, 27*, 1603719.

(205) Parker, D. Luminescent Lanthanide Sensors for pH, pO_2 and Selected Anions. *Coord. Chem. Rev.* **2000***, 205*, 109-130.

(206) Chen, J.; Yi, F. Y.; Yu, H.; Liu, X.; Han, L.; Pang, G. A Highly Robust Terbium Coordination Polymer as a Multiresponsive Luminescent Sensor for Detecting Pollutant Anions. *Eur. J. Inorg. Chem* **2016***, 2016*, 3994-3998.

(207) Zhou, Z. Y.; Han, Y. H.; Xing, X. S.; Du, S. W. Microporous Lanthanide Metal–Organic Frameworks with Multiple 1D Channels: Tunable Colors, White-Light Emission, and Luminescent Sensing for Iron(II) and Iron(III). *ChemPlusChem* **2016***, 81*, 798-803.

(208) Diaz-Torres, R.; Alvarez, S. Coordinating Ability of Anions and Solvents Towards Transition Metals and Lanthanides. *Dalton Trans.* **2011***, 40*, 10742-10750.

(209) Benmansour, S.; Pérez-Herráez, I.; López-Martínez, G.; Gómez García, C. J. Solvent-Modulated Structures in Anilato-Based 2D Coordination Polymers. *Polyhedron* **2017***, 135*, 17-25.

(210) Zheng, X.; Sun, C.; Lu, S.; Liao, F.; Gao, S.; Jin, L. New Porous Lanthanide-Organic Frameworks: Synthesis, Characterization, and Properties of Lanthanide 2,6-Naphthalenedicarboxylates. *Angewandte Chemie International Edition* **2004***, 2004*, 3262-3268.

(211) Ma, S.; Yuan, D.; Wang, X. S.; Zhou, H. C. Microporous Lanthanide Metal-Organic Frameworks Containing Coordinatively Linked Interpenetration: Syntheses, Gas Adsorption Studies, Thermal Stability Analysis, and Photoluminescence Investigation. *Inorg. Chem.* **2009***, 48*, 2072-2077.

(212) Luo, F.; Batten, S. R. Metal-Organic Framework (MOF): Lanthanide(III)-Doped Approach for Luminescence Modulation and Luminescent Sensing. *Dalton Trans.* **2010***, 39*, 4485-4488.

(213) Decadt, R.; Van Hecke, K.; Depla, D.; Leus, K.; Weinberger, D.; Van Driessche, I.; Van Der Voort, P.; Van Deun, R. Synthesis, Crystal Structures, and Luminescence Properties of Carboxylate Based Rare-Earth Coordination Polymers. *Inorg. Chem.* **2012***, 51*, 11623-11634.

(214) Datcu, A.; Roques, N.; Jubera, V.; Maspoch, D.; Fontrodona, X.; Wurst, K.; Imaz, I.; Mouchaham, G.; Sutter, J. P.; Rovira, C.; Veciana, J. Three-Dimensional Porous Metal–Radical Frameworks Based on Triphenylmethyl Radicals. *Chem. Eur. J.* **2012***, 18*, 152-162.

(215) Li, H.; Shi, W.; Zhao, K.; Niu, Z.; Li, H.; Cheng, P. Highly Selective Sorption and Luminescent Sensing of Small Molecules Demonstrated in a Multifunctional Lanthanide Microporous Metal–Organic Framework Containing 1D Honeycomb-Type Channels. *Chem. Eur. J.* **2013***, 19*, 3358-3365.

(216) Biswas, S.; Jena, H. S.; Goswami, S.; Sanda, S.; Konar, S. Synthesis and Characterization of Two Lanthanide (Gd3+ and Dy3+)-Based Three-Dimensional Metal Organic Frameworks with Squashed Metallomacrocycle Type Building Blocks and their Magnetic, Sorption, and Fluorescence Properties Study. *Cryst. Growth Des.* **2014***, 14*, 1287-1295.

(217) Roy, S.; Chakraborty, A.; Maji, T. K. Lanthanide–organic Frameworks for Gas Storage and as Magneto-Luminescent Materials. *Coord. Chem. Rev.* **2014***, 273–274*, 139-164.

(218) Li, B.; Wen, H. M.; Cui, Y.; Qian, G.; Chen, B. Multifunctional Lanthanide Coordination Polymers. *Progress in Polymer Science* **2015***, 48*, 40-84.

(219) Wu, J.; Zhang, H.; Du, S. Tunable Luminescence and White Light Emission of Mixed Lanthanide-Organic Frameworks Based on Polycarboxylate Ligands. *J. Mater. Chem. C* **2016***, 4*, 3364-3374.

(220) Harbuzaru, B. ; Corma, A.; Rey, F.; Jordà, J. ; Ananias, D.; Carlos, L. ; Rocha, J. A Miniaturized Linear pH Sensor Based on a Highly Photoluminescent Self-Assembled Europium(III) Metal–Organic Framework. *Angewandte Chemie International Edition* **2009***, 48*, 6476-6479.

(221) Gütlich, P.; Gaspar, A. B.; Garcia, Y. Spin State Switching in Iron Coordination Compounds. *Beilstein Journal of Organic Chemistry* **2013***, 9*, 342-391.

(222) Halcrow, M. A. In *Structure:Function Relationships in Molecular Spin-Crossover Materials;* Spin-Crossover Materials; John Wiley & Sons Ltd: 2013; pp 147-169.

(223) Gütlich, P.; Goodwin, H. A. *Top. Curr. Chem.* **2004***, 233*, 1-49.

(224) Murray, K. S. In *The Development of Spin-Crossover Research;* Spin-Crossover Materials; John Wiley & Sons Ltd: 2013; pp 1-54.

(225) Bousseksou, A.; Molnar, G.; Salmon, L.; Nicolazzi, W. Molecular Spin Crossover Phenomenon: Recent Achievements and Prospects. *Chem. Soc. Rev.* **2011***, 40*, 3313-3335.

(226) Gütlich, P.; Hauser, A.; Spiering, H. Thermal and Optical Switching of Iron(II) Complexes. *Angew. Chem. Int. Ed.* **1994***, 33*, 2024-2054.

(227) Halcrow, M. A. Iron(II) Complexes of 2,6-di(pyrazol-1-Yl)pyridines—A Versatile System for Spin-Crossover Research. *Coord. Chem. Rev.* **2009***, 253*, 2493-2514.

(228) Sato, O.; Tao, J.; Zhang, Y. Z. Control of Magnetic Properties through External Stimuli. *Angew. Chem. Int. Ed.* **2007***, 46*, 2152-2187.

(229) Gütlich, P.; Garcia, Y.; Goodwin, H. A. Spin Crossover Phenomena in Fe(II) Complexes. *Chem. Soc. Rev.* **2000***, 29*, 419-427.

(230) Nihei, M.; Shiga, T.; Maeda, Y.; Oshio, H. Spin Crossover Iron(III) Complexes. *Coord. Chem. Rev.* **2007***, 251*, 2606-2621.

(231) Barrett, S. A.; Kilner, C. A.; Halcrow, M. A. Spin-Crossover in $[Fe(3\text{-}bpp)_2]BF4]_2$ in Different Solvents - A Dramatic Stabilisation of the Low-Spin State in Water. *Dalton Trans.* **2011***, 40*, 12021-12024.

(232) Halcrow, M. A. The Spin-States and Spin-Transitions of Mononuclear Iron(II) Complexes of Nitrogen-Donor Ligands. *Polyhedron* **2007***, 26*, 3523-3576.

(233) Hauser, A.; Jeftić, J.; Romstedt, H.; Hinek, R.; Spiering, H. Cooperative Phenomena and Light-Induced Bistability in Iron(II) Spin-Crossover Compounds. *Coord. Chem. Rev.* **1999***, 190–192*, 471-491.

(234) Gaspar, A. B.; Seredyuk, M.; Gütlich, P. Spin Crossover in Iron(II) Complexes: Recent Advances. *J. Mol. Struct.* **2009***, 924-926*, 9-19.

(235) Halcrow, M. A. Structure:Function Relationships in Molecular Spin-Crossover Complexes. *Chem. Soc. Rev.* **2011***, 40*, 4119-4142.

(236) Murray, K. S. Advances in Polynuclear Iron(II), Iron(III) and Cobalt(II) Spin-Crossover Compounds. *Eur. J. Inorg. Chem* **2008**, 3101-3121.

(237) Harding, D. J.; Harding, P.; Phonsri, W. Spin Crossover in Iron(III) Complexes. *Coord. Chem. Rev.* **2016***, 313*, 38-61.

(238) Hauser, A. Ligand Field Theoretical Considerations. *Top. Curr. Chem.* **2004***, 233*, 49-58.

(239) Hayami, S.; Komatsu, Y.; Shimizu, T.; Kamihata, H.; Lee, Y. H. Spin-Crossover in Cobalt(II) Compounds Containing Terpyridine and its Derivatives. *Coord. Chem. Rev.* **2011***, 255*, 1981-1990.

(240) Krivokapic, I.; Zerara, M.; Daku, M. L.; Vargas, A.; Enachescu, C.; Ambrus, C.; Tregenna-Piggott, P.; Amstutz, N.; Krausz, E.; Hauser, A. Spin-Crossover in Cobalt(II) Imine Complexes. *Coord. Chem. Rev.* **2007***, 251*, 364-378.

(241) Goodwin, H. A. Spin Crossover in Cobalt(II) Systems. in: Spin Crossover in Transition Metal Compounds II. . *Topics in current chemistry* **2004***, 234*, 23-47.

(242) Real, J. A.; Gaspar, A. B.; Munoz, M. C. Thermal, Pressure and Light Switchable Spin-Crossover Materials. *Dalton Trans.* **2005**, 2062-2079.

(243) Figgis, B. N.; Lewis, J. In *The Magnetic Properties of Transition Metal Complexes;* Progress in Inorganic Chemistry; John Wiley & Sons, Inc.: 2007; pp 37-239.

(244) König, E. In *Structural Changes Accompanying Continuous and Discontinuous Spin-State Transitions;* Progress in Inorganic Chemistry; John Wiley & Sons, Inc.: 2007; Vol. 35, pp 527-622.

(245) Halcrow, M. A. The Foundation of Modern Spin-Crossover. *Chem. Commun.* **2013***, 49*, 10890-10892.

(246) Kershaw Cook, L. J.; Kulmaczewski, R.; Mohammed, R.; Dudley, S.; Barrett, S. A.; Little, M. A.; Deeth, R. J.; Halcrow, M. A. A Unified Treatment of the Relationship between Ligand Substituents and Spin State in a Family of Iron(II) Complexes. *Angewandte Chemie International Edition* **2016***, 55*, 4327-4331.

(247) Money, V. A.; Elhaik, J.; Radosavljevic Evans, I.; Halcrow, M. A.; Howard, J. A. K. A Study of the Thermal and Light Induced Spin Transition in $[FeL_2](BF_4)_2$ and $[FeL_2](ClO_4)_2$ L = 2,6-di(3-methylpyrazol-1-yl)pyrazine. *Dalton Trans.* **2004**, 65-69.

(248) Roberts, T. D.; Tuna, F.; Malkin, T. L.; Kilner, C. A.; Halcrow, M. A. An Iron(II) Complex Exhibiting Five Anhydrous Phases, Two of which Interconvert by Spin-Crossover with Wide Hysteresis. *Chem. Sci.* **2012***, 3*, 349-354.

(249) Lazar, H. Z.; Forestier, T.; Barrett, S. A.; Kilner, C. A.; Letard, J. F.; Halcrow, M. A. Thermal and Light-Induced Spin-Crossover in Salts of the Heptadentate Complex Tris(4-{pyrazol-3-yl}-3-aza-3-butenyl)amine]Iron(II). *Dalton Trans.* **2007**, 4276-4285.

(250) Létard, J. F.; Guionneau, P.; Goux-Capes, L. *Top. Curr. Chem.* **2004***, 235*, 221-249.

(251) Garcia, Y.; Ksenofontov, V.; Mentior, S.; Dîrtu, M. M.; Gieck, C.; Bhatthacharjee, A.; Gütlich, P. *Chem. Eur. J.* **2008***, 14*, 3745-3758.

(252) McGravey, J. J.; Lawthers, I. Photochemically-induced perturbation of the A ⇌ T equilibrium in Fe complexes by pulsed laser irradiation in the metal-to-ligand charge-transfer absorption band. *J. Chem. Soc. , Chem. Commun.* 1982*, 16*, 906-907.

(253) Decurtins, S.; Gütlich, P.; Köhler, C. P.; Spiering, H.; Hauser, A. Light-Induced Excited Spin State Trapping in a Transition-Metal Complex: The Hexa-1-Propyltetrazole-Iron (II) Tetrafluoroborate Spin-Crossover System. *Chem. Phys. Lett.* **1984***, 105*, 1-4.

(254) Decurtins, S.; Gutlich, P.; Hasselbach, K. M.; Hauser, A.; Spiering, H. Light-Induced Excited-Spin-State Trapping in Iron(II) Spin-Crossover Systems. Optical Spectroscopic and Magnetic Susceptibility Study. *Inorg. Chem.* **1985***, 24*, 2174-2178.

(255) Buchen, T.; Gütlich, P.; Sugiyarto, K. H.; Goodwin, H. A. High-Spin → Low-Spin Relaxation in $[Fe(bpp)_2](CF_3SO_3)_2 \cdot H2O$ After LIESST and Thermal Spin-State Trapping—Dynamics of Spin Transition Versus Dynamics of Phase Transition. *Chem. Eur. J.* **1996***, 2*, 1134-1138.

(256) Hauser, A. Reversibility of Light-Induced Excited Spin State Trapping in the $Fe(ptz)_6(BF_4)_2$, and the $Zn_{1-x}Fex(ptz)_6(BF_4)_2$ Spin-Crossover Systems. *Chem. Phys. Lett.* **1986***, 124*, 543-548.

(257) Hauser, A.; Adler, J.; Gütlich, P. Light-Induced Excited Spin State Trapping (LIESST) in $[Fe(2\text{-}Mephen)_3]^{2+}$ Embedded in Polymer Matrices. *Chem. Phys. Lett.* **1988***, 152*, 468-472.

(258) Hauser, A. Cooperative Effects on the HS→LS Relaxation in the $[Fe(ptz)_6](BF_4)_2$ Spin-Crossover System. *Chem. Phys. Lett.* **1992***, 192*, 65-70.

(259) Hauser, A. Light-Induced Spin Crossover and the High-Spin→low-Spin Relaxation; Spin Crossover in Transition Metal Compounds II. *Top. Curr. Chem.* **2004***, 234*, 155-198.

(260) Marcén, S.; Lecren, L.; Capes, L.; Goodwin, H. A.; Létard, J. F. Critical Temperature of the LIESST Effect in a Series of Hydrated and Anhydrous Complex Salts $[Fe(bpp)_2]X_2$. *Chem. Phys. Lett.* **2002***, 358*, 87-95.

(261) Shimamoto, N.; Ohkoshi, S. I.; Sato, O.; Hashimoto, K. One-Shot-Laser-Pulse-Induced Cooperative Charge Transfer Accompanied by Spin Transition in a Co-Fe Prussian Blue Analog at Room Temperature. *Chem. Lett.* **2002***, 31*, 486-487.

(262) Freysz, E.; Montant, S.; Létard, S.; Létard, J. F. Single Laser Pulse Induces Spin State Transition within the Hysteresis Loop of an Iron Compound. *Chem. Phys. Lett.* **2004***, 394*, 318-323.

(263) Bonhommeau, S.; Molnár, G.; Galet, A.; Zwick, A.; Real, J. A.; McGarvey, J. J.; Bousseksou, A. One Shot Laser Pulse Induced Reversible Spin Transition in the Spin-Crossover Complex $[Fe(C_4H_4N_2)\{Pt(CN)_4\}]$ at Room Temperature. *Angew. Chem. Int. Ed.* **2005***, 44*, 4069-4073.

(264) Coronado, E.; Giménez-López, M. C.; Giménez-Saiz, C.; Romero, F. M. Spin Crossover Complexes as Building Units of Hydrogen-Bonded Nanoporous Structures. *CrystEngComm* **2009***, 11*, 2198-2203.

(265) Ben Djamâa, A.; Clemente-León, M.; Coronado, E.; López-Jordà, M. Insertion of FeII Complexes with Schiff Base Ligands Derived from Imidazole Or Pyridine into 3D Bimetallic oxalate-Based Ferromagnets. *Polyhedron* **2013***, 64*, 142-150.

(266) Sanchez-Sanchez, C.; Desplanches, C.; Clemente-Juan, J. M.; Clemente-León, M.; Coronado, E. Photomagnetic Properties of an Fe(Ii) Spin-Crossover Complex of 6-(3,5-Diamino-2,4,6-Triazinyl)-2,2prime Or Minute]-Bipyridine and its Insertion into 2D and 3D Bimetallic oxalate-Based Networks. *Dalton Trans.* **2017***, 46*, 2680-2689.

(267) Ki, W.; Li, J.; Eda, G.; Chhowalla, M. Direct White Light Emission from Inorganic-Organic Hybrid Semiconductor Bulk Materials. *J. Mater. Chem.* **2010***, 20*, 10676-10679.

(268) Humphreys, C. J. Solid-State Lighting. *MRS Bull* **2008***, 33*, 459-470.

(269) Crawford, M. H. LEDs for Solid-State Lighting: Performance Challenges and Recent Advances. *IEEE J. Sel. Topics in Quantum Electron.* **2009***, 15*, 1028-1040.

(270) Coppo, P.; Duati, M.; Kozhevnikov, V. N.; Hofstraat, J. W.; De Cola, L. White-Light Emission from an Assembly Comprising Luminescent Iridium and Europium Complexes. *Angew. Chem. Int.. Ed.* **2005***, 44*, 1806-1810.

(271) Yam, F. K.; Hassan, Z. Innovative Advances in LED Technology. *Microelectron. J.* **2005***, 36*, 129-137.

(272) Huang, J.; Li, G.; Wu, E.; Xu, Q.; Yang, Y. Achieving High-Efficiency Polymer White-Light-Emitting Devices. *Adv Mater* **2006***, 18*, 114-117.

(273) D'Andrade, B. Lighting: White Phosphorescent LEDs Offer Efficient Answer. *Nat Photon* **2007***, 1*, 33-34.

(274) Zhao, Y. S.; Fu, H. ; Hu, F. ; Peng, A. ; Yang, W. ; Yao, J. Tunable Emission from Binary Organic One-Dimensional Nanomaterials: An Alternative Approach to White-Light Emission. *Adv Mater* **2008***, 20*, 79-83.

(275) Rogach, A. ; Gaponik, N.; Lupton, J. ; Bertoni, C.; Gallardo, D. ; Dunn, S.; Li Pira, N.; Paderi, M.; Repetto, P.; Romanov, S. ; O'Dwyer, C.; Sotomayor Torres, C. ; Eychmüller, A. Light-Emitting Diodes with Semiconductor Nanocrystals. *Angew. Chem. Int.. Ed.* **2008***, 47*, 6538-6549.

(276) Wiesmann, C.; Bergenek, K.; Linder, N.; Schwarz, U. T. Photonic Crystal LEDs – Designing Light Extraction. *Laser. Photon. Rev.* **2009***, 3*, 262-286.

(277) Wang, M. S.; Guo, S. P.; Li, Y.; Cai, L. Z.; Zou, J. P.; Xu, G.; Zhou, W. W.; Zheng, F. K.; Guo, G. C. A Direct White-Light-Emitting Metal - Organic Framework with Tunable Yellow-to-White Photoluminescence by Variation of Excitation Light. *J. Am. Chem. Soc.* **2009***, 131*, 13572-13573.

(278) Chen, L.; Lin, C. C.; Yeh, C. W.; Liu, R. S. Light Converting Inorganic Phosphors for White Light-Emitting Diodes. *Materials* **2010***, 3*, 2172-2195.

(279) Lin, C. C.; Liu, R. S. Advances in Phosphors for Light-Emitting Diodes. *J. Phys. Chem. Lett.* **2011***, 2*, 1268-1277.

(280) Fang, X.; Roushan, M.; Zhang, R.; Peng, J.; Zeng, H.; Li, J. Tuning and Enhancing White Light Emission of III Based Inorganic and Organic Hybrid Semiconductors as Single-Phased Phosphors. *Chem. Mater.* **2012***, 24*, 1710-1717.

(281) Chang, M. H.; Das, D.; Varde, P. V.; Pecht, M. Light Emitting Diodes Reliability Rev. *Microelectron. Reliab.* **2012***, 52*, 762-782.

(282) Ki, W.; Li, J. A Semiconductor Bulk Material that Emits Direct White Light. *J. Am. Chem. Soc.* **2008***, 130*, 8114-8115.

(283) Mitschke, U.; Bauerle, P. The Electroluminescence of Organic Materials. *J. Mater. Chem.* **2000***, 10*, 1471-1507.

(284) Geffroy, B.; le Roy, P.; Prat, C. Organic Light-Emitting Diode (OLED) Technology: Materials, Devices and Display Technologies. *Polym. Int.* **2006***, 55*, 572-582.

(285) Misra, A.; Kumar, P.; Kamalasanan, N. M.; Chandra, S. White Organic LEDs and their Recent Advancements. *Semiconductor Science and Technology* **2006***, 21*, R35-R47.

(286) Wong, W. Y.; Ho, C. L. Heavy Metal Organometallic Electrophosphors Derived from Multi-Component Chromophores. *Coord. Chem. Rev.* **2009***, 253*, 1709-1758.

(287) Gather, M. C.; Köhnen, A.; Meerholz, K. White Organic Light-Emitting Diodes. *Adv Mater* **2011***, 23*, 233-248.

(288) Sessolo, M.; Bolink, H. J. Hybrid Organic–Inorganic Light-Emitting Diodes. *Adv Mater* **2011***, 23*, 1829-1845.

(289) Zhou, G.; Wong, W. Y.; Yang, X. New Design Tactics in OLEDs using Functionalized 2-phenylpyridine-Type Cyclometalates of Iridium(III) and Platinum(II). *Chem. Asian J.* **2011***, 6*, 1706-1727.

(290) Xiao, L.; Chen, Z.; Qu, B.; Luo, J.; Kong, S.; Gong, Q.; Kido, J. Recent Progresses on Materials for Electrophosphorescent Organic Light-Emitting Devices. *Adv Mater* **2011***, 23*, 926-952.

(291) Thejo Kalyani, N.; Dhoble, S. J. Organic Light Emitting Diodes: Energy Saving Lighting technology—A Review. *Renew. Sust. Energ. Rev.* **2012***, 16*, 2696-2723.

(292) Furman, J. D.; Warner, A. Y.; Teat, S. J.; Mikhailovsky, A. A.; Cheetham, A. K. Tunable, Ligand-Based Emission from Inorganic-Organic Frameworks: A New Approach to Phosphors for Solid State Lighting and Other Applications. *Chem. Mater.* **2010***, 22*, 2255-2260.

(293) Sun, C. Y.; Wang, X. L.; Zhang, X.; Qin, C.; Li, P.; Su, Z. M.; Zhu, D. X.; Shan, G. G.; Shao, K. Z.; Wu, H.; Li, J. Efficient and Tunable White-Light Emission of Metal-organic Frameworks by Iridium-Complex Encapsulation. *Nat. Comm.* **2013***, 4*, 2717.

(294) Rao, X.; Huang, Q.; Yang, X.; Cui, Y.; Yang, Y.; Wu, C.; Chen, B.; Qian, G. Color Tunable and White Light Emitting Tb^{3+} and Eu^{3+} Doped Lanthanide Metal-Organic Framework Materials. *J. Mater. Chem.* **2012***, 22*, 3210-3214.

(295) Zhao, Q.; Huang, C.; Li, F. Phosphorescent Heavy-Metal Complexes for Bioimaging. *Chem. Soc. Rev.* **2011***, 40*, 2508-2524.

(296) Zhao, Q.; Li, F.; Huang, C. Phosphorescent Chemosensors Based on Heavy-Metal Complexes. *Chem. Soc. Rev.* **2010***, 39*, 3007-3030.

(297) Wong, W. Y.; Ho, C. L. Organometallic Photovoltaics: A New and Versatile Approach for Harvesting Solar Energy using Conjugated Polymetallaynes. *Acc. Chem. Res.* **2010***, 43*, 1246-1256.

(298) Wong, K. M. C.; Yam, V. W. W. Luminescence Platinum(II) Terpyridyl complexes—From Fundamental Studies to Sensory Functions. *Coord. Chem. Rev.* **2007***, 251*, 2477-2488.

(299) Thompson, M. The Evolution of Organometallic Complexes in Organic Light-Emitting Devices. *MRS Bull* **2007***, 32*, 694-701.

(300) Lamansky, S.; Djurovich, P.; Murphy, D.; Abdel-Razzaq, F.; Lee, H. E.; Adachi, C.; Burrows, P. E.; Forrest, S. R.; Thompson, M. E. Highly Phosphorescent Bis-Cyclometalated Iridium Complexes: Synthesis, Photophysical Characterization, and use in Organic Light Emitting Diodes. *J. Am. Chem. Soc.* **2001***, 123*, 4304-4312.

(301) Schwartz, G.; Reineke, S.; Rosenow, T. C.; Walzer, K.; Leo, K. Triplet Harvesting in Hybrid White Organic Light-Emitting Diodes. *Advanced Functional Materials* **2009***, 19*, 1319-1333.

(302) Lo, K. K. W.; Tsang, K. H. K.; Sze, K. S.; Chung, C. K.; Lee, T. K. M.; Zhang, K. Y.; Hui, W. K.; Li, C. K.; Lau, J. S. Y.; Ng, D. C. M.; Zhu, N. Non-Covalent Binding of Luminescent Transition Metal Polypyridine Complexes to Avidin, Indole-Binding Proteins and Estrogen Receptors. *Coord. Chem. Rev.* **2007***, 251*, 2292-2310.

(303) Chou, P. T.; Chi, Y. Phosphorescent Dyes for Organic Light-Emitting Diodes. *Chem. Eur. J.* **2007***, 13*, 380-395.

(304) Chi, Y.; Chou, P. T. Transition-Metal Phosphors with Cyclometalating Ligands: Fundamentals and Applications. *Chem. Soc. Rev.* **2010***, 39*, 638-655.

(305) Chen, Z. Q.; Bian, Z. Q.; Huang, C. H. Functional IrIII Complexes and their Applications. *Adv Mater* **2010***, 22*, 1534-1539.

(306) Zhao, Q.; Liu, S. J.; Huang, W. Promising Optoelectronic Materials: Polymers Containing Phosphorescent Iridium(III) Complexes. *Macromol. Rapid. Commun.* **2010***, 31*, 794-807.

(307) You, Y.; Park, S. Y. Phosphorescent Iridium(III) Complexes: Toward High Phosphorescence Quantum Efficiency through Ligand Control. *Dalton Trans.* **2009**, 1267-1282.

(308) Ulbricht, C.; Beyer, B.; Friebe, C.; Winter, A.; Schubert, U. S. Recent Developments in the Application of Phosphorescent Iridium(III) Complex Systems. *Adv Mater* **2009***, 21*, 4418-4441.

(309) Lin, M.; Tang, Q.; Xing, G.; Li, D.; Zeng, H.; Ling, Q. The Synthesis and Luminescent Properties of Trichromatic Iridium Complexes Based on 2-(4-bromophenyl)-1-hydrogen-benzimidazole. *Synth. Met.* **2017***, 223*, 87-93.

(310) Lu, C. W.; Wang, Y.; Chi, Y. Metal Complexes with Azolate-Functionalized Multidentate Ligands: Tactical Designs and Optoelectronic Applications. *Chem. Eur. J.* **2016***, 22*, 17892-17908.

(311) You, Y.; Nam, W. Photofunctional Triplet Excited States of Cyclometalated Ir(III) Complexes: Beyond Electroluminescence. *Chem. Soc. Rev.* **2012***, 41*, 7061-7084.

(312) Zhao, Q.; Jiang, C. Y.; Shi, M.; Li, F. Y.; Yi, T.; Cao, Y.; Huang, C. H. Synthesis and Photophysical, Electrochemical, and Electrophosphorescent Properties of a Series of Iridium(III) Complexes Based on Quinoline Derivatives and Different β-Diketonate Ligands. *Organometallics* **2006***, 25*, 3631-3638.

(313) Zhao, Q.; Liu, S.; Shi, M.; Wang, C.; Yu, M.; Li, L.; Li, F.; Yi, T.; Huang, C. Series of New Cationic Iridium(III) Complexes with Tunable Emission Wavelength and Excited State Properties: Structures, Theoretical Calculations, and Photophysical and Electrochemical Properties. *Inorg. Chem.* **2006***, 45*, 6152-6160.

(314) Li, L.; Zhang, S.; Xu, L.; Han, L.; Chen, Z. N.; Luo, J. An Intensely Luminescent Metal-Organic Framework Based on a Highly Light-Harvesting Dyclo-Metalated Iridium(III) Unit Showing Effective Detection of Explosives. *Inorg. Chem.* **2013***, 52*, 12323-12325.

(315) Ohsawa, Y.; Sprouse, S.; King, K. A.; DeArmond, M. K.; Hanck, K. W.; Watts, R. J. Electrochemistry and Spectroscopy of Ortho-Metalated Complexes of Iridium(III) and Rhodium(III). *J. Phys. Chem.* **1987***, 91*, 1047-1054.

(316) Sprouse, S.; King, K. A.; Spellane, P. J.; Watts, R. J. Photophysical Effects of Metal-Carbon .Sigma. Bonds in Ortho-Metalated Complexes of Iridium(III) and Rhodium(III). *J. Am. Chem. Soc.* **1984***, 106*, 6647-6653.

(317) Neve, F.; La Deda, M.; Crispini, A.; Bellusci, A.; Puntoriero, F.; Campagna, S. Cationic Cyclometalated Iridium Luminophores: Photophysical, Redox, and Structural Characterization. *Organometallics* **2004***, 23*, 5856-5863.

(318) Lepeltier, M.; Kwok-Ming Lee, T.; Kam-Wing Lo, K.; Toupet, L.; Le Bozec, H.; Guerchais, V. Synthesis, Structure, and Photophysical and Electrochemical Properties of Cyclometallated Iridium(III) Complexes with Phenylated Bipyridine Ligands. *Eur. J. Inorg. Chem.* **2005***, 2005*, 110-117.

(319) Christou, G.; Gatteschi, D.; Hendrickson, D. N.; Sessoli, R. Single Molecule Magnets. *MRS Bulletin* **2000**, 66-71.

(320) Sessoli, R.; Gatteschi, D.; Caneschi, A.; Novak, M. A. Magnetic Bistability in a Metal-Ion Cluster. *Nature* **1993***, 365*, 141-143.

(321) Thomas, L.; Lionti, F.; Ballou, R.; Gatteschi, D.; Sessoli, R.; Barbara, B. Macroscopic Quantum Tunnelling of Magnetization in a Single Crystal of Nanomagnets. *Nature* **1996***, 383*, 145-147.

(322) Misra, S. K. In *Single-Molecule Magnets and Magnetic Quantum Tunneling;* Multifrequency Electron Paramagnetic Resonance; Wiley-VCH Verlag GmbH & Co. KGaA: 2011; pp 845-874.

(323) Winpenny, R. E. P.; McInnes, E. J. L. In *Molecular Nanomagnets;* Molecular Materials; John Wiley & Sons, Ltd: 2010; pp 281-348.

(324) Gatteschi, D.; Sessoli, R.; Villain, J. In *Molecular Nanomagnets;* oxford University Press: oxford, 2006; , pp 408.

(325) Jeon, I. R.; Clerac, R. Controlled Association of Single-Molecule Magnets (SMMs) into Coordination Networks: Towards a New Generation of Magnetic Materials. *Dalton Trans.* **2012***, 41*, 9569-9586.

(326) Novak, M. A.; Sessoli, R.; Caneschi, A.; Gatteschi, D. Magnetic Properties of a Mn Cluster Organic Compound. *J Magn Magn Mater* **1995***, 146*, 211-213.

(327) Milios, C. J.; Vinslava, A.; Wernsdorfer, W.; Moggach, S.; Parsons, S.; Perlepes, S. P.; Christou, G.; Brechin, E. K. A Record Anisotropy Barrier for a Single-Molecule Magnet. *J. Am. Chem. Soc.* **2007***, 129*, 2754-2755.

(328) Milios, C. J.; Inglis, R.; Vinslava, A.; Bagai, R.; Wernsdorfer, W.; Parsons, S.; Perlepes, S. P.; Christou, G.; Brechin, E. K. Toward a Magnetostructural Correlation for a Family of Mn6 SMMs. *J. Am. Chem. Soc.* **2007***, 129*, 12505-12511.

(329) Tasiopoulos, A. J.; Vinslava, A.; Wernsdorfer, W.; Abboud, K. A.; Christou, G. Giant Single-Molecule Magnets: A $\{Mn_{84}\}$ Torus and its Supramolecular Nanotubes. *Angew. Chem.* **2004***, 116*, 2169-2173.

(330) Ishikawa, N.; Sugita, M.; Ishikawa, T.; Koshihara, S. Y.; Kaizu, Y. Lanthanide Double-Decker Complexes Functioning as Magnets at the Single-Molecular Level. *J. Am. Chem. Soc.* **2003***, 125*, 8694-8695.

(331) Freedman, D. E.; Harman, W. H.; Harris, T. D.; Long, G. J.; Chang, C. J.; Long, J. R. Slow Magnetic Relaxation in a High-Spin Iron(II) Complex. *J. Am. Chem. Soc.* **2010***, 132*, 1224-1225.

(332) Aromí, G.; Brechin, E. K. In *Synthesis of 3d Metallic Single-Molecule Magnets;* Winpenny, R., Ed.; Single-Molecule Magnets and Related Phenomena; Springer Berlin Heidelberg: Berlin, Heidelberg, 2006; Vol. 122, pp 1-67.

(333) Gómez-Coca, S.; Cremades, E.; Aliaga-Alcalde, N.; Ruiz, E. Huge Magnetic Anisotropy in a Trigonal-Pyramidal Nickel(II) Complex. *Inorg. Chem.* **2014***, 53*, 676-678.

(334) Craig, G. A.; Marbey, J. J.; Hill, S.; Roubeau, O.; Parsons, S.; Murrie, M. Field-Induced Slow Relaxation in a Monometallic Manganese(III) Single-Molecule Magnet. *Inorg. Chem.* **2015***, 54*, 13-15.

(335) Ishikawa, R.; Miyamoto, R.; Nojiri, H.; Breedlove, B. K.; Yamashita, M. Slow Relaxation of the Magnetization of an MnIII Single Ion. *Inorg. Chem.* **2013***, 52*, 8300-8302.

(336) Lecren, L.; Wernsdorfer, W.; Li, Y. G.; Vindigni, A.; Miyasaka, H.; Clérac, R. One-Dimensional Supramolecular Organization of Single-Molecule Magnets. *J. Am. Chem. Soc.* **2007***, 129*, 5045-5051.

(337) Lü, Z.; Yuan, M.; Pan, F.; Gao, S.; Zhang, D.; Zhu, D. Syntheses, Crystal Structures, and Magnetic Characterization of Five New Dimeric Manganese(III) Tetradentate Schiff Base Complexes Exhibiting Single-Molecule-Magnet Behavior. *Inorg. Chem.* **2006***, 45*, 3538-3548.

(338) Stamatatos, T. C.; Foguet-Albiol, D.; Stoumpos, C. C.; Raptopoulou, C. P.; Terzis, A.; Wernsdorfer, W.; Perlepes, S. P.; Christou, G. Initial Example of a Triangular Single-Molecule Magnet from Ligand-Induced Structural Distortion of a $[Mn^{III}_3O]^{7+}$ Complex. *J. Am. Chem. Soc.* **2005***, 127*, 15380-15381.

(339) Vallejo, J.; Pascual-Álvarez, A.; Cano, J.; Castro, I.; Julve, M.; Lloret, F.; Krzystek, J.; De Munno, G.; Armentano, D.; Wernsdorfer, W.; Ruiz-García, R.; Pardo, E. Field-Induced Hysteresis and Quantum Tunneling of the Magnetization in a Mononuclear Manganese(III) Complex. *Angew. Chem.* **2013***, 52*, 14075-14079.

(340) Grigoropoulos, A.; Pissas, M.; Papatolis, P.; Psycharis, V.; Kyritsis, P.; Sanakis, Y. Spin-Relaxation Properties of a High-Spin Mononuclear $Mn^{III}O_6$-Containing Complex. *Inorg. Chem.* **2013***, 52*, 12869-12871.

(341) Shyu, H. L.; Wei, H. H.; Wang, Y. Structure and Magnetic Properties of Dinuclear $[Mn^{III}(salen)(H_2O)]_2(ClO_4)_2$ and Polynuclear $[Mn^{III}(salen)(NO_3)]_n$. *Inorg. Chim. Acta* **1999***, 290*, 8-13.

(342) Miyasaka, H.; Saitoh, A.; Abe, S. Magnetic Assemblies Based on Mn(III) Salen Analogues. *Coord. Chem. Rev.* **2007***, 251*, 2622-2664.

(343) Miyasaka, H.; Clérac, R.; Wernsdorfer, W.; Lecren, L.; Bonhomme, C.; Sugiura, K. I.; Yamashita, M. A Dimeric Manganese(III) Tetradentate Schiff Base Complex as a Single-Molecule Magnet. *Angew. Chem.* **2004***, 116*, 2861-2865.

(344) Miyasaka, H.; Yamashita, M. A Look at Molecular Nanosized Magnets from the Aspect of Inter-Molecular Interactions. *Dalton Trans.* **2007**, 399-406.

(345) Alotto, P.; Guarnieri, M.; Moro, F. Redox Flow Batteries for the Storage of Renewable Energy: A Review. *Renew. Sustain. Energy. Rev.* **2014***, 29*, 325-335.

(346) Ejigu, A.; Edwards, M.; Walsh, D. A. Synergistic Catalyst-Support Interactions in a Graphene-Mn_3O_4 Electrocatalyst for Vanadium Redox Flow Batteries. *ACS Catal.* **2015***, 5*, 7122-7130.

(347) Armaroli, N.; Balzani, V. The Hydrogen Issue. *ChemSusChem* **2011***, 4*, 21-36.

(348) Kibsgaard, J.; Gorlin, Y.; Chen, Z.; Jaramillo, T. F. Meso-Structured Platinum Thin Films: Active and Stable Electrocatalysts for the oxygen Reduction Reaction. *J. Am. Chem. Soc.* **2012***, 134*, 7758-7765.

(349) Zhang, J.; Sasaki, K.; Sutter, E.; Adzic, R. R. Stabilization of Platinum oxygen-Reduction Electrocatalysts using Gold Clusters. *Science* **2007***, 315*, 220-222.

(350) Hu, X.; Brunschwig, B. S.; Peters, J. C. Electrocatalytic Hydrogen Evolution at Low Overpotentials by Cobalt Macrocyclic Glyoxime and Tetraimine Complexes. *J. Am. Chem. Soc.* **2007***, 129*, 8988-8998.

(351) Jacques, P. A.; Artero, V.; Pécaut, J.; Fontecave, M. Cobalt and Nickel Diimine-Dioxime Complexes as Molecular Electrocatalysts for Hydrogen Evolution with Low Overvoltages. *Proceedings of the National Academy of Sciences* **2009***, 106*, 20627-20632.

(352) Dempsey, J. L.; Winkler, J. R.; Gray, H. B. Mechanism of H2 Evolution from a Photogenerated Hydridocobaloxime. *J. Am. Chem. Soc.* **2010***, 132*, 16774-16776.

(353) Karunadasa, H. I.; Chang, C. J.; Long, J. R. A Molecular Molybdenum-oxo Catalyst for Generating Hydrogen from Water. *Nature* **2010***, 464*, 1329-1333.

(354) Losse, S.; Vos, J. G.; Rau, S. Catalytic Hydrogen Production at Cobalt Centres. *Coord. Chem. Rev.* **2010***, 254*, 2492-2504.

(355) Helm, M. L.; Stewart, M. P.; Bullock, R. M.; DuBois, M. R.; DuBois, D. L. A Synthetic Nickel Electrocatalyst with a Turnover Frequency Above 100,000 s^{-1} for H_2 Production. *Science* **2011***, 333*, 863-866.

(356) Artero, V.; Chavarot-Kerlidou, M.; Fontecave, M. Splitting Water with Cobalt. *Angew. Chem. Internat. Ed.* **2011***, 50*, 7238-7266.

(357) Lakadamyali, F.; Reisner, E. Photocatalytic H_2 Evolution from Neutral Water with a Molecular Cobalt Catalyst on a Dye-Sensitised TiO_2 Nanoparticle. *Chem. Commun.* **2011***, 47*, 1695-1697.

(358) Muckerman, J. T.; Fujita, E. Theoretical Studies of the Mechanism of Catalytic Hydrogen Production by a Cobaloxime. *Chem. Commun.* **2011***, 47*, 12456-12458.

(359) Rose, M. J.; Gray, H. B.; Winkler, J. R. Hydrogen Generation Catalyzed by Fluorinated Diglyoxime Iron Complexes at Low Overpotentials. *J. Am. Chem. Soc.* **2012***, 134*, 8310-8313.

(360) Li, L.; Duan, L.; Wen, F.; Li, C.; Wang, M.; Hagfeldt, A.; Sun, L. Visible Light Driven Hydrogen Production from a Photo-Active Cathode Based on a Molecular Catalyst and Organic Dye-Sensitized P-Type Nanostructured NiO. *Chem. Commun.* **2012***, 48*, 988-990.

(361) Wang, W.; Rauchfuss, T. B.; Bertini, L.; Zampella, G. Unsensitized Photochemical Hydrogen Production Catalyzed by Diiron Hydrides. *J. Am. Chem. Soc.* **2012***, 134*, 4525-4528.

(362) Singh, W. M.; Baine, T.; Kudo, S.; Tian, S.; Ma, X. A. N.; Zhou, H.; DeYonker, N. J.; Pham, T. C.; Bollinger, J. C.; Baker, D. L.; Yan, B.; Pham, T. C.; Zhao, X. Electrocatalytic and Photocatalytic Hydrogen Production in Aqueous Solution by a Molecular Cobalt Complex. *Angew. Chem. Internat. Ed.* **2012***, 51*, 5941-5944.

(363) Jasion, D.; Barforoush, J. M.; Qiao, Q.; Zhu, Y.; Ren, S.; Leónard, K. C. Low-Dimensional Hyperthin FeS2 Nanostructures for Efficient and Stable Hydrogen Evolution Electrocatalysis. *ACS Catal.* **2015***, 5*, 6653-6657.

(364) Matsumoto, T.; Nagahama, T.; Cho, J.; Hizume, T.; Suzuki, M.; Ogo, S. Preparation and Reactivity of a Nickel Dihydride Complex. *Angew. Chem. Internat. Ed.* **2011***, 123*, 10766-10768.

(365) Nann, T.; Ibrahim, S. ; Woi, P. M.; Xu, S.; Ziegler, J.; Pickett, C. Water Splitting by Visible Light: A Nanophotocathode for Hydrogen Production. *Angew. Chem. Internat. Ed.* **2010***, 49*, 1574-1577.

(366) Reece, S. Y.; Hamel, J. A.; Sung, K.; Jarvi, T. D.; Esswein, A. J.; Pijpers, J. J. H.; Nocera, D. G. Wireless Solar Water Splitting using Silicon-Based Semiconductors and Earth-Abundant Catalysts. *Science* **2011***, 334*, 645-648.

(367) Duan, L.; Bozoglian, F.; Mandal, S.; Stewart, B.; Privalov, T.; Llobet, A.; Sun, L. A Molecular Ruthenium Catalyst with Water-oxidation Activity Comparable to that of Photosystem II. *Nat Chem* **2012***, 4*, 418-423.

(368) Du, P.; Eisenberg, R. Catalysts made of Earth-Abundant Elements (Co, Ni, Fe) for Water Splitting: Recent Progress and Future Challenges. *Energy Environ. Sci.* **2012***, 5*, 6012-6021.

(369) Bauer, R.; Werner, H. A. F. Investigations on a Homogeneous Wilkinson's Catalyst for the Water Photolysis. *Int. J. Hydrogen Energy* **1994***, 19*, 497-499.

(370) Lakadamyali, F.; Kato, M.; Muresan, N., M.; Reisner, E. Selective Reduction of Aqueous Protons to Hydrogen with a Synthetic Cobaloxime Catalyst in the Presence of Atmospheric oxygen. *Angew. Chem. Internat. Ed.* **2012***, 51*, 9381-9384.

(371) Skyllas-Kazacos, M.; Chakrabarti, M. H.; Hajimolana, S. A.; Mjalli, F. S.; Saleem, M. Progress in Flow Battery Research and Development. *J. Electrochem. Soc.* **2011***, 158*, R55-R79.

(372) Wang, S.; Zhao, X.; Cochell, T.; Manthiram, A. Nitrogen-Doped Carbon Nanotube/Graphite Felts as Advanced Electrode Materials for Vanadium Redox Flow Batteries. *J. Phys. Chem. Lett.* **2012***, 3*, 2164-2167.

(373) Imanishi, N.; Morikawa, T.; Kondo, J.; Takeda, Y.; Yamamoto, O.; Kinugasa, N.; Yamagishi, T. Lithium Intercalation Behavior into Iron Cyanide Complex as Positive Electrode of Lithium Secondary Battery. *J. Power Sources* **1999***, 79*, 215-219.

(374) Mizuno, Y.; Okubo, M.; Asakura, D.; Saito, T.; Hosono, E.; Saito, Y.; Oh-ishi, K.; Kudo, T.; Zhou, H. Impedance Spectroscopic Study on Interfacial Ion Transfers in Cyanide-Bridged Coordination Polymer Electrode with Organic Electrolyte. *Electrochim. Acta* **2012***, 63*, 139-145.

(375) Moritomo, Y.; Takachi, M.; Kurihara, Y.; Matsuda, T. Thin Film Electrodes of Prussian Blue Analogues with Rapid Li^+ Intercalation. *Appl. Phys. Express* **2012***, 5*, 041801.

(376) Wang, X.; Hou, Y.; Zhu, Y.; Wu, Y.; Holze, R. An Aqueous Rechargeable Lithium Battery using Coated Li Metal as Anode. *Scientific Reports* **2013***, 3*, 1401.

(377) Kaveevivitchai, W.; Jacobson, A. J. Exploration of Vanadium Benzenedicarboxylate as a Cathode for Rechargeable Lithium Batteries. *J. Power Sources* **2015***, 278*, 265-273.

(378) Omarova, M.; Koishybay, A.; Yesibolati, N.; Mentbayeva, A.; Umirov, N.; Ismailov, K.; Adair, D.; Babaa, M. R.; Kurmanbayeva, I.; Bakenov, Z. Nickel Hexacyanoferrate Nanoparticles as a Low Cost Cathode Material for Lithium-Ion Batteries. *Electrochim. Acta* **2015***, 184*, 58-63.

(379) Yesibolati, N.; Umirov, N.; Koishybay, A.; Omarova, M.; Kurmanbayeva, I.; Zhang, Y.; Zhao, Y.; Bakenov, Z. High Performance Zn/$LiFePO_4$ Aqueous Rechargeable Battery for Large Scale Applications. *Electrochim. Acta* **2015***, 152*, 505-511.

(380) Emery, N.; Sougrati, M. T.; Panabière, E.; Bach, S.; Fraisse, B.; Jumas, J. C.; Pereira-Ramos, J. P.; Willmann, P. Unidimensional Unit Cell Variation and Fe^{+3}/Fe^{+4} Redox Activity of Li_3FeN_2 in Li-Ion Batteries. *J. Alloys Compounds* **2017***, 696*, 971-979.

(381) Wessells, C. D.; Peddada, S. V.; Huggins, R. A.; Cui, Y. Nickel Hexacyanoferrate Nanoparticle Electrodes for Aqueous Sodium and Potassium Ion Batteries. *Nano Lett.* **2011***, 11*, 5421-5425.

(382) Wang, L.; Lu, Y.; Liu, J.; Xu, M.; Cheng, J.; Zhang, D.; Goodenough, J. B. A Superior Low-Cost Cathode for a Na-Ion Battery. *Angew. Chem. Internat. Ed.* **2013***, 52*, 1964-1967.

(383) Lee, H. W.; Wang, R. Y.; Pasta, M.; Woo Lee, S.; Liu, N.; Cui, Y. Manganese Hexacyanomanganate Open Framework as a High-Capacity Positive Electrode Material for Sodium-Ion Batteries. *Nat. Comm.* **2014***, 5*, 5280.

(384) Sharma, N.; Tapia-Ruiz, N.; Singh, G.; Armstrong, A. R.; Pramudita, J. C.; Brand, H. E. A.; Billaud, J.; Bruce, P. G.; Rojo, T. Rate Dependent Performance Related to Crystal Structure Evolution of $Na_{0.67}Mn_{0.8}Mg_{0.2}O_2$ in a Sodium-Ion Battery. *Chem. Mater.* **2015***, 27*, 6976-6986.

(385) Su, D.; McDonagh, A.; Qiao, S. Z.; Wang, G. High-Capacity Aqueous Potassium-Ion Batteries for Large-Scale Energy Storage. *Adv Mater* **2017***, 29*, 1604007-n/a.

(386) Wu, C. M.; Pan, P. I.; Cheng, Y. W.; Liu, C. P.; Chang, C. C.; Avdeev, M.; Lin, S. K. The Mechanism of the Sodiation and Desodiation in Super P Carbon Electrode for Sodium-Ion Battery. *J. Power Sources* **2017***, 340*, 14-21.

(387) Zhan, X.; Shirpour, M. Evolution of Solid/Aqueous Interface in Aqueous Sodium-Ion Batteries. *Chem. Commun.* **2017***, 53*, 204-207.

(388) Tanabe, K. K.; Cohen, S. M. Postsynthetic Modification of Metal-Organic Frameworks-a Progress Report. *Chem. Soc. Rev.* **2011***, 40*, 498-519.

(389) Morozan, A.; Jaouen, F. Metal Organic Frameworks for Electrochemical Applications. *Energy Environ. Sci.* **2012***, 5*, 9269-9290.

(390) Zhang, Z.; Yoshikawa, H.; Awaga, K. Monitoring the Solid-State Electrochemistry of Cu(2,7-AQDC) (AQDC = Anthraquinone Dicarboxylate) in a Lithium Battery: Coexistence of Metal and Ligand Redox Activities in a Metal-Organic Framework. *J. Am. Chem. Soc.* **2014***, 136*, 16112-16115.

(391) Aubrey, M. L.; Long, J. R. A Dual-Ion Battery Cathode Via oxidative Insertion of Anions in a Metal-Organic Framework. *J. Am. Chem. Soc.* **2015***, 137*, 13594-13602.

(392) Yao, M.; Senoh, H.; Araki, M.; Sakai, T.; Yasuda, K. Organic Positive-Electrode Materials Based on Dialkoxybenzoquinone Derivatives for use in Rechargeable Lithium Batteries. *ECS Trans.* **2010***, 28*, 3-10.

(393) Senoh, H.; Yao, M.; Sakaebe, H.; Yasuda, K.; Siroma, Z. A Two-Compartment Cell for using Soluble Benzoquinone Derivatives as Active Materials in Lithium Secondary Batteries. *Electrochim. Acta* **2011***, 56*, 10145-10150.

(394) Barrès, A. L.; Geng, J.; Bonnard, G.; Renault, S.; Gottis, S.; Mentré, O.; Frayret, C.; Dolhem, F.; Poizot, P. High-Potential Reversible Li Deintercalation in a Substituted Tetrahydroxy-P-Benzoquinone Dilithium Salt: An Experimental and Theoretical Study. *Chem. Eur. J.* **2012***, 18*, 8800-8812.

(395) Reddy, A. L. M.; Nagarajan, S.; Chumyim, P.; Gowda, S. R.; Pradhan, P.; Jadhav, S. R.; Dubey, M.; John, G.; Ajayan, P. M. Lithium Storage Mechanisms in Purpurin Based Organic Lithium Ion Battery Electrodes. *Scientific Reports* **2012***, 2*, 960.

(396) Hanyu, Y.; Ganbe, Y.; Honma, I. Application of Quinonic Cathode Compounds for Quasi-Solid Lithium Batteries. *J. Power Sources* **2013***, 221*, 186-190.

(397) Huskinson, B.; Marshak, M. P.; Suh, C.; Er, S.; Gerhardt, M. R.; Galvin, C. J.; Chen, X.; Aspuru-Guzik, A.; Gordon, R. G.; Aziz, M. J. A Metal-Free Organic-Inorganic Aqueous Flow Battery. *Nature* **2014***, 505*, 195-198.

(398) Zeng, R.; Xing, L.; Qiu, Y.; Wang, Y.; Huang, W.; Li, W.; Yang, S. Polycarbonyl(Quinonyl) Organic Compounds as Cathode Materials for Sustainable Lithium Ion Batteries. *Electrochim. Acta* **2014***, 146*, 447-454.

(399) Song, Z.; Qian, Y.; Liu, X.; Zhang, T.; Zhu, Y.; Yu, H.; Otani, M.; Zhou, H. A Quinone-Based Oligomeric Lithium Salt for Superior Li-Organic Batteries. *Energy Environ. Sci.* **2014***, 7*, 4077-4086.

(400) Lin, K.; Chen, Q.; Gerhardt, M. R.; Tong, L.; Kim, S. B.; Eisenach, L.; Valle, A. W.; Hardee, D.; Gordon, R. G.; Aziz, M. J.; Marshak, M. P. Alkaline Quinone Flow Battery. *Science* **2015***, 349*, 1529.

(401) Son, E. J.; Kim, J. H.; Kim, K.; Park, C. B. Quinone and its Derivatives for Energy Harvesting and Storage Materials. *J. Mater. Chem. A* **2016***, 4*, 11179-11202.

(402) Ding, Y.; Yu, G. A Bio-Inspired, Heavy-Metal-Free, Dual-Electrolyte Liquid Battery Towards Sustainable Energy Storage. *Angew. Chem. Internat. Ed.* **2016***, 55*, 4772-4776.

(403) Wedege, K.; Drazevic, E.; Konya, D.; Bentien, A. Organic Redox Species in Aqueous Flow Batteries: Redox Potentials, Chemical Stability and Solubility. *Scientific Reports* **2016***, 6*, 39101.

(404) Dawut, G.; Lu, Y.; Zhao, Q.; Liang, J.; Tao, Z. L.; Chen, J. Quinones as Electrode Materials for Rechargeable Lithium Batteries. *Acta Physico-Chimica Sinica* **2016***, 32*, 1593.

(405) Ding, Y.; Li, Y.; Yu, G. Exploring Bio-Inspired Quinone-Based Organic Redox Flow Batteries: A Combined Experimental and Computational Study. *Chem* **2016***, 1*, 790-801.

(406) Le Gall, T.; Reiman, K. H.; Grossel, M. C.; Owen, J. R. Poly(2,5-Dihydroxy-1,4-Benzoquinone-3,6-Methylene): A New Organic Polymer as Positive Electrode Material for Rechargeable Lithium Batteries. *J. Power Sources* **2003***, 119–121*, 316-320.

(407) Xiang, J.; Chang, C.; Li, M.; Wu, S.; Yuan, L.; Sun, J. A Novel Coordination Polymer as Positive Electrode Material for Lithium Ion Battery. *Crys. Grow. Desi.* **2008***, 8*, 280-282.

(408) Armand, M.; Tarascon, J. M. Building Better Batteries. *Nature* **2008***, 451*, 652-657.

(409) Luo, C.; Zhu, Y.; Xu, Y.; Liu, Y.; Gao, T.; Wang, J.; Wang, C. Graphene oxide Wrapped Croconic Acid Disodium Salt for Sodium Ion Battery Electrodes. *J. Power Sources* **2014***, 250*, 372-378.

Chapter 1

Monomeric building blocks of the type $A_3[M^{III}(C_6O_4X_2)_3]$. Key role of the cation in the crystallization of chiral tris(anilato)metalate magnetic anions

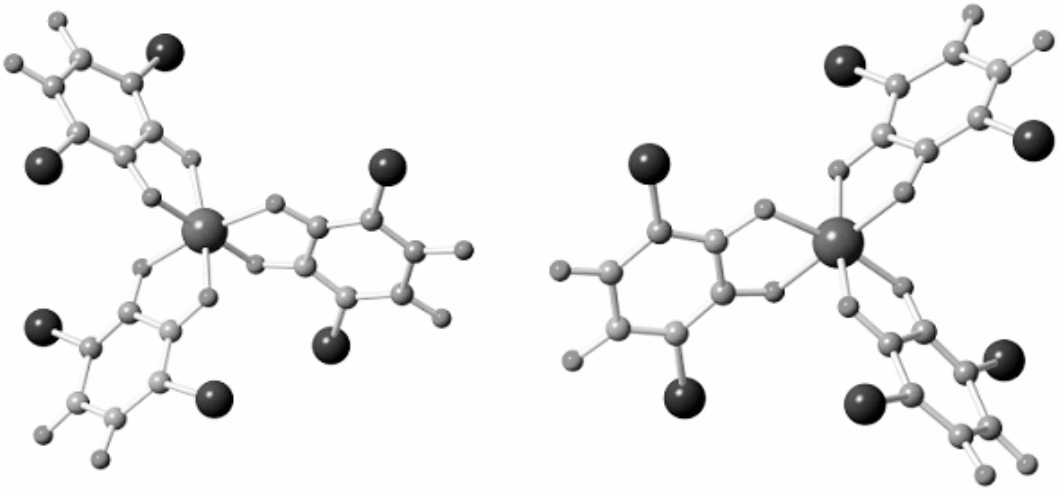

1. Introduction

In this chapter we will present the synthesis and characterization of a complete series of monomeric tris(anilato)metallate complexes (Figure 1.1) formulated as $[M^{III}(C_6O_4X_2)_3]^{3-}$ where M^{III} = Cr, Fe and Ga; X = Cl, Br and NO_2 with a wide variety of cations as K^+, tetra-phenyl-, tri-phenyl-alkyl- and tetra-alkyl-phospohonium cations: $[PPh_4]^+$, $[PPh_3R]^+$ and $[PR_4]^+$ or tetra-alkyl ammonium cations: $[NR_4]^+$ and $[Nhep_4]^+$. This study is motivated by three main reasons: (i) there were very few reported examples of monomeric $A_3[M^{III}(C_6O_4X_2)_3]$ compounds[1,2] until very recently,[3-6] (ii) no study of the influence of the size and symmetry of the cation on the final structure of these salts has been done to date and (iii) we need a library of precursor salts of the type $A_3[M^{III}(C_6O_4X_2)_3]$ in order to prepare hetero-metallic two dimensional magnets of the series $A[M^{II}M^{III}(C_6O_4X_2)_3]$ with different A^+ cations, similar to the ones prepared with the oxalato ligand.[7,8]

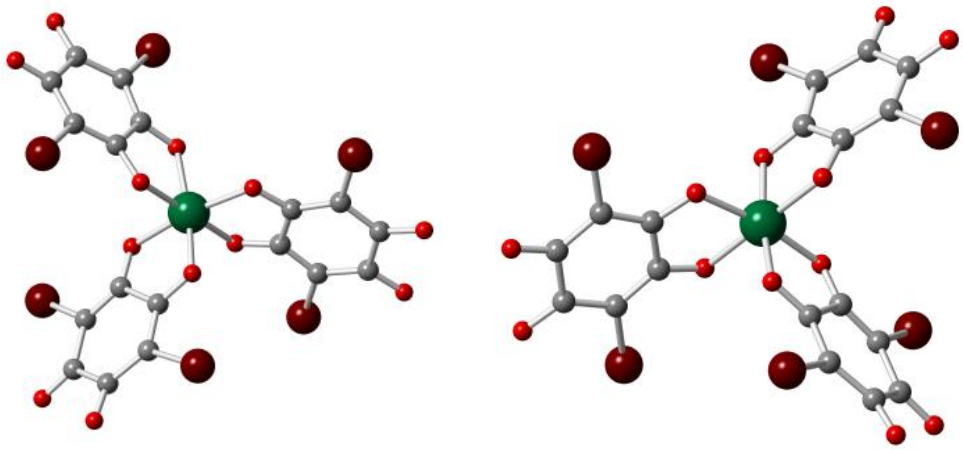

Δ-$[Cr(C_6O_4Br_2)_3]^{3-}$ **Λ-$[Cr(C_6O_4Br_2)_3]^{3-}$**

Figure 1.1*. Structure of both enantiomers of the monomeric tris(anilato)metallate*

Thus, in this chapter we will present the synthesis, spectroscopic, structural and magnetic characterization of a series of compounds formulated as $A_3[M^{III}(C_6O_4X_2)_3]$ (M^{III} = Cr, Fe and Ga; X = Cl, Br and NO_2; A = K^+, PPh_3Et^+, PPh_3Pr^+, PBu_4^+, $NHep_4^+$, NBu_4^+ and PPh_4^+). We will describe the non-innocent role played by the cation in determining the presence or absence of chirality in the single crystals obtained. Here we also explore the idea that cations with C_3 symmetry, particularly the ones of the type PPh_3R^+ with aromatic rings, must stabilise the structure by extra π-π

interactions, facilitating the, otherwise very difficult, synthesis of these monomeric anilato precursors. This assumption will be confirmed with the results presented in this chapter.

Some studies about the role of the counter-ion reveal that they may play an important role in the final structure in some coordination compounds. However this role is basically based on the coordination ability of the anion.[9] In the compounds we present here, the key role of the cation is much more subtle due to the fact that, in all compounds, the obtained anion is of the type $[M^{III}(C_6O_4X_2)_3]^{3-}$ but the final structure strongly depends on the number of $\pi-\pi$ anion-cation interactions.

The nature, size and presence or not of aromatic rings in the cations also significantly affects the solubility of the final compounds, changing radically between inorganic cations as K^+ and organic ones as NBu_4^+, PBu_4^+ and $PPhR_3^+$.

2. Experimental Section

2.1. Synthesis

General Remarks: The ammonium and phosphonium salts [PPh_3Et]Br, [PPh_3Pr]Br, [PBu_4]Br, [NBu_4]Br, [$NHep_4$]Cl and [PPh_4]Br are commercially available and were used without further purification. NaOH, KOH, chloranilic acid ($H_2C_6O_4Cl_2$), bromanilic acid ($H_2C_6O_4Br_2$) and the metal salts $FeCl_3{\cdot}6H_2O$, $CrCl_3{\cdot}6H_2O$, $GaCl_3$ and $Ga(NO_3)_3$ are also commercially available and were used as received without further purification. The sodium salt of nitranilic acid $Na_2[C_6O_4(NO_2)_2]$ was prepared according to the literature.[10]

Synthesis of $[PPh_3Et]_3[Cr(C_6O_4Cl_2)_3]$ (1). A solution of $CrCl_3{\cdot}6H_2O$ (533 mg, 2 mmol) in H_2O (5 mL) was added drop-wise to an aqueous solution (45 mL) prepared by the mixture of: (i) $H_2C_6O_4Cl_2$ (1255 mg, 6 mmol) in water (25 mL) at 60 °C, (ii) NaOH (480 mg, 12 mmol) in water (10 mL) and (iii) [PPh_3Et]Br (2228 mg, 6 mmol) in water (10 mL). The resulting solution was heated at 60 °C for 1 hour, allowed to cool at room temperature and extracted with three portions of 50 mL of CH_2Cl_2. The resulting deep red lower CH_2Cl_2 fractions were collected and the solvent removed using a rotavap. The obtained deep red lacquer solid was recrystallized with N,N-dimethylformamide (DMF) to afford **1** as a burgundy crystalline powder (1609

mg, yield 52 %). *Elemental Anal*. calc. for $C_{78}H_{60}Cl_6CrP_3O_{12}$ (M_w = 1546.94): C: 60.56; H: 3.91; Found: C: 60.06; H: 3.79. *FT-IR* (υ_{max}/cm^{-1}, KBr pellet): 3415(s), 3232(m), 1638(m), 1530(s), 1438(m), 1401(m), 1351(s), 1307(m), 1114(m), 1001(m), 841(m), 734(m), 691(m), 610(m), 572(w), 529(w), 509(w), 447(w). The phase purity of this compound was confirmed by powder X-ray diffraction analysis (see below).

Synthesis of $[PPh_3Et]_3[Cr(C_6O_4Br_2)_3]$ (2). This compound was prepared as **1** but using $H_2C_6O_4Br_2$ (1787 mg, 6 mmol) instead of $H_2C_6O_4Cl_2$. **2** was obtained as a burgundy crystalline powder (1705 mg, yield 47 %). *Elemental Anal.* Calc. for $C_{78}H_{60}Br_6CrP_3O_{12}$ (M_w = 1813.65): C, 51.65; H, 3.34; Found: C, 51.99; H, 3.58. *FT-IR* (υ_{max}/cm^{-1}, KBr pellet): 3415(s), 3234(w), 1637(m), 1521(s), 1438(m), 1400(m), 1341(s), 1288(m), 1114(m), 987(m), 808(m), 734(m), 691(m), 596(m), 558(w), 529(w), 502(w), 405(w). The phase purity of this compound was confirmed by powder X-ray diffraction analysis (see below).

Synthesis of $[PPh_3Et]_3[Ga(C_6O_4Br_2)_3]$ (3). A solution of $GaCl_3$ (141 mg, 0.8 mmol) in H_2O (5 mL) was added drop-wise to an aqueous solution (45 mL) prepared by the mixture of: (i) $H_2C_6O_4Br_2$ (715 mg, 2.4 mmol) in water (25 mL) at 60 °C, (ii) NaOH (192 mg, 4.8 mmol) in water (10 mL) and (iii) $[PPh_3Et]Br$ (891 mg, 2.4 mmol) in water (10 mL). The resulting solution was heated at 60 °C for 1 hour, allowed to cool to room temperature and extracted with three portions of 50 mL of CH_2Cl_2. The resulting deep red lower CH_2Cl_2 fractions were collected and the solvent the solvent removed using a rotavap. The obtained deep red lacquer solid was recrystallized with N,N-dimethylformamide (DMF) to afford **3** as a red crystalline powder (952 mg, yield 65 %). *Elemental Anal.* Calc. for $C_{78}H_{60}Br_6GaP_3O_{12}$ (M_w = 1831.37): C, 51.15; H, 3.30; Found: C, 51.40; H, 2.93. *FT-IR* (υ_{max}/cm^{-1}, KBr pellet): 3417(s), 3222(m), 1639(s), 1530(s), 1438(m), 1400(s), 1344(m), 1288(m), 1114(m), 984(m), 810(m), 733(m), 691(m), 589(m), 560(w), 529(w), 501(w). The phase purity of this compound was confirmed by powder X-ray diffraction analysis (see below).

Synthesis of $[PPh_3Et]_3[Fe(C_6O_4(NO_2)_2)_3]$ (4). This compound was prepared as compound **3** but using $Na_2[C_6O_4(NO_2)_2]$ (658 mg, 2.4 mmol). Since a sodium salt is used, the use of a base is not needed. Compound **4** was obtained as an orange-brown crystalline powder (209 mg, 16 %). *Elemental Anal.* Calc. for $C_{78}H_{60}N_6FeP_3O_{24}$ (M_w = 1614.11): C, 58.04; H, 3.75; N, 5.21; Found: C, 55.67; H, 3.82; N, 5.29. *FT-IR*

(υ_{max}/cm^{-1}, KBr pellet): 3440(s), 3222(w), 1624(m), 1552(s), 1504(w), 1438(w), 1393(s), 1324(w), 1270(w), 1116(m), 1047(w), 910(w), 772(w), 744(w), 720(w), 688(m), 582(w), 504(w), 405(w). The phase purity of this compound was confirmed by powder X-ray diffraction analysis (see below).

Synthesis of $[PPh_3Pr]_3[Cr(C_6O_4Cl_2)_3]$ (5). This compound was prepared as compound **1** but using $[PPh_3Pr]Br$ (2312 mg, 6 mmol) instead of $[PPh_3Et]Br$. Compound **5** was obtained as deep purple thin needles (1907 mg, yield 60 %). *Elemental Anal.* Calc. for $C_{81}H_{66}Cl_6CrP_3O_{12}$ (M_w = 1589.02): C, 61.22; H, 4.19; Found: C, 60.59; H, 4.28. *FT-IR* (υ_{max}/cm^{-1}, KBr pellet): 3416(s), 3233(w), 1638(m), 1529(s), 1437(m), 1400(m), 1353(s), 1308(m), 1113(m), 1000(m), 841(m), 734(m), 690(m), 610(m), 570(w), 529(w), 508(w), 447(w). The phase purity of this compound was confirmed by powder X-ray diffraction analysis (see below).

Synthesis of $[PPh_3Pr]_3[Cr(C_6O_4Br_2)_3]$ (6). This compound was prepared as compound **1** but using $H_2C_6O_4Br_2$ (1787 mg, 6 mmol) instead of $H_2C_6O_4Cl_2$ and $[PPh_3Pr]Br$ (2312 mg, 6 mmol) instead of $[PPh_3Et]Br$. Compound **6** was obtained as a burgundy crystalline powder (1782 mg, yield 48 %). *Elemental Anal.* Calc. for $C_{81}H_{66}Br_6CrP_3O_{12}$ (M_w = 1855.73): C, 52.43; H, 3.59; Found: C, 52.06; H, 3.57. *FT-IR* (υ_{max}/cm^{-1}, KBr pellet): 3416(s), 3229(w), 1637(m), 1519(s), 1437(m), 1400(m), 1339(s), 1288(m), 1114(m), 986(m), 806(m), 736(m), 698(m), 595(m), 557(w), 530(w), 503(w). The phase purity of this compound was confirmed by powder X-ray diffraction analysis (see below).

Synthesis of $[PPh_3Pr]_3[Fe(C_6O_4(NO_2)_2)_3]$ (7). This compound was prepared as compound **3** but using $Na_2[C_6O_4(NO_2)_2]$ (658 mg, 2.4 mmol) instead of $H_2C_6O_4Cl_2$ and $[PPh_3Pr]Br$ (925 mg, 2.4 mmol) instead of $[PPh_3Et]Br$. Since a sodium salt is used, no base is needed. Compound **7** was obtained as an orange-brown crystalline powder (186 mg, yield 14 %). *Elemental Anal.* Calc. for $C_{81}H_{66}N_6FeP_3O_{24}$ (M_w = 1656.19): C, 58.74; H, 4.02; N, 5.07; Found: C, 58.74; H, 4.06; N, 5.01. *FT-IR* (υ_{max}/cm^{-1}, KBr pellet): 3415(s), 3233(w), 1638(m), 1618(s), 1551(m), 1438(w), 1399(s), 1270(w), 1113(m), 995(w), 775(w), 721(w), 689(w), 669(w), 618(m), 529(w), 477(w). The phase purity of this compound was confirmed by powder X-ray diffraction analysis (see below).

Synthesis of $[PBu_4]_3[Cr(C_6O_4(NO_2)_2)_3]$ (8). This compound was prepared as compound **3** but using $Na_2[C_6O_4(NO_2)_2]$ (658 mg, 2.4 mmol) instead of $H_2C_6O_4Cl_2$, $CrCl_3{\cdot}6H_2O$ (213 mg, 0.8 mmol) instead of $FeCl_3{\cdot}6H_2O$ and $[PBu_4]Br$ (814 mg, 2.4 mmol) instead of $[PPh_3Et]Br$. Since a sodium salt is used, not base is needed. Compound **8** was recrystallized with a 2:1 mixture of Ethanol and DMF to afford **8** orange plate-like single crystals suitable for single-crystals X-ray structure determination (787 mg, yield 65 %). *Elemental Anal.* Calc. for $C_{66}H_{108}N_6CrP_3O_{24}$ (M_w = 1514.51): C, 52.34; H, 7.19; N, 5.55; Found: C, 52.57; H, 7.08; N, 6.73. *FT-IR* (υ_{max}/cm^{-1}, KBr pellet): 3417(s), 2961(m), 2933(m), 2873(w), 1652(m), 1552(s), 1465(w), 1398(s), 1362(w), 1320(m), 1098(w), 1052(m), 963(w), 918(w), 862(w), 811(w), 776(m), 755(w), 720(m), 598(m), 508(w). The phase purity of this compound was confirmed by powder X-ray diffraction analysis (see below).

Synthesis of $[PBu_4]_3[Fe(C_6O_4(NO_2)_2)_3]$ (9). This compound was prepared as compound **3** but using $Na_2[C_6O_4(NO_2)_2]$ (658 mg, 2.4 mmol) instead of $H_2C_6O_4Cl_2$ and $[PBu_4]Br$ (814 mg, 2.4 mmol) instead of $[PPh_3Et]Br$. Since a sodium salt is used, not base is needed. Compound **9** was recrystallized with a 2:1 mixture of Ethanol and DMF to afford **9** orange plate-like single crystals suitable for single-crystals X-ray structure determination (787 mg, yield 65 %). *Elemental Anal.* Calc. for $C_{66}H_{108}N_6FeP_3O_{24}$ (M_w = 1518.36): C, 52.21; H, 7.17; N, 5.54; Found: C, 52.21; H, 6.71; N, 5.18. *FT-IR* (υ_{max}/cm^{-1}, KBr pellet): 3546(w), 3439(s), 3222(w), 2962(m), 2934(m), 2874(m), 1624(m), 1560(s), 1396(s), 1316(m), 1270(w), 1099(w), 1047(m), 1022(m), 918(w), 861(m), 775(m), 571(w), 505(w). The phase purity of this compound was confirmed by powder X-ray diffraction analysis (see below).

Synthesis of $[Nhep_4]_3[Cr(C_6O_4Cl_2)_3]$ (10). This compound was prepared as compound **3** but using $CrCl_3{\cdot}6H_2O$ (213 mg, 0.8 mmol) instead of $FeCl_3{\cdot}6H_2O$, $[Nhep_4]Br$ (780 mg, 1.6 mmol) instead of $[PPh_3Et]Br$ and NaOH (192 mg, 4.8 mmol) instead of KOH. Compound **10** was obtained as deep red plate-like crystals (991 mg, yield 65 %). *Elemental Anal.* Calc. for $C_{102}H_{180}Cl_6CrN_3O_{12}$ (M_w = 1905.25): C, 64.30; H, 9.52; N, 2.21; Found: C, 64.20; H, 9.54; N, 2.29. *FT-IR* (υ_{max}/cm^{-1}, KBr pellet): 3416(s), 2957(m), 2927(m), 2856(m), 1640(m), 1618(w), 1532(s), 1467(w), 1400(s), 1350(s), 1302(m), 1081(m), 1000(m), 840(m), 610(m), 570(w), 508(w), 474(w). The

isostructurality of this compound with compound **17** was confirmed by powder X-ray diffraction analysis (see below).

Synthesis of $[Nhep_4]_3[Cr(C_6O_4Br_2)_3]$ (11). This compound was prepared as compound **3** but using $CrCl_3{\cdot}6H_2O$ (213 mg, 0.8 mmol) instead of $FeCl_3{\cdot}6H_2O$, $H_2C_6O_4Br_2$ (715 mg, 2.4 mmol) instead of $H_2C_6O_4Cl_2$, $[Nhep_4]Br$ (780 mg, 1,6 mmol) instead of $[PPh_3Et]Br$ and NaOH (192 mg, 4.8 mmol) instead of KOH. Compound **11** was obtained as deep red plate-like crystals (1129 mg, yield 65 %). *Elemental Anal.* Calc. for $C_{102}H_{180}Br_6CrN_3O_{12}$ (M_w = 2171.95): C, 56.41; H, 8.35; N, 1.94; Found: C, 56.45; H, 8.25; N, 2.01. *FT-IR* (υ_{max}/cm^{-1}, KBr pellet): 3417(s), 3234(w), 2957(m), 2926(m), 2856(m), 1639(m), 1522(s), 1401(s), 1339(s), 1282(m), 1082(m), 983(m), 804(m), 596(m), 556(w), 502(w). The isostructurality of this compound with compound **16** was confirmed by powder X-ray diffraction analysis (see below).

Synthesis of $[PPh_4]_3[Fe(C_6O_4(NO_2)_2)_3]$ (12). This compound was prepared as compound **3** but using $Na_2[C_6O_4(NO_2)_2]$ salt (658 mg, 2.4 mmol) instead of $H_2C_6O_4Cl_2$ and $[PPh_4]Br$ (1006 mg, 2.4 mmol) instead of $[PPh_3Et]Br$. Since a sodium salt is used, no base is needed. Compound **12** was obtained as an orange-brown crystalline powder (914 mg, yield 65 %). *Elemental Anal.* Calc. for $C_{90}H_{60}N_6FeP_3O_{24}$ (M_w = 1758.24): C, 61.48; H, 3.44; N, 4.78. Found: C, 60.12; H, 3.57; N, 4.88. *FT-IR* (υ_{max}/cm^{-1}, KBr pellet): 3439(s), 3233(w), 1624(s), 1559(m), 1437(w), 1398(s), 1270(m), 1108(m), 997(w), 722(w), 689(w), 667(w), 527(m). The phase purity of this compound was confirmed by powder X-ray diffraction analysis (see below).

Synthesis of $K_3[Fe(C_6O_4Cl_2)_3]$ (13): A solution of $FeCl_3{\cdot}6H_2O$ (216 mg, 0.8 mmol) in H_2O (5 mL) was added drop-wise to an aqueous solution (45 mL) prepared by the mixture of: (i) $H_2C_6O_4Cl_2$ (502 mg, 2.4 mmol) in water (25 mL) at 60 °C and (ii) KOH (270 mg, 4.8 mmol) in water (10 mL). The resulting solution was heated at 60 °C for 1 hour and was rota-evaporated to remove the water. The obtained deep purple powder was dissolved in N,N-dimethylformamide (DMF) and filtered to eliminate the KCl impurities (insoluble in DMF). Slow evaporation of the filtrate affords **13** as deep purple rhombohedral crystals (714 mg, yield 90 %). *Elemental Anal.* Calc. for $C_{30}H_{28}N_4FeCl_6O_{16}K_3$ (M_w = 1086.42): C, 33.17; H, 2.60; N, 5.16. Found: C, 31.68; H, 2.4; N, 5.3. *FT-IR* (υ_{max}/cm^{-1}, KBr pellet): 3455(s), 2920(w), 1656(s), 1534(m), 1349(w), 1275(m), 1080(m), 987(w), 811(w), 610(w), 578(m). The

phase purity of this compound was confirmed by powder X-ray diffraction analysis (see below).

Synthesis of $K_3[Cr(C_6O_4Cl_2)_3]$ (14): This compound was prepared as compound **13** but using $CrCl_3·6H_2O$ (0.8 mmol, 213 mg) instead of $FeCl_3·6H_2O$. Compound **14** was obtained as deep purple rhombohedral crystals (726 mg, yield 92 %). *Elemental Anal.* Calc. for $C_{27}H_{21}N_3CrCl_6O_{15}K_3$ (M_w = 1009.47): C, 29.37; H, 1.93; N, 3.3. Found: C, 32.12; H, 2.1; N, 4.16. *FT-IR* (υ_{max}/cm^{-1}, KBr pellet): 3455(s), 3080(w), 1656(s), 1531(m), 1356(w), 1270(m), 1080(m), 994(w), 847(w), 610(w), 573(m). The phase purity of this compound was confirmed by powder X-ray diffraction analysis (see below).

Synthesis of $K_3[Fe(C_6O_4Br_2)_3]$ (15): This compound was prepared as compound **13** but using $H_2C_6O_4Br_2$ (715 mg, 2.4 mmol) instead of $H_2C_6O_4Cl_2$. Compound **15** was obtained as deep purple rhombohedral crystals (772 mg, yield 91 %). *Elemental Anal.* Calc. for $C_{30}H_{28}N_4FeBr_6O_{16}K_3$ (M_w = 1353.12): C, 26.63; H, 2.09; N, 4.14. Found: C, 24.45; H, 1.37; N, 4.2. *FT-IR* (υ_{max}/cm^{-1}, KBr pellet): 3455(s), 3090(w), 1641(s), 1525(m), 1335(w), 1300(m), 1090(m), 977(w), 801(w), 655(w), 588(m). The phase purity of this compound was confirmed by powder X-ray diffraction analysis (see below).

Synthesis of $K_3[Cr(C_6O_4Br_2)_3]$ (16): This compound was synthesized as compound **13** but using $CrCl_3·6H_2O$ (0.8 mmol, 213 mg) instead of $FeCl_3·6H_2O$ and $H_2C_6O_4Br_2$ (715 mg, 2.4 mmol) instead of $H_2C_6O_4Cl_2$. Compound **16** was obtained as deep purple rhombohedral crystals (761 mg, yield 90 %). *Elemental Anal.* Calc. for $C_{30}H_{28}N_4CrBr_6O_{16}K_3$ (M_w = 1349.27): C, 26.7; H, 2.09; N, 4.15. Found: C, 26.5; H, 2.09; N, 4.15. *FT-IR* (υ_{max}/cm^{-1}, KBr pellet): 3425(s), 2930(w), 1664(s), 1520(m), 1347(w), 1345(m), 1100(m), 987(w), 811(w), 670(w), 578(m). The phase purity of this compound was confirmed by powder X-ray diffraction analysis (see below).

Synthesis of $[NBu_4]_3[Fe(C_6O_4Cl_2)_3]$ (17): The synthesis of compound **17** was done following the same previously described method[11] but the crystallization was carried out in DMF. *Elemental Anal.* Calc. for $C_{66}H_{108}N_3FeCl_6O_{12}$ (M_w = 1404.14): C, 56.45; H, 7.75; N, 2.99. Found: C, 55.6; H, 7.05; N, 3.14. *FT-IR* (υ_{max}/cm^{-1}, KBr pellet): 3455(s), 2965(w), 1646(s), 1520(m), 1351(w), 1310(m), 995(m), 824(w),

735(w), 600(w), 576(m). The phase purity of this compound was confirmed by powder X-ray diffraction analysis (see below).

Synthesis of $[NBu_4]_3[Cr(C_6O_4Cl_2)_3]$ (18): The synthesis of compound **18** was performed following the same previously described method[11] but the crystallization has been carried out in DMF. *Elemental Anal.* Calc. for $C_{66}H_{108}N_3CrCl_6O_{12}$ (M_w = 1400.29): C, 56.61; H, 7.77; N, 3.00. Found: C, 54.73; H, 7.42; N, 3.4. *FT-IR* (υ_{max}/cm^{-1}, KBr pellet): 3455(s), 2965(w), 1646(s), 1532(m), 1300(w), 1300(m), 1000(m), 841(w), 745(w), 610(w), 571(m). The phase purity of this compound was confirmed by powder X-ray diffraction analysis (see below).

Synthesis of $[NBu_4]_3[Fe(C_6O_4Br_2)_3]$ (19): The synthesis of compound **19** was achieved following the same synthetic previously described method[11] but the crystallization was carried out in DMF. *Elemental Anal.* Calc. for $C_{66}H_{108}N_3FeBr_6O_{12}$ (M_w = 1670.84): C, 47.44; H, 6.51; N, 2.51. Found: C, 46.49; H, 5.81; N, 2.79. *FT-IR* (υ_{max}/cm^{-1}, KBr pellet): 3445(s), 2965(w), 1666(s), 1526(m), 1342(w), 1280(m), 982(m), 885(w), 800(w), 740(w), 583(m). The phase purity of this compound was confirmed by powder X-ray diffraction analysis (see below).

Synthesis of $[NBu_4]_3[Cr(C_6O_4Br_2)_3]$ (20): The synthesis of compound **20** was done following the same synthetic method previously described [11] but the crystallization was carried out in DMF. *Elemental Anal.* Calc. for $C_{66}H_{108}N_3CrBr_6O_{12}$ (M_w = 1666.99): C, 47.55; H, 6.53; N, 2.52. Found: C, 46.98; H, 6.2; N, 2.8. *FT-IR* (υ_{max}/cm^{-1}, KBr pellet): 3435(s), 2965(w), 1640(s), 1525(m), 1342(w), 1290(m), 982(m), 824(w), 735(w), 596(m). The phase purity of this compound was confirmed by powder X-ray diffraction analysis (see below).

Table 1.1 lists the 20 different compounds prepared in this chapter and summarizes the precursors used for their synthesis. We include the data of compounds **A**-**D**, although compounds **A**-**D** were prepared by other members of the group, we include here their structure since compounds **1**-**3** are isostructural to them. The structures will be described below, because compounds **A** and **B** are isostructural to compounds **1**-**3** (phase I, see below) and compounds **C** and **D** are isostructural to compounds **5** and **6** (phase II, see below).

Table 1.1. *Compounds of the type $A_3[M^{III}(C_6O_4X_2)_3]$ prepared in this chapter (compounds **A**-**D** are included for comparative purposes).*

ref	Formula	A^+	M(III) salt	X	phase
1	$(PPh_3Et)_3[Cr(C_6O_4Cl_2)_3]$	$(PPh_3Et)^+$	$CrCl_3{\cdot}6H_2O$	Cl	I
A	$(PPh_3Et)_3[Fe(C_6O_4Cl_2)_3]$	$(PPh_3Et)^+$	$FeCl_3{\cdot}6H_2O$	Cl	I
2	$(PPh_3Et)_3[Cr(C_6O_4Br_2)_3]$	$(PPh_3Et)^+$	$CrCl_3{\cdot}6H_2O$	Br	I
B	$(PPh_3Et)_3[Fe(C_6O_4Br_2)_3]$	$(PPh_3Et)^+$	$FeCl_3{\cdot}6H_2O$	Br	I
3	$(PPh_3Et)_3[Ga(C_6O_4Br_2)_3]$	$(PPh_3Et)^+$	$GaCl_3$	Br	I
4	$(PPh_3Et)_3[Fe(C_6O_4(NO_2)_2)_3]$	$(PPh_3Et)^+$	$FeCl_3{\cdot}6H_2O$	NO_2	VI
5	$(PPh_3Pr)_3[Cr(C_6O_4Cl_2)_3]$	$(PPh_3Pr)^+$	$CrCl_3{\cdot}6H_2O$	Cl	II
C	$(PPh_3Pr)_3[Fe(C_6O_4Cl_2)_3]$	$(PPh_3Pr)^+$	$FeCl_3{\cdot}6H_2O$	Cl	II
D	$(PPh_3Pr)_3[Ga(C_6O_4Cl_2)_3]$	$(PPh_3Pr)^+$	$Ga(NO_3)_3$	Cl	II
6	$(PPh_3Pr)_3[Cr(C_6O_4Br_2)_3]$	$(PPh_3Pr)^+$	$CrCl_3{\cdot}6H_2O$	Br	II
7	$(PPh_3Pr)_3[Fe(C_6O_4(NO_2)_2)_3]$	$(PPh_3Pr)^+$	$FeCl_3{\cdot}6H_2O$	NO_2	VII
8	$(PBu_4)_3[Cr(C_6O_4(NO_2)_2)_3]$	$(PBu_4)^+$	$CrCl_3{\cdot}6H_2O$	NO_2	III
9	$(PBu_4)_3[Fe(C_6O_4(NO_2)_2)_3]$	$(PBu_4)^+$	$FeCl_3{\cdot}6H_2O$	NO_2	III
10	$(Nhep_4)_3[Cr(C_6O_4Cl_2)_3]$	$(Nhep_4)^+$	$CrCl_3{\cdot}6H_2O$	Cl	IV
11	$(Nhep_4)_3[Cr(C_6O_4Br_2)_3]$	$(Nhep_4)^+$	$CrCl_3{\cdot}6H_2O$	Br	IV
12	$(PPh_4)_3[Fe(C_6O_4(NO_2)_2)_3]$	$(PPh_4)^+$	$FeCl_3{\cdot}6H_2O$	NO_2	V
13	$K_3[Cr(C_6O_4Cl_2)_3]$	K^+	$CrCl_3{\cdot}6H_2O$	Cl	VIII
14	$K_3[Fe(C_6O_4Cl_2)_3]$	K^+	$FeCl_3{\cdot}6H_2O$	Cl	VIII
15	$K_3[Cr(C_6O_4Br_2)_3]$	K^+	$CrCl_3{\cdot}6H_2O$	Br	VIII
16	$K_3[Fe(C_6O_4Br_2)_3]$	K^+	$FeCl_3{\cdot}6H_2O$	Br	VIII
17	$[NBu_4]_3[Cr(C_6O_4Cl_2)_3]$	$(NBu_4)^+$	$CrCl_3{\cdot}6H_2O$	Cl	IX
18	$[NBu_4]_3[Fe(C_6O_4Cl_2)_3]$	$(NBu_4)^+$	$FeCl_3{\cdot}6H_2O$	Cl	IX
19	$[NBu_4]_3[Cr(C_6O_4Br_2)_3]$	$(NBu_4)^+$	$CrCl_3{\cdot}6H_2O$	Br	IX
20	$[NBu_4]_3[Fe(C_6O_4Br_2)_3]$	$(NBu_4)^+$	$FeCl_3{\cdot}6H_2O$	Br	IX

2.2. Physical Properties

FT-IR spectra were performed on KBr pellets and collected with a Nexus-Nicolet 5700 spectrophotometer.

Magnetic measurements were performed with a Quantum Design MPMS-XL-5 SQUID magnetometer in the temperature range of 2 to 300 K with applied magnetic fields of 0.1 or 0.5 T on polycrystalline samples of all the compounds. Susceptibility data were corrected for the sample holder and for the diamagnetic contribution of the salts using Pascal's constants.[12]

2.3. Structural Characterization

Suitable single crystals of compounds **8** and **9** were mounted on a loop using a viscous hydrocarbon oil then transferred directly to the cold nitrogen stream for data collection. X-ray data were collected at 120 K for both compounds on a Supernova diffractometer equipped with a graphite-monochromated Enhance (Mo) X-ray Source (λ = 0.71073 Å). The program CrysAlisPro, Agilent Technologies Ltd., was used for unit cell determinations and data reduction. Empirical absorption correction was performed using spherical harmonics, implemented in the SCALE3 ABSPACK scaling algorithm. Crystal structures were solved by direct methods with the SIR92 program[13] and refined against all F^2 values with the SHELXL-2014 program[14], using the WinGX2014.1 graphical user interface.[15] All non-hydrogen atoms were refined anisotropically and hydrogen atoms were placed in calculated positions and refined isotropically with a riding model. Data collection and refinement parameters are given in Tables 1.3-1.5.

The X-ray powder diffractograms were collected for polycrystalline samples of all the compounds using a 0.5 mm glass capillary that was mounted and aligned on a Empyrean PANalytical powder diffractometer, using CuKα radiation (λ = 1.54177 Å) operating at 40 mA and 45 kV. A total of 3 scans, in spinning mode, were collected at room temperature in the 2θ range of 2-40º with a step size of 0.0131º.

3. Results and Discussion

3.1. Synthesis

The synthesis of the monomeric compounds has been done following the same synthetic method previously described,[6] with a simple one pot reaction of the corresponding M(III) chloride or nitrate salts with a solution containing the desired bulky cation and the deprotonated anilato-type dianion (simply obtained by adding two equivalents of NaOH or KOH to the corresponding anilic-type acid). In spite of the apparent simplicity of the synthetic route, the bulky cation plays a key role in determining the crystallization of chiral crystals with a unique enantiomer (Λ or Δ) in a single crystal, as this will be discussed later.

3.2. Infrared Spectroscopy

The IR spectra are displayed by anilato type ligand: $C_6O_4Cl_2^{2-}$ (compounds **1**, **5**, **10**, **13**, **14**, **17**, **18**, **A**, **C** and **D**, Figure 1.2), $C_6O_4Br_2^{2-}$ (compounds **2**, **3**, **6**, **11**, **15**, **16**, **19**, **20** and **B**, Figure 1.3) and $C_6O_4(NO_2)^{2-}$ (**4**, **7**, **8**, **9** and **12**, Figure 1.4). Table 1.2 displays the main IR bands and their assignments.

***Table 1.2**. Selected vibrational frequencies for compounds **1**-**20** grouped by the X group (compounds **A**-**D** are included for comparative purposes).*

Com.	M	X	A^+	ν(C=O)	ν(C=C) ν(C-O)	ν(C-C) ν(C-O)	ν(C-C) ν(C-O) δ(C-X)	δ(C-O) δ(C=O) ν(C-X)	ρ(C-X)
1	Cr	Cl	PPh_3Et^+	1638	1530	1350	1001	841	572
A	Fe	Cl	PPh_3Et^+	1641	1525	1348	997	838	573
5	Cr	Cl	PPh_3Pr^+	1638	1529	1353	1000	841	570
C	Fe	Cl	PPh_3Pr^+	1643	1526	1350	997	839	572
D	Ga	Cl	PPh_3Pr^+	1642	1524	1356	998	844	573
10	Cr	Cl	$Nhep_4^+$	1640	1532	1350	1000	840	570
13	Fe	Cl	K^+	1656	1534	1349	999	845	578
14	Cr	Cl	K^+	1656	1531	1356	1005	847	573
17	Fe	Cl	NBu_4^+	1646	1520	1351	995	824	576
18	Cr	Cl	NBu_4^+	1646	1532	1352	1000	841	571
2	Cr	Br	PPh_3Et^+	1637	1521	1341	987	808	558
B	Fe	Br	PPh_3Et^+	1637	1522	1339	980	803	560
3	Ga	Br	PPh_3Et^+	1639	1530	1344	984	810	560
6	Cr	Br	PPh_3Pr^+	1637	1519	1339	986	806	557
11	Cr	Br	$Nhep_4^+$	1639	1522	1339	984	804	556
15	Fe	Br	K^+	1641	1525	1335	977	801	588
16	Cr	Br	K^+	1664	1520	1347	987	811	561
19	Fe	Br	NBu_4^+	1666	1522	1342	983	808	583
20	Cr	Br	NBu_4^+	1640	1525	1342	982	805	596
4	Fe	NO_2	PPh_3Et^+	1624	1552	1393	1047	772	581
7	Fe	NO_2	PPh_3Pr^+	1638	1551	1399	1047	775	-
8	Cr	NO_2	PBu_4^+	1652	1552	1398	1052	776	-
9	Fe	NO_2	PBu_4^+	1624	1560	1392	1047	775	571
12	Fe	NO_2	PPh_4^+	1624	1559	1398	1049	776	-

In general, all the compounds show very similar IR spectra, indicating that all the $[M^{III}(C_6O_4X_2)_3]^{3-}$ anions present very close molecular structures. All the $A_3[M^{III}(C_6O_4X_2)_3]$ compounds show the corresponding bands in the 2800-3000 cm^{-1} range associated with the ν(C-H) vibrations of the alkyl chains of the cations, except in **12** where the cation is $[PPh_4]^+$. Additionally, all the complexes show a strong band

around 1640 cm^{-1} attributed to the ν(C=O) vibration mode of the non-coordinated C=O groups of the anilato ligands.[16] This band appears at lower wavenumbers in all the complexes compared to the free $H_2C_6O_4Cl_2$ ligand (where it appears at 1665 cm^{-1}) as a result of the weakening of the C=O bond upon coordination to the metal ions. All the compounds also show a very intense band at ca. 1530-1550 cm^{-1} attributed to the ν(C=C) and ν(C-O) vibrational modes and a strong band at around 1350 cm^{-1} corresponding to the ν(C-C) and ν(C-O) vibration modes. Additionally, all the compounds present a series of medium bands at ca. 1000, 840 and 570 cm^{-1} due to diverse C=O, C-O, C-C and C-X vibrational modes (see below).[16]

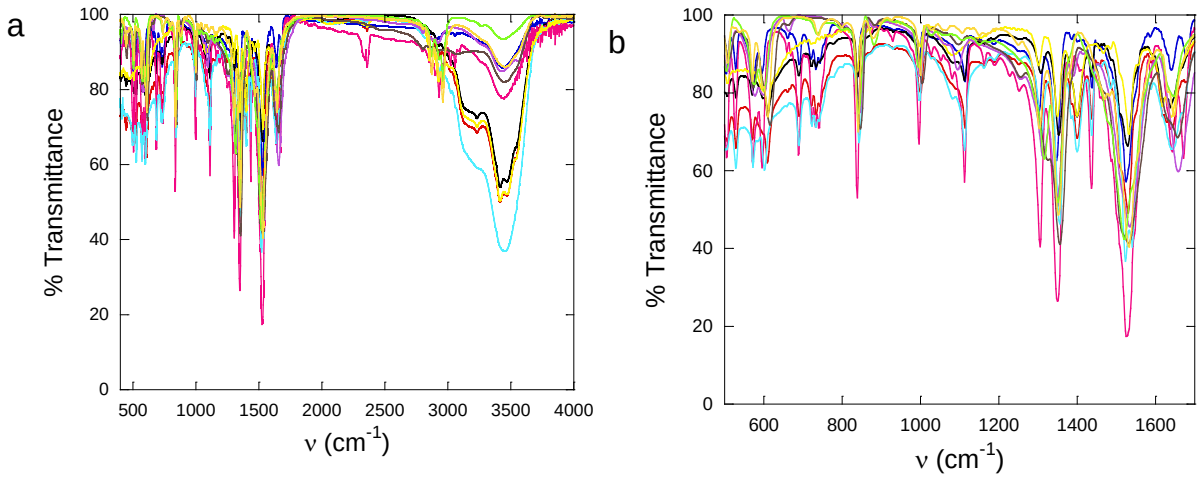

Figure 1.2: *FT-IR Spectra in* ***(a)*** *the 4000-400 cm^{-1} region and* ***(b)*** *the 1600-500 cm^{-1} region for the ten compounds containing the $[C_6O_4Cl_2]^{2-}$ ligand:* ***1*** *in red,* ***A*** *in blue,* ***5*** *in black,* ***C*** *in fuchsia,* ***D*** *in light blue,* ***10*** *in yellow ,* ***13*** *in brown,* ***14*** *in purple,* ***17*** *in orange and* ***18*** *in light green.*

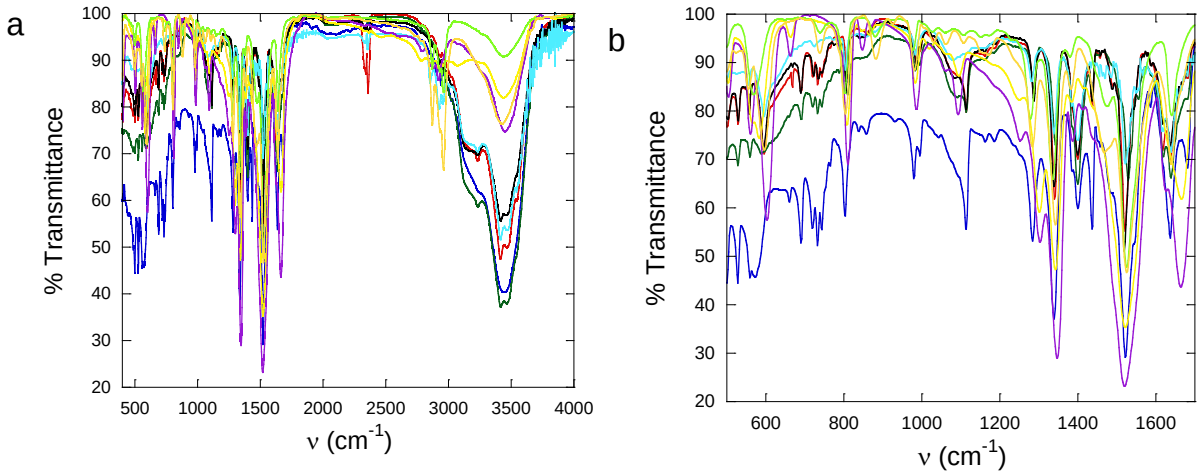

Figure 1.3: *FT-IR Spectra in* ***(a)*** *the 4000-400 cm^{-1} region and* ***(b)*** *the 1600-500 cm^{-1} region for the nine compounds containing the $[C_6O_4Br_2]^{2-}$ ligand:* ***2*** *in red,* ***B*** *in blue,* ***3*** *in green,* ***6*** *in black,* ***11*** *in light blue,* ***15*** *in purple,* ***16*** *in yellow,* ***19*** *in orange and* ***20*** *in light green.*

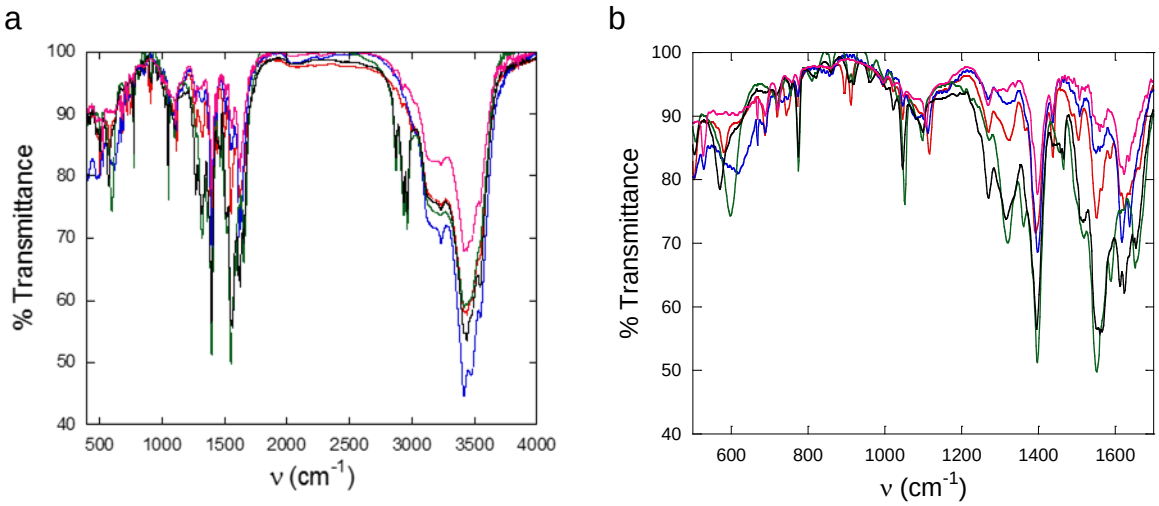

Figure 1.4: *FT-IR Spectra in the* ***(a)*** *4000-400 cm^{-1} region and* ***(b)*** *1600-500 cm^{-1} region for the five compounds containing the $[C_6O_4(NO_2)_2]^{2-}$ ligand:* ***4*** *in red,* ***7*** *in blue,* ***8*** *in green,* ***9*** *in black and* ***12*** *in fuchsia.*

3.3. X-Ray diffraction

Chiral compounds **A** , **B** and **1-3** crystallize in the trigonal chiral *R*3 space group (Phase I), whereas compounds **5**, **6**, **C** and **D** crystallize in the achiral but polar orthorhombic *P*2*cb* space group (Phase II) and finally compounds **8** and **9** crystallize in the centro-symmetric (neither chiral nor polar) triclinic *P*-1 space group (Phase III). It is a remarkable fact that these compounds show a progressive evolution from the

chiral and polar *R*3 space group (**1**-**3**, **A** and **B**) to the non chiral but polar orthorhombic *P*2*cb* space group (**5**, **6**, **C** and **D**) and finally the centrosymmetric (neither chiral nor polar) triclinic *P*-1 space group (**8** and **9**).

A summary of the data collection and structure refinements of compounds **8** and **9** is provided in Table 1.3.

***Table 1.3**. Crystal data for $[PBu_4]_3[Cr(C_6O_4(NO_2)_2)_3]$ (**8**) and $[PBu_4]_3[Fe(C_6O_4(NO_2)_2)_3]$ (**9**).*

Compound	**8**	**9**
Empirical formula	$C_{66}H_{108}N_6CrP_3O_{24}$	$C_{66}H_{108}N_6FeP_3O_{24}$
Formula weight	1514.49	1518.34
Crystal colour	orange	orange
Crystal size	0.10×0.09×0.01	0.12×0.04×0.04
Temperature (K)	120(2)	120(2)
Wavelength (Å)	0.71073	0.71073
Crystal system, *Z*	Triclinic, 2	Triclinic, 2
Space group	*P*-1	*P*-1
a (Å)	11.1016(8)	11.1092(12)
b (Å)	12.615(2)	12.6410(14)
c (Å)	30.134(3)	30.199(3)
α (°)	85.271(10)	85.474(9)
β (°)	85.275(7)	85.232(9)
γ (°)	68.409(10)	68.212(10)
V (Å^3)	3904.4(8)	3919.1(8)
ρ_{calc} (Mg/m^3)	1.288	1.287
μ(MoKα) (mm^{-1})	0.283	0.329
θ range (°)	2.92-25.05	3.08-27.99
Reflns. collected	29012	74345
Independent reflns. (R_{int})	13735 (0.1725)	16860 (0.2375)
Reflns used in refinement, *n*	13735	16860
L. S. parameters, *p*/ restraints, *r*	586 / 0	831 / 0
Absolute structure parameter	n.a.	n.a.
$R_1(F)$,[a] $I > 2\sigma(I)$	0.1058	0.1022
$wR_2(F^2)$,[b] all data	0.1953	0.2727
$S(F^2)$,[c] all data	0.954	0.978

[a]$R_1(F) = \Sigma||F_o|-|F_c||/\Sigma|F_o|$; [b]$wR_2(F^2) = [\Sigma w(F_o^2-F_c^2)^2/\Sigma wF_o^4]^{1/2}$; [c]$S(F^2) = [\Sigma w(F_o^2-F_c^2)^2/(n + r - p)]^{1/2}$

Crystal structure of $[PPh_3Et]_3[Cr(C_6O_4Cl_2)_3]$ (1), $[PPh_3Et]_3[Cr(C_6O_4Br_2)_3]$ (2), $[PPh_3Et]_3[Ga(C_6O_4Br_2)_3]$ (3), $[PPh_3Et]_3[Fe(C_6O_4Cl_2)_3]$ (A) and $[PPh_3Et]_3[Fe(C_6O_4Br_2)_3]$ (B): Although compounds **A** and **B** were prepared by other members of the group, we include here their structure since compounds **1**-**3** are isostructural to **A** and **B**. These five compounds are isostructural and crystallize in the chiral rhombohedral space group *R*3 (phase I). The asymmetric unit is formed by one $[M(C_6O_4X_2)_3]^{3-}$ anion and three $[PPh_3Et]^+$ cations, all of them located on a C_3 axis. These compounds show monomeric tris(haloanilato)metallate $[M(C_6O_4X_2)_3]^{3-}$ anions surrounded by $[PPh_3Et]^+$ cations (Figure 1.5a). The anions present the typical MO_6 octahedral geometry derived from the tris-chelated coordination environment described in previously published $[M^{III}(C_6O_4X_2)_3]^{3-}$ anions (Figure 1.5c and 1.5d).[1-3, 5, 17]

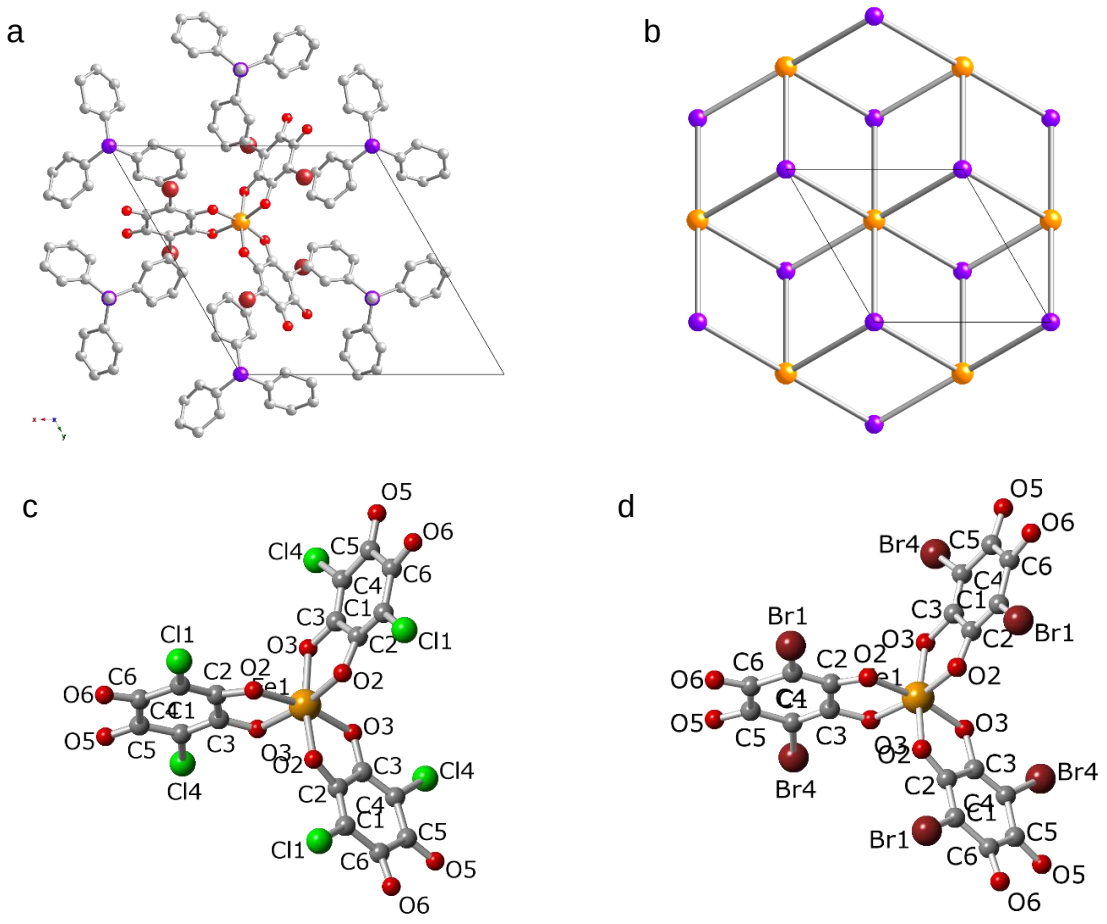

***Figure 1.5**. Structure of compounds **A** and **B**. (**a**) View of one$[Fe(C_6O_4X_2)_3]^{3-}$ anion surrounded by six $[PPh_3Et]^+$ cations showing the six π–π interactions. H atoms are omitted for clarity. (**b**) View of the relative disposition of the Fe (orange) and P (violet) atoms in the ab layer showing the six P surrounding each Fe and the three Fe around each P. **(c)** and **(d)** View of the two Λ-$[Fe(C_6O_4X_2)_3]^{3-}$ anions; (**c**) X = Cl and (**d**) X = Br with the labelling scheme. Colour code: Fe = orange, O = red, C = grey, Cl = green, Br = brown, P = violet.*

The Fe-O and the intra ligand C-C and C-O bond lengths show the expected tendency for mono-chelating anilato-type ligands. Thus, the C-O bond distances are significantly shorter for the two non coordinated oxygen atoms (O5 and O6, Table 1.4) than for the two coordinated ones (O2 and O3), in line with the loss of double bond character for the coordinated C=O groups. The cations present the expected tetrahedral geometry around the P atom and they all show the same orientation for the three phenyl aromatic rings in a way that the π–π interactions with the three surrounding anions are maximized (Figure 1.5a, Table 1.5). This disposition means that each anion presents a total of six π–π anilato/phenyl interactions, which is the maximum possible number of π–π interactions (Figure 1.5b).

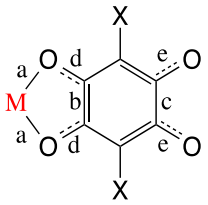

***Table 1.4**. Main bond lengths (Å) in the $[M(C_6O_4X_2)_3]^{3-}$ anions in compounds $[PPh_3Et]_3[Fe(C_6O_4Cl_2)_3]$ (**A**), $[PPh_3Et]_3[Fe(C_6O_4Br_2)_3]$ (**B**), $[PPh_3Pr]_3[Fe(C_6O_4Cl_2)_3]$ (**C**), $[PPh_3Pr]_3[Ga(C_6O_4Br_2)_3]$ (**D**), $[PBu_4]_3[Cr(C_6O_4(NO_2)_2)_3]$ (**8**) and $[PBu_4]_3[Fe(C_6O_4(NO_2)_2)_3]$ (**9**).*

atoms	type	A (Fe)	B (Fe)	C (Fe)	D (Ga)	8 (Cr)	9 (Fe)
M-O	a	2.00(2)	1.98(3)	2.003(7)	1.959(6)	1.953(5)	2.014(4)
		1.99(2)	1.98(3)	2.007(8)	1.961(5)	1.962(5)	1.984(4)
				2.010(8)	1.970(6)	1.985(5)	1.993(4)
						1.951(5)	2.017(4)
						1.959(5)	1.995(4)
						1.969(5)	2.014(4)
C2-C3	b	1.556(17)	1.57(5)	1.522(14)	1.511(12)	1.507(10)	1.517(9)
C12-C13				1.54(2)[a]	1.524(17)[c]	1.505(11)	1.501(8)
C22-C23						1.512(10)	1.504(10)
C5-C6	c	1.57(4)	1.51(5)	1.534(16)	1.557(13)	1.550(12)	1.554(9)
C15-C16				1.55(2)[b]	1.565(18)[d]	1.550(12)	1.551(9)
C25-C26						1.567(11)	1.551(11)
C2-O2	d	1.34(3)	1.33(4)	1.309(11)	1.309(10)	1.298(8)	1.276(7)
C12-O12				1.296(13)	1.270(10)	1.292(9)	1.285(7)
C22-O22						1.288(9)	1.296(7)
C3-O3	d	1.25(2)	1.19(5)	1.312(12)	1.314(9)	1.300(9)	1.288(7)
C13-O13						1.288(9)	1.294(7)
C23-O23						1.282(9)	1.281(7)
C5-O5	e	1.23(3)	1.24(4)	1.240(12)	1.222(11)	1.249(10)	1.227(7)
C15-O15						1.220(9)	1.217(8)
C25-O25						1.212(9)	1.215(8)
C6-O6	e	1.19(3)	1.27(4)	1.229(13)	1.238(10)	1.224(9)	1.216(7)
C16-O16				1.221(12)	1.220(10)	1.229(9)	1.226(7)
C26-O26						1.201(9)	1.217(8)

[a]C12-C12[*]; [b]C16-C16[*] (* = x, -y+1,-z+1); [c]C12-C12[#]; [d]C16-C16[#] (# = x, -y, -z+2)

Crystal structure of $[PPh_3Pr]_3[Cr(C_6O_4Cl_2)_3]$ (5), $[PPh_3Pr]_3[Cr(C_6O_4Br_2)_3]$ (6), $[PPh_3Pr]_3[Fe(C_6O_4Cl_2)_3]$ (C) and $[PPh_3Pr]_3[Ga(C_6O_4Cl_2)_3]$ (D): Although compounds **C** and **D** were prepared by other members of the group, we include here their structure since compounds **5** and **6** are isostructural to **C** and **D**. These four compounds are isostructural and crystallize in the orthorhombic *P*2*cb* space group (Phase II). Compound **D** is the first characterized $[Ga(C_6O_4X_2)_3]^{3-}$ anion, given that all the previously published trisanilatometallate anions are based on Fe, Cr or In.[1-5] The asymmetric unit contains half $[M^{III}(C_6O_4X_2)_3]^{3-}$ anion located on a C_2 axis, one $[PPh_3Pr]^+$ cation located on a general position and another half cation located on a C_2 axis. The geometry and bond distances (Table 1.4) of the cations and the anions in **C** and **D** are very similar to those observed in the chiral compounds **A** and **B** but present a different distribution, due to the different symmetry.

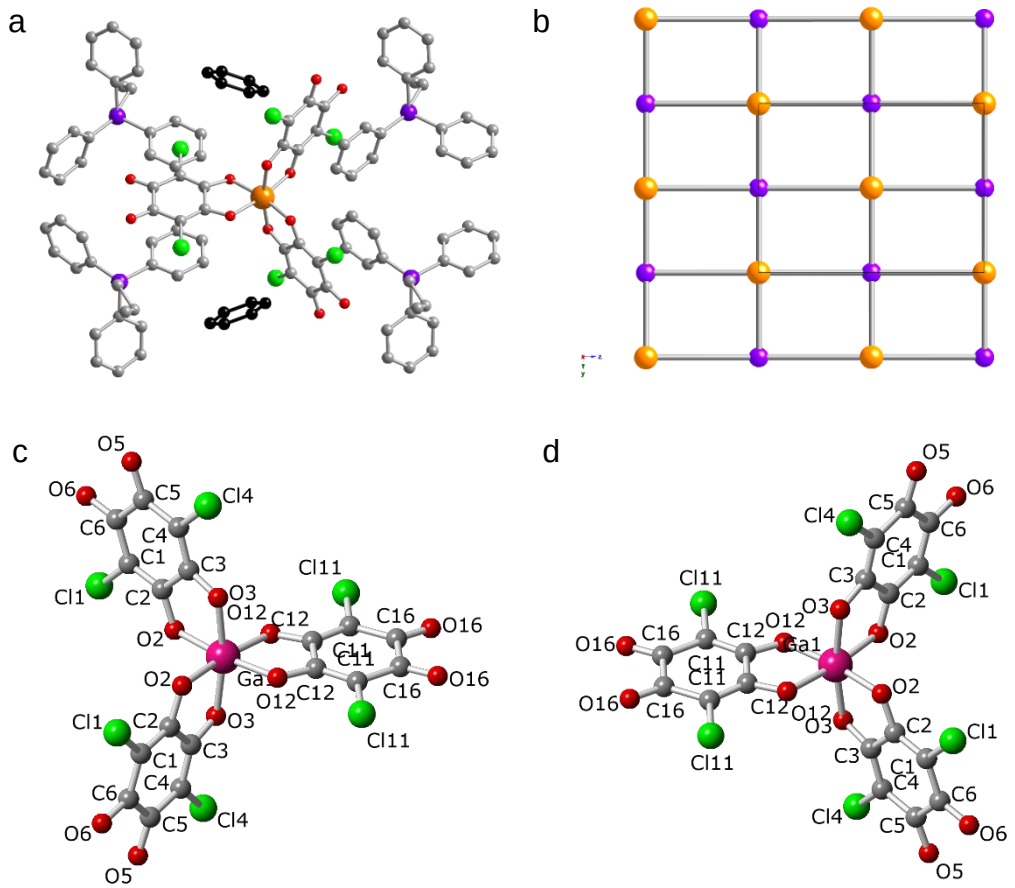

***Figure 1.6**. Structure of compounds **C** and **D**. (**a**) View of one$[Fe(C_6O_4Cl_2)_3]^{3-}$ anion surrounded by six $[PPh_3Pr]^+$ cations showing the four π–π interactions. H atoms are omitted for clarity. (**b**) View of the relative disposition of the Fe (orange) and P (violet) atoms in the bc layer showing the four P surrounding each Fe and the three Fe around each P. View of a Λ-$[Ga(C_6O_4Cl_2)_3]^{3-}$ **(c)** and a Δ-$[Ga(C_6O_4Cl_2)_3]^{3-}$ **(d)** anion in **D** with the labelling scheme. Colour code: Fe = orange, Ga = pink, O = red, C = grey, Cl = green and P = violet.*

The structure of **C** and **D** also shows monomeric octahedral $[M^{III}(C_6O_4Cl_2)_3]^{3-}$ anions surrounded by cations, as in **A** and **B**, but in **C** and **D** each anion only has π-π interactions with four neighbouring cations (Figure 1.6a, Table 1.5), giving rise to a square lattice where each anion is surrounded by four cations and vice-versa (Figure 1.6b). The two π–π missing interactions do not occur because the phenyl ring of the cation located in this direction is further away and presents an almost perpendicular orientation (black rings in Figure 1.6a), precluding any π–π interaction in this direction. This fact implies a weaker π-π stabilization and may be at the origin of the disorder found in the $[PPh_3Pr]^+$ cation containing these perpendicular phenyl rings. As expected, this crystal is not chiral since a racemic mixture of the two enantiomers was found (Figures 1.6c and 1.6d).

Crystal structure of $[PBu_4]_3[Cr(C_6O_4(NO_2)_2)_3]$ (8) and $[PBu_4]_3[Fe(C_6O_4(NO_2)_2)_3]$ (9): These two achiral compounds are isostructural and crystallize in the triclinic *P*-1 space group (phase III). As observed in phase II compounds, in **8** and **9** both enantiomers are present in the crystal (Figures 1.7c and 1.7d), , therefore, these compounds are not chiral.

The asymmetric unit is formed by three independent cations and one $[M^{III}(C_6O_4(NO_2)_2)_3]^{3-}$ anion (where M^{III} is Cr in **8** and Fe in **9**) located on general positions. The structure is formed by isolated octahedral $[M^{III}(C_6O_4(NO_2)_2)_3]^{3-}$ anions surrounded by tetrahedral $[PBu_4]^+$ cations. These two compounds represent the first structurally characterized examples of tris(nitranilato)metallate anions, since to date only complexes with anilato derivatives with X = Cl, Br or I have been characterized.[1-5] The overall geometry and bond distances of the $[M^{III}(C_6O_4(NO_2)_2)_3]^{3-}$ anions are similar to the ones previously described in other tris(anilato)metallate anions (Table 1.4). Nonetheless, these phase III compounds show two original aspects: (i) the cations do not have any aromatic rings and (ii) the anions contain non planar $[C_6O_4(NO_2)_2]^{2-}$ ligands due to the fact that the NO_2 groups are rotated with angles in the range of 37° to 67° with respect to the aromatic anilato ring. These singularities lead to a structure where each anion is surrounded by four cations in a near tetrahedral environment and each cation is surrounded by two anions (Figures 1.7a and 1.7b) with no significant anion-cation interactions except for the electrostatic ones.

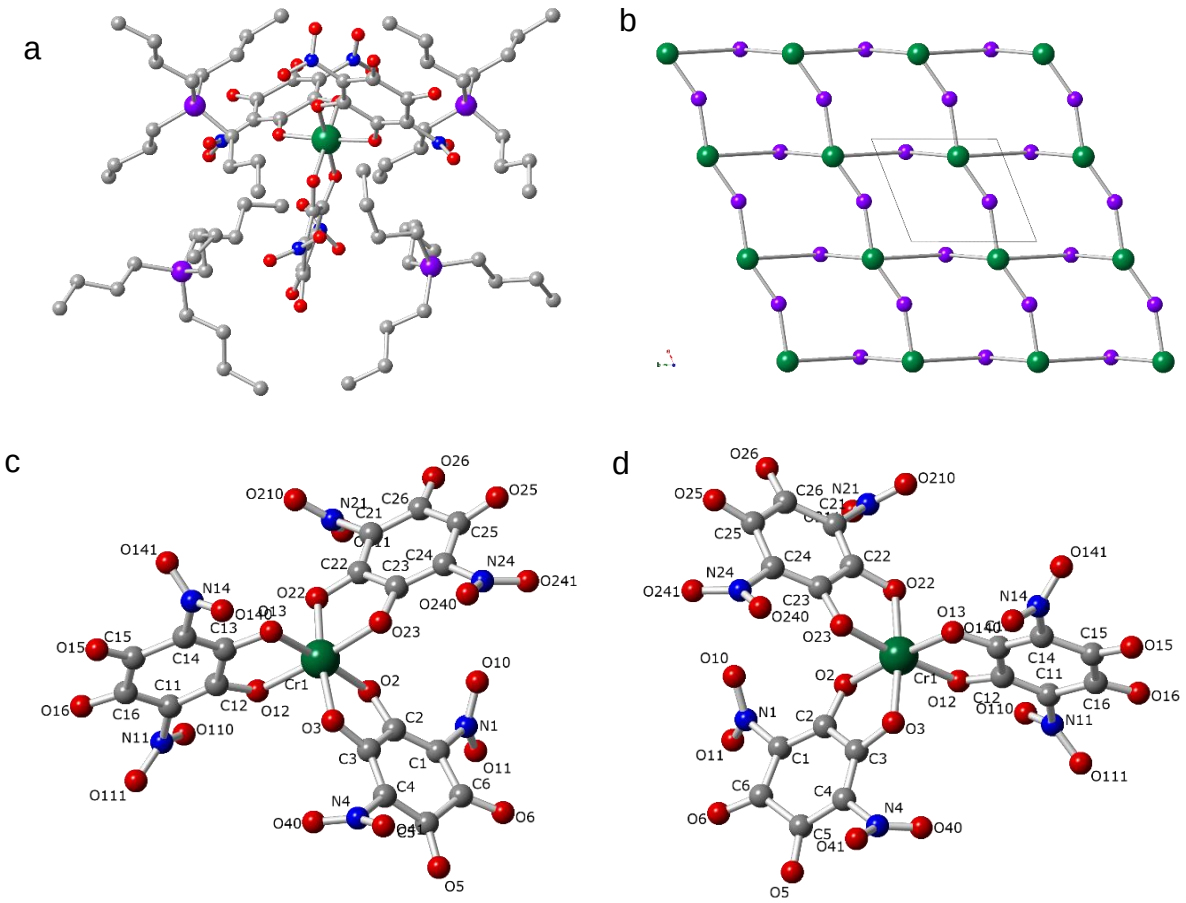

***Figure 1.7**. Structure of compounds **8** and **9**. **(a)** View of one $[M(C_6O_4(NO_2)_2)_3]^{3-}$ anion surrounded by four PBu_4^+ cations. H atoms are omitted for clarity. **(b)** View of the relative disposition of the Cr (green) and P (violet) atoms in the ab layer showing the four P surrounding each Cr and the two Cr around each P. **(c)** and **(d)** View of the two enantiomers of the novel anion $[Cr(C_6O_4(NO_2)_2)_3]^{3-}$ in **8** **(c)** Λ enantiomer and **(d)** Δ enantiomer. Colour code: Cr = green, O = red, C = grey, N = blue and P = violet*

3.3.1. Discussion of the structures

The most remarkable fact in the previously described structures is the enantiopure crystallization of the tris(anilato)metallate anion in compounds **1**-**3**, **A** and **B** (with formula $[M^{III}(C_6O_4X_2)_3]^{3-}$ where X = Cl and Br) when the cation $[PPh_3Et]^+$ acts as counter cation. In fact, this is the only cation that forces the already cited enantiopure crystallization. We have been able to prepare two complete series of isostructural compounds of formulas $[PPh_3Et]_3[M^{III}(C_6O_4X_2)_3]$ with M/X = Cr/Cl (**1**), Cr/Br (**2**) and Ga/Br (**3**), all of them presenting the same structure (phase I) as the Fe/Cl (**A**) and Fe/Br (**B**) derivatives (phase I) and $[PPh_3Pr]_3[M^{III}(C_6O_4X_2)_3]$ with M/X =

Cr/Cl (**5**) and Cr/Br (**6**), both presenting the same structure (phase II) asthe Fe/Cl (**C**) and Ga/Cl (**D**) derivatives (phase I)

With other cations as $[PPh_3Pr]^+$, $[PBu_4]^+$, $[NHep_4]^+$ and $[PPh_4]^+$ or for X = NO_2, racemic crystals were obtained in all cases. Nevertheless, despite numerous attempts using different methods and conditions, we have not been able to crystallize any compound of phases IV to IX, a clear proof of the great difficulty to crystallize these monomeric anions. In fact, until very recently, only two of these anions had been crystallized.[1, 2]

We can, therefore, conclude that in the $[M^{III}(C_6O_4X_2)_3]^{3-}$ anions (M^{III} = Cr, Fe and Ga; X = Cl and Br), the observed structure only depends on the counter cation used but not on M^{III} nor X. On the other hand, when X = NO_2 the anion plays a major role in the final structure and, accordingly, the structures are different to those observed for X = Cl and Br. Thus, the $[PPh_3Et]^+$ and $[PPh_3Pr]^+$ salts of the $[M^{III}(C_6O_4(NO_2)_2)_3]^{3-}$ anions are different and different to those observed for X = Cl and Br. This fact is attributed to the lack of planarity of the X = NO_2 anilato derivative, which exerts a steric impediment, preventing a close π–π interaction between the anilato rings and the phenyl groups of the cations.

As mentioned before, the cation-anion π–π interactions play a key role and seem to be the reason of the unexpected chirality observed for the $[PPh_3Et]^+$ salts, in which there are six close π–π interactions around each anion (Figure 1.5a, Table 1.5). Since these six π–π interactions appear only if all the anions present the same chirality, we can deduce that the obtained structure is chiral in order to maximize the π–π interactions between the aromatic anilato and phenyl rings. As a matter of fact, this sextuple phenyl-embrace (SPE) interaction[18] has been shown to be responsible for obtaining chirals 3D oxalate-based lattice with an attractive energy estimated to be as high as 125 kJ/mol with the closely related $[PPh_3Me]^+$ cation.[19] But, it has to be noted that in the oxalate example the interaction is established between the phenyl rings and the $C_2O_4^{2-}$ ligands whereas in compounds **1-3, A** and **B** the interaction is established between the phenyl rings of the $[PPh_3Et]^+$ cation and the aromatic rings of the anilato-type ligand, so, that interaction must be stronger than in the oxalate case. Thus, the presence of only one enantiomer in the chiral phase I compounds (Λ in the solved crystals of **A** and **B**) is driven by the possibility to maximize the number

of π–π interactions (during the one-pot synthesis we use a racemic mixture of the anions). Therefore, half of the crystals present one chirality and the other half the opposite one.

This hypothesis is confirmed by the fact that in compounds **5**, **6**, **C** and **D**, which contain the closely related $[PPh_3Pr]^+$ cation, there are only four π–π anion-cation interactions (Table 1.5) and, accordingly, the tendency to crystallize with only one enantiomer is less favourable than in compounds **A** and **B** from the energetic point of view. Due to this lower π–π stabilization energy, we obtain the statistically more favourable achiral phase since the solution contains a racemic mixture of both enantiomers.

Finally, compounds **8** and **9** contain the non-planar nitranilato $[C_6O_4(NO_2)_2]^{2-}$ ligand and $[PBu_4]^+$ cations that do not present aromatic rings, precluding the formation of any π–π interaction. Due to this lack of π–π interactions, the resulting crystals are not chiral and contain both enantiomers of the anions $[M(C_6O_4(NO_2)_2)_3]^{3-}$.

The structural parameters of the π–π interactions in compounds **A**-**D** are shown in Table 1.5.

Table 1.5*. Structural parameters of the of the π–π interactions in compounds **A**-**D**: centroid-centroid distances ($C_g \cdots C_g$), distances between average planes (d) and angles between the normal to the average planes of the aromatic rings (α)*

Compound	Interactions	Cation ring	Anion ring	$C_g \cdots C_g$ (Å)	d (Å)	α (°)
A	3	C11-C16	C1-C6	3.66	3.50	15.4
	3	C31'-C36'	C1-C6	3.39	3.19	15.5
B	3	C21'-C26'	C1-C6	3.75	3.62	15.0
	3	C31-C36	C1-C6	3.45	3.23	17.9
C	2	C121-C126	C1-C6	3.52	3.46	5.6
	2	C101-C106	C11-C16	3.45	3.41	4.2
D	2	C101-C106	C1-C6	3.51	3.45	5.6
	2	C121-C126	C11-C16	3.46	3.44	3.5

3.4. X-Ray Powder Diffraction

According to their X-ray powder diffractograms, we can group the 24 compounds (**1**-**20** and **A**-**D**) into nine isostructural families (phases I to IX, Figures 1.8 to 1.14).

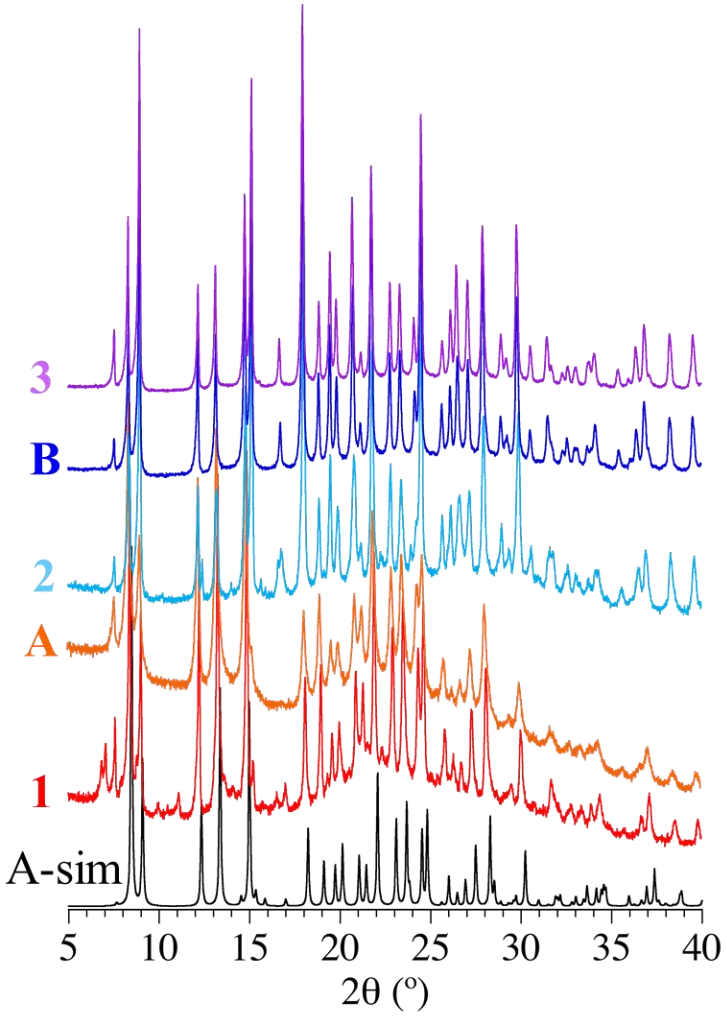

Figure 1.8. *Experimental and simulated (for **A**) X-ray powder diffractograms for phase I compounds: $(PPh_3Et)_3[M(C_6O_4X_2)_3]$ with M/X = Cr/Cl (**1**), Fe/Cl (**A**), Cr/Br (**2**), Fe/Br (**B**) and Ga/Br (**3**).*

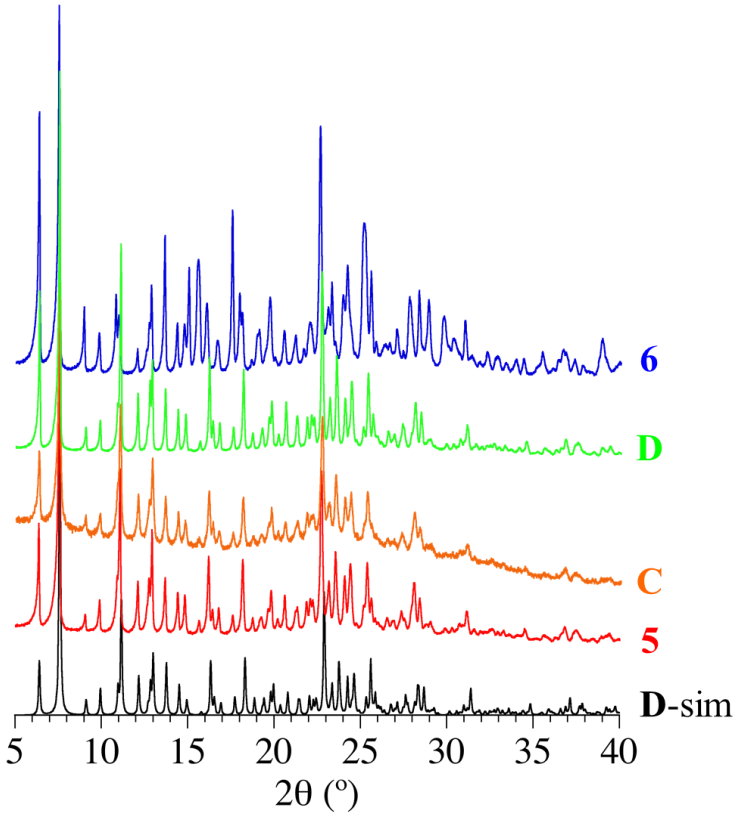

Figure 1.9. *Experimental and simulated X-ray powder diffractograms for phase II compounds: $(PPh_3Pr)_3[M(C_6O_4X_2)_3]$ with M/X = Cr/Cl (**5**), Fe/Cl (**C**), Ga/Cl (**D**) and Cr/Br (**6**).*

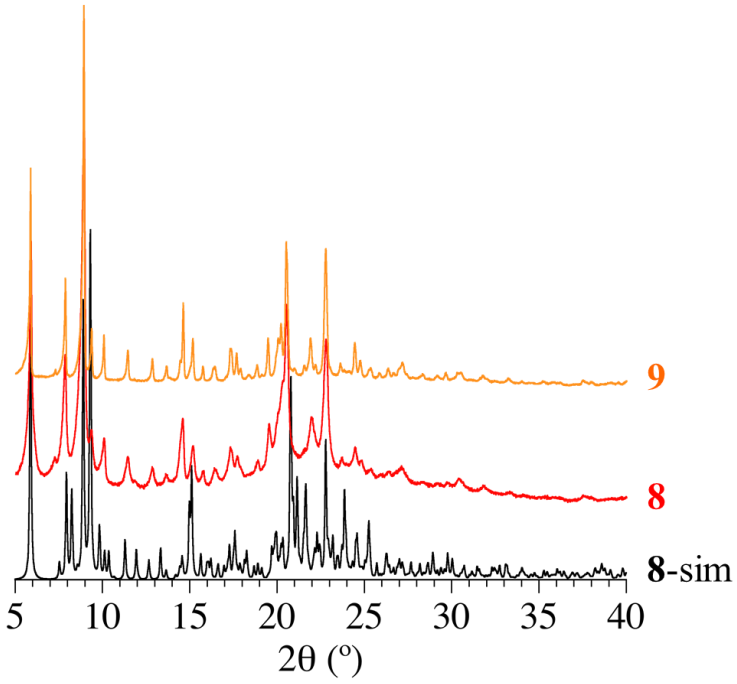

Figure 1.10. *Experimental and simulated X-ray powder diffractograms for phase III compounds: $(PBu_4)_3[M(C_6O_4X_2)_3]$ with M/X = Cr/NO_2 (**8**) and Fe/NO_2 (**9**).*

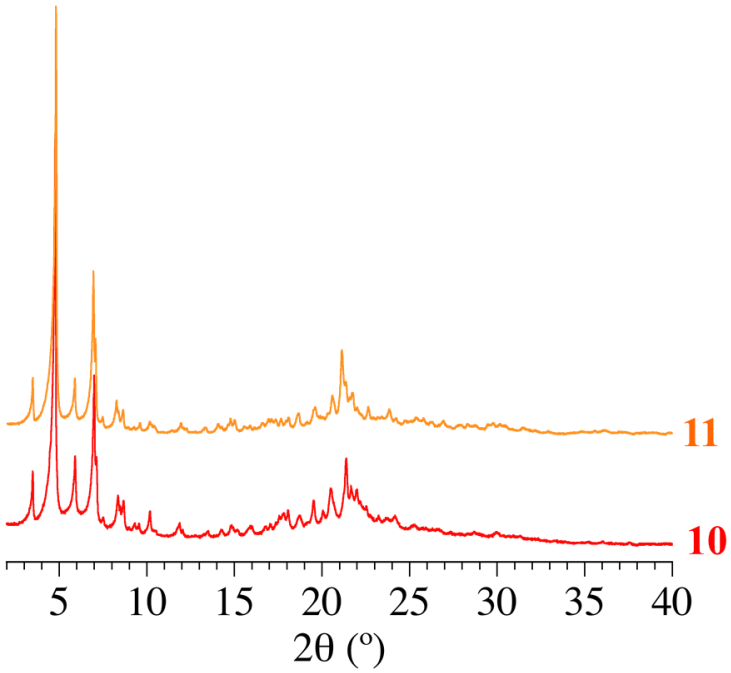

Figure 1.11. *Experimental X-ray powder diffractograms for phase IV compounds: $(Nhep_4)_3[M(C_6O_4X_2)_3]$ with M/X = Cr/Cl (**10**) and Cr/Br (**11**).*

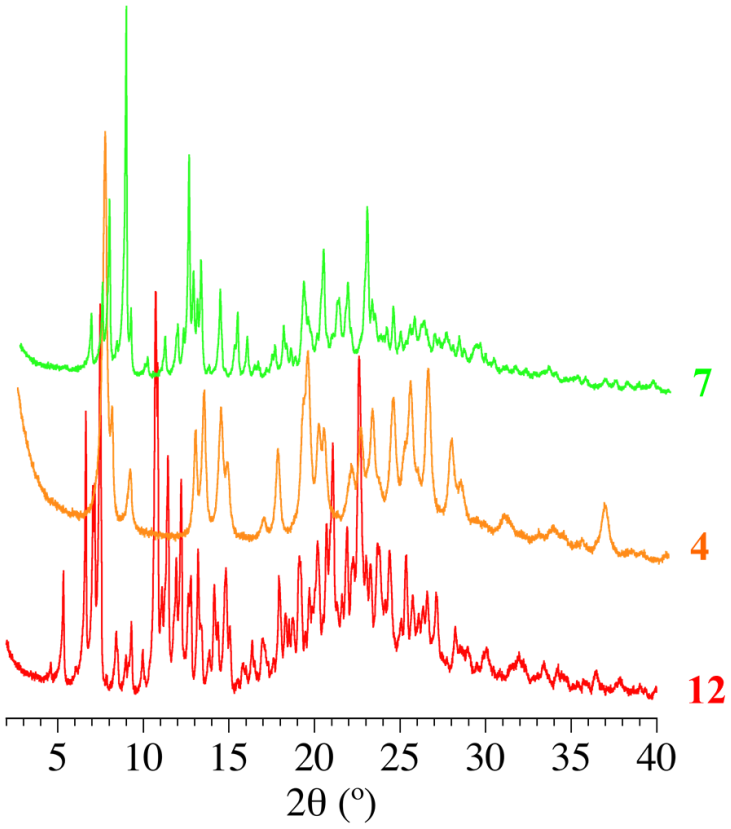

Figure 1.12. *Experimental X-ray powder diffractograms for compounds $(PPh_4)_3[Fe(C_6O_4(NO_2)_2)_3]$ (**12**, phase V), $(PPh_3Et)_3[Fe(C_6O_4(NO_2)_3]$ (**4**, phase VI) and $(PPh_3Pr)_3[Fe(C_6O_4(NO_2)_3]$ (**7**, phase VII).*

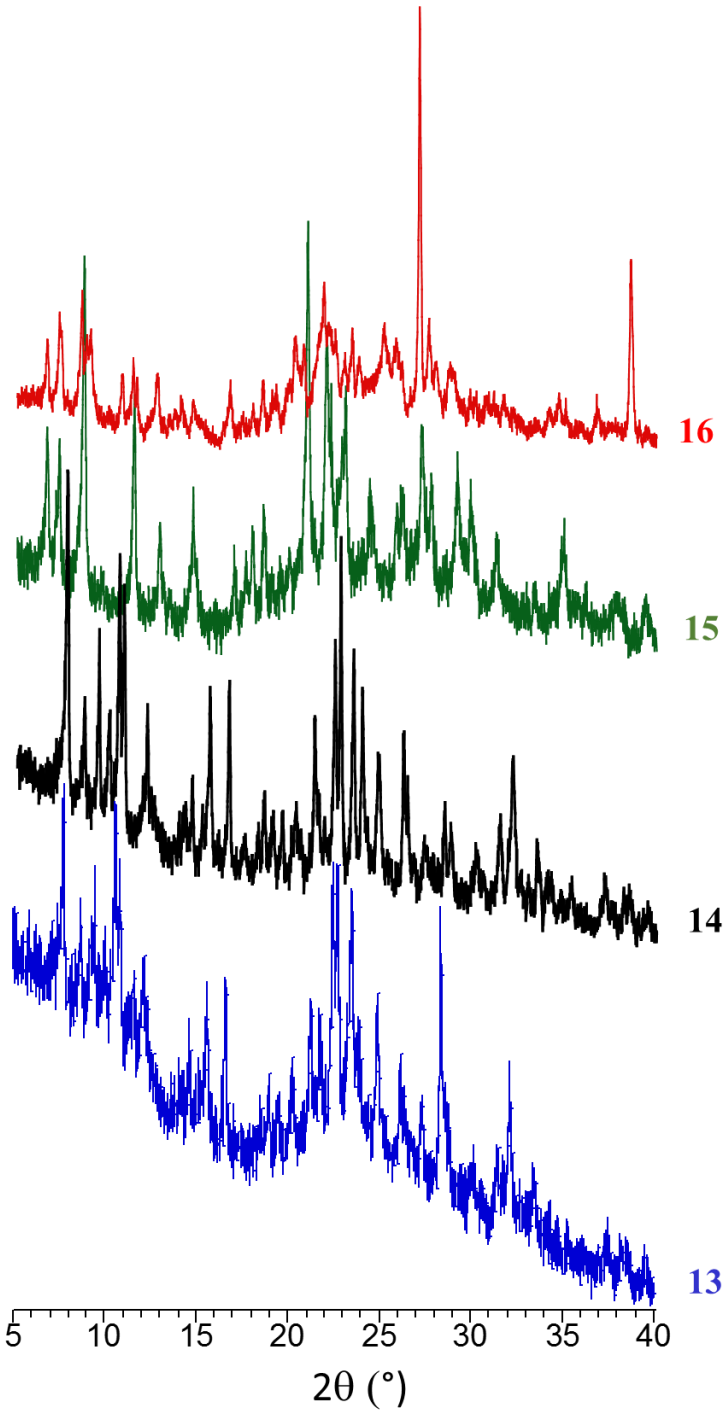

Figure 1.13. *Experimental X-ray powder diffractograms for phase VIII compounds: $K_3[Cr(C_6O_4Cl_2)_3]$ (**13**), $K_3[Fe(C_6O_4Cl_2)_3]$ (**14**), $K_3[Cr(C_6O_4Br_2)_3]$ and (**15**) $K_3[Fe(C_6O_4Br_2)_3]$ (**16**).*

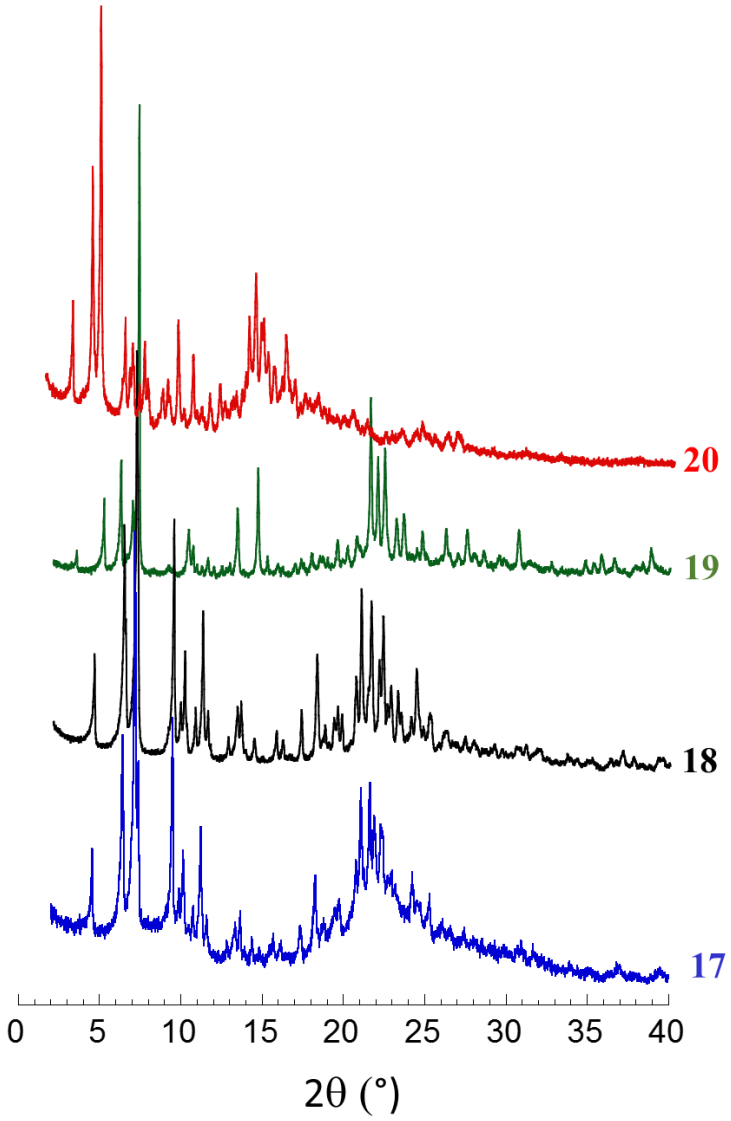

Figure 1.14. *Experimental X-ray powder diffractograms for phase IX compounds:* $[NBu_4]_3[Cr(C_6O_4Cl_2)_3]$ (***17***), $[NBu_4]_3[Fe(C_6O_4Cl_2)_3]$ (***18***), $[NBu_4]_3$ $[Cr(C_6O_4Br_2)_3]$ (***19***) *and* $[NBu_4]_3$ $[Fe(C_6O_4Br_2)_3]$ (***20***).

3.5. Magnetic Properties

We have only measured the magnetic properties of the Cr(III) and Fe(III) compounds, since Ga(III) is diamagnetic. The plots of $\chi_m T$ *vs.* T (χ_m is the molar magnetic susceptibility per M(III) ion) are very similar in all cases, showing a constant value of ca. 1.8-1.9 cm^3 K mol^{-1} for the Cr(III) compounds and ca. 4.5-4.8 cm^3 K mol^{-1} for the Fe(III) derivatives. These values are close to the expected ones for non-interacting S = 3/2 for Cr(III) and S = 5/2 for Fe(III) ions (1.875 and 4.375 cm^3 K mol^{-1}, respectively) (Figures 1.15 and 1.16 for the Cr(III) and Fe(III) compounds).

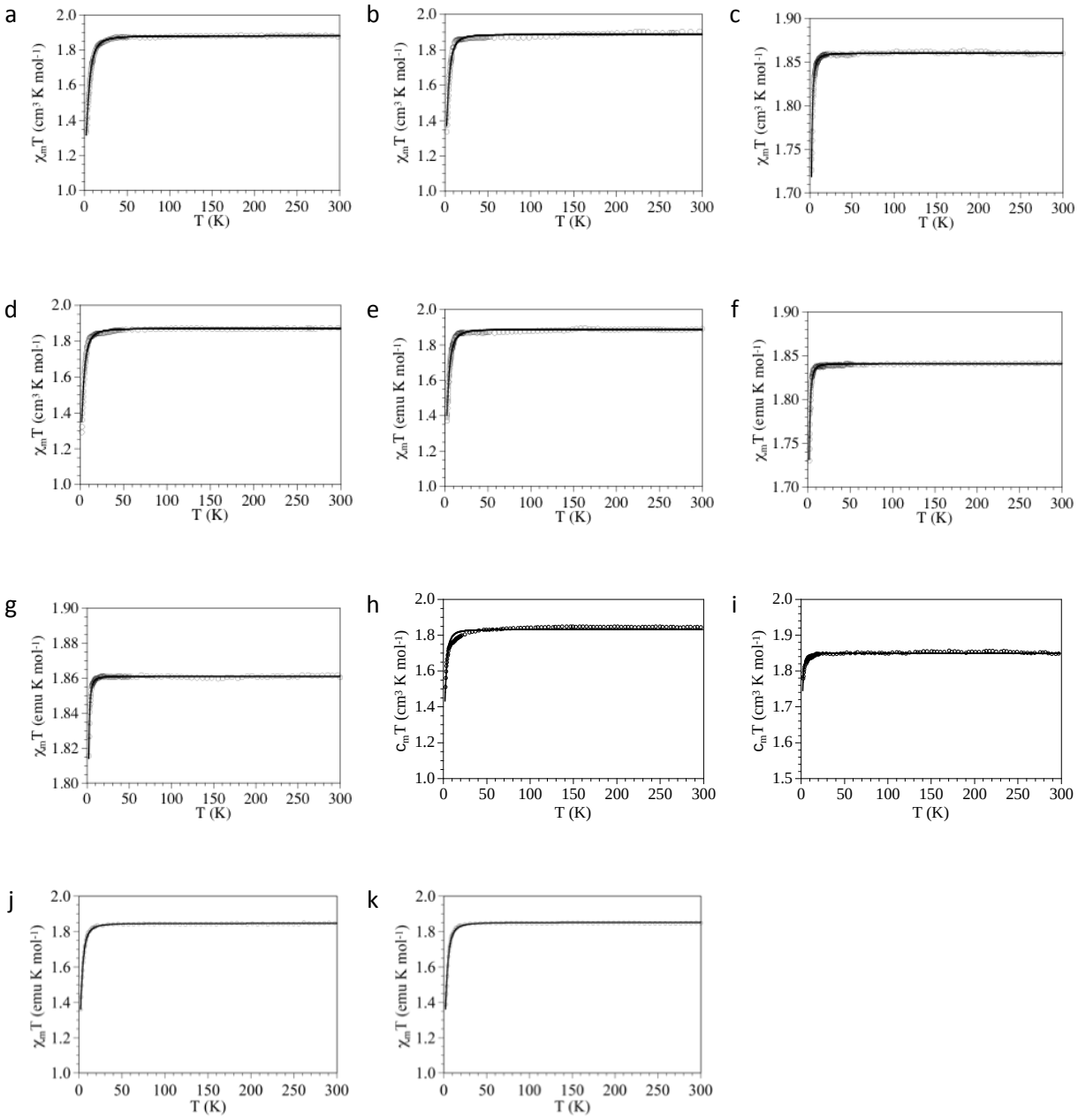

Figure 1.15. *Thermal variation of the $\chi_m T$ product for all the Cr(III) compounds:* ***(a)*** *$(PPh_3Et)_3[Cr(C_6O_4Cl_2)_3]$ (**1**);* ***(b)*** *$(PPh_3Et)_3[Cr(C_6O_4Br_2)_3]$ (**2**);* ***(c)*** *$(PPh_3Pr)_3[Cr(C_6O_4Cl_2)_3]$ (**5**);* ***(d)*** *$(PPh_3Pr)_3[Cr(C_6O_4Br_2)_3]$ (**6**);* ***(e)*** *$(PBu_4)_3[Cr(C_6O_4(NO_2)_2)_3]$ (**8**);* ***(f)*** *$(Nhet_4)_3[Cr(C_6O_4Cl_2)_3]$ (**10**);* ***(g)*** *$(Nhep_4)_3[Cr(C_6O_4Br_2)_3]$ (**11**);* ***(h)*** *$K_3[Cr(C_6O_4Cl_2)_3]$ (**13**);* ***(i)*** *$K_3[Cr(C_6O_4Br_2)_3]$ (**15**)* ***(j)*** *$(NBu_4)_3[Cr(C_6O_4Cl_2)_3]$ (**17**) and* ***(k)*** *$(NBu_4)_3[Cr(C_6O_4Br_2)_3]$ (**19**). Solid lines are the best fit to the isolated monomer model with zero field splitting (see table 1.6).*

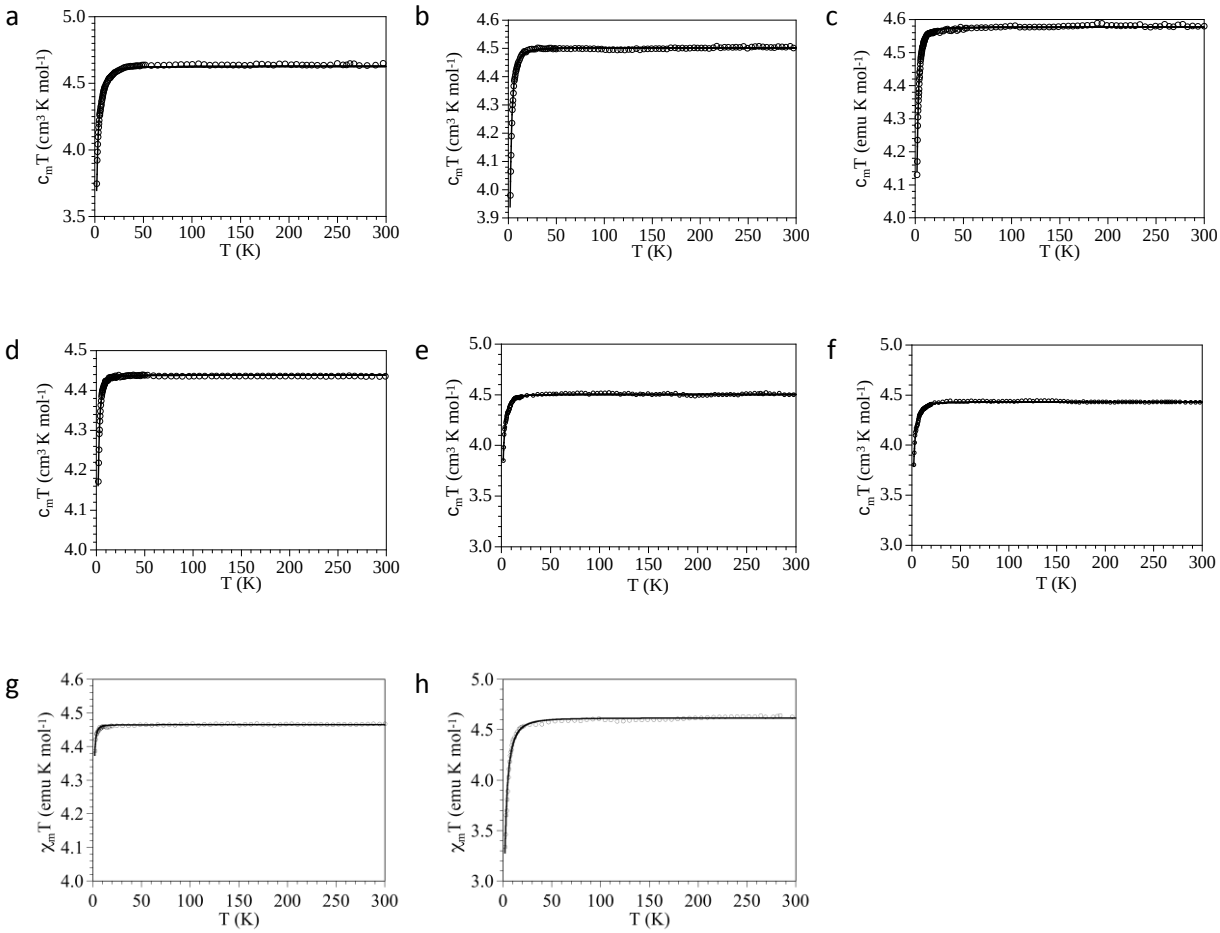

Figure 1.16. *Thermal variation of the χ_mT product for all the Fe(III) compounds:* ***(a)*** *$(PPh_3Et)_3[Fe(C_6O_4(NO_2)_2)_3]$ (**4**);* ***(b)*** *$(PPh_3Pr)_3[Fe(C_6O_4(NO_2)_2)_3]$ (**7**);* ***(c)*** *$(PBu_4)_3[Fe(C_6O_4(NO_2)_2)_3]$ (**9**);* ***(d)*** *$(PPh_4)_3[Fe(C_6O_4(NO_2)_2)_3]$ (**12**);* ***(e)*** *$K_3[Fe(C_6O_4Cl_2)_3]$ (**14**);* ***(f)*** *$K_3[Fe(C_6O_4Br_2)_3]$ (**16**);* ***(g)*** *$(NBu_4)_3[Fe(C_6O_4Cl_2)_3]$ (**18**) and* ***(h)*** *$(NBu_4)_3[Fe(C_6O_4Br_2)_3]$ (**20**). Solid lines are the best fit to the isolated monomer model with zero field splitting (see table 1.6).*

On cooling the samples χ_mT remains constant in all cases down to *ca*. 5-10 K and shows a quite abrupt decrease at very low temperatures. This behaviour indicates that all the compounds are paramagnets with zero field splitting (ZFS) of the S = 3/2 or S = 5/2 ground spin state as indicated by the sharp decrease at very low temperatures. Accordingly, the magnetic properties of all the compounds are fitted to a simple model for S = 3/2 or S = 5/2 monomer with a ZFS.[20] This simple model reproduces very satisfactorily the magnetic data of all the compounds with the g and |D| values reported in Table 1.6. In all cases, the |D| values are low and within the normal range observed for isolated octahedral Cr(III) and Fe(III) complexes.[21] It has to be noted that the sing of D cannot be determined from powder magnetic

susceptibility measurements and that these D values could include a very weak intermolecular interaction.

***Table 1.6**. Magnetic parameters of all the Cr and Fe-containing compounds.*

Compound	Formula	S	g	|D| (cm-1)
1	$[PPh_3Et]_3[Cr(C_6O_4Cl_2)_3]$	3/2	2.003	5.5
2	$[PPh_3Et]_3[Cr(C_6O_4Br_2)_3]$	3/2	2.006	4.4
4	$[PPh_3Et]_3[Fe(C_6O_4(NO_2)_2)_3]$	5/2	2.057	2.2
5	$[PPh_3Pr]_3[Cr(C_6O_4Cl_2)_3]$	3/2	1.992	1.2
6	$[PPh_3Pr]_3[Cr(C_6O_4Br_2)_3]$	3/2	1.998	4.5
7	$[PPh_3Pr]_3[Fe(C_6O_4(NO_2)_2)_3]$	5/2	2.029	1.4
8	$[PBu_4]_3[Cr(C_6O_4(NO_2)_2)_3]$	3/2	2.007	4.3
9	$[PBu_4]_3[Fe(C_6O_4(NO_2)_2)_3]$	5/2	2.046	1.1
10	$[Nhet_4]_3[Cr(C_6O_4Cl_2)_3]$	3/2	1.982	1.0
11	$[NHep_4]_3[Cr(C_6O_4Br_2)_3]$	3/2	1.993	0.6
12	$[PPh_4]_3[Fe(C_6O_4(NO_2)_2)_3]$	5/2	2.014	0.8
13	$K_3[Cr(C_6O_4Cl_2)_3]$	3/2	1.977	3.0
14	$K_3[Fe(C_6O_4Cl_2)_3]$	5/2	2.029	1.6
15	$K_3[Cr(C_6O_4Br_2)_3]$	3/2	1.986	1.0
16	$K_3[Fe(C_6O_4Br_2)_3]$	5/2	2.013	1.6
17	$[NBu_4]_3[Cr(C_6O_4Cl_2)_3]$	3/2	1.984	4.0
18	$[NBu_4]_3[Fe(C_6O_4Cl_2)_3]$	5/2	2.020	0.4
19	$[NBu_4]_3[Cr(C_6O_4Br_2)_3]$	3/2	1.987	4.0
20	$[NBu_4]_3[Fe(C_6O_4Br_2)_3]$	5/2	2.054	3.7

4. Conclusions and perspectives

Up to 20 new compounds with general formula $A_3[M(C_6O_4X_2)_3]$ have been synthesized following a one-pot reaction between a M^{III} salt M^{III} = Cr, Fe and Ga) and three different anilato-derivative ligands $[C_6O_4X_2]^{2-}$ (X = Cl, Br and NO_2). Different A^+ cations were used (A = K^+, $[PPh_3Et]^+$, $[PPh_3Pr]^+$, $[PBu_4]^+$, $[NBu_4]^+$, $[NHep_4]^+$ and $[PPh_4]^+$) to study how the differences in the shape and size of the cation affect the structure of the corresponding salts. We have demonstrated the key role played by the cation. Thus, phase I compounds, containing the $[PPh_3Et]^+$ cation, crystallize in the chiral and polar *R*3 space group; phase II compounds, containing the $[PPh_3Pr]^+$ cation, crystallize in the non chiral but polar *P*2*cb* space group and finally, phase III compounds, containing the non planar $[C_6O_4(NO_2)_2]^{2-}$ ligand and a cation without aromatic rings, crystallize in the centrosymmetric so neither chiral nor polar, triclinic

P-1 space group. This evolution from chiral and polar (phase I) to non chiral but polar (phase II) and to centrosymmetric (neither chiral nor polar (phase III) is due to a loss of π–π interactions from six (phase I) to four (phase II) and finally zero (phase III). This absence of π-π interactions is also expected in all the other phases with non-aromatic cations. We have observed that this key role of the cation is due to the formation of π–π interactions and the number of these interactions mainly depends on the cation (except for X = NO_2, where the lack of planarity also plays an important role in the final geometry since it precludes the formation of close π-π interactions).

The crystallization of the chiral phase I compounds is an unexpected and unprecedented result in this tris(anilato)metalate complexes and has been attributed to the presence of six π–π interactions established between the anilato rings of the anion and the phenyl rings of the cation. In contrast, the use of other bulky cations or the change of X in the ligands from Cl or Br to NO_2, led to achiral compounds where the number of close π–π interactions is reduced from six to four and zero.

When the cation has aromatic rings, but X = NO_2, the structure is not chiral, probably because of the previously commented lack of planarity. Thus, although we do not have structural data for any salt with X = NO_2 and cations with aromatic rings, we can expect the formation of achiral crystals since the twisting of the NO2 groups preclude the formation of close π-π interactions.

Even though the important role that may play the π–π cation-anion interactions in the final observed structure was already well known, the compounds here presented have shown the capacity of these interactions to form chiral or achiral crystals even when using a racemic mixture of anions and cations. We have used this large series of compounds as precursors in the synthesis of different families of hetero-metallic extended networks with magnetic ordering and other interesting properties that will be presented in the following chapters.

It is well known that the size and structure of the cation also affects the solubility of the final salts. This is why we have decided to prepare the series of compounds $K_3[M^{III}(C_6O_4X_2)_3]$, which are the only water soluble tris(anilato)metallate salts. This solubility can be used to prepare the corresponding Ag^+ salts by methatesis reaction

with $Ag(NO_3)$, a very useful strategy already used to prepare many oxalato-based 2D multifunctional magnets.[22, 23]

5. References

(1) Spengler, R.; Lange, J.; Zimmermann, H.; Burzlaff, H.; Veltsistas, P. G.; Karayannis, M. I. Structure of $C_{36}H_{52}Cl_6InN_3O_{14}$. *Acta Cryst. B* **1995***, 51*, 174-177.

(2) Min, K. S.; Rhinegold, A. L.; Miller, J. S. tris(chloranilato)ferrate(III) Anionic Building Block Containing the (dihydroxo)oxodiiron(III) Dimer Cation: Synthesis and Characterization of $[(TPA)(OH)Fe^{III}OFe^{III}(OH)(TPA)][Fe(CA)_3]_{0.5}(BF_4)_{0.5}\cdot 1.5MeOH\cdot H_2O$ [TPA = tris(2-pyridylmethyl)amine; CA = Chloranilate]. *J. Am. Chem. Soc.* **2006***, 128*, 40-41.

(3) Atzori, M.; Artizzu, F.; Sessini, E.; Marchio, L.; Loche, D.; Serpe, A.; Deplano, P.; Concas, G.; Pop, F.; Avarvari, N.; Mercuri, M. L. Halogen-Bonding in a New Family of Tris(Haloanilato)Metallate(III) Magnetic Molecular Building Blocks. *Dalton Trans.* **2014***, 43*, 7006-7019.

(4) Atzori, M.; Pop, F.; Auban-Senzier, P.; Gómez-García, C. J.; Canadell, E.; Artizzu, F.; Serpe, A.; Deplano, P.; Avarvari, N.; Mercuri, M. L. Structural Diversity and Physical Properties of Paramagnetic Molecular Conductors Based on bis(ethylenedithio)tetrathiafulvalene (BEDT-TTF) and the tris(chloranilato)ferrate(III) Complex. *Inorg. Chem.* **2014***, 53*, 7028-7039.

(5) Benmansour, S.; Coronado, E.; Giménez-Saiz, C.; Gómez-García, C. J.; Rößer, C. Metallic Charge-Transfer Salts of Bis(Ethylenedithio)Tetrathiafulvalene with Paramagnetic Tetrachloro(Oxalato)Rhenate(IV) and Tris(Chloranilato)Ferrate(III) Anions. *Eur. J. Inorg. Chem* **2014***, 2014*, 3949-3959.

(6) Benmansour, S.; Gómez-Claramunt, P.; Vallés-García, C.; Mínguez Espallargas, G.; Gómez García, C. J. Key Role of the Cation in the Crystallization of Chiral Tris(Anilato)Metalate Magnetic Anions. *Cryst. Growth Des.* **2016***, 16*, 518-526.

(7) Bailar, J. C.; Jones, E. M.; Booth, H. S.; Grennert, M. Trioxalato Salts (Trioxalatoaluminiate, -Ferriate, -Chromiate, and -Cobaltiate). **1939**, 35-38.

(8) Che, C. M.; Kwong, S. S.; Poon, C. K.; Lai, T. F.; Mak, T. C. W. Cis Ruthenium Complexes of 1,4,8,11-tetraazacyclotetradecane (cyclam): Crystal and Molecular Structure of Cis-$[Ru(Cyclam)Cl_2]Cl$. *Inorg. Chem.* **1985***, 24*, 1359-1363.

(9) Mukherjee, P.; Drew, M. G. B.; Gómez-García, C. J.; Ghosh, A. The Crucial Role of Polyatomic Anions in Molecular Architecture: Structural and Magnetic Versatility of Five Nickel(II) Complexes Derived from A N,N,O-Donor Schiff Base Ligand. *Inorg. Chem.* **2009***, 48*, 5848-5860.

(10) Huang, Y.; Gao, H.; Twamley, B.; Shreeve, J. Highly Dense Nitranilates-Containing Nitrogen-Rich Cations. *J. Chem. - Eur. J.* **2009***, 15*, 917-923.

(11) Atzori, M.; Benmansour, S.; Mínguez Espallargas, G.; Clemente-León, M.; Abhervé, A.; Gómez-Claramunt, P.; Coronado, E.; Artizzu, F.; Sessini, E.; Deplano, P.; Serpe, A.; Mercuri, M. L.; Gómez García, C. J. A Family of Layered Chiral Porous Magnets Exhibiting Tunable Ordering Temperatures. *Inorg. Chem.* **2013***, 52*, 10031-10040.

(12) Bain, G. A.; Berry, J. F. Diamagnetic Corrections and Pascal's Constants. *J. Chem. Educ.* **2008***, 85*, 532-536.

(13) Altomare, A.; Burla, M. C.; Camalli, M.; Cascarano, G. L.; Giacovazzo, C.; Guagliardi, A.; Moliterni, A. G. G.; Polidori, G.; Spagna, R. SIR97: A New Tool for Crystal Structure Determination and Refinement. *J. Appl. Cryst.* **1999***, 32*, 115-119.

(14) Sheldrick, G. M. Crystal Structure Refinement with SHELXL. *Acta Cryst. C* **2015***, 71*, 3-8.

(15) Farrugia, L. J. WinGX Suite for Small-Molecule Single-Crystal Crystallography. *J. Appl. Cryst.* **1999***, 32*, 837-838.

(16) Pawlukojc, A.; Bator, G.; Sobczyk, L.; Grech, E.; Nowicka-Scheibe, J. Inelastic Neutron Scattering, Raman, Infrared and DFT Theoretical Studies on Chloranilic Acid. *J. Phys. Org. Chem.* **2003***, 16*, 709-714.

(17) Atzori, M.; Artizzu, F.; Marchio, L.; Loche, D.; Caneschi, A.; Serpe, A.; Deplano, P.; Avarvari, N.; Mercuri, M. L. Switching-on Luminescence in Anilate-Based Molecular Materials. *Dalton Trans.* **2015***, 44*, 15786-15802.

(18) Dance, I.; Scudder, M. The Sextuple Phenyl Embrace, a Ubiquitous Concerted Supramolecular Motif. *J. Chem. Soc. , Chem. Commun.* **1995**, 1039-1040.

(19) Russell, V. M.; Craig, D. C.; Scudder, M. L.; Dance, I. G. Interpenetrating Non-Molecular and Supramolecular (10,3)-a Nets Occurring with Chiral Recognition in Crystalline $(Ph_3MeP)_2[NaCr(Ox)_3]$. *CrystEngComm* **2000***, 2*, 16-23.

(20) O'Connor, C. J. In *Research Frontiers in Magnetochemistry;* 1993; .

(21) Boca, R. Zero-Field Splitting in Metal Complexes. *Coord. Chem. Rev.* **2004***, 248*, 757-815.

(22) Clemente-Leon, M.; Coronado, E.; Dias, J. C.; Soriano-Portillo, A.; Willett, R. D. Synthesis, Structure, and Magnetic Properties of [(S)-$[PhCH(CH_3)N(CH_3)_3]][Mn(CH_3CN)_{2/3}Cr(Ox)_3].(CH_3CN)$.(Solvate), a 2D Chiral Magnet Containing a Quaternary Ammonium Chiral Cation. *Inorg. Chem.* **2008***, 47*, 6458-6463.

(23) Clemente-Leon, M.; Coronado, E.; Gómez-García, C. J.; Soriano-Portillo, A. Increasing the Ordering Temperatures in Oxalate-Based 3D Chiral Magnets: The Series $[Ir(ppy)_2(bpy)][M(II)M(III)(ox)_3]\cdot 0.5H_2O$ (M(II)M(III) = MnCr, FeCr, CoCr, NiCr, ZnCr, MnFe, FeFe); bpy = 2,2'-bipyridine; ppy = 2-phenylpyridine; ox = Oxalate Dianion). *Inorg. Chem.* **2006***, 45*, 5653-5660.

Chapter 2

2D/3D heterometallic networks with M^{III}/M^{I}

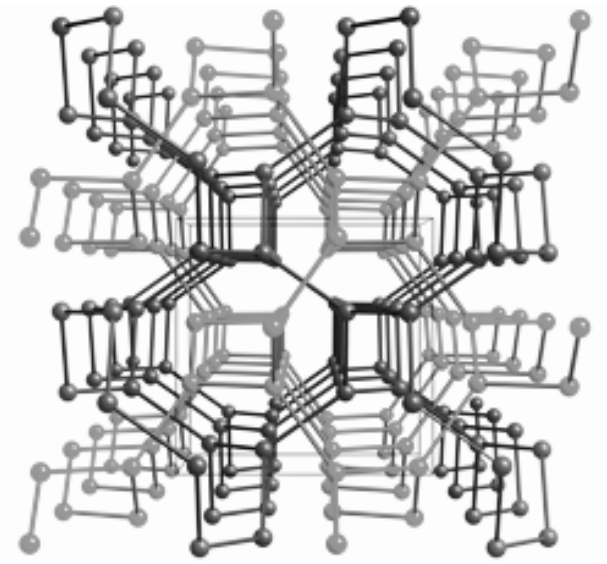

1. Introduction

The logical design of synthetic methods for the preparation of molecular materials (crystal engineering) is the key to obtain many materials based on the proper choice of the molecular precursors (building blocks) connected, mainly, by hydrogen and coordination bonding. The materials presented in this chapter have been prepared by using the most common building blocks in coordination chemistry, magnetic d-block metal ions and anionic ligands. These kind of ligands have been chosen due to their singular and precise abilities: (i) to act as bridges providing extended polynuclear complexes and (ii) to magnetically couple the metal ions they coordinate. Among the many anionic ligands used in coordination chemistry, oxalato is one of the most used one in the last two decades. Its use took off with the report made by Okawa et al.[1] in 1992 of a family of 2D oxalate-based honeycomb lattices formulated as $[NBu_4][M^{II}M^{III}(C_2O_4)_3]$ where M^{II} = Mn, Fe, Co, Ni and Cu and M^{III} = Cr and Fe. This family shows long range ferro and ferrimagnetic orderings at temperatures in the range of 6-48 K[1, 2] and present the same honeycomb layered structure already known for some M(III)/M(I) combinations.[3-8] After the report of the 2D oxalato-based M(III)M(II) many groups started to look for the 3D homochiral M(III)/M(II) lattice that was also known for some M(III)/M(I) combinations.[9, 10] This M(III)/M(II) 3D lattice was reported in 2000 and showed also magnetic order although at lower temperatures than the corresponding 2D lattices.[11] Since oxalate and anilate have the same bis-bidentate coordination modes, it is straightforward to think that it may be possible to prepare heterometalic 2D and 3D M(III)/M(I) lattices. The preparation of these two M(III)/M(I) lattices will further confirm the parallelism in the coordination chemistries of anilato and oxalato to build multifunctional materials, as previously done with the oxalate, but with different advantages since the anilato ligands can be easily modified and given that their large sizes, originate porous structures in some cases.[12]

In this chapter we present the first examples of both types of M(III)/M(I) lattices: $(NBu_3Me)_2[NaCr(C_6O_4Br_2)_3]$ (**21)**, which shows hexagonal 2D honeycomb lattices similar to those obtained for the M(III)/M(II) series[12] and $(NBu_3Me)_2[NaCr(C_6O_4Br_2)_3]$ (**22**) that shows a double interpenetrated chiral 3D-(10,3) lattice with opposite chiralities, resulting in achiral crystals. This double interpenetrated 3D lattice was already known in homometalic anilato-based compounds[13] but had never been

observed in oxalato-based compounds nor in heterometallic anilato-based compounds. Compounds **21** and **22** are polymorphs that were obtained in the same synthesis. Although we could not obtain good quality single crystals of compound **21**, we could verify with powder X-ray diffraction that this compound is isostructural to two other compounds prepared in our group: $[PBu_3Me]_2[NaCr(C_6O_4Br_2)_3]$ (**A**) and $[PPh_3Et]_2[KFe(C_6O_4Br_2)_3]\cdot 2DMF$ (**B**). Here we will describe the structure of compound **A** since it is isostructural to **21** (the only difference is the change of P by N in the cation). We will also present the structure of the 3D compound **22**. To the best of our knowledge, compounds **21** and **22** constitute the first example of a 2D/3D polymorphism in the anilato families. Note that this polymorphism has never been observed in the oxalate family.This fact shows the larger versatility of the anilato-type ligands compared to the oxalate one.

2. Experimental Section

2.1. Synthesis

General Remarks: N,N-Dimethylformamide (DMF), tributylmethylammoiun chloride $[PBu_3Me]Cl$, NaOH, bromanilic acid ($H_2C_6O_4Br_2$) and $CrCl_3\cdot 6H_2O$ are commercially available and were used as received without further purification.

The synthesis of the heterometallic $M^{III}M^{I}$ networks compounds has been done following the same synthetic method,[14] a one pot reaction between $CrCl_3$ with a solution containing the bulky cation NBu_3Me^+ and the deprotonated bromanilate dianion (simply obtained by adding two equivalents of NaOH the a bromanilic solution). The monovalent cation (Na^+) is also provided by the NaOH used to deprotonate de bromanilic acid.

Synthesis of $(NBu_3Me)_2[NaCr(C_6O_4Br_2)_3]$ (21 and **22).** A solution of $CrCl_3\cdot 6H_2O$ (213 mg, 0.8 mmol) in H_2O (5 mL) was added drop-wise to an aqueous solution (50 mL) containing $H_2C_6O_4Br_2$ (715 mg 2.4 mmol), NaOH (192 mg, 4.8 mmol) and $(NBu_3Me)Cl$ (566 mg, 2.4 mmol). This solution was heated at 60 °C for 30 minutes and then cooled to room temperature resulting in the formation of a violet precipitate. The solvent was removed by rotary evaporation and the resulting dark violet solid was stirred in 50 mL of absolute EtOH during 24 hours and then filtered. The solid obtained (i.e., the fraction non soluble in EtOH) was dissolved in DMF. After slow evaporation

of the solvent, purple prismatic single crystals of compound **22** (minor phase) were obtained mixed with a burgundy crystalline powder (major phase, compound **21**). For **22** the elemental ratio estimated by electron probe microanalysis (EPMA): Br/Cr/Na = 6.0/1.2/1.0 agrees with the calculated one (6/1/1) from the proposed formula. The powder X-ray diffractogram of the major phase (**21**) strongly suggests that it has the same 2D structure that compounds **A** and **B** (see next pages). *Elemental Anal.* Calc. for **21**: $C_{44}H_{60}Br_6O_{12}N_2CrNa$ (M_w = 1363.39): C, 38.76 %; H, 4.44 %; N, 2.06 %; Found: C, 38.87 %; H, 4.21 %; N 2.68 %. For **21** the elemental ratio estimated by electron probe microanalysis (EPMA): Br/Cr/Na = 6.0/1.2/1.0 agrees with the calculated one (6/1/1) from the proposed formula.

2.2. Physical Properties

The FT-IR spectrum of compound **21** was performed on a KBr pellet and collected with a Nexus-Nicolet 5700 spectrophotometer. C, H, N analysis of compound **21** was performed with a CE instrument EA 1110 CHNS analyser.

Magnetic measurements were performed with a Quantum Design MPMS-XL-5 SQUID magnetometer in the temperature range of 2 to 300 K with an applied magnetic field of 0.1 T on a polycrystalline sample of compound **21**. Isothermal magnetization measurements were performed on the same sample at 2 K with magnetic fields up to 5 T. Susceptibility data were corrected for the sample holder and for the diamagnetic contribution of the salts using Pascal's constants.[15]

For compound **22** we could only obtain a few single crystals and, therefore, we could only perform the single crystal X-ray structure analysis.

2.3. Structural Characterization

A suitable single crystal of compound **22** was mounted on a loop using a viscous hydrocarbon oil and then transferred directly to the cold nitrogen stream for data collection. X-ray data were collected at 120 K on a Supernova diffractometer equipped with a graphite-monochromated Enhance (Mo) X-ray Source (λ = 0.71073 Å). The program CrysAlisPro, Agilent Technologies Ltd., was used for unit cell determinations and data reduction. Empirical absorption correction was performed using spherical

harmonics, implemented in the SCALE3 ABSPACK scaling algorithm. The crystal structure was solved by direct methods with the SIR92 program[16] and refined against all F^2 values with the SHELXL-2014 program[17], using the WinGX2014.1 graphical user interface.[18] All non-hydrogen atoms were refined anisotropically and hydrogen atoms were placed in calculated positions and refined isotropically with a riding model. Data collection and refinement parameters are given in Table 2.2.

The X-ray powder diffractogram was collected for a polycrystalline sample of compound **21** using a 0.5 mm glass capillary that was mounted and aligned on a Empyrean PANalytical powder diffractometer, using CuKα radiation (λ = 1.54177 Å) operating at 40 mA and 45 kV. A total of 3 scans were collected at room temperature in the 2θ range of 2-40º in spinning mode with a step size of 0.0131º.

3. Results and Discussion

3.1. Infrared Spectroscopy

Compound **21**, besides the bands in the 2800-3000 cm^{-1} region, associated with the ν(C-H) vibrations of the alkyl chains of the cations, shows a weak to medium band in the region at *ca*. 1640 cm^{-1} corresponding to the ν (C=O) vibration mode of the C=O groups weakly coordinated to the Na^+ ions (Figure 2.1).[1] Additionally, compounds **21** shows a very intense band at ca. 1520 cm^{-1} corresponding to the ν(C=C) and ν(C-O) vibrational modes as well as a strong band at ca. 1350 cm^{-1} attributed to the ν(C-C) and ν(C-O) modes. Finally, in the low energy region compound **21** shows medium bands at *ca*. 1000, 830 and 600 cm^{-1} corresponding to diverse C=O, C-O, C-C and C-X vibrational modes (Table 2.1).

Table 2.1: *Selected vibrational frequencies (cm^{-1}) and assignments for compounds **A**, **B** (for comparison purposes) and **21**.*

Compound	M^{III}	X	ν(C=O)	ν(C=C) ν(C-O)	ν(C-C) ν(C-O)	ν(C-C) ν(C-O) δ(C-X)	δ(C-O) δ(C=O) ν(C-X)	ρ(C-X)
A	Cr	Br	1644	1521	1346	985	809	603
B	Fe	Cl	1641	1525	1348	997	839	573
21	Cr	Br	1642	1522	1348	986	810	604

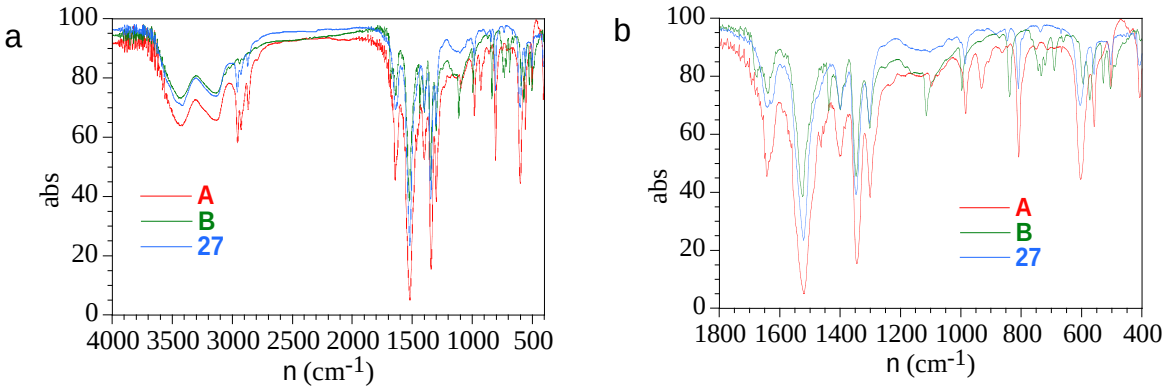

Figure 2.1*: FT-IR Spectra for compounds **A**, **B** (for comparison purposes) and **21** in the **(a)** 4000-400 cm^{-1} and **(b)** 1800-400 cm^{-1} regions.*

3.2. X-Ray Diffraction

Table 2.2: *Crystallographic data for compound* **22**.

Compound	**22**
Empirical formula	$C_{44}H_{60}Br_6O_{12}N_2CrNa$
Formula weight	1363.39
Crystal colour	purple
Crystal size	0.17 x 0.14 x 0.07
Temperature (K)	120(2)
Wavelength (Å)	0.71073
Crystal system	Cubic
Z	*8*
Space group	*I*-43*d*
a (Å)	22.4250(9)
b (Å)	22.4250(9)
c (Å)	22.4250(9)
α (°)	90
ß (°)	90
γ (°)	90
V (Å^3)	11277.1(8)
ρ_{calc} (Mg/m^3)	1.606
μ($Mo_{K\alpha}$) (mm^{-1})	4.517
θ range (°)	2.87–25.09
Reflns collected	148006
Independent reflns (R_{int})	1679(0.1582)
Reflns used in refinement, *n*	1679
L. S. parameters, *p*/ restraints, *r*	103/0
$R1(F)$,[a] $I > 2\sigma(I)$	0.0633
$wR2(F^2)$, [b]all data	0.1729
$S(F^2)$,[c] all data	1.123

[a]$R_1(F) = \Sigma||F_o|-|F_c||/\Sigma|F_o|$; [b]$wR_2(F^2) = [\Sigma w(F_o^2-F_c^2)^2/\Sigma wF_o^4]^{1/2}$;
[c]$S(F^2) = [\Sigma w(F_o^2-F_c^2)^2/(n+r-p)]^{1/2}$

Crystal structure of $[NBu_3Me]_2[NaCr(C_6O_4Br_2)_3]$ (21). This compound is isostructural to compounds $[PBu_3Me]_2[NaCr(C_6O_4Br_2)_3]$ (**A**) and $[PPh_3Et]_2[KFe(C_6O_4Cl_2)_3]\cdot 2DMF$ (**B**) prepared in our group. Therefore, here we will describe the structure of these compounds to show the structure of compound **21**. Compounds **A** and **B** present very similar crystal structures formed by cationic and anionic layers alternating along the [101] direction (Figure 2.2a). The anionic layer, formulated as $[M^IM^{III}(C_6O_4X_2)_3]^{2-}$ with $M^I/M^{III}/X$ = Na/Cr/Br (**A**) and K/Fe/Cl (**B**), shows the well-known honeycomb 2D structure where M^I and M^{III} ions are connected through $(C_6O_4X_2)^{2-}$ bridging ligands and occupy alternating vertices of the hexagons (Figure 2.2b). Each M^I ion is connected to three M^{III} ions through three anilato-type bridges

and vice versa. In both compounds the M^{I} and the M^{III} ions are perfectly located and do not present any disorder.

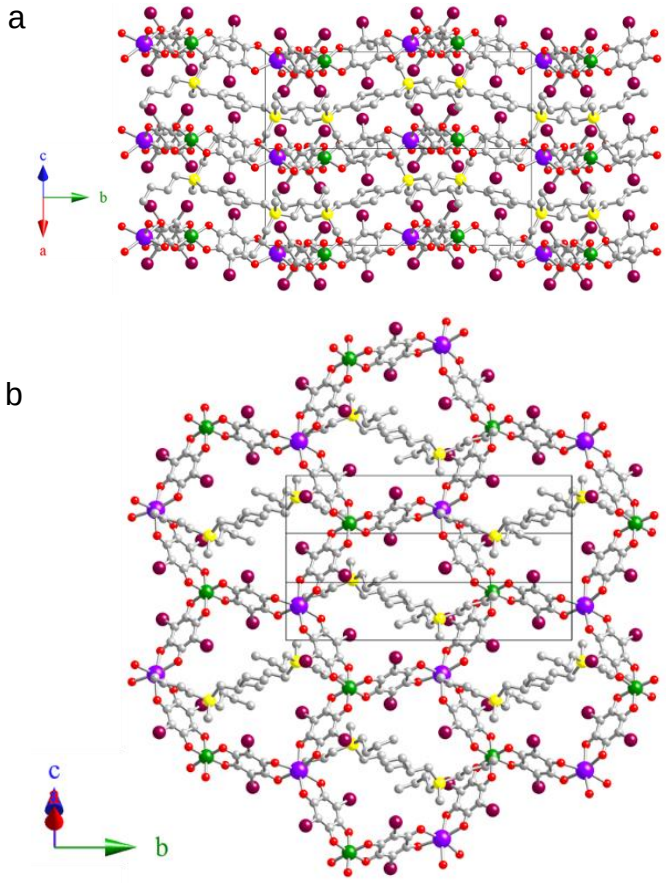

Figure 2.2: *Structure of compound **A** (similar to **B** and **21**) **(a)** View of the alternating anion/cation layers **(b)** View of the hexagonal honeycomb layer with the $(PBu_3Me)^+$ cations in the hexagons. Colour code: Cr = green, Na = violet, O = red, C = grey, Br = brown and P = yellow. H atoms have been omitted for clarity.*

The cationic layer contains bulky PBu_3Me^+ (**A**) or PPh_3Et^+ (**B**) cations located above and below the hexagons of the anionic layers. In both compounds, one of the larger groups of the cations (butyl group in **A**, phenyl group in **B**) are partially inserted inside the hexagons, whereas the remaining groups are located between the layers (Figure 2.2a). The phenyl ring inserted in the anionic layer in compound **B** presents π–π interactions with one anilato ring (interplanar distance of 3.299 Å, Figure 2.3a). Besides, in **B** there are two DMF molecules located inside the hexagons (Figure 2.3a).

This structure is very similar to the one observed in the closely related $[M^{II}M^{III}(C_6O_4X_2)_3]^-$ compounds.[12] However, there are some important differences: (i) in

the $M^{II}M^{III}$ layers with the cation $[(H_3O)(phz)_3]^+$ (phz = phenazine) the M^{II} ions have a water molecule connected (or close) to the M^{II} ion, (ii) the charge in the $M^{II}M^{III}$ layers is -1 per hexagon compared to -2 in compounds **A**, **B** and **21** and (iii) the layers are eclipsed when the cation is $[(H_3O)(phz)_3]^+$ whereas they are alternated in compounds **A**, **B** and **21** (Figure 2.3b). However, when the cation changes in the $[MnCr(C_6O_4X_2)_3]^-$ layers,[12] those layers could be also alternated. Some examples of $[MnCr(C_6O_4X_2)_3]^-$ alternated layers are the ones prepared with $(NBu_4)^+$ and with four spin crossover cations.[3,19]

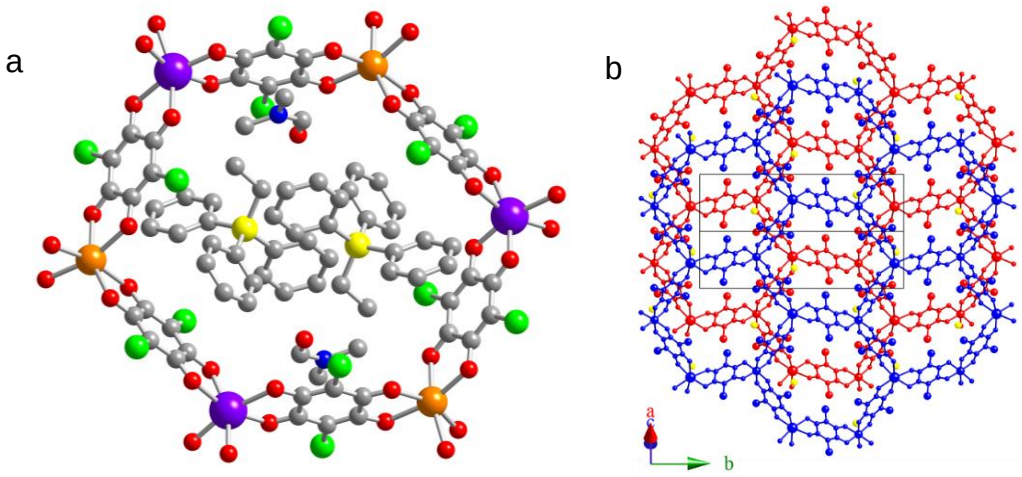

Figure 2.3: *Structure of compound **B** **(a)** View of the two dmf molecules and $(PPh_3Et)^+$ cations located in each hexagon showing the π–π interactions between the phenyl and the anilato rings (dotted lines). **(b)** View of two consecutive anionic layers in **B** showing the alternating disposition. Colour code in **(a)**: Fe = orange, K = violet, O = red, C = grey, Cl = green, N = blue and P = yellow. H atoms have been omitted for clarity.*

It is important to highlight tthat in the oxalato-based family, among the more than one hundred reported structures of the type $[MM'(C_2O_4)_3]^{n-}$, there are only five examples[3-6] of the type $[NaCr(C_2O_4)_3]^{2-}$, only one[7] of the type $[NaFe(C_2O_4)_3]^{2-}$ and one[8] of the type $[KFe(C_2O_4)_3]^{2-}$. In the five examples of $[NaCr(C_2O_4)_3]^{2-}$ layers the cations are either partially oxidized planar BEDT-$TTF^{+2/3}$ molecules (located perpendicular to the anionic layers)[3, 4, 7] or di-cations as $[Mg(H_2O)_6]^{2+}$,[5] $[Ni(cyclam)]^{2+}$ and $[Cu(tren)(H_2O)]^{2+}$.[6] The only reported examples of $[NaFe(C_2O_4)_3]^{2-}$ and $[KFe(C_2O_4)_3]^{2-}$ layers contains partially oxidized BEDT-$TTF^{+0.5}$ cations located perpendicular to the anionic layers.[7, 8] In none of these seven examples the cationic and anionic layers are interpenetrated as observed in **A** and **B**. The smaller size of the oxalato-based

hexagons (which are half the size of the anilato-based ones) may be the reason for this lack of interpenetration in the oxalato family in contrast with the anilato one.

Crystal structure of $(NBu_3Me)_2[NaCr(C_6O_4Br_2)_3]$ (22). This compound presents a 3D structure formed by two interlocked 3D (10,3) lattices (figure 2.4). Each lattice is formed by the union of $[Cr(C_6O_4Br_2)_3]^{3-}$ units with Na(I) and Cr(III) cations that alternate along the lattice and present the same chirality. Each Cr(III) ion is, therefore, connected to three different Na(I) ions by three bridging bromoanilate ligands and vice versa. In this way, each metal ion appears as tris-chelated with a D_3 local symmetry. Since all the metal centres present the same chirality, the structure is formed by non-planar 10 membered rings where each vertex is connected to three metals in a 3D (10,3) lattice. Although each of the two interpenetrated lattices is chiral, they present opposite chiralities giving rise to an achiral 3D structure based on chiral lattices. This structure is similar to the one recently reported for the homo-metallic compounds $[NBu_4]_2[M^{II}_2(dhbq)_3]$ (M^{II} = Mn, Fe, Ni, Co, Zn and Cd) (dhbq = $C_6O_4H_2^{2-}$) and $[NBu_4]_2[Mn_2(C_6O_4Cl_2)_3]$,[13] and to the 3D oxalato-based (10,3) lattices.[11, 20] The $(NBu_3Me)^+$ cations are located in the cavities formed by the two interpenetrated lattices (figure 2.4a) with a shortest N-N distance of 9.71 Å.

Interestingly, in compounds **A** and **22** the anionic lattices are isomeric $[NaCr(C_6O_4Br_2)_3]^{2-}$ and the cations are almost identical $(PBu_3Me)^+$ in **A** and $(NBu_3Me)^+$ in **22**. It is surprising that a simple change of a P by a N atom in the centre of the bulk cation may lead to such a drastic change in the structure. In order to elucidate and optimize the synthesis of the 2D and 3D lattices, it would be interesting to investigate the role played by the synthetic conditions and the bulky cations in the final structure. In fact, as already mentioned, **22** crystallizes with a major phase (**21**) that corresponds to the 2D structure observed in **A**, as deduced from powder X-ray data. This finding suggests that the 2D and 3D polymorphs are very close in energy, being the 2D phase slightly more stable and, therefore, the major one. In the analogous oxalate system, the 3D (10,3) structure is typically obtained with the use of chiral templating cations such as $[M(L)_3]^{n+}$ (L = bidentate ligand as bpy, ppy, phen,...).[11] In contrast, compound **22** gives rise to a double interpenetrated 3D (10,3) lattice even if the cation $(NBu_3Me)^+$ has no D_3 symmetry nor is chiral. Although very scarce, there are also some examples of oxalato-based (10,3) lattices prepared with achiral cations,[21-24] including the closely

related compound $(PPh_3Me)_2[NaCr(C_2O_4)_3]$.[20] Interestingly, this compound is the only 3D oxalato-based lattice with a monocation. It has the same cation than **A** and presents the same anionic lattice than **22** (although with oxalato instead of bromanilato).

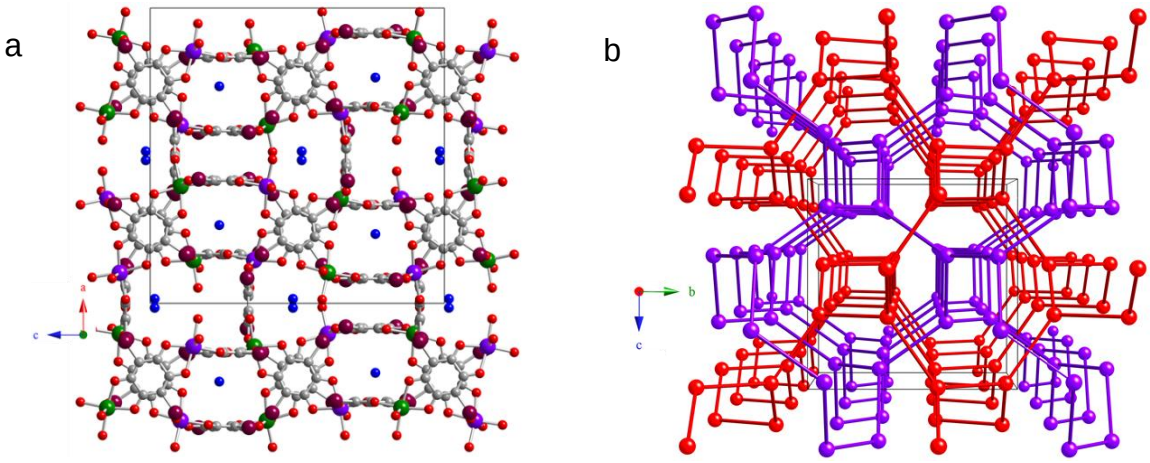

***Figure 2.4**. **(a)** View of the structure of compound **22** along the b direction. **(b)** Perspective view of the positions of the metal atoms in both interpenetrated sub-lattices (red and violet). Colour code in **(a)**: Cr = green, Na = violet, O = red, C = grey, Br = brown and N = blue. H and C atoms of the cations have been omitted for clarity.*

The M^{III}-O bond distances in the $[M^{III}(C_6O_4X_2)_3]^{3-}$ units in **A** and **B** (Table 3) are similar to those observed in the monomeric $[M^{III}(C_6O_4X_2)_3]^{3-}$ units reported and shown in chapter one.[25-27] Compound **22** shows a much longer average Cr-O bond distance (2.154 Å) than compound **A** (1.967 Å) because in compound **22** the M positions correspond to a 50/50 mixture of Cr and Na ions (and the Na-O bond distances are ca. 2.3 Å in **A**). The intra-ligand C-C and C-O bond lengths of the side of the anilato ligand coordinated to the M^{III} ions vary significantly when compared with the typical C-O and C-C values for terminal anilato ligands. Thus, the C-O bond distances increase from 1.20-1.25 Å, when the O atoms are terminal, to 1.26-1.30 Å in **A, B** and **22** (Table 2.3). The corresponding OC-CO bond distance decreases from 1.53-1.60 Å to 1.51-1.54 Å in the three compounds since it partially loses its single-bond character (Table 2.3). In contrast, the C-O and C-C bond distances of the side of the anilato ligand coordinated to the alkali ions do not show any important variation (the C-O bonds are in the range of 1.22-1.24 Å and the C-C bonds in the range of 1.55-1.57 Å) (Table 2.3). This fact agrees with the weaker coordination of the anilato ligand to the alkaline ions (as shown by the longer M^{I}-O bond distances of ca. 2.3 Å in compounds **A** and **B**)

***Table 2.3**. Bond lengths (Å) in the anilate ligands and around the M centres in **A, B** and **22**.*

Atoms	A (M = Cr)	B (M = Fe)	22 (M = Cr/Na)
M-O2	1.976(3)	2.058(3)	2.170(7)
M-O3	1.970(3)	2.087(3)	2.138(7)
M-O12	1.956(3)	2.050(3)	2.170(7)
M-O13	1.963(3)	2.080(4)	2.138(7)
M-O22	1.972(3)	2.019(4)	2.170(7)
M-O23	1.966(3)	2.030(4)	2.138(7)
C2-O2	1.283(5)	1.268(6)	1.256(10)
C3-O3	1.288(5)	1.284(5)	1.263(11)
C5-O5	1.223(5)	1.242(6)	1.256(10)
C6-O6	1.225(5)	1.224(5)	1.263(11)
C12-O12	1.300(5)	1.266(6)	1.256(10)
C13-O13	1.295(5)	1.287(6)	1.263(11)
C15-O15	1.230(5)	1.235(6)	1.256(10)
C16-O16	1.224(5)	1.236(5)	1.263(11)
C22-O22	1.289(5)	1.275(7)	1.256(10)
C23-O23	1.288(5)	1.294(6)	1.263(11)
C25-O25	1.216(5)	1.231(6)	1.256(10)
C26-O26	1.224(5)	1.250(6)	1.263(11)
C2-C3	1.514(6)	1.525(6)	1.572(12)
C5-C6	1.567(5)	1.562(6)	1.572(12)
C12-C13	1.527(6)	1.531(6)	1.572(12)
C15-C16	1.564(6)	1.548(6)	1.572(12)
C22-C23	1.517(6)	1.542(6)	1.572(12)
C25-C26	1.565(6)	1.565(7)	1.572(12)

3.2.1. Discussion of the structures

Compounds **A** and **B**, as well as compound **21** present very similar 2D structures. The honeycomb anionic layered distribution is well known in anilato M(III)/M(II) heterometallic compounds.[12] Albeit, there are some important differences between the M(III)/M(II) and the M(III)/M(I) structures. The first one is the disposition of the layers: The M(III)/M(II) and M(II)/M(II) compounds with the $[(H_3O)(phz)_3]^+$ cation present all eclipsed layers[12] whereas in compounds **A**, **B** and **21** the layers are alternated.[19]

One of the most remarkable facts in the compounds here presented is the obtaining of both, 2D and 3D structures, in the same synthesis (**21** and **22**) for the first time. Furthermore, although the 3D interlocked lattice structure was already known with the oxalato ligand,[9, 10] this is the first time that it is observed in an heterometallic anilato-based network.

3.3. X-Ray Powder Diffraction

Compound **21**, (the major phase in the synthesis of **22**) was analyzed with the XRPD technique to check the purity of thephase in the sample by comparing with the simulated diffractogram from the solved structure (compound **A**). The unit cell parameters obtained in the Pawley refinements (performed by Guillermo Minguez) are displayed in Table 2.4 and give the following results: for compound **A**: a = 10.0477 Å, b = 23.7359 Å, c = 12.6179 Å, α = 90º, β = 104.55º, γ = 90º, space group: *P2₁*, R_{wp} = 2.556, GOF = 1.781. For compound **21**: a = 9.7957 Å, b = 24.7850 Å, c = 12.5540 Å, α = 90º, β = 107.74º, γ = 90º, space group: *P2₁*, R_{wp} = 3.229, GOF = 2.420. Note that the differences between the unit cells determined by single crystal data and powder diffraction data are caused by the different experimental temperatures (120 K for single crystal *vs*. room temperature for powder measurements).

Table 2.4. *Unit cell parameters from Pawley refinements for compounds **A** and **22** and those from single crystal diffraction data.*

	a (Å)	b (Å)	c (Å)	α (°)	β (°)	γ (°)	R_{wp}	GOF	sp. gr.
A (crystal)	9.8809	23.8659	12.4131	90	104.868	90			*P2₁*
A (powder)	10.0477	23.7359	12.6179	90	104.55	90	2.556	1.781	*P2₁*
21 (powder)	9.7957	24.7850	12.5540	90	107.74	90	3.229	2.420	*P2₁*

As clearly shown in Figures 2.5 and 2.6, the diffractogram of compound **21**, the major phase obtained in the synthesis of **22** can be indexed within the 2D structure found in compound **A**, indicating that both polymorphs: 2D (**21**) and 3D (**22**), are obtained simultaneously.

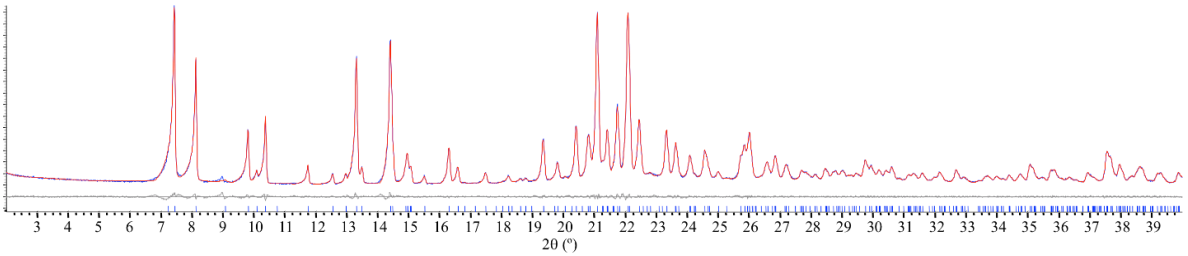

Figure 2.5. *Observed (blue) and calculated (red) profiles and difference plots ($I_{obs} - I_{calcd}$; gray) of the Pawley refinements (2θ range of 2.0–40.0°) for compound $(PBu_3Me)_2[NaCr(C_6O_4Br_2)_3]$ (**A**)*

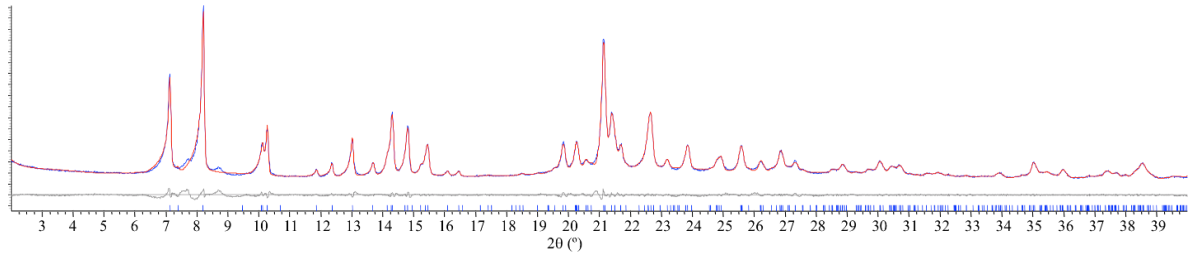

Figure 2.6. *Observed (blue) and calculated (red) profiles and difference plots ($I_{obs} - I_{calcd}$; gray) of the Pawley refinements (2θ range 2.0–40.0°) for the 2D polymorph $(NBu_3Me)_2[NaCr(C_6O_4Br_2)_3]$ (**21**).*

3.4. Magnetic Properties

Since only few crystals of compound **22** were obtained, we have only measured the magnetic properties of compound **21** whose Pawley refinement confirms that it is a pure 2D phase.

The product of the molar magnetic susceptibility per formula unit times the temperature ($\chi_m T$) for compound **21** shows a value of *ca*. 1.9 $cm^3\,K\,mol^{-1}$ at room temperature, confirming the presence of isolated S = 3/2 Cr(III) ions with g ≈ 2. When the sample is cooled down, $\chi_m T$ remains constant down to *ca*. 10 K. Below this temperature it shows a sharp decrease to reach a value of ca. 1.75 $cm^3\,K\,mol^{-1}$ at 2 K (Figure 2.7). This behaviour suggests the presence in **21** of isolated Cr(III) with a zero field splitting (ZFS) of the S = 3/2 ground spin sate.

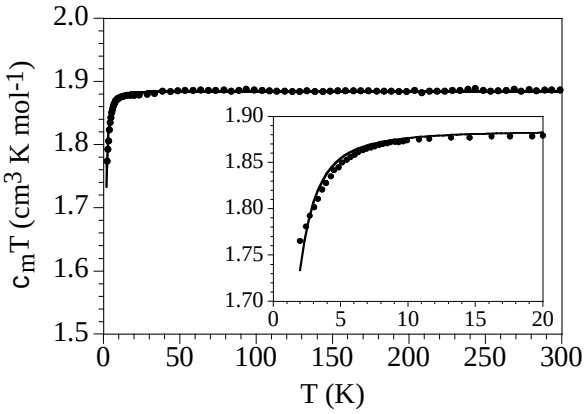

Figure 2.7. *Thermal variation of $\chi_m T$ for the Cr(III) compound **21**. Solid line is the best fit to the isolated monomer model with zero field splitting. Inset shows the low temperature region.*

Given that Na^+ cations are diamagnetic and do not give rise any magnetic coupling, compound **21** can be considered, from the magnetic point of view, as being formed by isolated $[Cr^{III}(C_6O_4X_2)_3]^{3-}$ units. For this reason, the magnetic properties of compound **21** have been fit with a simple model for isolated S = 3/2 ions with ZFS.[28] This model reproduces very satisfactorily the magnetic properties of compound **21** in the whole temperature range with g = 1.998 and |D| = 1.11 cm^{-1} (solid line in Figure 2.7). It has to be mentioned that the sign of the zero field splitting parameter cannot be determined from powder susceptibility measurements and that the presence of a very weak antiferromagnetic contribution in the D parameter cannot be discarded. The values of g and |D| are similar to those reported for the related isolated $[Cr^{III}(C_6O_4X_2)_3]^{3-}$ monomers[25-27] (see chapter one) in agreement with their resemblance from the magnetic point of view. The paramagnetic nature of compound **21** is confirmed by the isothermal magnetization at 2 K (Figure 2.8) that can be well reproduced with a simple Brillouin function for S = 3/2 with a g value very close to 2 (solid line in Figure 2.8).

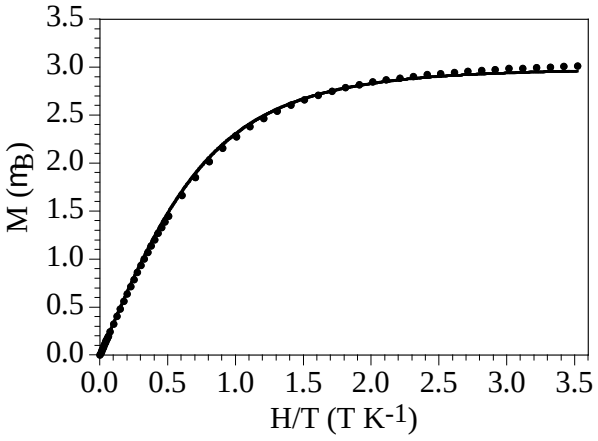

Figure 2.8. *Isothermal magnetization of compound **21** at 2 K. Solid line is the best fit to the Brillouin function for S = 3/2 with g = 1.984.*

4. Conclusions and perspectives

We have prepared for the first time heterometallic a honeycomb M(III)M(I) 2D lattice (**21**) and also the first heterometallic M(III)/M(I) 3D-(10,3) anilate-based lattice (**22**). Furthermore, compounds **21** and **22** constitute the first example of 2D/3D polymorphism in the anilato-based family. Moreover, this polymorphism has never been observed in the oxalato family.

These structures further confirm the ability of the anilato-type ligands to act as bis-chelating ligands, as was observed in the oxalato series. This ability should lead to the synthesis of magnetically ordered M(III)/M(II) 3D-(10-3) lattices, which is, after the results reported in this chapter, the only remaining challenge in the oxalato/anilato analogy.[11]

Studies to try to find a rational way to obtain these 3D M(III)/M(II) lattices are under way. A second improvement in the 2D series is the insertion of functional cations with a second interesting property, something that will be shown in the next chapters.

5. References

(1) Tamaki, H.; Zhong, Z. J.; Matsumoto, N.; Kida, S.; Koikawa, M.; Achiwa, N.; Hashimoto, Y.; Okawa, H. Design of Metal-Complex Magnets. Syntheses and Magnetic Properties of Mixed-Metal Assemblies $\{NBu_4[MCr(ox)_3]\}X$ (NBu_4^+ = Tetra(n-Butyl)Ammonium Ion; Ox^{2-} = Oxalate Ion; M = Mn^{2+}, Fe^{2+}, Co^{2+}, Ni^{2+}, Cu^{2+}, Zn^{2+}). *J. Am. Chem. Soc.* **1992***, 114*, 6974-6979.

(2) Atovmyan, L. O.; Shilov, G. V.; Lyubovskaya, R. N.; Zhilyaeva, E. I.; Ovanesyan, N. S.; Pirumova, S. I.; Gusakovskaya, I. G.; Morozov, Y. G. Crystal-Structure of the Molecular Ferromagnet $NBu_4[MnCr(C_2O_4)_3]$ (Bu = n-C_4H_9). *Jetp Lett.* **1993***, 58*, 766-769.

(3) Martin, L.; Day, P.; Horton, P.; Nakatsuji, S.; Yamada, J.; Akutsu, H. Chiral Conducting Salts of BEDT-TTF Containing a Single Enantiomer of tris(oxalato)chromate(III) Crystallised from a Chiral Solvent. *J. Mater. Chem.* **2010***, 20*, 2738-2742.

(4) Martin, L.; Day, P.; Nakatsuji, S.; Yamada, J.; Akutsu, H.; Horton, P. A Molecular Charge Transfer Salt of BEDT-TTF Containing a Single Enantiomer of Tris(oxalato)chromate(III) Crystallised from a Chiral Solvent. *CrystEngComm* **2010***, 12*, 1369-1372.

(5) Suh, J. S.; Shin, J. Y.; Yoon, C.; Lee, K. W.; Suh, I. H.; Lee, J. H.; Ryu, B. Y.; Lim, S. S. The Crystal and Molecular Structure of Sodium Magnesium tris(oxalato)chromate(III) Decahydrate, $NaMg[Cr(Ox)_3]\cdot 10H_2O$. *Bull. Korean Chem. Soc.* **1994***, 15*, 245-249.

(6) Suh, M. P.; Jeon, J. W.; Moon, H. R.; Min, K. S.; Choi, H. J. Self-Assembly of Hybrid Solids Consisting of 2D Supramolecular Networks and Intercalated Metal Complexes. *C. R. Chim.* **2005***, 8*, 1543-1551.

(7) Kurmoo, M.; Graham, A. W.; Day, P.; Coles, S. J.; Hursthouse, M. B.; Caulfield, J. L.; Singleton, J.; Pratt, F. L.; Hayes, W. Superconducting and Semiconducting Magnetic Charge Transfer Salts: $(BEDT\text{-}TTF)_4AFe(C_2O_4)_3$.Cntdot.$C_6H_5CN$ (A = H_2O, K, NH_4). *J. Am. Chem. Soc.* **1995***, 117*, 12209-12217.

(8) Coronado, E.; Curreli, S.; Gimenez-Saiz, C.; Gómez-García, C. J. The Series of Molecular Conductors and Superconductors $ET_4[AFe(C_2O_4)_3]\cdot PhX$ (ET = bis(ethylenedithio)tetrathiafulvalene; $(C_2O_4)^{2-}$ = oxalate; $A^+ = H_3O^+$, K^+; X = F, Cl, Br, and I): Influence of the Halobenzene Guest Molecules on the Crystal Structure and Superconducting Properties. *Inorg. Chem.* **2012***, 51*, 1111-1126.

(9) Butler, K. R.; Snow, M. R. Absolute Configuration of the Tris-(1,10-phenanthroline)nickel(II) and tris(oxalato)cobaltate(III) Complex Ions by X-Ray Structure Analysis. *J. Am. Chem. Soc.* **1971**, 565-569.

(10) Decurtins, S.; Schmalle, H. W.; Schneuwly, P.; Ensling, J.; Guetlich, P. A Concept for the Synthesis of 3-Dimensional Homo- and Bimetallic Oxalate-Bridged Networks $[M_2(ox)_3]_n$. Structural, Moessbauer, and Magnetic Studies in the Field of Molecular-Based Magnets. *J. Am. Chem. Soc.* **1994***, 116*, 9521-9528.

(11) Coronado, E.; Galán-Mascarós, J. R.; Gómez-García, C. J.; Martínez-Agudo, J. M. Molecule-Based Magnets Formed by Bimetallic Three-Dimensional Oxalate Networks and Chiral tris(bipyridyl) Complex Cations. the Series $[Z(II)(Bpy)_3][ClO_4][M(III)M(II)(ox)_3]$ Z(II) = Ru, Fe, Co, and Ni; M(II) = Mn, Fe, Co, Ni, Cu, and Zn; ox = Oxalate Dianion). *Inorg. Chem.* **2001***, 40*, 113-120.

(12) Atzori, M.; Benmansour, S.; Mínguez Espallargas, G.; Clemente-León, M.; Abhervé, A.; Gómez-Claramunt, P.; Coronado, E.; Artizzu, F.; Sessini, E.; Deplano, P.; Serpe, A.; Mercuri, M. L.; Gómez-García, C. J. A Family of Layered Chiral Porous Magnets Exhibiting Tunable Ordering Temperatures. *Inorg. Chem.* **2013***, 52*, 10031-10040.

(13) Abrahams, B. F.; Hudson, T. A.; McCormick, L. J.; Robson, R. Coordination Polymers of 2,5-Dihydroxybenzoquinone and Chloranilic Acid with the (10,3)-a Topology. *Cryst. Growth Des.* **2011***, 11*, 2717-2720.

(14) Benmansour, S.; Valles-García, C.; Gómez-Claramunt, P.; Minguez Espallargas, G.; Gómez-García, C. J. 2D and 3D Anilato-Based Heterometallic M(I)M(III) Lattices: The Missing Link. *Inorg. Chem.* **2015***, 54*, 5410-5418.

(15) Bain, G. A.; Berry, J. F. Diamagnetic Corrections and Pascal's Constants. *J. Chem. Educ.* **2008***, 85*, 532-536.

(16) Altomare, A.; Burla, M. C.; Camalli, M.; Cascarano, G. L.; Giacovazzo, C.; Guagliardi, A.; Moliterni, A. G. G.; Polidori, G.; Spagna, R. SIR97: A New Tool for Crystal Structure Determination and Refinement. *J. Appl. Cryst.* **1999***, 32*, 115-119.

(17) Sheldrick, G. M. Crystal Structure Refinement with SHELXL. *Acta Cryst. C* **2015***, 71*, 3-8.

(18) Farrugia, L. J. WinGX Suite for Small-Molecule Single-Crystal Crystallography. *J. Appl. Cryst.* **1999***, 32*, 837-838.

(19) Abherve, A.; Clemente-León, M.; Coronado, E.; Gómez-García, C. J.; Verneret, M. One-Dimensional and Two-Dimensional Anilate-Based Magnets with Inserted Spin-Crossover Complexes. *Inorg. Chem.* **2014***, 53*, 12014-12026.

(20) Russell, V. M.; Craig, D. C.; Scudder, M. L.; Dance, I. G. Interpenetrating Non-Molecular and Supramolecular (10,3)-a Nets Occurring with Chiral Recognition in Crystalline $(Ph_3MeP)_2[NaCr(Ox)_3]$. *CrystEngComm* **2000***, 2*, 16-23.

(21) Clemente-León, M.; Coronado, E.; López-Jorda, M.; Waerenborgh, J. C. Multifunctional Magnetic Materials obtained by Insertion of Spin-Crossover Fe-III Complexes into Chiral 3D Bimetallic Oxalate-Based Ferromagnets. *Inorg. Chem.* **2011***, 50*, 9122-9130.

(22) Coronado, E.; Galan Mascaros, J. R.; Giménez-López, M. C.;´ Almeida, M.; Waerenborgh, J. C. Spin Crossover FeII Complexes as Templates for Bimetallic Oxalate-Based 3D Magnets. *Polyhedron* **2007***, 26*, 1838-1844.

(23) Clemente-Leon, M.; Coronado, E.; López-Jordá, M.; Mínguez Espallargas, G.; Soriano-Portillo, A.; Waerenborgh, J. C. Multifunctional Magnetic Materials obtained by Insertion of a Spin-Crossover Fe^{III} Complex into Bimetallic Oxalate-Based Ferromagnets. *Chem. Eur. J.* **2010***, 16*, 2207-2219.

(24) Shen, H.; Bu, W.; Liao, D.; Jiang, Z.; Yan, S.; Wang, G. Three-Dimensional Oxalate-Bridged Heterometal Supramolecular Complex with a Large Helical Tunnel of 21.191 × 9.294 $Å^2$. *Inorg. Chem.* **2000***, 39*, 2239-2242.

(25) Atzori, M.; Artizzu, F.; Sessini, E.; Marchio, L.; Loche, D.; Serpe, A.; Deplano, P.; Concas, G.; Pop, F.; Avarvari, N.; Mercuri, M. L. Halogen-Bonding in a New Family of tris(haloanilato)metallate(III) Magnetic Molecular Building Blocks. *Dalton Trans.* **2014***, 43*, 7006-7019.

(26) Atzori, M.; Pop, F.; Auban-Senzier, P.; Gomez-Garcia, C. J.; Canadell, E.; Artizzu, F.; Serpe, A.; Deplano, P.; Avarvari, N.; Mercuri, M. L. Structural Diversity and Physical Properties of Paramagnetic Molecular Conductors Based on bis(ethylenedithio)tetrathiafulvalene (BEDT-TTF) and the tris(chloranilato)ferrate(III) Complex. *Inorg. Chem.* **2014***, 53*, 7028-7039.

(27) Atzori, M.; Artizzu, F.; Marchio, L.; Loche, D.; Caneschi, A.; Serpe, A.; Deplano, P.; Avarvari, N.; Mercuri, M. L. Switching-on Luminescence in Anilate-Based Molecular Materials. *Dalton Trans.* **2015***, 44*, 15786-15802.

(28) O'Connor, C. J. Magnetochemistry-Advances in Theory and Experimentation. *Prog. Inorg. Chem.* **1982***, 29*, 203-283.

Chapter 3

2D heterometalic honeycomb lattices with new template molecules

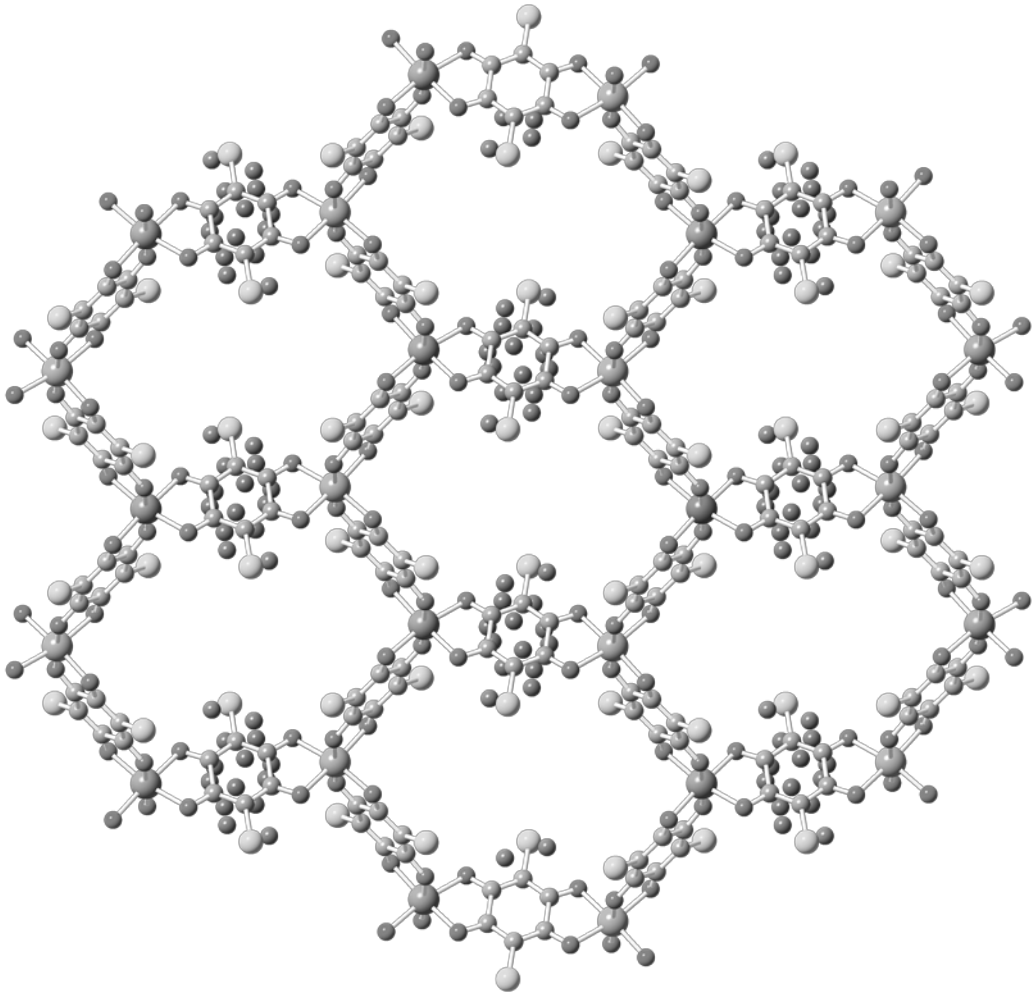

1. Introduction

The search for new metal organic frameworks (MOFs) and porous coordination polymers (PCPs) has increased exponentially during the past few years, as shown in several bibliographic databases such as Scopus or Web of science. According to the Web of Science, there are 5315 publications that contain PCP as keyword since 1998, with 634 in 2016 and with 57.29 average citations per item. Since 1995, 40119 items have been published with MOF as keyword, with 6203 works published in 2016. These 21st century materials have a porous ordered network that allows its use in gas storage and gas separation[1-4], water adsorption[5], sensors[6, 7], catalysis[8], photocatalysis for water splitting[9], luminescence,[10] energy storage and transfer,[11-13] biomedical applications[14]… In order to look for better materials for these applications, one of the most important characteristics to pursue is a larger pore size.

Crystal engineering plays an important role in this topic, due to the fact that, not only the correct choice of the starting materials is important but also the control of the final packing of the molecules. As an example, in 2013 our group along with Mercuri's one, we published a new series of anilato-based compounds where the T_c changes with the X group of the anilato ligand.[15] In this publication, two different families of compounds were presented: $[(H_3O)(phez)_3][M^{III}Mn(C_6O_4X_2)_3]$ (M^{III} = Cr and Fe, phez = phenazine; X = Cl, Br) and $[N(Bu)_4][CrMn(C_6O_4X_2)_3]$ (X = Cl, Br, I, H). In the first series the layers are eclipsed but in the second one the layers are alternated due to presence of the NBu_4^+ cations. This fact precludes the formation of hexagonal channels (that may host solvent/gas molecules) needed to form MOFs. These channels were indeed found in anilato-based compounds synthesized in the presence of phenazine, which is present in the final structure acting as a template that favours the eclipsed disposition of the 2D honeycomb layer. This template effect of the phenazine molecules proves that the final geometry of the anilato-based coordination polymers and the presence of porosity can be controlled by choosing the appropriate templating agents. In this chapter we will show that other molecules, as some benzene derivatives, show a similar template effect in the formation of eclipsed stackings and, therefore, in the presence of porosity. Thus, we have prepared two different families of compounds: the first one contains NBu_4^+ as cation and, thanks to the presence of halo-benzene molecules, presents an eclipsed disposition of the honeycomb layers and, therefore, porosity. The second family also

present honeycomb anilato-based layers but the cation is $(H_3O)^+$ without any phenazine molecule. In this second family the template effect of the benzene derivative molecules also favours the formation of eclipsed packing and, therefore, of porosity. Here we present the synthesis and the structural and magnetic characterization of up to six 2D anilato-based honeycomb layers with benzene derivative molecules as templates and with eclipsed packing and, therefore, with porosity.

2. Experimental section

2.1. Synthesis

General Remarks: The synthesis of $K_3[Cr(C_6O_4Cl_2)_3]$, $K_3[Cr(C_6O_4Br_2)_3]$ and $(NBu_4)_3[Cr(C_6O_4Br_2)_3]$ is described in chapter one. All other materials and solvents were commercially available and used without further purification.

Synthesis of $(H_3O)[MnCr(C_6O_4Cl_2)_3]\cdot 2PhCl\cdot 6H_2O$ (23): A solution of $K_3[Cr(C_6O_4Cl_2)_3]$ (20.0 mg, 0.025 mmol) in a mixture of 2 mL of MeCN and 0.5 mL of MeOH was stirred for twenty minutes and placed on top of a solution of $MnCl_2\cdot 4H_2O$ (10.0 mg, 0.05 mmol) in a mixture of 1 mL of MeOH and 1.5 mL of chlorobenzene in a thin layering tube. In order to slow the diffusion, 1 mL of a mixture of MeOH and chlorobenzene (2:1) was placed in-between the two solutions. Crystals suitable for X-Ray diffraction were obtained after slow diffusion during two months at 18 ºC.

Synthesis of $(H_3O)[MnCr(C_6O_4Br_2)_3]\cdot 2PhCl\cdot 6H_2O$ (24): This compound was obtained as **23** but using $K_3[Cr(C_6O_4Br_2)_3]$ (26.5 mg, 0.025 mmol) instead of $K_3[Cr(C_6O_4Cl_2)_3]$. Crystals suitable for X-Ray diffraction were obtained after slow diffusion during two months at 18 ºC.

Synthesis of $(H_3O)[MnCr(C_6O_4Br_2)_3]\cdot 2PhBr\cdot 6H_2O$ (25): This compound was obtained as **24** but using bromobenzene instead of chlorobenzene.

Synthesis of $(H_3O)[MnCr(C_6O_4Br_2)_3]\cdot 2PhCH_3\cdot 6H_2O$ (26): This compound was obtained as **24** but using toluene instead of chlorobenzene.

Synthesis of $(NBu_4)[MnCr(C_6O_4Br_2)_3]\cdot PhBr\cdot 5H_2O$ (27): This compound was obtained by slow diffusion of a solution of $(NBu_4)_3[Cr(C_6O_4Br_2)_3]$ (16.7 mg, 0.01 mmol) in 2.5 mL of acetonitrile placed on top of a solution of $MnCl_2\cdot 4H_2O$ (27.7 mg,

0.14 mmol) in 2.5 mL of water. In order to slow the diffusion, a mixture of bromobenzene and THF (1:2) was placed in-between the two solutions. Crystals suitable for X-Ray diffraction were obtained after slow diffusion for two months at 18 ºC.

2.2. Physical Properties

Magnetic measurements were performed with a Quantum Design MPMS-XL-5 SQUID magnetometer in the temperature range of 2 to 300 K with different applied DC magnetic fields in the range of 1 mT to 1 T on polycrystalline samples of all the compounds. Isothermal hysteresis measurements were performed at 2 K with magnetic fields from -5 to 5 T. AC susceptibility measurements were performed on the same samples with a field of 0.395 mT (3.95 Gauss) oscillating at different frequencies in the range of 1-1000 Hz. Susceptibility data were corrected for the sample holder and for the diamagnetic contribution of the salts using Pascal's constants.[16]

2.3. Structural Characterization

Suitable single crystals of compounds **23, 24** and **27** were mounted on a loop using a viscous hydrocarbon oil to coat the crystals and then transferred directly to the cold nitrogen stream for data collection. X-ray data were collected at 120 K for the three compounds on a Supernova diffractometer equipped with a graphite-monochromated Enhance (Mo) X-ray Source (λ = 0.71073 Å). The program CrysAlisPro, Agilent Technologies Ltd., was used for unit cell determinations and data reduction. Empirical absorption correction was performed using spherical harmonics, implemented in the SCALE3 ABSPACK scaling algorithm. Crystal structures were solved by direct methods with the SIR92 program[17] and refined against all F^2 values with the SHELXL-2014 program[18], using the WinGX2014.1 graphical user interface.[19] All non-hydrogen atoms were refined anisotropically and hydrogen atoms were placed in calculated positions and refined isotropically with a riding model. Data collection and refinement parameters are given in Table 3.1.

The X-ray powder diffractograms were collected for polycrystalline samples of all the compounds using a 0.5 mm glass capillary that was mounted and aligned on a Empyrean PANalytical powder diffractometer, using CuKα radiation (λ = 1.54177 Å)

operating at 40 mA and 45 kV. A total of 3 scans were collected at room temperature in the 2θ range of 2-40º in spinning mode with a step size of 0.0131º.

3. Results and Discussion

3.1. X-Ray Diffraction

***Table 3.1**. Crystallographic data compounds **23**, **24** and **27**.*

	23	**24**	**27**
Empirical formula	$C_{30}H_{27}Cl_8O_8MnCr$	$C_{30}H_{27}Br_8O_8MnCr$	$C_{40}H_{51}NBr_7O_{17}MnCr$
Formula weight	1098.08	1261.7	1484.09
Temperature K	120(2)	120(2)	120(2)
Wavelength (Å)	0.71073	0.71073	0.71073
Crystal system	Monoclinic	Monoclinic	Monoclinic
Space group	$P2_1/n$	$P2_1/n$	$P2_1/n$
a (Å)	7.5892(2)	7.8052(6)	9.9557(5)
b(Å)	23.1064(5)	23.1026(13)	23.6054(10)
c(Å)	11.4474(3)	11.5753(7)	12.2129
α (°)	90	90	90
β (°)	92.256(2)	90.039(7)	105.187(5)
γ (°)	90	90	90
V (Å^3)	2005.85(9)	2087.3(2)	2769.9
ρ_{cal} (mg m^{-3})	1.790	2.141	1.723
μ (mm^{-1})	1.199	6.511	5.533
Crystal size (mm^3)	0.10x0.08x 0.03	0.13x0.04x0.03	0.10x0.06x0.02
θ range (°)	3.281 to 25.040	3.520 to 25.053	3.347 to 25.035
Reflections collected	23295	21407	41364
Independent reflections (R_{int})	3530	3687	9777
Reflns used in refinement, n	3530	3687	9777
$R_1(F)$,[a] $I > 2\sigma(I)$	0.0730	0.1197	0.0998
$wR_2(F^2)$,[b] all data	0.1738	0.2701	0.2628
$S(F^2)$,[c] all data	1.074	1.120	1.072
Largest diff. peak	1.557	1.613	1.654
Largest diff. hole	-0.850	-0.915	-1.394

[a]$R1(F) = \Sigma||F_O|-|F_C||/\Sigma|F_O|$; [b]$wR2(F^2) = [\Sigma w(F_O^2-F_C^2)^2/\Sigma wF_O^4]^{1/2}$; [c]$S(F^2) = [\Sigma w(F_O^2-F_C^2)^2/(n + r - p)]^{1/2}$

Structure of $(H_3O)[MnCr(C_6O_4X_2)_3]\cdot 2PhCl\cdot 6H_2O$; X = Cl (23) and Br (24). Both compounds are isostructural and crystallize in the monoclinic $P2_1/n$ space group.The asymmetric unit contains one metal centre corresponding to ½ Mn(II) and ½ Cr(III), one anilato $(C_6O_4X_2)^{2-}$, X = Cl (**23**) and Br (**24**) in general position , half anilato located on an inversion centre and one chloro-benzene molecule in general position. There are also six disordered water molecules and one oxonium cation with an occupancy factor of 1/2, resulting in the formula: $(H_3O)[MnCr(C_6O_4X_2)_3]\cdot 2PhCl\cdot 6H_2O$ with X = Cl (**23**) or Br (**24**).

The structure of the two compounds is based on anionic layers formulated as $[Mn^{II}Cr^{III}(C_6O_4X_2)_3]^-$ (X = Cl or Br) (Figure 3.1a) with the classical hexagonal honey-comb 2D structure (Figure 1b). In between the anionic layers there are six water molecules and one oxonium cation to compensate the negative charge of the anionic lattice. The inclusion of the cations in between the anionic layers gives rise to alternated cationic and anionic layers parallel to the *ab* plane with an interlayer Cr-Cr distance of c/2 = 7.686 Å in **23** and 7.899 Å in **24**. The longer inter-layer distance in **24** is attributed to the larger size of Br compared to Cl and to the fact that the halogen atoms are pointing towards the interlayer space and thus determine the interlayer distance.

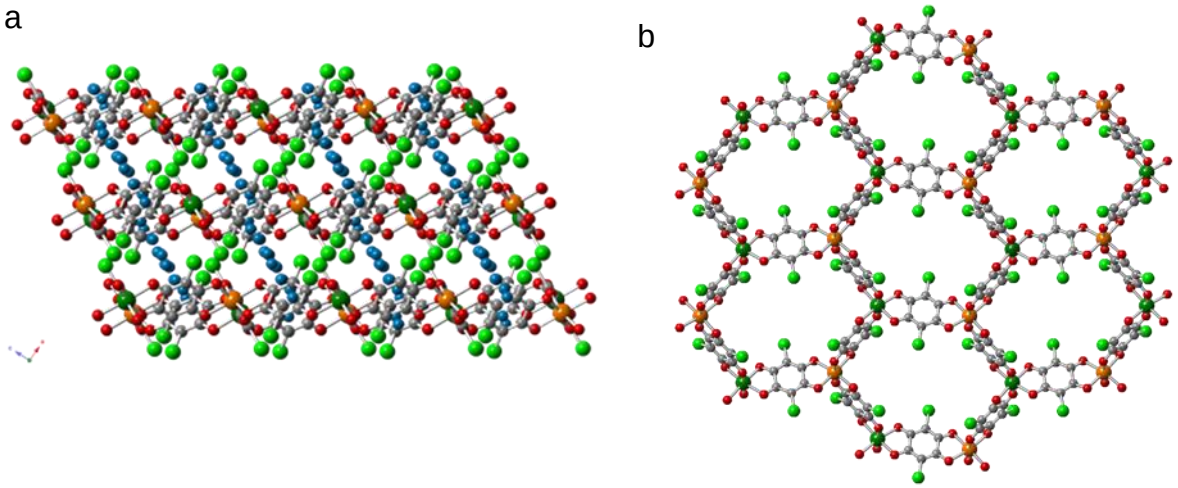

***Figure 3.1**. (**a**) Side view (down the b direction) of the layers in compound **23** (similar for **24**). (**b**) Side view (down the b direction) of the layers in compound **23** (similar for **24**) with water crystallization located in between the layers. (**c**) View of a honey-comb layer in **23**. Colour code: C = grey, O = red, O_w = light blue, Cl = light green, Cr = dark green and Mn = orange. Chloro-benzene molecules have been omitted for clarity.*

The layers are packed along the *a* direction in an eclipsed way, giving rise to slightly distorted hexagonal honeycomb channels running along the *a* direction (Figure 3.2a). In the *c* direction, the layers are packed in a rectangular way with the six water molecules and the oxonium cation inside those rectangular cavities (Figure 3.2b).

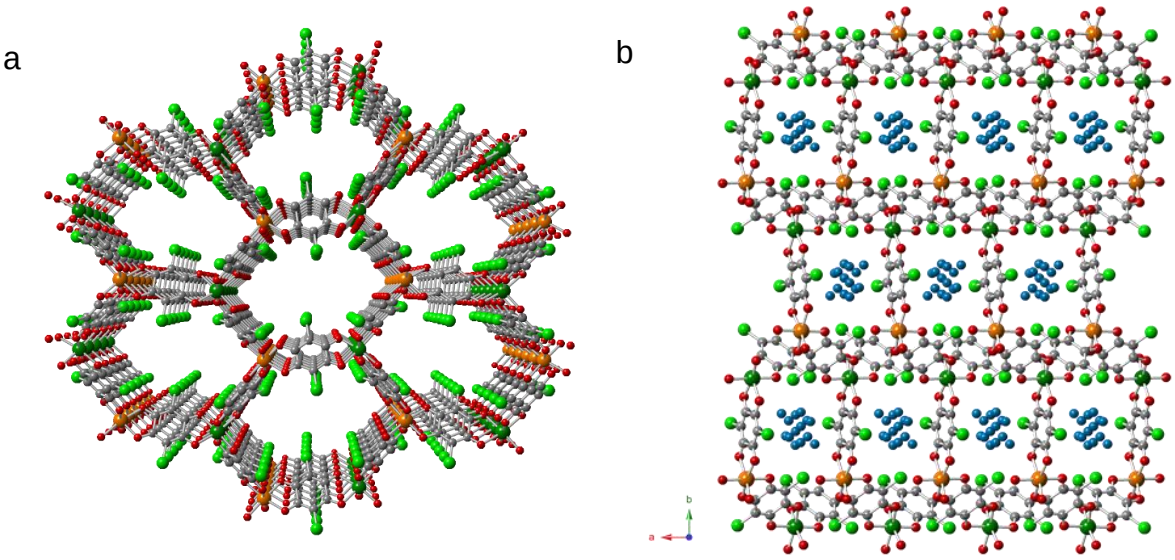

***Figure 3.2**. (**a**) Perspective view of the hexagonal channels in **23** running along the a axis. (**b**) View along the c axis showing the rectangular channels where the water and oxonium molecules are located. Colour code: C = grey, O = red, O_w = light blue, Cl = light green, Cr = dark green and Mn = orange. H atoms and chloro-benzene molecules have been omitted for clarity.*

The anionic layers contain Mn(II) and Cr(III) ions alternating in the vertices of the hexagons connected through bis-bidentate anilato ligands (chloranilato in **23** and bromanilato in **24**) that form the sides of the hexagons (Figure 3.1b). The metal ions alternate in the hexagons in such a way that each Mn(II) ions is surrounded by three Cr(III) ions and vice-versa (Figure 3.3a).

The metal ions are surrounded by three chelating anilato ligands in a distorted octahedral coordination geometry. The M-O bonds are all in the range of 2.046-2.084 Å for **23** and of 2.022-2.097 Å for **24** (Table 3.2). The *cis* and *trans* angles are also similar for both compounds. Thus, the *cis* angles are in the range of 77.6-103.7º for **23** and of 77.6-102.7º for **24**, and the *trans* angles are in the range of 165.6-177.8º for **23** and of 165.7-177.4º for **24** (Table 3.3). These values are very similar to those found in previously reported $A[MnCr(C_6O_4X_2)_3]$ compounds (X = Cl and Br; A = NBu_4^+, $[(H_3O)(phz)_3]^+$, $[Fe^{III}(sal_2\text{-trien})]^+$, $[Fe^{III}(4\text{-OH-sal}_2\text{-trien})]^+$, $[Fe^{III}(sal_2\text{-epe})]^+$ and $[Fe^{III}(5\text{-Cl-sal}_2\text{-trien})]^+$).[15, 20-22]

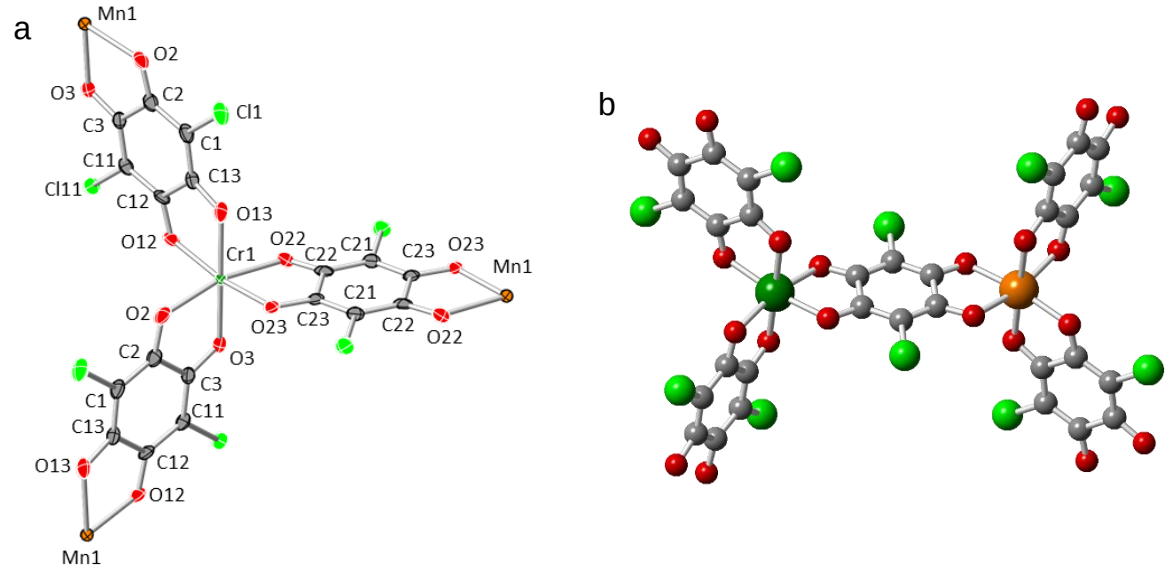

Figure 3.3. *(**a**) ORTEP drawing of the coordination around a Cr(III) ion showing the labelling scheme in **23** (similar in **24** but changing Cl by Br) (**b**) View of two neighbouring metal centres. Colour code: C = grey, O = red, Cl = light green, Cr = dark green and Mn = orange.*

A very interesting aspect of these structures is the presence of an eclipsed packing of the layers. A close look at the structure shows that this packing may be attributed to the presence of two chloro-benzene molecules located inside the hexagonal cavities and oriented almost perpendicular to the layers (Figure 3.4).

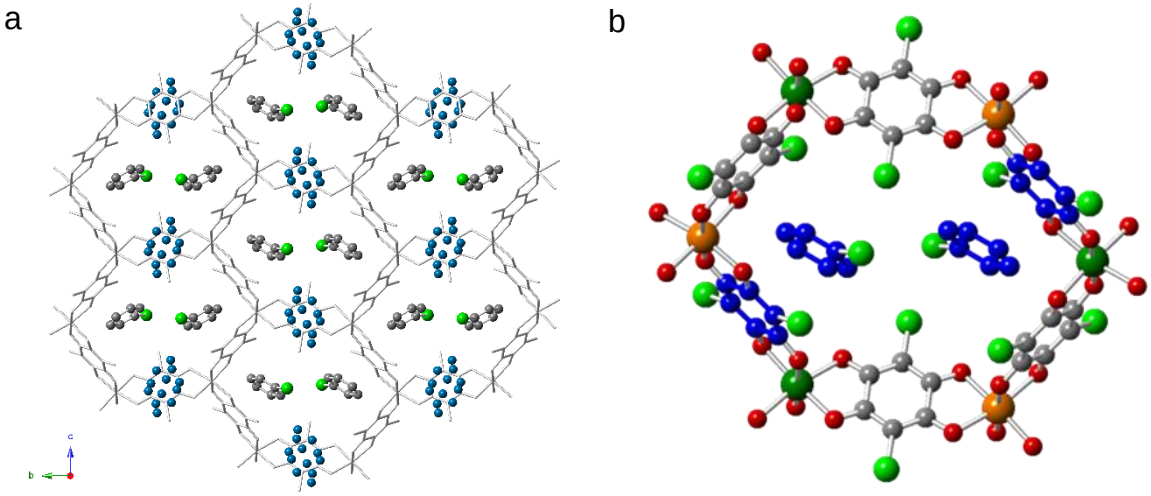

Figure 3.4*. (**a**) View down the a axis of an hexagonal layer with the template chloro-benzene molecules in the hexagonal cavities. **(b)** View of one hexagon showing the π–π interactions between the choro-benzene molecules and the aromatic rings of the anilato ligand (in blue).*

This orientation forces the Cl atoms of the chloro-benzene molecules to occupy the space above and below each hexagonal cavity, preventing the alternating

packing of the layers. In other words, the chloro-benzene molecules block the space above and below the hexagonal cavities and, accordingly, consecutive layers must stack in an eclipsed way to reduce the steric hindrance of the Cl atoms of the PhCl molecules. A close look at these PhCl molecules shows that they are located almost perpendicular to the hexagonal cavities due to the π-π stacking interactions with the aromatic rings of the anilato ligands (Figure 3.4). The offset angles and the plane distances (21.58° and 3.624 Å for **23** and 21.58° and 3.624 Å for **24**) of these π-π interactions are within the typical range found in many other π-π interactions (3.3-3.8 Å and angles around 20º) as defined by Janiak.[23]

***Table 3.2**. Main bond lengths (Å) around the metals centres in **23**-**24** (M(1) = Cr(III)/Mn(II)).*

23		***24***	
Atoms	distance (Å)	Atoms	distance (Å)
M(1)-O(12)	2.046(5)	M(1)-O(12)#1	2.069(12)
M(1)-O(23)	2.067(5)	M(1)-O(26)#2	2.071(13)
M(1)-O(3)	2.073(4)	M(1)-O(3)	2.068(12)
M(1)-O(2)	2.074(5)	M(1)-O(2)	2.090(12)
M(1)-O(13)	2.076(5)	M(1)-O(13)#1	2.021(12)
M(1)-O(22)	2.084(5)	M(1)-O(22)	2.097(11)

Symmetry transformations used to generate equivalent atoms:
#1 = x+1/2,-y+1/2,z-1/2; #2 = x-1/2,-y+1/2,z+1/2.

***Table 3.3**. Main bond angles (°) around the metals centres in **23**-**24** (M(1) = Cr(III)/Mn(II)).*

23		***24***	
atoms	**angle (°)**	**atoms**	**angle (°)**
O(12)-M(1)-O(23)	169.33(17)	O(13)#1-M(1)-O(3)	89.7(5)
O(12)-M(1)-O(3)	100.10(18)	O(13)#1-M(1)-O(12)#1	78.3(5)
O(23)-M(1)-O(3)	90.55(17)	O(3)-M(1)-O(12)#1	102.7(5)
O(12)-M(1)-O(2)	88.94(18)	O(13)#1-M(1)-O(26)#2	169.0(5)
O(23)-M(1)-O(2)	94.10(18)	O(3)-M(1)-O(26)#2	94.3(5)
O(3)-M(1)-O(2)	77.62(17)	O(12)#1-M(1)-O(26)#2	90.8(5)
O(12)-M(1)-O(13)	78.08(17)	O(13)#1-M(1)-O(2)	99.2(5)
O(23)-M(1)-O(13)	91.26(17)	O(3)-M(1)-O(2)	77.6(5)
O(3)-M(1)-O(13)	177.72(19)	O(12)#1-M(1)-O(2)	177.4(5)
O(2)-M(1)-O(13)	103.63(18)	O(26)#2-M(1)-O(2)	91.7(4)
O(12)-M(1)-O(22)	100.88(18)	O(13)#1-M(1)-O(22)	99.5(5)
O(23)-M(1)-O(22)	78.18(18)	O(3)-Cr(1)-O(22)	165.7(4)
O(3)-M(1)-O(22)	90.21(17)	O(12)#1-Cr(1)-O(22)	89.9(4)
O(2)-M(1)-O(22)	165.61(18)	O(26)#2-Cr(1)-O(22)	78.7(4)
O(13)-M(1)-O(22)	88.81(18)	O(2)-Cr(1)-O(22)	90.1(4)

Symmetry transformations used to generate equivalent atoms:
#1 = x+1/2,-y+1/2,z-1/2; #2 = x-1/2,-y+1/2,z+1/2.

Structure of $(NBu_4)[MnCr(C_6O_4Br_2)_3]\cdot PhBr\cdot 5H_2O$ (27): This compound crystallizes in the monoclinic $P2_1$ space group). The asymmetric unit contains one Cr(III), one Mn(II), three anilato ligands $(C_6O_4Br_2)^{2-}$, one tetrabutylamonium (NBu_4^+) cation, one disordered bromo-benzene molecule and five water molecules, all located on general positions. The total formula is, therefore, $(NBu_4)[MnCr(C_6O_4Br_2)_3]\cdot PhBr\cdot 5H_2O$.

The structure consists of anionic layers formulated as $[Mn^{II}Cr^{III}(C_6O_4Br_2)_3]^-$ with a slightly distorted hexagonal honeycomb 2D structure (Figure 3.5b). The NBu_4^+ cation and the bromo-benzene molecules are located inside the hexagonal channels, occupying opposite vertices. The NBu_4^+ cation compensates the negative charge of the anionic lattice and the bromo-benzene stabilizes the final structure with π–π interactions between them and the aromatic rings of the anilato ligands.

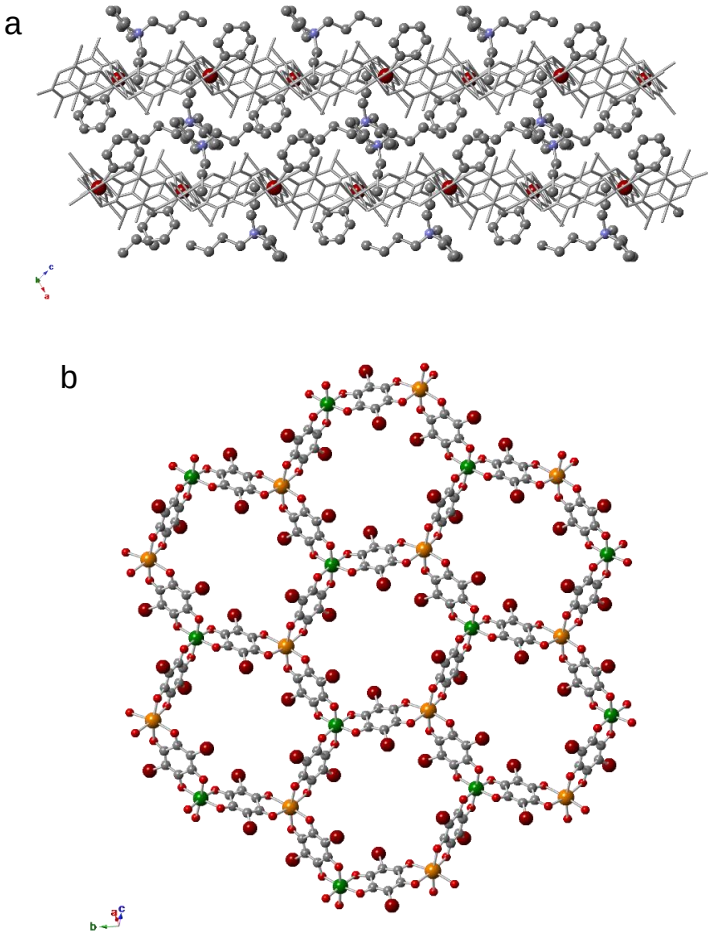

***Figure 3.5**. (**a**) Side view (down the b axis) of the layers in compound **27**. (**b**) View of a honeycomb layer in **27**. Colour code: C = grey, O = red, N = blue, Br = brown, Cr = dark green and Mn = orange. H atoms, NBu_4^+ cations and bromo-benzene molecules have been omitted for clarity.*

The cations are located in-between the anionic layers, giving rise to an alternation of anionic and cationic layers along the *c* axis with an interlayer distance of c/2 = 10.196 Å. This value is much higher than in the 2D layers where the cations are bulky cations such as $[(H_3O)(phez)_3]^+$,[15] resulting in more separated anionic layers. For example, in compounds **23** and **24**, the distances c/2 are 7.686 and 7.805 Å, respectively. Another example of anilato based-compound where the anionic layers are close in between them are neutral anilato layers with the cations located inside the hexagons of the anionic layers is the one published by Clemente et al[20, 24], where the distances c/2 between the Mn of different layers are between ca. 7.571 – 8.445 Å.

The layers are packed along the *a* axis in an eclipsed way, giving rise to slightly distorted hexagonal channels along the *a* axis (figure 3.6a). Along the *c* axis, chains of alternated metals bonded by anilato ligands (figure 3.6b) could be observed.

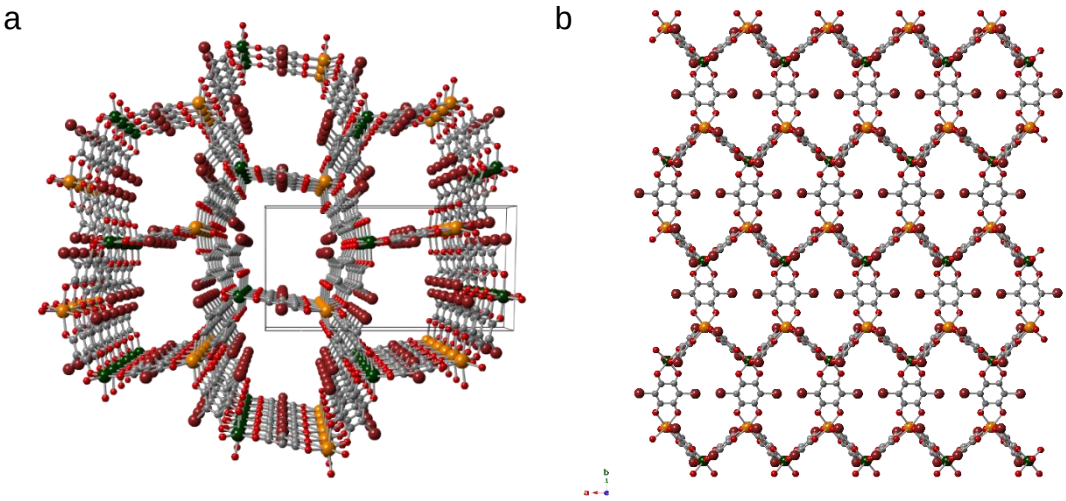

***Figure 3.6**. (**a**) Perspective view of the hexagonal channels in **27** running along the a axis. (**b**)View along the c axis of the structure of **27**. Colour code: C = grey, O = red, N = blue, Br = deep red, Cr = dark green and Mn = orange. H atoms, NBu_4^+ cations and bromobenzene molecules have been omitted for clarity.*

The anionic layers contain Mn(II) and Cr(III) ions in the vertices of the hexagons connected through bis-bidentate bromoanilato ligands that form the sides of the hexagons (Figure 3.7b). The metal ions alternate in the hexagons in such a way that each Mn(II) ions is surrounded by three Cr(III) ions and vice-versa (Figure 3.7b).

The metal ions are surrounded by three chelating anilato ligands giving rise to a distorted octahedral coordination geometry. The M-O bonds are all in the range of 1.947-2.213 Å for **27.** The *cis* angles are in the range of 74.6-108.2º and *trans* are in the range of 165.7-174.6º (Table 3.5). These values are very similar to those found in all the previously reported A[MnCr($C_6O_4X_2$)$_3$] compounds (X = Cl and Br; A = NBu_4^+, $[(H_3O)(phz)_3]^+$, $[Fe^{III}(sal_2\text{-trien})]^+$, $[Fe^{III}(4\text{-OH-sal}_2\text{-trien})]^+$, $[Fe^{III}(sal_2\text{-epe})]^+$ and $[Fe^{III}(5\text{-Cl-sal}_2\text{-trien})]^+$)[15] and to those found in all the 2D anilato compounds with Cr(III)-Mn(II).[15, 21, 22, 25-29]

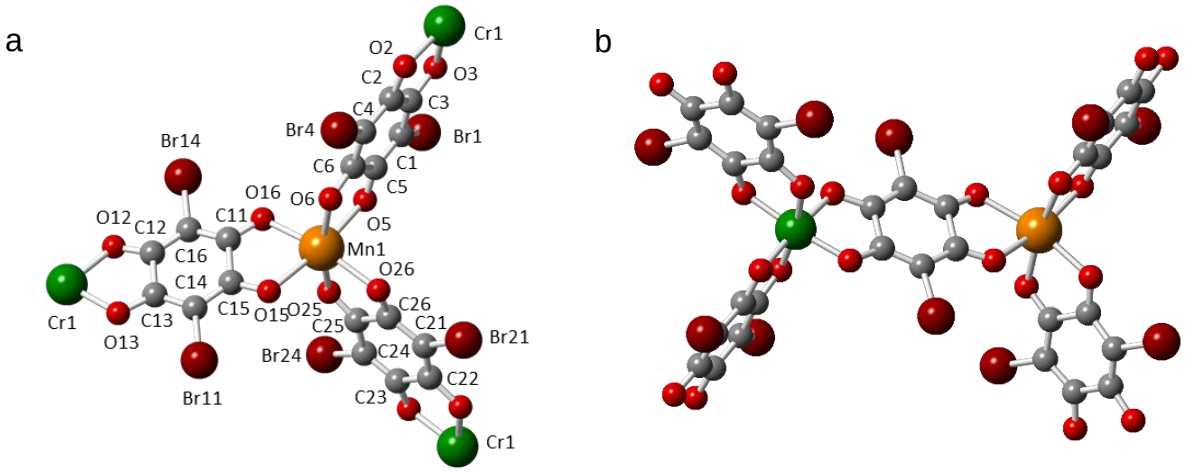

Figure 3.7. *(**a**) View of the coordination around a Mn(II) ion showing the labelling scheme in **27**. (**b**) View of two neighbouring metal centres. Colour code: C = grey, O = red, Br = deep red, Cr = dark green and Mn = orange.*

As it was pointed out before, the bromo-benzene molecules have a very important role in determining the eclipsed packing of the layers. In compound **27** even if there is only one bromo-benzene molecule (since half of the hexagonal cavity is occupied by the NBu_4^+ cation, Figure 3.8), its disposition is also almost perpendicular to the hexagonal cavity (Figure 3.8), as in **23** and **24**. This almost orthogonal orientation is also due to the presence of π-π interactions with the aromatic ring of one anilato ligand and results in a similar template effect that leads to an eclipsed packing. Although the PhBr molecule is slightly disordered, we have estimated an offset angle of *ca*. 20º and an inter-planar distance of *ca*. 3.5 Å, values typical of those found in many other π-π interactions.[23]

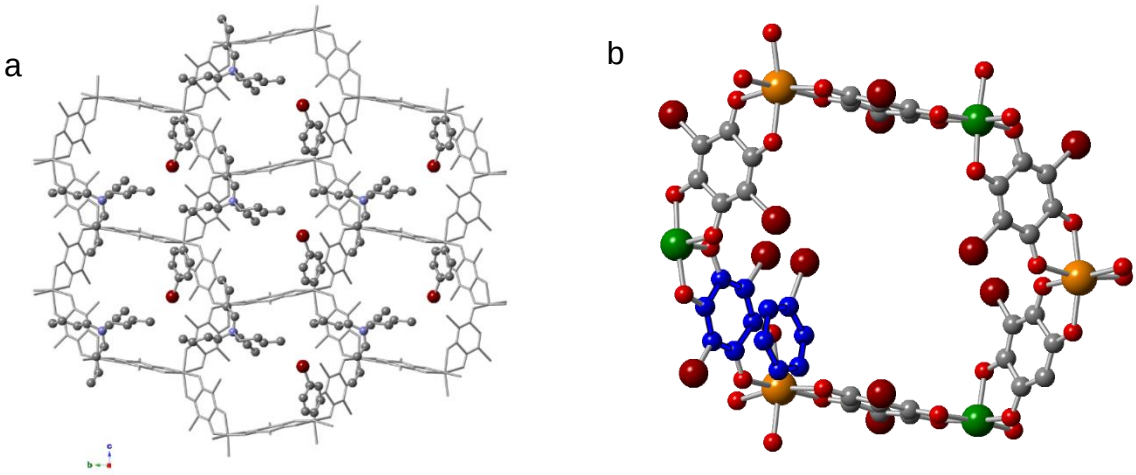

***Figure 3.8**. (**a**) (**a**) View down the a axis of an hexagonal layer with the bromo-benzene molecule and the NBu_4^+ cation in the cavities. **(b)** View of one hexagon showing the $\pi-\pi$ interactions between the bromo-benzene molecules and the aromatic rings of the anilato ligand (in blue)*

***Table 3.4**. Main bond lengths (Å) around the metals centres in **27**.*

Atoms	distance (Å)	Atoms	distance (Å)
Cr(1)-O(23)	1.947(16)	Mn(1)-O(6)	2.157(18)
Cr(1)-O(2)	1.952(16)	Mn(1)-O(25)#1	2.160(18)
Cr(1)-O(3)	1.969(15)	Mn(1)-O(5)	2.166(18)
Cr(1)-O(13)	1.970(16)	Mn(1)-O(15)#2	2.173(18)
Cr(1)-O(12)	1.975(17)	Mn(1)-O(16)#2	2.181(18)
Cr(1)-O(22)	1.983(15)	Mn(1)-O(26)#1	2.213(19)

Symmetry transformations used to generate equivalent atoms: #1 x+1/2,-y+1/2,z 1/2; #2 x-1/2,-y+1/2,z+1/2

***Table 3.5**. Main bond angles (°) around the metals centres in **27**.*

Atoms	angle (°)	Atoms	angle (°)
O(23)-Cr(1)-O(2)	90.8(7)	O(6)-Mn(1)-O(25)#1	165.7(7)
O(23)-Cr(1)-O(3)	93.9(6)	O(6)-Mn(1)-O(5)	74.6(6)
O(2)-Cr(1)-O(3)	82.0(6)	O(25)#1-Mn(1)-O(5)	92.6(7)
O(23)-Cr(1)-O(13)	96.8(6)	O(6)-Mn(1)-O(15)#2	108.2(7)
O(2)-Cr(1)-O(13)	171.7(7)	O(25)#1-Mn(1)-O(15)#2	85.5(7)
O(3)-Cr(1)-O(13)	94.3(6)	O(5)-Mn(1)-O(15)#2	168.9(7)
O(23)-Cr(1)-O(12)	174.6(7)	O(6)-Mn(1)-O(16)#2	94.6(6)
O(2)-Cr(1)-O(12)	92.9(7)	O(25)#1-Mn(1)-O(16)#2	92.7(7)
O(3)-Cr(1)-O(12)	90.4(7)	O(5)-Mn(1)-O(16)#2	94.5(7)
O(13)-Cr(1)-O(12)	79.8(7)	O(15)#2-Mn(1)-O(16)#2	74.7(7)
O(23)-Cr(1)-O(22)	83.2(6)	O(6)-Mn(1)-O(26)#1	99.4(7)
O(2)-Cr(1)-O(22)	92.4(6)	O(25)#1-Mn(1)-O(26)#1	73.7(7)
O(3)-Cr(1)-O(22)	173.7(7)	O(5)-Mn(1)-O(26)#1	89.8(7)
O(13)-Cr(1)-O(22)	91.7(7)	O(15)#2-Mn(1)-O(26)#1	100.1(6)
O(12)-Cr(1)-O(22)	92.7(7)	O(16)#2-Mn(1)-O(26)#1	165.9(7)

Symmetry transformations used to generate equivalent atoms:
#1 x+1/2, y+1/2,z-1/2; #2 x-1/2,-y+1/2,z+1/2.

3.2. X-Ray Powder Diffraction

Compounds **23**-**27** were analysed with XRPD to check the phase purity in the samples using the simulated diffractograms from the solved structures. Unfortunately, sample **23** was very poorly crystalline and we could not compare this sample with the others, although since 23 and 24 are isostructural, we can use sample **24** as a reference. The X-ray powder diffractograms show important similarities in the samples **24**-**26** that suggest that these samples are all isostructural (Figure 3.9) and, therefore, we can assume that samples **25** and **26** present the same structure than compounds **23** and **24**, whose structure has been previously described.

Compound **27** was also checked for phase purity (Figure 3.9). This sample is more crystalline than the other samples and its diffractogram corresponds to the simulated one from the single crystal X-ray structure of compound **27**.

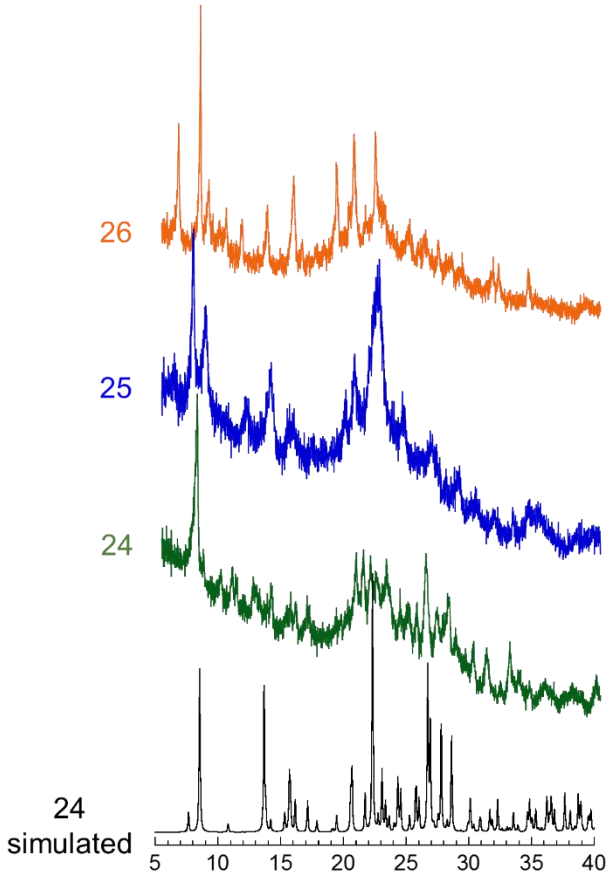

***Figure 3.9**. Experimental and simulated (in black) X-ray powder diffractograms for compounds **24**-**26**.*

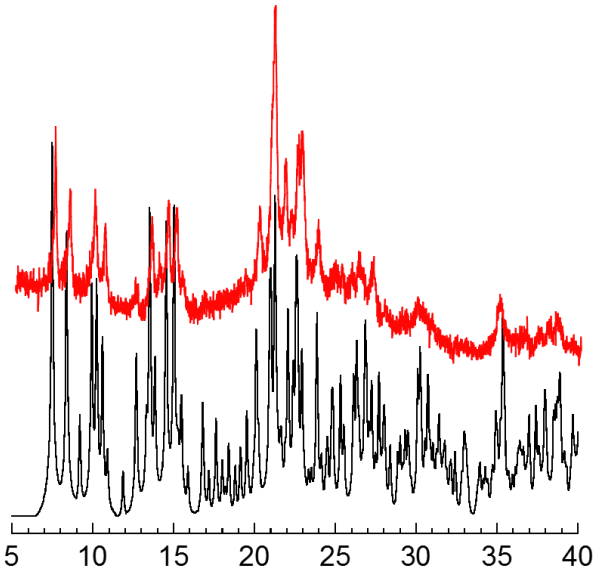

***Figure 3.10**. Experimental and simulated (in black) X-ray powder diffractograms for compound **27**.*

3.3. Magnetic properties

These five different compounds can be separated into two main groups based on their magnetic behaviour: compounds **23** and **27** present a long-range ferrimagnetic ordering at low temperatures due to the antiferromagnetic coupling between the Cr and Mn ions. In contrast, compounds **24-26** present a metamagnetic behaviour with critical fields of ca. 200 mT at 2 K (Table 3.6).

***Table 3.6**. Summary of the magnetic properties of compounds **23**-**27**.*

compound	cation	Solvent	Anilato	Magn. prop.	T_c (K)[2]	H_c (mT)[1]
23	H_3O^+	PhCl	$C_6O_4Cl_2^{2-}$	Ferrimagnetic Order	10.5	90
24	H_3O^+	PhCl	$C_6O_4Br_2^{2-}$	Metamagnetic	3.6	210
25	H_3O^+	PhBr	$C_6O_4Br_2^{2-}$	Metamagnetic	3.6	200
26	H_3O^+	$PhCH_3$	$C_6O_4Br_2^{2-}$	Metamagnetic	3.5	190
27	NBu_4^+	PhBr	$C_6O_4Br_2^{2-}$	Ferrimagnetic Order	9.5	33

[1]*Coercive field (in **23** and **27**) or critical metamagnetic field at 2 K in **24**-**26**.*
[2]*Critical temperature of the antiferromagnetic long range ordering (T_N) in **24**-**26**.*

The ferrimagnetic compounds **23** and **27** show antiferromagnetic (AF) Cr-Mn interactions mediated through the bridging anilato ligands that lead to a long range ferrimagnetic ordering at low temperatures, since the ground spin states of Cr^{III} and Mn^{II} are different (3/2 and 5/2, respectively). This behaviour is typically confirmed by the presence of a minimum at low temperatures in the thermal variation of the magnetic moment (represented as the product of the molar magnetic susceptibility per $Mn^{II}Cr^{III}$ couple times the temperature, $\chi_m T$). Compounds **23** and **27** show $\chi_m T$ values of *ca*. 6.4 cm^3 K mol^{-1} at room temperature, close to the expected value (4.375 + 1.875 = 6.25 cm^3 K mol^{-1}) for a couple of non-interacting Mn^{II} and Cr^{III} ions. When the temperature is lowered, $\chi_m T$ shows a continuous decrease (since the magnetic coupling is antiferromagnetic and the total magnetic moment is reduced as the temperature decreases), reaching a minimum at ca. 16 K for **23** and 18 K for **27** (since the two ground spin states are not fully cancelled), followed by a sharp increase at lower temperatures and a maximum at ca. 10 K for both compounds, suggesting the presence of a long range ferrimagnetic ordering (figures 3.11 and 3.12).

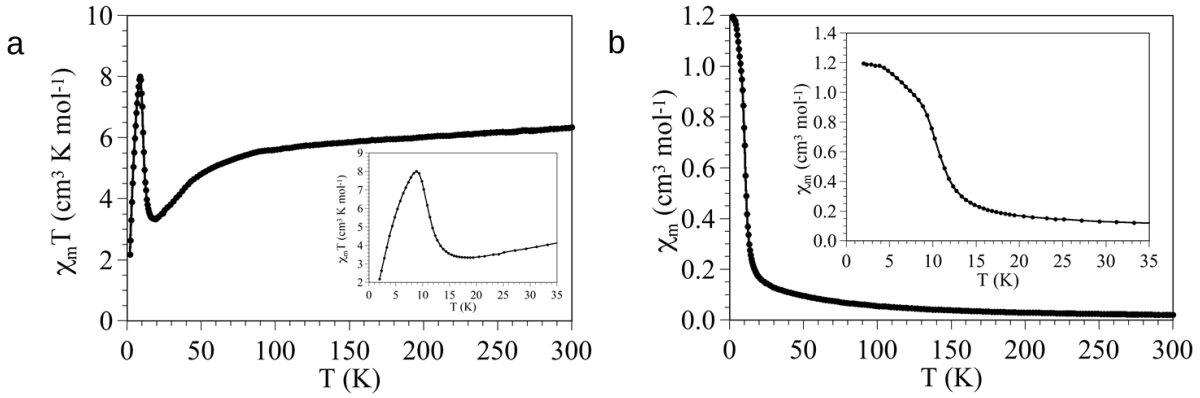

***Figure 3.11**: Thermal variation of $\chi_m T$ **(a)** and χ_m **(b)** for compound **23**. Insets show the low temperature region.*

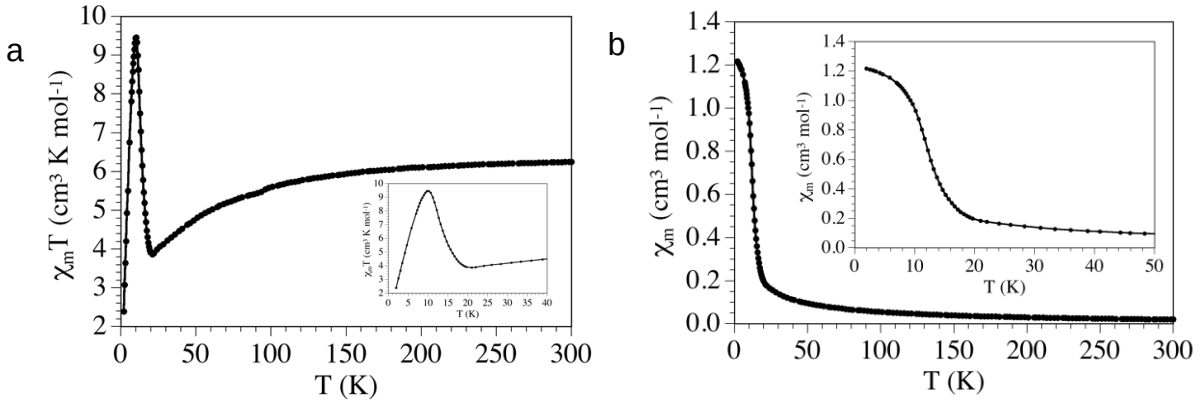

***Figure 3.12**: Thermal variation of $\chi_m T$ **(a)** and χ_m **(b)** for compound **27**. Insets show the low temperature region.*

The thermal variation of χ_m (Figures 3.11 and 3.12) shows a sharp increase for both samples at *ca*. 10-11 K, further suggesting the presence of a long range ferrimagnetic ordering at these temperatures.

Magnetic susceptibility measurements with an oscillating magnetic field at different frequencies in the range of 1-1000 Hz (AC susceptibility) were performed in order to confirm the long range order and obtain a more accurate value for T_c. These measurements show frequency-independent peaks in both, the in phase (χ_m') and out-of-phase (χ_m") susceptibilities in both compounds, confirming the presence of the long range ordering (figures 3.13 and 3.14). Thus, compound **23** shows a peak in χ_m' at *ca*. 10.0 K and a χ_m" signal starting at *ca*.10.5 K that can be considered as T_c (Figure 3.13). In compound **27** the peak in χ_m' is observed at *ca*. 9.0 K and the χ_m"

signal appears at *ca*. 9.5 K. We can, therefore, conclude that compounds **23** and **27** present ferrimagnetic long range ordering at 10.5 and 9.5 K, respectively.

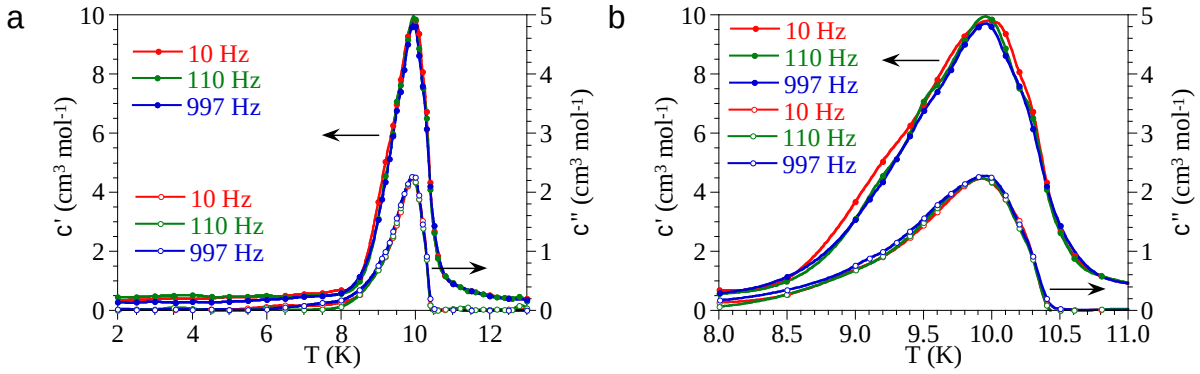

***Figure 3.13**: **(a)** Thermal variation of χ_m' (filled circles, left scale) and χ_m'' (empty circles, right scale) at different frequencies for compound **23**. **(b)** Zoom of the AC peak.*

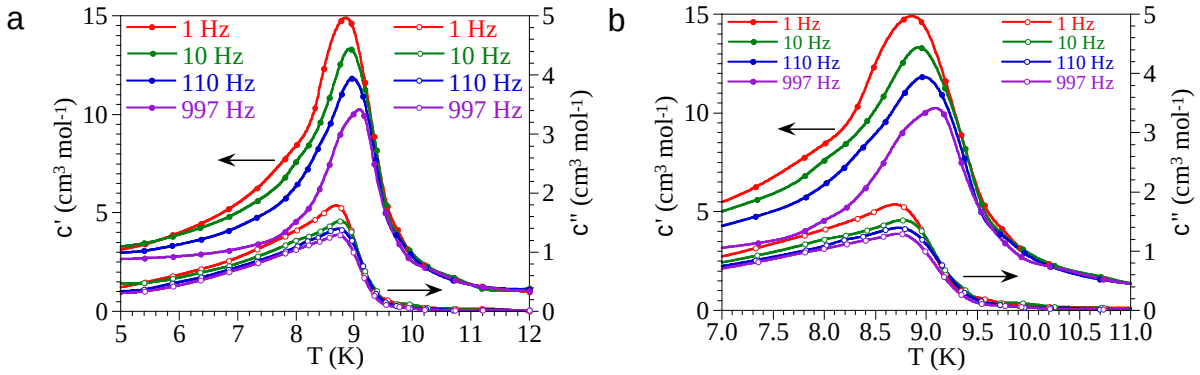

***Figure 3.14**: **(a)** Thermal variation of χ_m' (filled circles, left scale) and χ_m'' (empty circles, right scale) at different frequencies for compound **27**. **(b)** Zoom of the AC peak.*

The ferrimagnetic nature of the coupling in these Mn-Cr compounds is further confirmed by the hysteresis cycles of the isothermal magnetization below the ordering temperature. These measurements show at 2 K saturation values of *ca*. 2 μ_B (Figures 3.15 and 3.16), which is the expected value for a S = 1 resulting from the antiferromagnetic coupling of a Mn(II) ion with S = 5/2 and a Cr(III) ion with S = 3/2. The isothermal magnetization also shows a linear increase even at high fields, further confirming the ferrimagnetic Mn-Cr coupling. These measurements also provide an additional proof of the magnetic ordering presented by these layered materials since both compounds present hysteresis cycles below the ordering temperatures with coercive fields of *ca.* 90 mT (900 G) for compound **23** and 33 mT (330 G) for **27**.

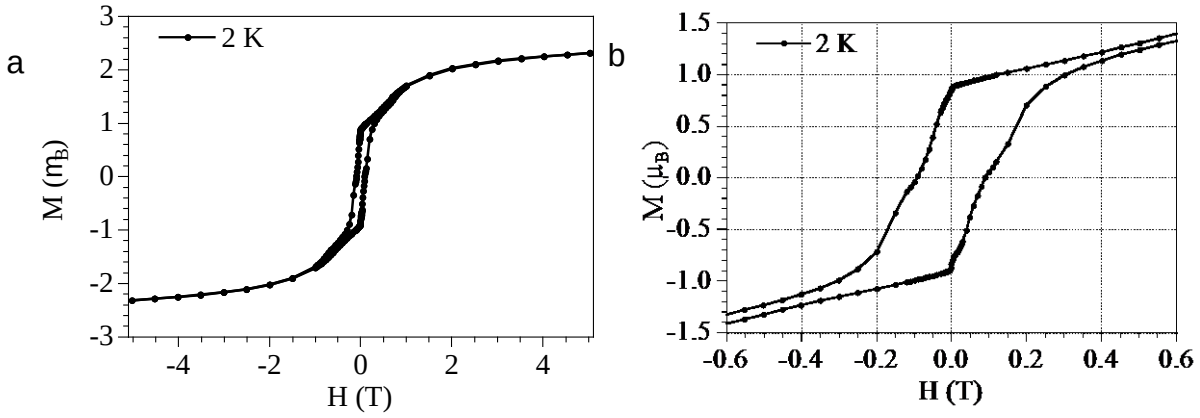

***Figure 3.15**: **(a)** Hysteresis cycle at 2 K for compound **23**. **(b)** Zoom of the low field region.*

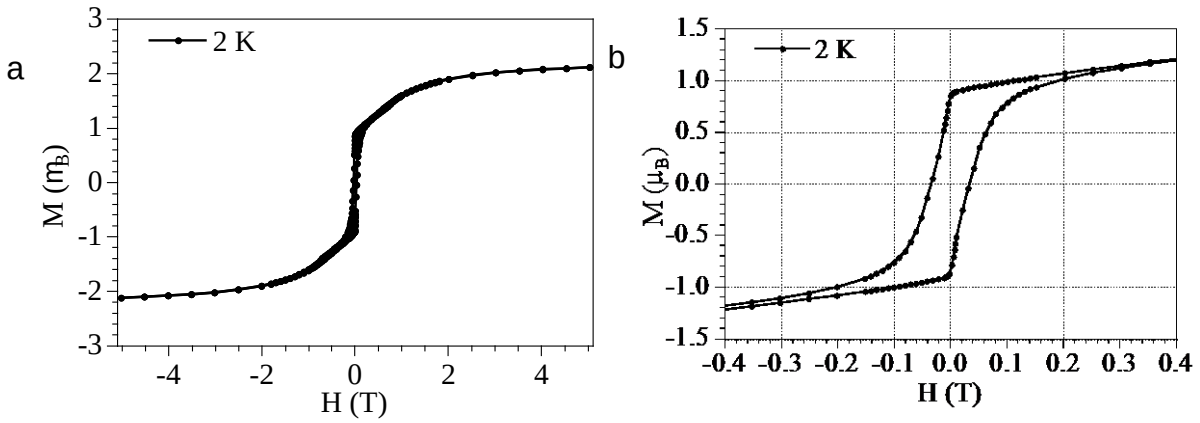

***Figure 3.16**: **(a)** Hysteresis cycle at 2 K for compound **27**. **(b)** Zoom of the low field region.*

On the other side, compounds **24**-**26** show a different behaviour. They all show $\chi_m T$ values at room temperature of *ca*. 6.4-6.5 cm^3 K mol^{-1} (Figure 3.17) in agreement with the expected value for a couple of non-interacting Cr(III) and Mn(II) ions. When the samples are cooled, $\chi_m T$ remains almost constant down to ca. 80 K and below this temperature $\chi_m T$ progressively decreases to reach values of *ca*. 1.7 cm^3 K mol^{-1} at 2 K. This behaviour resembles that observed in compounds **23** and **27** and indicates the presence of an antiferromagnetic Mn-Cr coupling (as observed in compounds **23** and **27**) although in compounds **24**-**26** there are no minima in the $\chi_m T$ plot. A second important difference is the presence of a sharp peak at ca. 3.5 K in the three compounds. This sharp peak is also visible in the χ_m *vs*. T plot at *ca*. 3.5 K (insets in figure 3.17). This peak suggests the presence of an antiferromagnetic long range ordering in compounds **24**-**26** with a T_N of *ca*. 3.5 K.

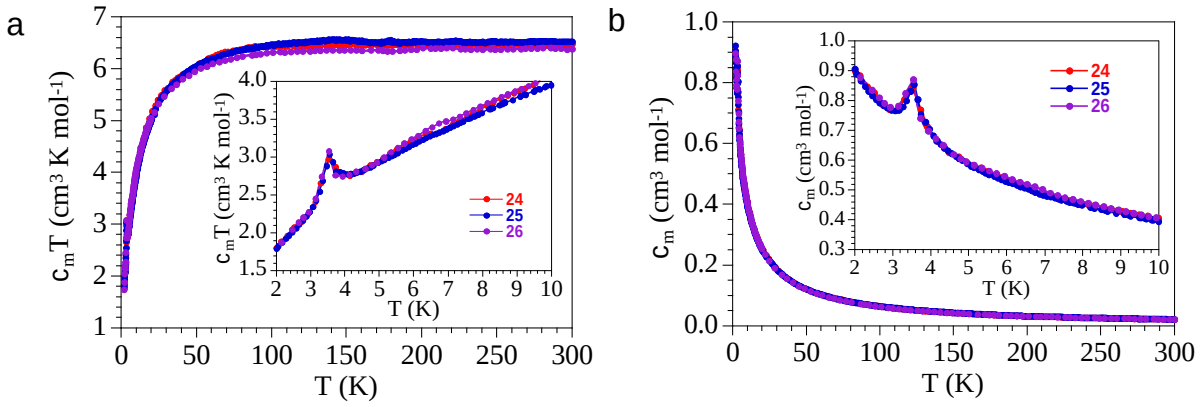

***Figure 3.17**: Thermal variation of $\chi_m T$ **(a)** and χ_m **(b)** for compounds **24**-**26**. Insets shows zooms of the low temperature regions.*

In order to confirm the antiferromagnetic long range ordering we have performed AC susceptibility measurements at different frequencies as well as DC susceptibility measurements with different applied DC fields. AC susceptibility measurements for the three compounds show the presence of a frequency-independent peak at 3.5-3.6 K in the in-phase susceptibility (χ_m') but no signal in the out-of-phase susceptibility (χ_m"), as expected for an antiferromagnetic long range ordering (Figure 3.18). These measurements confirm, therefore, the presence of a long range antiferromagnetic ordering at T_N = 3.5-3.6 K in compounds **24**-**26**. In compound **26** the peak is smoother than in compounds **24** and **25**.

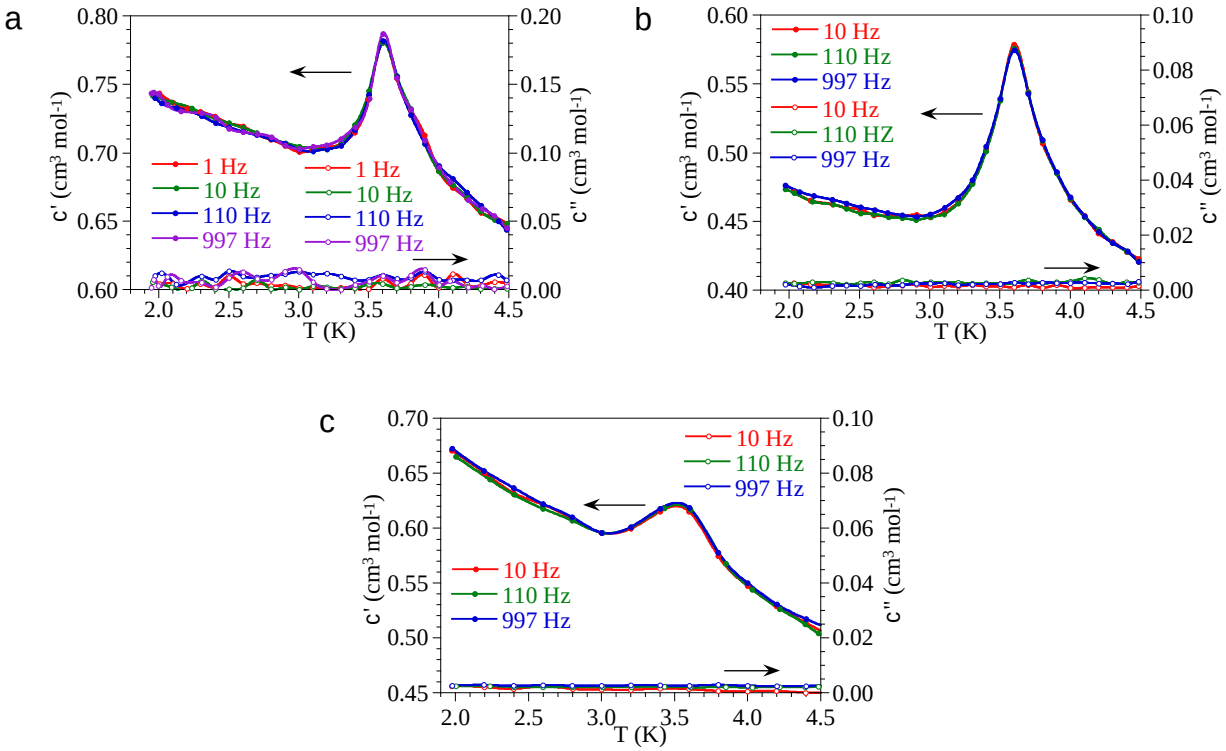

***Figure 3.18**: Thermal variation of χ_m' (filled circles, left scale) and χ_m" (empty circles, right scale) at different frequencies for compounds **24 (a)**, **25 (b)** and **26 (c)**.*

The isothermal magnetization measurements at 2 K further confirm this behaviour. Thus, the magnetization shows in the three compounds a linear increase with the magnetic field and does not reach saturation even at 5 T (Figures 3.19 - 3.21), supporting the antiferromagnetic ordering at 2 K. Interestingly, the isothermal magnetization show a small jump in the magnetization at fields of around 200 mT (2000 G) in the three compounds (210 mT in **24**, 200 mT in **25** and 190 mT in **26**). Furthermore, in compounds **25** and **26** this jump shows a hysteretic behaviour with values of *ca*. 200 and 190 mT in the increasing field scan and *ca*. 150 and 160 mT in the decreasing field scan in **25** and **26**, respectively (Figures 3.20b and 3.21b). Compound **24** shows a softer jump and does not show any noticeable hysteresis in the jump. This behaviour suggest that compounds **24**-**26** behave as metamagnets with critical fields of ca. 200 mT. For fields below ca. 200 mT (2000 G) they show an antiferromagnetic ordering at ca. 3.5 K whereas for fields above ca. 200 mT the antiferromagnetic ordering is cancelled and the compounds are paramagnetic. Since we know that the intra-layer magnetic coupling should result in a ferrimagnetic ordering, we assume that the antiferromagnetic ordering corresponds to a weak

antiferromagnetic interlayer interaction that can be overpassed with a critical magnetic field of *ca*. 200 mT (2000 G) in the three compounds.

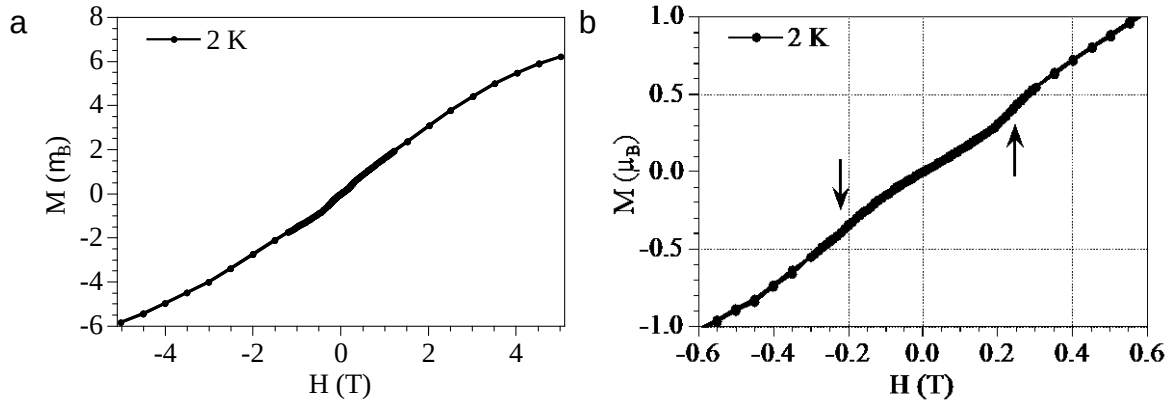

***Figure 3.19**: **(a)** Hysteresis cycle at 2 K for compound **24**. **(b)** Zoom of the low field region. The arrows indicate the jumps observed at ca. 200 mT.*

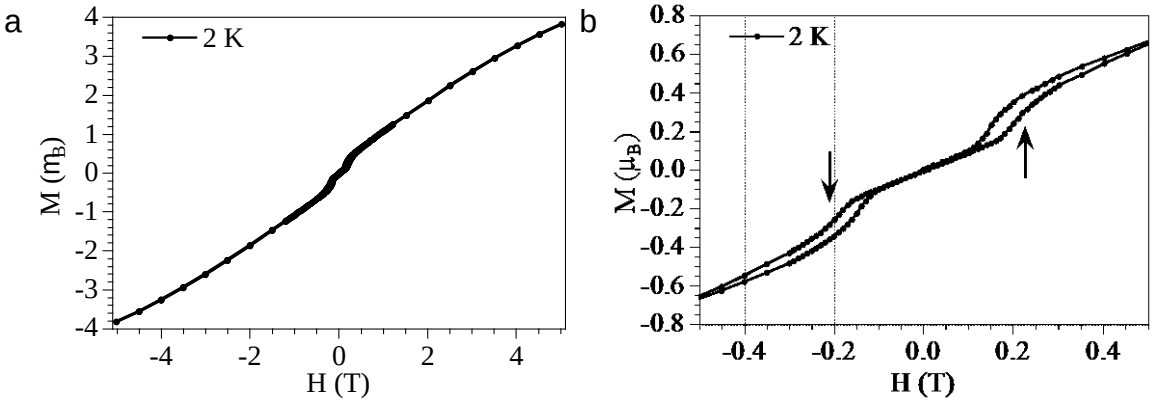

***Figure 3.20**: **(a)** Hysteresis cycle at 2 K for compound **25**. **(b)** Zoom of the low field region. The arrows indicate the jumps observed at ca. 200 mT.*

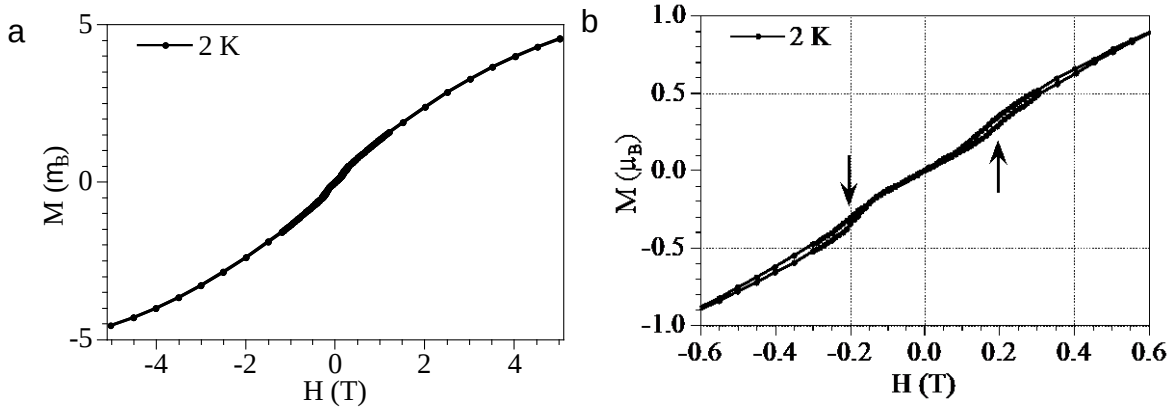

***Figure 3.21**: **(a)** Hysteresis cycle at 2 K for compound **26**. **(b)** Zoom of the low field region. The arrows indicate the jumps observed at ca. 200 mT.*

A further confirmation of this metamagnetic behaviour is provided by the susceptibility measurements with different applied DC magnetic fields above and below the critical field. These measurements show, as expected, that the peak observed in the susceptibility at *ca*. 3.5 K disappears for fields above ca. 200 mT in the three samples (Figure 3.22), confirming the metamagnetic behaviour and the critical field determined from isothermal magnetization measurements at 2 K.

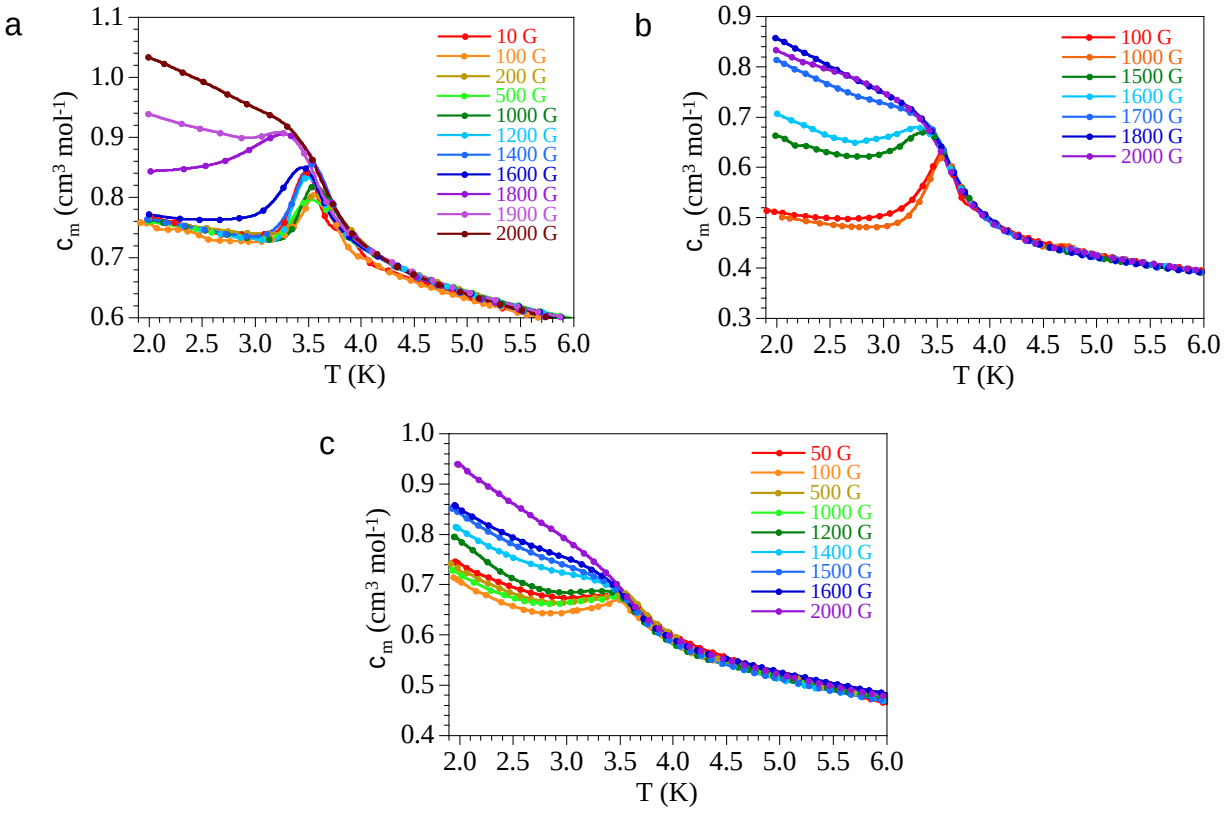

***Figure 3.22**: Thermal variation of χ_m with different applied DC fields for compounds **24 (a)**, **25 (b)** and **26 (c)**.*

The long range ferrimagnetic ordering observed in compounds **23** and **27** is the expected one and has been observed in all the $[MnCr(C_6O_4X_2)_3]^-$ honeycomb lattices prepared to date.[15, 20] The ordering temperatures are also similar to those observed in other $[MnCr(C_6O_4X_2)_3]^-$ lattices and the coercive fields found in compounds **23** and **27** at 2 K (90 and 33 mT, respectively) are within the range observed in the other reported $[MnCr(C_6O_4X_2)_3]^-$ honeycomb lattices (4.5-92 mT).[15, 20]

The most surprising result is the absence of this ferrimagnetic ordering in compounds **24**-**26** (since they present the same $[MnCr(C_6O_4X_2)_3]^-$ honeycomb lattice) and the presence of an antiferromagnetic ordering with a metamagnetic behaviour.

Although, as expected, in compounds **24**-**26** the Cr-Mn magnetic coupling is antiferromagnetic, the absence of a ferrimagnetic ordering has to be attributed to the presence of a weak antiferromagnetic inter-layer coupling that orders antiferromagnetically the layers at *ca*. 3.5 K. This weak antiferromagnetic coupling can be cancelled with magnetic fields above ca. 200 mT in the three samples, resulting in the metamagnetic behaviour observed in the three compounds. If we analyse the structure of compounds **24**-**26** we can observe that these compounds differ from the already reported $[MnCr(C_6O_4X_2)_3]^-$ lattices in the absence of a bulky cation that separates the layers. In the other reported $[MnCr(C_6O_4X_2)_3]^-$ lattices the cations are bulky $[(H_3O)(phz)_3]^+$ units[15] or bulky SCO cations as $[Fe^{III}(sal_2\text{-trien})]^+$, $[Fe^{III}(4\text{-OH-}sal_2\text{-trien})]^+$, $[Fe^{III}(sal_2\text{-epe})]^+$ and $[Fe^{III}(5\text{-Cl-}sal_2\text{-trien})]^+$.[20] In compounds **24**-**26** the negative charge of the layers is neutralized by small H_3O^+ cations and, accordingly, the layers are very close (the interlayer distance is only 6.47 Å in compound **24** and it must be very similar in the other two compounds since they are isostructural). This short distance and the presence of Br atoms in the bromanilato ligands explains the weak antiferromagnetic inter-layer coupling observed in these compounds. In fact, in **24** there is a very short Br···Cl distance of only 3.48(2) Å established between the Br atom of one bromanilato ligand and the Cl atom of the chloro-benzene molecule in the neighbouring layer. This distance is shorter than the sum of the Van der Waals radii of both atoms (1.75 + 1.85 = 3.6 Å). This halogen interaction would be responsible of the weak antiferromagnetic interlayer coupling (and ordering) observed in compounds **24**-**26**. Compound **23** presents the same structure than **24** and the interlayer distance is also very small (6.20 Å) but it contains chloranilato instead of bromanilato as ligand. The change of Br (in **24**-**26**) by Cl (in **23**) reduces the inter-layer coupling (since the Cl orbitals are smaller). Accordingly, we do not observe the antiferromagnetic ordering in **23**. In compound **23** the shortest Cl···Cl distance between a Cl atom of the chloranilato ligand and the chloro-benzene molecule of the neighbouring layer is also short (3.448(4) Å) but this distance is only slightly below the sum of the Van der Waals radii of two Cl atoms (3.5 Å) and, therefore, the magnetic coupling is expected to be weaker. Compound **27** also contains bromanilato as ligand but the bulky NBu_4^+ cations preclude any antiferromagnetic coupling between the layers and, accordingly, compound **27** shows the expected ferrimagnetic ordering. In fact, the distance between consecutive

planes in compound **27** is 8.66 Å, much longer than the distances observed in compounds **23** and **24**.

4. Conclusions and perspectives

In this chapter, we present five different 2D honeycomb compounds based on the anilato ligand with benzene derivatives as template molecules and oxonium or NBu_4^+ as counter-cations: $(H_3O)[MnCr(C_6O_4X_2)_3]\cdot 2PhZ\cdot 6H_2O$; X/Z = Cl/Cl (**23**), Br/Cl (**24**), Br/Br (**25**) and Br/CH_3 (**26**) and $(NBu_4)[MnCr(C_6O_4Br_2)_3]\cdot PhBr\cdot 5H_2O$ (**27**).

The key role of the benzene derivatives as template molecules to achieve 2D eclipsed honeycomb structures with hexagonal channels is clearly proved with compound **27**, since this structure was obtained in an alternated configuration when no template molecules were added.[15] The other compounds are novel since there were no previous examples of 2D anilate-based compounds with oxonium as counter-cations without bulky molecules.

Regarding the magnetic properties of these five compounds, **23** and **27** present ferrimagnetic ordering due to an antiferrimagnetic coupling of the Cr^{III} and Mn^{II} though the anilato ligand-bridge. In contrast, **24**-**26**, present a metamagnetic coupling due to the fact that, although the Cr-Mn magnetic coupling is antiferromagnetic, a weak antiferromagnetic inter-layer coupling prevents the ferrimagnetic ordering. This weak antiferromagnetic coupling can be cancelled with magnetic fields above *ca.* 200 mT in the three samples, resulting in the metamagnetic behaviour observed. This behaviour could be attributed to the absence of bulky cations separating the layers and to the presence of bromanilato ligands that favour the interlayer antiferromagnetic coupling.

Future work include the synthesis of layered compounds with other X and Z groups. In the cases of oxonium as counter-cations, the key role of the X and Z groups in the magnetic behaviour needs to be further studied. Furthermore, for the compounds with oxonium as counter-cation, the possible removal of the water molecules of the channels in order to test the capacity of the channels to reversibly host gas or other solvent molecules is another interesting future task to confirm that these structures may act as MOFs and the possible impact on the magnetic properties triggered by these guest molecules.

5. References

(1) Barea, E.; Montoro, C.; Navarro, J. A. Toxic Gas Removal--Metal-Organic Frameworks for the Capture and Degradation of Toxic Gases and Vapours. *Chem. Soc. Rev.* **2014***, 43*, 5419-5430.

(2) Pang, J.; Jiang, F.; Wu, M.; Liu, C.; Su, K.; Lu, W.; Yuan, D.; Hong, M. A Porous Metal-Organic Framework with Ultrahigh Acetylene Uptake Capacity Under Ambient Conditions. *Nat. Commun.* **2015***, 6*, 7575.

(3) Wang, B.; Cote, A. P.; Furukawa, H.; O'Keeffe, M.; Yaghi, O. M. Colossal Cages in Zeolitic Imidazolate Frameworks as Selective Carbon Dioxide Reservoirs. *Nature* **2008***, 453*, 207-211.

(4) Schoedel, A.; Ji, Z.; Yaghi, O. M. The Role of Metal–organic Frameworks in a Carbon-Neutral Energy Cycle. *Nature Energy* **2016***, 1*, 16034.

(5) Canivet, J.; Fateeva, A.; Guo, Y.; Coasne, B.; Farrusseng, D. Water Adsorption in MOFs: Fundamentals and Applications. *Chem. Soc. Rev.* **2014***, 43*, 5594-5617.

(6) Kreno, L. E.; Leong, K.; Farha, O. K.; Allendorf, M.; Van Duyne, R. P.; Hupp, J. T. Metal-Organic Framework Materials as Chemical Sensors. *Chem. Rev.* **2012***, 112*, 1105-1125.

(7) Liu, D.; Lu, K.; Poon, C.; Lin, W. Metal-Organic Frameworks as Sensory Materials and Imaging Agents. *Inorg. Chem.* **2014***, 53*, 1916-1924.

(8) Nandasiri, M. I.; Jambovane, S. R.; McGrail, B. P.; Schaef, H. T.; Nune, S. K. Adsorption, Separation, and Catalytic Properties of Densified Metal-Organic Frameworks. *Coord. Chem. Rev.* **2016***, 311*, 38-52.

(9) Wang, S.; Wang, X. Multifunctional Metal-Organic Frameworks for Photocatalysis. *Small* **2015***, 11*, 3097-3112.

(10) Hu, Z.; Deibert, B. J.; Li, J. Luminescent Metal-Organic Frameworks for Chemical Sensing and Explosive Detection. *Chem. Soc. Rev.* **2014***, 43*, 5815-5840.

(11) Wang, L.; Han, Y.; Feng, X.; Zhou, J.; Qi, P. Metal–organic Frameworks for Energy Storage: Batteries and Supercapacitors. *Coord. Chem. Rev.* **2016***, 307*, 361-381.

(12) Furukawa, H.; Cordova, K. E.; O'Keeffe, M.; Yaghi, O. M. The Chemistry and Applications of Metal-Organic Frameworks. *Science* **2013***, 341*, 1230444.

(13) So, M. C.; Wiederrecht, G. P.; Mondloch, J. E.; Hupp, J. T.; Farha, O. K. Metal-Organic Framework Materials for Light-Harvesting and Energy Transfer. *Chem. Commun.* **2015***, 51*, 3501-3510.

(14) Horcajada, P.; Gref, R.; Baati, T.; Allan, P. K.; Maurin, G.; Couvreur, P.; Férey, G.; Morris, R. E.; Serre, C. Metal-Organic Frameworks in Biomedicine. *Chem. Rev.* **2012***, 112*, 1232-1268.

(15) Atzori, M.; Benmansour, S.; Mínguez Espallargas, G.; Clemente-León, M.; Abhervé, A.; Gómez-Claramunt, P.; Coronado, E.; Artizzu, F.; Sessini, E.; Deplano, P.; Serpe, A.; Mercuri, M. L.; Gómez García, C. J. A Family of Layered Chiral Porous Magnets Exhibiting Tunable Ordering Temperatures. *Inorg. Chem.* **2013***, 52*, 10031-10040.

(16) Bain, G. A.; Berry, J. F. Diamagnetic Corrections and Pascal's Constants. *J. Chem. Educ.* **2008***, 85*, 532-536.

(17) Altomare, A.; Burla, M. C.; Camalli, M.; Cascarano, G. L.; Giacovazzo, C.; Guagliardi, A.; Moliterni, A. G. G.; Polidori, G.; Spagna, R. SIR97: A New Tool for Crystal Structure Determination and Refinement. *J. Appl. Cryst.* **1999***, 32*, 115-119.

(18) Sheldrick, G. M. Crystal Structure Refinement with SHELXL. *Acta Cryst. C* **2015***, 71*, 3-8.

(19) Farrugia, L. J. WinGX Suite for Small-Molecule Single-Crystal Crystallography. *J. Appl. Cryst.* **1999***, 32*, 837-838.

(20) Abhervé, A.; Clemente-León, M.; Coronado, E.; Gómez-García, C. J.; Verneret, M. One-Dimensional and Two-Dimensional Anilate-Based Magnets with Inserted Spin-Crossover Complexes. *Inorg. Chem.* **2014***, 53*, 12014-12026.

(21) Benmansour, S.; Coronado, E.; Giménez-Saiz, C.; Gómez-García, C. J.; Rößer, C. Metallic Charge-Transfer Salts of Bis(Ethylenedithio)Tetrathiafulvalene with Paramagnetic Tetrachloro(Oxalato)Rhenate(IV) and Tris(Chloranilato)Ferrate(III) Anions. *Eur. J. Inorg. Chem* **2014***, 2014*, 3949-3959.

(22) Benmansour, S.; Valles-García, C.; Gómez-Claramunt, P.; Minguez Espallargas, G.; Gómez-García, C. J. 2D and 3D Anilato-Based Heterometallic M(I)M(III) Lattices: The Missing Link. *Inorg. Chem.* **2015***, 54*, 5410-5418.

(23) Janiak, C. A Critical Account on π–π Stacking in Metal Complexes with Aromatic Nitrogen-Containing Ligands. *J. Chem. Soc. , Dalton Trans.* **2000**, 3885-3896.

(24) Abhervé, A.; Mañas-Valero, S.; Clemente-León, M.; Coronado, E. Graphene Related Magnetic Materials: Micromechanical Exfoliation of 2D Layered Magnets Based on Bimetallic Anilate Complexes with Inserted $[Fe^{III}(Acac_2\text{-Trien})]^+$ and $[Fe^{III}(Sal_2\text{-Trien})]^+$ Molecules. *Chem. Sci.* **2015***, 6*, 4665-4673.

(25) Abherve, A.; Clemente-Leon, M.; Coronado, E.; Gómez-García, C. J.; Verneret, M. One-Dimensional and Two-Dimensional Anilate-Based Magnets with Inserted Spin-Crossover Complexes. *Inorg. Chem.* **2014***, 53*, 12014-12026.

(26) Benmansour, S.; Gómez-García, J. C. A Heterobimetallic Anionic 3,6-Connected 2D Coordination Polymer Based on Nitranilate as Ligand. *Polymers* **2016***, 8*, 89.

(27) Atzori, M.; Artizzu, F.; Sessini, E.; Marchio, L.; Loche, D.; Serpe, A.; Deplano, P.; Concas, G.; Pop, F.; Avarvari, N.; Mercuri, M. L. Halogen-Bonding in a New Family of tris(haloanilato)metallate(III) Magnetic Molecular Building Blocks. *Dalton Trans.* **2014***, 43*, 7006-7019.

(28) Atzori, M.; Artizzu, F.; Marchio, L.; Loche, D.; Caneschi, A.; Serpe, A.; Deplano, P.; Avarvari, N.; Mercuri, M. L. Switching-on Luminescence in Anilate-Based Molecular Materials. *Dalton Trans.* **2015***, 44*, 15786-15802.

(29) Benmansour, S.; Gómez-Claramunt, P.; Vallés-García, C.; Mínguez Espallargas, G.; Gómez-García, C. J. Key Role of the Cation in the Crystallization of Chiral Tris(Anilato)Metalate Magnetic Anions. *Cryst. Growth Des.* **2016***, 16*, 518-526.

Chapter 4

Lanthanoid compounds based on the anilato ligand: the key role of the solvents

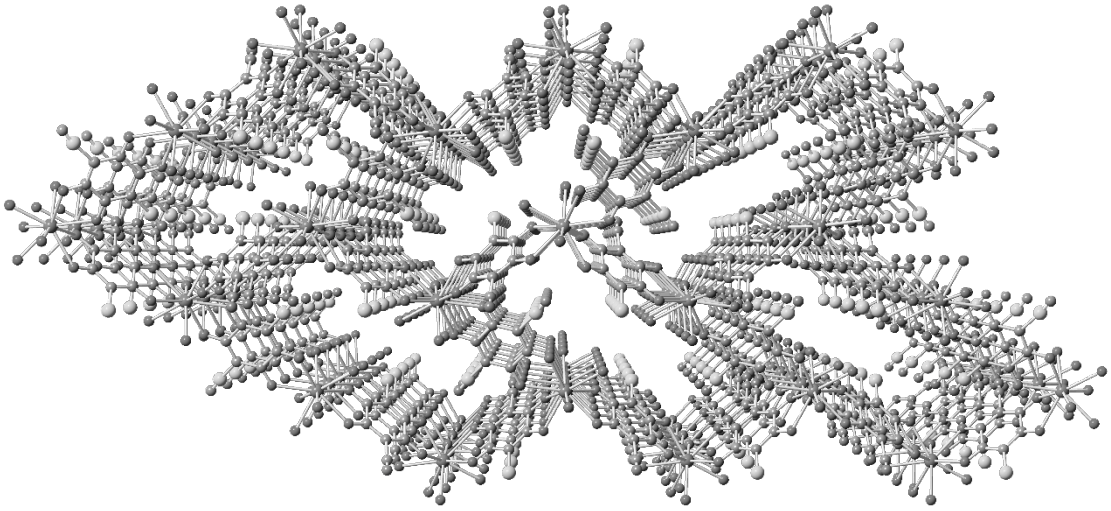

1. Introduction

The 2-chloro-5-cyano-3,6-dihydroxybenzoquinone (X = Cl, X' = CN, Scheme 1) is a quinoide-based ligand with photoluminescent properties in solid state[1] and in solution.[2] This functional ligand may be useful, not only to synthesize the equivalent 2D molecular magnets and extend their T_c range, but also to add an extra functionality, opening the door to the preparation of molecular materials combining three different properties such as magnetic ordering (provided by the combination of metals), luminescence (provided by the ligand) and a third functionality such as SCO[3], SMM[4], porosity[5]… provided by the cation inserted in between the layers.

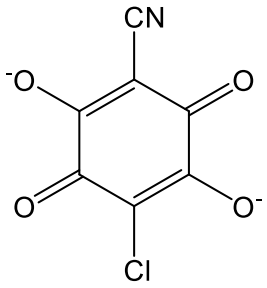

***Scheme 4.1**: 2-chloro-5-cyano-3,6-dihydroxybenzoquinone ligand.*

In this chapter we study the luminescence of the 2-chloro-5-cyano-3,6-dihydroxy-benzoquinone ligand combined with trivalent lanthanide ions. Publications based on lanthanide ions have increased widely in the past few years due to their structural versatility[6] and their potential to form luminescent compounds.[7] These ions are characterized by the availability of the 4f orbitals, from $4f^0$ to $4f^{14}$ (from La^{+3} to Lu^{+3}). This configuration results in a long range of electronic energy levels that can give rise to luminescent properties[8-14] and also interesting magnetic properties.[15-17]

Nevertheless, due to the partly-forbidden f-f transitions, the direct excitation of the lanthanide ions does not lead to a strong luminescence by itself. A solution to this drawback is the use of "antennas" (also known as luminescence sensitizers) that act absorbing the incident light and transferring this excitation to one of the excited states of the lanthanide metal by intramolecular transfer and, finally, if there is no quenching process, luminescence is produced.

In contrast to most luminescent compounds, the emission arising from the rare earth ions essentially depends on the energy levels of the ion,[18] and it is rather independent of the environment. The reason is intrinsic to the electronic structure of the lanthanides family, characterized by internal 4f orbitals. In the lanthanides the light emission occurs due to transitions inside the 4f shell, f-f transitions.[19] In contrast to transition metals, where conduction electrons at the d orbitals are exposed to the electronic screening of the first and second coordination spheres, in the case of lanthanides the 4f shell is well shielded by “closed” 5s and 5p orbitals, and thus spectral diffusion due to surrounding charges is dramatically prevented. This also applies to ions forming coordination compounds and supramolecular complexes. As a result, in those complexes the role of ligands is more related to the recombination dynamics. Ligands enable additional de-activation pathways without influencing the energy levels of the 4f shields. Thanks to that, the ion emission can be improved by tailoring the energy splitting with respect to the surrounding molecules. This is the so-called antenna effect (or sensitization).[10] This strategy consists on taking advantage of the intense absorption bands of organic chromophores to increase the energy transfer to the lanthanide ions via intramolecular de-activation pathways.

The viability as a luminescent sensitizer of the heterosubstituted chlorocyananilato ligand will be tested in this chapter using different lanthanide ions and different solvents coordinated to these ions. The key role of the solvent in these compounds will be analysed from both structural and luminescent points of view. In this chapter, four lanthanide-based compounds are presented. Two of them are Praseodymium-based compounds with formulas $[Pr_2(C_6O_4(CN)Cl)_3(DMF)_3]$ (**28**) and $[Pr_2(C_6O_4(CN)Cl)_3(DMSO)_6]$ (**29**). The other two are the Ytterbium-based compounds $[Yb_2(C_6O_4(CN)Cl)_3(DMSO)_4]\cdot 2H_2O$ (**30**) and $[(H_3O)K][Yb_2(C_6O_4(CN)Cl)_3(\mu\text{-}OH)_2]$ (**31**). Their structural, magnetic and luminescent properties will be discussed.

2. Experimental section

2.1. Synthesis

General Remarks: All the reagents and solvents were commercially available and used as received, without further purification.

Synthesis of $K_2(C_6O_4(CN)Cl)$: An aqueous solution of KOH 6 M (7.5 mL) was slowly added under stirring to an aqueous solution (37.5 mL) of 2,3-dicyano-5,6-dichloro-1,4-benzoquinone (1.25 g, 5.5 mmol). The resulting solution was concentrated at 60 °C to half of the initial volume. The resulting solution was kept 48 hours at 4 °C, resulting in a red microcrystalline powder that was filtered and washed with a 3 M KOH aqueous solution and acetone.

Synthesis of $[Pr_2(C_6O_4(CN)Cl)_3(DMF)_6]$ (28): A solution of $Pr(NO_3)_3{\cdot}6H_2O$ (4.35 mg, 0.01 mmol) in 2.5 mL of MeOH was carefully layered on top of a solution of $K_2(C_6O_4(CN)Cl)$ (4.14 mg, 0.015 mmol) in 2.5 mL of DMF and left to stand at room temperature. After two weeks, red prismatic crystals suitable for X-Ray diffraction were collected.

Synthesis of $[Pr_2(C_6O_4(CN)Cl)_3(DMSO)_6]$ (29): A solution of $Pr(NO_3)_3{\cdot}6H_2O$ (4.35 mg, 0.01 mmol) in 2.5 mL of MeOH was carefully layered on top of a solution of $K_2(C_6O_4(CN)Cl)$ (4.14 mg, 0.015 mmol) in 2.5 mL of DMSO and left to stand at room temperature. After ten days, red block crystals suitable for X-Ray diffraction were collected.

Synthesis of $[Yb_2(C_6O_4(CN)Cl)_3(DMSO)_4]{\cdot}2H_2O$ (30): A solution of $Yb(NO_3)_3{\cdot}5H_2O$ (4.5 mg, 0.01 mmol) in 2.5 mL of MeOH was carefully layered on top of a solution of $K_2(C_6O_4(CN)Cl)$ (4.14 mg, 0.015 mmol) in 2.5 mL of DMSO and left to stand at room temperature. After ten days, red block crystals suitable for X-Ray diffraction were collected.

Synthesis of $[(H_3O)K][Yb_2(C_6O_4(CN)Cl)_3(\mu\text{-}OH)_2]$ (31): A solution of $Yb(NO_3)_3{\cdot}5H_2O$ (4.5 mg, 0.01 mmol) in 2.5 mL of MeOH was carefully layered on top of a solution of $K_2(C_6O_4(CN)Cl)$ (4.14 mg, 0.015 mmol) in 2.5 mL of H_2O and left to

stand at room temperature. After three weeks, red plate crystals suitable for X-Ray diffraction were collected.

2.2. Structural Characterization

Suitable single crystals of compounds **28**-**31** were mounted on a loop using a viscous hydrocarbon oil and transferred directly to the cold nitrogen stream for data collection. X-ray data were collected at 120 K for all compounds on a Supernova diffractometer equipped with a graphite-monochromated Enhance (Mo) X-ray Source (λ = 0.71073 Å). The program CrysAlisPro, Agilent Technologies Ltd., was used for unit cell determinations and data reduction. Empirical absorption correction was performed using spherical harmonics, implemented in the SCALE3 ABSPACK scaling algorithm. Crystal structures were solved by direct methods with the Shelxt and refined against all F^2 values with the SHELXL-2014 program,[21] using the WinGX2014.1 graphical user interface.[22] All non-hydrogen atoms were refined anisotropically and hydrogen atoms were placed in calculated positions and refined isotropically with a riding model. Data collection and refinement parameters are given in Table 4.1.

The X-ray powder diffractograms were collected for polycrystalline samples of all the compounds using a 0.5 mm glass capillary that was mounted and aligned on a Empyrean PANalytical powder diffractometer, using Cu$K\alpha$ radiation (λ = 1.54177 Å) operating at 40 mA and 45 kV. A total of 3 scans were collected at room temperature in the 2θ range of 2-40º with a step size of 0.0131º.

2.3. Physical Properties

Magnetic measurements were performed with a Quantum Design MPMS-XL-5 SQUID magnetometer in the temperature range of 2-300 K with applied magnetic fields of 0.1 or 0.5 T on polycrystalline samples of all the compounds. Susceptibility data were corrected for the sample holder and for the diamagnetic contribution of the salts using Pascal's constants.[23]

2.4. Luminescent Properties

The luminescence measurements have been carried out holding the samples in a positioning stage with micrometer resolution and exciting the sample with an Ar laser using the 488 nm (visible) and 364 nm (ultraviolet) lines in continuous wave operation. Both lasers were aligned on the same optical path, so they could be consecutively used at the same measuring point. The excitation was focused using a large focal length microscope objective driving to a spot size of few micrometers. A beam splitter was employed to collect the luminescence using the same objective (back-scattering configuration). The collected light was dispersed by a 1 m focal length spectrograph, and detected with a silicon detector.

3. Result and discussion

3.1. X-Ray Diffraction

We have solved the X-ray crystal structure of the four compounds presented in this chapter. These four compounds contain the asymmetric 2-chloro-5-cyano-3,6-dihydroxybenzoquinone and either Pr(III) or Yb(III) and can be formulated as: $[Pr_2(C_6O_4(CN)Cl)_3(DMF)_6]$ **(28)**, $[Pr_2(C_6O_4(CN)Cl)_3(DMSO)_6]$ **(29)**, $[Yb_2(C_6O_4(CN)Cl)_3(DMSO)_4]\cdot 2H_2O$ **(30)** and $[(H_3O)K][Yb_2(C_6O_4(CN)Cl)_3(\mu\text{-}OH)_2]$ **(31)**. The data collection and refinement parameters of these four compounds are given in Table 4.1.

Structure of $[Pr_2(C_6O_4(CN)Cl)_3(DMF)_6]$ (28). This compound crystallizes in the monoclinic P21*/n* space group. The asymmetric unit contains one praseodymium ion, one and a half anilato ligands and three DMF molecules coordinated to the Pr(III) ion, giving rise to the extended formula $[Pr_2(C_6O_4(CN)Cl)_3(DMF)_6]$. The coordination environment around the Pr(III) ions and the labelling scheme is displayed in Figure 4.1.

***Table 4.1**. Crystallographic data for compounds **1**-**4**.*

	28	**29**	**30**	**31**
Empirical formula	$C_{39}H_{42}Cl_3N_9O_{18}Pr_2$	$C_{33}H_{36}Cl_3N_3O_{18}S_6Pr_2$	$C_{29}H_{28}Cl_3N_3O_{18}S_4Yb_2$	$C_{21}H_7Cl_3N_3O_{16}Yb_2K$
Formula weight (g/mol)	1312.98	1343.21	1287.24	1048.86
Temperature K	120(2)	120(2)	120(2)	120(2)
Wavelength (Å)	0.71073	0.71073	0.71073	0.71073
Crystal system	Monoclinic	Monoclinic	Triclinic	Monoclinic
Space group	*P* $2_1/n$	*P* $2_1/n$	*P* -1	*C* 2/*m*
a (Å)	10.6585(10)	9.6262(3)	9.9354	10.3502(8)
b(Å)	13.7163(10)	16.3853(4)	10.6195	16.3660(5)
c(Å)	18.3196(14)	15.3240(4)	10.7752	10.1654(5)
α (°)	90	90	112.010	90
β (°)	98.863	91.765	93.135	109.567
γ (°)	90	90	95.19	90
V ($Å^3$)	2646.3(4)	2415.88(11)	1044.39(7)	1622.49(17)
ρ_{cal} (mg m^{-3})	1.633	1.797	2.021	2.329
μ (mm^{-1})	2.045	2.488	4.916	6.200
Crystal size (mm^3)	0.08x0.05x0.02	0.06x0.05x0.02	0.09x0.08x0.03	0.15x0.08x0.01
θ range (°)	2.808-25.136	2.761-25.067	3.048-25.033	3.274-25.019
Reflections collected	35858	3830	11481	4739
Independent reflections (R_{int})	4705 (0.0898)	4278 (0.1180)	3682 (0.0594)	1488 (0.0400)
Reflec used in refinement, *n*	4705	4278	3682	1488
$R_1(F)$,[a] $I > 2\sigma(I)$	0.0442	0.0606	0.0394	0.0384
$wR_2(F^2)$,[b] all data	0.1139	0.1497	0.1010	0.0986
$S(F^2)$,[c] all data	1.052	1.067	1.071	1.101
Largest diff. peak	1,616	1,419	1,775	2,918
Largest diff. hole	-0,865	-1,004	-1,100	-1,334

[a]$R1(F) = \Sigma||F_O|-|F_C||/\Sigma|F_O|$; [b]$wR2(F^2) = [\Sigma w(F_O^2-F_C^2)^2/\Sigma wF_O^4]^{1/2}$; [c]$S(F^2) = [\Sigma w(F_O^2-F_C^2)^2/(n+r-p)]^{1/2}$

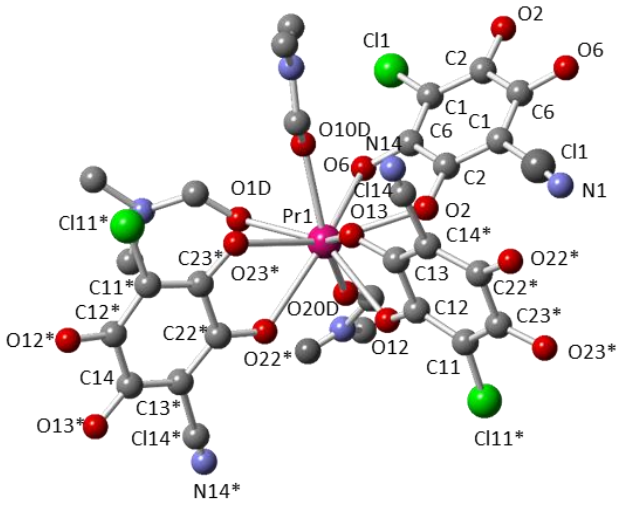

Figure 4.1: *Coordination environment of the Pr(III) ions in compound* ***28*** *showing the labelling scheme. Colour code: Pr = pink, C = grey, O = red, N = blue, Cl = light green. H atoms have been omitted for clarity.*

The structure of this compound consists of neutral layers (Figure 4.2a) with the classical (6,3)-topology (Figure 4.2b) where each metal ion is connected to three other metal atoms through bridging anilato ligands forming rings containing six metal atoms (Figure 4.3a). The six-membered rings present a rectangular geometry resulting from a large distortion of the hexagons. Four of the six anilato ligands that constitute the sides of the distorted hexagons are located with the anilato plane almost orthogonal to the plane of the hexagon ("edge on" orientation, E) and the other two with the anilato plane almost parallel to the hexagon plane ("face on" orientation, F). This particular (4E-2F) orientation gives rise to the large distortions leading to a rectangular lattice (although with the same 6,3-topology) rather than the well known hexagonal honeycomb layers, previously observed in other anilato compounds.[24, 25] The rectangles present a spike-like disposition: the rectangles are located in parallel rows with orthogonal orientations between the rectangles of consecutive rows (Figure 4.2b).

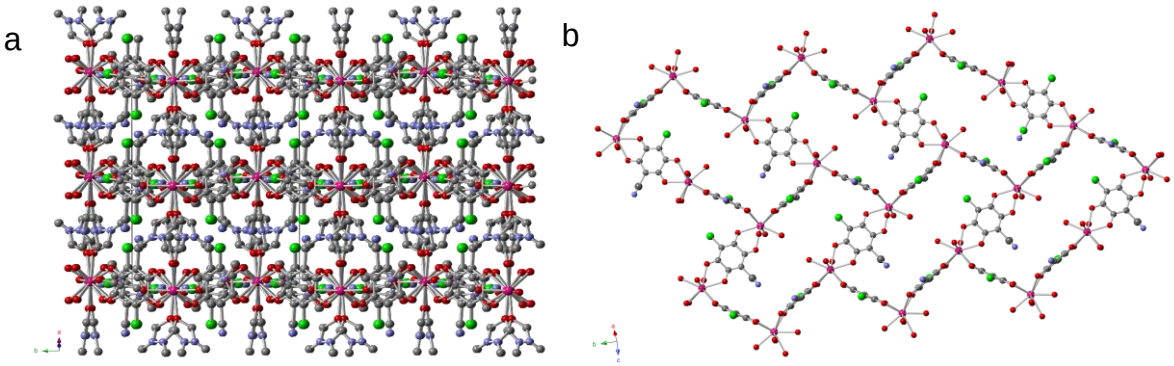

Figure 4.2: *structure of compound* ***28****.* ***(a)*** *Side view of the layers.* ***(b)*** *View of one layer showing the spike-like disposition of the rectangular cavities.*

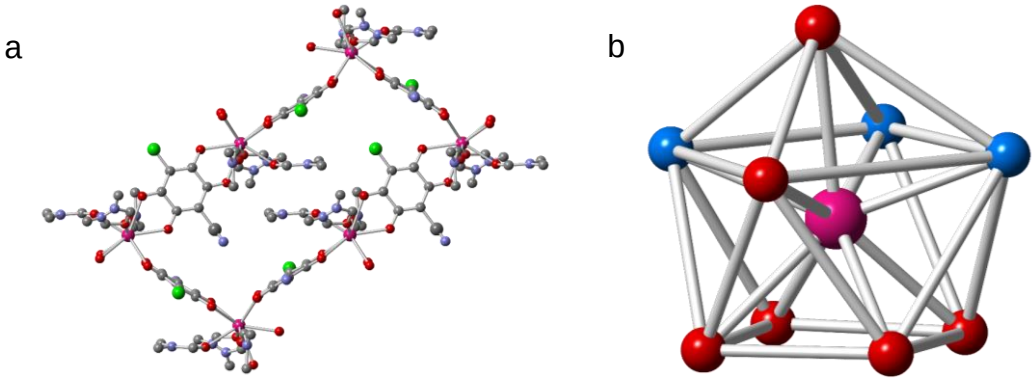

Figure 4.3: *structure of compound* ***28****.* ***(a)*** *View of one rectangular cavity.* ***(b)*** *mono-capped square anti-prism geometry of the nona-coordinated Pr(III) ion.*

The Pr(III) ions are nona-coordinated with six oxygen atoms coming from three chelating anilato ligands (in red in figure 4.3b) and three oxygen atoms from the three coordinated DMF molecules (in blue in figure 4.3b). The Pr ions have a mono-capped square anti-prism coordination geometry (figure 4.3b), where the three DMF molecules occupy positions in the same square face. The main Ln-O bond distances for this compound are listed in table 4.2.

Table 4.2. *Main Ln-O bond distances for compound* ***28****.*

Atoms	distance (Å)	Atoms	distance (Å)
Pr(1)-O(10D)	2.425(4)	Pr(1)-O(22)	2.518(4)
Pr(1)-O(20D)	2.436(5)	Pr(1)-O(12)	2.521(4)
Pr(1)-O(1D)	2.468(4)	Pr(1)-O(23)	2.568(4)
Pr(1)-O(2)	2.507(4)	Pr(1)-O(6)	2.588(4)
Pr(1)-O(13)	2.507(4)		

The large deviation from 120º of the three different Pr-Pr-Pr angles, inside the six-membered rings, (101.06º, 78.11º and 170.68º) clearly show the large distortion of the cavity from the hexagonal geometry (Figure 4.4a). The sum of the deviations of the three angles from the ideal value of 120° is 111.51º. The rectangular layers are packed in an eclipsed way, giving rise to rectangular channels filled by DMF molecules (Figure 4.4b).

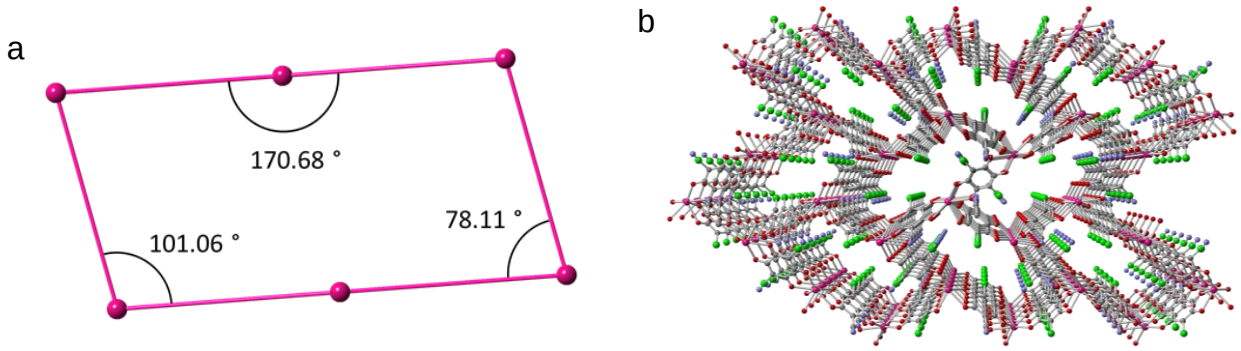

Figure 4.4: (a) *View of a rectangular cavity in compound* ***28*** *showing the three different Pr-Pr-Pr angles. Only the positions of the Pr(III) ions have been drawn* ***(b)*** *View of the rectangular channels along the b axis in compound* ***28****. DMF molecules and H atoms are omitted for clarity*

Structure of $[Pr_2(C_6O_4(CN)Cl)_3(DMSO)_6]$ (29): This compound crystallizes in the same monoclinic $P2_1/n$ group than compound **1** although the structures are quite different. The asymmetric unit of **29** contains one praseodymium ion, one and a half anilato ligand and three DMSO molecules coordinated to the Pr(III) ion, giving rise to the formula $[Pr_2(C_6O_4(CN)Cl)_3(DMSO)_6]$. The coordination environment around the Pr(III) ions and the labelling scheme are displayed in Figure 4.5.

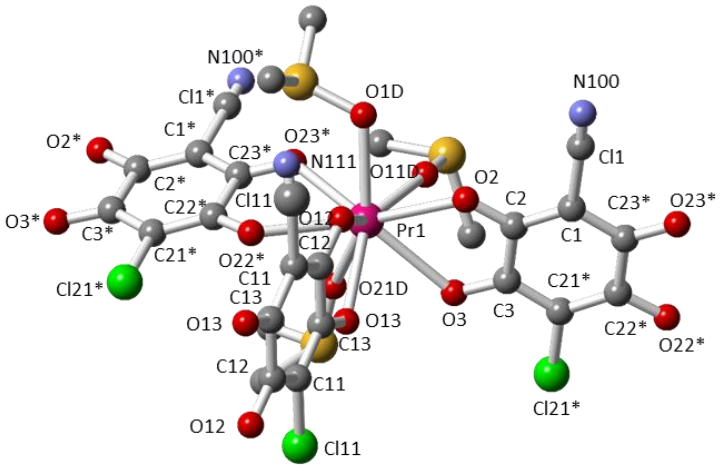

Figure 4.5: *Coordination environment of the Pr(III) ions in compound **29** showing the labelling scheme. Colour code: Pr = pink, C = grey, O = red, N = blue, Cl = light green, S = yellow. H atoms have been omitted for clarity.*

The structure of this compound is formed by neutral corrugated layers (Figure 4.6a) where each metal ion is connected to three other metal atoms through bridging anilato ligands forming rings containing six metal atoms with a very distorted hexagonal geometry. The Pr(III) ions are located on the vertex of the hexagons and the anilato ligands on the edges, giving rise to the a distorted honeycomb lattice with a 6,3 topology (Figure 4.6b). These distorted hexagonal rings present two “edge-on” and four “face-on” oriented anilato ligands, giving rise to a 2E-4F disposition of the anilato ligands (Figure 4.7a), in contrast to the 4E-2F disposition observed in **28**.

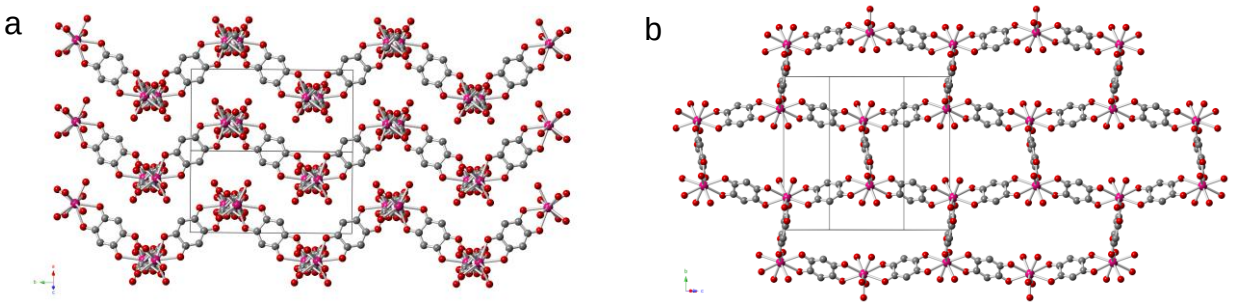

Figure 4.6: *structure of compound* ***29****.* ***(a)*** *Side view of the corrugated layers.* ***(b)*** *View of the distorted hexagonal cavities in the direction perpendicular to the layer. The Cl and CN groups of the anilato ligands have been omitted and only the O atom of the DMSO molecules is displayed for clarity.*

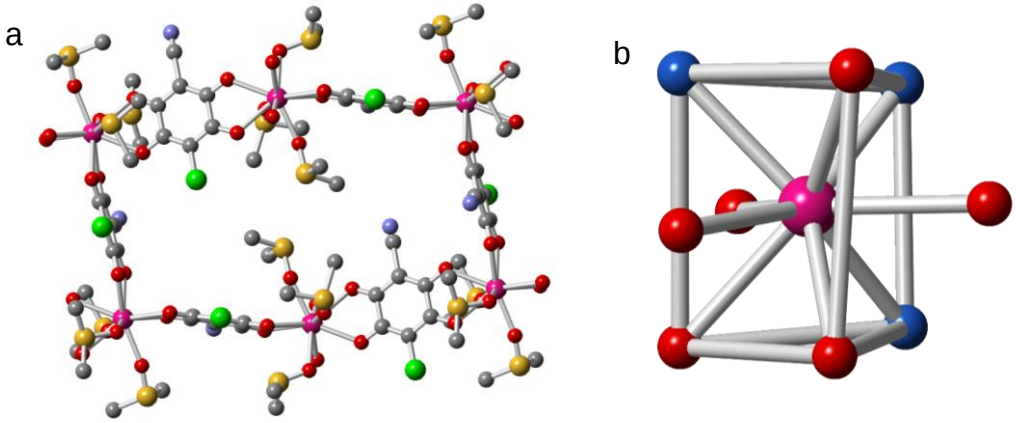

Figure 4.7: *structure of compound* ***29****.* ***(a)*** *View of one isolated distorted hexagonal cavity with the solvents coordinated to the Pr(III) ions.* ***(b)*** *tri-capped trigonal prism geometry of the nona-coordinated Pr(III) ion.*

The Pr(III) ions are also nona-coordinated (as in **28**) with six oxygen atoms coming from three anilato ligands (in red in Figure 4.7b) and three oxygens atoms from the three coordinated DMSO molecules (in blue in Figure 4.7b). The Pr ions have a tri-capped trigonal prism coordination geometry (figure 4.7b), where two of the DMSO molecules are coordinated in one triangular face and the third one to the other triangular face. The three anialto ligands connect one position of a triangular face with one equatorial position. The main Ln-O bond distances for this compound are given in table 4.3.

Table 4.3. *Main Ln-O bond distances for compound* ***29****.*

Atoms	distance (Å)	Atoms	distance (Å)
Pr(1)-O(11D)	2.406(6)	Pr(1)-O(12)	2.540(6)
Pr(1)-O(21D)	2.420(7)	Pr(1)-O(3)	2.551(6)
Pr(1)-O(1D)	2.435(6)	Pr(1)-O(23)	2.558(6)
Pr(1)-O(13)	2.517(6)	Pr(1)-O(22)	2.562(5)
Pr(1)-O(2)	2.527(5)		

The smaller deviation from 120º of the three different Pr-Pr-Pr angles inside the deformed hexagonal cavity (ca. 100.62°, 163.98° and 91.79°), confirm that the distortions in **29** are smaller than in **28** (Figure 4.8a). In fact, in **29** the sum of the deviations of the three angles from the ideal value of 120° is 91.57°, *ca*. 20º smaller than the value found in compound **28** (111.51º). The hexagonal layers are packed in an eclipsed way, giving rise to hexagonal channels filled with the coordinated DMSO molecules (Figure 4.8b).

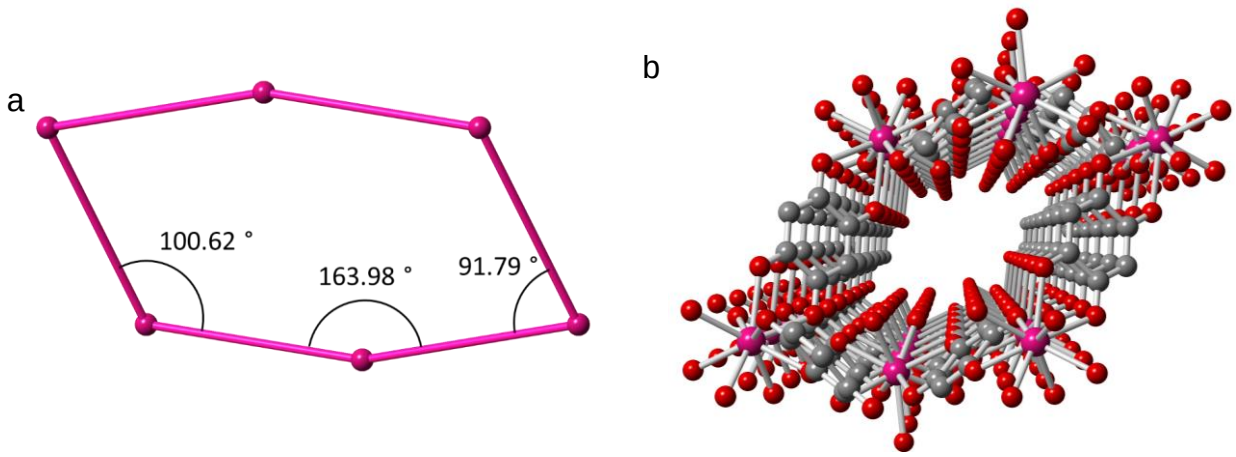

Figure 4.8: (a) *View of a distorted hexagonal cavity in* ***29*** *showing the three different Pr-Pr-Pr angles. Only the positions of the Pr(III) ions have been drawn.* ***(b)*** *Perspective view of one deformed hexagonal channel along the c direction in* ***29****. The Cl and CN groups of the anilato ligands have been omitted and only the O atom of the DMSO molecules is displayed for clarity.*

Structure of $[Yb_2(C_6O_4(CN)Cl)_3(DMSO)_4]\cdot 2H_2O$ (30): This compound crystallizes in the trigonal P-*1* space group The asymmetric unit contains one ytterbium ion, one and a half anilato ligands and two DMSO molecules coordinated to the Yb(III) ion, giving rise to the extended formula $[Yb_2(C_6O_4(CN)Cl)_3(DMSO)_4]$. The

coordination environment around the Yb(III) ions and the labelling scheme are displayed in Figure 4.9.

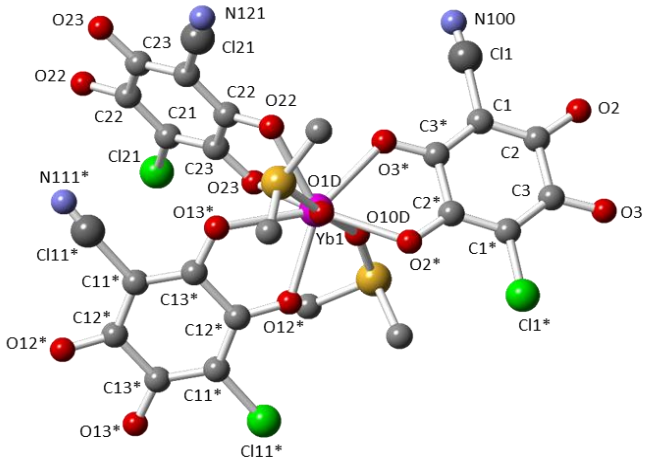

Figure 4.9: *Coordination environment of the Yb(III) ions in compound* ***30*** *showing the labelling scheme. Colour code: Yb = pink, C = grey, O = red, N = blue, Cl = light green, S = yellow. H atoms have been omitted for clarity.*

The structure of this compound consists of neutral almost planar hexagonal layers (Figure 4.10a) where each Yb(III) ion is connected to three other metal atoms through bridging anilato ligands forming rings containing six metal atoms with a distorted hexagonal geometry (Figure 4.10b).

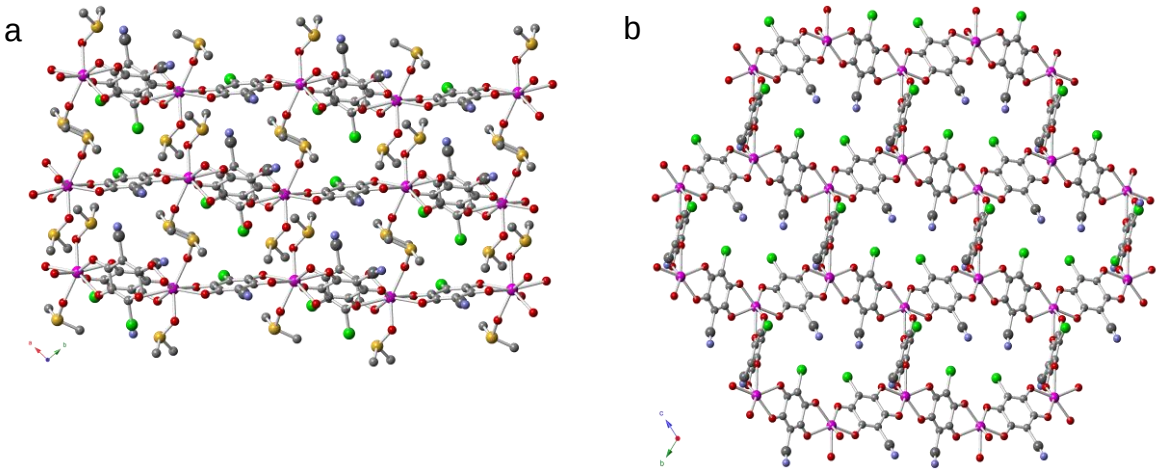

Figure 4.10: *structure of compound* ***30****.* ***(a)*** *Side view of the layers.* ***(b)*** *View of the distorted hexagonal cavities in the direction perpendicular to the layer. In* ***(b)*** *only the O atom of the DMSO molecules is displayed for clarity.*

The Yb(III) ions are located on the vertex of the distorted hexagons and the anilato ligands on the edges, originating a distorted 2D honeycomb layer with 6,3 topology. The distorted hexagonal rings show two “edge-on” and four “face-on” oriented anilato ligands, giving rise to a 2E-4F disposition of the anilato ligands (Figure 4.11a), as observed in **29** and in contrast to the 4E-2F disposition observed in **28**.

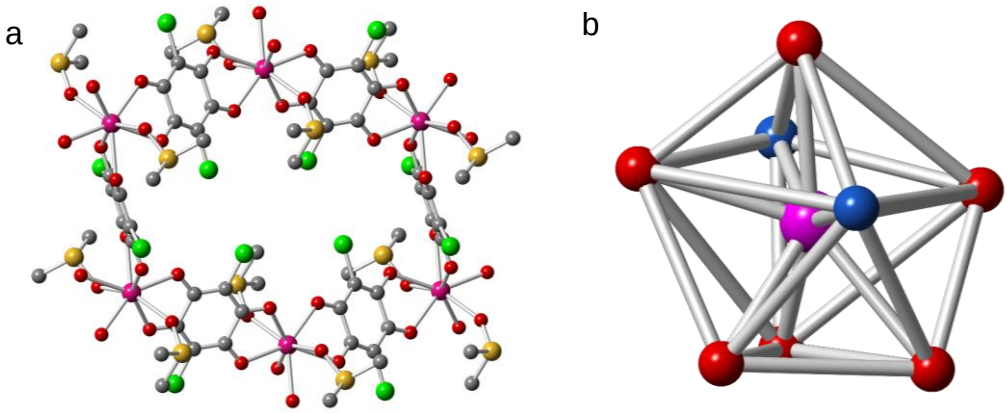

Figure 4.11: *structure of compound* ***30****.* ***(a)*** *View of one isolated distorted hexagonal cavity with the solvents coordinated to the Yb(III) ions.* ***(b)*** *triangular dodecahedron geometry of the octa-coordinated Yb(III) ion.*

The Yb(III) ions are octa-coordinated, in contrast to the Pr(III) ions in compounds **28** and **29**, that are nona-coordinated. This difference has to be attributed to the smaller size of Yb(III) compared to Pr(III). The coordination sphere of the Yb(III) ions is formed by six oxygen atoms from three anilato ligands (in red in figure 4.11b) and two oxygen atoms from the two coordinated DMSO molecules (in blue in figure 4.11a). The Yb ions have a triangular dodecahedron geometry (figure 4.11b). The main Ln-O bond distances for this compound are listed in table 4.4.

Table 4.4. *Main Ln-O bond distances for compound* ***30****.*

Atoms	distance (Å)	Atoms	distance (Å)
Yb(1)-O(1D)	2.210(5)	Yb(1)-O(3)	2.315(5)
Yb(1)-O(10D)	2.285(5)	Yb(1)-O(22)	2.335(5)
Yb(1)-O(23)	2.302(5)	Yb(1)-O(2)	2.341(5)
Yb(1)-O(12)	2.311(5)	Yb(1)-O(13)	2.461(5)

The deviation from 120º of the three different Yb-Yb-Yb angles inside the deformed hexagonal rings (78.41°, 149.46° and 127.77°) are smaller than in **28** and **29**. (Figure 4.12a). Thus, in **30** the sum of the deviations of the three angles from the ideal value of 120° is 78.82° a value smaller than those found in **28** (111.51º) and **29** (91.57º). This value confirms that in **30** the hexagonal cavities are less distorted as a result of the smaller coordination number found in this compound that generates less steric hindrance in the anilato ligands and, accordingly, a more regular geometry in the cavities (when there are no additional coordination solvents the hexagonal cavities are regular, as observed in the layers formed with transition metal). As in **28** and **29**, the hexagonal layers are packed in an eclipsed way, giving rise to hexagonal channels that contain the coordinated DMSO molecules (Figure 4.12b).

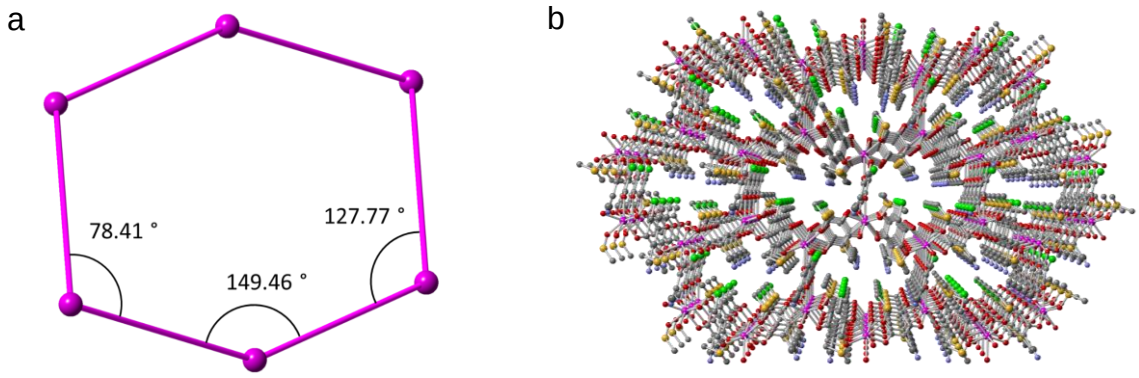

Figure 4.12: (a) *View of a distorted hexagonal cavity in* ***30*** *showing the three different Yb-Yb-Yb angles. Only the positions of the Yb(III) ions have been drawn.* ***(b)*** *Perspective view of the hexagonal channels along the c direction in compound* ***30****.*

Structure of $[(H_3O)K][Yb_2(C_6O_4(CN)Cl)_3(\mu\text{-}OH)_2]\cdot 7H_2O$ (31): This compound crystallizes in the monoclinic C2/*m* group The asymmetric unit contains half Yb(III) ion, 1/4 potassium ion, 1/4 and 1/2 anilato ligands, half coordinated OH^- anion and two crystallization water molecules, giving rise to the extended formula $[(H_3O)K][Yb_2(C_6O_4(CN)Cl)_3(\mu\text{-}OH)_2]\cdot 7H_2O$. The presence of one H_3O^+ cation is deduced from the change balance although the X-ray structure does not allow to confirm this point. The coordination environment around the Yb(III) ions and the labelling scheme are displayed in Figure 4.13.

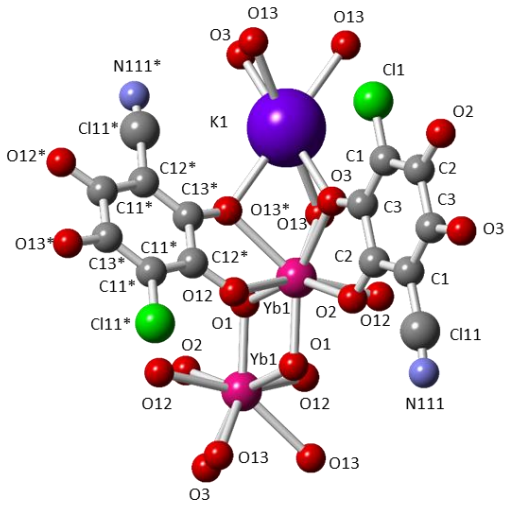

Figure 4.13. *Coordination environment of the Yb(III) ions in* ***31*** *showing the labelling scheme.*

This compound forms a 3D structure that can be described as layers parallel to the *ab* plane connected through anilato bridges along the *c* direction (Figure 4.14). The layers are formed by $Yb_2(OH)_2$ dimers connected through anilato ligands to form a square lattice where each $Yb_2(OH)_2$ unit is connected to four other $Yb_2(OH)_2$ units through four anilato bridges in a (4,4)-2D square lattice. Additionally, there are K^+ ions connecting non consecutive $Yb_2(OH)_2$ units in the squares (Figure 4.15).

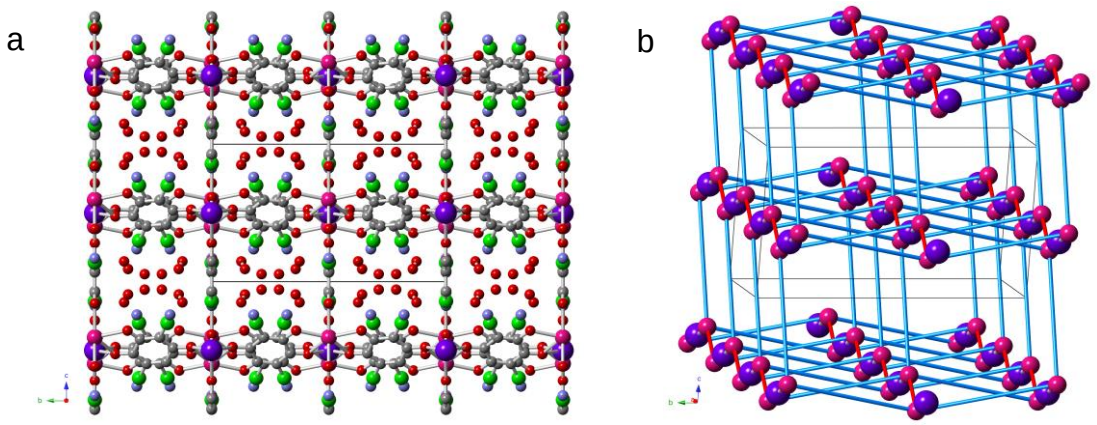

Figure 4.14: *Structure of compound* ***31****:* ***(a)*** *View down the a direction of the layers parallel to the ab plane and the anilato bridges connecting the layers along the c direction.* ***(b)*** *Schematic view of the connectivity in* ***31****. Blue lines represent the anilato bridges and red lines the double OH bridges connecting the Yb(III) ions. Colour code: Yb = pink, C = grey, O = red, N = blue, Cl = light green, K = purple.*

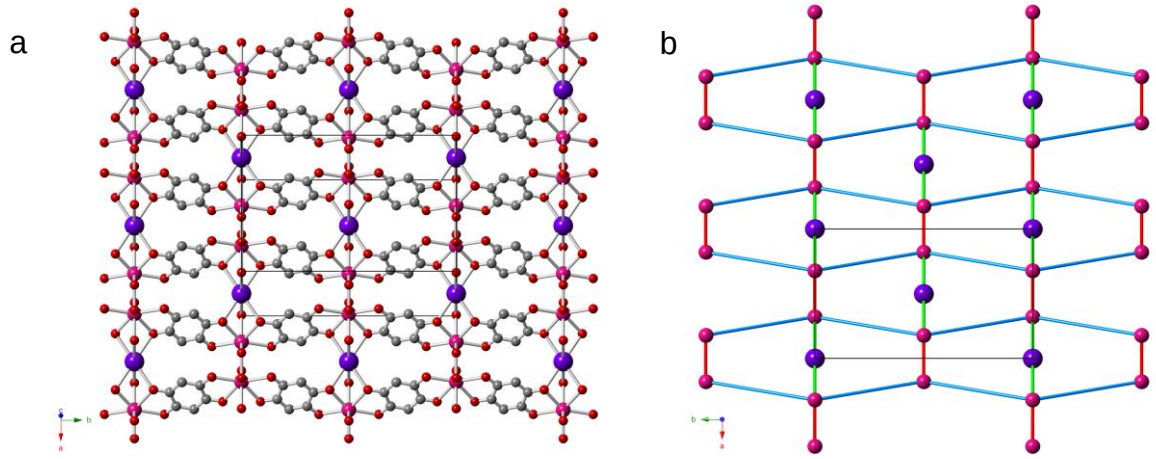

Figure 4.15: *Structure of **31**: **(a)** View of a (4,4) square layer down the c direction. The Cl and CN groups and the water molecules have been omitted for clarity. **(b)** Schematic view of the connectivity in **31**. Blue lines represent the anilato bridges, red lines the double OH bridges connecting the Yb(III) ions and green lines the K-O-Yb connections though anilato-oxygen atoms. Colour code: Yb = pink, C = grey, O = red, N = blue, Cl = light green, K = purple.*

The Yb (III) ions are octa-coordinated (as in compound **30**) with six oxygen atoms coming from three anilato ligands and two oxygen atoms from two bridging OH^- anions in a triangular dodecahedron geometry as in **30** (Figure 4.16a). The OH^- anions (in blue in Figure 4.16a) connect each Yb(III) with another one, forming $[Yb_2(OH)_2]^{4+}$ dimers, (Figure 4.16a). Each $Yb_2(OH)_2$ unit is connected to other four $Yb_2(OH)_2$ units through anilato bridges and to two more Yb_2 dimers though K^+ ions with a triple K-O-Yb bridge (Figure 4.16b). The main Ln-O bond distances for this compound are displayed in table 4.5.

Table 4.5. *Main Ln-O bond distances for compound **31**.*

Atoms	distance (Å)	Atoms	distance (Å)
Yb(1)-O(1)#1	2.197(7)	Yb(1)-O(3)	2.354(8)
Yb(1)-O(1)	2.202(8)	Yb(1)-O(2)	2.366(7)
Yb(1)-O(12)	2.354(5)	Yb(1)-O(13)#2	2.396(5)
Yb(1)-O(12)#2	2.354(5)	Yb(1)-O(13)	2.396(5)

Symmetry transformations used to generate equivalent atoms: #1 -x+2,-y+1,-z+1 and #2 x,-y+1,z

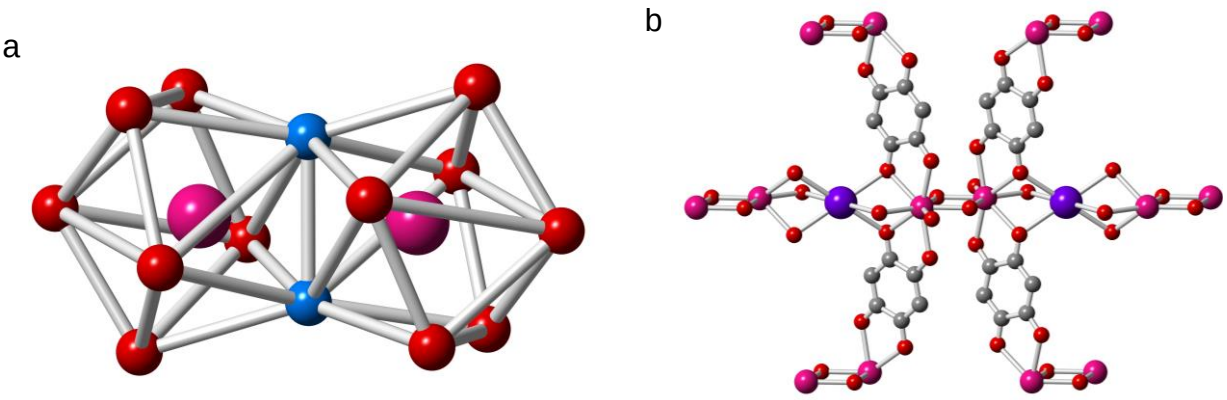

Figure 4.16: (a) *View of the coordination environment around the Yb(III) ions in the $Yb_2(OH)_2$ dimers (O atoms form the OH groups are displayed in blue).* ***(b)*** *View of a $Yb_2(OH)_2$ dimer connected to four other dimers through four anilato bridges and to two other dimers through two K bridges. The Cl and CN groups and the water molecules have been omitted for clarity. Colour code: Yb = pink, C = grey, O = red and K = purple.*

3.2. X-Ray Powder Diffraction

The phase purity of the bulk for **28**-**31** was checked with the XRPD technique, comparing the experimental diffractograms with the simulated ones generated by Mercury program from the solved structures (Figures 4.17-4.20).

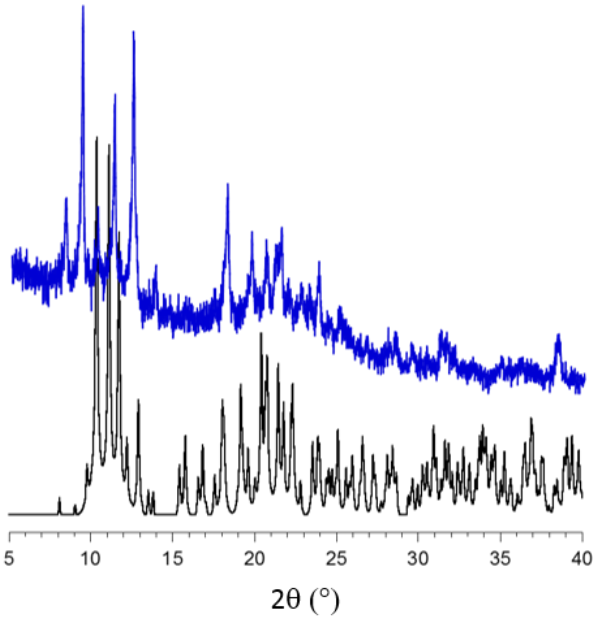

Figure 4.17 *Simulated (in black) and experimental X-ray powder diffractograms for compound* ***28****.*

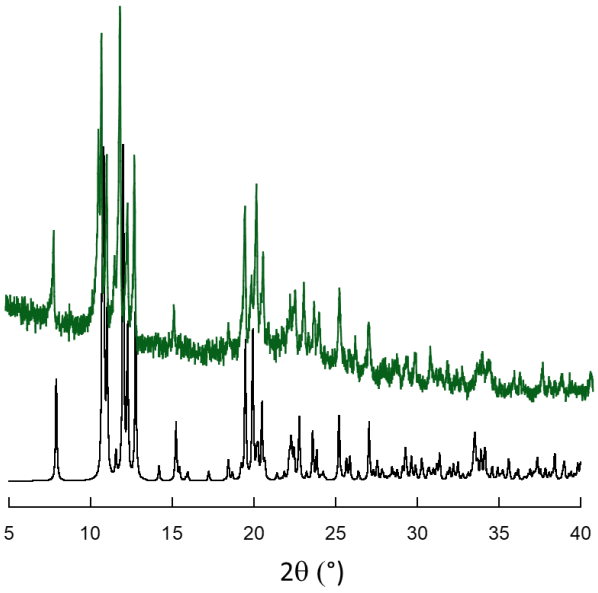

Figure 4.18 *Simulated (in black) and experimental X-ray powder diffractograms for compound* ***29****.*

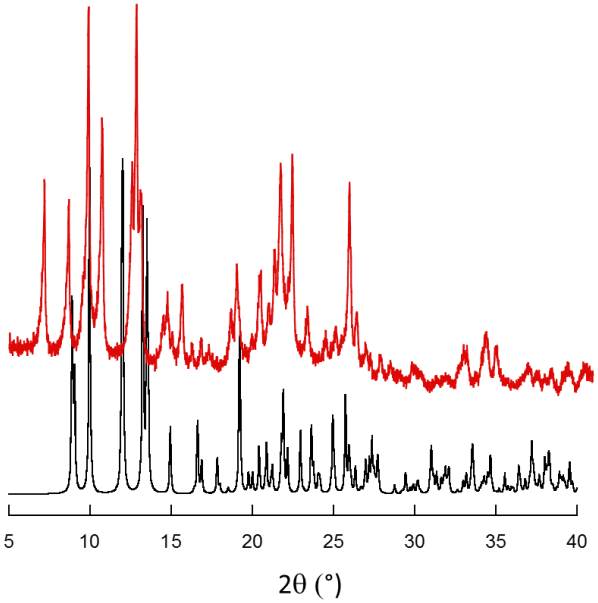

Figure 4.19 *Simulated (in black) and experimental X-ray powder diffractograms for compound* ***30****.*

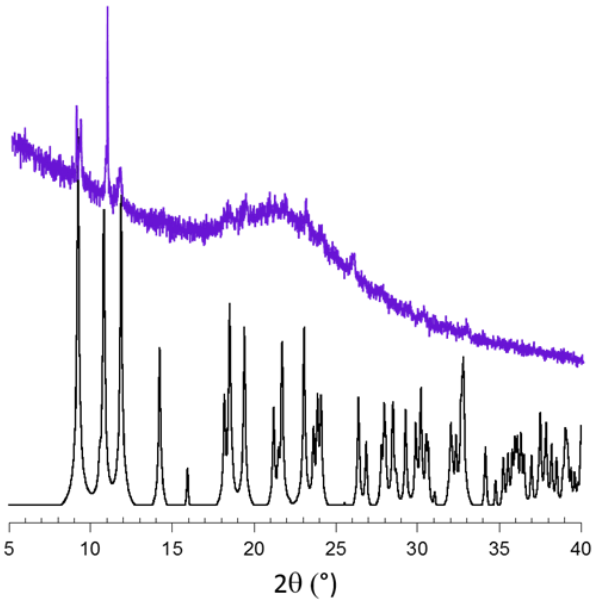

Figure 4.20 *Simulated (in black) and experimental X-ray powder diffractograms for compound* ***31****.*

3.4. Magnetic Properties

Compounds **28**-**31** have, as expected, very similar magnetic behaviour since all of them are based on isolated lanthanide ions. Only compound **31** has more than one metallic centre, but, since K^+ ions are diamagnetic, it does not affect the magnetic properties. Besides, anilato-type ligands are known to give rise to very weak (if any) antiferromagnetic couplings when coordinated to lanthanide ions.[26]

Thus, the thermal variation of the $\chi_m T$ product for the couples of compounds containing the same lanthanide ions are similar: 3.25 and 3.15 cm^3 K mol^{-1} at room temperature for compounds **28** and **29** respectively (Figure 4.21), close to the value expected for two Pr(III) ions (3.2 cm^3 K mol^{-1}), and 5.25 and 5.20 cm^3 K mol^{-1} at room temperature for compounds **30** and **31** respectively (Figure 4.22), close to the value expected for two Yb(III) ions (5.14 cm^3 K mol^{-1}). When the temperature is lowered, the $\chi_m T$ product shows a continuous decrease to reach a value of ca. 0.25 cm^3 K mol^{-1} for compounds **28** and **29**. This decrease is due to the depopulation of the Stark levels as observed in others lanthanide-based anilato compounds.[26] In compounds **30** and **31** the decrease is softer than in **28** and **29**, reaching values of ca. 2.0 and

3.0 cm^3 K mol^{-1} respectively. This decrease is also due to the depopulation of the Stark levels. Nevertheless, the presence of a very weak, almost negligible, antiferromagnetic coupling cannot be excluded.

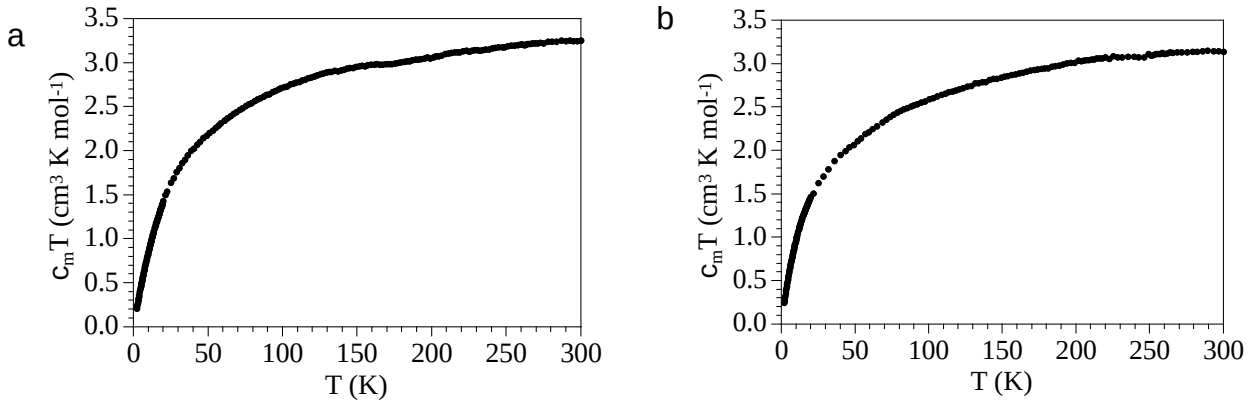

Figure 4.21: *Thermal variation of $\chi_m T$ for the two compounds containing Pr(III) ions:* ***(a)*** *compound* ***28*** *and* ***(b)*** *compound* ***29****.*

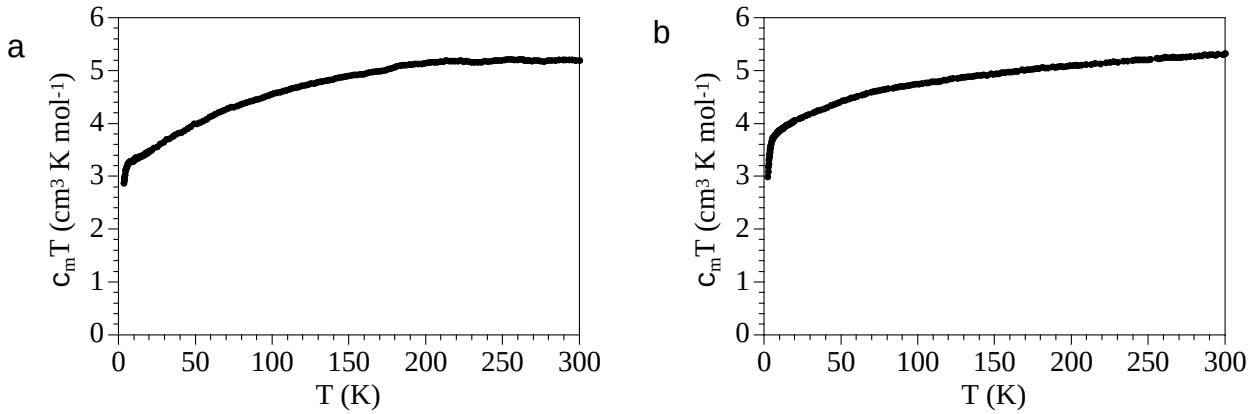

Figure 4.22: *Thermal variation of $\chi_m T$ for the two compounds containing Pr(III) ions :* ***(a)*** *compound* ***30*** *and* ***(b)*** *compound* ***31****.*

3.5. Luminescent Properties

In compounds **28**-**30** the energy transfer is activated via the 2-chloro-5-cyano-3,6-dihydroxybenzoquinone ligand. Therefore, the contribution of the ligand to the light emission must be taken into account since, in certain situations, such emission could be as intense as the lanthanide contribution. In solution the luminescence of the chlorocyanoanilato presents a broad emission band (500-600 nm) centered at,

corresponding to a $^3T \rightarrow {}^0S$ transition. This transition can be excited with blue and green light (resonant excitation) by direct population of the ^1S state using shorter wavelengths (UV excitation).[2] However, the optical properties of the chromophores might vary after crystallization[26] and, therefore, the measurements in solution may not be representative of our compounds. Accordingly, we have measured as reference of the chlorocyanoanilato ligand its potassium salt: $K_2(C_6O_4(CN)Cl)$. The spectrum of this salt was measured in the same conditions as for the crystals of the lanthanoid-based compounds. These measurements show very similar spectra for the potassium salt and for compounds **28**-**30** using UV (364 nm) and visible excitation (488 nm) (Figure 4.23). These spectra consist of a broad band located at *ca*. 675 nm with a full width at half-maximum (FWHM) of about 120 nm. We can, therefore, observe a notable red-shift and broadening of the band in solid state with respect to the emission found in solution[2] (where the emission band is observed at 500-600 nm and the FWHM was *ca*. 100nm).

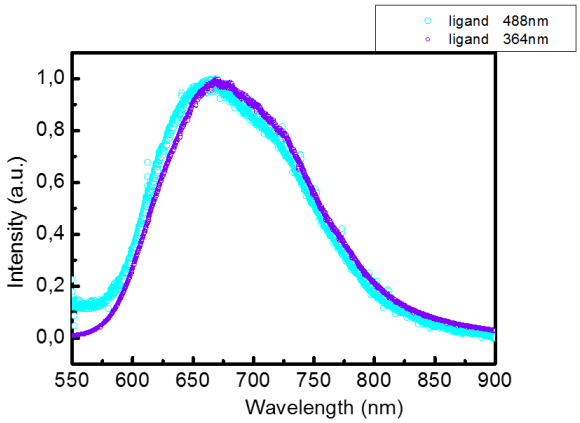

Figure 4.23: *Emission spectrum of the potassium salt of 2-chloro-5-cyano-3,6-dihydroxybenzoquinone in solid state under UV excitation (364 nm, blue line) and under visible excitation (488 nm, violet line).*

With the information of the ligand emission we can discuss the spectra shown in figure 4.24, which correspond to the emission of compounds **28** and **30** (Pr^{3+} and Yb^{3+}, respectively) under UV (364 nm, figure 4.24a) and visible excitations (488 nm, figure 4.24b). As described in the experimental section, the optical measurements have been carried with confocal microscopy in back-scattering configuration. This technique allows us to obtain images and luminescence spectra of the surface with high lateral resolution (of the order of microns).

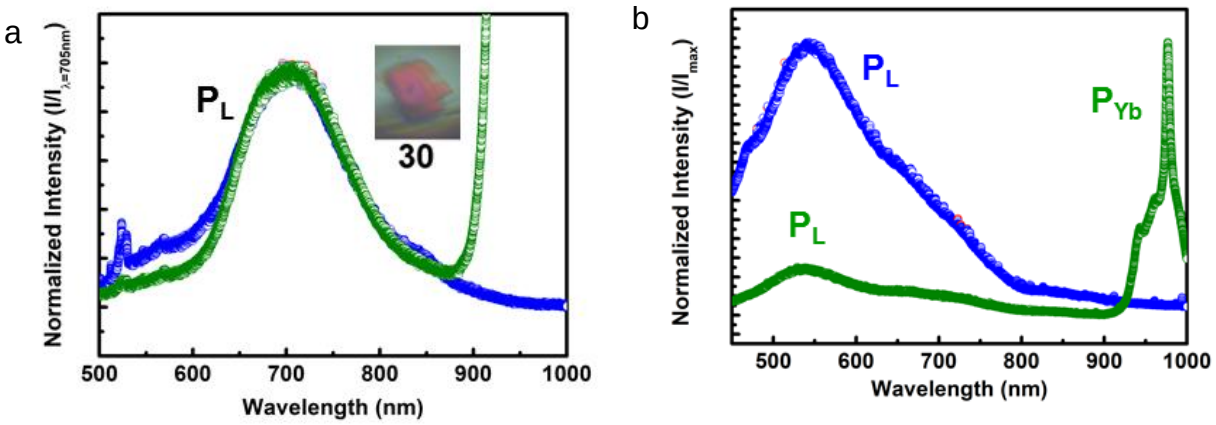

Figure 4.24: (a) *Luminescence obtained from the compounds **28** (blue) and **30** (green) excited at 364 nm wavelength; Inset shows a crystal of **30**. All the spectra are normalized to its maximum.* ***(b)*** *Luminescence from the same crystals excited at 488 nm. The spectra are normalized to the P_L peak.*

It is worth to note that we have not found significant differences when comparing emission from crystals of the same compound, only variations on the light intensity that we can attribute to the geometry and orientation of a given crystal (see inset of figure 4.24a with a crystal of compound **30**). In the case of compound **28**, the spectra are mainly formed by a broad emission band covering the visible part of spectra ~ 600-800 nm (labelled as P_L). However, even though both spectra are covering the same area, they present different structure and we can clearly distinguish different spectral components in each case (i.e. peaks of different nature). In the case of compound **30** we can identify the P_L broad band, but for compound **30** the most important contribution comes from a narrow peak located at 980 nm, labeled as P_{Yb}. This peak is the well-known signature the Yb^{3+} ion corresponding to the transition from the only excited state to the ground state, $^2F_{5/2} \rightarrow {}^2F_{7/2}$.[27, 28] Since no more transitions can be related to the Yb^{3+} ion, we should ascribe P_L to the ligand.

To clarify this point, we have also acquired luminescence spectra under resonant excitation (488 nm). These spectra show a much more intense P_L peak for **28** than from **30**, (Figure 4.24b). Moreover, in the case of compound **30** the main component still comes from the previously mentioned P_{Yb} peak corresponding to the $^2F_{5/2} \rightarrow {}^2F_{7/2}$ transition.[27, 28] With these results, we can tentatively propose the energy

transfer diagram depicted in figure 4.25, which allows us to discuss about the sensitization mechanism.

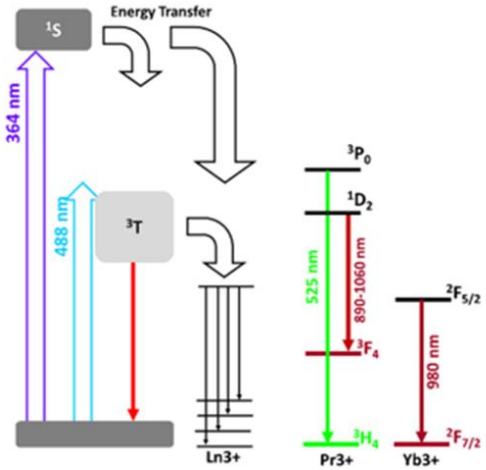

***Figure 4.25**: Diagram for the main pathways available for energy transfer and sensitization*

The dynamics under UV and visible excitations are associated to two different energy transfer pathways. In some cases, sensitized compounds could be excited through the ^1S level of the ligand, and then, an important part of the absorbed energy would be transferred to the ^3T state. Since the $^3T \rightarrow {}^1S$ transition usually present long lifetimes, the energy transfer rate to the lanthanide ions will be enabled (i.e. the ions will be sensitized). In the case of compound **30** the transfer towards the lanthanide is clearly favoured, since $^2F_{5/2}$ is located at slightly lower energy with respect to the ^3T band of the ligand. In **28** the closest state, $^3P_0$, is found at higher energies thanthe ones of the ligand.[27, 29] There is no contribution from the Pr(III) ion in compound **28** to the P_L peak. This can be understood as a combination of factors: i) firstly, the oscillator strength of the transition $^3P_0 \rightarrow {}^3H_4$ is very low, then, a weak luminescence is expected; ii) secondly, the presence of $^1D_2$ in resonance to ^3T, de-activates the transfer to $^3P_0$, notice that the emission from $^1D_2$ does not fit with the P_L peak.[27, 28] In any case, energy transferred to ^3T is thermalized to the low energy tail and the transfer from this band to the lanthanide ion is not optimized for compound **28**. Roughly speaking Pr(III) ions would be in competition with ^3T for the energy transfer from ^1S, resulting in a poor sensitization of the ions. In a similar way, excited states of compound **28** are not populated when exciting resonant to ^3T. For this reason, the emission of Yb^{3+} compounds does not seem to be affected when exciting resonant to

^{3}T. This demonstrates that the energy transfer to the lanthanide mainly occurs from ^{3}T.

Compound **29** does not show any significant emission. Thus, the luminescence emission coming from this compound is comparable to the luminescence emission coming from the substrate, and no contribution from the Pr(III) ions is appreciable when exciting at 364 nm (Figure 4.26).

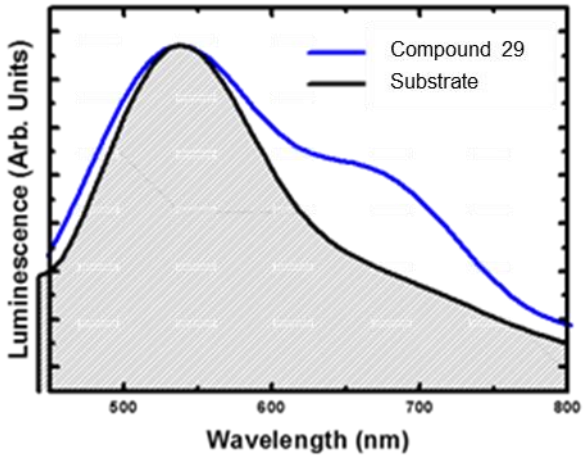

Figure 4.26 *Luminescence of compound* ***29.*** *Both spectra are normalized to its maximum for a better comparison.*

4. Conclusions and Perspectives

In this chapter we have presented four different compounds based on the 2-chloro-5-cyano-3,6-dihydroxybenzoquinone ligand and lanthanide ions with different solvents that complete the coordination sphere of the lanthanide ions. Compounds **28** and **29** are praseodymium-based 2D networks with DMF and DMSO as solvent formulated as $[Pr_2(C_6O_4(CN)Cl)_3(DMF)_6]$ (**28**) and $[Pr_2(C_6O_4(CN)Cl)_3(DMSO)_6]$ (**29**).

Compounds **30** and **31** are ytterbium-based 2D and 3D networks respectively. Compound **30** has DMSO as solvent and the formula $[Yb_2(C_6O_4(CN)Cl)_3(DMSO)_4]\cdot 2H_2O$ while **31** has H_2O as solvent and, besides Yb(III) ions, it also contains K^+ ions and two bridging hydroxide anions connecting two Yb(III) ions: $[(H_3O)K][Yb_2(C_6O_4(CN)Cl)_3(\mu\text{-}OH)_2]$.

The structure of **28** consists of neutral layers with the well known (6,3)-topology forming rings with six metal atoms. The six-membered rings present a rectangular geometry resulting from a large distortion of the hexagons. The origin of this large distortion resides in the spatial orientation of the three anilato ligands surrounding the metal centres. This orientation forces four of the six anilato ligands that constitute the sides of the distorted hexagons to be located with the anilato plane almost orthogonal to the plane of the hexagon ("edge on" orientation, E) and the other two with the anilato plane almost parallel to the hexagon plane ("face on" orientation, F). This particular (4E-2F) orientation gives rise to the large distortions leading to a rectangular lattice (although with the same 6,3-topology) rather than the well known hexagonal honeycomb layers. The rectangles present a spike-like disposition: they are located in parallel rows with orthogonal orientations between the rectangles of consecutive rows.

Changing DMF (**28**) by DMSO (**29**) in the Pr(III) compound results in important structural changes: in **29** the layers are corrugated and the cavities are distorted hexagons with two "edge-on" and four "face-on" oriented anilato ligands, giving rise to a 2E-4F disposition of the anilato ligands, in contrast with the 4E-2F disposition observed in **28**. This difference in the structure is confirmed by the deviation from 120º of the three different Pr-Pr-Pr angles, inside the six-membered rings, which are 101.06º, 78.11º and 170.68º in **28** and 100.62°, 163.98° and 91.79° in **29**. The larger deviation of the angles from 120º in **28** with respect to **29** (adding up to 111.51º for **28** versus 91.57° for **29**) clearly shows the large distortion of the cavity from the hexagonal geometry.

In both cases, the Pr(III) ions are nona-coordianted with six oxygen atoms coming from three chelating anilato ligands and three oxygen atoms coming from the three coordinated solvent molecules (DMF for **28** and DMSO for **29**).

Compound **30** has the same solvent than **29**, but now we replace Pr(III) by the smaller Yb(III) ion. The first and main difference is the coordination number of the lanthanide ion: while Pr(III) ions are nona-coordinated, Yb(III) ions are octa-coordinated (six oxygen atoms come from three anilato ligands and two oxygen

atoms come from the two coordinated DMSO molecules). This difference has to be attributed to the smaller size of Yb(III) compared to Pr(III).

Moreover, both compounds present neutral hexagonal layers with the same 2E-4F disposition of the anilato ligands. The deviation from 120º of the three different Yb-Yb-Yb angles inside the distorted hexagonal rings (78.41°, 149.46° and 127.77°) are smaller than in **28** and **29**. The sum of the deviations of the three angles from the ideal value of 120° is 78.82°, smaller than for **28** (111.51º) and **29** (91.57º), confirming that in **30** the hexagonal cavities are less distorted as a result of the smaller coordination number of the Yb(III) centres.

A surprising result was observed when changing DMSO by water as solvent with Yb(III). In this case, the change of solvent has led to a complete change of the structure, as observed in the 3D compound **31**. This compound presents unique features as the presence of K^+ ions and double OH^- bridges connecting two Yb(III) centres. These unprecedented structural features in the chemistry of lanthanoids with anilato ligands have to be attributed exclusively to the change of the solvent and shows the key role that may play the solvent in the structure (and properties) of these anilato based lattices.

The luminescent properties of the 2-chloro-5-cyano-3,6-dihydroxy-benzoquinone ligand and of compounds **28**-**30** show a strong emission at *ca*. 980 nm corresponding to the Yb(III) ions in compound **30** and a broad band emission at *ca*. 600-800 nm which is more intense in compound **28**. The analysis of these bands allows a tentative proposal of the energy transfer diagram.

As future work we will perform a complete study of the luminescent properties of other lanthanoid metal ions with other solvents in order to check their quenching capacity in these lattices and to obtain the best conditions for luminiscence.

5. References

(1) Rehwol, R. E.; Chasen, B. L.; Li, J. B. 2-Chloro-5-Cyano-3,6-Dihydroxybenzoquinone, a New Analytical Reagent for the Spectrophotometric Determination of Calcium(II). *Anal. Chem.* **1966***, 38*, 1018-1019.

(2) Atzori, M.; Artizzu, F.; Marchio, L.; Loche, D.; Caneschi, A.; Serpe, A.; Deplano, P.; Avarvari, N.; Mercuri, M. L. Switching-on Luminescence in Anilate-Based Molecular Materials. *Dalton Trans.* **2015***, 44*, 15786-15802.

(3) Halcrow, M. A. Structure: Function Relationships in Molecular Spin-Crossover Complexes. *Chem. Soc. Rev.* **2011***, 40*, 4119-4142.

(4) Williams, J. M.; Ferraro, J. R.; Thorn, R. J.; Carlson, K. D.; Geiser, U.; Wang, H. H.; Kini, A. M.; Whangbo, M. H. In *Organic Superconductors (Including Fullerenes), Synthesis, Structure, Properties and Theory;* Crimes, R. N., Ed.; Prentice Hall: Englewood Cliffs, NJ, 1992; .

(5) Zhou, H.; Long, J. R.; Yaghi, O. M. Introduction to Metal–Organic Frameworks. *Chem. Rev.* **2012***, 112*, 673-674.

(6) Alipour, M.; Akintola, O.; Buchholz, A.; Mirzaei, M.; Eshtiagh-Hosseini, H.; Görls, H.; Plass, W. Size-Dependent Self-Assembly of Lanthanide-Based Coordination Frameworks with Phenanthroline-2,9-Dicarboxylic Acid as a Preorganized Ligand in Hybrid Materials. *Eur. J. Inorg. Chem.* **2016***, 2016*, 5356-5365.

(7) Guillou, O.; Daiguebonne, C.; Calvez, G.; Bernot, K. A Long Journey in Lanthanide Chemistry: From Fundamental Crystallogenesis Studies to Commercial Anticounterfeiting Taggants. *Acc. Chem. Res.* **2016***, 49*, 844-856.

(8) Chandler, B. D.; Cramb, D. T.; Shimizu, G. K. H. Microporous Metal-Organic Frameworks Formed in a Stepwise Manner from Luminescent Building Blocks. *J. Am. Chem. Soc.* **2006***, 128*, 10403-10412.

(9) Harbuzaru, B. ; Corma, A.; Rey, F.; Atienzar, P.; Jordá, J. ; García, H.; Ananias, D.; Carlos, L.; Rocha, J. Metal–Organic Nanoporous Structures with Anisotropic Photoluminescence and Magnetic Properties and their use as Sensors. *Angew. Chem. Int. Ed.* **2008***, 47*, 1080-1083.

(10) Binnemans, K. Lanthanide-Based Luminescent Hybrid Materials. *Chem. Rev.* **2009***, 109*, 4283-4374.

(11) Armelao, L.; Quici, S.; Barigelletti, F.; Accorsi, G.; Bottaro, G.; Cavazzini, M.; Tondello, E. Design of Luminescent Lanthanide Complexes: From Molecules to Highly Efficient Photo-Emitting Materials. *Coord. Chem. Rev.* **2010***, 254*, 487-505.

(12) Rocha, J.; Carlos, L. D.; Paz, F. A. A.; Ananias, D. Luminescent Multifunctional Lanthanides-Based Metal-Organic Frameworks. *Chem. Soc. Rev.* **2011***, 40*, 926-940.

(13) Senthil Kumar, K.; Schafer, B.; Lebedkin, S.; Karmazin, L.; Kappes, M. M.; Ruben, M. Highly Luminescent Charge-Neutral Europium(III) and Terbium(III) Complexes with Tridentate Nitrogen Ligands. *Dalton Trans.* **2015***, 44*, 15611-15619.

(14) Zhao, Y.; He, L.; Qin, S.; Tao, G. H. Tunable Luminescence of Lanthanide (Ln = Sm, Eu, Tb) Hydrophilic Ionic Polymers Based on Poly(N-methyl-4-vinylpyridinium-Co-styrene) Cations. *Polym. Chem.* **2016***, 7*, 7068-7077.

(15) Pointillart, F.; Cador, O.; Le Guennic, B.; Ouahab, L. Uncommon Lanthanide Ions in Purely 4f Single Molecule Magnets. *Coord. Chem. Rev.* **2017***, 346, 150-175*.

(16) Sorace, L.; Benelli, C.; Gatteschi, D. Lanthanides in Molecular Magnetism: Old Tools in a New Field. *Chem. Soc. Rev.* **2011***, 40*, 3092-3104.

(17) Long, J.; Habib, F.; Lin, P. H.; Korobkov, I.; Enright, G.; Ungur, L.; Wernsdorfer, W.; Chibotaru, L. F.; Murugesu, M. Single-Molecule Magnet Behavior for an Antiferromagnetically Superexchange-Coupled Dinuclear Dysprosium(III) Complex. *J. Am. Chem. Soc.* **2011***, 133*, 5319-5328.

(18) Bunzli, J. C. G.; Piguet, C. Taking Advantage of Luminescent Lanthanide Ions. *Chem. Soc. Rev.* **2005***, 34*, 1048-1077.

(19) Peijzel, P. S.; Meijerink, A.; Wegh, R. T.; Reid, M. F.; Burdick, G. W. A Complete 4fn Energy Level Diagram for all Trivalent Lanthanide Ions. *J. Solid Stat. Chem.* **2005***, 178*, 448-453.

(20) Altomare, A.; Burla, M. C.; Camalli, M.; Cascarano, G. L.; Giacovazzo, C.; Guagliardi, A.; Moliterni, A. G. G.; Polidori, G.; Spagna, R. SIR97: A New Tool for Crystal Structure Determination and Refinement. *J. Appl. Cryst.* **1999***, 32*, 115-119.

(21) Sheldrick, G. M. Crystal Structure Refinement with SHELXL. *Acta Cryst. C* **2015***, 71*, 3-8.

(22) Farrugia, L. J. WinGX Suite for Small-Molecule Single-Crystal Crystallography. *J. Appl. Cryst.* **1999***, 32*, 837-838.

(23) Bain, G. A.; Berry, J. F. Diamagnetic Corrections and Pascal's Constants. *J. Chem. Educ.* **2008***, 85*, 532-536.

(24) Abhervé, A.; Clemente-León, M.; Coronado, E.; Gómez-García, C. J.; Verneret, M. One-Dimensional and Two-Dimensional Anilate-Based Magnets with Inserted Spin-Crossover Complexes. *Inorg. Chem.* **2014***, 53*, 12014-12026.

(25) Atzori, M.; Benmansour, S.; Mínguez Espallargas, G.; Clemente-León, M.; Abhervé, A.; Gómez-Claramunt, P.; Coronado, E.; Artizzu, F.; Sessini, E.; Deplano, P.; Serpe, A.; Mercuri, M. L.; Gómez García, C. J. A Family of Layered Chiral Porous Magnets Exhibiting Tunable Ordering Temperatures. *Inorg. Chem.* **2013***, 52*, 10031-10040.

(26) Benmansour, S.; López-Martínez, G.; Canet-Ferrer, J.; Gómez-García, J. C. A Family of Lanthanoid Dimers with Nitroanilato Bridges. *Magnetochemistry* **2016***, 2*, 32.

(27) Sontakke, A. D.; Ueda, J.; Katayama, Y.; Zhuang, Y.; Dorenbos, P.; Tanabe, S. Role of Electron Transfer in Ce^{3+} Sensitized Yb^{3+} Luminescence in Borate Glass. *J. Appl. Phys.* **2015***, 117*, 013105.

(28) Carnall, W. T.; Crosswhite, H.; Crosswhite, H. M. Energy Level Structure and Transition Probabilities in the Spectra of the Trivalent Lanthanides in LaF3. **1995**.

(29) Kristianpoller, N.; Shmilevich, A.; Weiss, D.; Chen, R.; Khaidukov, N. Luminescence of $LiKYF_5:Pr^{3+}$ Crystals. *Radiat. Meas.* **2001***, 33*, 637-640.

Chapter 5

Spin crossover compounds based on anilato ligand

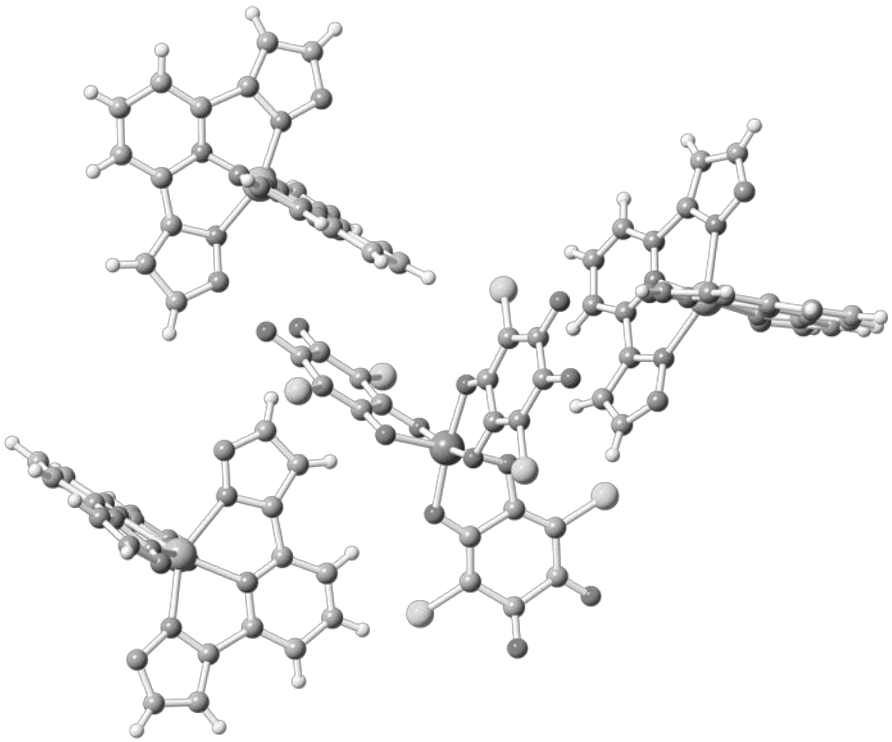

1. Introduction

Electronic bistability, i.e. the presence of two different electronic states under the same external conditions, is one of the most desired properties in Materials Science. This bistability confers a memory effect to a material that can be used for information storage and sensing applications. One of the best known examples of bistability are spin crossover (SCO) complexes.[1-6] Although these complexes show at least two different magnetic states: high spin (HS) and low spin (LS), only a few of them present bi-stability since this property requires the presence of a hysteresis loop. Among these bistable systems, Fe(II) compounds are the most studied ones due to the drastic changes in their optical and magnetic properties when going from the LS (S = 0) to the HS (S = 2) configuration.[2, 7, 8] Although less studied and less abundant, there are also Fe(III) SCO complexes with bistability.[9]

Unfortunately, the control of the presence/absence of bistability and of its characteristics (such as the transition temperature or the hysteresis width) in SCO complexes has not been achieved yet. This is mainly due to the fact that there are many factors that play a role in the presence of SCO in a complex and in the appearance of hysteresis when the SCO takes place. Thus, besides the well known role played by the metal ion and the ligand in the magnitude of the ligand field, there are other many subtle factors that determine the characteristics of the spin transition. These factors include (i) the nature of the counter-ion when the SCO complexes are cationic,[10-12] (ii) the presence of intermolecular interactions (mainly H-bonds and $\pi-\pi$ interactions) between the SCO complexes,[13] and (iii) the presence/absence of solvent molecules (that may interact with the SCO complexes modifying the ligand field or may apply a chemical pressure effect).[7]

Classical examples of the key role played by counter-ions are the families of $[Fe(3\text{-bpp})_2]X$ salts, X being different counter-anions, where the change of the anions determines the presence/absence of SCO, the transition temperature and even the presence/absence of thermal hysteresis.[11, 12, 14, 15] The role played by the solvent was also deeply studied for the $[Fe(3\text{-bpp})_2](BF_4)_2 \cdot G$ family, where it has been proved that changing the solvent molecule also determines the presence/absence of SCO, its temperature and the presence/absence of hysteresis.[7] The complex $[Fe(bpp)_2](BF_4)_2 \cdot 3H_2O$ provides another interesting example where the removal of the

three water molecules changes the transition temperature from 168 K (cooling down) and 184 K (heating) to 288 K and causes the loss of the hysteresis. For the Fe^{II} SCO complex $[Fe(bpp)(H_2L)](ClO_4)_2(CH_3COCH_3)_{1.5}$ (bpp = 2,6-bis(pyrazol-3-yl)pyridine, H_2L = 2,6-bis(5-(2-methoxyphenyl)pyrazol-3-yl)pyridine) the reversible exchange of solvents leads to drastic changes in the SCO properties.[16] Finally, the key role of the intermolecular interactions in neutral SCO complexes is evidenced in the family of complexes $[Fe(abpt)_2(L)_2]$ (L = nitrile derivative), where the change in L does not change the complex structure but results in a change in the intermolecular interactions and, accordingly, in the characteristics of the spin transition.[13]

In this chapter we will show and discuss the key role played by a non-coordinated water molecule in the presence/absence of SCO, in the transition temperature and in the presence/absence of hysteresis in two related iron(II) complexes. These complexes, formulated as $[NBu_4][Fe(3\text{-}bpp)_2][Cr(C_6O_4X_2)_3].H_2O$; X = Cl (**32**) and Br(**33**); 3-bpp = 2,6-bis(pyrazol-3-yl)pyridine; $(C_6O_4X_2)^{2-}$ = dianion of the 3,6-disubstituted derivatives of 2,5-dihydroxy-1,4-benzoquinone) are isostructural and present isolated $[Fe(3\text{-}bpp)_2]^{2+}$ cations surrounded by chiral $[Cr(C_6O_4X_2)_3]^{3-}$ anions, NBu_4^+ cations and a H-bonded water molecule. These complexes show gradual spin transitions without hysteresis centred at *ca*. 181 and 183 K for X = Cl and Br, respectively. The loss of the water molecule H-bonded to one of the N atoms of a pyrazol ring results in an increase of the SCO in both compounds: from 181 to 208 K in **32** and from *ca.* 183 K to *ca.* 200 K in **33**, and in the appearance of a narrow hysteresis of *ca.* 5 K in compound **33**. The reversibility/irreversibility of this dehydration process and the key role played by the water molecule are discussed from structural data at different temperatures before and after dehydration. Additionally, compound **33** presents LIESST effect when irradiated with green light with a LIESST temperature of *ca.* 70 K.

Besides these two compounds, another similar compound with formula $[Fe(3\text{-}bpp)_2]_3[Cr(C_6O_4Cl_2)_3]_2{\cdot}6H_2O$ **(34)** will be also presented and its structure will be described. This compound is similar to **32** although there is no NBu_4^+ cation and the cation:anion stoichiometry is now 3:2. Interestingly, this change leads to the disappearing of the SCO transition in the $[Fe(3\text{-}bpp)_2]^{2+}$ cation, that is now in the high spin state at any temperature.

2. Experimental Section

2.1. Synthesis

General Remarks: The synthesis of the precursor complexes $[NBu_4]_3[Cr(C_6O_4Cl_2)_3]$, $[NBu_4]_3[Cr(C_6O_4Br_2)_3]$ and $K_3[Cr(C_6O_4Cl_2)_3]$ is described in chapter one. The SCO compound $[Fe(3\text{-bpp})_2](BF_4)_2$ was prepared according to the literature method.[17] All other reagents and solvents were commercially available and used without further purification.

Synthesis of $[NBu_4][Fe(3\text{-bpp})_2][Cr(C_6O_4Cl_2)_3].H_2O$ (32): A solution containing $[Fe(3\text{-bpp})_2](BF_4)_2$ (6.6 mg, 0.01 mmol) in 2 mL of MeCN was added dropwise to a solution of $[NBu_4]_3[Cr(C_6O_4Cl_2)_3]$ (14.2 mg, 0.01 mmol) in 2 mL of MeCN under stirring. After the addition was completed, a precipitate appeared and 2 mL of H_2O were added to dissolve it. The final solution was further stirred for 20 minutes, filtered and left to evaporate at room temperature covered by an aluminium foil with some small pinholes. After one week, deep brown cubic crystals suitable for X-ray diffraction were filtered. Phase purity was confirmed by the powder X-ray diffractogram that is identical to the one simulated using with Mercury program from the crystal structure of **32** (Figure 5.1).

Synthesis of $[NBu_4][Fe(3\text{-bpp})_2][Cr(C_6O_4Br_2)_3].H_2O$ (33): This compound was prepared as **32** but using $[NBu_4]_3[Cr(C_6O_4Br_2)_3]$ (16.6 mg, 0.01 mmol) instead of $(NBu_4)_3[Cr(C_6O_4Cl_2)_3]$. After one week, deep brown cubic crystals suitable for X-ray diffraction were filtered. Phase purity was confirmed by the powder X-ray diffractogram that is identical to the one simulated with Mercury program from the crystal structure of **33** (Figure 5.2).

Synthesis of $[Fe(3\text{-bpp})_2]_3[Cr(C_6O_4Cl_2)_3]_2 \cdot 6H_2O$ (34): This compound was obtained using the layering technique in thin tubes while trying to obtain a 2D compound with the cation $[Fe(3\text{-bpp})_2]^{2+}$. A solution of $K_3[Cr(C_6O_4Cl_2)_3]$ (24 mg, 0.03 mmol) in 2.5 mL of MeCN (stirred for twenty minutes) was placed on top of a solution of $MnCl_2 \cdot H_2O$ (20 mg, 0.1 mmol) in 2.5 mL of water (middle solution) and a solution of $[Fe(bpp)_2](BF_4)_2$ (26 mg, 0.04 mmol) in 1 mL of EtOH and 1.5 mL of THF (bottom solution). The mixture was left to stand at room temperature. After three months single crystals suitable to X-ray diffraction were collected.

To reproduce this synthesis in a rational way, a solution containing $[Fe(bpp)_2](BF_4)_2$ (26 mg, 0.04 mmol) in 2 mL of EtOH and 1.5 mL THF was added dropwise to a solution of $K_3[Cr(C_6O_4Cl_2)_3]$ (24 mg, 0.03 mmol) in 2.5 mL of MeCN and 2.5 mL H_2O under stirring. The final solution was further stirred for 20 minutes, filtered and left to evaporate at room temperature covered by an aluminium foil with some small pinholes. After three days, a microcrystalline powder was collected. Phase purity was confirmed by the powder X-ray difractogram that is identical to the one simulated, using Mercury program from the crystal structure of **34** (Figure 5.3).

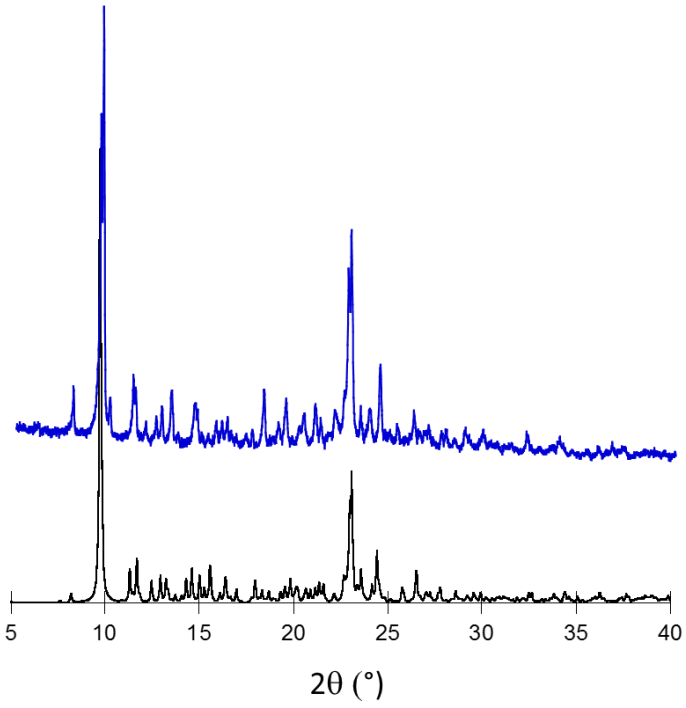

Figure 5.1*. Simulated (black) and experimental (blue) powder X-ray diffractograms for compound* ***1****.*

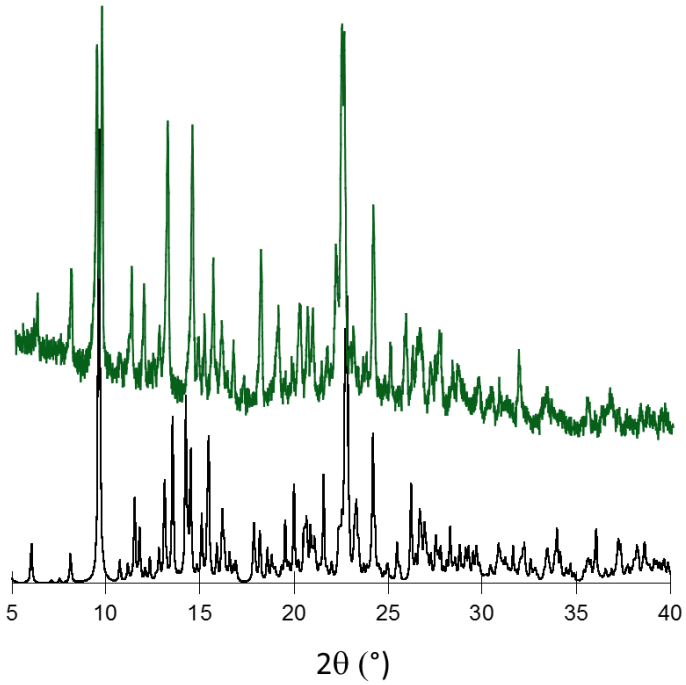

Figure 5.2**. Simulated (black) and experimental (green) powder X-ray diffractograms for compound **2

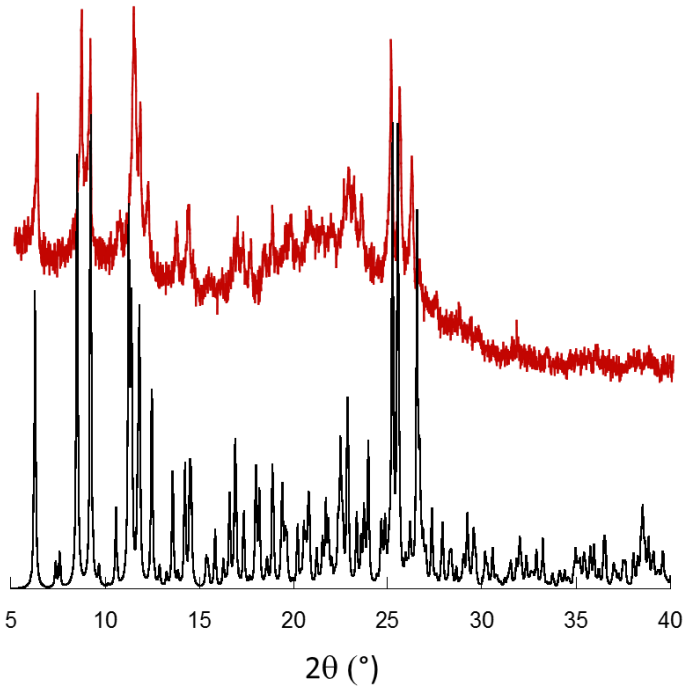

***Figure 5.3**. Simulated (black) and experimental (red) powder X-ray diffractograms for compound **3**.*

2.3. Physical Properties

Magnetic measurements were performed with a Quantum Design MPMS-XL-5 SQUID magnetometer in the 2-300 K temperature range with an applied magnetic field of 0.5 T on polycrystalline samples of the three compounds. Isothermal magnetization measurements were performed at 2 K with magnetic fields of up to 5 T. Susceptibility data were corrected for the sample holder and for the diamagnetic contribution of the salts using Pascal's constants.[18]

2.4. Structural Characterization

Single crystals of compounds **32, 33** and **34** were mounted on a loop using a viscous hydrocarbon and then transferred directly to the cold nitrogen stream for data collection. X-ray data were initially collected at 120 K (**32**$_{120}$ and **33**$_{120}$) and 220 K (**32**$_{220}$ and **33**$_{220}$). The samples were then heated up to 360 K (to remove the water molecule) and then cooled again to 120 K (**32d**$_{120}$ and **33d**$_{120}$). Finally, the crystal of compound **32** was immersed in water during 48 hours and the rehydrated crystal was measured at 200 K (**32h**$_{200}$).The unit cell parameters were measured every 5 or 10 K during the cooling and heating scans. X-ray data were collected on a Supernova diffractometer equipped with a graphite-monochromated Enhance (Mo) X-ray Source (λ = 0.71073 Å). The program CrysAlisPro, Oxford Diffraction Ltd., was used for unit cell determinations and data reduction. Empirical absorption correction was performed using spherical harmonics, implemented in the SCALE3 ABSPACK scaling algorithm. Crystal structures were solved and refined against all F^2 values using the SHELXL-2014 suite of programs.[19] Non-hydrogen atoms were refined anisotropically and hydrogen atoms were assigned fixed isotropic displacement parameters. A summary of the data collection and structure refinements is provided in Tables 5.1, 5.2 and 5.8.

The X-ray powder diffractograms were collected for polycrystalline samples of all the compounds using a 0.5 mm glass capillary that was mounted and aligned on a Empyrean PANalytical powder diffractometer, using CuKα radiation (λ = 1.54177 Å) operating at 40 mA and 45 kV. A total of 6 scans were collected at room temperature in the 2θ range of 2-40º in spinning mode with a step size of 0.0131º.

3. Results and Discussion

3.1. Single Crystal Structure

Structure of $[NBu_4][Fe(3\text{-}bpp)_2][Cr(C_6O_4X_2)_3].H_2O$, X = Cl (32) and Br (33).

Table 5.1*. Crystallographic data of compound* ***32*** *at 120 K (****32$_{120}$****), 220 K (****32$_{220}$****), 120 K after dehydration at 360 K (****32d$_{120}$****) and 200 K after immersion in water for 48 hours (****32h$_{200}$****).*

	32$_{120}$	**32$_{220}$**	**32d$_{120}$**	**32h$_{200}$**
Empirical formula	$C_{56}H_{56}Cl_6N_{11}O_{13}FeCr$	$C_{56}H_{56}Cl_6N_{11}O_{13}FeCr$	$C_{56}H_{54}Cl_6N_{11}O_{12}FeCr$	$C_{56}H_{58}Cl_6N_{11}O_{14}FeCr$
Formula weight	1411.67	1411.67	1377.65	1429.68
Temperature (K)	120(2)	220(2)	120(2)	200(2)
Wavelength (Å)	0.71073	0.71073	0.71073	0.71073
Crystal system	Monoclinic	Monoclinic	Monoclinic	Monoclinic
Space group	*P*21*n*	*P*21*n*	*Pn*	*P*21*n*
a (Å)	9.3111 (2)	9.4551(3)	9.2485(4)	9.4619(4)
b(Å)	27.2510(10)	28.6872(9)	27.4961(10)	28.6180(11)
c(Å)	23.5119(8)	24.1170(6)	24.3155(9)	24.1198(12)
α (°)	90	90	90	90
β (°)	99.150(3)	100.232(2)	96.368(4)	100.368
γ (°)	90	90	90	90
V (Å^3)	6322.2 (3)	6437.5(3)	6145.2(4)	6424.5(5)
ρ_{cal} (mg m^{-3})	1.481	1.450	1.502	1.470
μ (mm^{-1})	0.725	0.712	0.743	0.715
Crystal size (mm^3)	0.22x 0.05x0.04	0.23x 0.07x0.06	0.23x 0.07x0.06	0.23x 0.07x0.06
θ range (°)	3.236 - 25.039	2.840-25.056	2.869-25.067	2.943-25.056
Reflections collected	65494	24071	65218	27073
Independent reflections (R_{int})	11140	11367	20135	11330
Reflns used in refinement, *n*	11140	11367	20135	11330
$R_1(F)$,[a] $I > 2\sigma(I)$	0.1072	0.0684	0.1343	0.0986
$wR_2(F^2)$,[b] all data	0.2989	0.1971	0.2949	0.2126
$S(F^2)$,[c] all data	1.028	1.035	1.165	1.107
Largest diff. peak	1.013	1.561	1.025	0.838
Largest diff. hole	-0.586	-0.498	-1.616	-0.376

[a] $R1(F) = \Sigma||F_O|-|F_C||/\Sigma|F_O|$; [b] $wR2(F^2) = [\Sigma w(F_O^2-F_C^2)^2/\Sigma wF_O^4]^{1/2}$;

[c] $S(F^2) = [\Sigma w(F_O^2-F_C^2)^2/(n+r-p)]^{1/2}$

Compounds **32** and **33** are isostructural and only differ in the X group of the anilato-type ligand in the $[Cr(C_6O_4X_2)_3]^{3-}$ anion (X = Cl for **32** and X = Br for **33**). The asymmetric unit of both compounds is formed by an isolated $[Fe(3\text{-}bpp)_2]^{2+}$ cation, a $[NBu_4]^+$ cation, an isolated $[Cr(C_6O_4X_2)_3]^{3-}$ anion and a crystallization water molecule (Figure 5.4).

***Table 5.2**. Crystallographic data of compound **33** at 120 K (**33$_{120}$**), 220 K (**33$_{220}$**) and 120 K after dehydration at 360 K (**33d$_{120}$**).*

	33$_{120}$	**33$_{220}$**	**33d$_{120}$**
Empirical formula	$C_{56}H_{56}Br_6N_{11}O_{13}FeCr$	$C_{56}H_{56}Br_6N_{11}O_{13}FeCr$	$C_{56}H_{54}Br_6N_{11}O_{12}FeCr$
Formula weight (g/mol)	1678.37	1678.37	1660.36
Temperature (K)	120(2)	220(2)	120(2)
Wavelength (Å)	0.71073	0.71073	0.71073
Crystal system	Monoclinic	Monoclinic	Monoclinic
Space group	*P*21*n*	*P*21*n*	*Pn*
a (Å)	9.4573(2)	9.6344(2)	9.4903(2)
b(Å)	29.2787(8)	28.7075(5)	27.6039(5)
c(Å)	23.7813(5)	24.2300(5)	24.1284(5)
α (°)	90	90	90
β (°)	99.232(2)	99.915(2)	96.094(2)
γ (°)	90	90	90
V (Å^3)	6499.7	6601.4(2)	6285.2
ρ_{cal} (mg m^{-3})	1.722	1.668	1.754
μ (mm^{-1})	4.149	4.082	4.286
Crystal size (mm^3)	0.11x0.08x0.04	0.11x0.08x0.04	0.11x0.08x0.04
θ range (°)	2.915-25.044	2.927-25.039	2.819-25.057
Reflections collected	86642	73375	61410
Independent reflections (R_{int})	11488	11667	22010
Reflns used in refinement, *n*	11488	11667	22010
$R_1(F)$,[a] $I > 2\sigma(I)$	0.0807	0.0605	0.0572
$wR_2(F^2)$,[b] all data	0.1947	0.1654	0.0908
$S(F^2)$,[c] all data	1.049	1.026	0.998
Largest diff. peak	2.497	1.172	0.865
Largest diff. hole	-2.435	-0.833	-0.599

[a]$R1(F) = \Sigma||F_O|-|F_C||/\Sigma|F_O|$; [b]$wR2(F^2) = [\Sigma w(F_O^2-F_C^2)^2/\Sigma wF_O^4]^{1/2}$;

[c]$S(F^2) = [\Sigma w(F_O^2-F_C^2)^2/(n+r-p)]^{1/2}$

The structure consists of layers parallel to the *bc* plane (Figure 5.5a) containing $[Fe(3\text{-bpp})_2]^{2+}$ and $[NBu_4]^+$ cations, $[Cr(C_6O_4X_2)_3]^{3-}$ anion and the water molecule. The projection onto the *bc* plane of these layers shows rows containing $[Fe(3\text{-bpp})_2]^{2+}$ cations parallel to the *c* direction alternating (along *b*) with rows containing $[NBu_4]^+$ cations and $[Cr(C_6O_4X_2)_3]^{3-}$ anions with the water molecules (Figure 5.5b).

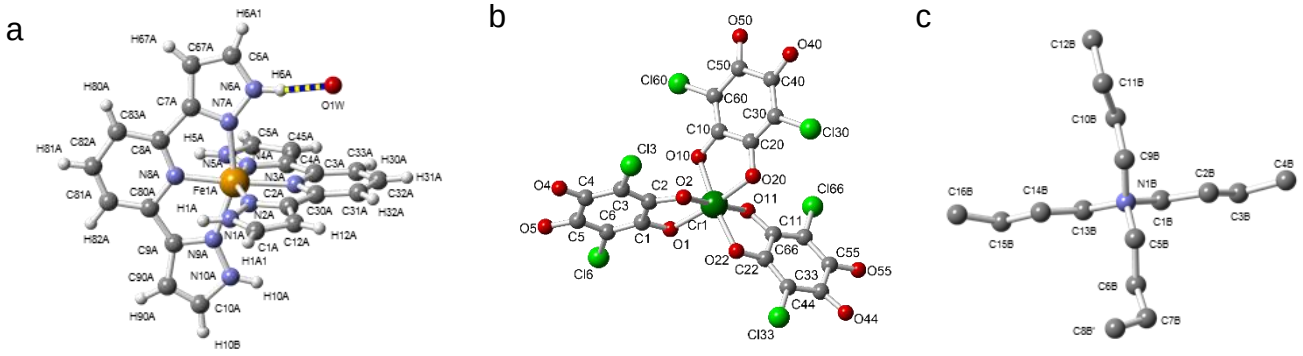

Figure 5.4: *Components of the asymmetric unit of compound **32** sowing the labelling scheme (same for **33** but with X = Br) **(a)** The $[Fe(3\text{-}bpp)_2]^{2+}$ cation with the H_2O molecule bonded to one H of the bpp ligand. **(b)** The $[Cr(C_6O_4Cl_2)_3]^{3-}$ anion and **(c)** the $[NBu_4]^+$ cation.*

The $[NBu_4]^+$ cations appear fully ordered and present three butyl groups with an all *trans* configuration and one butyl group with a *cis* configuration in the last C-C bond. (Figure 5.4c).

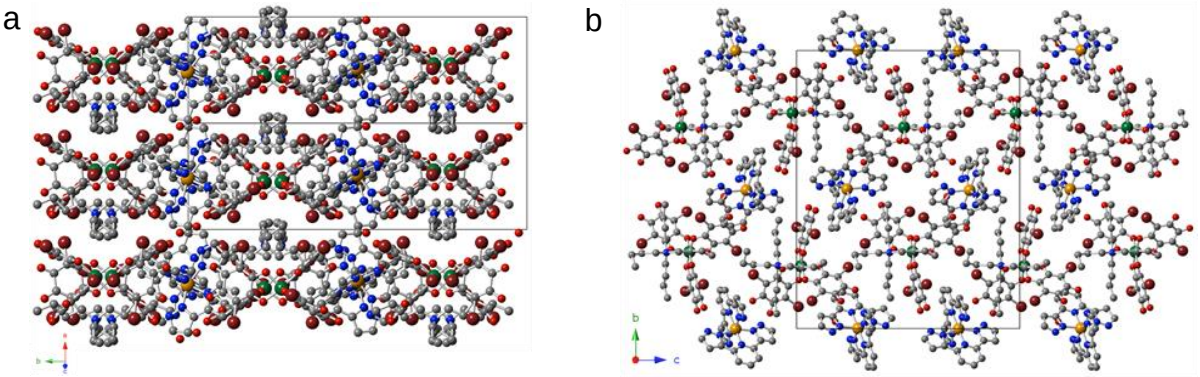

Figure 5.5. (a) *View of the structure of compound **33** (same for **32**) showing the layers parallel to the bc plane. **(b)** Projection of these layers into the bc plane showing the $[Fe(3\text{-}bpp)_2]^{2+}$ rows running along the c direction (at c = 1/4 and 3/2) and the parallel rows containing the $[NBu_4]^+$ cations and the $[Cr(C_6O_4Br_2)_3]^{3-}$ anions (at c = 0 and 1/2). H atoms have been omitted for clarity. Colour code: C = grey, N = blue, O = red, Fe = orange, Cr = green, Br = brown.*

The $[Cr(C_6O_4X_2)_3]^{3-}$ anions present the tris-chelate structure already observed in other similar $[M(C_6O_4X_2)_3]^{3-}$ anions (Figure 5.4b).[20-24] As expected, there is a racemic mixture of Δ- and Λ-$[Cr(C_6O_4X_2)_3]^{3-}$ anions, since the structure is not chiral and we use a racemic mixture of anions in the synthetic procedure. In compound **32,** each $[Cr(C_6O_4X_2)_3]^{3-}$ anion is surrounded by two $[Fe(3\text{-}bpp)_2]^{2+}$ and shows a weak π–π interaction established between the anilato rings and one of the two pyrazol rings of

the 3-bpp ligands (Figure 5.6). This weak π-π interaction shows a centroid-centroid distance of 3.878 Å and an offset angle of 21.84º, values slightly above the normal range defined by Janiak[25] for these interactions (3.3-3.8 Å and *ca*. 20º).[25] Compound **33** does not show any π-π anion-cation interaction since the centroid-centroid distance is much longer (4.462 Å) and the offset angle (13.41º) is far from 20º.

The $[Fe(3\text{-bpp})_2]^{2+}$ cations present the *mer* configuration. In both compounds the crystallization H_2O molecule is H-bonded to a H atom of one of the pyrazol rings (H···O = 1.843 Å and 1.874 Å; N-H···O = 158.04º and 160.39º in **32** and **33**, respectively at 120 K) (figure 5.6). The Fe-N bond distances in both compounds are strongly dependent on the temperature. Thus, at 120 K the Fe-N bond lengths are in the range of 1.996-2.038 Å for **32** and of 1.963-2.050 Å for **33** with average values of 2.0216 for **32** and 2.0213 Å for **33** (Tables 5.3 and 5.5).

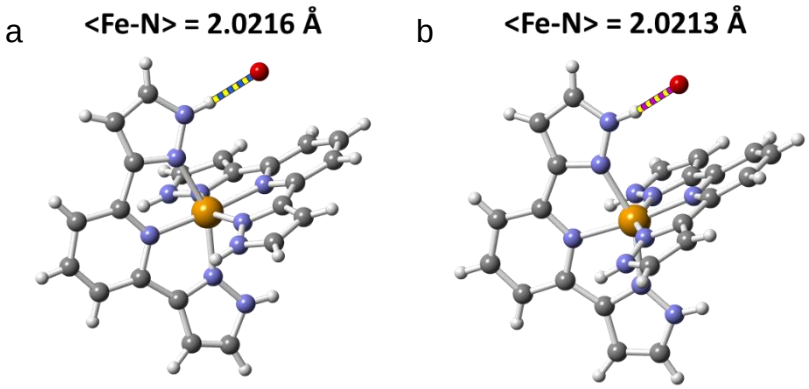

Figure 5.6. *View of the structure of the $[Fe(bpp)_2]^{2+}$ cation with the water molecule H-bonded to the bpp ligand in* ***(a)*** *compound* ***32*** *at 120 K,* ***(b)*** *compound* ***33*** *at 120 K.*

These values suggest that the Fe(II) centres are in the low spin (LS) configuration although there is a small fraction of *ca*. 15 % of Fe(II) centres in high spin (HS) at 120 K, since the average Fe-N distance in LS is *ca.* 2.00 Å and *ca*. 2.18 Å in HS.[26, 27] At 220 K, the average Fe-N bond distance increases to 2.166 Å for **32** and to 2.153 Å for **33** (Tables 5.3 and 5.5, figure 5.7), indicating that both complexes are now almost 100 % in HS configuration, in agreement with the magnetic measurements (see below). At this temperature, the water molecule is still H-bonded with the bpp ligand (figure 5.7).

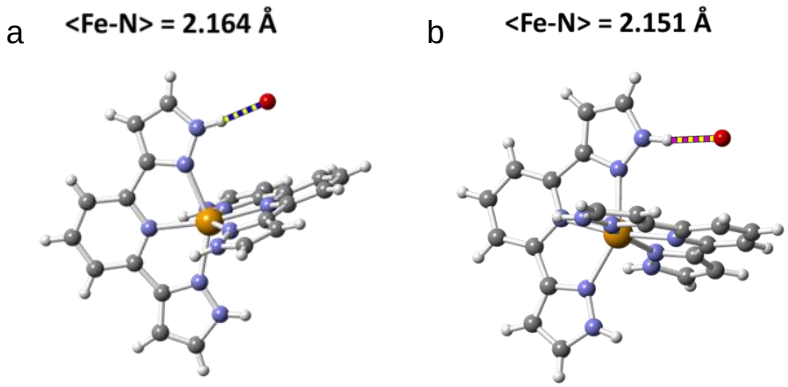

Figure 5.7. *View of the structure of the $[Fe(bpp)_2]^{2+}$ cation with the water molecule H-bonded to the bpp ligand in* ***(a)*** *compound* ***32*** *at 220 K.* ***(b)*** *Compound* ***33*** *at 220 K.*

After heating the crystals above 340 K, the water molecule is lost (figure 5.8). Interestingly, this loss is accompanied by a phase transition. In the new phase there are two different Fe(II) centres. When the dehydrated samples are cooled down to 120 K the two Fe(II) centres present average Fe-N bond lengths of 1.946 Å and 2.172 Å for **32** and 1.955 Å and 2.169 Å for **33**, indicating that one of the Fe(II) centres in each compound is in LS and the other is in HS, in agreement with the magnetic measurements (see below).

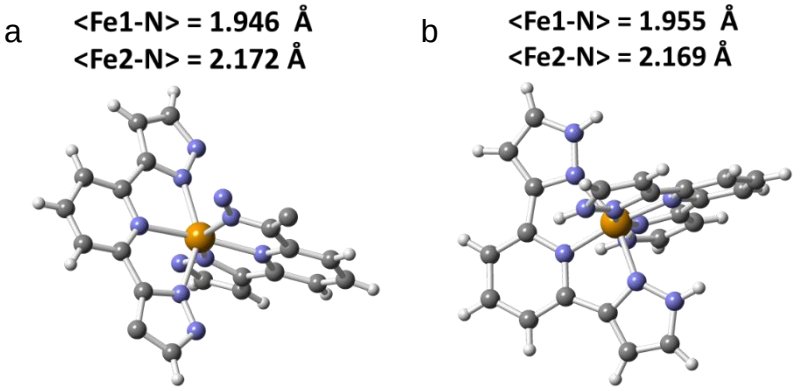

Figure 5.8. *View of the structure of the $[Fe(bpp)_2]^{2+}$ cation in* ***(a)*** *Compound* ***32*** *at 120 K after dehydration at 340 K, showing no water molecule attached and two crystallographic independent Fe(II) centres.* ***(b)*** *Compound* ***33*** *at 120 K after dehydration at 340 K, showing no water molecule attached and two crystallographic independent Fe(II) centres.*

An additional parameter that can be used to check the spin state of the metal centre is the Σ value, which is the sum of the deviation from 90° of the 12 *cis* angles around the Fe(II) centre. There is no Σ range of values stablished for high spin and low

spin, but, when two different metal centres are compared, the Σ value is much higher for the HS centres than for the LS ones. This same behaviour is found in compounds **32** and **33**, where values of Σ around 150º can be found for the HS configuration and ca. 100º for the LS one (see tables 5.4 and 5.6).

To check for the reversibility of the water release, the dehydrated crystals of compound **32** were immersed in water for two days and measured again. After rehydration the crystal was cooled to 200 K. At this temperature there is only one crystallographically independent Fe(II) which is in the HS state (the Fe-N average distance is 2.163 Å), confirming the reversibility of the water removal/uptake process. Surprisingly, after immersion in water for 48 h, the crystal uptakes two water molecules instead of only one. These two water molecules appear H-bonded to the two bpp ligands of the $[Fe(3\text{-bpp})_2]^{2+}$ cations (figure 5.9).

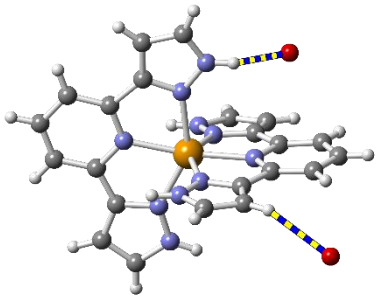

Figure 5.9. *View of the structure of the $[Fe(bpp)_2]^{2+}$ cation with the two water molecules H-bonded to the bpp ligand in compound* ***32*** *after immersion in water for 48 hours, showing only one independent Fe(II) and two molecules of water.*

Table 5.3*. Fe-N bond lengths (Å) in* ***32****.*

	32_{120}	**32_{220}**	**$32d_{120}$**		**$32h_{200}$**
Atoms	Fe(1A)	Fe(1A)	Fe(1A)	Fe(1D)	Fe(1A)
Fe(1Z)-N(8A)	1.963(10)	2.130(4)	1.919(18)	2.116(15)	2.124(6)
Fe(1Z)-N(3A)	2.005(8)	2.142(4)	1.923(18)	2.14(2)	2.138(6)
Fe(1Z)-N(4A)	2.021(8)	2.166(4)	1.924(18)	2.14(2)	2.165(6)
Fe(1Z)-N(2A)	2.039(8)	2.172(5)	1.926(19)	2.206(19)	2.170(7)
Fe(1Z)-N(9A)	2.050(10)	2.178(4)	1.976(18)	2.19(2)	2.180(6)
Fe(1Z)-N(7A)	2.050(9)	2.209(4)	2.010(19)	2.24(2)	2.201(7)

***Table 5.4**. Bond angles and Σ values (°) around the Fe centre in **32**.*

	32_{120}	32_{220}	$32d_{120}$		$32h_{200}$
Atoms	**Fe(1A)**	**Fe(1A)**	**Fe(1C)**	**Fe(1D)**	**Fe(1A)**
N(8)-Fe(1Z)-N(4)	100.9(4)	109.60(16)	94.8(8)	116.1(7)	109.3(2)
N(3)-Fe(1Z)-N(4)	77.6(3)	73.28(16)	79.3(8)	75.1(8)	73.3(2)
N(8)-Fe(1Z)-N(2)	105.7(3)	103.40(15)	106.4(8)	96.4(6)	103.4(2)
N(3)-Fe(1Z)-N(2)	76.0(3)	74.33(16)	79.5(8)	73.0(7)	74.5(2)
N(8)-Fe(1Z)-N(9)	76.1(5)	73.48(17)	79.6(8)	74.9(6)	73.5(2)
N(3)-Fe(1Z)-N(9)	107.6(4)	97.63(16)	101.6(8)	118.8(7)	97.9(2)
N(4)-Fe(1Z)-N(9)	95.4(4)	98.64(16)	93.8(8)	87.1(7)	98.5(2)
N(2)-Fe(1Z)-N(9)	88.6(3)	91.89(15)	89.3(8)	103.2(7)	91.7(2)
N(8)-Fe(1Z)-N(7)	79.1(4)	74.22(19)	78.8(7)	74.4(6)	74.4(3)
N(3)-Fe(1Z)-N(7)	97.1(4)	114.76(18)	100.2(8)	92.8(7)	114.3(3)
N(4)-Fe(1Z)-N(7)	89.8(3)	89.35(16)	90.5(8)	99.2(7)	89.2(2)
N(2)-Fe(1Z)-N(7)	97.5(3)	98.35(17)	94.3(7)	88.1(7)	98.6(2)
Σ	**117.0**	**149.6**	**95.1**	**153.9**	**148.1**

***Table 5.5**. Fe-N bond lengths (Å) in **33**.*

	33_{120}	33_{220}	$33d_{120}$	
Atoms	**Fe(1A)**	**Fe(1A)**	**Fe(1A)**	**Fe(1D)**
Fe(1Z)-N(8A)	1.996(8)	2.118(6)	2.130(9)	1.928(10)
Fe(1Z)-N(3A)	1.998(9)	2.124(6)	2.143(10)	1.916(10)
Fe(1Z)-N(4A)	2.034(9)	2.144(6)	2.195(11)	1.988(10)
Fe(1Z)-N(2A)	2.038(10)	2.163(6)	2.144(11)	1.976(10)
Fe(1Z)-N(9A)	2.027(8)	2.157(6)	2.217(11)	1.954(11)
Fe(1Z)-N(7A)	2.037(9)	2.209(6)	2.186(11)	1.965(11)

***Table 5.6**. Bond angles and sigma values (°) around the Fe centres in **33**.*

	33_{120}	33_{220}	$33d_{120}$	
Atoms	**Fe(1A)**	**Fe(1A)**	**Fe(1A)**	**Fe(1D)**
N(8)-Fe(1Z)-N(4)	108.6(4)	102.2(2)	93.2(4)	109.0(4)
N(3)-Fe(1Z)-N(4)	77.6(4)	74.2(2)	72.7(4)	79.0(4)
N(8)-Fe(1Z)-N(2)	96.3(3)	110.7(2)	121.1(4)	93.0(4)
N(3)-Fe(1Z)-N(2)	77.5(4)	73.6(2)	73.9(4)	79.1(4)
N(8)-Fe(1Z)-N(9)	77.4(3)	74.6(2)	73.8(4)	79.5(5)
N(3)-Fe(1Z)-N(9)	99.5(3)	115.5(2)	91.2(4)	101.8(4)
N(4)-Fe(1Z)-N(9)	96.3(3)	99.4(2)	88.1(4)	88.4(4)
N(2)-Fe(1Z)-N(9)	88.7(3)	87.8(2)	100.7(4)	94.9(4)
N(8)-Fe(1Z)-N(7)	77.1(3)	73.5(2)	74.5(4)	79.0(4)
N(3)-Fe(1Z)-N(7)	106.2(3)	96.5(2)	121.9(4)	99.8(4)
N(4)-Fe(1Z)-N(7)	88.3(3)	90.5(2)	103.4(4)	96.8(4)
N(2)-Fe(1X)-N(7)	97.8(3)	100.3(2)	87.3(4)	88.1(4)
Σ	**120.5**	**151.4**	**161.2**	**102.2**

As expected, the Σ values (Tables 5.4 and 5.6) are much higher in the HS than in the LS state, since sigma reflects the distortions of the coordination environment and these are expected to be higher for the HS configuration than for the LS, since the coordination sphere expands by *ca*. 10 %.[28]

It seem undeniable that the singularity of these compounds lies in the water attached to the $[Fe(bpp)_2]^{2+}$ by a hydrogen bond. To check the strength of this bond, we have performed the analysis suggested by Steiner[29]. The main values are given in Table 5.7.

Table 5.7*. Bond distances and angles for the hydrogen bonds in* ***32*** *and* ***33****.*

	H···O (Å)	X···O (Å)	X-H···O (°)	Interaction type
32$_{120}$	1.843	2.688	160.39	Mostly electrostatic
32$_{220}$	1.852	2.706	166.65	Mostly electrostatic
32h$_{200}$	1.843	2.707	166.43	Mostly electrostatic
32h$_{200}$	2.707	3.413	152.98	Electrostatic/disper.
33$_{120}$	1.874	2.709	158.04	Mostly electrostatic
33$_{220}$	1.850	2.701	165.59	Mostly electrostatic

All hydrogen bonds are mostly electrostatic and moderate. The only exception is the one present in the rehydrated structure in the second molecule of water. In this case, the hydrogen bond has a weak character and presents a higher distance between the water molecule and the H of the pirazol ring in the bpp ligand. This H-bond is longer because it is established between the water molecule and a C-H group of the pyrazol ring instead of a N-H group. In the monohydrated structure there are 224 $Å^3$ of empty space. This is filled with water after immersing the crystal in water for 48 hours. The weak character of this hydrogen bond, might prevent the absorption of a second water molecule during the original synthesis. Thus, this second water molecule is only incorporated when the compound is immersed in water.

In order to study the changes produced in both compounds after heating the samples above 340 K, we have performed a detailed structural study as a function of the temperature for both compounds. First, we have measured the unit cell of a single crystal of compounds **32** and **33** in the temperature range 120-360 K while heating the crystal. The β parameter and the unit cell volume show the expected increase with temperature (Figures 5.10 and 5.11). At *ca.* 180-190 K the β angle for both compounds shows an anomalous increase, suggesting the occurrence of a SCO around this

temperature (in agreement with the magnetic measurements, see below). This fact suggests that the structural variations in the $[Fe(bpp)_2]^{2+}$ cation during the SCO transition affect mainly this parameter. Upon further heating, both the volume and the β angle of **32** and **33** continue to steadily increase until approximately 340 K, where there is an abrupt decrease of *ca.* 200 Å^3 in the unit cell volume of both compounds that indicates the loss of one water molecule. The β angle also shows the same abrupt decrease for both compounds, indicating the reorganization of the bpp ligand after the loss of water. (Figures 5.10 and 5.11). Once the water molecule is lost, when the temperature is decreased, an abrupt decrease of the β angle value can be observed at *ca.* 180 K, indicating again the presence of a SCO around this temperature in the dehydrated crystal. On further cooling to 120 K the unit cell volume and the β angle do not recover the initial values, indicating that, as expected, the water loss at *ca.* 330-340 K is irreversible under this conditions (the crystals are surrounded by a nitrogen jet in the cryostat of the X-ray diffractometer).

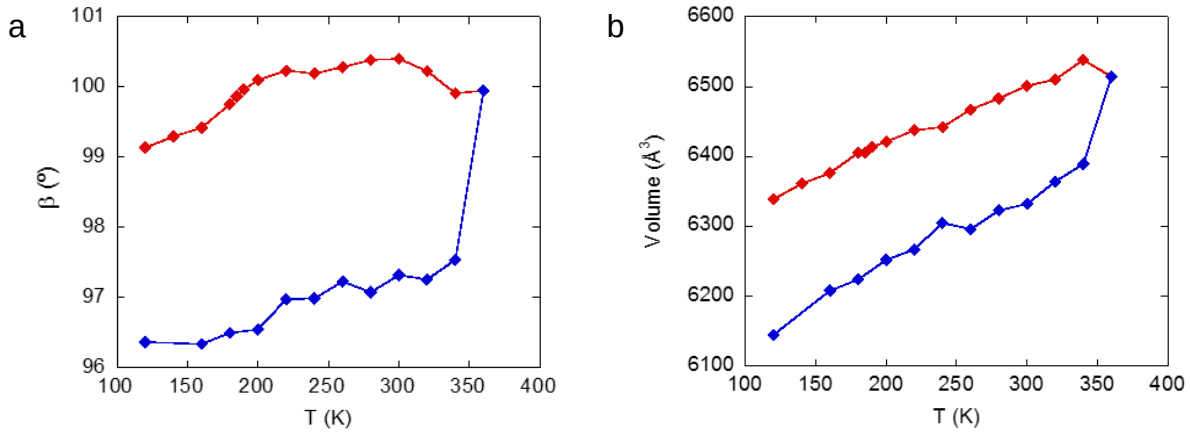

Figure 5.10. *Thermal variation of* ***(a)*** *the β angle and* ***(b)*** *the unit cell volume in the heating (red) and cooling (blue) scans for compound* ***32****.*

The unit cell volume shows similar anomalies due to the SCO and the loss of water. Thus, the unit cell volume shows a linear increment as the temperature is increased from 120 K to the SCO temperature, where there is an abrupt increase. Above the SCO, the volume increases again until 340 K, where it shows an abrupt decrease of *ca*. 200 Å^3 due to the water loss. When cooling down from 360 K to 120 K a constant lessening was observed, as in the β angle study, and a more abrupt decrease of the volume at the SCO transition temperature is detected. The volume

values are different than the ones obtained during the heating process further confirming the irreversibility of the water loss under the mentioned conditions.

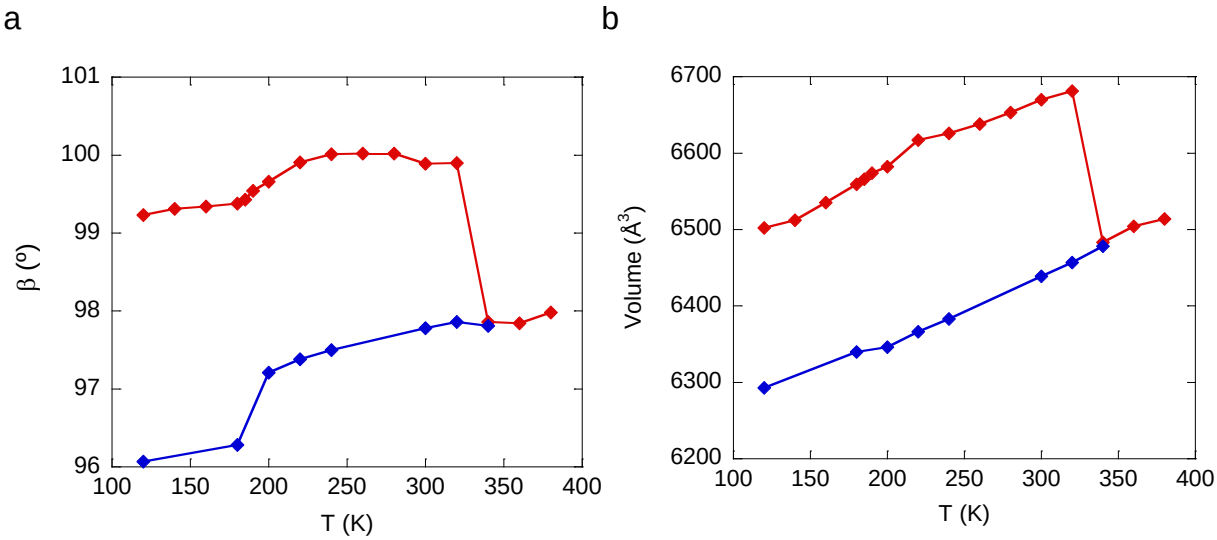

Figure 5.11. *Thermal variation of* ***(a)*** *the* β *angle and* ***(b)*** *the unit cell volume in the heating (red) and cooling (blue) scans for compound* ***33****.*

Structure of $[Fe(3\text{-bpp})_2]_3[Cr(C_6O_4Cl_2)_3]_2\cdot 6H_2O$ (34). Compound **34** crystallizes in the trigonal *R*-3 space group. The asymmetric unit is formed by three $[Fe(3\text{-bpp})_2]^{2+}$ cations, two $[Cr(C_6O_4Cl_2)_3]^{3-}$ anions and four water molecules, giving a total formula of $[Fe(3\text{-bpp})_2]_3[Cr(C_6O_4Cl_2)_3]_2\cdot 4H_2O$. A summary of the data collection and structure refinements is provided in Table 5.8.

The structure of compound **34** consists of $[Fe(3\text{-bpp})_2]^{+2}$ cations surrounded by $[Cr(C_6O_4Cl_2)_3]^{3-}$ anions and vice versa (Figure 5.12a). In this structure the water molecules are not H-bonded to any H of the bpp ligand. The $[Fe(3\text{-bpp})_2]^{+2}$ cations and the $[Cr(C_6O_4Cl_2)_3]^{3-}$ anions have the same structure found in the two previous compounds (Figure 5.12b). Despite the large number of aromatic rings in the cation and anion, there are no π-π interactions in this compound (the closest C_g-C_g distance is 4.167 Å with and offset angle of 15.91º, values out of the normal range proposed by Janiak for a normal π-π interactions.[25]

Table 5.8**. Crystallographic data for compound **34

	34
Empirical formula	$C_{408}H_{216}Cl_{48}N_{120}O_{130}Fe_{12}Cr_8$
Formula weight (g/mol)	11666.79
Temperature (K)	120(2)
Wavelength (Å)	0.71073
Crystal system	Trigonal
Space group	*R-3* (#148).
a (Å)	41.5988(8)
b(Å)	41.5988(8)
c(Å)	22.6478(4)
α (°)	90
β (°)	90
γ (°)	120
V (Å^3)	33940.5
ρ_{cal} (mg m^{-3})	1.712
μ (mm^{-1})	0.941
Crystal size (mm^3)	0.20x0.04x0.03
θ range (°)	3.274 - 25.064
Reflections collected	139605
Independent reflections (R_{int})	13305
Reflns used in refinement, *n*	13305
$R_1(F)$,[a] $I > 2\sigma(I)$	0.0605
$wR_2(F^2)$,[b] all data	0.1569
$S(F^2)$,[c] all data	1.040
Largest diff. peak	2.141
Largest diff. hole	-1.079

[a]$R1(F) = \Sigma||F_O|-|F_C||/\Sigma|F_O|$; [b]$wR2(F^2) = [\Sigma w(F_O^2-F_C^2)^2/\Sigma wF_O^4]^{1/2}$;
[c]$S(F^2) = [\Sigma w(F_O^2-F_C^2)^2/(n+r-p)]^{1/2}$

There are two independent Fe(II) ions with average Fe-N bond distances of 2.185 and 2.190 Å (Table 5.9). These values indicate that both Fe(II) centres are in the high spin configuration at 120 K, in agreement with the magnetic measurements (see below). Note that compound **34** contains the same $[Fe(3\text{-bpp})_2]^{2+}$ cation than compounds **32** and **33** and even the same $[Cr(C_6O_4X_2)_3]^{3-}$ anion. The only differences are the cation:anion stoichiometry (1:1 in **32** and **33** and 3:2 in **34**), the presence of a NBu_4^+ cation and a H-bonded water molecule in **32** and **33**. Compound **34**, therefore, illustrates the key role that may play the anion-cation and the solvent-cation interactions in the SCO phenomenon.

a b

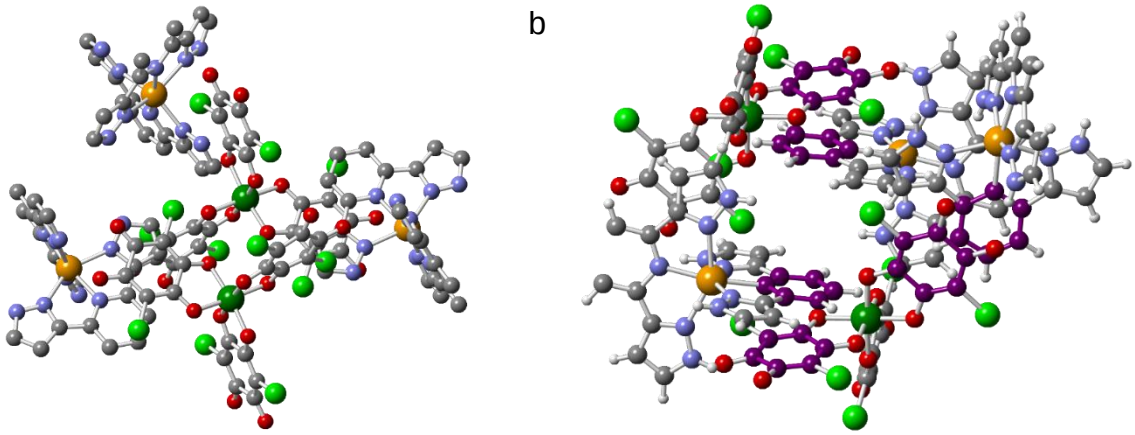

Figure 5.12. *Structure of compound* ***34*** ***(a)*** *View of two* $[Cr(C_6O_4Cl_2)_3]^{3-}$ *anions surrounded by three* $[Fe(3\text{-}bpp)_2]^{+2}$ *cations (H atoms are omitted for clarity) and* ***(b)*** *view of the anion-cation interactions. Colour code: C = grey, N = blue, O = red, Fe = orange, Cr = green, Cl = light green, H = white.*

Table 5.9*. Fe-N Bond lengths (Å) in compound* ***34.***

	34	
Atoms	Z = A	Z = B
Fe(1Z)-N(8Z)	2.170(4)	2.156(5)
Fe(1Z)-N(3Z)	2.151(4)	2.176(4)
Fe(1Z)-N(4Z)	2.192(4)	2.181(4)
Fe(1Z)-N(2Z)	2.214(4)	2.196(4)
Fe(1Z)-N(9Z)	2.195(4)	2.246(5)
Fe(1Z)-N(7Z)	2.189(4)	2.184(5)
<Fe(1Z)-N>	**2.185**	**2.190**

3.2. Powder X-Ray Diffraction

Compounds **32**, **33** and **34** were analysed with the XRPD technique to check for phase purity in the samples by comparison with the simulated diffractogram from the solved structures (Figures 5.1, 5.2 and 5.3). In all cases the experimental diffractograms are similar to the simulated ones from the single crystal X-ray structure.

3.3. Magnetic Properties

Compound **32** shows at room temperature a $\chi_m T$ value of 5.2 cm^3 K mol^{-1}, the expected value for a Cr(III) with g = 2 (1.875 cm^3 K mol^{-1}) plus a Fe(II) with g ≈ 2.1 (*ca*. 3.3 $cm^3 \cdot K \cdot mol^{-1}$) (Figure 5.13a). When the temperature is decreased the $\chi_m T$ product remains constant down to ca. 200 K. Below this temperature, $\chi_m T$ shows a smooth decrease in the temperature-range of 200-100 K and reaches a plateau of *ca*. 2.4 cm^3

K mol^{-1} at *ca*.100 K. Below 100 K, χ_mT remains constant and shows an abrupt decrease below *ca*. 5 K to reach a value of *ca*. 1.2 cm^3 K mol^{-1} at 2 K (Figure 5.13a). The χ_mT value at room temperature indicates that all the Fe(II) centres of the [Fe(3-bpp)$_2$]$^{2+}$ cation are in the HS configuration (S = 2) at 300 K. The decrease of χ_mT observed between *ca*. 200 K and 100 K corresponds to a smooth SCO taking place in the [Fe(3-bpp)$_2$]$^{2+}$ cation. The low temperature value (ca. 2.4 cm^3 K mol^{-1}) indicates that the SCO is not complete and that *ca*. 15 % of the Fe(II) centres remain in the HS configuration. This value agrees with the structure results at 120 K (see above). The abrupt decrease observed at very low temperatures is simply due to the presence of a zero field splitting (ZFS) of the Fe(II) fraction in HS state and of the paramagnetic S = 3/2 Cr(III) ion. Since the SCO is smooth, in order to determine the SCO temperature we have calculated the derivative of χ_mT with the temperature. The plot of $\delta(\chi_m T)/\delta T$ *vs*. T (Figure 5.13b) shows that the SCO is smooth and takes place in the range 200-100 K with a major inflexion point at ca. 180 K and no hysteresis between the cooling and warming scans. We can conclude that this compound shows a smooth almost complete spin transition centred at ca. 180 K.

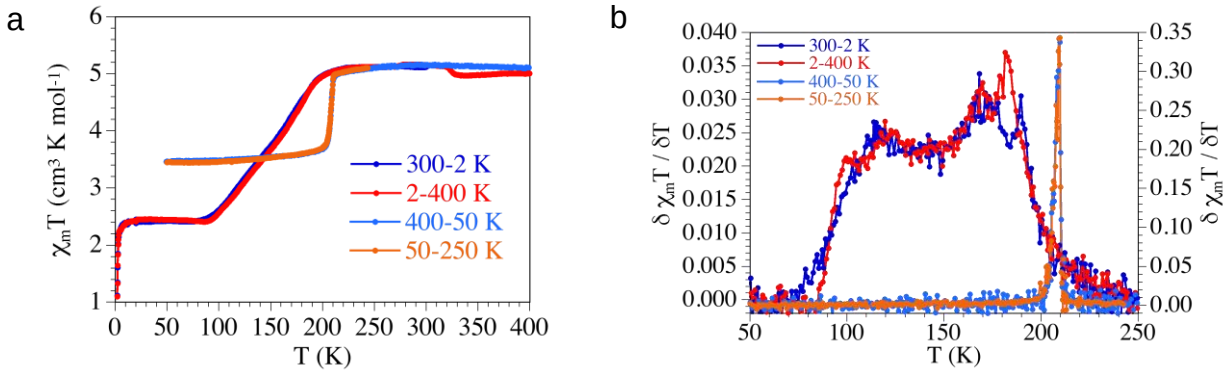

Figure 5.13. *Magnetic properties of* ***32****:* ***(a)*** *Thermal variation of the χ_mT product.* ***(b)*** *Thermal variation of $\delta(\chi_m T)/\delta T$ showing the SCO before (left scale) and after (right scale) the water loss.*

After the initial thermal cycle, we heated the sample up to 400 K to force the loss of the water molecule as observed in the crystallographic study, (see above). This heating scan shows the same behaviour than the cooling scan with a smooth SCO between 100 and 200 K. In contrast, when the dehydrated sample is cooled, we can observe a sharp SCO transition at *ca*. 208 K with a decrease of χ_mT from *ca*. 5.2 cm^3 K mol^{-1} to *ca*. 3.6 cm^3 K mol^{-1} (Figure 5.13a). This decrease of *ca*. 1.6 cm^3 K mol^{-1}

corresponds to half the expected jump for a complete SCO of all the Fe(II) centres. We can, therefore, conclude that only 1/2 of the Fe(II) centres show the SCO. This result is in full agreement with the structural data that show that the dehydrated phase contains two independent Fe(II) centres, one in the HS and the other in the LS state (see above). When the dehydrated sample was immersed in water for 48 hours, left to dry at room temperature and measured again, the original behaviour of the hydrated sample is observed again, proving that the water loss is a reversible process.

Compound **33** also shows at room temperature a $\chi_m T$ value of *ca*. 5.2 cm^3 K mol^{-1}, corresponding to the expected value for a Cr(III) with g = 2 (1.875 cm^3 K mol^{-1}) plus a Fe(II) with g ≈ 2.1 (*ca*. 3.3 $cm^3 \cdot K \cdot mol^{-1}$). When the temperature is decreased $\chi_m T$ remains constant down to ca. 220 K and shows a smooth decrease to reach a value of ca. 3.0 cm^3 K mol^{-1} at ca. 90 K (Figure 5.14a). Below this temperature $\chi_m T$ remains constant down to ca. 5 K where it shows an abrupt decrease to reach a value of *ca*. 1.2 cm^3 K mol^{-1} at 2 K. As in compound **32**, the room temperature $\chi_m T$ value indicates that all the Fe(II) centres of the $[Fe(3\text{-bpp})_2]^{2+}$ cation are in the HS configuration (S = 2) at 300 K. The smooth decrease of $\chi_m T$ observed between *ca*. 220 K and 90 K corresponds to a SCO of the $[Fe(3\text{-bpp})_2]^{2+}$ cation. The low temperature value (ca. 3.0 cm^3 K mol^{-1}) indicates that the SCO is not complete and that ca. 1/3 of the Fe(II) centres remain in the HS configuration. This value agrees with the structure results at 120 K (see above). The abrupt decrease observed at very low temperatures is, as in **32,** due to the presence of a zero field splitting (ZFS) of the Fe(II) fraction in HS state and of the paramagnetic S = 3/2 Cr(III) ion. The plot of $\delta(\chi_m T)/\delta T$ *vs*. T (Figure 5.14b) shows a broad maximum at *ca*. 180 K and no hysteresis in the initial cooling and heating scan, confirming that the SCO is smooth with an inflexion point at *ca*. 180 K. We can conclude that this compound shows a smooth incomplete SCO centred at 180 K, in agreement with the structural data.

After the initial thermal cycle, the sample was heated to 400 K to remove the water molecule (as observed in the crystallographic study and in compound **32**, see above). This heating scan shows the same behaviour than the initial cooling one (Figure 5.14a). When the dehydrated sample is cooled again, it shows, as compound **32**, an abrupt decrease at 196 K in the cooling scan and 202 K in the heating scan with a jump from c.a. 5.2 cm^3 K mol^{-1} to c.a. 3.8 cm^3 K mol^{-1}. This jump of c.a.

1.4 cm^3 K mol^{-1} corresponds to *ca*. 1/2 of the Fe(II) centres, as observed in **32**, suggesting that compound **33** presents the same structural phase transition when dehydrated, with two independent Fe(II) centres with HS and LS configurations, again in agreement with the structural data (see above). The plot of $\delta(\chi_m T)/\delta T$ *vs*. T (Figure 5.14b) shows sharp maxima at ca. 196 and 202 K in the cooling and heating scans, respectively, confirming the temperatures of the SCO and the presence of a small hysteresis of ca. 6 K. Finally, as in compound **32**, the dehydrated sample was immersed in water for 48 hours, allowed to dry and measured again. These measurements show that the sample recovers the initial behaviour, confirming the total reversibility of the water loss process.

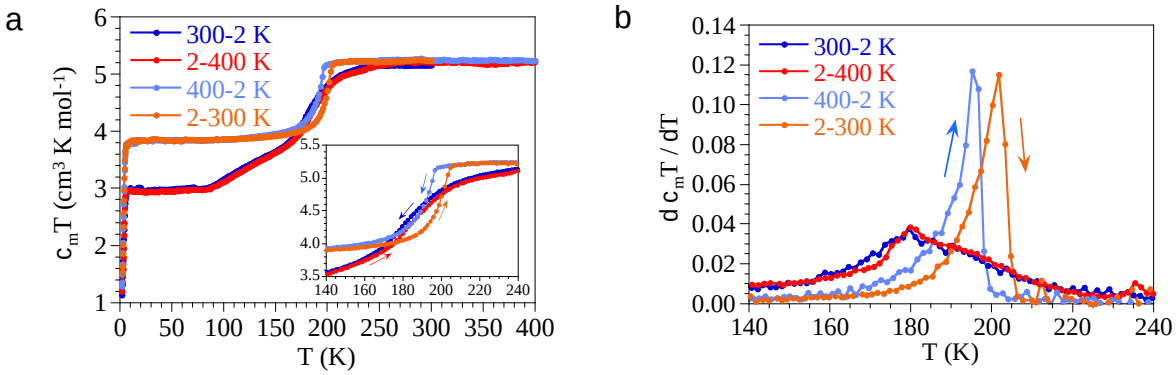

Figure 5.14. *Magnetic properties of **33**: **(a)** Thermal variation of the $\chi_m T$ product in two consecutive cooling and warming scans. Inset shows the SCO region **(b)** Thermal variation of $\delta(\chi_m T)/\delta T$ showing the SCO before (left scale) and after (right scale) the water loss.*

The change in the magnetic properties observed between the hydrated and dehydrated samples in compounds **32** and **33** can be attributed to two different effects, both related to the water removal/uptake: electronic and steric effects. The electronic effect is related to the change in electron density in the 3-pbb ligand when the H-bond between the water molecule and the pyrazole ring is removed. This H-bond increases the electron density in the ligand since the water acts as an electron donor (H-acceptor), leading to an increase in the metal-ligand interaction and, thus, in the ligand field. So, when the water molecule is present, the ligand field should be higher and also the SCO temperature. On the other hand, the steric effects are due to the rearrangement of the ligand when the water molecule is removed. The orientation of the 3-bpp ligand will slightly change in order to increase the metal-ligand interaction and, accordingly, the ligand field will increase in the dehydrated form and also the SCO

temperature, as observed experimentally. Since the experimental effect is an increase in the SCO temperature in both compounds (Figures 5.13b and 5.14b), this rearrangement effect must be more effective than the electronic one. This idea is further supported by the values of the Σ parameter in the HS state for both samples in de hydrated and dehydrated forms (Tables 5.4 and 5.6). Thus, when the water molecule is removed, the Σ(HS) parameter increases from 148.1º to 153.9º in **32** and from 151.0º to 161.2º in **33**. This larger values of Σ in the dehydrated form suggest that the distortions are higher in the dehydrated form because the ligands are more free to rearrange in order to minimize the steric repulsions.

Compound **34** shows a $\chi_m T$ value of *ca*. 14.15 cm^3 K mol^{-1} at room temperature, which is the expected value for two S= 3/2 Cr(III) ions and three S = 2 high spin Fe(II) centres (Figure 5.15). When the temperature decreases $\chi_m T$ remains constant down to ca. 50 K and below this temperature $\chi_m T$ shows a progressive decrease to reach a value of ca. 7.2 cm^3 K mol^{-1} at 2 K. This behaviour indicates that the sample remains in HS in all the temperature range and no SCO is observed. The decrease observed at low temperatures is simply due to the ZFS of the Cr(III) and the HS Fe(II) centres. We also heated the sample up to 400 K in order to remove the crystallization water molecules but no differences in the magnetic properties are observed after heating the sample (Figure 5.15).

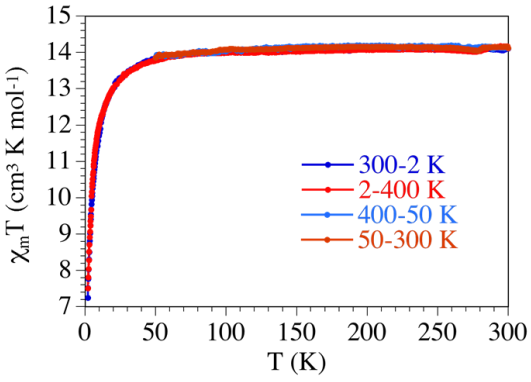

Figure 5.15: (a) *Thermal variation of the $\chi_m T$ product for compound **34** in two consecutive cooling and heating scans up to 400 K.*

3.4. LIESST effect in compounds 32 and 33

LIESST (Light-Induced Excited Spin-State Trapping) effect measurements were performed for compounds **32** and **33** although the effect was only observed for compound **33**. The samples were irradiated with green light (λ = 532 nm) at low temperatures (10 K) until the magnetization saturates. In compound **32** after several hours of irradiation no increase of the magnetization was observed. In contrast, in compound **33** after *ca*. 3 hours of irradiation the magnetization reached saturation at a value of *ca*. 3.5 cm^3 K mol^{-1}, indicating that *ca*. 1/3 of the Fe(II) centres that were in LS have been excited to the HS configuration (Figure 5.16a). Since the stable state at 10 K is the LS, these Fe(II) centres in HS are in a meta-stable state. After 3 hours the irradiation was stopped and the temperature was increased at a rate of 0.3 K/min. In this process, the sample gets thermic energy and some more Fe(II) centres are excited from LS to HS. Thus, the plot shows a maximum of ca. 4.0 cm^3 K mol^{-1} at *ca*. 40 K. This value indicates that *ca*. 1/2 of the Fe(II) centres that were in LS have been excited to the HS state (Figure 5.16b). At higher temperatures the Fe(II) centres have energy enough to transit from the meta-stable HS state to the stable state at low temperatures (LS). This HS to LS transition occurs at a T_{LIEEST} of *ca*. 65 K (Figure 5.16b). When the temperature is further increased the sample shows again the SCO at *ca.* 185 K, as observed in the initial cooling scan (Figure 5.16a).

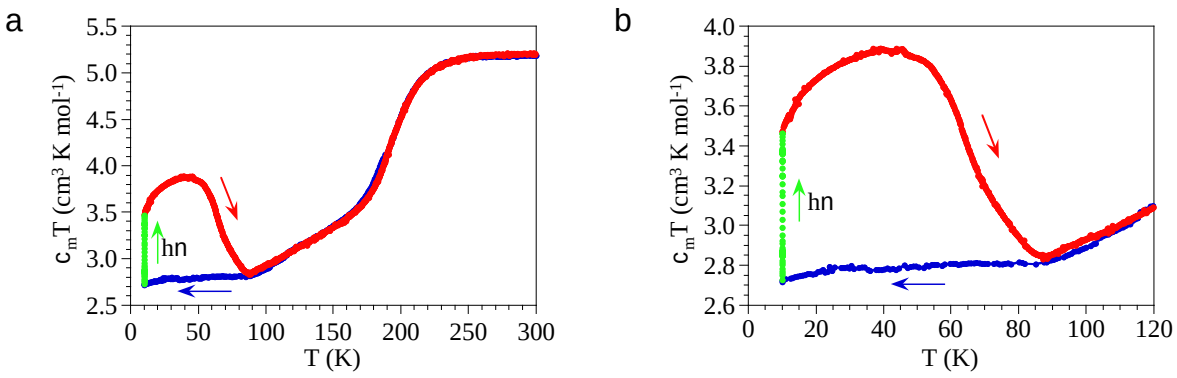

***Figure 5.16**. LIESST measurement of **33**: **(a)** Thermal variation of the χ_mT product (i) cooling scan without irradiation (blue dots), (ii) irradiation at 10 K with green light (green dots) and (iii) heating scan after irradiation without irradiation (red dots). **(b)** Zoom of the low temperature region.*

3. Conclusions and perspectives

In this chapter we have presented three anilato-based compounds with the $[Fe(bpp)_2]^{2+}$ SCO cation. Compounds **32** and **33** also have a $[NBu_4]^+$ cation to compensate the charge and a H_2O molecule H-bonded to the bpp ligand. This water molecule plays a key role in the SCO properties of the two compounds. In both compounds the removal of the water molecule increases the SCO temperature and gives rise to a small hysteresis of 6 K in the SCO in compound **33**. Additionally, this water removal originates a phase transition in the dehydrated samples. In this dehydrated phase there are two independent Fe(II) centres: one of them shows an abrupt SCO whereas the second one remains in the HS state at any temperature. Furthermore, we have demonstrated that the water removal process is reversible upon immersion of the crystals in water. Interestingly, the rehydrated samples behave as the original ones even if they uptake two water molecules instead of one. The recovered water molecule that was present in the original structure is bonded by a moderate H-bond whilst the second water molecule is bonded by a weak H-bond. This second water molecule is able to enter the structure due to the fact that there is an empty space of 224 $Å^3$. Further studies to check if this water molecule could enter before the dehydration process and to check if other solvents such as methanol, ethanol or acetonitrile could also interact with the cation are in progress.

Compound **34** in an interesting example since it has the same SCO $[Fe(3\text{-}bpp)_2]^{2+}$ cation than compounds **32** and **33** and also the same $[Cr(C_6O_4X_2)_3]^{3-}$ anion but with a different stoichiometry and no NBu_4^+ cation. Additionally, compound **34** has no water molecules H-bonded to the cation. These slight changes produce a drastic change in the magnetic properties since compounds **34** does not show any SCO in contrast to **32** and **33**. Compound **34**, therefore, illustrates the key role that may play the anion-cation and the solvent-cation interactions in the SCO phenomenon.

The possibility to include other anilato-based anions and other bulky cations with an additional functionality in these compounds in order to modify the SCO properties and prepare bistable multifunctional materials is a challenge that remains to be done.

4. References

(1) Bousseksou, A.; Molnar, G.; Salmon, L.; Nicolazzi, W. Molecular Spin Crossover Phenomenon: Recent Achievements and Prospects. *Chem. Soc. Rev.* **2011**, *40*, 3313-3335.

(2) Gütlich, P.; García, Y.; Goodwin, H. A. Spin Crossover Phenomena in Fe(II) Complexes. *Chem. Soc. Rev.* **2000**, *29*, 419-427.

(3) Halcrow, M. A. In *Structure: Function Relationships in Molecular Spin-Crossover Materials;* Spin-Crossover Materials; John Wiley & Sons Ltd: 2013; pp 147-169.

(4) Halcrow, M. A. The Foundation of Modern Spin-Crossover. *Chem. Commun.* **2013**, *49*, 10890-10892.

(5) Murray, K. S. In *The Development of Spin-Crossover Research;* Spin-Crossover Materials; John Wiley & Sons Ltd: 2013; pp 1-54.

(6) Real, J. A.; Gaspar, A. B.; Muñoz, M. C. Thermal, Pressure and Light Switchable Spin-Crossover Materials. *Dalton Trans.* **2005**, 2062-2079.

(7) Barrett, S. A.; Kilner, C. A.; Halcrow, M. A. Spin-Crossover in $[Fe(3\text{-}bpp)_2]BF_4]_2$ in Different Solvents - A Dramatic Stabilisation of the Low-Spin State in Water. *Dalton Trans.* **2011**, *40*, 12021-12024.

(8) Gütlich, P.; Hauser, A.; Spiering, H. Thermal and Optical Switching of Iron(II) Complexes. *Angew. Chem. Int. Ed.* **1994**, *33*, 2024-2054.

(9) Nihei, M.; Shiga, T.; Maeda, Y.; Oshio, H. Spin Crossover Iron(III) Complexes. *Coord. Chem. Rev.* **2007**, *251*, 2606-2621.

(10) Buchen, T.; Gütlich, P.; Sugiyarto, K. H.; Goodwin, H. A. High-Spin → Low-Spin Relaxation in $[Fe(bpp)_2](CF_3SO_3)_2$ H_2O After LIESST and Thermal Spin-State Trapping Dynamics of Spin Transition Versus Dynamics of Phase Transition. *Chem. Eur. J.* **1996**, *2*, 1134-1138.

(11) Clemente-Leon, M.; Coronado, E.; Gimenez-Lopez, M. C.; Romero, F. M.; Asthana, S.; Desplanches, C.; Letard, J. F. Structural, Thermal and Photomagnetic Properties of Spin Crossover $[Fe(bpp)_2]^{2+}$ Salts Bearing $[Cr(L)(ox)_2]^-$ Anions. *Dalton Trans.* **2009**, 8087-8095.

(12) Clemente-León, M.; Coronado, E.; Giménez-López, M. C.; Romero, F. M. Structural, Thermal, and Magnetic Study of Solvation Processes in Spin-Crossover $[Fe(bpp)_2]Cr(L)(ox)_2]_2 \cdot nH_2O$ Complexes. *Inorg. Chem.* **2007**, *46*, 11266-11276.

(13) Dupouy, G.; Marchivie, M.; Triki, S.; Sala-Pala, J.; Salaun, J. Y.; Gómez-García, C. J.; Guionneau, P. The Key Role of the Intermolecular Pi-Pi Interactions in the Presence of Spin Crossover in Neutral $[Fe(abpt)_2A_2]$ Complexes (A = Terminal Monoanion N Ligand). *Inorg. Chem.* **2008**, *47*, 8921-8931.

(14) Coronado, E.; Giménez-López, M. C.; Giménez-Saiz, C.; Romero, F. M. Spin Crossover Complexes as Building Units of Hydrogen-Bonded Nanoporous Structures. *CrystEngComm* **2009**, *11*, 2198-2203.

(15) Giménez-López, M. C.; Clemente-León, M.; Coronado, E.; Romero, F. M.; Shova, S.; Tuchagues, J. P. Structural Transformations and Magnetic Effects Induced by Solvent Exchange in the Spin Crossover Complex $[Fe(bpp)_2][Cr(Bpy)(Ox)_2]_2$. *Eur. J. Inorg. Chem* **2005***, 2005*, 2783-2787.

(16) Costa, J. S.; Rodriguez-Jimenez, S.; Craig, G. A.; Barth, B.; Beavers, C. M.; Teat, S. J.; Aromi, G. Three-Way Crystal-to-Crystal Reversible Transformation and Controlled Spin Switching by a Nonporous Molecular Material. *J. Am. Chem. Soc.* **2014***, 136*, 3869-3874.

(17) Sugiyarto, K. H.; Goodwin, H. A. Coordination of Pyridine-Substituted Pyrazoles and their Influence on the Spin State of Iron(II). *Aust. J. Chem.* **1988***, 41*, 1645-1663.

(18) Bain, G. A.; Berry, J. F. Diamagnetic Corrections and Pascal's Constants. *J. Chem. Educ.* **2008***, 85*, 532-536.

(19) Sheldrick, G. M. Crystal Structure Refinement with SHELXL. *Acta Cryst. C* **2015***, 71*, 3-8.

(20) Atzori, M.; Artizzu, F.; Sessini, E.; Marchio, L.; Loche, D.; Serpe, A.; Deplano, P.; Concas, G.; Pop, F.; Avarvari, N.; Mercuri, M. L. Halogen-Bonding in a New Family of Tris(Haloanilato)Metallate(III) Magnetic Molecular Building Blocks. *Dalton Trans.* **2014***, 43*, 7006-7019.

(21) Atzori, M.; Pop, F.; Auban-Senzier, P.; Gómez-García, C. J.; Canadell, E.; Artizzu, F.; Serpe, A.; Deplano, P.; Avarvari, N.; Mercuri, M. L. Structural Diversity and Physical Properties of Paramagnetic Molecular Conductors Based on Bis(Ethylenedithio)Tetrathiafulvalene (BEDT-TTF) and the Tris(chloranilato)ferrate(III) Complex. *Inorg. Chem.* **2014***, 53*, 7028-7039.

(22) Atzori, M.; Artizzu, F.; Marchio, L.; Loche, D.; Caneschi, A.; Serpe, A.; Deplano, P.; Avarvari, N.; Mercuri, M. L. Switching-on Luminescence in Anilate-Based Molecular Materials. *Dalton Trans.* **2015***, 44*, 15786-15802.

(23) Benmansour, S.; Gómez-Claramunt, P.; Vallés-García, C.; Mínguez Espallargas, G.; Gómez García, C. J. Key Role of the Cation in the Crystallization of Chiral Tris(Anilato)Metalate Magnetic Anions. *Cryst. Growth Des.* **2016***, 16*, 518-526.

(24) Benmansour, S.; Coronado, E.; Giménez-Saiz, C.; Gómez-García, C. J.; Rößer, C. Metallic Charge-Transfer Salts of bis(ethylenedithio)tetrathiafulvalene with paramagnetic tetrachloro(oxalato)rhenate(IV) and tris(chloranilato)ferrate(III) Anions. *Eur. J. Inorg. Chem* **2014***, 2014*, 3949-3959.

(25) Janiak, C. A Critical Account on π–π Stacking in Metal Complexes with Aromatic Nitrogen-Containing Ligands. *J. Chem. Soc. , Dalton Trans.* **2000**, 3885-3896.

(26) Guionneau, P.; Marchivie, M.; Bravic, G.; Letard, J. F.; Chasseau, D. Structural Aspects of Spin Crossover. Example of the $[(FeLn)\text{-}L\text{-}II(NCS)_2]$ Complexes. *Top. in Curr. Chem.* **2004***, 234*, 97-128.

(27) Halcrow, M. A. The Spin-States and Spin-Transitions of Mononuclear Iron(II) Complexes of Nitrogen-Donor Ligands. *Polyhedron* **2007***, 26*, 3523-3576.

(28) Milin, E.; Benaicha, B.; El Hajj, F.; Patinec, V.; Triki, S.; Marchivie, M.; Gómez-García, C. J.; Pillet, S. Magnetic Bistability in Macrocycle-Based FeII Spin-Crossover Complexes: Counter Ion and Solvent Effects. *Eur. J. Inorg. Chem* **2016***, 2016*, 5305-5314.

(29) Steiner, T. The Hydrogen Bond in the Solid State. *Angew. Chem. Int. Ed.* **2002***, 41*, 48-76.

Chapter 6

Luminescent compounds based on anilato ligand

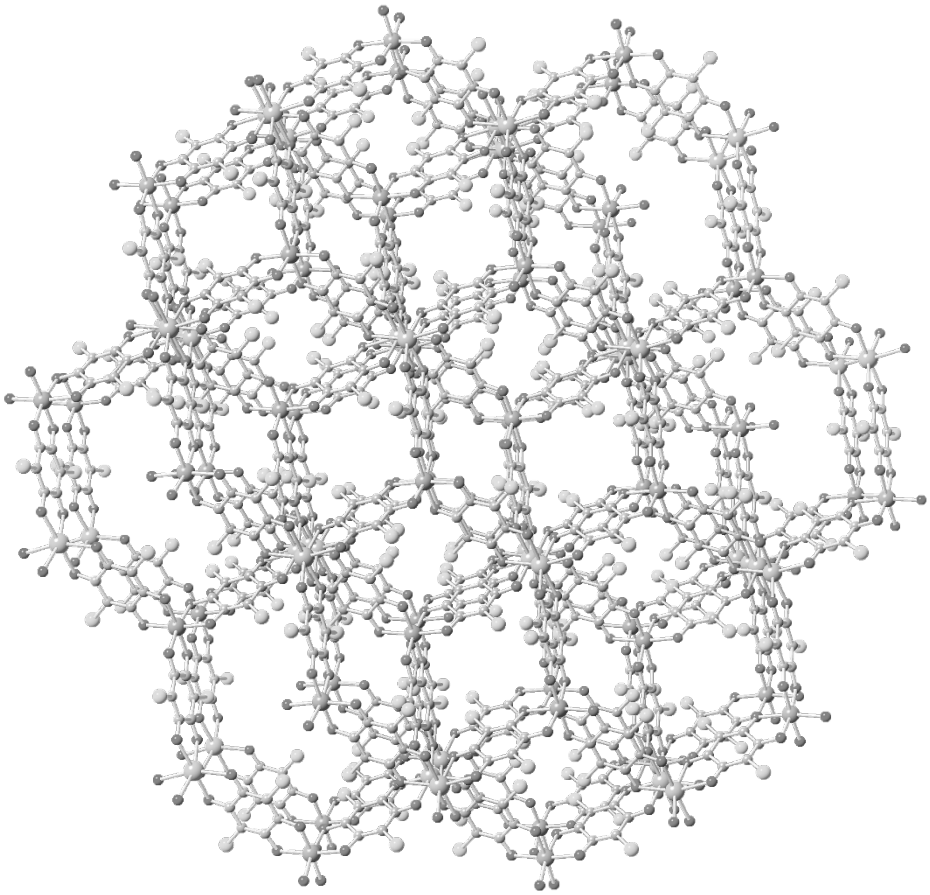

1. Introduction

In this chapter we present the results obtained when trying to combine the ferrimagnetic anionic anilato based $[M^{II}M^{III}(C_6O_4X_2)_3]^-$ layers with a luminescent cation as $[Ir(ppy)_2(bpy)]^+$. These attempts led to two different kind of compounds containing the luminescent $[Ir(ppy)_2(bpy)]^+$ cation: (i) two monomeric salts: $[Ir(ppy)_2(bpy)]_2[(H_3O)[Cr(C_6O_4X_2)_3]\cdot H_2O$ with X = Cl **(35)** and Br **(36)** containing isolated paramagnetic $[Cr(C_6O_4X_2)_3]^{3-}$ anions (X = Cl and Br) and (ii) a series of six compounds formulated as $[Ir(bpy)(ppy)_2][MnCr(C_6O_4X_2)_3]\cdot 2G\cdot 2CH_3CN\cdot H_2O$ with X/G = Cl/PhF (**37**), Cl/PhCl (**38**), Cl/PhBr (**39**), Br/PhF (**40**), Br/PhCl (**41**) and Br/PhBr (**41**), where the luminescent cation $[Ir(ppy)_2(bpy)]^+$ is inserted between the ferrimagnetic anilato-based anionic layers. In this chapter we report the synthesis, structure, magnetic and luminescence properties of all these compounds.

As will be discussed in this chapter, the halo-benzene molecules (PhF, PhCl and PhBr) play a key role for obtaining the well-known honeycomb 2D structure. In fact, all the attempts to obtain the 2D phase without using a halo-benzene as solvent lead to compounds **35** and **36** for all the concentrations, solvents and anilato precursors used: $A_3[Cr(C_6O_4X_2)_3]$, X = Cl and Br; A = K^+, NBu_4^+, PPh_3Et^+ and Mn^{2+}.

2. Experimental section

2.1. Synthesis

General Remarks: The synthesis of $K_3[Cr(C_6O_4Cl_2)_3]$ and $K_3[Cr(C_6O_4Br_2)_3]$ are described in chapter one. The compound $[Ir(ppy)_2(bpy)]Cl$ was prepared following the literature.[1, 2] All other reagents and solvents are commercially available and we used as received without further purification.

Synthesis of $[Ir(ppy)_2(bpy)]_2(H_3O)[Cr(C_6O_4Cl_2)_3]\cdot H_2O$ (35): This compound was obtained by serendipity while trying to obtain the 2D phase. A solution of $K_3[Cr(C_6O_4Cl_2)_3]$ (12.0 mg, 0.015 mmol) and $MnCl_2\cdot 4H_2O$ (3.0 mg, 0.015 mmol) in 4 mL of water was placed on top of a solution of $[Ir(bpy)(ppy)_2]Cl$ (10.5 mg, 0.015 mmol) in 4 mL of MeCN. Compound **35** crystallizes as red block crystals suitable for X-ray diffraction after one week at 18 ºC.

The same compound was obtained using other solvents as CH_2Cl_2, CH_2Br_2, $CHCl_3$, $CHBr_3$, THF, and MeOH, other concentrations in the range 0.0025-0.015 M and other precursor anilato salts as $(NBu_4)_3[Cr(C_6O_4Cl_2)_3]$, $(PPh_3Et)_3[Cr(C_6O_4Cl_2)_3]$ and $Mn_3[Cr(C_6O_4Cl_2)_3]_2$.

Synthesis of $[Ir(ppy)_2(bpy)]_2(H_3O)[Cr(C_6O_4Br_2)_3]\cdot H_2O$ (36): This compound was obtained as compound **35** but using $K_3[Cr(C_6O_4Br_2)_3]$ (16 mg, 0.015 mmol) instead of $K_3[Cr(C_6O_4Cl_2)_3]$. Compound **36** also crystallizes as Red hexagonal prismatic crystals suitable for X-ray diffraction after one week at 18 ºC.

As observed with compound **35**, compound **36** could also be obtained using different solvents, concentrations and precursor tris(anilato)chromate salts.

Synthesis of $[Ir(bpy)(ppy)_2][MnCr(C_6O_4Cl_2)_3]\cdot 2PhF\cdot 2CH_3CN\cdot H_2O$ (37): This compound was obtained by slow diffusion of a solution of $K_3[Cr(C_6O_4Cl_2)_3]$ (24 mg, 0.03 mmol) in 6 mL of MeCN (and stirred during several minutes) placed on top of a solution of $[Ir(bpy)(ppy)_2]Cl$ (21 mg, 0.03 mmol) and $MnCl_2\cdot 4H_2O$ (12 mg, 0.06 mmol) in 2 mL of MeOH and 4 mL of PhF. Red microneedles were obtained after one month at 18 ºC.

Synthesis of $[Ir(bpy)(ppy)_2][MnCr(C_6O_4Cl_2)_3]\cdot 2PhCl\cdot 2CH_3CN\cdot H_2O$ (38): This compound was obtained by slow diffusion of a solution of $K_3[Cr(C_6O_4Cl_2)_3]$ (5.2 mg, 0.0075 mmol) in 3 mL of MeCN (and stirred during several minutes) placed on top of a solution of $[Ir(bpy)(ppy)_2]Cl$ (5.8 mg, 0.0075 mmol) and $MnCl_2\cdot 4H_2O$ (3 mg, 0.015 mmol) in 1 mL of MeOH and 2 mL of PhCl. Red plates crystals suitable for X-Ray diffraction were obtained after three months at 18ºC.

Synthesis of $[Ir(bpy)(ppy)_2][MnCr(C_6O_4Cl_2)_3]\cdot 2PhBr\cdot 2CH_3CN\cdot H_2O$ (39): This compound was synthesized as compound **38** but adding PhBr instead of PhCl. Red prismatic crystals suitable for X-Ray diffraction were obtained after three months at 18ºC.

Synthesis of $[Ir(bpy)(ppy)_2][MnCr(C_6O_4Br_2)_3]\cdot 2PhF\cdot 2CH_3CN\cdot H_2O$ (40): This compound was obtained by slow diffusion of a solution of $K_3[Cr(C_6O_4Br_2)_3]$ (16 mg, 0.015 mmol) in 3 mL of MeCN (and stirred during several minutes) placed on top of a solution of $[Ir(bpy)(ppy)_2]Cl$ (11 mg, 0.015 mmol) and $MnCl_2\cdot 4H_2O$ (6 mg, 0.03 mmol)

in 1 mL of MeOH and 2 mL of PhF. A red crystalline powder formed by ultrathin needles was obtained after one month at 18 ºC.

Synthesis of $[Ir(bpy)(ppy)_2][MnCr(C_6O_4Br_2)_3]\cdot 2PhCl\cdot 2CH_3CN\cdot H_2O$ (41): This compound was obtained as compound **40** but adding PhCl instead of PhF. A red crystalline powder formed by ultrathin needles was obtained after one month at 18 ºC.

Synthesis of $[Ir(bpy)(ppy)_2][MnCr(C_6O_4Br_2)_3]\cdot 2PhBr\cdot 2CH_3CN\cdot H_2O$ (42): This compound was obtained as compound **40** but adding PhBr instead of PhF. A red crystalline powder formed by ultrathin needles was obtained after one month at 18 ºC.

2.2. Physical Properties

FT-IR spectra were performed on KBr pellets and collected with a Nexus-Nicolet 5700 spectrophotometer.

Magnetic measurements were performed with a Quantum Design MPMS-XL-5 SQUID magnetometer in the 2-300 K temperature range with an applied magnetic field of 0.5 T on polycrystalline samples of all the compounds. Isothermal hysteresis measurements were performed at 2 K with magnetic fields from -5 to 5 T. AC susceptibility measurements were performed on the same samples with a field of 0.395 mT (3.95 Gauss) oscillating at different frequencies in the range of 1-1000 Hz. Susceptibility data were corrected for the sample holder and for the diamagnetic contribution of the salts using Pascal's constants.[3]

2.3. Structural Characterization

Suitable single crystals of compounds **35, 36, 38** and **39** were mounted on a loop using a viscous hydrocarbon oil and then transferred directly to the cold nitrogen stream for data collection. X-ray data were collected at 120 K on a Supernova diffractometer equipped with a graphite-monochromated Enhance (Mo) X-ray Source (λ = 0.71073 Å). The program CrysAlisPro, Agilent Technologies Ltd., was used for unit cell determinations and data reduction. Empirical absorption correction was performed using spherical harmonics, implemented in the SCALE3 ABSPACK

scaling algorithm. Crystal structures were solved and refined against all F^2 values with the SHELXL-2014 program[4], using the WinGX2014.1 graphical user interface.[5] All non-hydrogen atoms were refined anisotropically and hydrogen atoms were placed in calculated positions and refined isotropically with a riding model. Data collection and refinement parameters are given in Tables 6.2 and 6.5.

The X-ray powder diffractograms were collected for polycrystalline samples of all the compounds using a 0.5 mm glass capillary that was mounted and aligned on a Empyrean PANalytical powder diffractometer, using CuKα radiation (λ = 1.54177 Å) operating at 40 mA and 45 kV. A total of 3 or 6 scans were collected at room temperature in the 2θ range of 2-40º with a step size of 0.0131º.

2.4. Luminescent Properties

The optical measurements for compounds **35** and **36** have been evaluated by means of scanning confocal microscopy using an excitation light of 405 nm. This technique allows simultaneous analysis of the emission spectra from a surface of hundreds of square microns in order to obtain an average spectra representative of the scanning area. Although this fact limits the spectral resolution of the set-up it is well suited for semi-quantitative discussion of the optical properties of crystalline materials.

The luminescent properties for the 2D compounds (**37**-**42**) have been evaluated following the following procedure: the samples were held in a positioning stage with micrometer resolution. The luminescence experiments were carried out exciting the sample with visible (488 nm line from Ar laser) and ultra violet (364 nm from another Ar laser) light in continuous wave operation. Both lasers were aligned on the same optical path, so they could be consecutively used at the same measuring point. The excitation was focused using a large focal length microscope objective driving to a spot size of few micrometers. A beam splitter was employed to collect the luminescence using the same objective (back-scattering configuration). The collected light was dispersed by a 1 m focal length spectrograph, and detected with a silicon detector.

3. Results and discussion

3.1. Infrared Spectroscopy

Compounds **37**-**42** show similar IR spectra, suggesting that the anionic lattice must be similar in the six compounds (Figures 6.1-6.6). In all cases the IR spectra confirm the presence of the $[Ir(bpy)(ppy)_2]^+$ cation. The main bands and their assignments are displayed in Table 6.1.

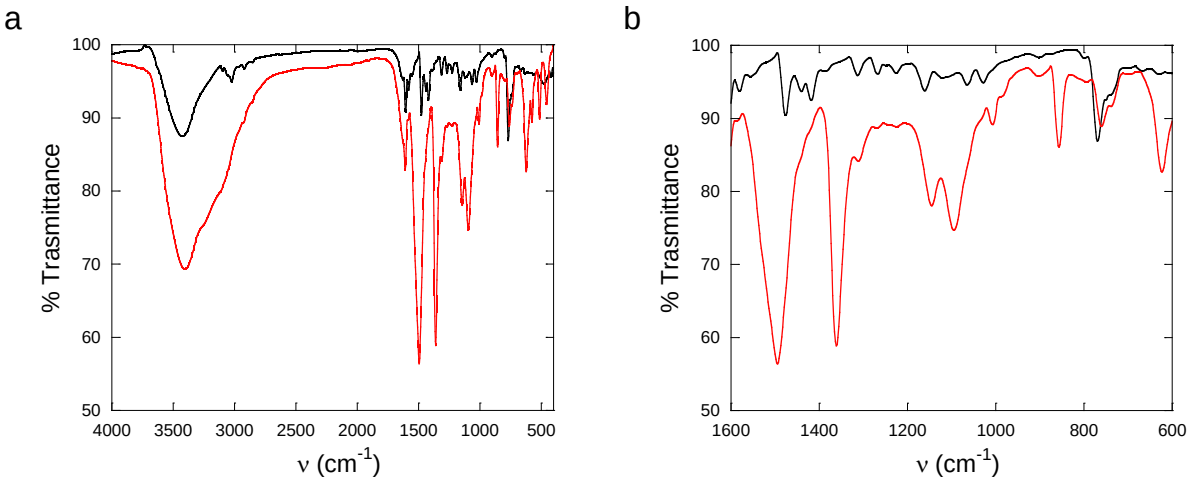

***Figure 6.1**. FT-IR spectra of compound **37** (in red) and the salt $[Ir(bpy)(ppy)_2]Cl$ (in black) in the region 4000-400 cm^{-1} (**a**) and 1600-600 cm^{-1} (**b**).*

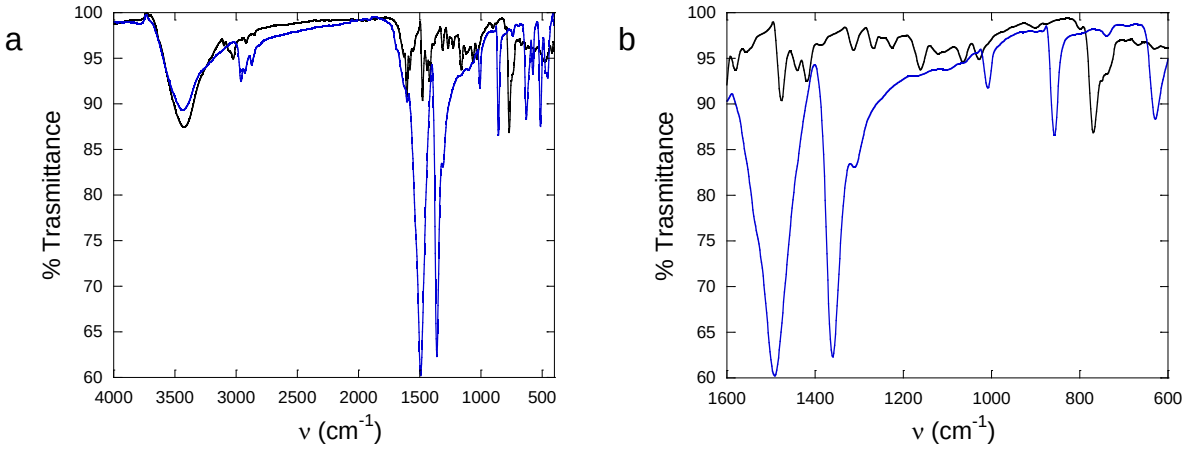

***Figure 6.2**. FT-IR spectra of compound **38** (in blue) and the salt $[Ir(bpy)(ppy)_2]Cl$ (in black) in the region 4000-400 cm^{-1} (**a**) and 1600-600 cm^{-1} (**b**).*

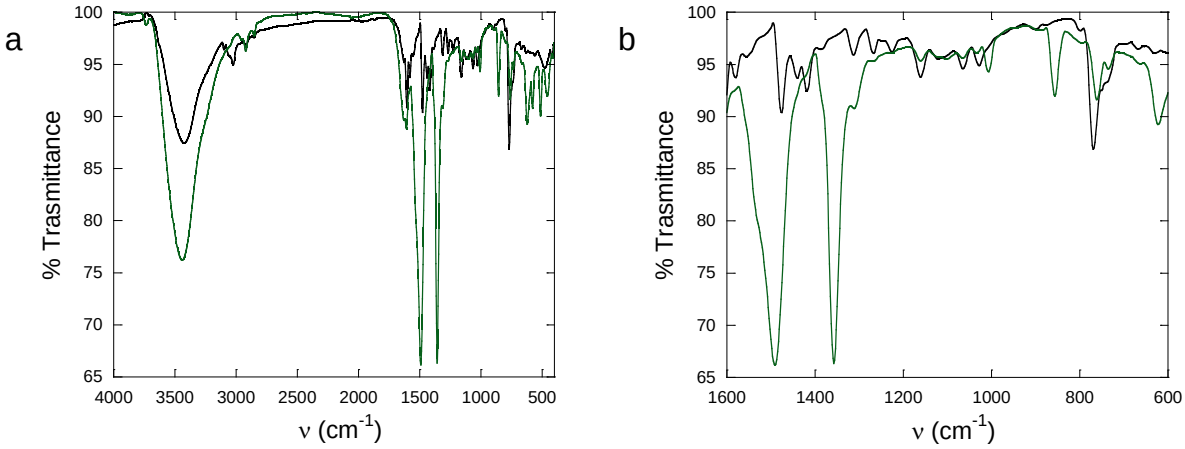

***Figure 6.3**. FT-IR spectra of compound **39** (in green) and the salt [Ir(bpy)(ppy)$_2$]Cl (in black) in the region 4000-400 cm^{-1} (**a**) and 1600-600 cm^{-1} (**b**).*

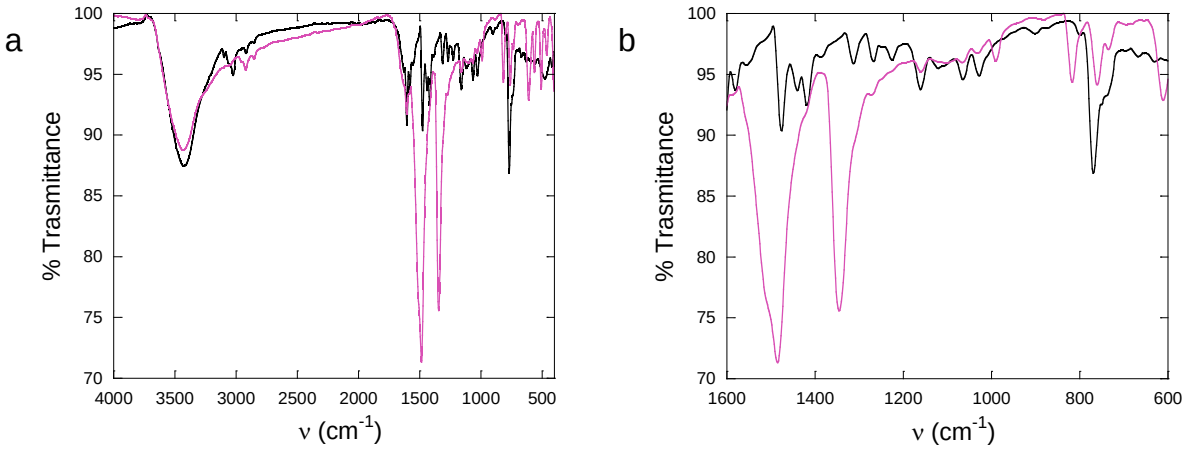

***Figure 6.4**. FT-IR spectra of compound **40** (in pink) and the salt [Ir(bpy)(ppy)$_2$]Cl (in black) in the region 4000-400 cm^{-1} (**a**) and 1600-600 cm^{-1} (**b**).*

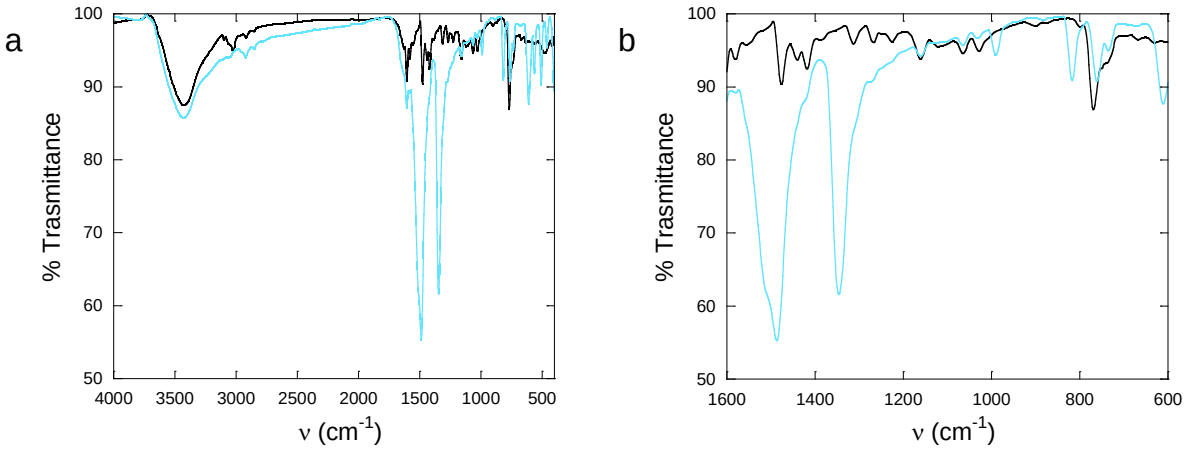

***Figure 6.5**. FT-IR spectra of compound **41** (in blue) and the salt [Ir(bpy)(ppy)$_2$]Cl (in black) in the region 4000-400 cm^{-1} (**a**) and 1600-600 cm^{-1} (**b**).*

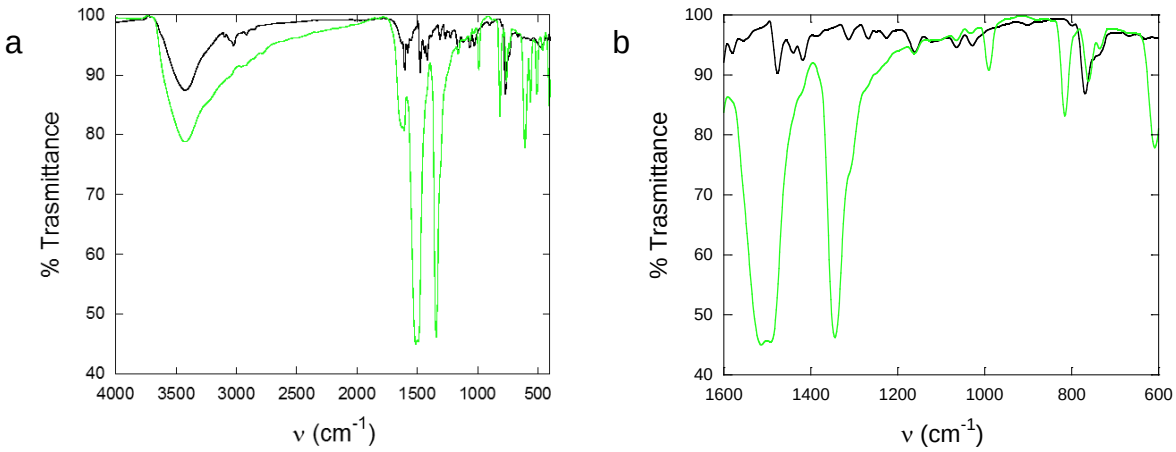

***Figure 6.6**. FT-IR spectra of compound **42** (in green) and the salt [Ir(bpy)(ppy)$_2$]Cl (in black) in the region 4000-400 cm^{-1} (**a**) and 1600-600 cm^{-1} (**b**).*

***Table 6.1**. IR bands (in cm^{-1}) and assignments of [Ir(bpy)(ppy)$_2$]Cl and compounds **37-42**.*

Compound	ν(C=O) ν(C=N) ν(C=C)$_{ring}$			ν(C=C)$_{ring}$ ν(C-O)	δ(C-O) / δ(C=O) ν(C-X) / δ(C-H) ν(C=C)$_{ring}$			δ(C-X) γ(C-H)		ρ(C-X)
[Ir(bpy)(ppy)$_2$]Cl	1475 1440 1415	1320	1260 1220	1160	1060	1030			765	
37	1490	1360	1310		1060	1010		855		630
38	1490	1360	1310	1145	1100		1005	850	750	625
39	1490	1360	1310	1160	1100	1065		850	765	
40	1490	1350	1255	1160	1060	1025	1000	815	760	630
41	1490	1350	1275	1160	1060	1025	1000	813	760	615
42	1490	1350	1270	1160	1065	1030	1000	815	760	615

ν = stretching, d = in-plane bending, γ = out-of-plane bending

As can be observed in Table 6.1, the main characteristic vibrational bands of the Iridium complex are present in compounds **37**-**42**, confirming the presence of this cation. In the 1500-1200 cm^{-1} region, the bands of the Iridium complex are mostly overlapped by the intense carbonyl stretching vibration of the anilato ligand. Nevertheless, the less intense bands of the Iridium complex in the 1200-1000 cm^{-1} region, which can be mostly assigned to stretching vibrations of the bypiridyl and pyiridil rings, can be clearly observed. Finally the most intense band in the Ir complex around 750 cm^{-1}, which can be assigned to the in-plane deformation of the bpy and ppy ligands, is clearly visible in the six compounds. Thus, FT-IR spectra clearly confirms the presence of the [Ir(bpy)(ppy)$_2$]$^+$ cation in compounds **37**-**42**.

3.2. X-Ray Diffraction

As indicated above, we have obtained two different families of compounds containing the $[Ir(ppy)_2(bpy)]^+$ cation: (a) $[Ir(ppy)_2(bpy)]_2(H_3O)[Cr(C_6O_4X_2)_3]\cdot H_2O$ with X = Cl (**35**) and Br (**36**), containing the monomeric $[Cr(C_6O_4X_2)_3]^{3-}$ anion and (b) $[Ir(bpy)(ppy)_2][MnCr(C_6O_4X_2)_3]\cdot 2G\cdot 2CH_3CN\cdot H_2O$ with X/G = Cl/PhF (**37**), Cl/PhCl (**38**), Cl/PhBr (**39**), Br/PhF (**40**), Br/PhCl (**41**) and Br/PhBr (**42**), where the $[Ir(ppy)_2(bpy)]^+$ cation is located between the ferrimagnetic anilato-based anionic layers $[MnCr(C_6O_4X_2)_3]^-$.

Crystal structure of $[Ir(ppy)_2(bpy)]_2(H_3O)[Cr(C_6O_4X_2)_3]\cdot H_2O$, X = Cl (35) and Br (36)

Table 6.2*. Crystallographic data for compounds **35** and **36**.*

	35	**36**
Empirical formula	$C_{82}H_{45}N_8O_{14}Cl_6CrIr_2$	$C_{82}H_{45}N_8O_{14}Br_6CrIr_2$
Formula weight (g/mol)	2015.43	2282.13
Temperature K	120(2)	120(2)
Wavelength (Å)	0.71073	0.71073
Crystal system	Trigonal	Trigonal
Space group	*P*-3*c*1 #165	*P*-3*c*1 #165
a (Å)	14.4878(2)	14.5058(3)
b(Å)	14.4878(2)	14.5058(3)
c(Å)	22.1861(3)	22.2622(4)
α (°)	90	90
β (°)	90	90
γ (°)	120	120
V (Å^3)	4032.89(12)	4056.78(18)
ρ_{cal} (mg m^{-3})	1.659	1.867
μ (mm^{-1})	3.690	6.426
Crystal size (mm)	0.20x0.20x0.18	0.11x0.08x 0.07
θ range (°)	3.247-25.040	3.243 to 25.045
Reflections collected	18684	26965
Independent reflections (R_{int})	2387	2395
Reflns used in refinement, *n*	2387	2395
$R_1(F)$,[a] $I > 2\sigma(I)$	0.0610	0.0809
$wR_2(F^2)$,[b] all data	0.1707	0.2744
$S(F^2)$,[c] all data	1.217	1.116
Largest diff. Peak	5.446	4.731
Largest diff. Hole	-1.501	-3.320

[a] $R1(F) = \Sigma||F_O|-|F_C||/\Sigma|F_O|$; [b] $wR2(F^2) = [\Sigma w(F_O^2-F_C^2)^2/\Sigma wF_O^4]^{1/2}$;

[c] $S(F^2) = [\Sigma w(F_O^2-F_C^2)^2/(n + r - p)]^{1/2}$

Both compounds are isostructural and crystallize in the trigonal P-*3c1* space group The asymmetric unit contains 1/3 of the anion $[Cr(C_6O_4X_2)_3]^{3-}$ (X = Cl in **35** and Br in **36**), 2/3 of the cation $[Ir(ppy)_2(bpy)]^+$, 1/3 of H_3O^+ and 1/3 of H_2O. The corresponding formula is, therefore, $[Ir(ppy)_2(bpy)]_2(H_3O)[Cr(C_6O_4X_2)_3]\cdot H_2O$ (X = Cl in **35** and Br in **36**). Data collection and refinement parameters are given in Table 6.2.

The structure of both compounds shows isolated trishaloanilato cromate(III) anions running along the *c* axis (Figure 6.7a) surrounded by six $[Ir(ppy)_2(bpy)]^+$ cations in a distorted octahedral disposition with six $\pi-\pi$ interactions between the anilato rings and the aromatic rings of the bpy and ppy ligands of the cation (Figure 6.7b). Each $[Ir(ppy)_2(bpy)]^+$ cation is surrounded by three $[Cr(C_6O_4X_2)_3]^{3-}$ anions, giving rise to a corrugated hexagonal 2D network (Figures 6.8a and 6.8b) with the same topology that the layers in CdI_2 and $CdCl_2$ structure types (Figure 6.8c).

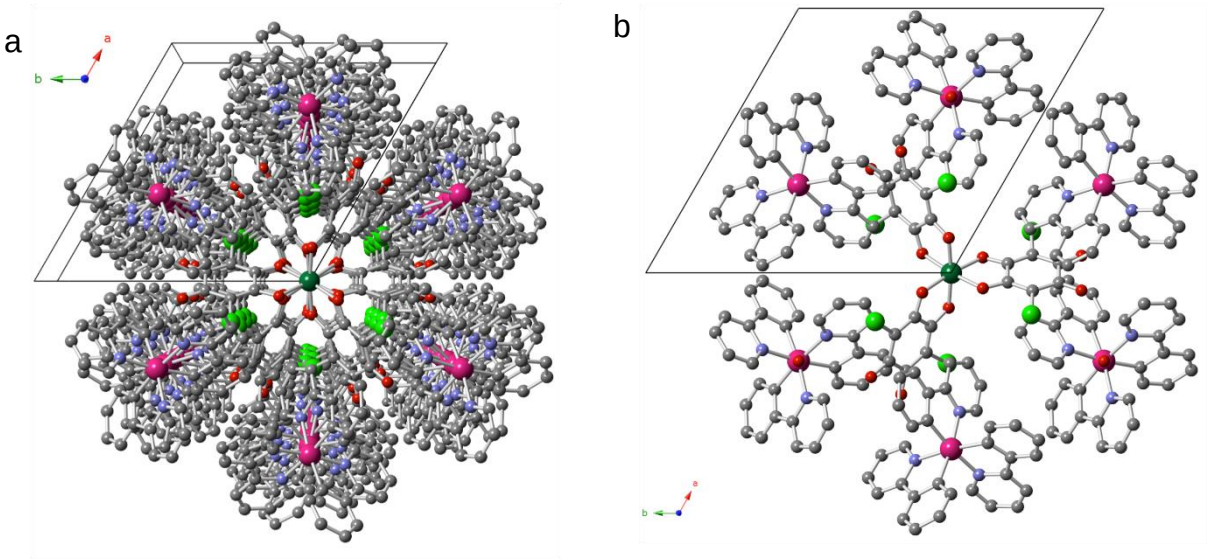

***Figure 6.7**. Structure of compound **35** (similar in **36**). **(a)** Perspective view of a row of $[Cr(C_6O_4Cl_2)_3]^{3-}$ anions surrounded by $[Ir(bpy)(ppy)_2]^+$ cations. **(b)** View of one $[Cr(C_6O_4Cl_2)_3]^{3-}$ anion surrounded by six $[Ir(bpy)(ppy)_2]^+$ cations. Colour code: Cr = dark green, Ir = pink, O = red, C = grey, Cl = light green, N = blue*

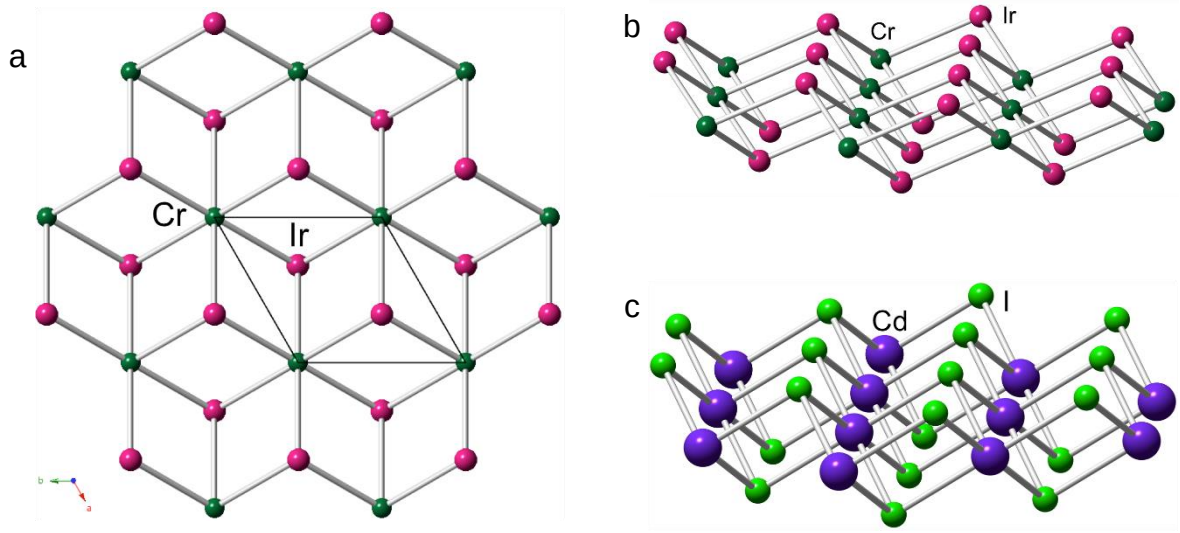

***Figure 6.8**. Structure of compound **35** (similar in **36**). **(a)** View of the positions of the Ir and Cr metals in the ab plane showing the six Ir metals around each Cr and the three Cr ions around each Ir metal. **(b)** Side view of the same layer showing the lack of planarity. **(c)** Side view of a layer of CdI_2.*

The anions present the typical distorted MO_6 octahedral geometry derived from the tris-chelated coordination environment described in the previously published $[M^{III}(C_6O_4X_2)_3]^{3-}$ anions (Figure 6.9a).[6-10] The Cr-O bond distances and angles (Tables 6.3 and 6.4) are similar to those found in other similar $[Cr(C_6O_4X_2)_3]^{3-}$ anions.[6-10] The $[Ir(ppy)_2(bpy)]^+$ cation also shows the expected distorted octahedral coordination geometry observed in other compounds with this cation (Figure 6.9b).[11-13] The Ir-C and Ir-N bond distances and angles (Tables 6.3 and 6.4) are also similar to those found in the same cation in other compouds.[11-13] Note that there is a positional disorder between the three ligands coordinated to the Ir atom (two ppy and one bpy) and, therefore, it is impossible to determine the exact nature (N or C) of the six atoms connected to the Ir atom. In average, each connected atom contains 2/3 of N and 1/3 of C since 4 of the six atoms are N and the remaining two are C.

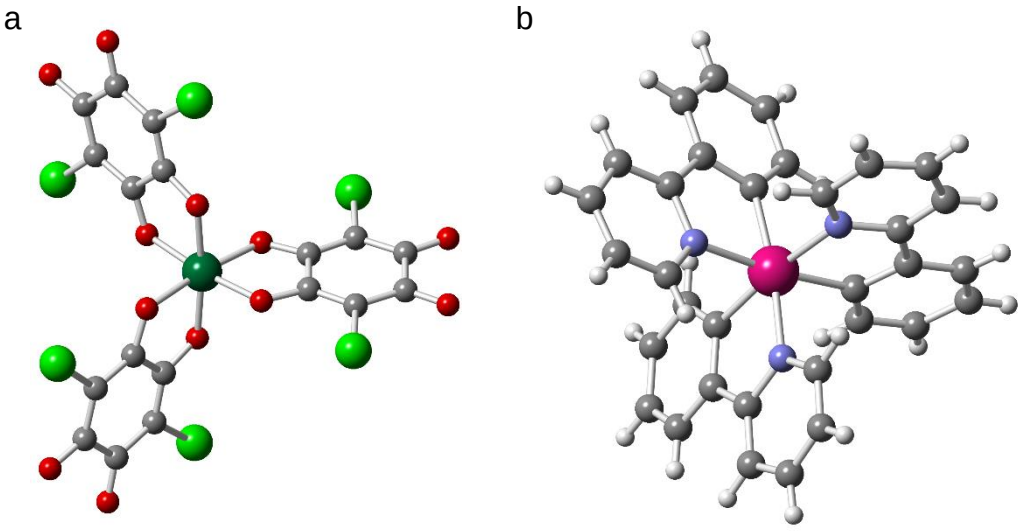

***Figure 6.9**. Structure of **1** (similar in **2**). **(a)** View of the $[Cr(C_6O_4Cl_2)_3]^{3-}$ anion. **(b)** View of the $[Ir(bpy)(ppy)_2]^+$ cation. Colour code: Cr = dark green, Ir = pink, O = red, C = grey, Cl = light green, N = blue, H = white.*

The 2:1 cation:anion stoichiometry found in this compound requires the presence of an oxonium cation, H_3O^+ to compensate the -3 anionic charge. Although the H atoms of the H_3O^+ cation could not be located in the X-ray structure, we assume that one of the two water molecules must be protonated, resulting in the formula $[Ir(ppy)_2(bpy)]_2(H_3O)[Cr(C_6O_4X_2)_3]\cdot H_2O$, X = Cl (**35**) and Br(**36**).

***Table 6.3**. Main bond lengths (Å) around the metals centres in **35** and **36**.*

Atoms	35	36
Cr(1)-O(2)	1.984(8)	1.962(11)
Cr(1)-O(2) #1	1.984(8)	1.962(11)
Cr(1)-O(2) #2	1.984(8)	1.962(11)
Cr(1)-O(2) #3	1.984(8)	1.962(11)
Cr(1)-O(2) #4	1.984(8)	1.962(11)
Cr(1)-O(2) #5	1.984(8)	1.962(11)
Ir(10)-N(101)#6	2.062(8)	2.068(11)
Ir(10)-C(101)#6	2.062(8)	2.068(11)
Ir(10)-N(101)#7	2.062(8)	2.068(11)
Ir(10)-C(101)#7	2.062(8)	2.068(11)
Ir(10)-N(112)#6	2.074(9)	2.081(14)
Ir(10)-N(112)#7	2.074(9)	2.081(14)

Symmetry transformations:
#1 -x,-x+y,-z+1/2; #2 -y,x-y,z;
#3 y,x, z+1/2; #4 -x+y,-x,z;
#5 x-y, y,-z+1/2; #6 -y+1,x-y,z;
#7 -x+y+1,-x+1,z

***Table 6.4**. Main angles (°) around the metals centres in **35** and **36**.*

Atoms	35	36	Atoms	35	36
O(2)#1-Cr(1)-O(2)	91.5(4)	173.3(5)	C(101)#6-Ir(10)-C(101)	95.5(3)	95.5(4)
O(2)#1-Cr(1)-O(2)#2	173.2(3)	90.4(6)	N(101)#6-Ir(10)-N(101)	95.5(3)	95.5(4)
O(2)-Cr(1)-O(2)#2	93.7(3)	94.7(5)	C(101)-Ir(10)-C(101)#7	95.5(3)	95.5(4)
O(2)#1-Cr(1)-O(2)#3	93.7(3)	80.6(6)	N(101)-Ir(10)-C(112)#6	89.1(3)	89.0(4)
O(2)-Cr(1)-O(2)#3	173.2(3)	94.7(5)	C(101)#6-Ir(10)-N(112)#6	79.0(4)	79.0(6)
O(2)#2-Cr(1)-O(2)#3	81.5(4)	94.7(5)	C(101)-Ir(10)-N(112)#6	89.1(3)	89.0(4)
O(2)#1-Cr(1)-O(2)#4	81.5(4)	94.7(5)	N(101)-Ir(10)-C(112)#7	173.1(3)	173.5(5)
O(2)-Cr(1)-O(2)#4	93.7(3)	90.4(6)	C(101)-Ir(10)-N(112)#7	173.1(3)	173.5(5)
O(2)#2-Cr(1)-O(2)#4	93.7(3)	80.6(6)	N(112)#6-Ir(10)-N(112)#7	96.7(4)	96.8(6)
O(2)#3-Cr(1)-O(2)#4	91.5(4)	173.3(5)	N(101)#6-Ir(10)-C(112)	173.1(3)	173.5(5)
O(2)#1-Cr(1)-O(2)#5	93.7(3)	94.7(5)	N(101)-Ir(10)-C(112)	79.0(4)	79.0(6)
O(2)-Cr(1)-O(2)#5	81.5(4)	80.6(6)	N(101)#7-Ir(10)-C(112)	89.1(3)	89.0(4)
O(2)#2-Cr(1)-O(2)#5	91.5(4)	173.3(5)	C(112)#6-Ir(10)-C(112)	96.7(4)	96.8(6)
O(2)#3-Cr(1)-O(2)#5	93.7(3)	90.4(6)	C(101)-Ir(10)-N(112)	79.0(4)	79.0(6)
O(2)#4-Cr(1)-O(2)#5	173.2(3)	94.7(5)	N(112)#6-Ir(10)-N(112)	96.7(4)	96.8(6)

Symmetry transformations: #2 -y,x-y,z; #3 y,x,-z+1/2; #4 -x+y,-x,z; #5 x-y,-y,-z+1/2; #6 -y+1,x-y,z; #7 -x+y+1,-x+1,z

Crystal structure of $[Ir(bpy)(ppy)_2][MnCr(C_6O_4Cl_2)_3]\cdot 2G\cdot 2CH_3CN\cdot H_2O$, G = PhCl (38) and PhBr (39): Both compounds are isostructural and crystallize in the triclinic *P*-1 space group The asymmetric unit contains one $[Ir(bpy)(ppy)_2]^+$ cation, one $[MnCr(C_6O_4Cl_2)_3]^-$ anion, two halo-benzene molecules, two acetonitrile molecules and a water molecule. Thus the asymmetric unit matches the chemical formula: $[Ir(bpy)(ppy)_2][MnCr(C_6O_4Cl_2)_3]\cdot 2G\cdot 2CH_3CN\cdot H_2O$, G = PhCl (**38**) and PhBr (**39**). Since both compounds are isostructural and present the same compositions, differing only in the solvent molecules, they are solvates. The structure of both compounds consists of anionic layers formulated as $[Mn^{II}Cr^{III}(C_6O_4Cl_2)_3]^-$ with the classical hexagonal honeycomb 2D structure and layers of $[Ir(bpy)(ppy)_2]^+$ cations to compensate the negative charge. The most original aspect of this structure is the presence of two consecutive anionic layers alternating with one cationic layer (Figure 6.10a) instead of the typical alternation of one anionic and one cationic layer. Water and acetonitrile molecules are located in the cationic layers while the halo-benzene molecules (PhCl in **38** and PhBr in **39**) are located in the anionic layers, adding an extra stabilization by $\pi-\pi$ stacking with the aromatic rings of the anilato ligand. Data collection and refinement parameters are given in Table 6.5.

***Table 6.5**. Crystallographic data compounds **38** and **39**.*

	38	**39**
Empirical formula	$C_{66}H_{42}N_6O_{13}Cl_8MnCrIr$	$C_{66}H_{40}N_6O_{12}Cl_6Br_2MnCrIr$
Formula weight (g/mol)	1709.85	1780,73
Temperature K	120(2)	120(2)
Wavelength (Å)	0.71073	0.71073
Crystal system	Triclinic	Triclinic
Space group	*P*-1 #2.	*P*-1 #2
a (Å)	13.2080(10)	13.3038(6)
b(Å)	13.4119(9)	13.4201(8)
c(Å)	20.8703(13)	20.3225(10)
α (°)	78.052(5)	83.773(4)
β (°)	77.417(6)	84.347(4)
γ (°)	65.475(7)	64.794(5)
V (Å^3)	3254.3(4)	3258.0(3)
ρ_{cal} (mg m^{-3})	1.733	1.805
μ (mm^{-1})	2.793	3.932
Crystal size (mm)	0.08x0.05x0.04	0.08x0.04x0.02
θ range (°)	2.792-25.057	3.336-25.046
Reflections collected	52247	21965
Independent reflections (R_{int})	11492	11330
Reflns used in refinement, *n*	11492	11330
$R_1(F)$,[a] $I > 2\sigma(I)$	0.056	0.0857
$wR_2(F^2)$,[b] all data	0.1321	0.1802
$S(F^2)$,[c] all data	1.029	1.018
Largest diff. Peak	3.534	3.358
Largest diff. Hole	-1.563	-2.314

[a]$R1(F) = \Sigma||F_O|-|F_C||/\Sigma|F_O|$; [b]$wR2(F^2) = [\Sigma w(F_O^2-F_C^2)^2/\Sigma wF_O^4]^{1/2}$;

[c]$S(F^2) = [\Sigma w(F_O^2-F_C^2)^2/(n+r-p)]^{1/2}$

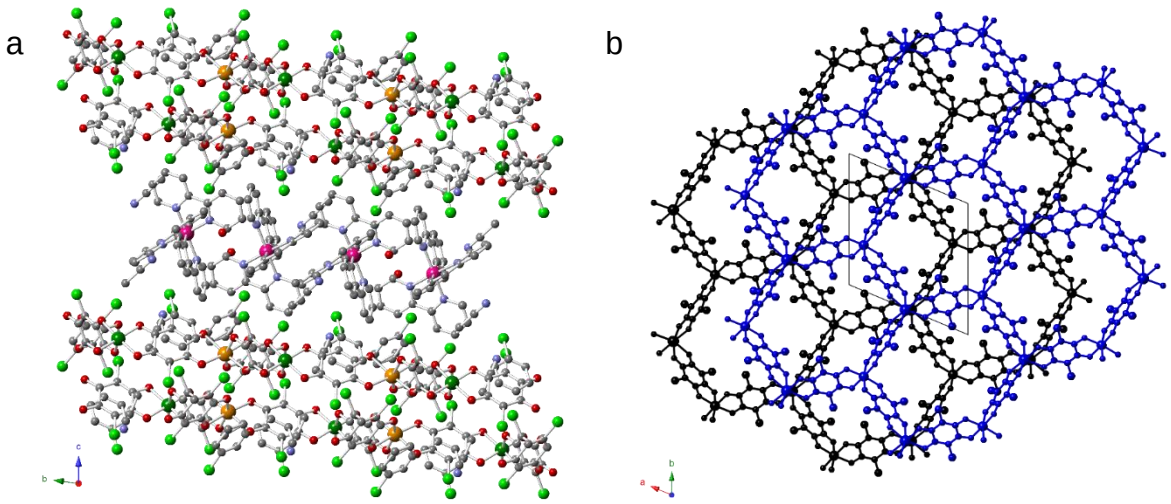

***Figure 6.10**. Structure of compound **38** (similar in **39**): **(a)** Side view (down the a direction) of the packing of the layers. **(b)** View of the alternated disposition of the two consecutive anionic layers (in blue and black) down the c axi.s Colour code in **(a)**: Cr = dark green, Mn = orange, Ir = pink, O = red, C = grey, Cl = light green, N = blue.*

The two consecutive anionic layers have an alternated disposition (Figure 6.10b), precluding the formation of hexagonal channels. The distance between the average planes of the metal centres in the two consecutive anionic layers is, as expected, shorter for the PhCl derivative (4.148 Å in **38** *vs*. 4.283 Å in **39**). As already indicated, the presence of the halo-benzene template molecules is essential for obtaining these kinds of structures. In fact, all the attempts to obtain the 2D honeycomb layers with this $[Ir(bpy)(ppy)_2]^+$ cation without adding a halo-benzene resulted in the formation of the monomeric phases **35** and **36**. The halo-benzene molecules are located in the hexagonal cavities of the honeycomb layers forming short π-π interactions with the anilato aromatic rings (Figure 6.11).

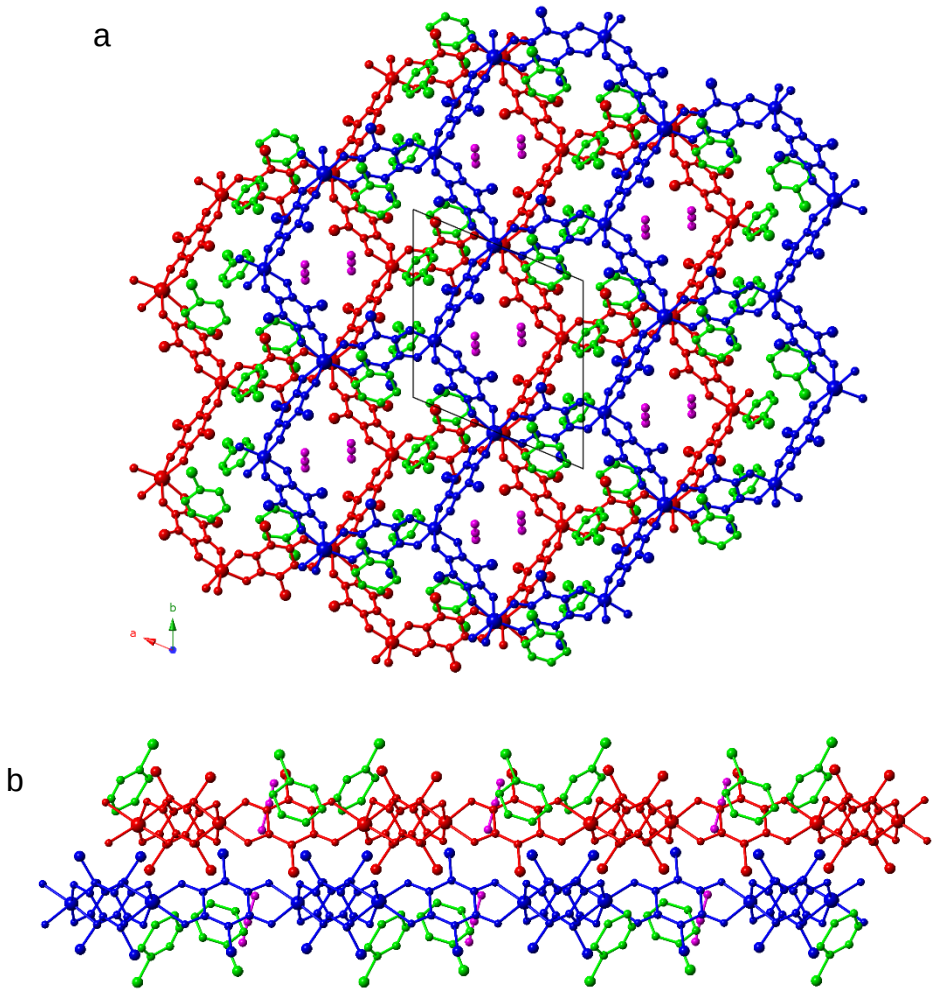

***Figure 6.11**. Structure of compound **38** (similar in **39**): View of two consecutive anionic layers showing the location of the template halo-benzene molecules (in green) and the acetonitrile molecules (in pink) down the c axis **(a)** and the b axis **(b)** showing the π–π stacking between the anilato ring and the halo-benzene molecules.*

The π-π interactions between the halo-benzene molecules and the anilato ligands are 3.476 and 3.435 Å and the offset angles are 19.87 and 21.09º for **38** and **39**, respectively, values typical for π–π interactions as defined by Janiak (C_g-C_g distances 3.3-3.8 Å and offset angles close to 20º).[14]

The anionic layers contain Mn(II) and Cr(III) ions alternating in the vertices of the hexagons connected through bis-bidentate chloranilato ligands that form the sides of the hexagons (Figure 6.12). The metal ions alternate in the hexagons in such a way that each Mn(II) ions is surrounded by three Cr(III) ions and vice-versa (Figure 6.13a). These structures, unlike the ones presented in other chapters in this Thesis, are non centro-symmetric and, therefore, the metal centres could be perfectly assigned. Furthermore, since the metal ions present different chiralities (as observed in the other anilato and oxalato-based honeycomb layers) we can observe that in the solved crystals of compounds **38** and **39** the Mn(II) ions are Δ whereas the Cr(III) are Λ (Figure 6.13b).

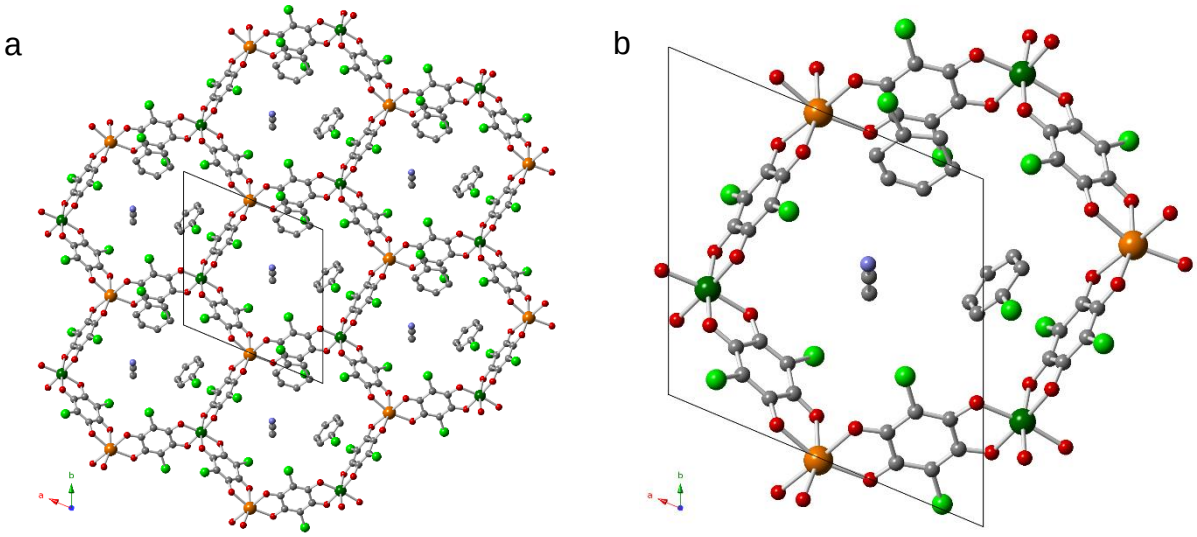

***Figure 6.12**. Structure of compound **38** (similar in **39**): **(a)** View of one hexagonal honeycomb layer down the c direction. **(b)** View of one hexagon down the c direction showing the π-π interactions between the chloro-benzene molecules and the anilato rings. Colour code: Cr = dark green, Mn = orange, O = red, C = grey, Cl = light green.*

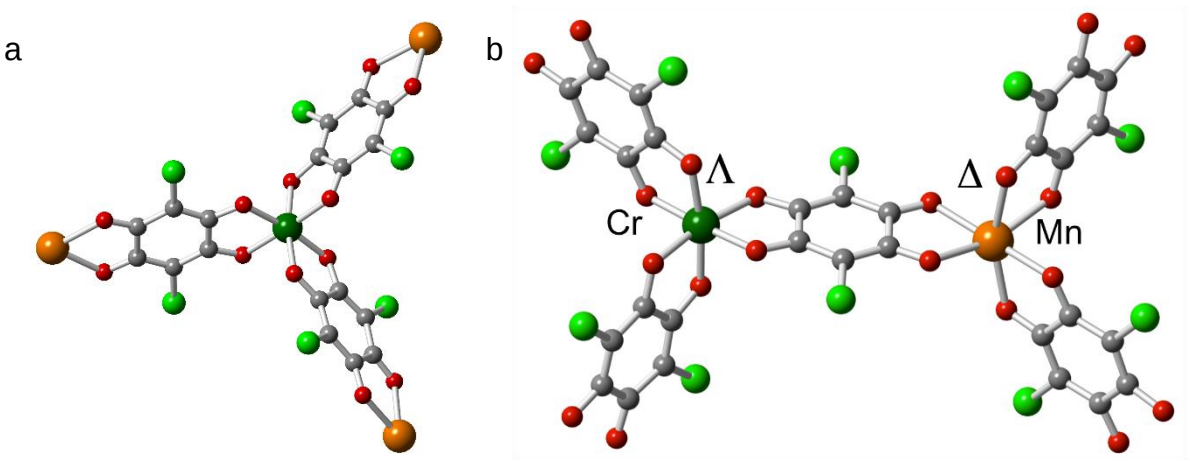

***Figure 6.13**. Structure of compound **38** (similar in **39**): **(a)** View of one Cr(III) ion surrounded by three Mn(II) ions. **(b)** View of two neighbouring metal centres with alternating chiralities. Colour code: Cr = dark green, Mn = orange, O = red, C = grey, Cl = light green.*

The metal ions are surrounded by three chelating anilato ligands giving rise to a distorted octahedral coordination geometry (Figure 6.13a). The M-O bonds (in the range of 1.969-1.989 Å in **38** and of 1.965-1.987 Å in **39**, (Table 6.6) are similar to those found in other related 2D honeycomb M(II)M(III) layers, including those presented here in other chapters.[6, 9, 10, 15-17] The *cis* and *trans* angles are also similar in both compounds (Table 6.7). Thus, the *cis* angles are in the range of 81.6-84.2º in **38** and of 81.5-95.9º in **39**, and the *trans* angles are in the range of 169.71-171.85º in **38** and of 170.4-176.5º in **39** (Table 6.7). These values are very similar to those found in all the reported A[MnCr($C_6O_4X_2$)$_3$] compounds (X = Cl and Br; A = NBu_4^+, $[(H_3O)(phz)_3]^+$, $[Fe^{III}(sal_2\text{-trien})]^+$, $[Fe^{III}(4\text{-OH-}sal_2\text{-trien})]^+$, $[Fe^{III}(sal_2\text{-epe})]^+$ and $[Fe^{III}(5\text{-Cl-}sal_2\text{-trien})]^+$).[15, 18]

***Table 6.6**. Main bond lengths (Å) around the metals centres in compounds **38** and **39**.*

Atoms	38	39
Cr(1)-O(22)	1.969(5)	1.967(9)
Cr(1)-O(13)	1.969(4)	1.965(8)
Cr(1)-O(3)	1.971(4)	1.982(8)
Cr(1)-O(12)	1.974(5)	1.987(8)
Cr(1)-O(2)	1.976(5)	1.975(8)
Cr(1)-O(23)	1.989(5)	1.979(8)
Mn(1)-O(15)	2.153(5)	2.197(8)
Mn(1)-O(5)	2.166(5)	2.214(8)
Mn(1)-O(6)	2.169(5)	2.150(8)
Mn(1)-O(26)	2.172(5)	2.207(8)
Mn(1)-O(16)	2.199(5)	2.203(8)
Mn(1)-O(25)	2.200(5)	2.163(8)

***Table 6.7**. Main angles (°) around the metals centres in compounds **38** and **39**.*

Atoms	38	39	Atoms	38	39
O(22)-Cr(1)-O(13)	92.23(19)	170.4(3)	O(15)-Mn(1)-O(5)	100.21(19)	87.3(3)
O(22)-Cr(1)-O(3)	90.7(2)	94.7(3)	O(15)-Mn(1)-O(6)	110.23(18)	160.6(3)
O(13)-Cr(1)-O(3)	177.0(2)	91.7(3)	O(5)-Mn(1)-O(6)	74.98(17)	75.0(3)
O(22)-Cr(1)-O(12)	171.85(19)	92.8(3)	O(15)-Mn(1)-O(26)	97.74(18)	89.9(3)
O(13)-Cr(1)-O(12)	81.83(19)	81.5(3)	O(5)-Mn(1)-O(26)	161.92(19)	172.4(3)
O(3)-Cr(1)-O(12)	95.3(2)	171.2(3)	O(6)-Mn(1)-O(26)	96.81(18)	108.6(3)
O(22)-Cr(1)-O(2)	92.1(2)	95.4(3)	O(15)-Mn(1)-O(16)	74.33(18)	74.6(3)
O(13)-Cr(1)-O(2)	97.39(18)	92.6(3)	O(5)-Mn(1)-O(16)	100.28(17)	86.8(3)
O(3)-Cr(1)-O(2)	81.70(18)	81.8(3)	O(6)-Mn(1)-O(16)	173.77(18)	96.2(3)
O(12)-Cr(1)-O(2)	94.2(2)	93.0(3)	O(26)-Mn(1)-O(16)	86.58(18)	99.2(3)
O(22)-Cr(1)-O(23)	81.6(2)	82.2(3)	O(15)-Mn(1)-O(25)	159.20(17)	92.7(3)
O(13)-Cr(1)-O(23)	91.01(19)	90.1(3)	O(5)-Mn(1)-O(25)	89.58(18)	98.7(3)
O(3)-Cr(1)-O(23)	90.21(19)	95.9(3)	O(6)-Mn(1)-O(25)	89.96(18)	97.7(3)
O(12)-Cr(1)-O(23)	92.9(2)	89.6(3)	O(26)-Mn(1)-O(25)	74.12(18)	74.3(3)
O(2)-Cr(1)-O(23)	169.71(19)	176.5(3)	O(16)-Mn(1)-O(25)	85.94(18)	165.9(3)

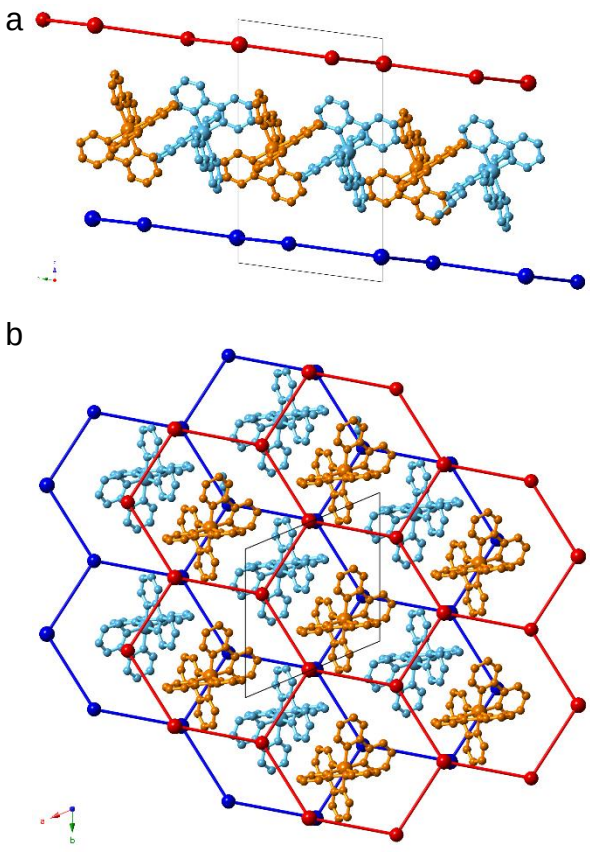

***Figure 6.14**. Structure of compound **38** (similar in **39**): **(a)** View, down the c direction, of one cationic layer and the anionic layers above and below. **(b)** View down the c direction of the same layers. Only the positions of the Cr(III) and Mn(II) ions are shown in the anionic layers.*

The $[Ir(bpy)(ppy)_2]^+$ cations are located above and below the hexagonal cavities of the anionic layers in such a way that half of the cations (light blue in Figure 6.14) lays in the centre of the hexagonal cavities of the anionic layer above (dark blue in Figure 6.14) and the other half (orange in Figure 6.14) lays on the hexagonal cavities of the layer below (red in Figure 6.14).

3.3. X-Ray Powder Diffraction

All the compounds were analysed with the XRPD technique to check for phase purity in the samples by comparing with the simulated diffractograms from the solved structures (Figures 6.15 and 6.16). Compounds **35** and **36** show a good crystallinity and a good agreement with the simulated ones, generated with Mercury program, from their respective single crystals X-ray structures. Compounds **37**-**42** are much more difficult to crystallize and, accordingly present a much lower crystallinity. Nevertheless, we can assume that they all are isostructural (although the exact number of solvent crystallization molecules may varies).

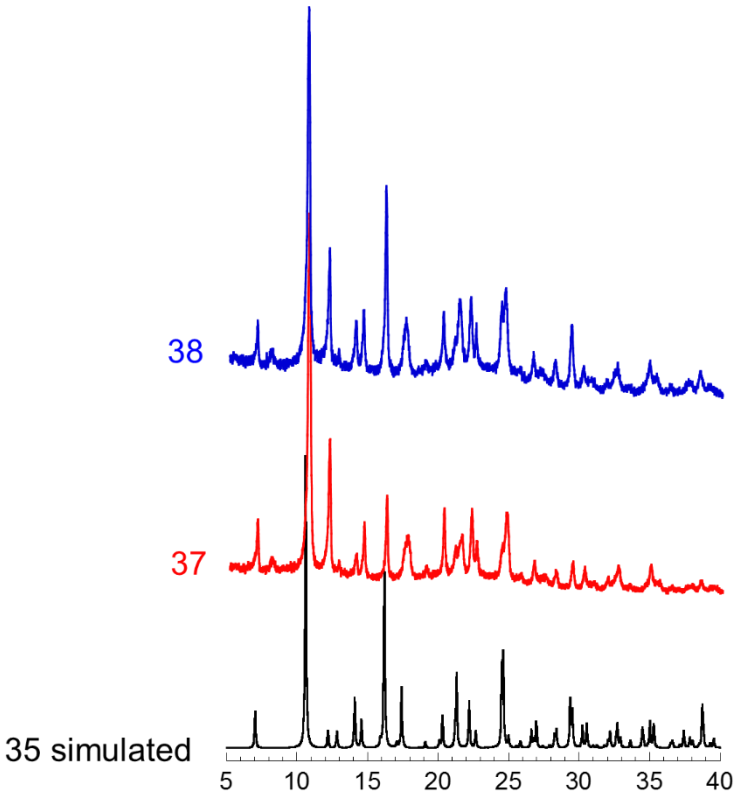

***Figure 6.15**. Experimental and simulated (black) X-ray powder diffractograms for **35** (red) and **36** (blue).*

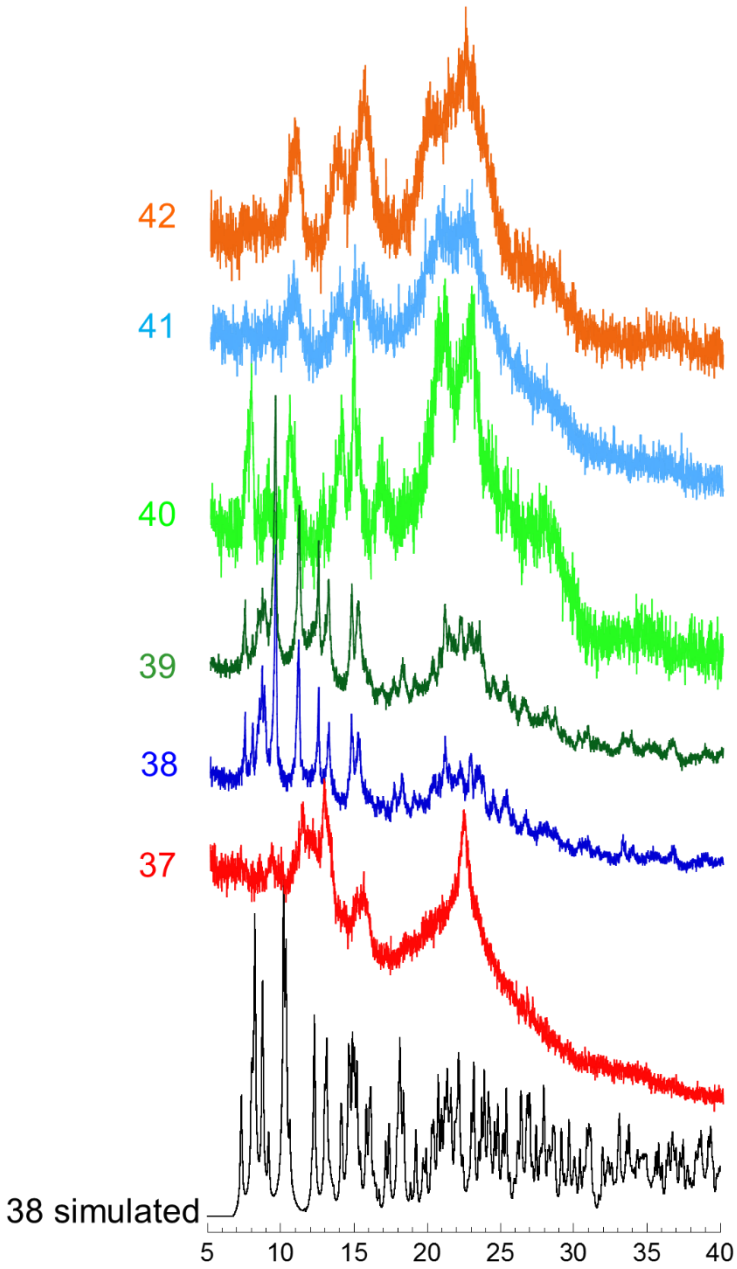

***Figure 6.16**. Experimental and simulated (black) X-ray powder diffractograms for **37**-**42**.*

3.4. Magnetic Properties

Compounds **35** and **36** show very similar magnetic properties. The thermal variation of $\chi_m T$ (χ_m is the molar magnetic susceptibility per formula) shows a constant value of *ca*. 1.9 cm^3 K mol^{-1} for both compounds (Figure 6.17). This value is very close to the expected one for an isolated Cr(III) ion with a d^3 configuration and a S = 3/2 spin ground state. On cooling the samples, $\chi_m T$ remains constant in both

compounds down to *ca*. 20 K and shows a smooth and progressive decrease at lower temperatures. This behaviour indicates that both compounds are essentially paramagnetic and present a zero field splitting (ZFS) of the S = 3/2 ground spin state. Accordingly, we have fit the magnetic properties of the two compounds to a simple model for a S = 3/2 monomer with a ZFS.[19] This simple model reproduces very satisfactorily the magnetic data of both compounds in the whole temperature range with g = 2.0084 and |D| = 1.6 cm^{-1} for **35** and g = 2.0076 and |D| = 1.4 cm^{-1} for **36** (solid lines in Figure 6.17). Both |D| values are low and within the normal range observed for isolated octahedral Cr(III) complexes.[20] It has to be noted that the sign of D cannot be determined from powder magnetic susceptibility measurements and that these D values could include a very weak intermolecular antiferromagnetic interaction.

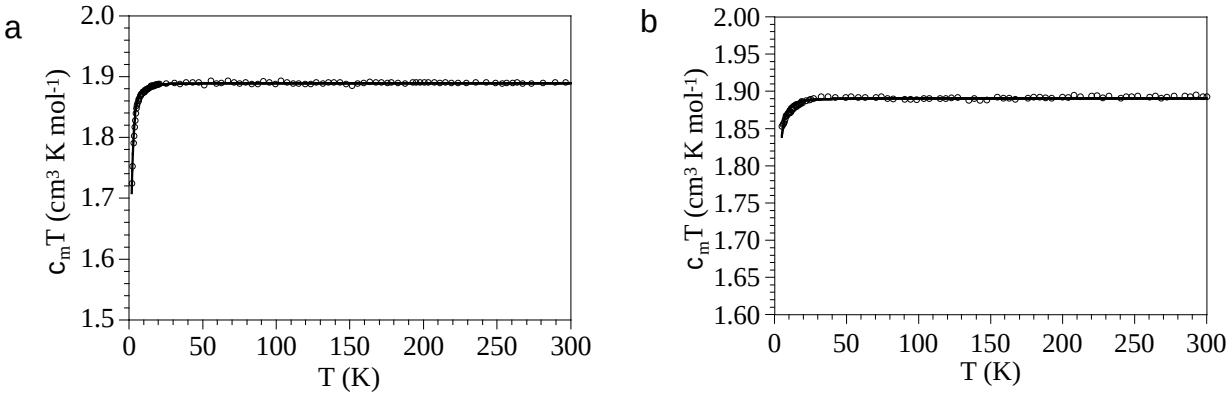

***Figure 6.17**. Thermal variation of the χ_mT product for compounds **35 (a)** and **36 (b)**. Solid lines are the best fit to the isolated S = 3/2 monomer model with a zero field splitting*

Compounds **37**-**42** present a different magnetic behaviour due to the presence of Cr^{III} and M^{II} ions. These compounds show the presence of antiferromagnetic (AF) Cr-Mn interactions mediated through the anilato-ligand bridges, as clearly shown by the thermal variation of their magnetic moment (represented as the product of the molar magnetic susceptibility per $Mn^{II}Cr^{III}$ couple times the temperature, χ_mT). Since the ground spin states of Cr^{III} and Mn^{II} are different (3/2 and 5/2, respectively) this AF interaction leads to a ferrimagnetic coupling that results in a ferrimagnetic long range ordering at low temperatures. The χ_mT product shows for **37**- **42** at room temperature values in the range of 6.2-6.5 cm^3 K mol^{-1} (Figure 6.18), close to the expected value for isolated S = 3/2 Cr(III) and S = 5/2 Mn(II) ions with g = 2 (6.25 cm^3 K mol^{-1}). When

the temperature is lowered, $\chi_m T$ shows a continuous decrease (since the magnetic coupling is antiferromagnetic and the total magnetic moment is reduced as the temperature decreases), reaching a minimum at ca. 20 K (since the two ground spin states are not fully cancelled), followed by a sharp increase at lower temperatures and a maximum at ca. 11 K in all the compounds, indicating the presence of a long range ferrimagnetic ordering (Figure 6.18). The magnetic susceptibility plots (Figure 6.18), show abrupt jumps at ca.10-11 K in all cases, also supporting the presence of a long range magnetic ordering around 10 K.

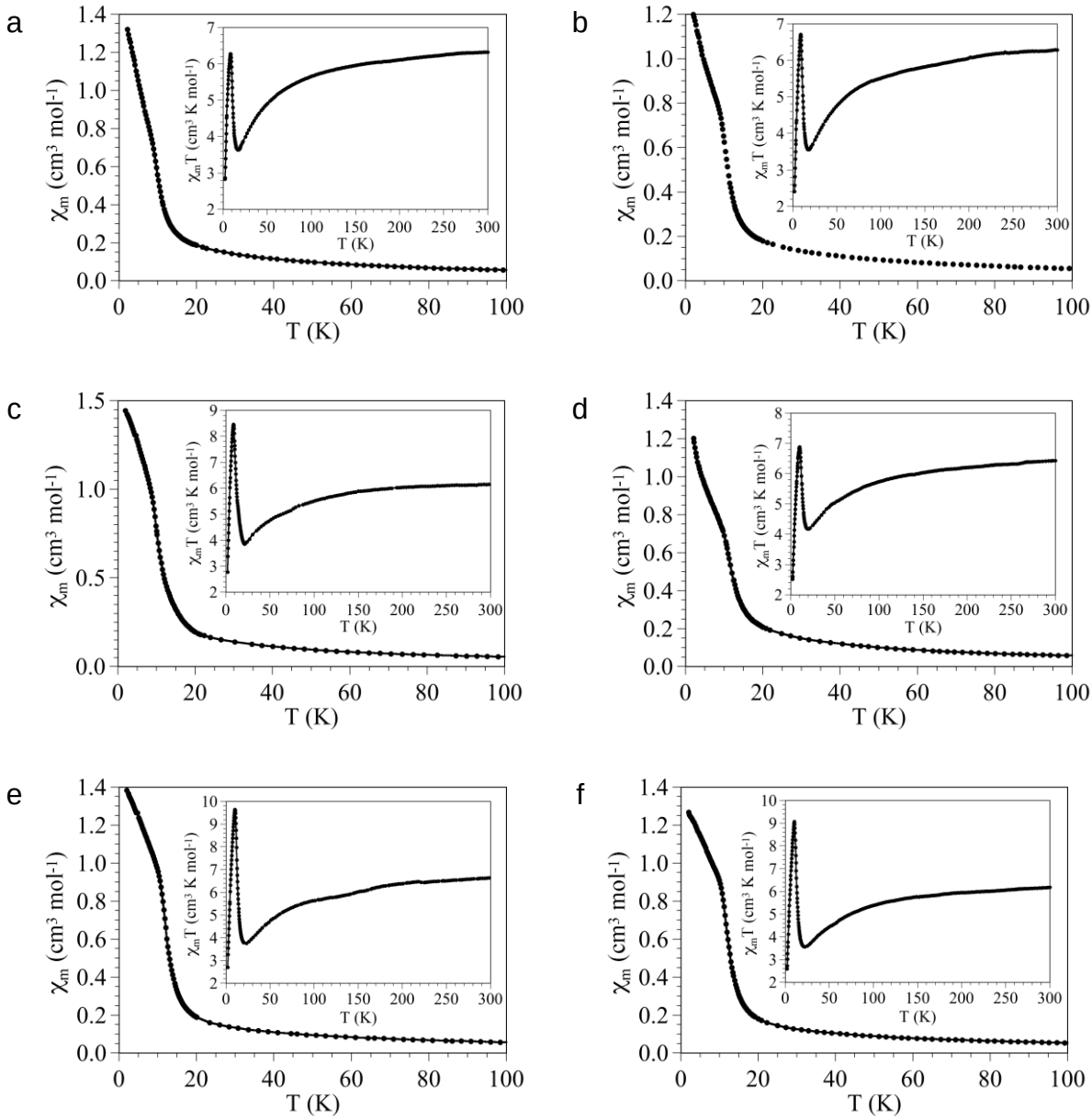

***Figure 6.18**: Thermal variation of χ_m in the temperature range 2-100 K for compounds **(a) 37**, **(b) 38**, **(c) 39**, **(d) 40**, **(e) 41** and **(f) 42**. Insets show the thermal variations of the $\chi_m T$ products.*

To confirm the presence of a long range ferrimagnetic ordering and determine the ordering temperature in a more precise way we have performed susceptibility measurements with an oscillating magnetic field at different frequencies in the range of 1-1000 Hz (AC susceptibility). These measurements show frequency-independent peaks in both, the in phase (χ_m') and the out of phase (χ_m") susceptibilities in the three compounds with chloranilato (**37**-**39**) and a slightly frequency dependent signal in the three samples with bromanilato (**40**-**42**), confirming the presence of a long range ordering in all the samples (Figures 6.19-6.24). The presence of a slightly frequency-dependent signal in compounds **40**-**42** may be attributed to the small size of the crystals in the polycrystalline samples and/or to the lower crystallinity of these compounds, in agreement with the observed trend in the powder X-ray diffractograms (see above).

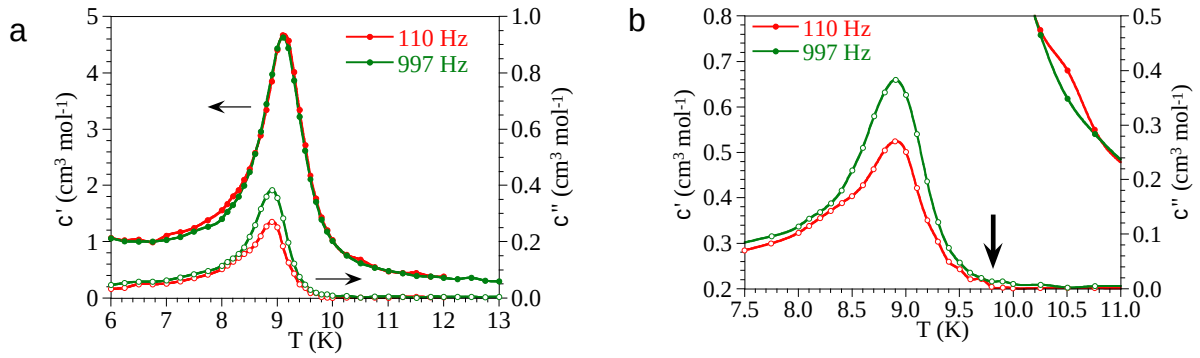

***Figure 6.19**: **(a)** Thermal variation of the in-phase (χ_m', filled symbols, left scale) and out-of-phase (χ"$_m$, empty symbols, right scale) susceptibilities at different frequencies for compound **37**. **(b)** Zoom of the out-of-phase susceptibility. The arrow indicates T_c.*

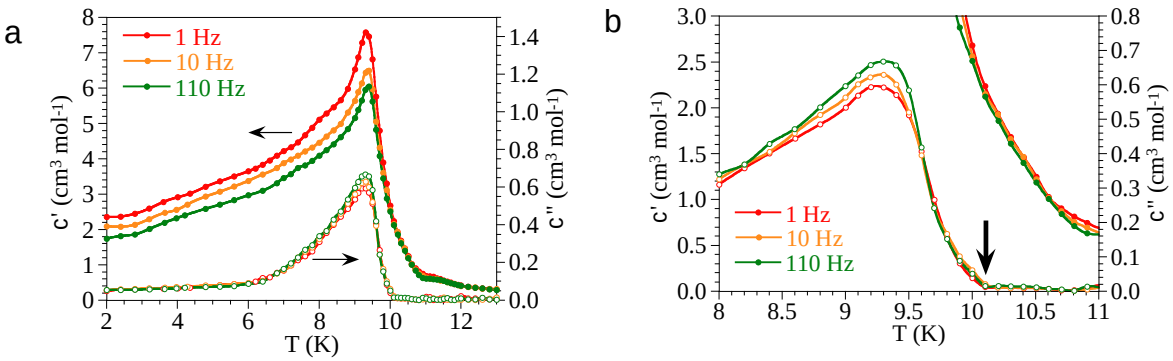

***Figure 6.20**: **(a)** Thermal variation of the in-phase (χ_m', filled symbols, left scale) and out-of-phase (χ"$_m$, empty symbols, right scale) susceptibilities at different frequencies for compound **38**. **(b)** Zoom of the out-of-phase susceptibility. The arrow indicates T_c.*

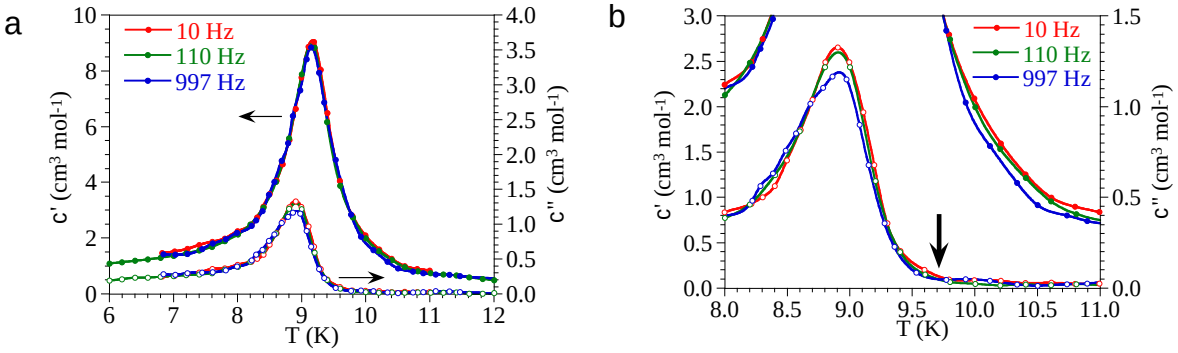

***Figure 6.21**: **(a)** Thermal variation of the in-phase (χ_m', filled symbols, left scale) and out-of-phase (χ''_m, empty symbols, right scale) susceptibilities at different frequencies for compound **39**. **(b)** Zoom of the out-of-phase susceptibility. The arrow indicates T_c*

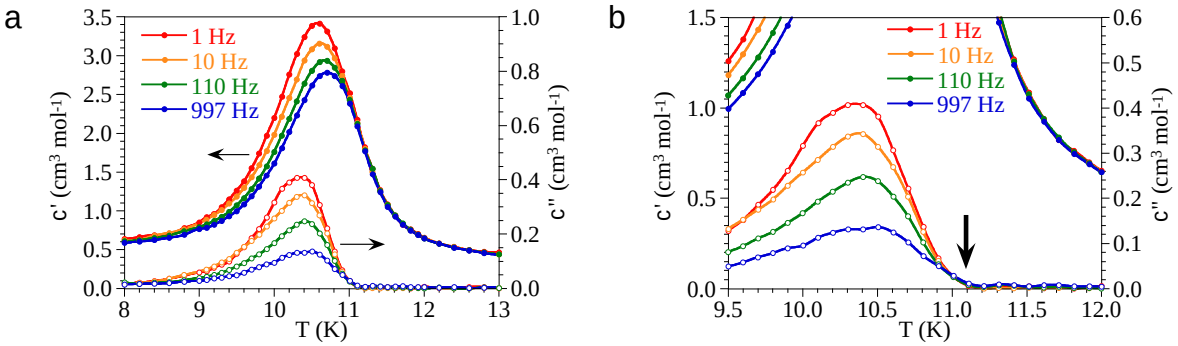

***Figure 6.22**: **(a)** Thermal variation of the in-phase (χ_m', filled symbols, left scale) and out-of-phase (χ''_m, empty symbols, right scale) susceptibilities at different frequencies for compound **40**. **(b)** Zoom of the out-of-phase susceptibility. The arrow indicates T_c.*

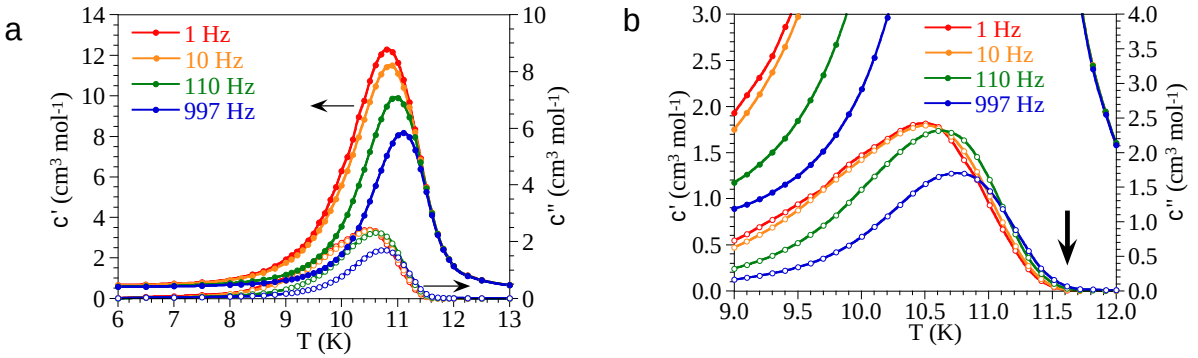

***Figure 6.23**: **(a)** Thermal variation of the in-phase (χ_m', filled symbols, left scale) and out-of-phase (χ''_m, empty symbols, right scale) susceptibilities at different frequencies for compound **41**. **(b)** Zoom of the out-of-phase susceptibility. The arrow indicates T_c.*

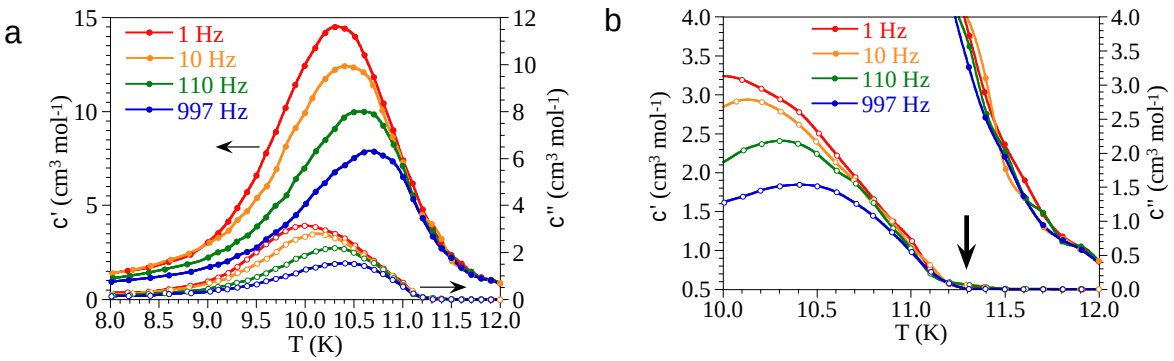

***Figure 6.24**: **(a)** Thermal variation of the in-phase (χ_m', filled symbols, left scale) and out-of-phase (χ''_m, empty symbols, right scale) susceptibilities at different frequencies for compound **42**. **(b)** Zoom of the out-of-phase susceptibility. The arrow indicates T_c.*

Although all the compounds show similar AC behaviours, the positions of the peaks change with X (Figures 6.19-6.24). As previously reported,[15] when the X group of the anilato ligand changes, T_c changes. The trend is the same that the one observed in the series $(NBu_4)[MnCr(C_6O_4X_2)_3]$ (X = H, Cl, Br and I): the higher the electronegativity of X, the lower the ordering temperature. Thus, in compounds **37**-**39**, where X = Cl, the ordering temperatures (9.8, 10.1 and 9.7 K in **37**-**39**, respectively) are lower than in compounds **40**-**42**, where X = Br (11.1, 11.6 and 11.3 K in **40**-**42**, respectively). This modulation of T_c with the electronegativity of X can be easily explained with the inductive effect of X: when the electronegativity of X increases, the electron density on the anilato ring decreases and the magnetic coupling through this anilato ring weakens, resulting in a lower T_c. As expected, the change of the halo-benzene (PhF, PhCl and PhBr) does not result in any important change in T_c, since the influence of the halo-benzene on the electron density of the anilato ring is rather low. Further studies with other anilato-derivative ligands with X = H, I, $-CH_3$, NO_2, CN… are under way in order to further modulate the ordering temperature.

The ferrimagnetic nature of the coupling in all the Mn-Cr compounds is further confirmed by the isothermal magnetization measurements at 2 K that show no saturation even at high fields (Figures 6.25-6.30). These measurements also provide an additional proof of the magnetic ordering presented by these layered materials since all compounds present hysteresis at 2 K, below the ordering temperatures with coercive fields of ca. 92 (**37**), 52 (**38**), 31 (**39**), 120 (**40**), 110 (**41**) and 88 mT (**42**).

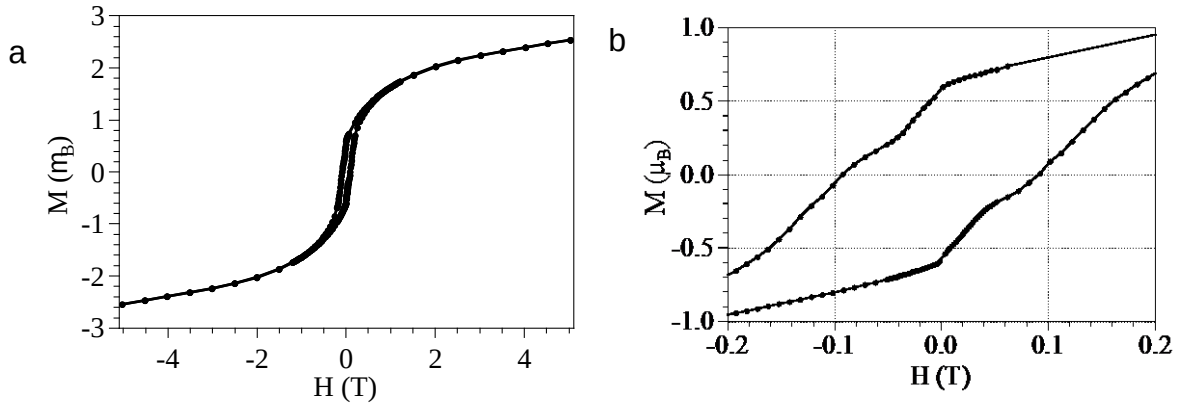

***Figure 6.25**: **(a)** Hysteresis cycle at 2 K for compounds **37**. **(b)** Zoom of the low field region.*

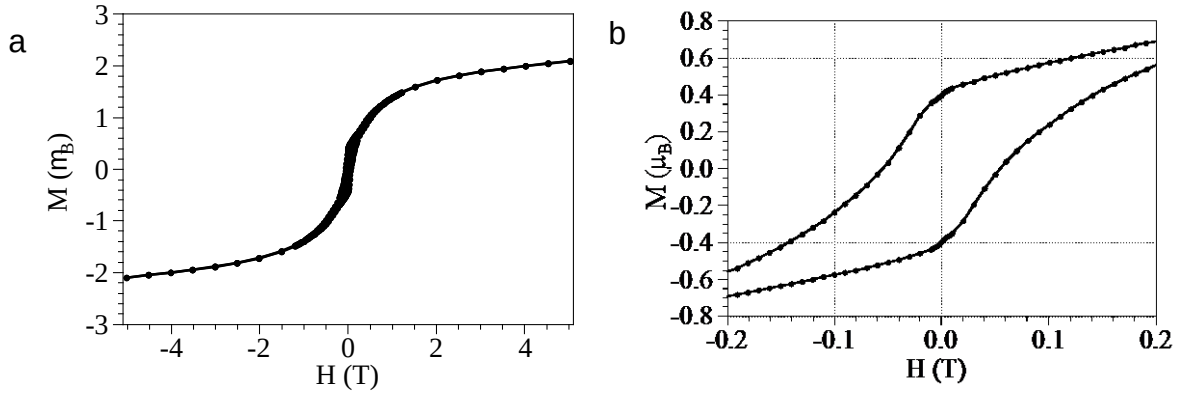

***Figure 6.26**: **(a)** Hysteresis cycle at 2 K for compounds **38**. **(b)** Zoom of the low field region.*

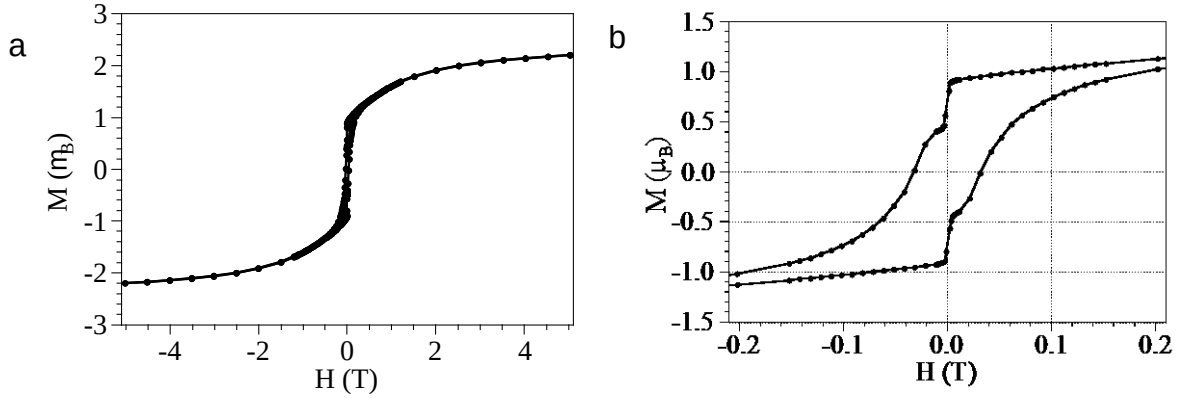

***Figure 6.27**: **(a)** Hysteresis cycle at 2 K for compounds **39**. **(b)** Zoom of the low field region.*

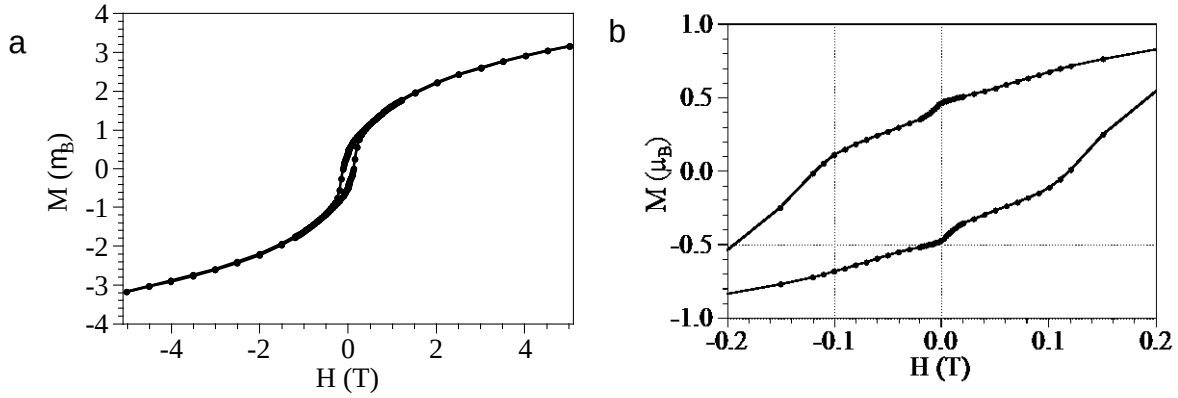

***Figure 6.28**: **(a)** Hysteresis cycle at 2 K for compounds **40**. **(b)** Zoom of the low field region.*

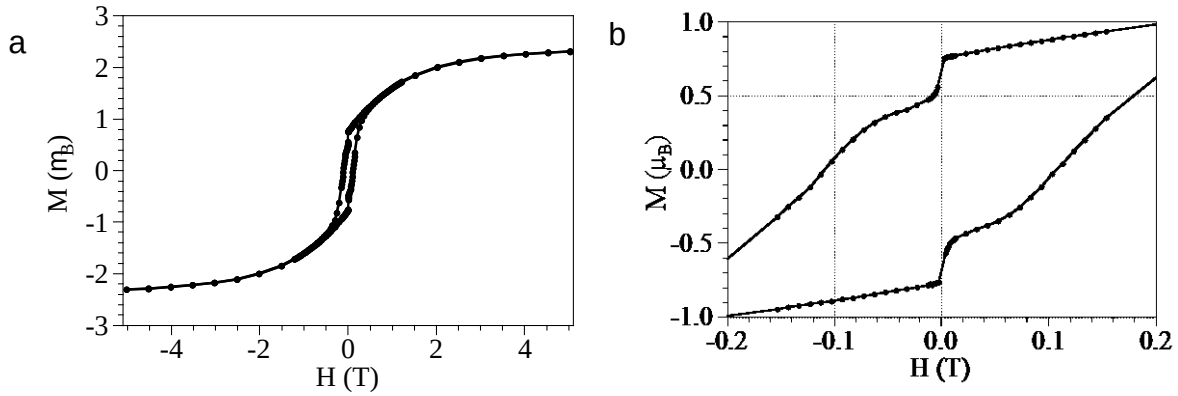

***Figure 6.29**: **(a)** Hysteresis cycle at 2 K for compounds **41**. **(b)** Zoom of the low field region.*

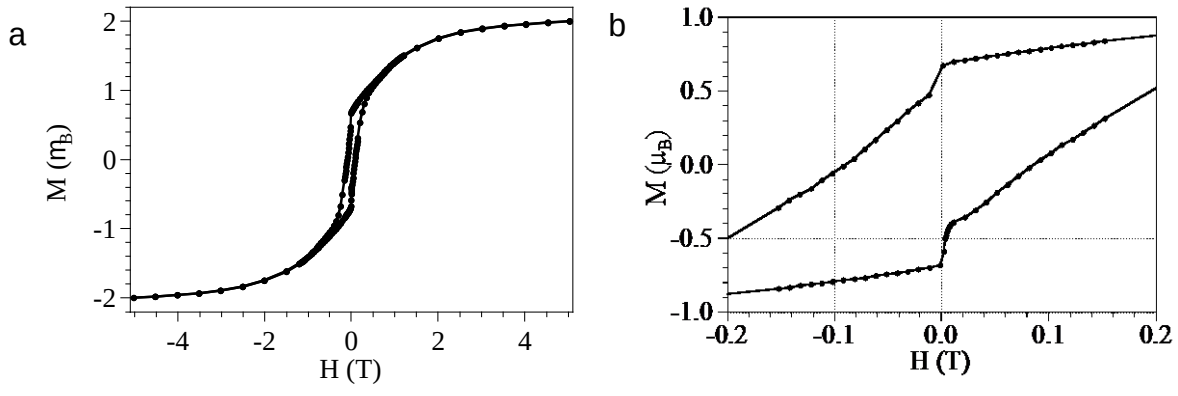

***Figure 6.30**: **(a)** Hysteresis cycle at 2 K for compounds **42**. **(b)** Zoom of the low field region.*

3.5. Luminescent Properties

Compounds **35** and **36** show luminescence due to the $[Ir(ppy)_2(bpy)]^+$ cation. The emission peak maximum, when excite at 488 nm wavelenght, appears for both compounds at *ca.* 580 nm (Figure 6.31), indicating that the anilato-based anion does not interfere with the emission properties of the $[Ir(ppy)_2(bpy)]^+$ cation as the maximum appears at the same wavelength observed in the $[Ir(ppy)_2(bpy)]^+$ cation itself[21] and in others slightly modified compounds based on the $[Ir(ppy)_2(bpy)]^+$ cation.[22]

For systems containing chelating and neutral ligands, such as $[Ir(ppy)_2(bpy)]Cl$, two luminescent pathways are feasible. The first one is the metal-to-ligand charge transfer (^{3}MLCT) and the second one is a $^3\pi-\pi^*$ ligand charge (LC) transition. Due to the fact that these two transitions have similar energies, it is difficult to discern between them. Indeed, Güdel et al.[23, 24] conclude that, in this mixed-ligand systems, the emission can be attributed to strong mixing between the MLCT and the LC excited states.

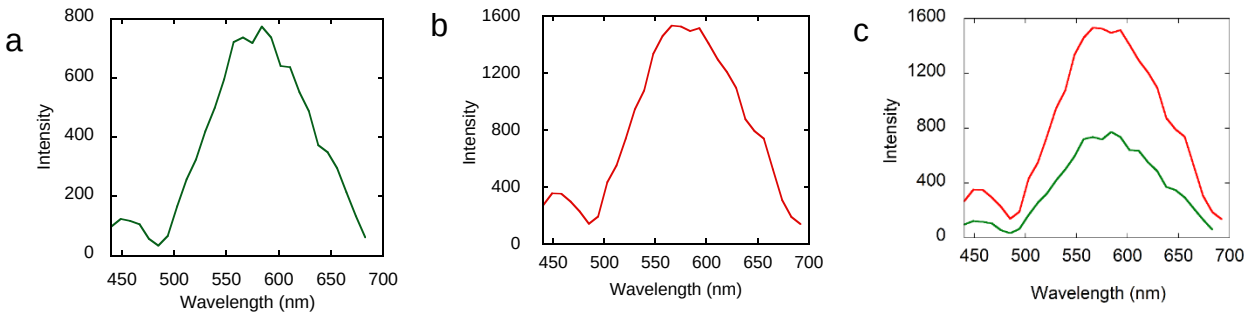

***Figure 6.31**: Emission spectrum for **(a)** compound **35**, **(b)** compound **36** and **(c)** both compounds, showing the larger intensity of compound **36** (in red).*

Figure 6.31 shows the emission spectra of single crystals of compounds **35** and **36** acquired in identical conditions. The scanning optical set-up that we use allows to compare the results obtained for two different compounds since the resulting optical spectra are the spatial average over the whole crystal image, improving the reproducibility of the measurement. We systematically observe a higher intensity in the emission of compound **36**. To explain this larger intensity in compound **36** would require advanced micro-spectroscopy characterization techniques such as excitation luminescence spectroscopy and time resolved

luminescence. It is well known that the molecular mass of the radicals highly influences the emission efficiency, because it is related with the energy of the vibrational modes, which are important de-activation channels. In this sense, the higher mass of bromoanilato might increase the emission efficiency, explaining the higher emission intensity observed in compound **36**.

Compounds **38**, **40**, **41** and **42** show a weak emission peak at 488 nm (Figure 6.32). This emission is only slightly more intense than the emission of the substrate and much lower that the emission of the ligand (Figure 6.32), suggesting that the 2D anilato-based honeycomb layers quench the emission of the iridium-based cation.

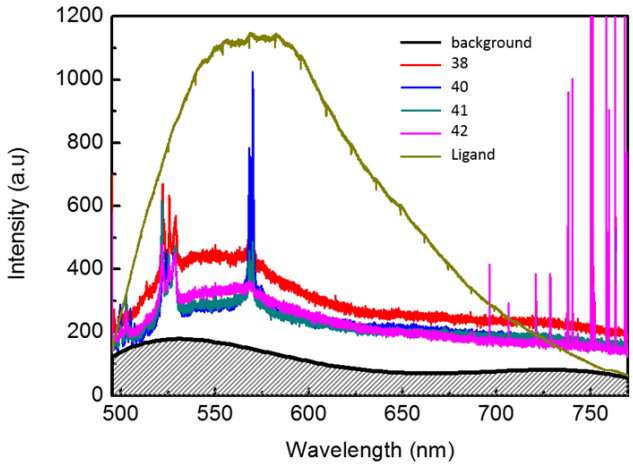

***Figure 6.32**: Emission spectra of compounds **38** and **40**-**42**, compared with the emission spectrum of the substrate.*

4. Conclusions and perspectives

In this chapter, we have presented ten different compounds distributed into two families. The first family is composed by two 0D compounds based on the tris(anilato)cromate $[Cr(C_6O_4X_2)_3]^{3-}$ (X = Cl and Br) anion and the luminescent $[Ir(ppy)_2(bpy)]^+$ cation. These two compounds present the paramagnetic behaviour characteristic of an isolated Cr^{III} ion and luminescent properties with a maximum of *ca*. 575 nm characteristic of the $[Ir(ppy)_2(bpy)]^+$ cation. The luminescent spectra is wide enough to assure that the compounds are going to emit white light. For this kind of systems that contain chelating and neutral ligands, such as $[Ir(ppy)_2(bpy)]Cl$, two luminescent pathways are feasible. The metal-to-ligand charge transfer (^{3}MLCT) and

the $^3\pi-\pi^*$ ligand charge (LC) transition. These two transitions have similar energies, so it is difficult to exactly know which one is taking place. In fact, Güdel et al. conclude that, in these mixed-ligand systems, the emission can be attributed to a strong mixing between the MLCT and the LC excited states.[23, 24]

The second family is composed by six 2D honeycomb hexagonal anilato-based layers with the same $[Ir(ppy)_2(bpy)]^+$ luminescent cation, formulated as $[Ir(bpy)(ppy)_2][MnCr(C_6O_4X_2)_3]\cdot 2PhZ\cdot 2CH_3CN\cdot H_2O$ (X = Cl, Br; Z = F, Cl, Br). These compounds present the, well known, 2D honeycomb anilato-based layered structure with the $[Ir(ppy)_2(bpy)]^+$ cation in-between the layers but with an unprecedented characteristic: there are two consecutive anilato layers per cationic layer. These two consecutive anilato layers are located in a alternated configuration, avoiding the formation of hexagonal channels.

The ferrimagnetic coupling of the Cr^{III} and Mn^{II} ions through the anilato ligands results in long range ferrimagnetic orderings at *ca*. 10-11 K for all the compounds. The differences in the T_c when changing the X group that were reported previously,[15] have also been observed in these compounds, with T_c around 10 K for X = Cl and 11.5 K for X = Br. In contrast, the change of the halo-benzene molecule located in the hexagonal cavities does not produces any significant change in T_c since this solvent molecule changes very slightly the electron density on the anilato ligand.

Regarding the luminescent properties of these compounds, no significant luminescence has been found. The emission spectra of the three compounds with X = Br and Z = F, Cl and Br and with X = Cl and Z = Cl (**38**, **40**, **41** and **42**) was weaker than the cation emission in all the cases, indicating that the anilato layers quench the emission of the cation.

As future perspectives, we would like to insert other new luminescent compounds into the anilato layers. In particular, other derivatives of the $[Ir(ppy)_2(bpy)]^+$ with different emission spectra.[13, 25, 26] Moreover, we are planning to insert the neutral luminescent compound $[Ir(ppy)_3]$ in-between neutral anilato layers such as $[M^{III}M^{III}(C_6O_4X_2)_3]$ (M^{III} = Fe, Cr, Al, Ln; X = Cl, Br) using PhZ molecules as templates.

5. References

(1) Sprouse, S.; King, K. A.; Spellane, P. J.; Watts, R. J. Photophysical Effects of Metal-Carbon .Sigma. Bonds in Ortho-Metalated Complexes of Iridium(III) and Rhodium(III). *J. Am. Chem. Soc.* **1984***, 106*, 6647-6653.

(2) Ohsawa, Y.; Sprouse, S.; King, K. A.; DeArmond, M. K.; Hanck, K. W.; Watts, R. J. Electrochemistry and Spectroscopy of Ortho-Metalated Complexes of Iridium(III) and Rhodium(III). *J. Phys. Chem.* **1987***, 91*, 1047-1054.

(3) Bain, G. A.; Berry, J. F. Diamagnetic Corrections and Pascal's Constants. *J. Chem. Educ.* **2008***, 85*, 532-536.

(4) Sheldrick, G. M. Crystal Structure Refinement with SHELXL. *Acta Cryst. C* **2015***, 71*, 3-8.

(5) Farrugia, L. J. WinGX Suite for Small-Molecule Single-Crystal Crystallography. *J. Appl. Cryst.* **1999***, 32*, 837-838.

(6) Atzori, M.; Artizzu, F.; Sessini, E.; Marchio, L.; Loche, D.; Serpe, A.; Deplano, P.; Concas, G.; Pop, F.; Avarvari, N.; Mercuri, M. L. Halogen-Bonding in a New Family of Tris(haloanilato)metallate(III) Magnetic Molecular Building Blocks. *Dalton Trans.* **2014***, 43*, 7006-7019.

(7) Min, K. S.; Rhinegold, A. L.; Miller, J. S. Tris(Chloranilato)Ferrate(III) Anionic Building Block Containing the (Dihydroxo)Oxodiiron(III) Dimer Cation: Synthesis and Characterization of $[(TPA)(OH)Fe^{III}OFe^{III}(OH)(TPA)][Fe(CA)_3]_{0.5}(BF_4)0.5CA{\cdot}1.5MeOH{\cdot}H_2O$ [TPA = tris(2-pyridylmethyl)amine; CA = chloranilate]. *J. Am. Chem. Soc.* **2006***, 128*, 40-41.

(8) Spengler, R.; Lange, J.; Zimmermann, H.; Burzlaff, H.; Veltsistas, P. G.; Karayannis, M. I. Structure of $C_{36}H_{52}Cl_6InN_3O_{14}$. *Acta Cryst. B* **1995***, 51*, 174-177.

(9) Atzori, M.; Artizzu, F.; Marchio, L.; Loche, D.; Caneschi, A.; Serpe, A.; Deplano, P.; Avarvari, N.; Mercuri, M. L. Switching-on Luminescence in Anilate-Based Molecular Materials. *Dalton Trans.* **2015***, 44*, 15786-15802.

(10) Benmansour, S.; Coronado, E.; Giménez-Saiz, C.; Gómez-García, C. J.; Rößer, C. Metallic Charge-Transfer Salts of Bis(Ethylenedithio)Tetrathiafulvalene with Paramagnetic Tetrachloro(Oxalato)Rhenate(IV) and Tris(Chloranilato)Ferrate(III) Anions. *Eur. J. Inorg. Chem* **2014***, 2014*, 3949-3959.

(11) Clemente-León, M.; Coronado, E.; Gómez-García, C. J.; Soriano-Portillo, A. Increasing the Ordering Temperatures in Oxalate-Based 3D Chiral Magnets: the series $Ir(ppy)_2(bpy)]M^{II}M^{III}(ox)_3]{\cdot}0.5H_2O$ ($M^{II}M^{III}$ = MnCr, FeCr, CoCr, NiCr, ZnCr, MnFe, FeFe); bpy = 2,2-bipyridine; ppy = 2-phenylpyridine; ox = Oxalate Dianion). *Inorg. Chem.* **2006***, 45*, 5653-5660.

(12) Sun, C. Y.; Wang, X. L.; Zhang, X.; Qin, C.; Li, P.; Su, Z. M.; Zhu, D. X.; Shan, G. G.; Shao, K. Z.; Wu, H.; Li, J. Efficient and Tunable White-Light Emission of Metal-organic Frameworks by Iridium-Complex Encapsulation. *Nat. Comm.* **2013***, 4*, 2717.

(13) Li, L.; Zhang, S.; Xu, L.; Han, L.; Chen, Z. N.; Luo, J. An Intensely Luminescent Metal-Organic Framework Based on a Highly Light-Harvesting Dyclo-Metalated Iridium(III) Unit Showing Effective Detection of Explosives. *Inorg. Chem.* **2013***, 52*, 12323-12325.

(14) Janiak, C. A Critical Account on π–π Stacking in Metal Complexes with Aromatic Nitrogen-Containing Ligands. *J. Chem. Soc. , Dalton Trans.* **2000**, 3885-3896.

(15) Atzori, M.; Benmansour, S.; Mínguez Espallargas, G.; Clemente-León, M.; Abhervé, A.; Gómez-Claramunt, P.; Coronado, E.; Artizzu, F.; Sessini, E.; Deplano, P.; Serpe, A.; Mercuri, M. L.; Gómez García, C. J. A Family of Layered Chiral Porous Magnets Exhibiting Tunable Ordering Temperatures. *Inorg. Chem.* **2013***, 52*, 10031-10040.

(16) Benmansour, S.; Vallés-García, C.; Gómez-Claramunt, P.; Mínguez Espallargas, G.; Gómez-García, C. J. 2D and 3D Anilato-Based Heterometallic M(I)M(III) Lattices: The Missing Link. *Inorg. Chem.* **2015***, 54*, 5410-5418.

(17) Benmansour, S.; Gómez-Claramunt, P.; Vallés-García, C.; Mínguez Espallargas, G.; Gómez García, C. J. Key Role of the Cation in the Crystallization of Chiral Tris(Anilato)Metalate Magnetic Anions. *Cryst. Growth Des.* **2016***, 16*, 518-526.

(18) Abherve, A.; Clemente-León, M.; Coronado, E.; Gómez-García, C. J.; Verneret, M. One-Dimensional and Two-Dimensional Anilate-Based Magnets with Inserted Spin-Crossover Complexes. *Inorg. Chem.* **2014***, 53*, 12014-12026.

(19) O'Connor, C. J. In *Research Frontiers in Magnetochemistry;* 1993; .

(20) Boca, R. Zero-Field Splitting in Metal Complexes. *Coord. Chem. Rev.* **2004***, 248*, 757-815.

(21) King, K. A.; Watts, R. J. Dual Emission from an Ortho-Metalated Iridium(III) Complex. *J. Am. Chem. Soc.* **1987***, 109*, 1589-1590.

(22) Slinker, J. D.; Gorodetsky, A. A.; Lowry, M. S.; Wang, J.; Parker, S.; Rohl, R.; Bernhard, S.; Malliaras, G. G. Efficient Yellow Electroluminescence from a Single Layer of a Cyclometalated Iridium Complex. *J. Am. Chem. Soc.* **2004***, 126*, 2763-2767.

(23) Colombo, M. G.; Hauser, A.; Guedel, H. U. Evidence for Strong Mixing between the LC and MLCT Excited States in Bis(2-phenylpyridinato-C2,N')(2,2'-bipyridine)Iridium(III). *Inorg. Chem.* **1993***, 32*, 3088-3092.

(24) Colombo, M. G.; Güdel, H. U. Synthesis and High-Resolution Optical Spectroscopy of bis2-(2-thienyl)pyridinato-C3,N'](2,2'-Bipyridine)Iridium(III). *Inorg. Chem.* **1993***, 32*, 3081-3087.

(25) Bunzli, A. M.; Constable, E. C.; Housecroft, C. E.; Prescimone, A.; Zampese, J. A.; Longo, G.; Gil-Escrig, L.; Pertegas, A.; Orti, E.; Bolink, H. J. Exceptionally Long-Lived Light-Emitting Electrochemical Cells: Multiple Intra-Cation Small Pi]-Stacking Interactions in $Ir(C^N)_2(N^N)]PF_6]$ Emitters. *Chem. Sci.* **2015***, 6*, 2843-2852.

(26) Wong, M. Y.; Xie, G.; Tourbillon, C.; Sandroni, M.; Cordes, D. B.; Slawin, A. M. Z.; Samuel, I. D. W.; Zysman-Colman, E. Formylated Chloro-Bridged Iridium(Iii) Dimers as OLED Materials: Opening Up New Possibilities. *Dalton Trans.* **2015***, 44*, 8419-8432.

Chapter 7

Single Molecule Magnet compounds inserted between anilato layers

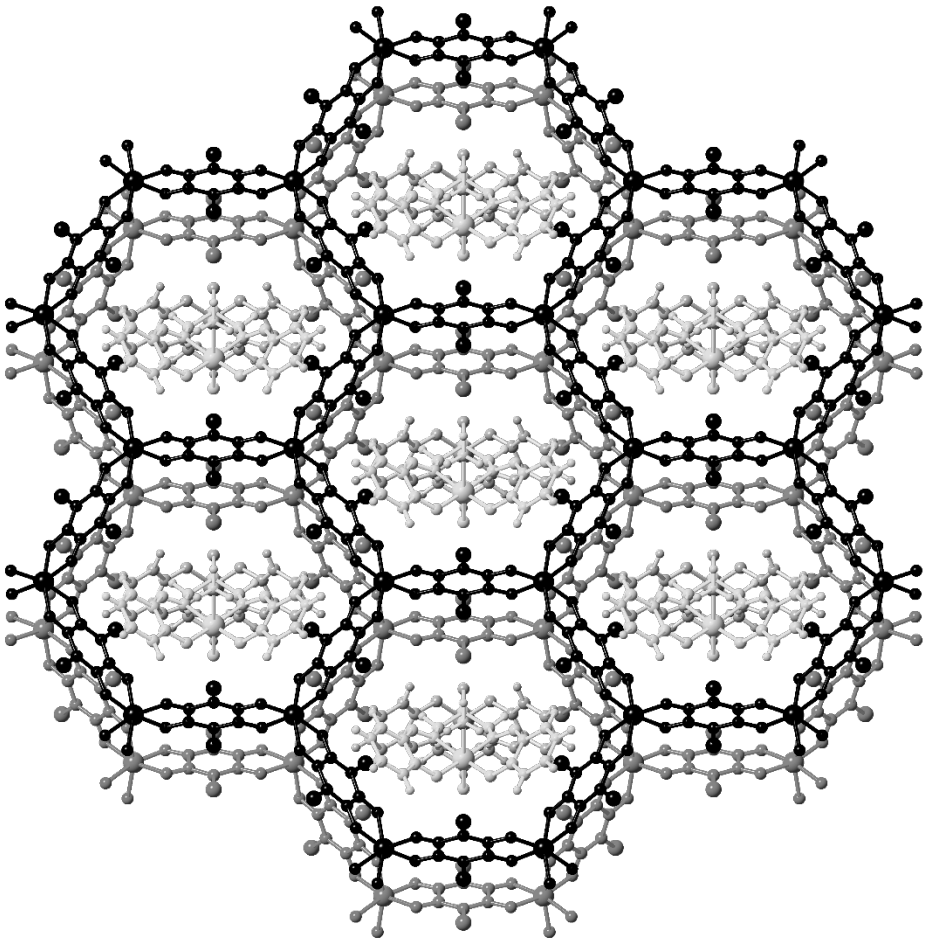

1. Introduction

In this chapter, we report the synthesis and characterization of four compounds containing the cations $[Mn(salen)(H_2O)]^+$ (salen = 2,2′-ethylenebis(nitrilomethylidene)diphenol) and $[Mn(salpn)(H_2O)]^+$ (salpn = N,N'-(propane)bis(salicyldeneiminate)) inserted in between anilato layers combining Cr(III) and Mn(II) with $C_6O_4Cl_2^{2-}$ and $C_6O_4Br_2^{2-}$. These four compounds can be formulated as $[Mn(salpn)(H_2O)][CrMn(C_6O_4X_2)_3]$ with X = Cl (**43**) and Br (**44**) and $[Mn(salen)(H_2O)][CrMn(C_6O_4X_2)_3]$ with X = Cl (**45**) and Br (**46**).

Only compounds **43** and **44**, containing the $[Mn(salpn)(H_2O)(MeO)]^+$ cation, crystallize in single crystals suitable for X-Ray diffraction. For these compounds we present the crystal structure, powder X-ray diffractograms, magnetic measurements and infrared spectra. Compounds **45** and **46**, with the cation $[Mn(salen)(H_2O)]^+$, could not be obtained with good quality single crystals although the IR spectroscopy and magnetic measurements confirm the presence of the cation and the 2D structure, as we will show below.

The presence of these SMM cations inserted into the honeycomb anilato layers does not necessarily imply the presence of SMM behaviour since the SMM behaviour depends on many factors and interactions and a slight change in the structure could dramatically affect the SMM behaviour. 2D oxalate lattices containing SMM cations are the best example of this unpredictable behaviour.[1, 2]

2. Experimental section

2.1. Synthesis

General Remarks: The synthesis of $K_3[Cr(C_6O_4Cl_2)_3]$ and $K_3[Cr(C_6O_4Br_2)_3]$ is described in chapter one. The SMM cations $[Mn(salpn)(H_2O)](ClO_4)$[3] and $[Mn(salen)(H_2O)](ClO_4)$[4] were prepared according to the literature. All the other reagents and solvents were commercially available and used as received, without further purification.

Synthesis of $[Mn(salpn)(H_2O)(MeO)][CrMn(C_6O_4Cl_2)_3]$ (43): A solution of $MnCl_2{\cdot}4H_2O$ (5.0 mg, 0.025 mmol) and $K_3[Cr(C_6O_4Cl_2)_3]$ (9.9 mg, 0.0125 mmol) in 0.5 mL of MeOH and 2 mL of MeCN was placed on top of a solution of

[Mn(salpn)(H_2O)](ClO_4) (11.3 mg, 0.0125 mmol) in 1.5 mL of fluorobenzene and 1 mL of MeCN. In between the two solutions, a stopper solution of fluorobencene and MeCN (1:2) was placed in order to slow down the diffusion. Black primsatic single crystals suitable for X-Ray diffraction were obtained after *ca*. two months at 18 ºC.

Synthesis of [Mn(salpn)(H_2O)(MeO)][CrMn($C_6O_4Br_2$)$_3$] (44): Compound **44** was synthesized as compound **43** but using K_3[Cr($C_6O_4Br_2$)$_3$] (13.2 mg, 0.0125 mmol) instead of K_3[Cr($C_6O_4Cl_2$)$_3$]. Brown primatic single crystals suitable for X-Ray diffraction were obtained after *ca.* two months at 18 ºC.

Synthesis of [Mn(salen)(H_2O)(MeO)][CrMn($C_6O_4Cl_2$)$_3$] (45): Compound **45** was synthesized as compound **43** but using [Mn(salen)(H_2O)](ClO_4) (11.0 mg, 0.0125 mmol), instead of [Mn(salpn)(H_2O)](ClO_4). After *ca.* three months, brown hedgehog-like small crystals were obtained and filtered. Unfortunately, these crystals were not suitable for single crystal X-Ray diffraction.

Synthesis of [Mn(salen)(H_2O)(MeO)][CrMn($C_6O_4Br_2$)$_3$] (46): Compound **46** was synthesized as compound **43** but using [Mn(salen)(H_2O)](ClO_4) (11.0 mg, 0.0125 mmol) instead of [Mn(salpn)(H_2O)](ClO_4). After *ca.* three months, small brown hedgehog-like crystals were obtained and filtered. Unluckily, these crystals were not suitable for X-Ray diffraction.

2.2. Physical Properties

FT-IR spectra were performed on KBr pellets and collected with a Nexus-Nicolet 5700 spectrophotometer.

Magnetic measurements were performed with a Quantum Design MPMS-XL-5 SQUID magnetometer in the 2-300 K temperature range with an applied magnetic fields of 0.5 T on polycrystalline samples of all the compounds. Isothermal hysteresis measurements were performed at 2 K with magnetic fields from -5 to 5 T. AC susceptibility measurements were performed on the same samples with a field of 0.395 mT (3.95 Gauss) oscillating at different frequencies in the range 1-1000 Hz. Susceptibility data were corrected for the sample holder and for the diamagnetic contribution of the salts using Pascal's constants.[5]

2.3. Structural Characterization

Suitable single crystals of compounds **43** and **44** were mounted on a loop using a viscous hydrocarbon oil and then transferred directly to the cold nitrogen stream for data collection. X-ray data were collected at 120 K for both compounds on a Supernova diffractometer equipped with a graphite-monochromated Enhance (Mo) X-ray Source (λ = 0.71073 Å). The program CrysAlisPro, Agilent Technologies Ltd., was used for unit cell determinations and data reduction. Empirical absorption correction was performed using spherical harmonics, implemented in the SCALE3 ABSPACK scaling algorithm. Crystal structures were solved by direct methods with the SIR92 program[6] and refined against all F^2 values with the SHELXL-2014 program[7], using the WinGX2014.1 graphical user interface.[8] All non-hydrogen atoms were refined anisotropically and hydrogen atoms were placed in calculated positions and refined isotropically with a riding model. Data collection and refinement parameters are given in Table 7.2.

The X-ray powder diffractograms were collected for polycrystalline samples of all the compounds using a 0.5 mm glass capillary that was mounted and aligned on a Empyrean PANalytical powder diffractometer, using Cu$K\alpha$ radiation (λ = 1.54177 Å) operating at 40 mA and 45 kV. A total of 4 scans were collected at room temperature in the 2θ range of 2-40º with a step size of 0.0131º.

3. Results and Discussion

3.1. Infrared Spectroscopy

The four compounds show very similar IR spectra indicating that the anionic lattice must be similar in all cases (Figures 7.1-7.4). In compounds **45** and **46** the IR spectra confirm that both compounds contain the $[Mn(salen)(H_2O)]^+$ cation. Magnetic measurements further confirm the presence of a Mn(II) cation as will be shown below. In compounds **43** and **44**, the presence of the $[Mn(salpn)(H_2O)]^+$ cation was also confirmed by the single crystal structure.

All compounds show the characteristic vibrational bands of the SMM cations $[Mn(salen)(H_2O)]^+$ and $[Mn(salpn)(H_2O)]^+$ in the 600-1300 cm^{-1} region (see Table 7.1), confirming the presence of these cations. At higher frequencies the anilato bands

overlap with those of the SMM-cations. The wide bands appearing at ca. 1150 cm^{-1} in the perchlorate salts of the SMM cation spectra are due to the counter ion $(ClO_4)^-$ and do not appear on the anilato-based compounds. The bands at *ca.* 1200-1300 cm^{-1} are due to the Mn-OH_2 or Mn-OHMe bonds of the SMM cations.

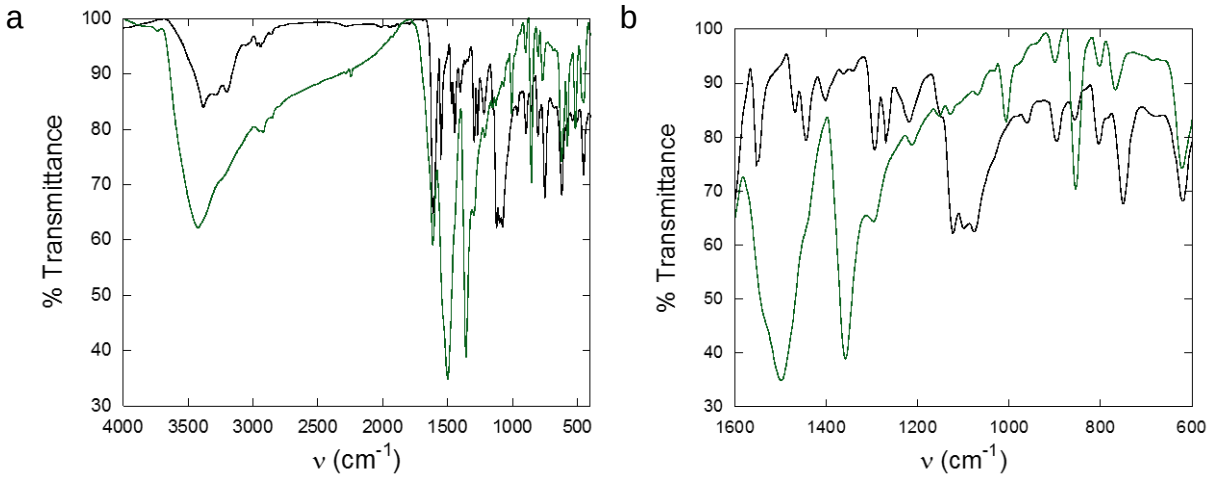

***Figure 7.1**. FT-IR spectra of compound **43** and the salt [Mn(salpn)(H_2O)](ClO_4) (in black) in the region 4000-400 cm^{-1} (**a**) and 1600-600 cm^{-1} (**b**).*

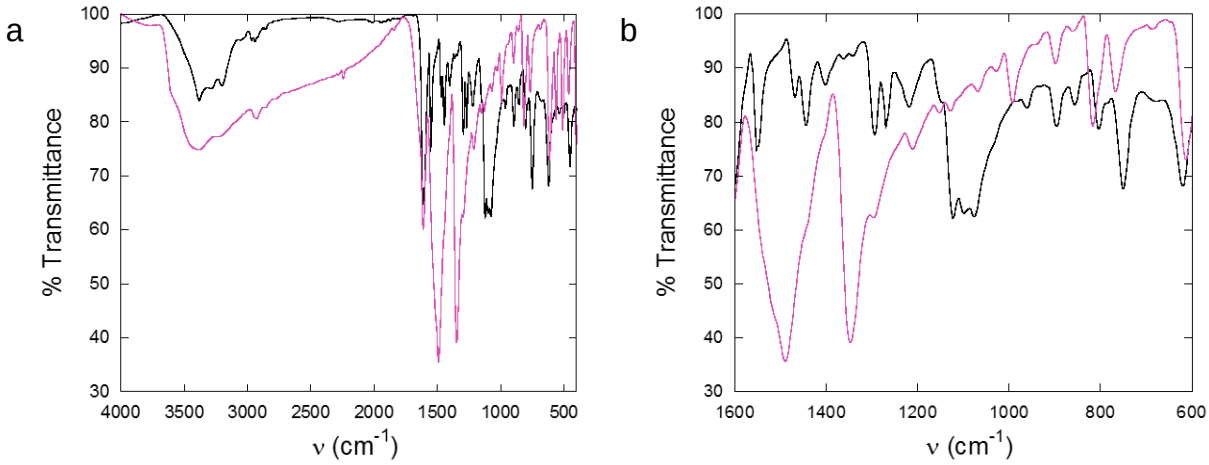

***Figure 7.2**. FT-IR spectra of compound **44** and the salt [Mn(salpn)(H_2O)](ClO_4) (in black) in the region 4000-400 cm^{-1} (**a**) and 1600-600 cm^{-1} (**b**).*

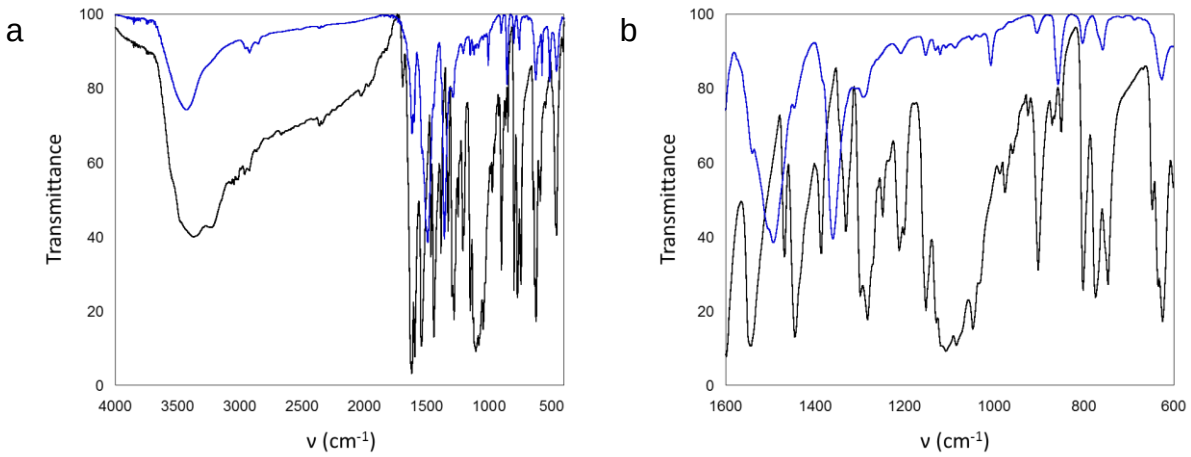

***Figure 7.3**. FT-IR spectra of compound **45** and the salt [Mn(salen)(H₂O)](ClO₄) (in black) in the region 4000-400 cm⁻¹ (**a**) and 1600-600 cm⁻¹ (**b**).*

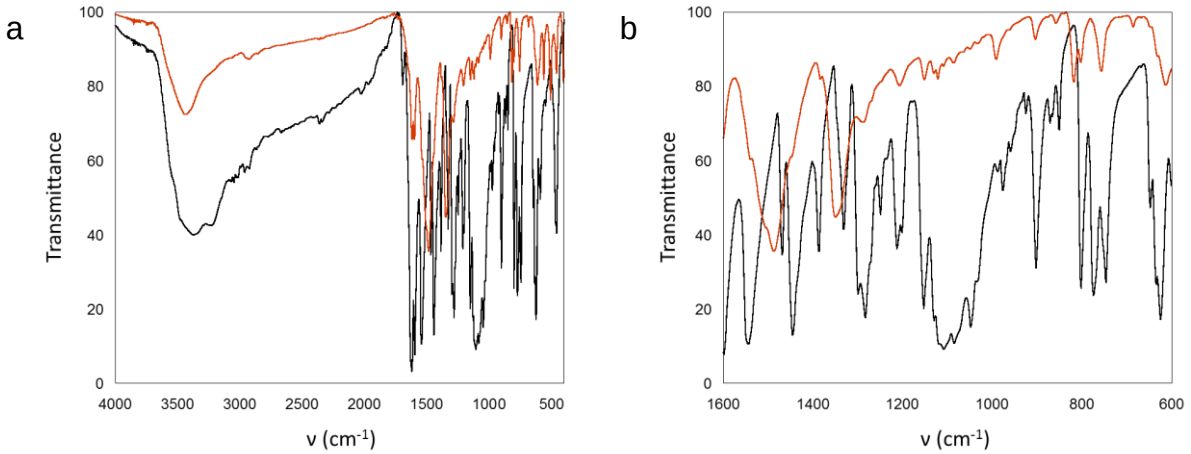

***Figure 7.4**. FT-IR spectra of compound **46** and the salt [Mn(salen)(H₂O)](ClO₄) (in black) in the region 4000-400 cm⁻¹ (**a**) and 1600-600 cm⁻¹ (**b**).*

***Table 7.1**. IR bands (in cm⁻¹) and assignments of [Mn(salpn)(H₂O)](ClO₄), [Mn(salen)(H₂O)](ClO₄) and compounds **1-4**.*

Ref.	ν(C=O) ν(C=N) ν(C=C)ring			ν(C=C)ring ν(C-O)	δ(C-O) / δ(C=O) ν(C-X) / δ(C-H) ν(C=C)ring			δ(C-X) γ(C-H)					ρ(C-X)
[Mn(salpn)(H₂O)](ClO₄)	1555 1465 1445	1400	1290 1270	1215		1120	1095 1075	965	900	850	805	750	625
[Mn(salen)(H₂O)](ClO₄)	1545 1465 1445	1390 1330	1295	1280 1245	1215 1205	1155 1110	1085 1045	975	905	865 850	800	775 745	625
1	1500	1360	1295	1210	1150	1125	1065	1005	900	850	805	765	620
2	1490	1350	1295	1210	1150	1125	1065	1025 990	895	820		765	610
3	1495	1360	1285	1200	1150	1125		1005	900	860	800	750	625
4	1490	1350	1285	1205	1050	1025	1085	990	900	855	815 800	755	615

ν stretching, δ in-plane bending and γ out-of-plane bending

3.2. X-Ray Diffraction

Compounds **43** and **44** are isostructural and crystallize in the orthorhombic C*mc*2_1 space group. The asymmetric unit contains half $[Mn(salpn)(H_2O)(MeOH)]^+$ cation, located on a two fold axis, one metal centre with occupancy 1/3, located on a C_3 axis, corresponding to ½ Mn(II) and ½ Cr(III), one anilato ligand $(C_6O_4X_2)^{2-}$, X = Cl (**43**) and Br (**44**) located on a general position, half anilato ligand located on a two-fold axis and one acetonitrile and three water crystallization molecules, located on general positions. This asymmetric unit generates the formula $[Mn(salpn)(H_2O)(MeOH)][MnCr(C_6O_4X_2)_3]\cdot 6H_2O\cdot 2MeCN$ (X = Cl in **43** and Br in **44**). Data collection and refinement parameters are given in Table 7.2.

***Table 7.2**. Crystallographic data of compounds **43** and **44**.*

	43	**44**
Empirical formula	$C_{40}H_{38}Cl_6N_4O_{22}Mn_2Cr$	$C_{40}H_{38}Br_6N_4O_{22}Mn_2Cr$
Formula weight	1301.33	1568.04
Temperature K	120(2)	120(2)
Wavelength (Å)	0.71073	0.71073
Crystal system	Orthorombic	Orthorombic
Space group	*Cmc* 21 (#36).	*Cmc* 21 (#36).
a (Å)	24.6611(11)	24.5553(6)
b(Å)	13.1453(4)	13.2113(3)
c(Å)	16.2232(8)	16.8455(4)
α (°)	90	90
β (°)	90	90
γ (°)	90	90
V (Å^3)	5259.2(4)	5464.8
ρ_{cal} (mg m^{-3})	1.595	1.877
μ (mm^{-1})	1.059	5.083
Crystal size (mm^3)	0.08x0.04x0.02	0.10x0.06x0.02
θ range (°)	3.304-27.950	3.313-25.047
Reflections collected	22977	23953
Independent reflections (R_{int})	5643	4935
Reflns used in refinement, *n*	5643	4935
$R_1(F)$,[a] $I > 2\sigma(I)$	0.0864	0.0793
$wR_2(F^2)$,[b] all data	0.2157	0.1613
$S(F^2)$,[c] all data	1.028	1.211
Largest diff. peak	0.695	1.622
Largest diff. hole	-0.597	-1.192

[a]$R1(F) = \Sigma||F_O|-|F_C||/\Sigma|F_O|$; [b]$wR2(F^2) = [\Sigma w(F_O^2-F_C^2)^2/\Sigma wF_O^4]^{1/2}$; [c]$S(F^2) = [\Sigma w(F_O^2-F_C^2)^2/(n + r - p)]^{1/2}$

The structure of both compounds consists of anionic layers formulated as $[Mn^{II}Cr^{III}(C_6O_4X_2)_3]^-$ (X = Cl or Br) (Figure 7.5a) with the classical hexagonal honey-comb 2D structure (Figure 7.5b). Each hexagon contains a $[Mn(salpn)(H_2O)(MeOH)]^+$

cation to compensate the negative charge of the anionic $[Mn^{II}Cr^{III}(C_6O_4X_2)_3]^-$ lattice. The inclusion of the cations inside the hexagonal holes of the anionic layer gives rise to overall neutral layers parallel to the *ab* plane with an interlayer distance of *c*/2 = 8.112 and 8.423 Å in **43** and **44**, respectively (Figure 7.5a). The longer inter-layer distance in **44** is attributed to the larger size of Br compared to Cl since the halogen atoms are pointing towards the interlayer space and play an active role in determining the interlayer distance (Figure 7.5a).

The layers are packed along the *c* direction in an almost eclipsed way, giving rise to hexagonal channels running along the *c* direction (Figure 7.6a). The $[Mn(salpn)(H_2O)(MeOH)]^+$ cations and the crystallization CH_3CN and water molecules are located in these hexagonal channels. (Figure 7.6b).

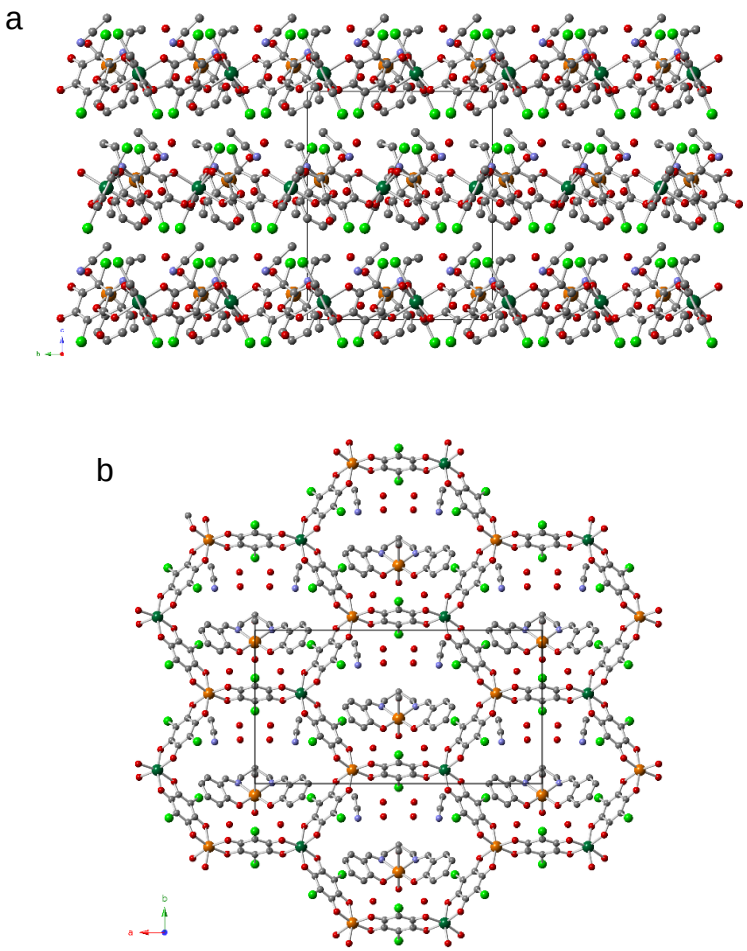

***Figure 7.5**. **(a)** Side view (down the a direction) of the layers in compound **43** (similar for **44**). **(b)** View of a honey-comb layer in **43**. Colour code: C = grey, O = red, N = blue, Cl = light green, Cr = dark green and Mn = orange. H atoms have been omitted for clarity.*

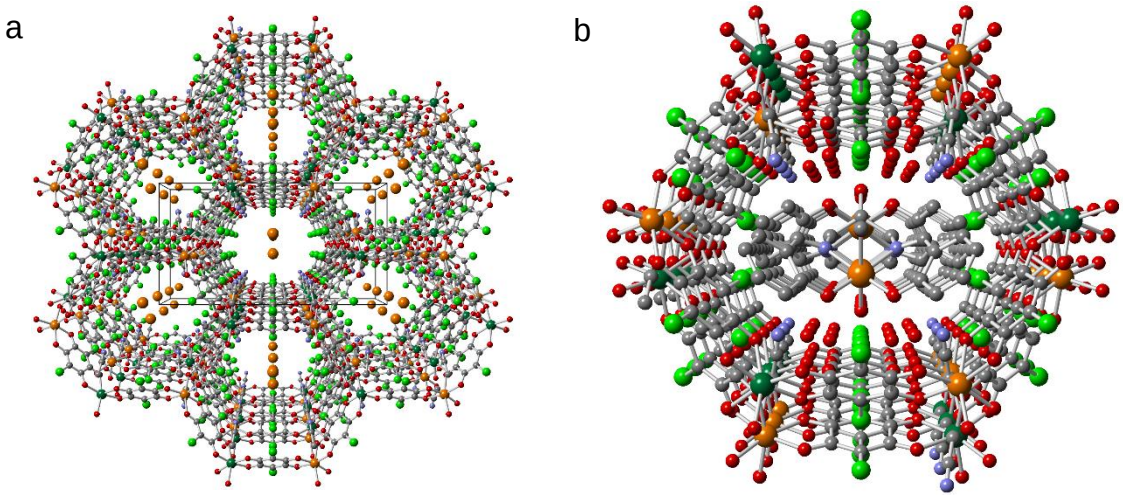

***Figure 7.6**. **(a)** Perspective view of the hexagonal channels in **43** running along the c axis. Only the Mn atom of the [Mn(salpn)(H_2O)(MeOH)]$^+$ cations are drawn for clarity. **(b)** Perspective view of one hexagonal channel showing the [Mn(salpn)(H_2O)(MeOH)]$^+$ cations and the CH_3CN and water molecules located inside. Colour code: C = grey, O = red, N = blue, Cl = light green, Cr = dark green and Mn = orange. H atoms have been omitted for clarity.*

The anionic layers contain Mn(II) and Cr(III) ions alternating in the vertices of the hexagons connected through bis-bidentate anilato ligands (chloranilato in **43** and bromanilato in **44**) that form the sides of the hexagons (Figure 7.7b). The metal ions alternate in the hexagons in such a way that each Mn(II) ion is surrounded by three Cr(III) ions and vice-versa (Figure 7.7a).

Each Mn(II) or Cr(III) centre is located on a C_3 axis surrounded by three anilato ligands with a local D_3 symmetry and a propeller-like arrangement (Figure 7.7a). Consecutive metal centres show opposite chirality (Figure 7.7b) to generate a planar honey-comb lattice. Since the structure is centro-symmetric (as observed in $[(H_3O)(phez)_3][MnM^{III}(C_6O_4Br_2)_3]$ (M^{III} = Cr and Fe)[9] and the metal centres are located on the C_3 axis, there is only one crystallographically independent metal atom in **43** and **44**. This crystallographic equivalence does not imply a disorder in the positions of the metal atoms inside the layers since in any single layer the metal atoms are always situated in alternating positions. The equivalence arises from a different dispositions of the Mn(II) and Cr(III) centres in different layers, as observed in $[(H_3O)(phez)_3][MnCr(C_6O_4Cl_2)_3]$ (where the Mn and Cr centres are well localized in each layer).[9]

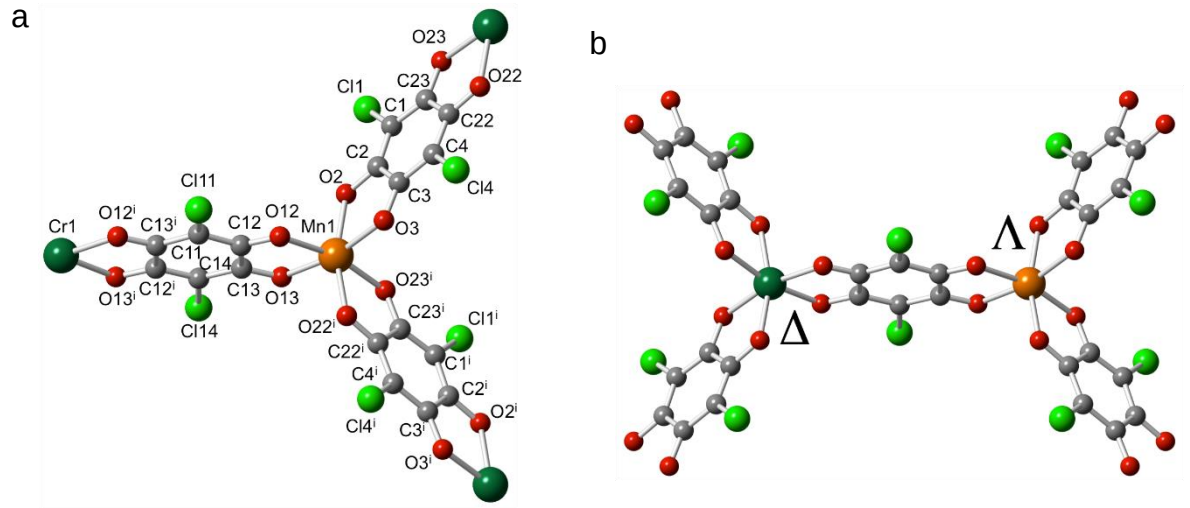

Figure 7.7. (a) *View of the coordination around a Mn(II) ion showing the labelling scheme in* ***43*** *(similar in* ***44*** *but changing Cl by Br)* ***(b)*** *View of two neighbouring metal centres with alternating chirality. Colour code: C = grey, O = red, Cl = light green, Cr = dark green and Mn = orange.*

The metal ions are surrounded by three chelating anilato ligands giving rise to a distorted octahedral coordination geometry (Figure 7.7a). The M-O bonds are all in the range of 2.033-2.099 Å in **43** and 2.044-2.092 Å in **44** (Table 7.3). The *cis* and *trans* angles are also similar in both compounds. Thus, the *cis* angles are in the range of 77.5-100.4º in **43** and 76.6-101.7º in **44**, and the *trans* angles are in the range of 163.5-167.4º in **43** and 163.2-167.4º in **44** (Table 7.4). These values are very similar to those found in all the reported A[MnCr($C_6O_4X_2$)$_3$] compounds (X = Cl and Br; A = NBu_4^+, $[(H_3O)(phz)_3]^+$, $[Fe^{III}(sal_2\text{-trien})]^+$, $[Fe^{III}(4\text{-OH-}sal_2\text{-trien})]^+$, $[Fe^{III}(sal_2\text{-epe})]^+$ and $[Fe^{III}(5\text{-Cl-}sal_2\text{-trien})]^+$).[9, 10]

The $[Mn(salpn)(H_2O)(MeOH)]^+$ cations are located inside the hexagonal cavities of the $[MnCr(C_6O_4X_2)_3]^-$ lattice with short π-π interactions between the anilato rings of the anionic lattice and the phenyl rings of the salpn ligand. The offset angles and the plane distances are, respectively, 21.82º and 3.404 Å for **43** and 22.61º and 3.394 Å for **44**. These values fit in the typical π–π interaction range distances 3.3-3.8 Å defined by Janiak.[11] (Figure 7.8a) The cation shows a bent structure (Figure 7.8) as clearly shown by the dihedral angle (49.48º in **43** and 50.70º in **44**) formed by the two phenyl rings of the ligand.

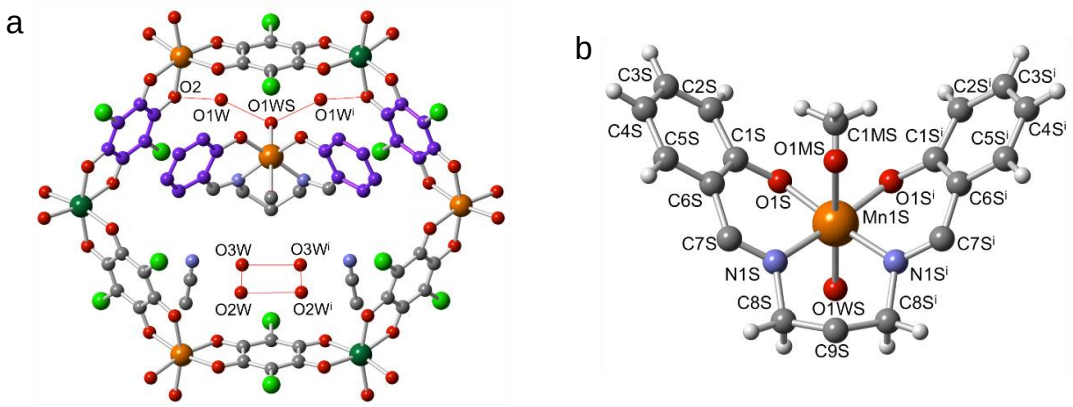

Figure 7.8. (a) *View of a [Mn(salpn)(H_2O)(MeO)]$^{+}$ cation inside the hexagonal cavity in* ***43*** *showing its bent structure and the parallel disposition of the phenyl rings of the salpn ligand and the anilato rings (in violet). H-bonds are shown as thin red lines. H atoms have been omitted for clarity* ***(b)*** *View of the [Mn(salpn)(H_2O)(MeO)]$^{+}$ cation with its labelling scheme. Colour code: C = grey, O = red, N = blue, Cl = light green, Cr = dark green and Mn = orange.*

The Mn(II) ion in the [Mn(salpn)(H_2O)(MeOH)]$^{+}$ cation shows a distorted octahedral coordination geometry. The equatorial positions are occupied by two oxygen (O1S and O1S*) and two nitrogen (N1S and N1S*) atoms from the salpn ligand. The axial positions are occupied by a water molecule (O1WS) and a methanol molecule (O1MS). The equatorial Mn-O and Mn-N bond distances (1. 873(9) and 2.004(13) Å in **43** and 1.857(13) and 2.003(16) Å in **44**, respectively) are much shorter than the axial ones (Mn1S-O1WS = 2.154(15) and 2.16(2) Å in **43** and **44** and Mn1S-O1MS = 2.32(2) and 2.348(19) Å in **43** and **44**, respectively, Table 7.3 and Figure 7.8b).

Besides the π-π interactions with the anilato ligands, the cation also shows two H-bonds between the coordinated water molecule (O1WS) and two crystallization water molecules of the cavity (O1W and O1W^{i}, Figure 7.8a) with a O1WS···O1W distance of 2.645 and 2.555 Å in **43** and **44**, respectively. Finally, the crystallization water molecules are involved in four types of H-bonds: (i) O2W is H-bonded to O3W with a O2W···O3W distance of 2.42 and 2.17 Å in **43** and **44**, respectively, (ii) O2W is H-bonded to O2W^{i} with a O2W···O2W^{i} distance of 2.67 and 2.41 Å in **43** and **44**, respectively, (iii) O3W is H-bonded with O3W^{i} with a O3W···O3W^{i} distance of 2.57 and 2.66 Å in **43** and **44**, respectively and (iv) O1W is H-bonded to O2 from the anilato ligand with a O1W···O2 distance of 2.94 and 3.04 Å in **43** and **44**, respectively (Figure

7.8a). The shortest O···O distances observed in **44** are due to the larger volume of the Br atoms that reduce the available space for the crystallization water molecules in **44**.

***Table 7.3**. Main bond lengths (Å) around the metals centres in compounds **43** and **44** (M(1) = Cr(III)/Mn(II)).*

Atoms	43	44
M(1)-O(13)	2.033(10)	2.052(16)
M(1)-O(22)	2.061(9)	2.092(14)
M(1)-O(3)	2.062(10)	2.071(16)
M(1)-O(12)	2.064(9)	2.051(14)
M(1)-O(23)	2.073(10)	2.091(14)
M(1)-O(2)	2.099(9)	2.044(15)
Mn(1S)-O(1S)#2	1.873(9)	1.857(13)
Mn(1S)-O(1S)	1.873(9)	1.857(13)
Mn(1S)-N(1S)#2	2.004(13)	2.003(16)
Mn(1S)-N(1S)	2.004(13)	2.003(16)
Mn(1S)-O(1WS)	2.154(15)	2.16(2)
Mn(1S)-O(1MS)	2.32(2)	2.348(19)

***Table 7.4**. Main bond angles (°) around the metals centres in compounds **43** and **44** (M(1) = Cr(III), Mn(II)).*

Atoms	43	44
O(2)-M(1)-O(12)	100.4(4)	101.7(6)
O(2)-M (1)-O(13)	94.0(4)	94.7(6)
O(12)-M (1)-O(13)	77.7(3)	78.4(5)
O(2)-M(1)-O(3)	77.5(3)	76.6(6)
O(12)-M(1)-O(3)	94.5(4)	94.3(6)
O(13)-M(1)-O(3)	167.4(4)	167.4(6)
O(2)-M(1)-O(23)	91.4(4)	91.6(6)
O(12)-M(1)-O(23)	166.2(4)	164.5(6)
O(13)-M(1)-O(23)	94.3(4)	92.9(6)
O(3)-M(1)-O(23)	95.2(3)	96.4(5)
O(2)-M(1)-O(22)	163.5(3)	163.2(5)
O(12)-M(1)-O(22)	92.2(4)	90.6(5)
O(13)-M(1)-O(22)	99.1(4)	99.2(6)
O(3)-M(1)-O(22)	90.4(4)	91.0(6)
O(23)-M(1)-O(22)	77.7(4)	78.2(5)

One of the most interesting features of these structures is the presence of large hexagonal channels (due to the *quasi* eclipsed packing of the layers, Figure 7.9) with internal diameters of 15.334(3) and 16.766(3) Å in **43** and 15.392(4) and 16.657(4) Å in **44**. These values indicate that the distortion of the hexagonal cavity is slightly higher in **43**. These hexagonal channels represent ca. 21 % of the total space.

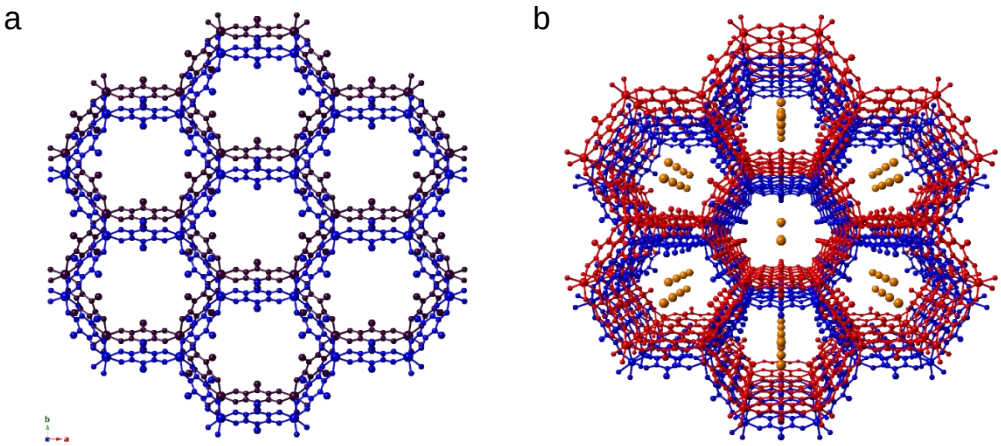

***Figure 7.9**. (**a**) View of two consecutive honey-comb layers showing the quasi eclipsed packing in **43** (similar to **44**). **(b)** Perspective view of the channels showing equivalent layers with the same colour. Only the Mn atoms of the cations are shown.*

3.3. X- Ray Powder Diffraction

Compounds **43** and **44** were analysed with the XRPD technique to check for phase purity in the samples by comparison with the simulated diffractogram, generated with Mercury program, from the solved structures of **43**. These difractograms show that both compounds are isostructural and have the same structure that the solved crystals (Figure 7.10).

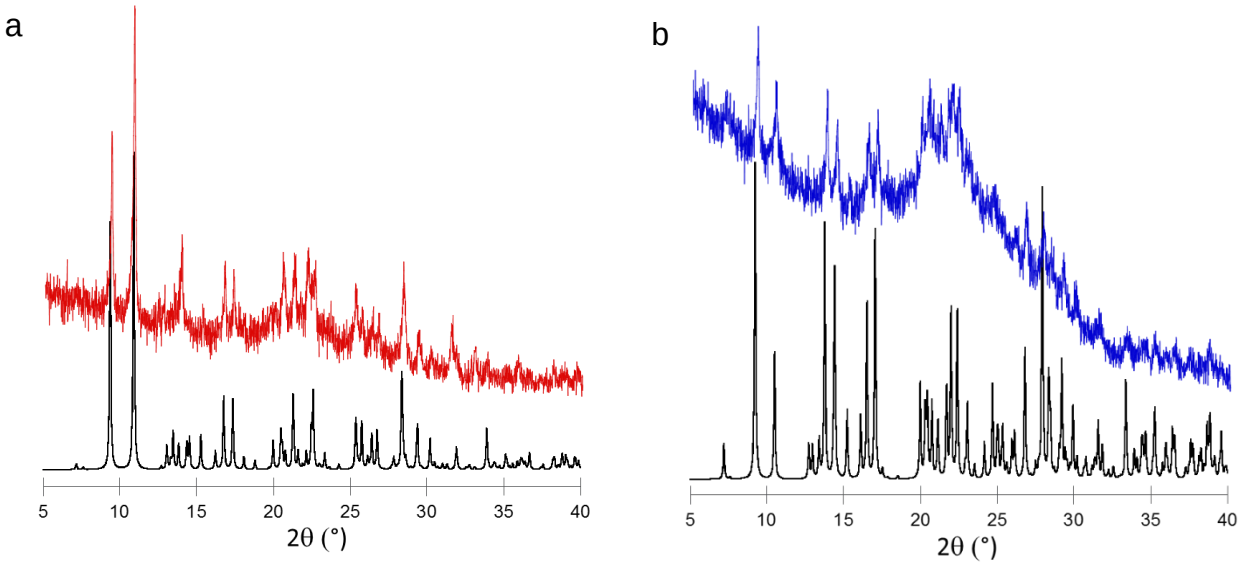

Figure 7.10. Experimental and simulated (in black) X-ray powder diffractograms for compounds **43 (a)** and **44 (b)**.

Compounds **45** and **46** were also analysed with the XRPD technique to check for phase purity in the samples by comparison with the simulated diffractogram from the solved structures of **43**, but the crystallinity of these compounds was very poor and no conclusions about the isostructurality could be obtained.

3.4. Magnetic Properties

The four compounds present a very similar magnetic behavior due to the presence of Cr^{III} and M^{II} ions. These compounds show the presence of antiferromagnetic (AF) Cr-Mn interactions mediated through the anilato-ligand bridges, as clearly shown by the thermal variation of their magnetic moment (represented as the product of the molar magnetic susceptibility per $Mn^{II}Cr^{III}$ couple times the temperature, $\chi_m T$). Since the ground spin states of Cr(III) and Mn(II) are different (3/2 and 5/2, respectively) this AF interaction leads to a ferrimagnetic coupling that results in a ferrimagnetic long range ordering at low temperatures. Accordingly, $\chi_m T$ shows, at room temperature, values of *ca*. 9.0 cm^3 K mol^{-1} for compounds **43** and **44** and *ca*. 9.5 cm^3 K mol^{-1} for **45** and **46** (Figures 7.11-7.14). All of them are close to the expected one (4.375 + 1.875 + 3.0 = 9.25 cm^3 K mol^{-1} for g = 2) for a non-interacting couple of Mn(II) and Cr(III) ions from the anilato network plus one Mn(III) from the $[Mn(salpn)(H_2O)(MeOH)]^+$ or the $[Mn(salen)]^+$ cation (we do not consider any solvent molecule attached to the salen-based cation since we were not able to fully identify it). When the temperature is lowered, $\chi_m T$ shows a continuous decrease (since the magnetic coupling is antiferromagnetic and the total magnetic moment is reduced as the temperature decreases), reaching a minimum at *ca*. 15-16 K in all compounds (since the two ground spin states are not fully cancelled), followed by a sharp increase at lower temperatures and a maximum at ca. 11-12 K in all compounds and a second sharp increase at *ca*. 4 K for the four compounds, indicating the presence of a long range ferrimagnetic ordering (figures 7.11-7.14). Further on, the nature of this second sharp increase will be discussed.

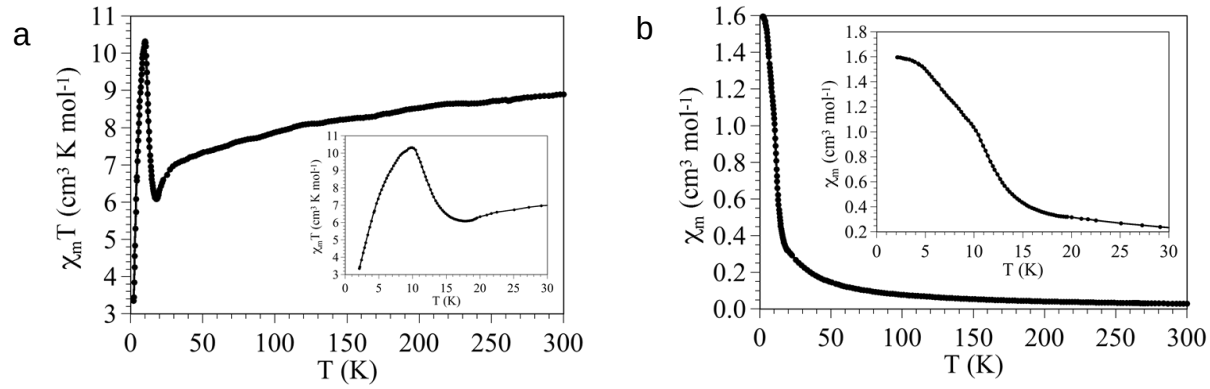

***Figure 7.11**: Magnetic properties of compounds **43**: **(a)** thermal variation of $\chi_m T$ and **(b)** Thermal variation of χ_m. Insets show the low temperature regions.*

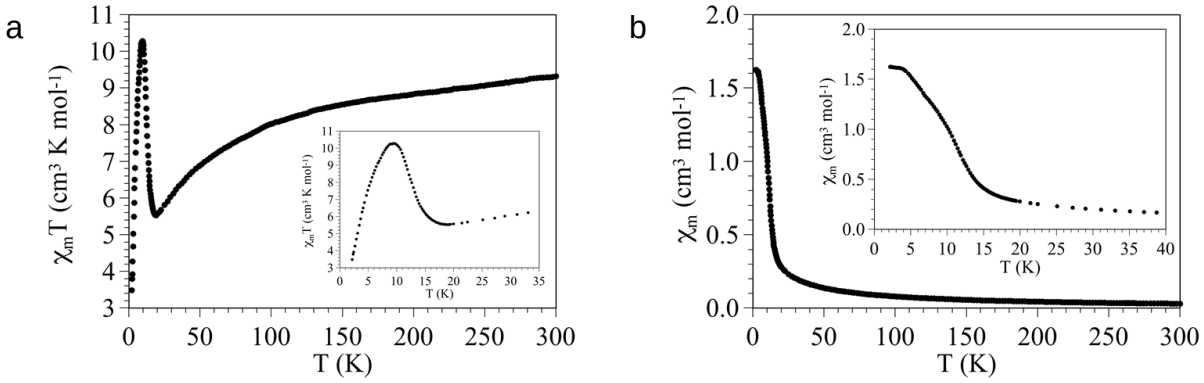

***Figure 7.12**: Magnetic properties of compounds **44**: **(a)** thermal variation of $\chi_m T$ and **(b)** Thermal variation of χ_m. Insets show the low temperature regions.*

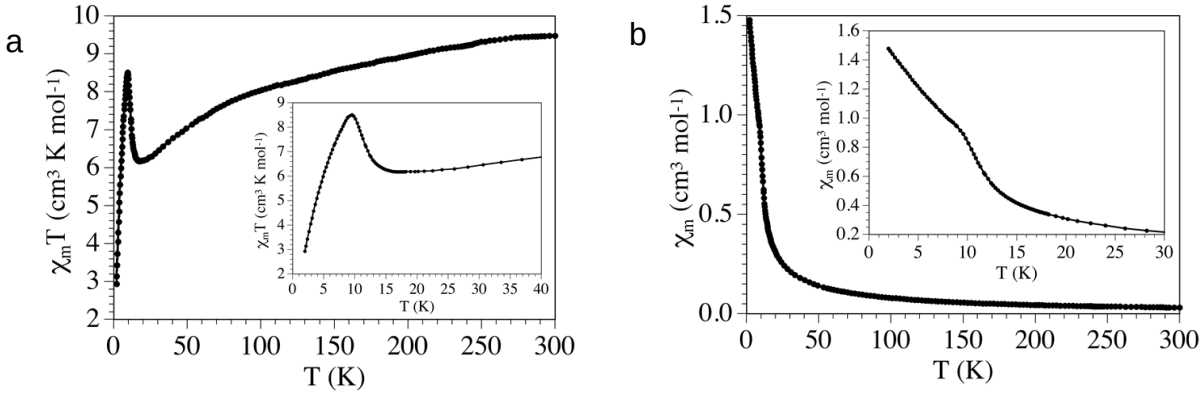

***Figure 7.13**: Magnetic properties of compounds **45**: **(a)** thermal variation of $\chi_m T$ and **(b)** Thermal variation of χ_m. Insets show the low temperature regions.*

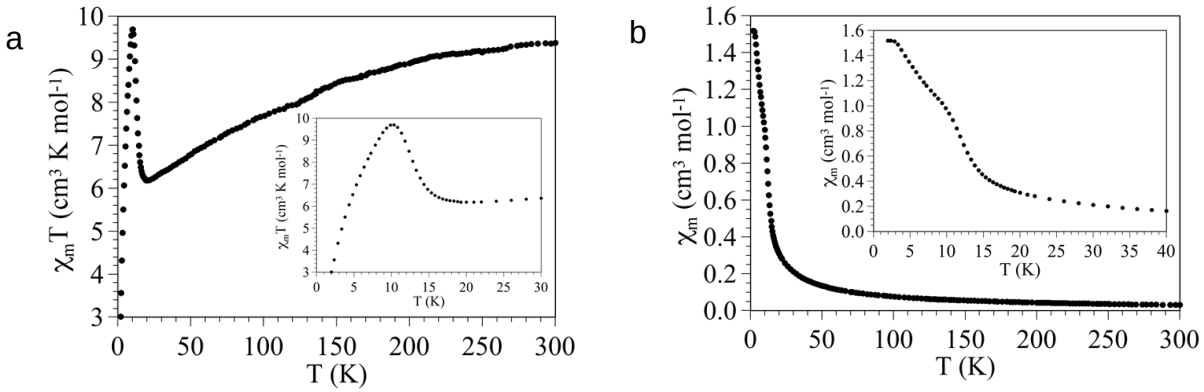

***Figure 7.14**: Magnetic properties of compounds **46**: **(a)** thermal variation of $\chi_m T$ and **(b)** Thermal variation of χ_m. Insets show the low temperature regions.*

In order to confirm the long range order and to obtain a more accurate value for T_c we have performed AC susceptibility measurements with an oscillating magnetic field at different frequencies in the range 1-1000 Hz. These measurements show frequency-independent peaks in both, the in phase (χ_m') and in the out of phase (χ_m") susceptibilities in al compounds, confirming the presence of the long range ordering (figures 7.15-7.18). Thus, peaks in the in phase susceptibility χ_m' appear at *ca*. 11.7 (**43**), 11.6 (**44**), 10.3 (**45**), and 11.5 K (**46**).

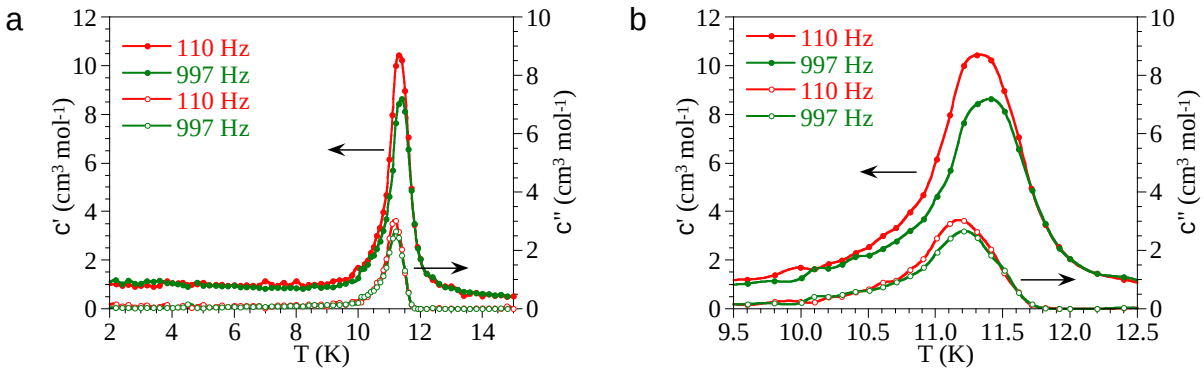

***Figure 7.15**. **(a)** Thermal variation of χ_m' (filled circles, left scale) and χ_m" (empty circles, right scale) at different frequencies for compound **43**. **(b)** Zoom of the AC peak.*

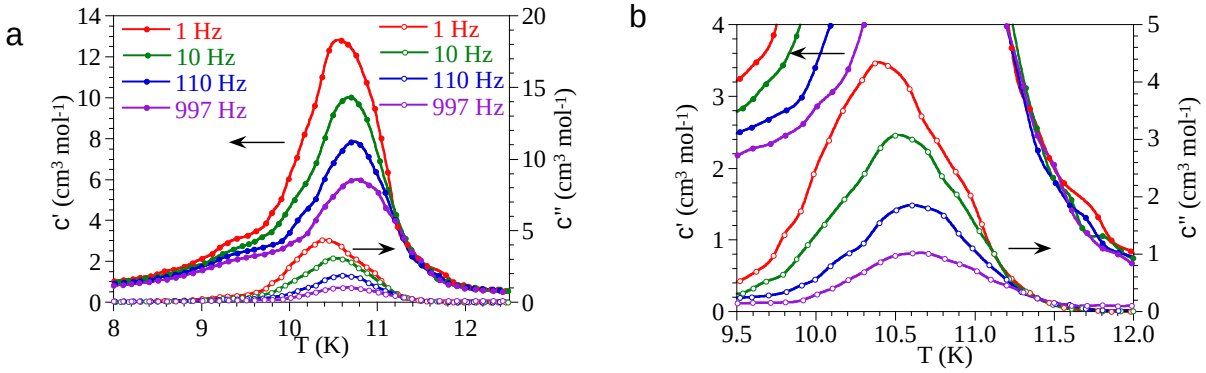

***Figure 7.16**. **(a)** Thermal variation of χ_m' (filled circles, left scale) and χ_m" (empty circles, right scale) at different frequencies for compound **44**. **(b)** Zoom of the AC peak.*

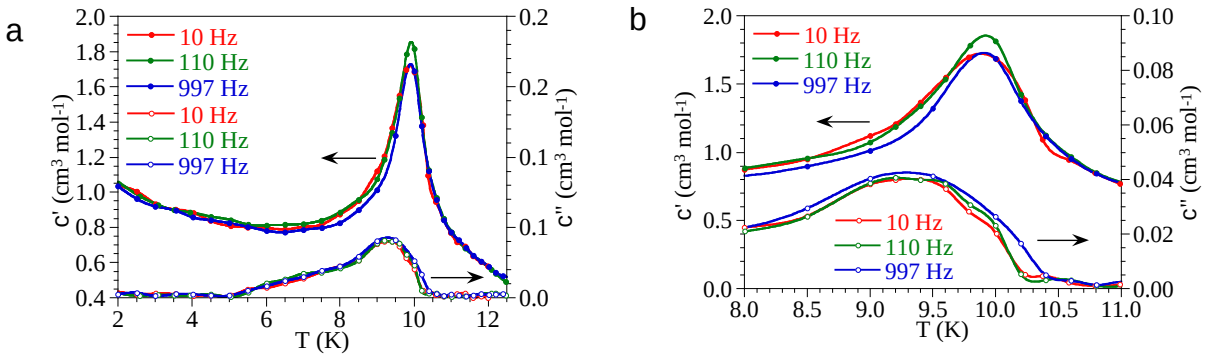

***Figure 7.17**. **(a)** Thermal variation of χ_m' (filled circles, left scale) and χ_m" (empty circles, right scale) at different frequencies for compound **45**. **(b)** Zoom of the AC peak.*

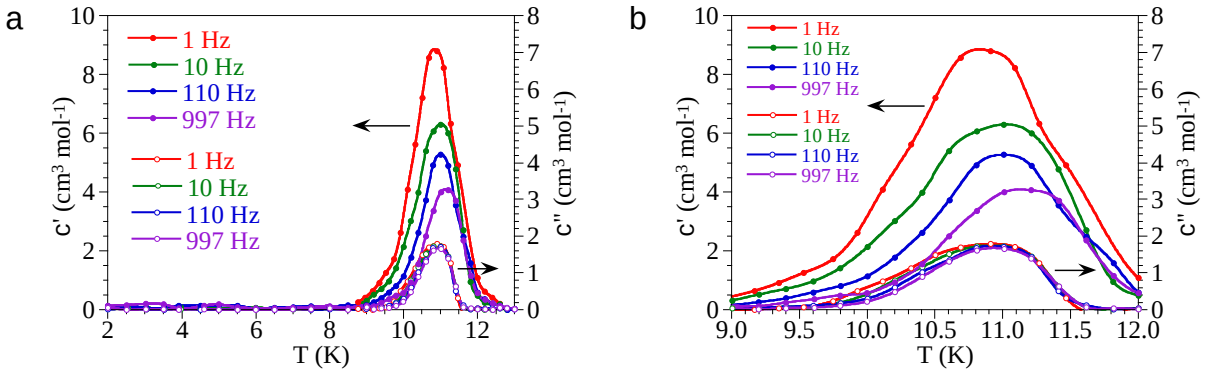

***Figure 7.18**. **(a)** Thermal variation of χ_m' (filled circles, left scale) and χ_m" (empty circles, right scale) at different frequencies for compound **46**. **(b)** Zoom of the AC peak.*

The ferrimagnetic nature of the coupling in all the Mn-Cr compounds is further confirmed by the isothermal magnetization measurements at 2 K that show a smooth increase of the magnetization with increasing fields and no saturation even at high

fields (Figures 7.19-7.22). These measurements also provide an additional proof of the magnetic ordering presented by these layered materials since all compounds present hysteresis below the ordering temperatures with coercive fields of ca. 92 (**43**), 100 (**44**), 40 (**45**) and 22 mT (**46**).

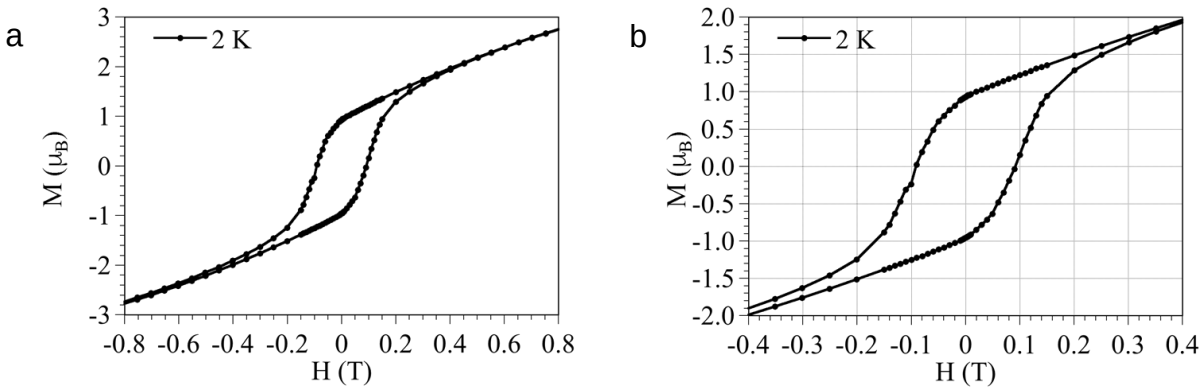

***Figure 7.19**. **(a)** Hysteresis cycle at 2 K for compound **43**. **(b)** Zoom of the low field region.*

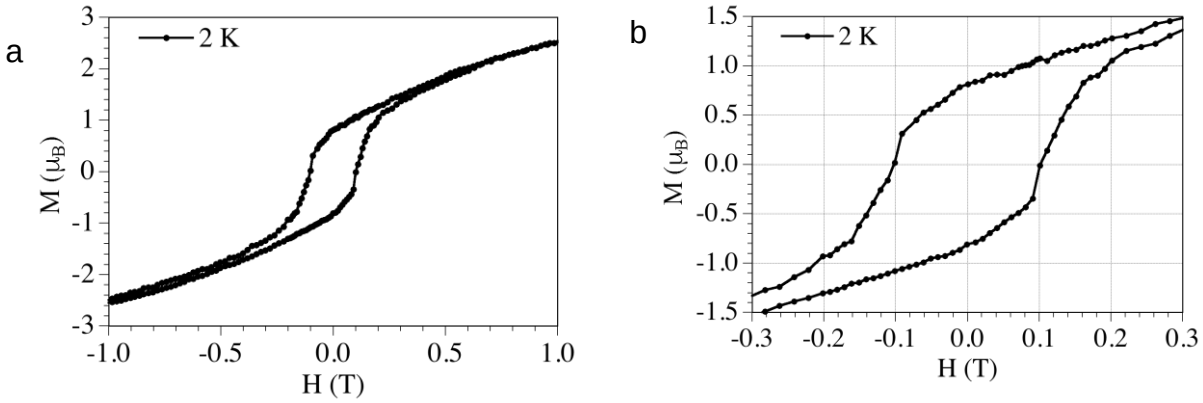

***Figure 7.20**. **(a)** Hysteresis cycle at 2 K for compound **44**. **(b)** Zoom of the low field region.*

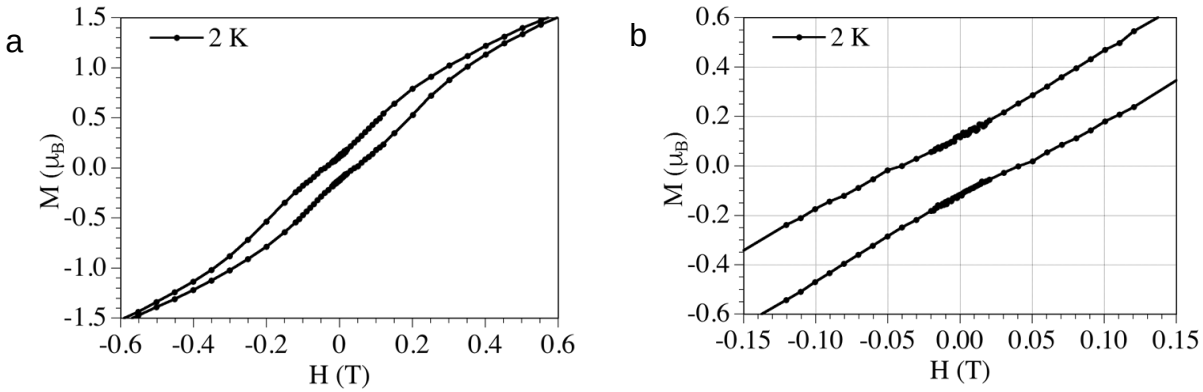

***Figure 7.21**. **(a)** Hysteresis cycle at 2 K for compound **45**. **(b)** Zoom of the low field region.*

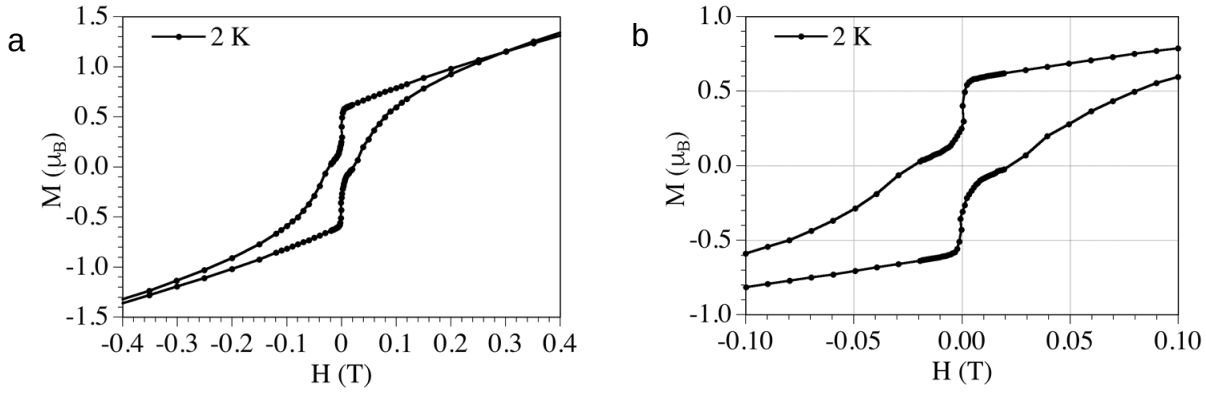

***Figure 7.22**. **(a)** Hysteresis cycle at 2 K for compound **46**. **(b)** Zoom of the low field region.*

4. Conclusions and perspectives

In this chapter we have presented two different families of anilato-based compounds with single molecule magnets inserted between anilato layers formulated as $[Mn(salpn)(H_2O)][CrMn(C_6O_4X_2)_3]$ with X = Cl (**43**) and Br (**44**) and $[Mn(salen)(H_2O)][CrMn(C_6O_4X_2)_3]$ with X = Cl (**45**) and Br (**46**). Compounds **43** and **44** show an eclipsed configuration with hexagonal channels containing the SMM cations.

The four compounds present a ferrimagnetic long range ordering with ordering temperatures of 11.7 (**43**), 11.6 (**44**), 10.3 (**45**), and 11.5 K (**46**) and coercive fields of 92 (**43**), 100 (**44**), 40 (**45**) and 22 mT (**46**) at 2 K. The lack of a signal attributed to the SMM cations suggests that these cations are not isolated in the structure of these compounds and present some interactions with the ferrimagnetic layers. The presence of a π-π interaction between the anilato rings and the aromatic rings of the salpn ligand on the cationic SMM in compounds **44** and **45** provides a possible pathway for such cation-anion interaction.

As future work, we plan to change the metal atoms M(III) and M(II) in order to change the ordering temperatures and to insert other SMM without aromatic rings to reduce the interactions between the SMM and the anilato-based lattice.

5. References

(1) Clemente-León, M.; Coronado, E.; López-Jordà, M. 2D and 3D Bimetallic Oxalate-Based Ferromagnets Prepared by Insertion of Mn^{III}-Salen Type Complexes. *Dalton Trans.* **2013***, 42*, 5100-5110.

(2) Clemente-León, M.; Coronado, E.; Gómez-García, C. J.; López-Jordà, M.; Camón, A.; Repollés, A.; Luis, F. Insertion of a Single-Molecule Magnet Inside a Ferromagnetic Lattice Based on a 3D Bimetallic Oxalate Network: Towards Molecular Analogues of Permanent Magnets. *Chem. Eur. J.* **2014***, 20*, 1669-1676.

(3) Ashmawy, F. M.; McAuliffe, C. A.; Parish, R. V. D.; Tames, J. Water Photolysis. Part 1. the Photolysis of Co-Ordinated Water in $\{MnL(H_2O)\}_2]ClO_4]_2$ (L = Dianion of Tetradentate O_2N_2-Donor Schiff Bases). A Model for the Manganese Site in Photosystem II of Green Plant Photosynthesis. *J. Chem. Soc. , Dalton Trans.* **1985***, 0*, 1391-1397.

(4) Shyu, H. L.; Wei, H. H.; Wang, Y. Structure and Magnetic Properties of Dinuclear $[Mn(III)(salen)(H_2O)]_2(ClO_4)_2$ and Polynuclear $[Mn(III)(salen)(NO_3)]N$. *Inorg. Chim. Acta* **1999***, 290*, 8-13.

(5) Bain, G. A.; Berry, J. F. Diamagnetic Corrections and Pascal's Constants. *J. Chem. Educ.* **2008***, 85*, 532-536.

(6) Altomare, A.; Burla, M. C.; Camalli, M.; Cascarano, G. L.; Giacovazzo, C.; Guagliardi, A.; Moliterni, A. G. G.; Polidori, G.; Spagna, R. SIR97: A New Tool for Crystal Structure Determination and Refinement. *J. Appl. Cryst.* **1999***, 32*, 115-119.

(7) Sheldrick, G. M. Crystal Structure Refinement with SHELXL. *Acta Cryst. C* **2015***, 71*, 3-8.

(8) Farrugia, L. J. WinGX Suite for Small-Molecule Single-Crystal Crystallography. *J. Appl. Cryst.* **1999***, 32*, 837-838.

(9) Atzori, M.; Benmansour, S.; Mínguez Espallargas, G.; Clemente-León, M.; Abhervé, A.; Gómez-Claramunt, P.; Coronado, E.; Artizzu, F.; Sessini, E.; Deplano, P.; Serpe, A.; Mercuri, M. L.; Gómez-García, C. J. A Family of Layered Chiral Porous Magnets Exhibiting Tunable Ordering Temperatures. *Inorg. Chem.* **2013***, 52*, 10031-10040.

(10) Abhervé, A.; Clemente-León, M.; Coronado, E.; Gómez-García, C. J.; Verneret, M. One-Dimensional and Two-Dimensional Anilate-Based Magnets with Inserted Spin-Crossover Complexes. *Inorg. Chem.* **2014***, 53*, 12014-12026.

(11) Janiak, C. A Critical Account on π–π Stacking in Metal Complexes with Aromatic Nitrogen-Containing Ligands. *J. Chem. Soc. , Dalton Trans.* **2000**, 3885-3896.

Chapter 8

Bifunctional electrode based on anilato ligand

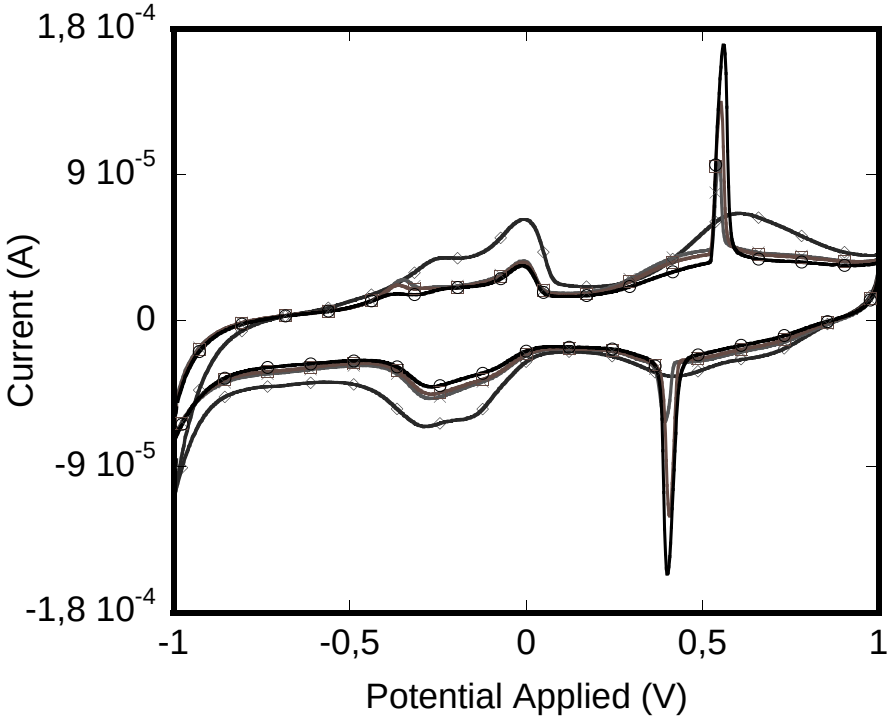

1. Introduction

In the last two decades, there has been an increasing interest on clean and renewable energy sources as alternative to fossil fuels.[1-4] For instance, the water-splitting reaction, which consists of the hydrogen and oxygen evolution half-reactions (HER and OER, respectively), has attracted great attention as a sustainable source of hydrogen.[5-7] This gas (H_2) is an attractive energy carrier that can be used to produce clean electricity in fuel cells, where the hydrogen oxidation and oxygen reduction reactions (HOR and ORR, respectively) convert chemical energy into electrical energy.[8] Furthermore, driving the HER with renewable sources of energy can lead to a sustainable source of hydrogen fuel that be used in a zero-emission fuel cell of combustion engine.

The hydrogen evolution reaction (HER, $2\ H^+ + 2\ e^- \rightarrow H_2$) that is, the cathodic reaction in electrochemical water splitting, is a classic example of a two-electron transfer reaction with one catalytic intermediate, H* (where * indicates a site on the electrode surface), and may occur through either the Volmer-Heyrovsky or the Volmer-Tafel mechanism as shown below.

Volmer step: $H^+ + e^- + * \rightarrow H^*$ **Equation 1**

Heyrovsky step: $H^* + H^+ + e^- \rightarrow H_2 + *$ **Equation 2**

Tafel step: $2H^* \rightarrow H_2 + 2\ *$ **Equation 3**

The hydrogen oxidation reaction (HOR) involves the same reaction steps as the HER although in the reverse direction. Achieving high energy efficiency for water splitting requires the use of a catalyst to minimize the necessary overpotential to drive the HER. Noble-metal catalysts, like platinum, are splendid H_2-evolution catalysts,[9, 10] but their high cost and the low availability of these compounds have slowed the implementation of hydrogen as an alternative fuel.

Until now, two kinds of methods have been developed to produce H_2 from water splitting photocatalytic and electrocatalytic HERs, in which many catalysts, such as metals, metal oxides, metal chalcogenides, and carbides, have been reported.

In particular, two-dimensional (2D) transition-metal-dichalcogenide (TMD) nanosheets have received much attention owing to their excellent catalytic activity and low cost compared to noble metals.[11, 12] The active S atoms on the exposed edges of TMDs could strongly bond with the H^+ ions in solution, enabling the effective reduction of H^+ ions to H_2.[13] Many advances have been also reported in last few years in the development of small molecules to catalyze H_2 formation from water and other solvents.[14-28] Unfortunately, an efficient water splitting method to produce hydrogen on a large scale using the sunlight as energy source (solar fuels)[29-32] is still far away from being a reality and only few compounds are proven to be efficient catalysts in presence of O_2.[33, 34]

The development of electrical energy storage systems is also very important to cope with the high-electricity demands of our modern society. Among all the storage systems, the best known and used examples of batteries are the alkaline ion intercalation batteries, such as rechargeable lithium-ion (Li^+) batteries, which are widely used for power conversion and storage systems.[35-42] However, the main problem with these Li-ion batteries is the high cost of large-scale energy storage due to the risk of explosion. Sodium (Na^+) and Potassium (K^+) batteries could be the perfect choice due to their low cost and the massive abundance of these elements[43-49]. In these alkaline-ion intercalation batteries, not only the alkaline-ion is important for the intercalation reaction, the anionic lattice that hosts these cations is also a key element. The geometry of the lattice, its ability to stablish bonds and the size of the holes or the separation in between the lattices are decisive characteristics for the intercalation reactions to occur. Depending on the geometry of the anionic part of these compounds, 2D or 3D metal-organic frameworks (materials with permanently porous crystalline structures that can host molecules inside) could be used.[45, 50-53]

Classically, only metallic complexes embedded in inorganic materials have been used for electrocatalysis and batteries fabrication. Its use as templates to produce inorganic scaffolds has gained some attraction in the last decade, specially the calcination of MOFs to produce various nanocomposites of carbon nanoforms decorated with metallic nanoparticles.[54, 55] The use of as-made metal-ligand coordination polymers (CPs) and metal-organic frameworks (MOFs) has been historically scarce, mainly because the lack of electrical conductivity in these materials.

However, crucial advances have been recently made in the field of electrically conductive 2D metal-organic nanomaterials.[56] These systems present good both symmetry and energy overlapped between metal nodes (with tendency for mixed valency) and organic linkers (generally aromatic compounds), which promotes charge transport and yields high conductivity values. Apart from the electrical conductivity, the presence of polytopic ligands promotes permanent porosity and magnetic superexchange, thus creating multifunctional materials, whose properties are tunable thanks to the easy chemical modification of the organic linkers. Moreover, 2D metal-organic nanomaterials offer a wide platform to achieve high-performance active materials. The use of 2D materials for electrocatalysis (ORR, OER and HER) and storage has being increasing recently.[51, 52, 57-60] This interest is due to the large contacting areas for electrolytes and high number of active sites, which means an increase of reaction activity of inorganic lattices during the electrochemical process. Besides, the 2D geometry facilitates the assembly into thin films for the preparation of electrochemical devices, greatly improving the electrodes geometry, which is another important factor in electro-catalytic performance.

Di-substituted benzoquinones derivatives (anilato-type) compounds have been extensively studied from the magnetic point of view.[61-67] Very recently a few examples of bifunctional anilato-based materials, which combine ferri or ferromagnetism with electrical conductivity have been reported.[67-70]

However, until now, there are no electrochemical studies of the extended 2D layers based on anilato ligand to determine their ability to act as electro-catalysts for hydrogen formation or as batteries[71-86]. Organic compounds present promising possibilities to act as such due to their high energy density,[87, 88] but practical applications have been unsuccessful to date because they normally present low discharge plateaus and poor cycling performances. However, some electrochemical studies of discrete quinone derivate have yielded good results. In some of these studies, the proposed mechanism is that the alkaline ion is coordinated by the quinone in a bis-bidentate way, which is the same coordination mode the anilato ligand adopts to form extended 2D layers.[71, 74, 77, 78]

In this chapter we present the in-*situ* electro-synthesis of a bifunctional electrode that catalyses HER and stores alkali cations based on a 2D nanomaterial formed by

Fe(III) centres connected via redox active chloranilato ligands. The Cl groups help to correct the low discharge plateaus by providing electroactivity.[89]

We also propose a possible mechanism explaining the experimental results at the end of this chapter, although the results presented are preliminary and further experiments are required to confirm the mechanism.

2. Experimental Section

2.1. Synthesis

General Remarks: All the reagents and solvents used in the following synthesis were commercially available and used as received, without further purification. The synthesis of compounds $K_3[Fe(C_6O_4Cl_2)_3]$ (**13**) and $K_3[Cr(C_6O_4Cl_2)_3]$ (**14**) are described in chapter one.

Synthesis of $Ag_3[Fe(C_6O_4Cl_2)_3]$ (A): A solution of $K_3[Fe(C_6O_4Cl_2)_3]$ (528 mg, 0.5 mmol) in water (20 mL) was mixed with a solution of $AgNO_3$ (255 mg, 1.5 mmol) in water (10 mL). The resulting solution was stirred for 10 minutes. The brown solid that appears was filtered and left to dry overnight to yield a brown powder.

Synthesis of a solution of $[Fe_2(C_6O_4Cl_2)_3]$ (47): A solution of $Ag_3[Fe(C_6O_4Cl_2)_3]$ (10 mg, 0.01 mmol) in MeOH (1.5 mL) was mixed with $FeCl_3 \cdot 6H_2O$ (2.7 mg, 0.01 mmol) in MeOH (0.5 mL). The resulting mixture was stirred for 15 minutes and filtered to remove the AgCl that precipitates. Electrochemical measurements were performed on the resulting solution (0.5 mM) after addition of 18 mL of water and KCl (149 mg, 2 mmol) or NaCl (117 mg, 2 mmol) as electrolyte.

2.2. Electrochemical measurements

Electrochemical experiments were performed on an AutoLab potenciostat PGSTAT204 using a three-electrode cell consisting of a glassy carbon (GC) disk working electrode (3 mm diameter), a Hydrogen reference electrode, and a Pt counter electrode. Before use, the GC working electrodes were polished with aqueous 0.05 μm alumina slurries on felt polishing pads and rinsed with deionized water felt polishing pads and rinsed with deionized water and acetone.

The general method for the electrochemical analysis of the chloranilic acid and the potassium salt precursors consisted in performing CV's between 1 and -1 V in a 20 mL solution of 0.5 mM of the anilate-based compounds: $H_2C_6O_4Cl_2$ (2.1 mg, 0.01 mmol) and $K_3[M^{III}(C_6O_4Cl_2)_3]$ (M^{III} = Fe and Cr) (7.9 mg, 0.01 mmol) and 0.1 M of the electrolyte: KCl (149 mg, 2 mmol) or NaCl (117 mg, 2 mmol) on a GC electrode modified with C by depositing approximately 10 μg of Carbon. Measurements were performed at a scan rate of 0.1 V/min.

Compound **47** was electrodeposited by performing CVs cycles and applying a fixed voltage of 0 V during 10 minutes in between each CV cycle on a 0.5 mM solution of compound **47**. The solution of **47** was prepared following the procedure shown in the synthetic part. GC electrodes can be also modified following the same procedure but replacing KCl with NaCl as electrolyte.

The general method to check if the electrodeposition was successful consisted in changing the solution of **47** and the electrolyte (KCl or NaCl) for a freshly prepared 0.1 M solution of the electrolyte (KCl or NaCl). If the narrow peaks continue appearing while performing CVs, then the electrodeposition took place.

All the measurements, except the one shown in figure 8.3, are performed with GC electrode modified with C.

3. Results and discussion

The potassium salts of the tris(chloroanilato)metallate compounds have been chosen for their high solubility in water. This property brings us two important advantages: the possibility of performing electrochemical measurements in water and the possibility to prepare the corresponding Ag^+ salts by a metathesis reaction with $Ag(NO_3)$, a useful strategy already used to prepare many oxalato-based 2D multifunctional magnets.[90, 91]

Once the Ag salts are prepared as $Ag_3[M^{III}(C_6O_4Cl_2)_3]$ (M(III) = Fe or Cr), Ag^+ cations can be removed by addition of $FeCl_3$, resulting in the precipitation of AgCl and leaving $[M^{III}(C_6O_4Cl_2)_3]^{3-}$ anions and Fe(III) cations in solution, which is the starting solution to perform the electro-synthesis of the new electrode material. All the solutions were freshly prepared before performing any electrochemical measurement. The GC electrode was modified with C in order to improve the conductivity of the electrode.

The electrochemical behaviour of the precursors was analysed in detail to check their redox behaviour. The cyclic voltammogram (CV) of $H_2C_6O_4Cl_2$ in water using KCl as electrolyte shows the reduction to the semiquinone form at *ca*. 0.2 V in the cathodic scan and the corresponding oxidation at *ca*. 0.6 V in the anodic scan (Figure 8.1, Table 8.1). On the other hand, to determine the redox processes of the anilato ligand when it is coordinated to iron(III) in compound **47**, we have performed the CV of a solution of $K_3[Cr(C_6O_4Cl_2)_3]$ (**14**) (Figure 8.1). This CV shows the redox process associated to the three anilato ligands coordinated to the trivalent metal, since Cr(III) is electrochemically inert in the studied potential range. These measurements, performed in an aqueous solution of $K_3[Cr(C_6O_4Cl_2)_3]$ (**14**) with KCl as electrolyte show that when the anilato ligand is coordinated, its redox processes take place at lower potentials (*ca*. 0.17 V in the anodic scan and *ca*. -0,12 V in the cathodic one, Figure 8.1, Table 8.1).

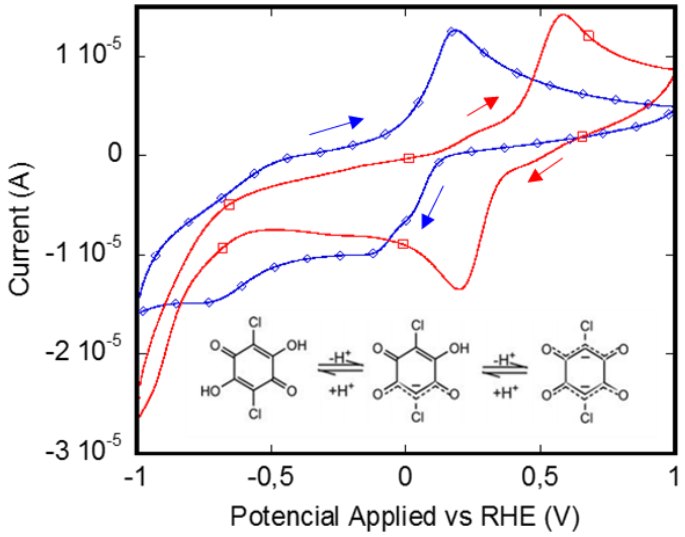

Figure 8.1 *CV of $H_2C_6O_6Cl_2$ (red) and $K_3[Cr(C_6O_4Cl_2)_3]$ (blue) recorded between -1.0 and 1.0 V (initial potential -1.0 V).*

As expected, the CV of $K_3[Fe(C_6O_4Cl_2)_3]$ (**13**) is more complex (Figure 8.2). It shows a multi-step redox behaviour with cathodic peaks at *ca*. 0.56 V (corresponding to the Fe(III)/Fe(II) reduction) and at *ca*. 0.3, 0.0 and -0.4 V, corresponding to the reduction of the three anilato ligands (Table 8.1). The corresponding oxidation peaks appear at *ca*. 0.8 V (for the Fe(II)/Fe(III) couple) and at *ca*. -0.6, -0.25 and 0.0 , corresponding to the oxidation of the three anilato ligands (Figure 8.2, Table 8.1).

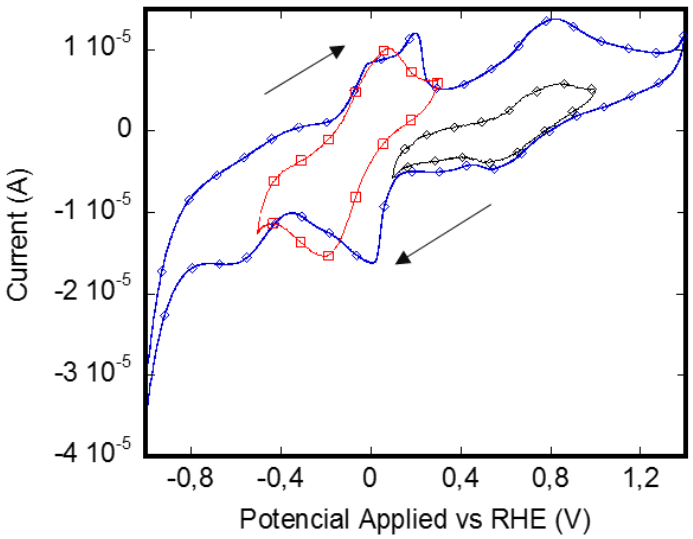

Figure 8.2: *CV of compound **13** (blue) recorded between -1 and +1.4 V (initial potential -1.0 V). This measurements show the oxidation-reduction of the anilato ligand after the oxidation-reduction of the Fe(III)/Fe(II) pair. Measurements of the anilato redox process (red) and the iron isolated redox process (black) of compound **13** are also shown.*

These measurements show that the reduction of the anilato ligands in the $K_3[Fe(C_6O_4Cl_2)_3]$ (**13**) complex takes place at lower potentials (*ca*. 0.3, 0.0 and -0.4 V) than the Fe(III)/Fe(II) reduction (0.56 V). Figure 8.2 also shows the CV measurements corresponding to the anilato redox processes (in red) and the iron ones (in black) of a solution of **13** with KCl as electrolyte. To observe these redox processes independently, we performed two different scans of a solution of compound **13**. The first one, to observe the anilato redox processes, was recorded between -0.6 and 0.3 V (initial potential -0.60 V, red curve) and the second one, to observe the iron redox processes, was performed between 0.1 and 1 V (initial potential 0.1 V, black curve). As can be observed in Figure 8.2, the redox processes of the anilato ligands are simpler when they are recorded independently than when both redox processes (chloranilato and iron) are measured simultaneously. This fact indicates that the redox process of the anilato ligand changes in presence of the iron redox process.

We can, therefore, conclude that there is a partial electron transfer between the iron centre and the coordinated anilato ligands. Thus, when the Fe(III) is reduced initially to Fe(II), there is a partial electron transfer to the anilato coordinated ligands (i.e., the Fe(II) centre facilitates the anilato reduction) and, accordingly, the reduction of the ligand becomes slightly easier and appears at a higher potential (0.3 V compared to -0.12 V in the Cr(III) complex, where the metal atom does not show any redox activity). The reduction of the second ligand also takes place at a higher potential (0.0 V) suggesting that the help of the Fe(II) centre compensates the increase of the negative charge of the complex when the anilato ligans are reduced. This effect is no longer observed in the reduction of the third ligand and, accordingly, this reduction takes place at a lower potential (-0.4 V). Note that this iron-anilato electron transfer fully agrees with the semiconducting and class II mixed valence behaviour observed in the 2D lattice $[Fe^{II}Fe^{III}(C_6O_4Cl_2)_3]^-$, where the chloranilato ligands connect Fe(III) and Fe(II) centres.[67]

Table 8.1. Electrochemical properties of $H_2C_6O_4Cl_2$, $K_3[Cr(C_6O_4Cl_2)_3]$ (**14**) and $K_3[Fe(C_6O_4Cl_2)_3]$ (**13**).

	anilato		iron	
Compound	**E_{anod} (V)**	**E_{cath} (V)**	**E_{anod} (V)**	**E_{cath} (V)**
$H_2C_6O_4Cl_2$	+0.60	+0.20	-	-
$K_3[Cr(C_6O_4Cl_2)_3]$ (**14**)	+0.18	-0.12	-	-
$K_3[Fe(C_6O_4Cl_2)_3]$ (**13**)	0.00 -0.25 -0.60	+0.20 0.00 -0.34	+0.80	+0.56
$K_3[Fe(C_6O_4Cl_2)_3]$ (**13**)[a]	+0.06	-0.20	-	-
$K_3[Fe(C_6O_4Cl_2)_3]$ (**13**)[b]	-	-	+0.82	+0.53

[a] scanning only the redox processes of the anilato ligands
[b] scanning only the redox processes of the iron centre.

In-situ electro-synthesis of a new catalyst $[Fe_2(C_6O_4Cl_2)_3]$ (47)

Since we have demonstrated that we can easily reduce the Fe(III) centres in compound **47**, we decided to perform reduction experiments by applying an electrochemical impedance of 0 V during ten minutes. This reduction generates Fe(II) centres with the corresponding flow of alkaline ions (K^+ or Na^+, depending on the electrolyte used) to compensate the Fe(III)/Fe(II) reduction, turning our system into a battery.

In order to check if the modification of the GC electrodes plays a role in the electrodeposition of compound **47**, we have performed these reduction experiments with both GC electrodes (with and without modification with C). Figure 8.3 shows the CVs performed with a non modified GC electrode. We have done up to forty CV + ten-minutes impedance cycles at 0 V to perform the Fe(III)/Fe(II) reduction and create a flow of K^+ from the 0.1 M KCl electrolyte solution. In these conditions we could observe the electrodeposition of a deep blue film on the electrode. After forty CV + ten-minutes impedance cycles at 0 V, the film was clearly seen and the GC electrode was removed from the solution. If the surface of the GC electrode is cleaned with a paper, some deep blue powder could be seen. During these cycles we could observe a sharp anodic peak at 0.55 V and the corresponding sharp cathodic peak at 0.40 V (Figure 8.3). These peaks are associated to the K^+ insertion/removal process in the film **47** that accompany the iron reduction/oxidation processes.

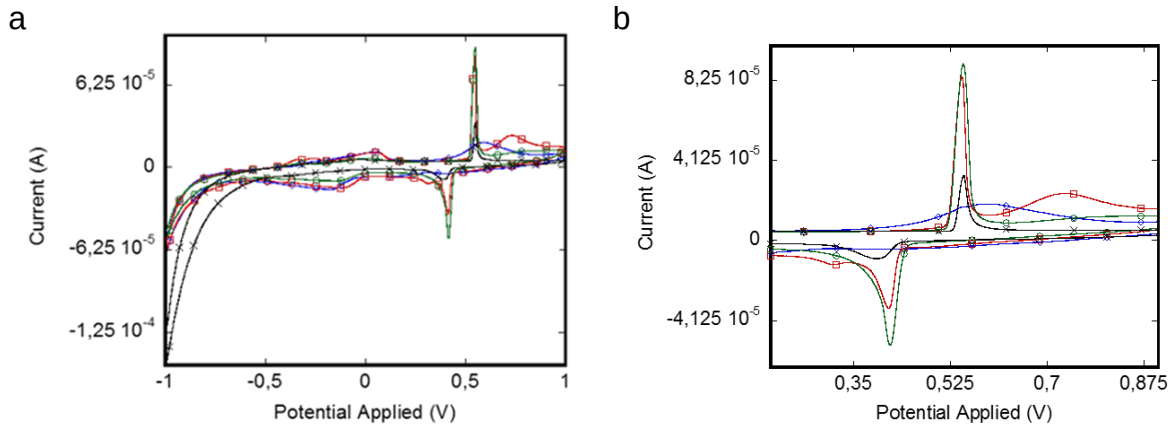

Figure 8.3. (a) *CV of a $Fe_2(C_6O_4Cl_2)_3$ film (**47**) obtained with CV + impedance cycles at 0 V with a non modified GC electrode. Cycles 1, 10, 20 and 40 are drawn in blue, red, green and black, respectively.* ***(b)*** *Zoom in the range of 0.2 – 0.9 V of the CV of a $Fe_2(C_6O_4Cl_2)_3$ film (**47**).*

As can be seen in Figure 8.3, this K^+ intercalation process is not fully reversible since the anodic peaks are more intense than the cathodic ones. This means that not all the alkali cations that enter in the structure come out. For this reason, after a finite number of cycles, the intercalation process start to decrease and finally disappears after *ca*. 40 cycles.

We have also performed the same experiment with a carbon-modified GC electrode (CMGC) with 10 μg of carbon (Figure 8.4). When carbon is deposited onto the GC electrode, the surface area increases and, therefore, the amount of film **47** electrodeposited is expected to increase.[92-95] Additionally, the anodic and cathodic currents increase approximately one order of magnitude (*ca*. 10^{-5} A without carbon *vs*. *ca*. 10^{-4} A with carbon). More important, the process is more reversible since the anodic and cathodic peaks have similar intensities.

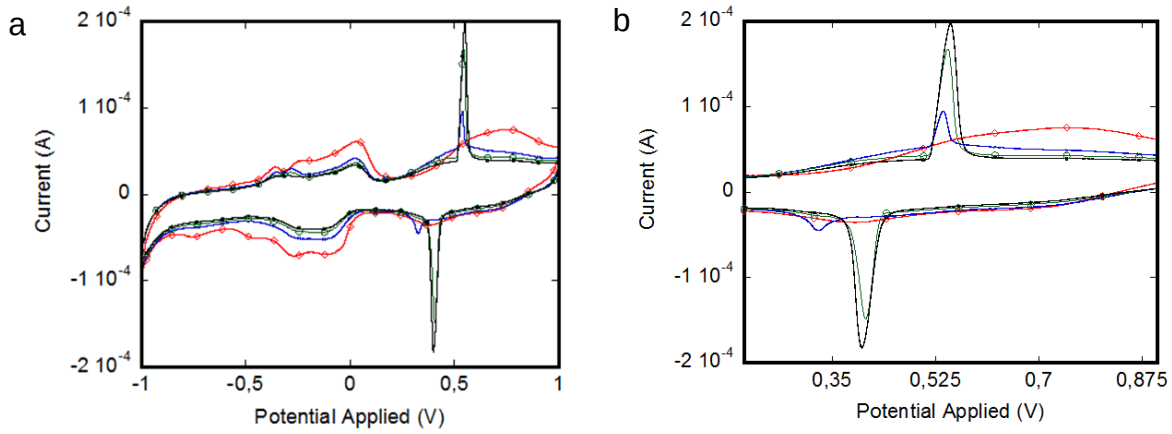

***Figure 8.4**. **(a)** CV of a $Fe_2(C_6O_4Cl_2)_3$ film (**47**) obtained with CV + impedance cycles at 0 V with a GC electrode without modification and KCl 0.1 M as electrolyte. Cycles 1, 10, 20 and 40 are drawn in red, black, blue and green, respectively. **(b)** Zoom in the range of 0.2 – 0.9 V of the CV of a $Fe_2(C_6O_4Cl_2)_3$ film (**47**).*

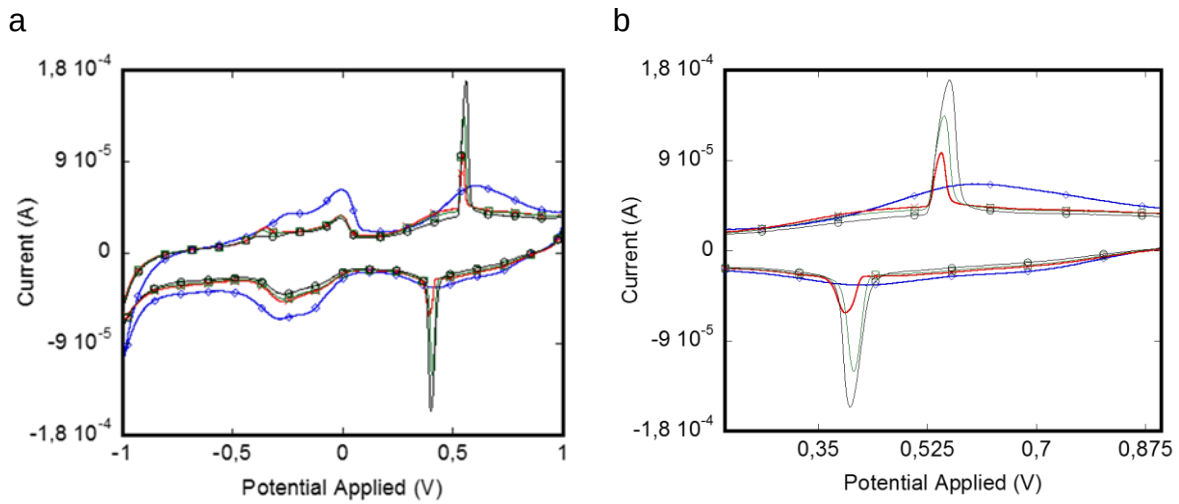

***Figure 8.5**. **(a)** CV of a $Fe_2(C_6O_4Cl_2)_3$ film (**47**) obtained with CV + impedance cycles at 0 V with a GC electrode without modification and NaCl 0.1 M as electrolyte. Cycles 1, 10, 20 and 40 are drawn in blue, black, red and green, respectively. **(b)** Zoom in the range of 0.2 – 0.9 V of the CV of a $Fe_2(C_6O_4Cl_2)_3$ film (**47**).*

To check if the amount of C deposited in the GC electrode affects the intercalation process, we have repeated the same experiment with a CMGC electrode containing 25 μg of C instead of 10 μg of C (Figure 8.6). This study clearly shows that the amount of C deposited does not affect the intensity of the intercalation peaks but it does improve the capacitance.

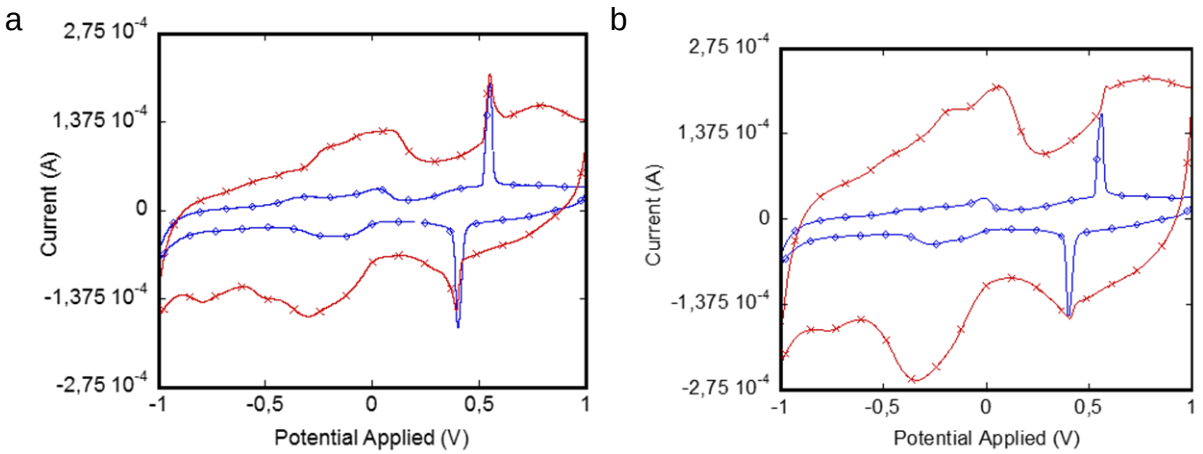

Figure 8.6: . *CV cycle 40th of a $Fe_2(C_6O_4Cl_2)_3$ film (**47**) obtained with CV + impedance cycles at 0 V with a CMGC electrode containing 10 μg (in blue) and 25 μg (in red) using as electrolyte KCl 0.1 M **(a)** or NaCl 0.1 M **(b)**.*

Although the CMGC electrodes show a better reversibility of the intercalation processes, the process is not fully reversible (Figure 8.7). Thus, the successive cycles in the CV of the films of **47** show that after *ca*. 60 cycles the intensity of the peaks decreases and after ca. 100 cycles the peaks disappear, indicating that the storage of alkali ions is not a fully reversible process.

Interestingly, as the intercalation process quenches we can observe the appearing of the Hydrogen Evolution Reaction (HER). This reaction takes place at higher values of potential as the number of cycles increases (Figures 8.6 and 8.7).

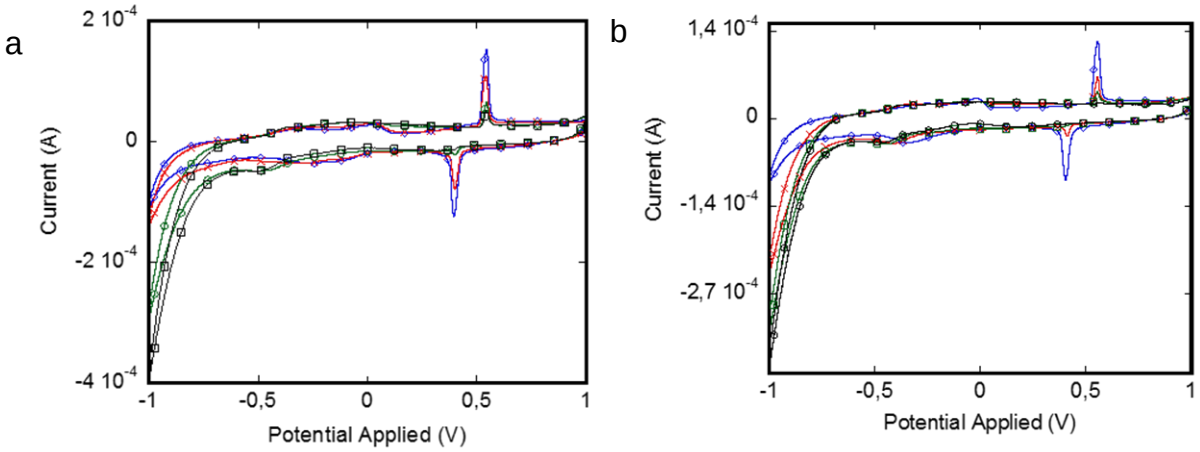

Figure 8.7. (a) *CV of a $Fe_2(C_6O_4Cl_2)_3$ film obtained with CV + impedance cycles at 0 V with a CMGC electrode with 10 μg of C and KCl 0.1 M as electrolyte. Cycles 60, 70, 80 and 85 are drawn in blue, red, green and black, respectively.* ***(b)*** *Same experiment but using NaCl 0.1 M as electrolyte. Cycles 60, 70, 80 and 100 are drawn in blue, red, green and black, respectively.*

In order to study the synergy of the two processes, we electrodeposited a film of compound **47** by performing 60 cycles of CV + ten-minutes impedance at 0 V with a CMGC electrode. Once the film **47** was formed, the solution was changed by a pure 0.1 M KCl in 18 mL of water and 2 mL of methanol, in order to stop the electrodeposition process and study the CV characteristics of the film (Figure 8.8).

As can be seen in Figure 8.8 (curves red and black), when the CV of film **47** stops at a higher potential, (-0.7 V instead of -1 V), the K^+ intercalation process takes place (peaks at 0.45 V in the anodic scan and 0.25 V in the cathodic one) but HER does not occur. However, as shown in Figure 8.8, HER evolves to higher values of potential (from -0.85 in curve blue to -0.65 in curve green) when the scans stop at a lower potential (-1 V).

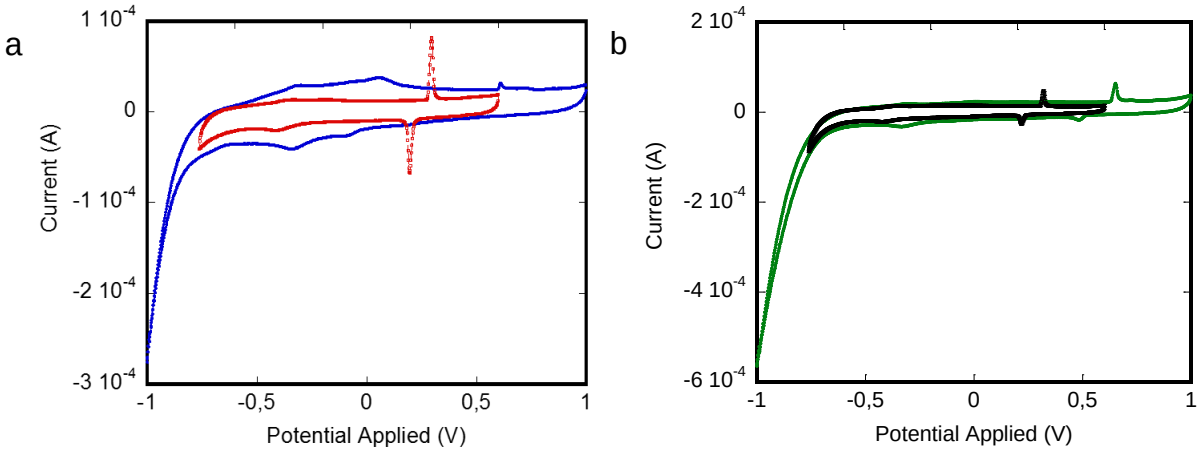

Figure 8.8: *CV of a film of* ***47*** *deposited with 60 cycles of CV + ten-minutes impedance at 0 V. The CV was performed after changing the original solution by a 0.1 M solution of KCl.* ***(a)*** *Cycle 5th performed in the range -1 V to 1 V (blue line) and cycle 30th in the range -0.7 V to 0.6 V (red line).* ***(b)*** *Cycle 35th performed in the range -1 V to 1 V (green line) or in the range -0.7 V to 0.6 V (black line).*

Accordingly, in order to check the reversibility and stability of the intercalation process we decided to stop the CV at -0.4 V to avoid the interference of the HER process. Thus, we have performed the CVs between -0.4 and 1 V. These CVs show no HER and a gradual decrease of the intercalation process that disappears after *ca*. 200 cycles (Figure 8.9).

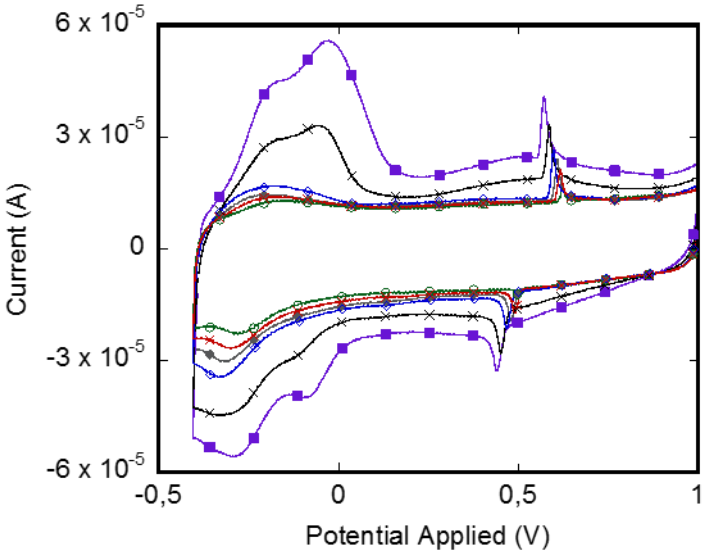

Figure 8.9: *CV of a film of* ***47*** *deposited with 60 cycles of CV + ten-minutes impedance at 0 V showing the decrease of the intercalation peaks as the number of cycles increase: cycles 1, 5, 20, 50, 100 and 200 are drawn in purple, black, blue, grey, green and red. The CV was performed after changing the original solution by a 0.1 M solution of KCl.*

The fact that HER evolves to higher potentials when the intercalation process starts to quench suggests that film **47** could be a good catalyst for hydrogen formation since this film reduced the over-potential required for the HER. In order to check this possibility we performed CVs in acidic medium.

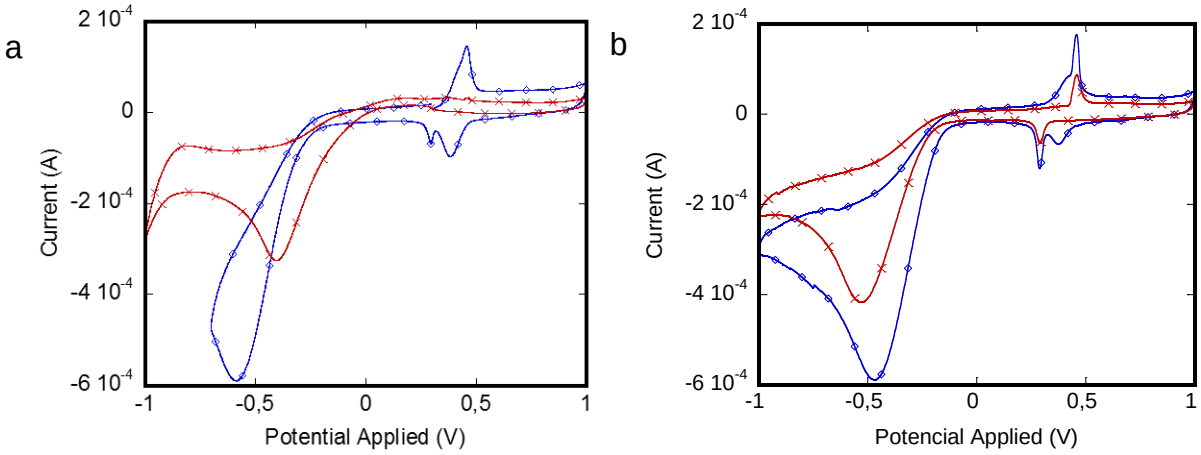

Figure 8.10: *CV of a film of **47** deposited with 40 cycles of CV + ten-minutes impedance at 0 V. **(a)** Cycle 1 (blue) and cycle 505 (red) in a 0.1 M KCl solution at pH = 2. **(b)** Cycle 1 (blue) and cycle 750 (red) of a 0.1 M NaCl solution at pH = 2.*

Thus, we electrodeposited a film of **47** with 40 cycles of CV + ten-minutes of impedance at 0 V. Once the film was deposited, we changed the original solution by a 0.1 M KCl (or NaCl) solution acidified to pH = 2 with concentrated HCl. The CVs of this film with KCl and NaCl as electrolytes are shown in Figures 8.10a and 8.10b, respectively.

Figure 8.10 shows how the HER process is further favoured as the number of cycles increases. When the electrolyte is KCl (Figure 8.10a), the HER starts at *ca*. -0.2 V in the initial scan and shifts *ca*. 0.3 V (to *ca*. +0.1 V) after 550 scans. This shift and the stability of the film (up to 500 cycles) constitute a very promising result of this electrodeposited film.

If the same experiment is carried out with NaCl as electrolyte instead of KCl, a completely different behaviour is observed: the HER process is not favoured as the number of cycles increases. As shown in Figure 8.10b, the HER in the initial cycle (blue line) takes place at a lower potential (-0.13 V) than after 750 cycles (-0.19 V, red line). This different behaviour may be related to the intercalation process. In NaCl the

intercalation peaks at *ca*. 0.3-0.5 V are still present after 750 cycles (Figure 8.10b, red line) but this is not the case in KCl (Figure 8.10a, red line). This result agrees with our previous observation showing that the HER in only favoured when the intercalation process is blocked (Figure 8.6). This result strongly suggests that both process are competitive: i.e., when the alkaline ions enter in the structure of the film, the H^+ do not enter and vice-versa.

Figure 8.11 compares the behaviour of the film **47** with both electrolytes (KCl and NaCl) and also with a C/Pt electrode at pH = 2, in order to compare our film with a typical C/Pt electrode. We can see that the HER initiates at lower potentials when using the C/Pt electrode (*ca*. 0 V) but this value is not far from the one observed for film **47** with KCl as electrolyte (*ca*. -0.1 V).

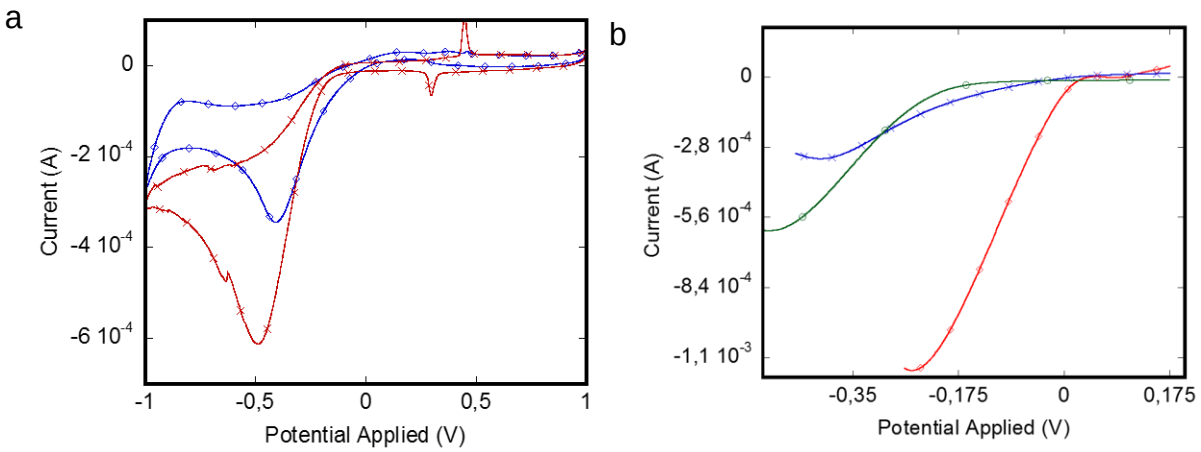

Figure 8.11. *CV of a film of* ***47*** *deposited with 40 cycles of CV + ten-minutes impedance at 0 V.* ***(a)*** *Cycle 500 with 0.1 M KCl (blue) or NaCl (red) as electrolyte at pH = 2.* ***(b)*** *Zoom of the starting point of the HER with KCl (red) and NaCl (green) as electrolyte (red) and with a C/Pt electrode (blue).*

These results indicate that the Na^+ ions can enter/exit the film lattice even after 500 cycles (red line in Figure 8.11a) in contrast to K^+ ions that cannot enter in the film lattice after 500 cycles (blue line in Figure 8.10a). Since Na^+ is smaller than K^+, a possible reason to explain this fact could be the ionic size: the smaller ion is expected to enter/exit more easily than the large one.

Physical deposition of **47** was also performed by adding a few drops of a methanol solution of compound **47** into the GC electrode and allowing the solvent to

evaporate. In this way we can obtain a film (**47ev**) deposited in a few minutes in absence of any alkaline ions. When this film **47ev** is characterized by CV, we observe no alkali ion intercalation (no narrow peaks are observed, Figure 8.12). A possible reason for this lack of intercalation in film **47ev** may be the fact that the electrodeposited film **47** slowly crystallizes forming hexagonal channels where the alkaline ions can enter. In contrast, the fast formation of film **47ev** prevents the formation of these ordered hexagonal channels, precluding the entrance of the alkaline ions. Additionally, the presence of K^+ or Na^+ ions in the solution when the film is formed may template the formation of the hexagonal channels, as can be clearly observed in the crystal structure of compounds $Na_2(H_2O)_{24}[M^{II}_2(C_6O_4H_2)_3]$ (M^{II} = Mn and Cd), that presents hexagonal channels where hydrated Na^+ cations are located (Figure 8.12).[96] Note that a similar template behaviour was observed in chapter 3 of this Thesis, where benzene derivative molecules template the formation of eclipsed stacks and hexagonal channels in contrast to the alternating packing observed when these template molecules are not present. In the case of film **47** the template effect of the Na^+ and K^+ cations is very effective because the film is formed and deposited at a very slow rate. In contrast, film **47ev** is formed very fast and most probably the layers are stacked in an alternating way, precluding the formation of the hexagonal channels. This structural difference will explain the lack of intercalation observed in film **47ev**.

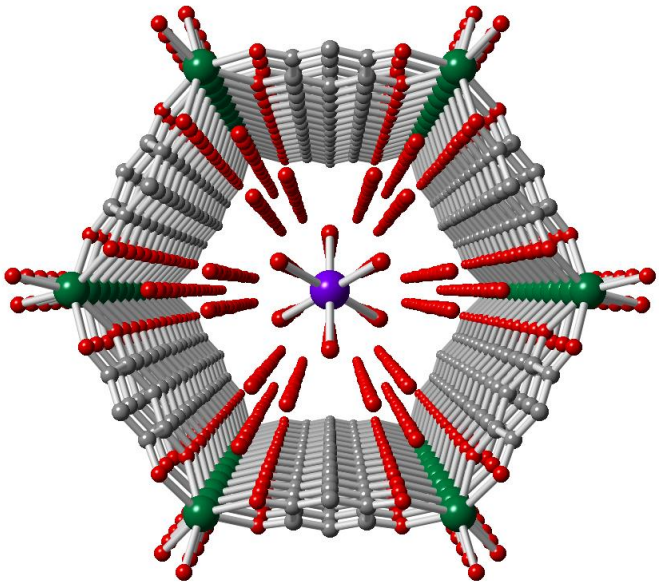

Figure 8.12. *Perspective view of one hexagonal channel in compound $Na_2(H_2O)_{24}[Cd^{II}_2(C_6O_4H_2)_3]$ showing the chains of Na^+ cations and water molecules inside. Colour code: C = grey, O = red, Na = purple, Cd = green.*

4. Conclusions and perspectives

In this chapter we present a chloranilato-based electrodeposited film (**47**) that constitutes a bifunctional electrode able to store Na^+ and K^+ ions and catalyse the hydrogen evolution reaction (HER). To explain this bifunctionality, we propose the following mechanism: when the building blocks ($Fe^{3+}_{(ac)}$, $[Fe^{III}(C_6O_4Cl_2)]^{3-}$ and $Na^+_{(ac)}$ or K^+) in the original solution are submitted to a 0 V impedance for ten minutes some $Fe^{3+}_{(ac)}$ cations must reduce to $Fe^{2+}_{(ac)}$ cations that react with the $[Fe^{III}(C_6O_4Cl_2)]^{3-}$ anions to form the well known $[Fe^{II}Fe^{III}(C_6O_4Cl_2)_3]^-$ honeycomb 2D lattice,[63, 67] or with reduced $[Fe^{II}(C_6O_4Cl_2)]^{4-}$ anions to form the also well known $[Fe^{II}Fe^{II}(C_6O_4Cl_2)_3]^{2-}$ 2D honeycomb lattice lattice.[96, 97] The formation of both lattices requires the insertion of cations (Na^+ or K^+) in the hexagonal channels to form structure similar to that depicted in figure 8.11.

Once the film is formed and reduced, we must have $Na_2[Fe^{II}(C_6O_4Cl_2)]$ or $K_2[Fe^{II}(C_6O_4Cl_2)]$ electrodeposited in the GC electrode. When successive CVs are performed and the appropriate voltage is reached, the Fe(II) centres oxidise to Fe(III) and the alkali cations have to leave the channels in order to balance the charge. This mechanism would explain the narrow peaks that appear near the Fe(III)/Fe(II) redox processes (Figures 8.3 to 8.8). As observed in many other electrodeposited films, the intercalation process is not fully reversible, probably due to a slow diffusion rate of the alkali ions through the hexagonal channels compared to the CV scan rate. As a result of this non fully reversibility of the intercalation process, after a certain number of cycles (that, depending on the type of electrolyte and electrode, may vary from 60 to 700) the intercalation is quenched. Note also that a possible intercalation of the Na^+ and K^+ ions in between the anionic layers cannot be discarded at this point since 2D diffusion is more efficient that 1D. This 2D diffusion may be at the origin of the high number of redox cycles needed to saturate the film (up to several hundreds in some cases). A second possible reason explaining the lack of total reversibility may be the coordination of the alkali ions to the oxygen atoms of the chloranilato ligands. In fact, there are some examples of anilato-based lattices similar to those proposed in film **47**, where Na^+ ions are coordinated to the oxygen atoms of the anilato ligands.[62, 67] This mechanism for the alkali ions insertion is the one proposed in the majority of quinones-based batteries.[71, 74, 77, 78] A third possibility is a progressive degradation of the film during the

redox cycles due to a release of some anilato ligands leading to vacant structures where water molecules replace anilato ligands, as those observed in the many examples of anilato-based chains (Figure 8.12).[98-104]

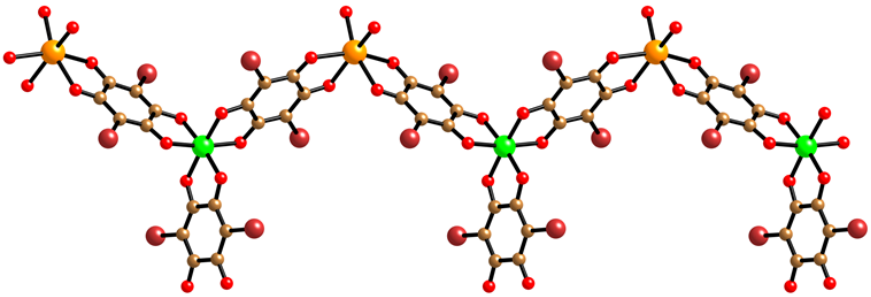

Figure 8.12: *Structure of an anilate-based chain where half of the M(III) centres are bonded to only two anilato ligands and the two coordination position vacancies are filled with water.*

Once all the available positions for the Na^+ or K^+ cations are filled, the successive reduction processes do not show any intercalation of alkali ions. At this moment, only H^+ can enter to compensate the reduction of the iron centres. This mechanism explains why the quenching of the alkali ions intercalation is accompanied by the HER. The H^+ diffuse thanks to the water molecules present in the hexagonal channels of the film and arrive close to the Fe(II) positions where they are reduced by these Fe(II) centres. Most probably, the H^+ binds to one oxygen atom of an anilato ligand coordinated to the Fe(II) centre. This hypothesis is consistent with the observation of mono-protonated anilato ligands that are coordinated to metals.[105, 106] The resulting effect is the Fe(II)/Fe(III)-catalysed H_2 evolution observed in the "alkali-saturated" films. These two processes, ion intercalation and HER are antagonists since only when the intercalation quenches, HER is observed. The initial prevalence of the alkali ion intercalation process may be simply due to the much higher concentration of the alkali ions (0.1 M) compared to the H^+ concentration.

As future work, we are planning further experiments with other cations (including bulky ones as NBu_4^+) to verify if the quenching of the intercalation process leads to HER from the initial cycles. We also plan to include other alkali ions as electrolytes (Li^+, Rb^+ and Cs^+) and to change their concentrations and the pH to study the role of the diffusion rate and ion concentrations on the HER potential. These study will lead to an optimization of the electrodeposition conditions in order to obtain a more efficient

anilato-based HER catalyst. Finally, we also plan to electrodeposit this film in other electrodes as ITO in order to isolate the film and perform a complete characterization of its structure and properties (IR, Raman and EPR spectroscopies, elemental and metal analysis, magnetic measurements, conductivity measurements, X-Ray powder diffractograms,...)

Any case, regardless of the mechanism, the fact that HER evolves at higher potentials with film the GC electrodes containing electrodeposited film **47** strongly suggests that this film could be a good catalyst for hydrogen formation. Additionally, the high stability of the electrode during the HER at pH = 2 adds an extra interest to this film.

5. References

(1) Caban-Acevedo, M.; Stone, M. L.; Schmidt, J. R.; Thomas, J. G.; Ding, Q.; Chang, H. C.; Tsai, M. L.; He, J. H.; Jin, S. Efficient Hydrogen Evolution Catalysis using Ternary Pyrite-Type Cobalt Phosphosulphide. *Nat. Mater.* **2015***, 14*, 1245-1251.

(2) Cobo, S.; Heidkamp, J.; Jacques, P. A.; Fize, J.; Fourmond, V.; Guetaz, L.; Jousselme, B.; Ivanova, V.; Dau, H.; Palacin, S.; Fontecave, M.; Artero, V. A Janus Cobalt-Based Catalytic Material for Electro-Splitting of Water. *Nat. Mater.* **2012***, 11*, 802.

(3) Dresselhaus, M. S.; Thomas, I. L. Alternative Energy Technologies. *Nature* **2001***, 414*, 332-337.

(4) Navarro, R. M.; Peña, M. A.; Fierro, J. L. G. Hydrogen Production Reactions from Carbon Feedstocks: Fossil Fuels and Biomass. *Chem. Rev.* **2007***, 107*, 3952-3991.

(5) Jiao, Y.; Zheng, Y.; Jaroniec, M.; Qiao, S. Z. Design of Electrocatalysts for Oxygen- and Hydrogen-Involving Energy Conversion Reactions. *Chem. Soc. Rev.* **2015***, 44*, 2060-2086.

(6) Benck, J. D.; Hellstern, T. R.; Kibsgaard, J.; Chakthranont, P.; Jaramillo, T. F. Catalyzing the Hydrogen Evolution Reaction (HER) with Molybdenum Sulfide Nanomaterials. *ACS Catal.* **2014***, 4*, 3957-3971.

(7) Fei, H.; Dong, J.; Arellano-Jiménez, M. J.; Ye, G.; Dong Kim, N.; Samuel, E. L. G.; Peng, Z.; Zhu, Z.; Qin, F.; Bao, J.; Yacaman, M. J.; Ajayan, P. M.; Chen, D.; Tour, J. M. Atomic Cobalt on Nitrogen-Doped Graphene for Hydrogen Generation. *Nat Commun* **2015***, 6*, 8668.

(8) Gasteiger, H. A.; Kocha, S. S.; Sompalli, B.; Wagner, F. T. Activity Benchmarks and Requirements for Pt, Pt-Alloy, and Non-Pt Oxygen Reduction Catalysts for PEMFCs. *Applied Catalysis B: Environmental* **2005***, 56*, 9-35.

(9) Kibsgaard, J.; Gorlin, Y.; Chen, Z.; Jaramillo, T. F. Meso-Structured Platinum Thin Films: Active and Stable Electrocatalysts for the Oxygen Reduction Reaction. *J. Am. Chem. Soc.* **2012***, 134*, 7758-7765.

(10) Zhang, J.; Sasaki, K.; Sutter, E.; Adzic, R. R. Stabilization of Platinum Oxygen-Reduction Electrocatalysts using Gold Clusters. *Science* **2007***, 315*, 220-222.

(11) Ahmad, H.; Kamarudin, S. K.; Minggu, L. J.; Kassim, M. Hydrogen from Photo-Catalytic Water Splitting Process: A Review. *Renewable and Sustainable Energy Reviews* **2015***, 43*, 599-610.

(12) Liu, J.; Liu, Y.; Liu, N.; Han, Y.; Zhang, X.; Huang, H.; Lifshitz, Y.; Lee, S. T.; Zhong, J.; Kang, Z. Metal-Free Efficient Photocatalyst for Stable Visible Water Splitting Via a Two-Electron Pathway. *Science* **2015***, 347*, 970.

(13) Chang, K.; Mei, Z.; Wang, T.; Kang, Q.; Ouyang, S.; Ye, J. MoS2/Graphene Cocatalyst for Efficient Photocatalytic H_2 Evolution Under Visible Light Irradiation. *ACS Nano* **2014***, 8*, 7078-7087.

(14) Hu, X.; Brunschwig, B. S.; Peters, J. C. Electrocatalytic Hydrogen Evolution at Low Overpotentials by Cobalt Macrocyclic Glyoxime and Tetraimine Complexes. *J. Am. Chem. Soc.* **2007***, 129*, 8988-8998.

(15) Jacques, P. A.; Artero, V.; Pécaut, J.; Fontecave, M. Cobalt and Nickel Diimine-Dioxime Complexes as Molecular Electrocatalysts for Hydrogen Evolution with Low Overvoltages. *Proceedings of the National Academy of Sciences* **2009***, 106*, 20627-20632.

(16) Dempsey, J. L.; Winkler, J. R.; Gray, H. B. Mechanism of H2 Evolution from a Photogenerated Hydridocobaloxime. *J. Am. Chem. Soc.* **2010***, 132*, 16774-16776.

(17) Karunadasa, H. I.; Chang, C. J.; Long, J. R. A Molecular Molybdenum-Oxo Catalyst for Generating Hydrogen from Water. *Nature* **2010***, 464*, 1329-1333.

(18) Losse, S.; Vos, J. G.; Rau, S. Catalytic Hydrogen Production at Cobalt Centres. *Coord. Chem. Rev.* **2010***, 254*, 2492-2504.

(19) Helm, M. L.; Stewart, M. P.; Bullock, R. M.; DuBois, M. R.; DuBois, D. L. A Synthetic Nickel Electrocatalyst with a Turnover Frequency Above 100,000 s^{-1} for H_2 Production. *Science* **2011***, 333*, 863-866.

(20) Artero, V.; Chavarot-Kerlidou, M.; Fontecave, M. Splitting Water with Cobalt. *Angewandte Chemie International Edition* **2011***, 50*, 7238-7266.

(21) Lakadamyali, F.; Reisner, E. Photocatalytic H_2 Evolution from Neutral Water with a Molecular Cobalt Catalyst on a Dye-Sensitised TiO_2 Nanoparticle. *Chem. Commun.* **2011***, 47*, 1695-1697.

(22) Muckerman, J. T.; Fujita, E. Theoretical Studies of the Mechanism of Catalytic Hydrogen Production by a Cobaloxime. *Chem. Commun.* **2011***, 47*, 12456-12458.

(23) Rose, M. J.; Gray, H. B.; Winkler, J. R. Hydrogen Generation Catalyzed by Fluorinated Diglyoximeâ€“Iron Complexes at Low Overpotentials. *J. Am. Chem. Soc.* **2012***, 134*, 8310-8313.

(24) Li, L.; Duan, L.; Wen, F.; Li, C.; Wang, M.; Hagfeldt, A.; Sun, L. Visible Light Driven Hydrogen Production from a Photo-Active Cathode Based on a Molecular Catalyst and Organic Dye-Sensitized P-Type Nanostructured NiO. *Chem. Commun.* **2012***, 48*, 988-990.

(25) Wang, W.; Rauchfuss, T. B.; Bertini, L.; Zampella, G. Unsensitized Photochemical Hydrogen Production Catalyzed by Diiron Hydrides. *J. Am. Chem. Soc.* **2012***, 134*, 4525-4528.

(26) Singh, W. M.; Baine, T.; Kudo, S.; Tian, S.; Ma, X. A. N.; Zhou, H.; DeYonker, N. J.; Pham, T. C.; Bollinger, J. C.; Baker, D. L.; Yan, B.; Pham, T. C.; Zhao, X. Electrocatalytic and Photocatalytic Hydrogen Production in Aqueous Solution by a Molecular Cobalt Complex. *Angew. Chem. Inter. Ed.* **2012***, 51*, 5941-5944.

(27) Jasion, D.; Barforoush, J. M.; Qiao, Q.; Zhu, Y.; Ren, S.; Leonard, K. C. Low-Dimensional Hyperthin FeS_2 Nanostructures for Efficient and Stable Hydrogen Evolution Electrocatalysis. *ACS Catal.* **2015***, 5*, 6653-6657.

(28) Matsumoto, T.; Nagahama, T.; Cho, J.; Hizume, T.; Suzuki, M.; Ogo, S. Preparation and Reactivity of a Nickel Dihydride Complex. *Angew. Chem. Inter. Ed.* **2011***, 123*, 10766-10768.

(29) Nann, T.; Ibrahim, S. ; Woi, P. M.; Xu, S.; Ziegler, J.; Pickett, C. Water Splitting by Visible Light: A Nanophotocathode for Hydrogen Production. *Angew. Chem. Inter. Ed.* **2010***, 49*, 1574-1577.

(30) Reece, S. Y.; Hamel, J. A.; Sung, K.; Jarvi, T. D.; Esswein, A. J.; Pijpers, J. J. H.; Nocera, D. G. Wireless Solar Water Splitting using Silicon-Based Semiconductors and Earth-Abundant Catalysts. *Science* **2011***, 334*, 645-648.

(31) Duan, L.; Bozoglian, F.; Mandal, S.; Stewart, B.; Privalov, T.; Llobet, A.; Sun, L. A Molecular Ruthenium Catalyst with Water-Oxidation Activity Comparable to that of Photosystem II. *Nat. Chem.* **2012***, 4*, 418-423.

(32) Du, P.; Eisenberg, R. Catalysts made of Earth-Abundant Elements (Co, Ni, Fe) for Water Splitting: Recent Progress and Future Challenges. *Energy Environ. Sci.* **2012***, 5*, 6012-6021.

(33) Bauer, R.; Werner, H. A. F. Investigations on a Homogeneous Wilkinson's Catalyst for the Water Photolysis. *Int. J. Hydrogen Energy* **1994***, 19*, 497-499.

(34) Lakadamyali, F.; Kato, M.; Muresan, N., M.; Reisner, E. Selective Reduction of Aqueous Protons to Hydrogen with a Synthetic Cobaloxime Catalyst in the Presence of Atmospheric Oxygen. *Angew. Chem. Inter. Ed.* **2012***, 51*, 9381-9384.

(35) Imanishi, N.; Morikawa, T.; Kondo, J.; Takeda, Y.; Yamamoto, O.; Kinugasa, N.; Yamagishi, T. Lithium Intercalation Behavior into Iron Cyanide Complex as Positive Electrode of Lithium Secondary Battery. *J. Power Sources* **1999***, 79*, 215-219.

(36) Mizuno, Y.; Okubo, M.; Asakura, D.; Saito, T.; Hosono, E.; Saito, Y.; Oh-ishi, K.; Kudo, T.; Zhou, H. Impedance Spectroscopic Study on Interfacial Ion Transfers in Cyanide-Bridged Coordination Polymer Electrode with Organic Electrolyte. *Electrochim. Acta* **2012***, 63*, 139-145.

(37) Moritomo, Y.; Takachi, M.; Kurihara, Y.; Matsuda, T. Thin Film Electrodes of Prussian Blue Analogues with Rapid Li + Intercalation. *Appl. Phys. Express* **2012***, 5*, 041801.

(38) Wang, X.; Hou, Y.; Zhu, Y.; Wu, Y.; Holze, R. An Aqueous Rechargeable Lithium Battery using Coated Li Metal as Anode. *Scientific Reports* **2013***, 3*, 1401.

(39) Kaveevivitchai, W.; Jacobson, A. J. Exploration of Vanadium Benzenedicarboxylate as a Cathode for Rechargeable Lithium Batteries. *J. Power Sources* **2015***, 278*, 265-273.

(40) Omarova, M.; Koishybay, A.; Yesibolati, N.; Mentbayeva, A.; Umirov, N.; Ismailov, K.; Adair, D.; Babaa, M. R.; Kurmanbayeva, I.; Bakenov, Z. Nickel Hexacyanoferrate Nanoparticles as a Low Cost Cathode Material for Lithium-Ion Batteries. *Electrochim. Acta* **2015***, 184*, 58-63.

(41) Yesibolati, N.; Umirov, N.; Koishybay, A.; Omarova, M.; Kurmanbayeva, I.; Zhang, Y.; Zhao, Y.; Bakenov, Z. High Performance Zn/$LiFePO_4$ Aqueous Rechargeable Battery for Large Scale Applications. *Electrochim. Acta* **2015***, 152*, 505-511.

(42) Emery, N.; Sougrati, M. T.; Panabière, E.; Bach, S.; Fraisse, B.; Jumas, J. C.; Pereira-Ramos, J. P.; Willmann, P. Unidimensional Unit Cell Variation and Fe^{+3}/Fe^{+4} Redox Activity of Li_3FeN_2 in Li-Ion Batteries. *J. Alloys Compounds* **2017***, 696*, 971-979.

(43) Wessells, C. D.; Peddada, S. V.; Huggins, R. A.; Cui, Y. Nickel Hexacyanoferrate Nanoparticle Electrodes for Aqueous Sodium and Potassium Ion Batteries. *Nano Lett.* **2011***, 11*, 5421-5425.

(44) Wang, L.; Lu, Y.; Liu, J.; Xu, M.; Cheng, J.; Zhang, D.; Goodenough, J. B. A Superior Low-Cost Cathode for a Na-Ion Battery. *Angew. Chem. Inter. Ed.* **2013***, 52*, 1964-1967.

(45) Lee, H. W.; Wang, R. Y.; Pasta, M.; Woo Lee, S.; Liu, N.; Cui, Y. Manganese Hexacyanomanganate Open Framework as a High-Capacity Positive Electrode Material for Sodium-Ion Batteries. *Nature Communications* **2014***, 5*, 5280.

(46) Sharma, N.; Tapia-Ruiz, N.; Singh, G.; Armstrong, A. R.; Pramudita, J. C.; Brand, H. E. A.; Billaud, J.; Bruce, P. G.; Rojo, T. Rate Dependent Performance Related to Crystal Structure Evolution of $Na_{0.67}Mn_{0.8}Mg_{0.2}O_2$ in a Sodium-Ion Battery. *Chem. Mater.* **2015***, 27*, 6976-6986.

(47) Su, D.; McDonagh, A.; Qiao, S. Z.; Wang, G. High-Capacity Aqueous Potassium-Ion Batteries for Large-Scale Energy Storage. *Adv Mater* **2017***, 29*, 1604007.

(48) Wu, C. M.; Pan, P. I.; Cheng, Y. W.; Liu, C. P.; Chang, C. C.; Avdeev, M.; Lin, S. K. The Mechanism of the Sodiation and Desodiation in Super P Carbon Electrode for Sodium-Ion Battery. *J. Power Sources* **2017***, 340*, 14-21.

(49) Zhan, X.; Shirpour, M. Evolution of Solid/Aqueous Interface in Aqueous Sodium-Ion Batteries. *Chem. Commun.* **2017***, 53*, 204-207.

(50) Tanabe, K. K.; Cohen, S. M. Postsynthetic Modification of Metal-Organic Frameworks-a Progress Report. *Chem. Soc. Rev.* **2011***, 40*, 498-519.

(51) Morozan, A.; Jaouen, F. Metal Organic Frameworks for Electrochemical Applications. *Energy Environ. Sci.* **2012***, 5*, 9269-9290.

(52) Zhang, Z.; Yoshikawa, H.; Awaga, K. Monitoring the Solid-State Electrochemistry of Cu(2,7-AQDC) (AQDC = anthraquinone dicarboxylate) in a Lithium Battery: Coexistence of Metal and Ligand Redox Activities in a Metal-Organic Framework. *J. Am. Chem. Soc.* **2014***, 136*, 16112-16115.

(53) Aubrey, M. L.; Long, J. R. A Dual-Ion Battery Cathode Via Oxidative Insertion of Anions in a Metal-Organic Framework. *J. Am. Chem. Soc.* **2015***, 137*, 13594-13602.

(54) Lux, L.; Williams, K.; Ma, S. Heat-Treatment of Metal-Organic Frameworks for Green Energy Applications. *CrystEngComm* **2015***, 17*, 10-22.

(55) Xia, W.; Mahmood, A.; Zou, R.; Xu, Q. Metal-Organic Frameworks and their Derived Nanostructures for Electrochemical Energy Storage and Conversion. *Energy Environ. Sci.* **2015***, 8*, 1837-1866.

(56) Sun, L.; Campbell, M. G.; Dincă, M. Electrically Conductive Porous Metal–Organic Frameworks. *Angew. Chem. Int. Ed.* **2016***, 55*, 3566-3579.

(57) Dong, R.; Pfeffermann, M.; Liang, H.; Zheng, Z.; Zhu, X.; Zhang, J.; Feng, X. Large-Area, Free-Standing, Two-Dimensional Supramolecular Polymer Single-Layer Sheets for Highly Efficient Electrocatalytic Hydrogen Evolution. *Angew. Chem. Int. Ed.* **2015***, 54*, 12058-12063.

(58) Duan, J.; Chen, S.; Zhao, C. Ultrathin Metal-Organic Framework Array for Efficient Electrocatalytic Water Splitting. *Nat. Comm.* **2017***, 8*, 15341.

(59) Miner, E. M.; Fukushima, T.; Sheberla, D.; Sun, L.; Surendranath, Y.; Dinca, M. Electrochemical Oxygen Reduction Catalysed by Ni_3(Hexaiminotriphenylene)$_2$. *Nature Communications* **2016***, 7*, 10942.

(60) Dinca, M.; Long, J. R. Hydrogen Storage in Microporous Metal-Organic Frameworks with Exposed Metal Sites. *Angew. Chem. Int. Ed.* **2008***, 47*, 6766-6779.

(61) Abhervé, A.; Clemente-León, M.; Coronado, E.; Gómez-García, C. J.; Verneret, M. One-Dimensional and Two-Dimensional Anilate-Based Magnets with Inserted Spin-Crossover Complexes. *Inorg. Chem.* **2014***, 53*, 12014-12026.

(62) Benmansour, S.; Vallés-García, C.; Gómez-Claramunt, P.; Mínguez Espallargas, G.; Gómez-García, C. J. 2D and 3D Anilato-Based Heterometallic M(I)M(III) Lattices: The Missing Link. *Inorg. Chem.* **2015***, 54*, 5410-5418.

(63) Atzori, M.; Benmansour, S.; Mínguez Espallargas, G.; Clemente-León, M.; Abhervé, A.; Gómez-Claramunt, P.; Coronado, E.; Artizzu, F.; Sessini, E.; Deplano, P.; Serpe, A.; Mercuri, M. L.; Gómez García, C. J. A Family of Layered Chiral Porous Magnets Exhibiting Tunable Ordering Temperatures. *Inorg. Chem.* **2013***, 52*, 10031-10040.

(64) Atzori, M.; Pop, F.; Auban-Senzier, P.; Gomez-Garcia, C. J.; Canadell, E.; Artizzu, F.; Serpe, A.; Deplano, P.; Avarvari, N.; Mercuri, M. L. Structural Diversity and Physical Properties of Paramagnetic Molecular Conductors Based on bis(ethylenedithio)tetrathiafulvalene (BEDT-TTF) and the tris(chloranilato)ferrate(III) Complex. *Inorg. Chem.* **2014***, 53*, 7028-7039.

(65) Benmansour, S.; Coronado, E.; Giménez-Saiz, C.; Gómez-García, C. J.; Rößer, C. Metallic Charge-Transfer Salts of Bis(Ethylenedithio)Tetrathiafulvalene with paramagnetic tetrachloro(oxalato)rhenate(IV) and tris(chloranilato)ferrate(III) Anions. *Eur. J. Inorg. Chem* **2014***, 2014*, 3949-3959.

(66) Benmansour, S.; Gomez-Claramunt, P.; Valles-Garcia, C.; Minguez Espallargas, G.; Gomez Garcia, C. J. Key Role of the Cation in the Crystallization of Chiral tris(anilato)metalate Magnetic Anions. *Cryst. Growth Des.* **2016***, 16*, 518-526.

(67) Benmansour, S.; Abherve, A.; Gómez-Claramunt, P.; Vallés-García, C.; Gómez-García, C. J. Nanosheets of Two-Dimensional Magnetic and Conducting Fe(II)/Fe(III) Mixed-Valence Metal-Organic Frameworks. *ACS Appl. Mater. Interfaces* **2017***, 9*, 26210-26218.

(68) Jeon, I. R.; Negru, B.; Van Duyne, R. P.; Harris, T. D. A 2D Semiquinone Radical-Containing Microporous Magnet with Solvent-Induced Switching from Tc = 26 to 80 K. *J. Am. Chem. Soc.* **2015***, 137*, 15699-15702.

(69) Darago, L. E.; Aubrey, M. L.; Yu, C. J.; Gonzalez, M. I.; Long, J. R. Electronic Conductivity, Ferrimagnetic Ordering, and Reductive Insertion Mediated by Organic Mixed-Valence in a Ferric Semiquinoid Metal-Organic Framework. *J. Am. Chem. Soc.* **2015***, 137*, 15703-15711.

(70) DeGayner, J. A.; Jeon, I. R.; Sun, L.; D., M.; Harris, T. D. 2D Conductive Iron-Quinoid Magnets Ordering Up to Tc = 105 K Via Heterogenous Redox Chemistry. *J. Am. Chem. Soc.* **2017***, 139*, 4175-4184.

(71) Yao, M.; Senoh, H.; Araki, M.; Sakai, T.; Yasuda, K. Organic Positive-Electrode Materials Based on Dialkoxybenzoquinone Derivatives for use in Rechargeable Lithium Batteries. *ECS Transactions* **2010***, 28*, 3-10.

(72) Senoh, H.; Yao, M.; Sakaebe, H.; Yasuda, K.; Siroma, Z. A Two-Compartment Cell for using Soluble Benzoquinone Derivatives as Active Materials in Lithium Secondary Batteries. *Electrochim. Acta* **2011***, 56*, 10145-10150.

(73) Barrès, A. L.; Geng, J.; Bonnard, G.; Renault, S.; Gottis, S.; Mentré, O.; Frayret, C.; Dolhem, F.; Poizot, P. High-Potential Reversible Li Deintercalation in a Substituted Tetrahydroxy-P-Benzoquinone Dilithium Salt: An Experimental and Theoretical Study. *Chem. Eur. J.* **2012***, 18*, 8800-8812.

(74) Reddy, A. L. M.; Nagarajan, S.; Chumyim, P.; Gowda, S. R.; Pradhan, P.; Jadhav, S. R.; Dubey, M.; John, G.; Ajayan, P. M. Lithium Storage Mechanisms in Purpurin Based Organic Lithium Ion Battery Electrodes. *Scientific Reports* **2012***, 2*, 960.

(75) Hanyu, Y.; Ganbe, Y.; Honma, I. Application of Quinonic Cathode Compounds for Quasi-Solid Lithium Batteries. *J. Power Sources* **2013***, 221*, 186-190.

(76) Huskinson, B.; Marshak, M. P.; Suh, C.; Er, S.; Gerhardt, M. R.; Galvin, C. J.; Chen, X.; Aspuru-Guzik, A.; Gordon, R. G.; Aziz, M. J. A Metal-Free Organic-Inorganic Aqueous Flow Battery. *Nature* **2014***, 505*, 195-198.

(77) Zeng, R.; Xing, L.; Qiu, Y.; Wang, Y.; Huang, W.; Li, W.; Yang, S. Polycarbonyl(Quinonyl) Organic Compounds as Cathode Materials for Sustainable Lithium Ion Batteries. *Electrochim. Acta* **2014***, 146*, 447-454.

(78) Song, Z.; Qian, Y.; Liu, X.; Zhang, T.; Zhu, Y.; Yu, H.; Otani, M.; Zhou, H. A Quinone-Based Oligomeric Lithium Salt for Superior Li-Organic Batteries. *Energy Environ. Sci.* **2014***, 7*, 4077-4086.

(79) Lin, K.; Chen, Q.; Gerhardt, M. R.; Tong, L.; Kim, S. B.; Eisenach, L.; Valle, A. W.; Hardee, D.; Gordon, R. G.; Aziz, M. J.; Marshak, M. P. Alkaline Quinone Flow Battery. *Science* **2015***, 349*, 1529.

(80) Son, E. J.; Kim, J. H.; Kim, K.; Park, C. B. Quinone and its Derivatives for Energy Harvesting and Storage Materials. *J. Mater. Chem. A* **2016***, 4*, 11179-11202.

(81) Ding, Y.; Yu, G. A Bio-Inspired, Heavy-Metal-Free, Dual-Electrolyte Liquid Battery Towards Sustainable Energy Storage. *Angew. Chem. Inter. Ed.* **2016***, 55*, 4772-4776.

(82) Wedege, K.; Drazevic, E.; Konya, D.; Bentien, A. Organic Redox Species in Aqueous Flow Batteries: Redox Potentials, Chemical Stability and Solubility. *Scientific Reports* **2016***, 6*, 39101.

(83) Dawut, G.; Lu, Y.; Zhao, Q.; Liang, J.; Tao, Z. L.; Chen, J. Quinones as Electrode Materials for Rechargeable Lithium Batteries. *Acta Phys. Chim. Sinica* **2016***, 32*, 1593.

(84) Ding, Y.; Li, Y.; Yu, G. Exploring Bio-Inspired Quinone-Based Organic Redox Flow Batteries: A Combined Experimental and Computational Study. *Chem* **2016***, 1*, 790-801.

(85) Le Gall, T.; Reiman, K. H.; Grossel, M. C.; Owen, J. R. Poly(2,5-Dihydroxy-1,4-Benzoquinone-3,6-Methylene): A New Organic Polymer as Positive Electrode Material for Rechargeable Lithium Batteries. *J. Power Sources* **2003***, 119–121*, 316-320.

(86) Xiang, J.; Chang, C.; Li, M.; Wu, S.; Yuan, L.; Sun, J. A Novel Coordination Polymer as Positive Electrode Material for Lithium Ion Battery. *Cryst. Growth. Des.* **2008***, 8*, 280-282.

(87) Armand, M.; Tarascon, J. M. Building Better Batteries. *Nature* **2008***, 451*, 652-657.

(88) Luo, C.; Zhu, Y.; Xu, Y.; Liu, Y.; Gao, T.; Wang, J.; Wang, C. Graphene Oxide Wrapped Croconic Acid Disodium Salt for Sodium Ion Battery Electrodes. *J. Power Sources* **2014***, 250*, 372-378.

(89) Chen, H.; Poizot, P.; Dolhem, F.; Basir, N. I.; Mentré, O.; Tarascon, J. M. Electrochemical Reactivity of Lithium Chloranilate Vs Li and Crystal Structures of the Hydrated Phases. *Electrochem. Solid. State. Lett.* **2009***, 12*, A102-A106.

(90) Clemente-León, M.; Coronado, E.; Dias, J. C.; Soriano-Portillo, A.; Willett, R. D. Synthesis, Structure, and Magnetic Properties of [(S)-$[PhCH(CH_3)N(CH_3)_3]][Mn(CH_3CN)_{2/3}Cr(Ox)_3].(CH_3CN)$.(Solvate), a 2D Chiral Magnet Containing a Quaternary Ammonium Chiral Cation. *Inorg. Chem.* **2008***, 47*, 6458-6463.

(91) Clemente-Leon, M.; Coronado, E.; Gómez-García, C. J.; Soriano-Portillo, A. Increasing the Ordering Temperatures in Oxalate-Based 3D Chiral Magnets: The Series $[Ir(ppy)_2(bpy)][M(II)M(III)(Ox)_3]$ X 0.5 H_2O (M(II)M(III) = MnCr, FeCr, CoCr, NiCr, ZnCr, MnFe, FeFe); Bpy = 2,2'-Bipyridine; ppy = 2-Phenylpyridine; ox = Oxalate Dianion). *Inorg. Chem.* **2006***, 45*, 5653-5660.

(92) Frackowiak, E.; Béguin, F. Carbon Materials for the Electrochemical Storage of Energy in Capacitors. *Carbon* **2001***, 39*, 937-950.

(93) Pandolfo, A. G.; Hollenkamp, A. F. Carbon Properties and their Role in Supercapacitors. *J. Power Sources* **2006***, 157*, 11-27.

(94) Stoller, M. D.; Park, S.; Zhu, Y.; An, J.; Ruoff, R. S. Graphene-Based Ultracapacitors. *Nano Lett.* **2008***, 8*, 3498-3502.

(95) Zhu, Y.; Murali, S.; Stoller, M. D.; Ganesh, K. J.; Cai, W.; Ferreira, P. J.; Pirkle, A.; Wallace, R. M.; Cychosz, K. A.; Thommes, M.; Su, D.; Stach, E. A.; Ruoff, R. S. Carbon-Based Supercapacitors Produced by Activation of Graphene. *Science* **2011***, 332*, 1537-1541.

(96) Weiss, A.; Riegler, E.; Robl, C. Polymeric 2,5-Dihydroxy-1,4-Benzoquinone Transition-Metal Complexes $Na_2(H_2O)_{24}[M_2(C_6H_2O_4)_3]$ (M = Mn^{2+}, Cd^{2+}). *Z. Naturforsch. B: Chem. Sci.* **1986***, 41*, 1501-1505.

(97) Shilov, G. V.; Nikitina, Z. K.; Ovanesyan, N. S.; Aldoshin, S. M.; Makhaev, V. D. Phenazineoxonium Chloranilatomanganate and Chloranilatoferrate: Synthesis, Structure, Magnetic Properties, and Mossbauer Spectra. *Russ. Chem. Bull.* **2011***, 60*, 1209-1219.

(98) Abhervé, A.; Clemente-León, M.; Coronado, E.; Gómez-García, C. J.; Verneret, M. One-Dimensional and Two-Dimensional Anilate-Based Magnets with Inserted Spin-Crossover Complexes. *Inorg. Chem.* **2014***, 53*, 12014-12026.

(99) Abrahams, B. F.; Coleiro, J.; Ha, K.; Hoskins, B. F.; Orchard, S. D.; Robson, R. Dihydroxybenzoquinone and Chloranilic Acid Derivatives of Rare Earth Metals. *J. Chem. Soc. , Dalton Trans.* **2002**, 1586-1594.

(100) Abrahams, B. F.; Dharma, A. D.; Dyett, B.; Hudson, T. A.; Maynard-Casely, H.; Kingsbury, C. J.; McCormick, L. J.; Robson, R.; Sutton, A. L.; White, K. F. An Indirect Generation of 1D M^{II}-2,5-Dihydroxybenzoquinone Coordination Polymers, their Structural Rearrangements and Generation of Materials with a High Affinity for H_2, CO_2 and CH_4. *Dalton Trans.* **2016***, 45*, 1339-1344.

(101) Kabir, M. K.; Kawahara, M.; Kumagai, H.; Adachi, K.; Kawata, S.; Ishii, T.; Kitagawa, S. The Rational Syntheses of Manganese–chloranilate Compounds: Crystal Structures and Magnetic Properties. *Polyhedron* **2001***, 20*, 1417-1422.

(102) Kawata, S.; Kitagawa, S.; Kumagai, H.; Kudo, C.; Kamesaki, H.; Ishiyama, T.; Suzuki, R.; Kondo, M.; Katada, M. Rational Design of a Novel Intercalation System. Layer-Gap Control of Crystalline Coordination Polymers, $\{[Cu(CA)(H_2O)_M](G)\}_N$ (M = 2, G = 2,5-dimethylpyrazine and phenazine; m = 1, G = 1,2,3,4,6,7,8,9-Octahydrophenazine). *Inorg. Chem.* **1996***, 35*, 4449-4461.

(103) Kawata, S.; Kitagawa, S.; Kumagai, H.; Ishiyama, T.; Honda, K.; Tobita, H.; Adachi, K.; Katada, M. Novel Intercalation Host System Based on Transition Metal (Fe^{2+}, Co^{2+}, Mn^{2+}) Chloranilate Coordination Polymers. Single Crystal Structures and Properties. *Chem. Mater.* **1998***, 10*, 3902-3912.

(104) Kitagawa, S.; Kawata, S. Coordination Compounds of 1,4-Dihydroxybenzoquinone and its Homologues. Structures and Properties. *Coord. Chem. Rev.* **2002***, 224*, 11-34.

(105) Gao, H.; Zhang, X. M. Three Novel Bi(Iii) Complexes with in Situ Generated Anilate Ligands: Unusual Oxidation of Cyclohexanedione to Dihydroxy Benzoquinone. *Dalton Trans.* **2012***, 41*, 1562-1567.

(106) Molcanov, K.; Kojic-Prodic, B.; Meden, A. Small Pi-Stacking of Quinoid Rings in Crystals of Alkali Diaqua Hydrogen Chloranilates. *CrystEngComm* **2009***, 11*, 1407-1415.

Short Summary of the Thesis
(English & Spanish)

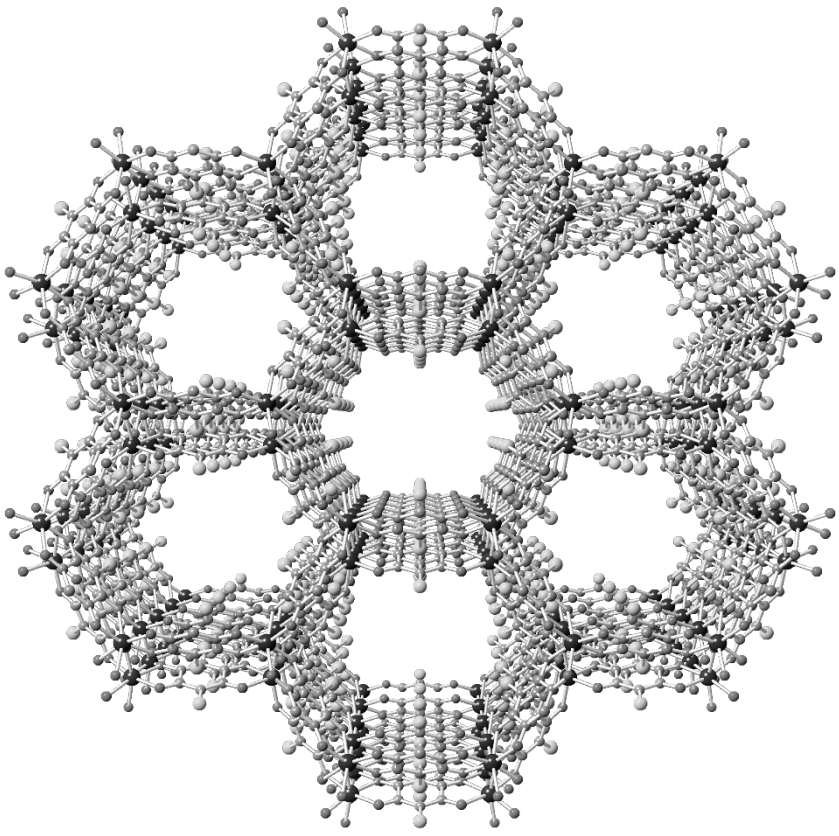

Summary.

In this Thesis work, we present different series of new molecule-based compounds prepared with anilato-derived ligands (anilato = $C_6O_4X_2^{2-}$ = 2,5-disubstituted-3,6-dihydroxy-1,4-benzoquinone) and different metal atoms including s, p, d and f-blocks metals.

In **chapter one** we present the synthesis and characterization of new anilato-based precursor salts with general formula $A_3[M(C_6O_4X_2)_3]$; (M^{III} = Fe, Cr and Ga; X = Cl, Br and NO_2). We have used different cations A^+ (A = K^+, $[PPh_3Et]^+$, $[PPh_3Pr]^+$, $[PBu_4]^+$, $[NBu_4]^+$, $[NHep_4]^+$, $[PPh_4]^+$ and K^+, compounds **1**-**20**) to study the role played by the shape and size of the cation on the structure and symmetry of the corresponding salts. This study shows that the salts with the $[PPh_3Et]^+$ cation and X = Cl or Br, crystallize in the chiral and polar *R*3 space group (phase I). With the closely related $[PPh_3Pr]^+$ cation the salts crystallize in the non-chiral but polar *P*2*cb* space group when X = Cl and Br (phase II). When X = NO_2 and the cation is PBu_4^+ then the salts crystallize in the neither chiral nor polar, triclinic *P*-1 space group (phase III). This evolution from chiral and polar (phase I) to non-chiral but polar (phase II) and to centrosymmetric, neither chiral nor polar (phase III), is due to a loss of cation-anion π–π interactions from six in phase I, four in phase II and finally zero in phase III. This key role of the cation in the number of π-π interactions is not observed for X = NO_2, where the lack of planarity also plays an important role in the final geometry since it precludes the formation of any π-π interactions.

In **chapter two** we present the first heterometallic honeycomb M(III)M(I) 2D lattice: $(NBu_3Me)_2[NaCr(C_6O_4Br_2)_3]$ (**21**) and also the first heterometallic M(III)/M(I) 3D-(10,3) anilato-based lattice: $(NBu_3Me)_2[NaCr(C_6O_4Br_2)_3]$ (**22**). This two compounds constitute the first example of 2D/3D polymorphism in the anilato-based family, a polymorphism that has never been observed in the oxalato family.

In **chapter three** we report the synthesis and characterization of four 2D honeycomb layers containing a trivalent metal (Cr^{III}) and a divalent metal (Mn^{II}) with H_3O^+ as counter-cation, and long range ferri-or antiferromagnetic ordering

formulated as $(H_3O)[MnCr(C_6O_4X_2)_3]\cdot 2PhZ\cdot 6H_2O$ with X/Z = Cl/Cl (**23**), Br/Cl (**24**), Br/Br (**25**), Br/CH_3 (**26**). We also present the first 2D anilato-based ferrimagnet with NBu_4^+ as counterion and an eclipsed disposition of the honeycomb layers: $(NBu_4)[MnCr(C_6O_4Br_2)_3]\cdot PhBr\cdot 5H_2O$ (**27**). In the series containing H_3O^+, the inclusion of different benzene derivative solvent molecules favours the eclipsed disposition of the layers, giving rise to hexagonal channels that contain the solvent molecules and originate porous magnets. This strategy has allowed the synthesis of eclipsed layers even with NBu_4^+ (compound **27**) improving previous results where the 2D hexagonal layers with $[NBu_4]^+$ were alternated, avoiding the formation of hexagonal channels. Compounds **23** and **27** present ferrimagnetic ordering due to an antiferromagnetic coupling of the Cr^{III} and Mn^{II} though the anilato ligand-bridge. In contrast, compounds **24**-**26** present a metamagnetic behaviour resulting from a weak antiferromagnetic inter-layer coupling that prevents the ferrimagnetic intralayer ordering. This weak antiferromagnetic coupling can be cancelled with magnetic fields above *c.a.* 200 mT in the three samples, resulting in the metamagnetic behaviour observed. This behaviour has been attributed to the absence of bulky cations separating the layers and to the presence of bromanilato ligands that favours the interlayer antiferromagnetic coupling.

In **chapter four** we present four compounds combining the asymmetric 2-chloro-5-cyano-3,6-dihydroxybenzoquinone ligand and lanthanide ions with different solvents filing its coordination sphere. Two of them (**28** and **29**) are praseodymium based 2D networks with DMF and DMSO as solvents and formulas $[Pr_2(C_6O_4(CN)Cl)_3(DMF)_6]$ (**28**) and $[Pr_2(C_6O_4(CN)Cl)_3(DMSO)_6]$ (**29**). The other compounds are Yb(III) based 2D and 3D networks formulated as $[Yb_2(C_6O_4(CN)Cl)_3(DMSO)_4]\cdot 2H_2O$ (**30**) and $[(H_3O)K][Yb_2(C_6O_4(CN)Cl)_3(\mu\text{-}OH)_2]$ (**31**), respectively. Since the 2-chloro-5-cyano-3,6-dihydroxy-benzoquinone ligand has luminescent properties, we have measured the luminescent properties of these compounds to verify the possible antenna-effect of this ligand on the of lanthanide ions.

In **chapter five** we present the combination of anilato-based compounds with cations having an extra functionality, as spin crossover (SCO). Thus, we

have prepared and characterized three anilato-based compounds with the $[Fe(bpp)_2]^{2+}$ SCO cation formulated as $[NBu_4][Fe(3\text{-}bpp)_2][Cr(C_6O_4X_2)_3].H_2O$ with X = Cl (**32**) and Br(**33**) and $[Fe(3\text{-}bpp)_2]_3[Cr(C_6O_4Cl_2)_3]_2\cdot 6H_2O$ **(34).** Compounds **32** and **33** have a H_2O molecule H-bonded to one bpp ligand that plays a key role in the SCO properties of the two compounds. The removal of this water molecule increases the SCO temperature in both compounds and gives rise to a small hysteresis of 6 K in the SCO in compound **33**. Furthermore, in the dehydrated phase there are two independent Fe(II) centres: one of them shows an abrupt SCO whereas the second one remains in the HS state at any temperature. We have demonstrated that the water removal is reversible and that the rehydrated samples behave as the original ones even if they uptake two water molecules instead of one. This second water molecule is able to enter the structure due to the fact that there is an empty space of 224 $Å^3$ and links through a weak H-bond. Compound **34** is an interesting example since it has the same SCO $[Fe(3\text{-}bpp)_2]^{2+}$ cation than compounds **32** and **33** and also the same $[Cr(C_6O_4X_2)_3]^{3-}$ anion but with a different stoichiometry and no NBu_4^+ cation. Additionally, compound **34** has no water molecules H-bonded to the cation. These slight changes produce a drastic change in the magnetic properties since compounds **34** does not show any SCO in contrast to **32** and **33**. Compound **34**, therefore, illustrates the key role that may play the anion-cation and the solvent-cation interactions in the SCO phenomenon.

In **chapter six** we present two different families of anilato-based compounds with the luminescent $[Ir(ppy)_2(bpy)]^+$ cation (ppy = phenylpiridine and bpy = bipirydine). The first series contains two monomeric salts: $[Ir(ppy)_2(bpy)]_2[(H_3O)[Cr(C_6O_4X_2)_3]\cdot H_2O$ with X = Cl **(35)** and Br **(36)** where isolated paramagnetic $[Cr(C_6O_4X_2)_3]^{3-}$ anions coexist with isolated $[Ir(ppy)_2(bpy)]^+$ cations. The second series of six anilato-based 2D layered compounds, which can be formulated as $[Ir(bpy)(ppy)_2][MnCr(C_6O_4X_2)_3]\cdot 2G\cdot 2CH_3CN\cdot H_2O$ with X/G = Cl/PhF (**37**), Cl/PhCl (**38**), Cl/PhBr (**39**), Br/PhF (**40**), Br/PhCl (**41**) and Br/PhBr (**41**), where the luminescent cation $[Ir(ppy)_2(bpy)]^+$ is inserted between the ferrimagnetic anilato-based anionic layers. Compounds **35** and **36** are paramagnetic and show the luminescence of the $[Ir(ppy)_2(bpy)]^+$ cation. The second series

presents the well-known honeycomb layered structure but with an unprecedented sequence where two consecutive anionic layers alternate with one cationic layer containing the $[Ir(ppy)_2(bpy)]^+$ cations. The ferrimagnetic coupling of the Cr^{III} and Mn^{II} ions through the anilato ligands results in long range ferrimagnetic orderings at *ca*. 10 K for X = Cl and 11.5 K for X = Br. These differences in the ordering temperature (T_c) are attributed to the inductive effect of the halogen atoms. In contrast, the change of the halo-benzene molecule located in the hexagonal cavities does not produces any significant change in T_c since this solvent molecule changes very slightly the electron density on the anilato ligand.

In **chapter seven** we present two different families of anilato-based compounds with single molecule magnets inserted between anilato layers formulated as $[Mn(salpn)(H_2O)][CrMn(C_6O_4X_2)_3]$ with X = Cl (**43**) and Br (**44**) and $[Mn(salen)(H_2O)][CrMn(C_6O_4X_2)_3]$ with X = Cl (**45**) and Br (**46**). Compounds **43** and **44** show an eclipsed configuration with hexagonal channels containing the SMM cations. The four compounds present a ferrimagnetic long range ordering with ordering temperatures of 10-12 K. The lack of a signal attributed to the SMM cations suggests that these cations are not isolated in the structure of these compounds and present some interactions with the ferrimagnetic layers. The presence of a π-π interaction between the anilato rings and the aromatic rings of the salpn ligand on the cationic SMM in compounds **44** and **45** provides a possible pathway for such cation-anion interaction.

In **chapter eight** we present a bifunctional anilato-based electrode that is able to store Na^+ and K^+ ions and electrocatalyse HER (hydrogen evolving reaction). Thus, this is a bifunctional compound capable of storing charge and electrocatalizing the HER process.

Resumen.

En esta Tesis presentamos varias series de compuestos moleculares basados en el ligando anilato (anilato = $C_6O_4X_2^{2-}$ = 2,5-disustituida-3,6-dihidroxi-1,4-benzoquinona) y diferentes átomos metálicos incluyendo metales de los bloques s, p, d y f.

En el **capítulo uno** presentamos la síntesis y caracterización de nuevas sales precursoras, basadas en el ligando anilato, con fórmula general $A_3[M(C_6O_4X_2)_3]$; (M^{III} = Fe, Cr y Ga; X = Cl, Br and NO_2). Hemos usado diferentes cationes A^+ (A = K^+, $[PPh_3Et]^+$, $[PPh_3Pr]^+$, $[PBu_4]^+$, $[NBu_4]^+$, $[NHep_4]^+$, $[PPh_4]^+$ y K^+, compuestos **1**-**20**) para estudiar el papel que juega la forma y el tamaño del catión en la estructura y simetría de las correspondientes sales. Este estudio muestra que las sales con el catión $[PPh_3Et]^+$ y X = Cl o Br, cristalizan en el grupo espacial *R3*, que es polar y quiral (fase I). Con el catión $[PPh_3Pr]^+$ y X = Cl o Br, cristalizan en el grupo espacial *P2cb*, que es polar pero no quiral (fase II). Cuando las sales de anilato contienen el grupo X = NO_2 y el catión PBu_4^+, cristalizan en el grupo espacial triclínico *P*-1, que no es ni polar ni quiral (fase III). Esta evolución de quiral y polar (fase I), a no quiral y polar (fase II), y finalmente a centrosimétrico, sin polaridad ni quiralidad (fase III), es debida a la pérdida de interacciones $\pi-\pi$ cation-anion, seis en la fase I, cuatro en la fase II y finalmente cero en la fase III. Este rol clave que juega el catión en el número de interacciones $\pi-\pi$, no se observa cuando X = NO_2, donde la falta de planaridad evita cualquier interacción $\pi-\pi$.

En el **capítulo dos** presentamos la primera red 2D tipo panal de abeja heterometálica con M(III)M(I): $(NBu_3Me)_2[NaCr(C_6O_4Br_2)_3]$ (**21**) y además la primera red heterometálica con M(III)M(I) 3D-(10,3): $(NBu_3Me)_2[NaCr(C_6O_4Br_2)_3]$ (**22**). Estos dos compuestos constituyen el primer ejemplo de polimorfismo 2D/3D en la familia de los compuestos basados en el ligando anilato. Este polimorfismo no se ha observado nunca en la familia de los oxalatos.

En el **capítulo tres**, reportamos la síntesis y caracterización de cuatro compuestos 2D con redes tipo panal de abeja formadas por un metal trivalente (Cr^{III}) y uno divalente (Mn^{II}) con cationes oxonio (H_3O^+) y ordenamiento de largo alcance ferrimagnético o antiferromagnético formuladas como

$(H_3O)[MnCr(C_6O_4X_2)_3]\cdot 2PhZ\cdot 6H_2O$ con X/Z = Cl/Cl (**23**), Br/Cl (**24**), Br/Br (**25**), Br/CH_3 (**26**). También presentamos la primera red 2D ferrimagnética basada en el ligando anilato con el catión NBu_4^+ y con disposición alternada de las capas aniónicas tipo panal de abeja: $(NBu_4)[MnCr(C_6O_4Br_2)_3]\cdot PhBr\cdot 5H_2O$ (**27**). En la serie que contiene el catión H_3O^+, la inclusión de diferentes derivados bencénicos favorece la disposición eclipsadas de las capas, dando lugar a canales hexagonales que contienen las moléculas de disolvente, originando imanes porosos. Esta estrategia ha permitido la síntesis de capas eclipsadas incluso con el catión NBu_4^+ (compuesto **27**), mejorando los resultados publicados en 2013,[1] donde las capas 2D hexagonales con NBu_4^+ tenían una disposición alternada, evitándose así la formación de canales hexagonales. Los compuestos **23** y **27** presentan un ordenamiento ferrimagnético debido a un acoplamiento antiferromagnético de los iones Cr^{III} y Mn^{II} a través de ligando anilato. Por el contrario, los compuestos **24** – **26**, presentan un acoplamiento metamagnético debido al débil acoplamiento Cr^{III} – Mn^{II} antiferromagnético entre las capas que evita el ordenamiento ferrimagnético. Este acoplamiento antiferromagnético débil se puede cancelar con campos magnéticos por encima de aproximadamente 200 mT en las tres muestras, resultando en el comportamiento metamagnético observado. Este comportamiento puede ser atribuido a la ausencia de cationes voluminosos que separan las capas y a la presencia del ligando bromoanilato, que favorece el acoplamiento antiferromagnético entre capas.

En el **capítulo cuatro** presentamos la familia que combina el ligando asimétrico 2-cloro-5-ciano-3,6-dihidroxibenzoquinona e iones lantanoides con diferentes disolventes completando la espera de coordinación. Dos de estos compuestos, (**28** y **29**) contienen el ion praseodimio y son estructuras 2D con DMF y DMSO como disolventes. Sus respectivas formulas son $[Pr_2(C_6O_4(CN)Cl)_3(DMF)_6]$ y $[Pr_2(C_6O_4(CN)Cl)_3(DMSO)_6]$. Los compuestos **30** y **31** contienen el ion yterbio y son redes 2D y 3D respectivamente. El compuesto **30** contiene DMSO como disolvente y su fórmula es $[Yb_2(C_6O_4(CN)Cl)_3(DMSO)_4]\cdot 2H_2O$ mientras que el **31** contiene H_2O como disolvente. Su fórmula final es $[(H_3O)K][Yb_2(C_6O_4(CN)Cl)_3(\mu\text{-}OH)_2]$. Dado que el ligando 2-cloro-5-ciano-3,6-dihidroxibenzoquinona tiene propiedades

luminiscentes, se han medido las propiedades luminiscentes de estos compuestos para verificar el posible efecto antena de este ligando con los iones lantanoides.

En el **capítulo cinco** presentamos la combinación de compuestos basados en el ligando anilato con cationes que presenten una funcionalidad extra, como la transición de espín. Así, hemos preparado tres compuestos basados en el ligando anilato con el catión de transición de espín $[Fe(bpp)_2]^{2+}$ formulados como $[NBu_4][Fe(3\text{-}bpp)_2][Cr(C_6O_4X_2)_3].H_2O$ con X = Cl (**32**) y Br(**33**) y $[Fe(3\text{-}bpp)_2]_3[Cr(C_6O_4Cl_2)_3]_2\cdot 6H_2O$ **(34)**. Los compuestos **32** y **33** contienen una molécula de H_2O unida mediante enlace de hidrógeno al ligando bpp que juega un papel fundamental en las propiedades de transición de espín en los dos compuestos. En ambos, la eliminación de la molécula de agua incrementa la temperatura de transición de espín y da lugar a una pequeña histéresis de 6 K en la transición de espín del compuesto **33**. Además, en la fase deshidratada hay dos centros de Fe(II) independientes: uno que muestra una transición de espín abrupta y otro que permanece en alto espín a cualquier temperatura. Hemos demostrado que esta eliminación de agua es un proceso reversible y que las muestras rehidratadas recuperan dos moléculas de agua en vez de una, y aun así se comportan como las originales. La segunda molécula de agua está unida mediante un enlace de hidrógeno débil y puede entrar en la estructura debido a que hay un espacio vacío de 224 $Å^3$. El compuesto **34** es un ejemplo interesante ya que tiene el mismo catión de transición de espín $[Fe(3\text{-}bpp)_2]^{2+}$ que los compuestos **32** y **33**, y el mismo anión $[Cr(C_6O_4X_2)_3]^{3-}$, pero con una estequiometria diferente, sin catión NBu_4^+ y sin agua unida mediante enlaces de hidrógeno al ligando bpp del catión. Estos pequeños cambios provocan un cambio brusco en las propiedades magnéticas ya que el compuesto **34** no muestra ninguna transición de espín en contraste con los compuestos **32** y **33**. Este compuesto ilustra el rol clave que tienen las interacciones anión-catión y disolvente-catión en el fenómeno de transición de espín.

En el **capítulo seis** se presentan dos familias de compuestos basadas en el ligando anilato con el catión luminiscente $[Ir(ppy)_2(bpy)]^+$ (ppy = fenilpiridina y bpy = bipiridina). La primera serie contiene dos compuestos monoméricos:

$[Ir(ppy)_2(bpy)]_2[(H_3O)[Cr(C_6O_4X_2)_3]\cdot H_2O$ con X = Cl **(35)** y Br **(36)** donde los aniones paramagnéticos $[Cr(C_6O_4X_2)_3]^{3-}$ aislados coexisten con cationes aislados $[Ir(ppy)_2(bpy)]^+$. La segunda serie está compuesta por seis compuestos basados en el ligando anilato formando capas 2D que se pueden formular como $[Ir(bpy)(ppy)_2][MnCr(C_6O_4X_2)_3]\cdot 2PhZ\cdot 2CH_3CN\cdot H_2O$ con X/G = Cl/PhF (**37**), Cl/PhCl (**38**), Cl/PhBr (**39**), Br/PhF (**40**), Br/PhCl (**41**) y Br/PhBr (**41**), donde los cationes $[Ir(ppy)_2(bpy)]^+$ se sitúan entre las capas aniónicas. Los compuestos **35** y **36** son paramagnéticos y presentan la luminiscencia del catión $[Ir(ppy)_2(bpy)]^+$. La segunda sería presenta la ya conocida estructura tipo panal de abeja, pero con una secuencia sin precedentes en la que dos capas aniónicas alternada por cada capa catiónica formada por los cationes $[Ir(ppy)_2(bpy)]^+$. El acoplamiento ferrimagnético de los iones Cr^{III} and Mn^{II} a través del ligando anilato resulta en ordenamiento ferrimagnéticos de largo alcance a aproximadamente 10 K para X = Cl y de 11.5 K para X = Br. Estas diferencias en la temperatura de orden (T_c) se atribuyen al efecto inductivo de los átomos de halógenos sobre el anillo aromático del ligando anilato. Por el contrario, el cambio de la molécula de halobenceno localizado en las cavidades hexagonales apenas afecta a la densidad electrónica en el ligando anilato.

En el **capítulo siete** presentamos dos familias de compuestos basados en el ligando anilato con cationes de imán molecular (SMM) insertados entre las capas y formulados como $[Mn(salpn)(H_2O)][CrMn(C_6O_4X_2)_3]$ con X = Cl (**43**) y Br (**44**) and $[Mn(salen)(H_2O)][CrMn(C_6O_4X_2)_3]$ con X = Cl (**45**) y Br (**46**). Los compuestos **43** y **44** tienen una configuración eclipsada con canales hexagonales donde se localizan los cationes SMM. Estos cuatro compuestos presentan ordenamiento ferrimagnético con temperaturas de orden de entre 10 – 12 K. La falta de señal atribuible al catión de SMM sugieren que estos cationes no están aislados en las estructuras de estos compuestos y que presentan algunas interacciones con las capas ferrimagnéticas. La presencia de interacciones $\pi - \pi$ entre el anillo aromático del ligando anilato y del anillo aromático del ligando salpn del catión SMM en los compuestos **44** y **45** generan una posible vía para estas interacciones catión-anión.

En el **capítulo ocho**, se presenta un electrodo bifuncional que es capaz tanto de almacenar iones Na^+ y K^+ como de catalizar el proceso HER (hydrogen evolving reaction). Este compuesto es, por lo tanto, un compuesto bifuncional capaz de almacenar carga y de electrocatalizar el proceso HER.